

Andrew Lyne, Francis Graham-Smith
and Benjamin Stappers

Pulsar Astronomy

Fifth Edition

PULSAR ASTRONOMY

Fifth Edition

After more than half a century since their unexpected discovery and identification as neutron stars, the observation and understanding of pulsars touch upon many areas of astronomy and astrophysics. The literature on pulsars is vast, and the observational techniques used now cover the whole of the electromagnetic spectrum from radio to gamma-rays. Now in its fifth edition, this volume has been reorganised and features new material throughout. It provides an introduction in historical and physical terms to the many aspects of neutron stars, including condensed matter, physics of the magnetosphere, supernovae and the development of the pulsar population, propagation in the interstellar medium, binary stars, gravitation and general relativity. The current development of a new generation of powerful radio telescopes, designed with pulsar research in mind, makes this survey and guide essential reading for a growing body of students and astronomers.

ANDREW LYNE has been at the forefront of pulsar research for over 50 years. He has discovered over two-thirds of the known pulsars, has more than 800 publications to his name and has received several awards, including the Herschel Medal of the Royal Astronomical Society and the Descartes Prize of the European Union. He is a Fellow of the Royal Society and was Director of Jodrell Bank Observatory (1997–2007).

FRANCIS GRAHAM-SMITH was Astronomer Royal (1982–90), Physical Secretary of the Royal Society (1988–94), Director of the Royal Greenwich Observatory (1976–81) and Director of Jodrell Bank Observatory (1981–88). He is the senior author of textbooks on optics and radio astronomy. The fifth edition of *Pulsar Astronomy* is the product of over 50 years of close collaboration in research at Jodrell Bank Observatory.

BENJAMIN STAPPERS is a professor of astrophysics at the University of Manchester. He has been at the forefront of many aspects of pulsar astronomy, from how they emit through to their use as gravitational wave detectors. He has been involved with the development and commissioning of pulsar instrumentation for telescopes including LOFAR, WSRT, Lovell, MeerKAT and the SKA. He currently holds a European Research Council Advanced Grant for searching for pulsars and fast transients.

Cambridge Astrophysics Series

Series editors:

Andrew King, Douglas Lin, Stephen Maran, Jim Pringle, Martin Ward and Robert Kennicutt

Titles available in the series

30. Globular Cluster Systems
by Keith M. Ashman and Stephen E. Zepf
33. The Origin and Evolution of Planetary Nebulae
by Sun Kwok
34. Solar and Stellar Magnetic Activity
by Carolus J. Schrijver and Cornelis Zwaan
35. The Galaxies of the Local Group
by Sidney van den Bergh
36. Stellar Rotation
by Jean-Louis Tassoul
37. Extreme Ultraviolet Astronomy
by Martin A. Barstow and Jay B. Holberg
39. Compact Stellar X-ray Sources
edited by Walter H. G. Lewin and Michiel van der Klis
40. Evolutionary Processes in Binary and Multiple Stars
by Peter Eggleton
41. The Physics of the Cosmic Microwave Background
by Pavel D. Naselsky, Dmitry I. Novikov and Igor D. Novikov
42. Molecular Collisions in the Interstellar Medium, 2nd Edition
by David Flower
43. Classical Novae, 2nd Edition
edited by M. F. Bode and A. Evans
44. Ultraviolet and X-ray Spectroscopy of the Solar Atmosphere
by Kenneth J. H. Phillips, Uri Feldman and Enrico Landi
45. From Luminous Hot Stars to Starburst Galaxies
by Peter S. Conti, Paul A. Crowther and Claus Leitherer
46. Sunspots and Starspots
by John H. Thomas and Nigel O. Weiss
47. Accretion Processes in Star Formation, 2nd Edition
by Lee Hartmann
48. Pulsar Astronomy, 4th Edition
by Andrew Lyne and Francis Graham-Smith
49. Astrophysical Jets and Beams
by Michael D. Smith
50. Maser Sources in Astrophysics
by Malcolm Gray
51. Gamma-ray Bursts
edited by Chryssa Kouveliotou, Ralph A. M. J. Wijers and Stan Woosley
52. Physics and Chemistry of Circumstellar Dust Shells
by Hans-Peter Gail and Erwin Sedlmayr
53. Cosmic Magnetic Fields
by Philipp P. Kronberg
54. The Impact of Binary Stars on Stellar Evolution
by Giacomo Beccari and Henri M. J. Boffin
55. Star-Formation Rates of Galaxies
edited by Andreas Zezas and Véronique Buat
56. Astrophysical Magnetic Fields: From Galaxies to the Early Universe
by Anvar Shukurov and Kandaswamy Subramanian
57. Pulsar Astronomy, 5th Edition
by Andrew Lyne, Francis Graham-Smith and Benjamin Stappers

PULSAR ASTRONOMY

FIFTH EDITION

ANDREW LYNE

University of Manchester

FRANCIS GRAHAM-SMITH

University of Manchester

BENJAMIN STAPPERS

University of Manchester



CAMBRIDGE

UNIVERSITY PRESS

University Printing House, Cambridge CB2 8BS, United Kingdom

One Liberty Plaza, 20th Floor, New York, NY 10006, USA

477 Williamstown Road, Port Melbourne, VIC 3207, Australia

314–321, 3rd Floor, Plot 3, Splendor Forum, Jasola District Centre,
New Delhi – 110025, India

103 Penang Road, #05–06/07, Visioncrest Commercial, Singapore 238467

Cambridge University Press is part of the University of Cambridge.

It furthers the University's mission by disseminating knowledge in the pursuit of
education, learning, and research at the highest international levels of excellence.

www.cambridge.org

Information on this title: www.cambridge.org/9781108495226

DOI: [10.1017/9781108861656](https://doi.org/10.1017/9781108861656)

© Andrew Lyne, Francis Graham-Smith and Benjamin Stappers 2022

This publication is in copyright. Subject to statutory exception
and to the provisions of relevant collective licensing agreements,
no reproduction of any part may take place without the written
permission of Cambridge University Press.

First published 2022

A catalogue record for this publication is available from the British Library.

Library of Congress Cataloging-in-Publication Data

Names: Lyne, A. G., author. | Graham-Smith, Francis, 1923– author. |
Stappers, Benjamin, 1972– author.

Title: Pulsar astronomy / Andrew Lyne, University of Manchester,
Francis Graham-Smith, University of Manchester,
Benjamin Stappers, University of Manchester.

Description: 5th edition. | Cambridge, United Kingdom ; New York, NY, USA :
Cambridge University Press, 2022. | Includes bibliographical references and index.

Identifiers: LCCN 2021061946 (print) | LCCN 2021061947 (ebook) |
ISBN 9781108495226 (hardback) | ISBN 9781108861656 (epub)

Subjects: LCSH: Pulsars.

Classification: LCC QB843.P8 L86 2022 (print) | LCC QB843.P8 (ebook) |
DDC 523.8/874–dc23/eng20220314

LC record available at <https://lccn.loc.gov/2021061946>

LC ebook record available at <https://lccn.loc.gov/2021061947>

ISBN 978-1-108-49522-6 Hardback

Cambridge University Press has no responsibility for the persistence or accuracy of
URLs for external or third-party internet websites referred to in this publication
and does not guarantee that any content on such websites is, or will remain,
accurate or appropriate.

Contents

<i>Preface</i>	<i>page xi</i>
Part I Discoveries and Techniques	1
1 The Discoveries	3
1.1 Predictions	3
1.2 The Radio Discovery	4
1.3 The <i>Nature</i> Letter of February 1968	7
1.4 Oscillations, Orbits, Rotation	8
1.5 The Identification with Neutron Stars	12
1.6 High-Energy Photons	14
1.7 Millisecond Pulsars	16
1.8 Binary Pulsars	18
1.9 Clocks and Relativistic Physics	18
1.10 The Growth of Pulsar Astronomy	19
2 Telescope Techniques, Radio to TeV	24
2.1 Radio Telescopes and Arrays	25
2.2 Focussing X-ray Telescopes	27
2.3 Gamma-ray Telescopes	29
3 Receiver Techniques and Data Analysis	34
3.1 Frequency Dispersion of Pulsed Signals	34
3.2 De-dispersion	36
3.3 Interstellar Multipath Scattering	39
3.4 Searching for Single Pulses	39
3.5 Searching for Periodic Pulses	40
3.6 Searches for Pulsars	42
3.7 The Detection of Binary Pulsar Systems	43
3.8 Searches for Millisecond Pulsars	46

3.9	Searches of Supernova Remnants and Globular Clusters	47
3.10	Sensitivity: Selection Effects	48
3.11	Current and Future Surveys	51
3.12	Combatting Radio Interference	52
4	Surveys and Population	54
4.1	The Surveys	54
4.2	Analysis Methods	55
4.3	The Observed Distribution of Normal Pulsars	58
4.4	The Derived Luminosity and Spatial Distributions	60
4.5	Pulsar Velocities and Ages	64
4.6	The Population of Millisecond Pulsars	66
4.7	The Galactic Centre Region	67
4.8	The Pulsar Birthrate	68
4.9	Gamma-ray Pulsars	71
5	Pulsar Timing	73
5.1	Pulsar Positions and the Earth's Orbit	74
5.2	The Römer Correction to the Barycentre	77
5.3	The General Relativistic Corrections	78
5.4	Fundamental Positional Reference Frames	80
5.5	Periods and Period Changes	80
5.6	Proper Motion	82
5.7	Gravitational Acceleration	83
5.8	Pulsar Ages and the Braking Index	84
5.9	Pulsars as Standard Clocks	87
6	Timing and Astrometry of Binary Pulsars	90
6.1	Parameters of a Binary Orbit	91
6.2	Annual Orbital Parallax	93
6.3	Relativistic Effects in Binary Orbits	94
6.4	The Relativistic Evolution of a Binary Orbit	95
6.5	The Double Pulsar Binary J0737–3039A/B	99
6.6	Tests of Gravitational Theory	100
6.7	Gravitational Waves	102
6.8	The Detection of Planetary Pulsar Systems	103
7	The Distances of the Pulsars	105
7.1	Pulsar Distances from Parallax	106
7.2	Kinematic Distances	108
7.3	Pulsar Distances from Neutral Hydrogen Absorption	110
7.4	Pulsar Distances from Optical Identifications	113

7.5	Radio Interstellar Scattering	114
7.6	The H II Regions	115
7.7	The Model Electron Distribution	115
7.8	The Accuracy of the Electron Density Model	117
Part II Observed Physical Characteristics		119
8	Pulse Profiles	121
8.1	High-Energy Profiles	122
8.2	X-ray Pulse Profiles	123
8.3	Optical and UV Pulse Profiles	125
8.4	Polar Cap and Outer Gap	127
8.5	The Radio Profiles	128
8.6	Integrated Pulse Widths	128
8.7	Radio Frequency Dependence	131
8.8	Beam Components, Core and Cone	133
8.9	The Overall Beam Shape	135
8.10	Polarisation	135
8.11	Millisecond Pulsars	137
9	The Variability of Pulsar Emission	139
9.1	Subpulses	139
9.2	Single Pulse Intensities and Pulse Nulling	142
9.3	Mode Changing	145
9.4	Drifting and Modulation	147
9.5	Drift Rates	151
9.6	Drifting after Nulling	153
9.7	Isolated Pulses: RRATs and FRBs	155
9.8	The Polarisation of Sub-pulses	157
9.9	Microstructure	157
9.10	Giant Pulses	160
10	Millisecond Pulsars	162
10.1	The Discoveries	162
10.2	The Evolution of Binary Systems	164
10.3	Solitary Millisecond Pulsars and Widows	167
10.4	The Eclipsing Cloud in the Millisecond Binaries	169
10.5	The Globular Cluster Pulsars	173
10.6	The Magnetic Fields of the Millisecond Pulsars	176
10.7	The Velocities of Millisecond Pulsars	177
10.8	Pulse Profiles of Millisecond Pulsars	178
10.9	Gamma-ray MSPs	178

11	Magnetars	181
11.1	The Soft Gamma-ray Repeaters (SGRs)	181
11.2	The Anomalous X-ray Pulsars (AXPs)	184
11.3	Other Emission from Magnetars	185
11.4	Other Possible Magnetar Manifestations	187
11.5	Demography and Origin of the Magnetars	188
12	Thermal X-rays from Neutron Stars	192
12.1	Binary X-ray Light Curves	195
12.2	Orbits and Companion Masses	196
12.3	The High-Mass X-ray Binaries (HMXBs)	198
12.4	The Low-Mass X-ray Binaries (LMXBs)	199
12.5	Peculiar Systems, Black Holes and Transients	201
12.6	Spin-Up, Accretion and Inertia	201
12.7	Magnetic Field Strength	203
12.8	The X-ray Bursters	204
12.9	The Rapid Burster	206
12.10	Quasi-periodic (QPO) and Kilohertz Oscillations	206
12.11	Thermal X-rays from Isolated Neutron Stars	207
12.12	Ultra-luminous X-ray Sources	209
Part III	Neutron Star Physics	211
13	Neutron Stars	213
13.1	White Dwarf Stars	214
13.2	Neutron Stars: The Equation of State	215
13.3	The Crust and the Neutron Fluid	217
13.4	Moments of Inertia	219
13.5	Rotation Rate: An Upper Limit	219
13.6	The Magnetic Fields of Neutron Stars	220
13.7	The Magnetosphere	221
14	Radius and Mass	226
14.1	Radii of Neutron Stars: Luminosity and Redshift	226
14.2	Masses: The Dynamics of Binaries	229
14.3	Masses of Neutron Stars in X-ray Binaries	230
14.4	Masses of Binary MSPs	230
14.5	Double Neutron Star Binaries	230
14.6	White Dwarf Binaries	232
14.7	Black Widow and Redback Binaries	233
14.8	Neutron Stars in X-ray Binaries	233
14.9	Summary	234

15	Glitches, Timing Noise, Nudot Switching	235
15.1	Glitches	235
15.2	Occurrence Rate	237
15.3	Glitch Size	237
15.4	Intervals between Glitches	237
15.5	Slowdown Rate after a Glitch	240
15.6	The Exponential Recoveries	243
15.7	Catastrophe Theories	245
15.8	Two-Component Models: Crust and Superfluid	246
15.9	Vorticity in the Neutron Fluid	246
15.10	Pinning and Unpinning	248
15.11	Summary of Glitch Theory	249
15.12	Alternative Glitch Theories	250
15.13	Timing Noise	251
15.14	Slowdown Switching	254
15.15	Precession	256
16	Location and Geometry of Emitters	258
16.1	High-Energy Emission: The Outer Gap and Current Sheet	258
16.2	Normal Radio Emission: The Polar Cap	261
16.3	The Beam Geometry	263
16.4	Observed Profile Widths	265
16.5	Radio Frequency Dependence	266
16.6	Sub-pulse Drifting	267
16.7	Polarisation Geometry	267
16.8	Integrated Polarisation Profiles	272
16.9	Orthogonal Polarisation Modes	274
16.10	Position Angle Swing Rates	276
16.11	Emission Height	277
16.12	Young Pulsars and Millisecond Pulsars	277
17	The Emission Mechanisms	280
17.1	The Two Locations	280
17.2	Aberration, Retardation and Magnetic Field Sweep-Back	283
17.3	The Outer Emission Regions: Curvature and Synchrotron Radiation	285
17.4	Radio Spectra	289
17.5	Power and Energy Density in the Polar Cap Radio Emitter	290
17.6	Polar Cap Radio Emission	290
17.7	Radio Propagation in the Magnetosphere	292
17.8	Polarisation	293
17.9	The Radio Emission Mechanism	294

Part IV Environments and the Interstellar Medium	297
18 Supernovae and Their Remnants: Pulsar Wind Nebulae	299
18.1 The Nature of Supernovae	299
18.2 Stellar Evolution and Stellar Collapse	301
18.3 Accretion-Induced Supernova Collapse	303
18.4 Luminosity Decay of the Remnant	303
18.5 Frequency of Occurrence of Supernovae	304
18.6 Supernova Remnants	306
18.7 The Crab Nebula	308
18.8 Continuum Radiation from the Crab Nebula	311
18.9 The Energy Supply	312
18.10 Associations between Pulsars and Supernovae	313
18.11 Pulsar Wind Nebulae	315
19 Interstellar Scintillation and Scattering	322
19.1 A Thin-Screen Model	323
19.2 Diffraction Theory of Scintillation	325
19.3 Thick (extended) Scattering Screen	326
19.4 The Fresnel Distance	327
19.5 Strong and Weak Scintillation	327
19.6 Distribution in Size of the Irregularities	328
19.7 Dynamic Scintillation Spectra	329
19.8 Discrete Structures	333
19.9 The Velocity of the Scintillation Pattern	335
19.10 Pulse Lengthening	337
19.11 Multiple Scattering	341
19.12 Observations of Pulse Lengthening	342
19.13 Apparent Source Diameters	345
19.14 Long-Term Intensity Variations	346
20 The Interstellar Magnetic Field	349
20.1 Optical and Radio Observations	349
20.2 Faraday Rotation in Pulsars	352
20.3 The Configuration of the Local Field	353
20.4 The Effect of H II Regions and Other Structure	357
20.5 The Intergalactic Magnetic Field	357
21 Prospects	359
<i>References</i>	364
<i>Index</i>	403

Preface

The last half century has seen a flood of research papers on pulsar astronomy, which is becoming a torrent as a new generation of radio telescopes come into service, joined by telescopes covering the spectrum up to the highest energy cosmic rays. Recent discoveries have covered a wide range of physics, from extreme condensed matter and black holes to general relativity, and astrophysics, from stellar evolution and the structure of our Galaxy to the huge energy concentration revealed by the fast radio bursts. To cover this range in a single text is a daunting task, in which the two authors of previous editions are joined by Professor Ben Stappers, head of pulsar research at Jodrell Bank Observatory. We aim to restate the basic physical principles in the light of modern observational techniques and recent discoveries, providing an introduction for new recruits and a guide to recent advances for established researchers. For this we rely on published papers, and we give an extensive bibliography that may be used a starting point for a deeper study. We are grateful for help from many colleagues around the world for illustrative material and to Peter Wilkinson and other staff members of the Jodrell Bank Centre for Astrophysics for scrutinising the text. Our colleague Chris Jordan provided invaluable technical support.

Part I

Discoveries and Techniques

1

The Discoveries

1.1 Predictions

In 1934, two astronomers, Walter Baade and Fritz Zwicky, proposed the existence of a new form of star, the neutron star, which would be the end point of stellar evolution. They wrote:

with all reserve we advance the view that a supernova represents the transition of an ordinary star into a neutron star, consisting mainly of neutrons. Such a star may possess a very small radius and an extremely high density.

These prophetic remarks seemed at the time to be beyond any possibility of actual observation, since a neutron star would be small, cold and inert, and would emit very little light. More than 30 years later, the discovery of the pulsars, and the realisation a few months later that they were neutron stars, provided a totally unexpected verification of the proposal.

The physical conditions inside a neutron star are very different from laboratory experience. Densities up to 10^{14} g cm $^{-3}$, and magnetic fields up to 10^{15} G (10^{11} tesla), are found in a star of solar mass but only about 20 kilometres in diameter (see Chapter 14). Predictions of these astonishing conditions were made before the discovery of pulsars. Oppenheimer and Volkoff in 1939 used a simple equation of state to predict the total mass, the density and the diameter; Hoyle, Narlikar and Wheeler in 1964 argued that a magnetic field of 10^{10} G might exist on a neutron star at the centre of the Crab Nebula; Pacini in 1967, just before the pulsar discovery, proposed that the rapid rotation of a highly magnetised neutron star might be the source of energy in the Crab Nebula.

Radio astronomers did not, however, set out to investigate the possibility that such bizarre objects might have detectable radio emissions. No prediction had been made of the extremely powerful lighthouse beam of radio waves, producing radio pulses as the rotation of the neutron star sweeps the beam across the observer's

line of sight. The observation of an astonishing and remarkably regular series of pulses was made by radio astronomers who were unfamiliar with the new theoretical concepts and who naturally took some time to connect their observations with predictions concerning some apparently unobservable objects.

1.1.1 X-rays

Another remarkable prediction was that condensed stars, either white dwarfs or neutron stars, should be observable sources of x-rays. Independent predictions were made by Zel'dovich and Guseynov (1964) and by Hayakawa and Matsouka (1964), introducing the concept of binary star systems as x-ray sources. If in a binary star system one star is a condensed object and the other is a more massive normal star that is losing mass through a stellar wind, there might be a very large rate of accretion onto the condensed star, and a hot, dense atmosphere would then develop. This atmosphere would radiate thermal x-rays.

Thermal x-ray emission from the surfaces or atmospheres of neutron stars provides unique information on their diameters, as explained in Chapter 12. There is also pulsed thermal and non-thermal emission, related to the rotation of beamed optical and gamma-ray emission, observed from mostly young pulsars (Chapter 6).

1.2 The Radio Discovery

At the start of the story we may ask why it was that pulsars were not discovered earlier than 1967. Their signals are very distinctive and often quite strong, so that, for example, the 250-ft Lovell radio telescope at Jodrell Bank was eventually used to produce audible trains of pulses from several pulsars. The possibility of discovery had existed for 10 years before it became reality. In fact, it turned out that pulsar signals had been recorded but not recognised when the Lovell telescope was used for a survey of background radiation several years before the actual discovery. The pulsar now known as PSR B0329+54 left a clear imprint on several of the survey recordings. The initial difficulty in the recognition of the pulsar radio signals was that radio astronomers were not expecting to find rapid fluctuations in the signals from any celestial source. An impulsive radio signal received by a radio telescope was regarded as interference, generated in the multitude of terrestrial impulsive sources, such as electrical machinery, power line discharges and automobile ignition, or by atmospheric lightning. Indeed, most radio receivers were designed to reject or smooth out impulsive signals and to measure only steady signals, averaged over several seconds of integration time. Even if a shorter integrating time was in use, a series of impulses appearing on a chart recorder would excite no comment;

interference of such regular appearance is to be expected and is often encountered from a simple device such as an electric cattle fence on a farm within a mile or two of the radio telescope.

Two attributes were lacking in the apparatus used in these previous surveys: a short response time and a repetitive observing routine, which would show that the apparently sporadic signals were in fact from a permanent celestial source. These were both features of the survey of the sky for scintillating radio sources designed by Antony Hewish, in the course of which the first pulsar was discovered.

1.2.1 *Interplanetary Scintillation*

Radio scintillation is the fluctuation of radio waves as they traverse turbulent ionised media, particularly the terrestrial ionosphere, the solar system (the heliosphere) and the interstellar medium (see Chapter 19). Hewish was working with a research student, Jocelyn Bell (now Prof. Bell-Burnell) to investigate the effect of the ionised heliosphere on radio signals from quasars. They constructed a large receiving antenna for a comparatively long radio wavelength, 3.7 m, making a transit radio telescope that was sensitive to weak discrete radio sources. At this long wavelength, the inter-planetary scintillation effects are large, but they only occur for radio sources with a very small angular diameter. Scintillation is therefore seen as a distinguishing mark of the quasars, since the larger radio galaxies do not scintillate; Hewish later used the results of a survey with this system to study the distribution and population of these very distant extragalactic sources. The observational technique involved a repeated survey of the sky, using a receiver with an unusually short time constant of less than a second, which would follow the radio scintillation fluctuations. In that pre-digital age, the recordings were made on long paper charts, at the rate of many metres per day.

The discovery was made by Jocelyn Bell within a month of the start of regular recordings in July 1967. Large fluctuations of signal were seen at about the same time on successive days. The characteristics of the signal looked unlike scintillation and very like terrestrial interference (Figure 1.1a). Hewish at first dismissed the fluctuating signal as interference, such as might be picked up from a passing motor car, but Bell persisted in searching the long recordings for any repeat of the signal. For several nights no signals appeared; as we now know, this must have been due to the random occurrence of interstellar scintillation. Then they re-appeared and continued to re-appear spasmodically. Bell soon noticed that that the fluctuating signal was appearing four minutes earlier each day, as expected for a signal of celestial origin observed with a transit telescope, and, in October, Hewish was persuaded that something new had turned up. What sort of celestial source could this be? He and his colleagues then used a recorder with an even faster response time

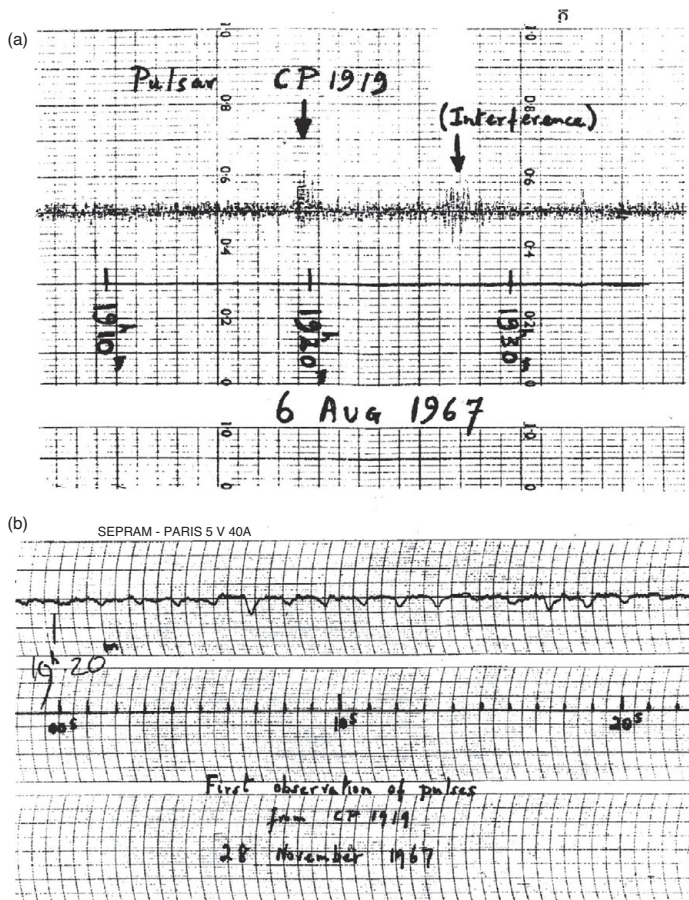


Figure 1.1 Discovery observations of the first pulsar. (a) The first recording of PSR B1919+21; the signal resembled the radio interference also seen on this chart; (b) Fast chart recording showing individual pulses as downward deflections of the trace (Hewish, private communication).

and, in November, they first saw the amazingly regular pulses having a repetition period of about 1.337 seconds. Could they be man-made? Possibly they originated on a space-craft? Possibly they were the first radio signals from an extraterrestrial civilisation?

The last possibility was disturbing. If it became known to the public that signals were being received that might have come from intelligent extraterrestrial sources – the ‘little green men’ of science fiction – the newspaper reporters would descend in strength on the observatory and destroy any chance of a peaceful solution to the problem. So there was intense activity but no communication for two months until, in February 1968, a classic paper appeared in *Nature* (Hewish *et al.* 1968).

1.3 The *Nature* Letter of February 1968

The announcement of the discovery contained a remarkable analysis of the pulsating signal, which already showed that the source must lie outside the Solar System and probably at a typical stellar distance; furthermore, the rapidity of the pulsation showed that the source must be very small and probably some form of condensed star, presumably either a white dwarf or a neutron star. The location outside the Solar System came from observations of the Doppler effect of the Earth's motion on the pulse periodicity; this phenomenon also led to a positional determination. (see Section 1.10.3). It is particularly interesting to see that the paper specifically mentions a neutron star as a possible origin, when at that time the existence of neutron stars was only hypothetical. Indeed, the flow of speculative theoretical papers that was let loose by the discovery did not even follow up this idea at first, exploring instead every possible configuration of the more familiar binary systems and white dwarf stars.

A few days before the *Nature* letter appeared, the discovery was discussed at a colloquium in Cambridge. The news spread rapidly, and radio astronomers immediately turned their attention to confirming the remarkable results. Only a fortnight separated the first paper and a *Nature* letter from Jodrell Bank Observatory (Davies *et al.* 1968) giving some remarkable extra details of the radio pulses from this first pulsar, now known as PSR B1919+21¹.

The locations and periodicities of three further pulsars were published in *Nature* in April (Pilkington *et al.* 1968). New discoveries of pulsars were made and announced by other observatories within a few months, and by the middle of the year, significant contributions were being made by at least eight radio observatories. In 2021 the catalogue of known pulsars contained nearly 3000 pulsars, sufficient for a statistical analysis of their distribution in period and across the sky, and their origins and lifetimes (Chapter 4).

The historian of science will enjoy the story of the theoretical papers that led to the identification of pulsars with neutron stars. It should be remembered that the very compact white dwarf stars were already observable and well understood, while the further stage of condensation represented by a neutron star existed in a theory familiar only to certain astrophysicists who were concerned with highly condensed states of matter. Suggestions based on the more familiar white dwarf stars, and particularly on their various possible modes of oscillation, poured out from the theorists.

¹ PSR stands for Pulsating Source of Radio. The numbers refer to its position, and the letter B refers to the B1950 system of coordinates. More recent pulsar discoveries are often referred to with a J prefix, which indicates the J2000 system of coordinates; in some cases both B and J names are used for the same source.

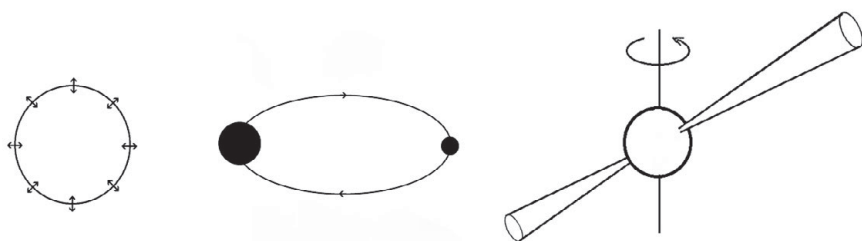


Figure 1.2 Early ideas put forward for the origin of the regular periodicity of pulsars: stellar oscillation, the orbital motion of condensed stars with gravitational focussing, or the rotation of a magnetised white dwarf or neutron star.

1.4 Oscillations, Orbits, Rotation

Although the identification of pulsars with rotating neutron stars is secure, it is of considerable interest to recall the two other possible explanations for the source of the periodicity of the pulses that were discussed during the first few months after the discovery (Figure 1.2). The very precise periodicity might be due to the oscillation of a condensed star or to a rapidly orbiting binary system. Both explanations were wide of the mark; nevertheless, the discovery of the pulsars did stimulate new work on oscillations, involving a re-examination of the equation of state of condensed matter, while the binary theory soon found application in the x-ray pulsars and, later, in the relativistic dynamics of the binary pulsar discovered in 1974.

1.4.1 Oscillations

In 1966, shortly before the discovery, Melzer and Thorne showed that a white dwarf star could have a resonant periodicity of about 10 s, for radial oscillation in the fundamental mode. No means of driving the oscillation was proposed. The period was determined by a combination of gravity and elasticity, but it was not far from the simple result of calculation using gravity alone. Dimensional arguments show that the period is independent of radius and proportional to $(G\rho)^{-\frac{1}{2}}$, where ρ is the density and G is the gravitational constant; for example, a white dwarf with density 10^7 g cm^{-3} would have a period of about 10 s if gravity alone provided the restoring force. Elasticity, which is in fact the dominant force in condensed stars, reduces the periodicity in white dwarfs to the order of 1 s. No shorter period seems to be possible for a fundamental mode, and higher order modes could not give such a simple pulse. The discovery of a pulsar with period 0.25 s among the first four therefore ruled out the oscillating white dwarf as a possible origin.

Melzer and Thorne had also calculated the period of oscillation of neutron stars. Here the fundamental modes of radial oscillation had periods in the range 1–10 ms, and no possibility seemed to exist for lengthening the periods by the necessary two orders of magnitude.

The oscillation theories were soon completely overtaken by the discoveries of two short-period pulsars, the Vela (89 ms) and Crab (33 ms) Pulsars, whose periods lay in the middle of the impossible gap between the theoretical oscillation periods of white dwarfs and neutron stars.

1.4.2 Planetary and Binary Orbits

Let us suppose that the pulsar period P is the orbital period of a planet, or satellite, in a circular orbit, radius R , around a much more massive condensed star with mass M (in units of the solar mass M_\odot). Then

$$R \approx 1500M^{1/3}P^{2/3} \text{ km.} \quad (1.1)$$

It is therefore just possible for a satellite to orbit a solar-mass white dwarf star of 1500 km radius with a period of 1 s, but the orbit would be grazing the surface. It would be more reasonable to consider a neutron star as the central object, when periods down to 1 ms would be possible. There are, however, two insuperable objections to the proposition that orbiting systems of this kind provide a model for pulsars.

The main difficulty concerns gravitational radiation, which is due to the varying quadrupole moment of any binary system. The energy loss through gravitational radiation would lead to a decrease in orbital period. A general formulation of the time scale τ of this change was given by Ostriker (1968) for a binary system with masses M and ϵM , with angular velocity $\Omega = 2\pi/P$:

$$\frac{1}{\tau} = \frac{1}{\Omega} \frac{d\Omega}{dt} = \frac{96}{5} \frac{\epsilon}{(1+\epsilon)^{1/3}} \frac{(GM)^{5/3}}{c^5} \Omega^{8/3}. \quad (1.2)$$

For a satellite in a 1 s orbit, with mass m , where $\epsilon = m/M$ is small, and $M = 1.0M_\odot$,

$$\tau = 2.7 \times 10^5 \epsilon^{-1} \text{ s.} \quad (1.3)$$

The time scale was evidently far too short unless the satellite mass was very small. Pacini and Salpeter (1968) soon established that early observations of the stability of the period showed that m must be less than $3 \times 10^{-8}M_\odot$.

Even the improbable hypothesis that such a small mass could be responsible for the radio pulses faced a second problem. The satellite would be orbiting in a very strong gravitational field, which would tend to disrupt it by tidal forces. Pacini and Salpeter showed that, even if it were made of high tensile steel, it could not withstand

these forces unless it was smaller than about 20 m in diameter. An added problem would be that the satellite would be liable to melt or evaporate in the very high radiation field of a pulsar.

The same situation evidently obtained *a fortiori* for a binary system, for which a very rapid change in period would be expected. Planetary and binary systems were therefore eliminated as possible origins for the clock mechanism of pulsars. Gravitational radiation itself does, however, recur in the pulsar story; PSR B1913+16 was eventually found, which is itself a member of a binary system with the short orbital period of $7\frac{3}{4}$ h, in which the orbital period decreases due to gravitational radiation at the rate of 30 ms per year (see Section 1.10.4).

1.4.3 Rotation and Slowdown

The maximum angular velocity Ω of a spinning star is determined by the centrifugal force on a mass at the equator. An estimate is easily obtained by assuming that the star is spherical with radius r ; the centrifugal force is then balanced by gravity when

$$\Omega^2 r = \frac{GM}{r^2}. \quad (1.4)$$

This is, of course, the same condition as for a satellite orbit grazing the surface. If the star has uniform density ρ , then the shortest possible rotational period P_{\min} is roughly

$$P_{\min} = (3\pi/G\rho)^{1/2}. \quad (1.5)$$

A period of 1 s therefore requires the density to be greater than 10^8 g cm $^{-3}$, which is just within the density range of white dwarf stars. Neutron stars, on the other hand, can rotate with a period as small as 1.5 ms, as demonstrated by the discovery of the first ‘millisecond’ pulsar PSR B1937+21.

The limit on rotational angular velocity is somewhat more severe than in this simple argument, because the star will distort into an oblate spheroid and tend to lose material in a disk-like extension of the equatorial region. The white dwarf theory was therefore already on the verge of impossibility for the first pulsars; the discovery of the short-period pulsars at once ruled it out completely.

The identification of pulsars with rotating neutron stars required the pulses to be interpreted as a ‘lighthouse’ effect, in which a beam of radiation is swept across the observer. This idea was supported by the observation by Radhakrishnan and Cooke (1969) that the plane of polarisation of radio waves from the Vela Pulsar swept rapidly in position angle during the pulse, in agreement with simple models of beamed emission. The radio source must then be localised, and directional, as well as powerful. This led Gold (1968) to his seminal note in *Nature*, in which he

suggested the identification with rotating neutron stars, the existence of a strong magnetic field, which drove a co-rotating magnetosphere, and the location of the radio source within the magnetosphere, probably close to the velocity-of-light cylinder. He also pointed out that rotational energy must be lost through magnetic dipole radiation, so that the rotation would be slowing down appreciably.

The early measurements of the period of the first pulsar PSR B1919+21 showed that no change was occurring larger than one part in 10^7 per year. This limit was very close to the actual changes that were measured a few years later, but the early null result could be used only to show that the stability of the period was in accord with the large angular momentum of a massive body in rapid rotation. Pacini (1968) showed that for a white dwarf, the limit on slowdown implied a magnetic field strength at the poles of less than 10^{12} G (10^8 tesla). He considered only magnetic dipole radiation in free space, which radiates away the rotational energy W at a rate

$$\frac{dW}{dt} = \frac{2\Omega^4}{3c^3} M_{\perp}^2 = \frac{\Omega^4}{3c^3} r^6 B_0^2 \sin^2 \alpha, \quad (1.6)$$

where $M_{\perp} \sim r^3 B_0 \sin \alpha$ is the component of the magnetic dipole moment orthogonal to the rotation axis, B_0 is the polar magnetic field at the stellar surface and α is the angle between the dipole axis and the rotation axis.

The slowdown of the Crab Pulsar was first measured by Richards and Comella (1969). From October 1968 to February 1969, the period lengthened uniformly by 36.48 ± 0.04 ns per day, i.e. by over 1 μ s per month. The rate of change was consistent with the known age of the Crab Nebula, confirming the association of the pulsar with the supernova explosion observed in AD 1054. Furthermore, the rate of change could be applied to the neutron star theory, giving an energy output from the spin-down alone that was sufficient for the excitation of the continuing synchrotron radiation from the Crab Nebula. This coincidence was the final proof of the identification, as pointed out in Gold's second *Nature* letter (1969).

The rate of rotational slowdown is now routinely measured for every newly discovered pulsar, and many continue to be monitored closely over many decades. For some young pulsars, the second differential is also obtainable, allowing investigation of the physics of the slow-down process (Chapter 5).

In retrospect, it is intriguing to consider what deduction might have been made from the measured variations of rotation period of the Vela Pulsar, if it had happened (as it nearly did) that those measurements had preceded those of the Crab Pulsar. The period of the Vela Pulsar was observed to be increasing slowly from November 1968 to February 1969, at the rate of 11 ns per day, but, at the end of February, a discontinuous decrease in period occurred, amounting to 200 ns. The change was known to have occurred in less than a week (Radhakrishnan & Manchester 1969; Reichley & Downs 1969). By the time that this anomalous step was announced, the

neutron star theory was already firmly established, and the decrease in period was regarded as an aberration rather than the typical behaviour. The step, or ‘glitch’, was at first interpreted on the basis of an abrupt change of moment of inertia, due to an overall shrinkage or a change of ellipticity in a ‘starquake’; it is now understood as the independent rotation of a superfluid within the neutron star (Chapter 15).

1.5 The Identification with Neutron Stars

Unknown to the theorists exploring the possibility that pulsars were white dwarf stars, and apparently also unnoticed by Hewish, Franco Pacini had already published a paper containing the solution to the nature of pulsars, again in *Nature* and only a few months before the discovery. This was the paper (Pacini 1967) in which he showed that a rapidly rotating neutron star, with a strong dipolar magnetic field, would act as a very energetic electric generator that could provide a source of energy for radiation from a surrounding nebula, such as the Crab Nebula. His work, and the original proposal by Baade and Zwicky, pointed the way to the subsequent discovery of the Crab Pulsar in the centre of the Nebula.

The two papers by Pacini and Gold set out very clearly the case for identifying the pulsars with rotating neutron stars. Between them, the two papers contained the basic theory and the vital connection with the observations. The remarkable part of the story is that the two men were working in offices practically next door to one another at the time of Gold’s paper, since Pacini was visiting Cornell University; nevertheless, Gold did not even know of Pacini’s earlier work, and there is no reference to it in his paper (Gold 1968). Collaboration was, of course, soon established, as may be seen in a paper from Pacini only a month later (Pacini 1968). These two should clearly share the credit for establishing the linkage between pulsars and neutron stars.

The confusion of theories persisted until the end of 1968, even though the correct theory had been clearly presented. Unfamiliarity with the concept of a neutron star seems to have been the main barrier to understanding, at least for the observers; it is interesting to see that both Hewish and Smith wrote forewords to a collection of *Nature* papers towards the end of 1968 in which they favoured explanations involving the more conventional white dwarf stars. The issue was settled dramatically by the discoveries of the two short-period pulsars: Vela, by Large, Vaughan and Mills (1968b), with a period of 89 ms, and the Crab, by Staelin and Reifenstein (1968), with a period of 33 ms (Comella *et al.* 1969). Only a neutron star could vibrate or rotate as fast as 30 times per second. Furthermore, as pointed out by Pacini and Gold, a rotation would slow down, but a vibration would not. Very soon a slowdown

was discovered in the period of the Crab Pulsar (Richards & Comella 1969), and the identification with a rotating neutron star was then certain. Furthermore, both the Crab and the Vela Pulsars are located within supernova remnants, providing a dramatic confirmation of the Baade–Zwicky prediction.

It happened almost 50 years after the discovery of pulsars that a white dwarf was found to be behaving almost exactly like a standard neutron star pulsar (Marsh *et al.* 2016). This was AR Sco, already well-known as a variable star in a binary system with an M star as companion. Pulses at a repetition period of 1.95 minutes were observed over the whole spectrum from radio to x-rays. This white dwarf pulsar is one of group of highly magnetised white dwarfs with magnetic dipole moments comparable to those of normal neutron star pulsars.

1.5.1 Physics of the Neutron Star

In Chapter 13 we review the physics of the neutron star itself. The general picture of a rapidly-rotating, highly-condensed and highly-magnetic star has been amply confirmed. Pulsar masses have been found to be mainly concentrated within the remarkably small range of $1.2\text{--}1.5M_{\odot}$; higher masses, up to $2M_{\odot}$, are found in some binary systems; these provide a useful constraint on the equation of state of the neutron fluid. The polar magnetic field is found to be of order $10^{12\text{--}15}$ G for normal pulsars and $10^{8\text{--}9}$ G for the millisecond pulsars (Chapter 10).

The neutron star was at first considered to comprise a simple neutron fluid with a density comparable to that of nuclear material, within a solid lower-density crystalline crust. The observation of glitches demonstrated that part of the fluid is a superfluid, which interpenetrates the crust and can rotate at a different speed; the interaction between these components is responsible for the step change in rotation rate.

The rapidly-rotating, highly-magnetised neutron star is surrounded by an energetic and electrically charged *magnetosphere* that co-rotates with the star and that extends out to a radial distance at which its linear velocity approaches the velocity of light. The magnetosphere, first analysed by Goldreich and Julian (1969) for a star in which the rotation and magnetic axes are aligned, has proved to be very complex, as may be seen from the 94 pages of ‘pulsar electrodynamics’ in Mestel’s classic work *Stellar Magnetism* (2003). It is often remarked that the origin of the radio, optical, x-ray and gamma-ray pulses through which we have gained so much astrophysical understanding itself remains a mystery; many pages of this book will be concerned with assembling the evidence that is slowly leading to an understanding of the source, or sources, of pulsar radiation.

1.6 High-Energy Photons

1.6.1 Optical Pulses from the Crab Pulsar

The possibility that pulsars might emit pulses of light as well as radio was tested on the first pulsar, PSR B1919+21, as early as May 1968. In the excitement, some over-optimistic positive results were reported at first from both Kitt Peak and Lick Observatories, but eventually every attempt was abandoned without any detection of optical pulsations or variation of any kind in several radio pulsars. Photometric equipment had, however, been assembled for searches for periodic fluctuations in white dwarf stars and, on 24 November 1968, a recording of the centre of the Crab Nebula was made by Willstrop (1969) in Cambridge without prior knowledge of the discovery of the radio pulsar a few days earlier in the USA. Although this recording was subsequently found to show the optical pulsations of the Crab Pulsar, it was stacked away with others for off-line computer analysis, and the discovery went instead to an enterprising team at the Steward Observatory in Arizona who were among three groups of observers fired with enthusiasm by the radio discovery of the Crab Pulsar.

The discovery of the optical pulses by Cocke, Disney and Taylor (1969) was published in a *Nature* letter; less usually, the actual event of the discovery was recorded on a tape recorder that was accidentally left running at the time. The excitement of the appearance of a pulse on a cathode ray tube, after a few minutes of integration, is well conveyed by the uninhibited (and unprintable) remarks of the observers. The discovery was made on 16 January 1969. Only three nights later, the light pulses were observed by two other groups, at McDonald Observatory and Kitt Peak Observatory. Shortly afterwards, a new television technique was applied to the 120-inch reflector at Lick Observatory, and a stroboscopic photograph of the pulsar was obtained. This showed two contrasting exposures, made at pulse maximum and minimum (Figure 1.3).

Subsequent observations have, of course, given very much more detail about the pulse timing, pulse shape, spectrum, and polarisation of these optical pulses; as might be expected, these are recorded in less dramatic form than the first paper by Cocke, Disney and Taylor, and their accidental historic tape recording.

1.6.2 X-ray Pulses from the Crab pulsar

The final link in the chain of discoveries about the Crab Pulsar was the extension of the spectrum into the x-ray and gamma-ray regions. The observations were necessarily made from above the Earth's atmosphere. In 1969 there was no x-ray telescope orbiting the Earth in a satellite, so that the only possibility lay in rocket flights. Astonishingly, two such rocket flights were successfully made, within a

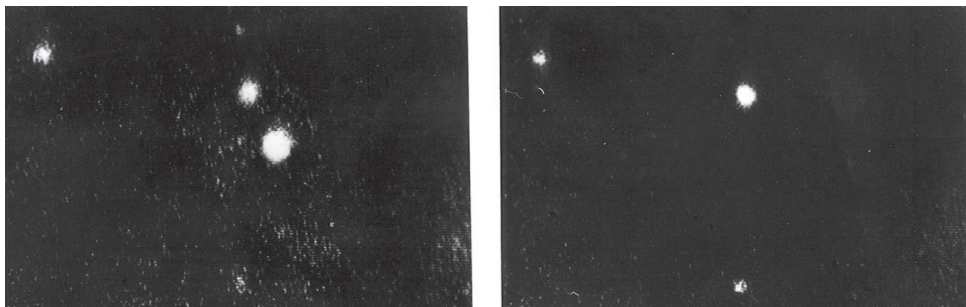


Figure 1.3 The Crab Pulsar. This pair of photographs was taken by a stroboscopic television technique, showing the pulsar on (left) and off (right) (Lick Observatory, reproduced by kind permission of the Royal Astronomical Society).

week of one another and only three months after the discovery of the optical pulses. The first was made by a team from the Naval Research Laboratory in Washington (Fritz *et al.* 1969) and the second from the Massachusetts Institute of Technology (Bradt *et al.* 1969). Both were completely successful, showing that the pulsed radiation extended to x-ray energies of several kilovolts; in fact, the total power radiated in the x-ray region was found to be at least 100 times that in visible light. The shape of the pulses was very nearly the same in x-rays as in light.

The Crab Nebula had been known and studied for several years as a source of x-rays. After the two rocket flights designed especially for the detection of periodic pulses had demonstrated the existence of the pulsar within the nebula, the recordings of an earlier rocket flight were re-examined; they showed that the pulses had been recorded but not recognised. This flight was in March 1968 (Boldt *et al.* 1969). Even this prediscovery recording turned out not to be the earliest, since a balloon-borne experiment in 1967 designed to measure the spectrum of the Crab Nebula up to x-ray energies of 20 keV was found to have recorded the periodic ‘light curve’ of the pulsar (Fishman, Harnden & Haymes 1969). There was sufficient accuracy in the periods obtainable from these two earlier experiments to show that the pulsar had been slowing down at the same average rate prior to the discovery as afterwards.

1.6.3 Gamma Rays

X-ray observations, and the gamma-ray observations that have now been made of many, mostly young, pulsars including the Crab and Vela Pulsars, involve detecting the arrival times of individual photons. A large optical telescope might record over 100 photons per pulse from the Crab Pulsar, but at the highest gamma-ray energies, a satellite-borne gamma-ray telescope might receive only one photon per hour. Nevertheless, precise timing over long observing sessions allows detection of

the periodicity and construction of the pulse profile. The techniques of gamma-ray telescopes, and the further extension of the spectrum to TeV energies by Cerenkov atmospheric shower detectors, are described in Chapter 2.

Both the Crab Pulsar and the Crab Nebula are observable almost continuously from radio frequencies at 30 MHz to gamma rays at above 100 GeV. Unpulsed radiation in the TeV region is observed from part of the Crab Nebula that is energised by a stream of particles emitted by the pulsar; this and other pulsar wind nebulae are described in Chapter 18.

The difficulty of relating the apparently random arrival of photons from a gamma-ray source to an underlying periodicity is illustrated by the source known as Geminga. This is one of the brightest gamma-ray sources in the sky, but without a radio detection, no periodicity could be found. Eventually the period of 237 ms was discovered in soft x-ray recordings, where the photon flux is very much greater, and a re-examination of the gamma-ray observations then showed the same periodicity (see Jackson *et al.* 2002 for an account of the x-ray and gamma-ray observations). Despite many attempts and some positive reports, no optical or radio pulses have yet been definitely observed from Geminga.

1.7 Millisecond Pulsars

For the first 15 years after the initial discoveries, the number of known pulsars grew to over 300. It seemed that the periods were distributed mainly from 100 ms to one second, and the rates of slowdown indicated that the pulsars with the shortest periods were the youngest. A monotonic slowdown through some millions of years would bring a pulsar towards its death when its period reached around one second. The search techniques seemed to be well matched to the population. This simple picture was disrupted by the discovery in 1982 of the pulsar B1937+21 by Backer and his collaborators (Backer *et al.* 1982): this pulsar has a period of only 1.56 ms, i.e. it is rotating 642 times per second. This was the first of the ‘millisecond’ pulsars, with periods mainly below 10 milliseconds and, significantly, with very low rates of slowdown. Search techniques that are sensitive to pulse periodicities as short as one millisecond have developed as computer speeds and data storage have improved (Chapter 3).

PSR B1937+21 was originally observed as a strong, highly-polarised radio source with a steep spectrum; the pulses were only discovered after an intensive analysis of recordings made with a very short integrating time constant. More general searches yielded only two more millisecond pulsars before the end of the decade, but new techniques involving rapid data sampling and Fourier analysis then began to yield many more. A further complication in this search was the discovery that a large proportion of the millisecond pulsars are in binary systems with short orbital periods, so that the observed pulsar period varies rapidly as the line-of-sight

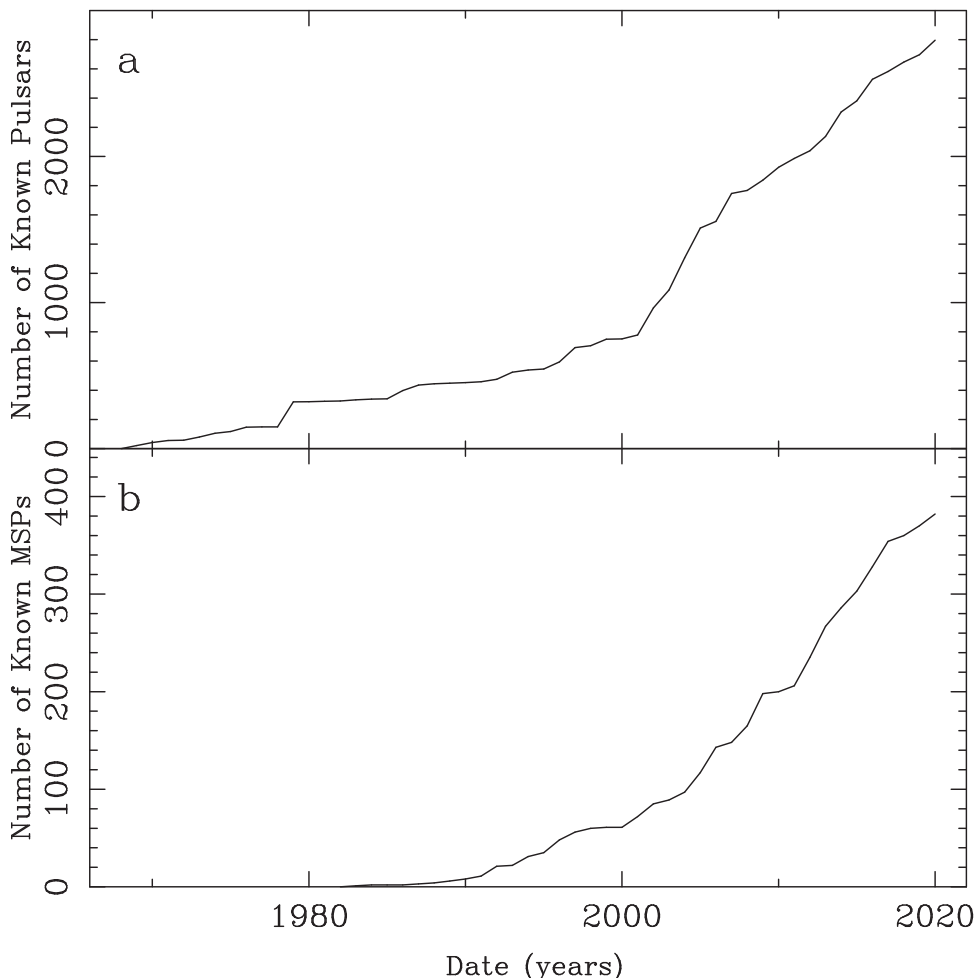


Figure 1.4 The time-line of the number of known pulsars: (a) all pulsars; (b) millisecond and other recycled pulsars with period < 30 ms.

velocity varies round the orbit. A major step forward was made by the gamma-ray observatory Fermi, carrying the Large Area Telescope (LAT), which confirmed and extended a list of discrete gamma-ray sources found by earlier satellite observatories; many of these were then found in radio observations to be millisecond pulsars. Furthermore, the gamma-ray observations could then be re-examined using the periodicities found by radio, and many of the discrete sources turned out to be pulsating at GeV energies with pulse shapes similar to the radio profiles (Chapter 8).

The improving success of search techniques, including the gamma-ray discoveries, is illustrated in Figure 1.4, which shows the time-line of the total number of known pulsars.

1.8 Binary Pulsars

The discovery of binary millisecond pulsars nicely substantiated a theory that linked the longer-period so-called normal pulsars, via the x-ray pulsars, to the whole class of millisecond pulsars. The x-ray pulsars were known to be binary systems, in which one component is a star with a large and expanding envelope spilling material onto a condensed star, heating part of the surface (or an accretion disk) to temperatures around 10^{6-7} K. The accretion process transfers angular momentum from the binary orbit to the condensed star, spinning it up to a periodicity approaching one millisecond.

The evolutionary scenario, which we develop in Chapter 10, starts with a binary pair of ordinary but massive stars. The more massive of the two evolves faster and eventually collapses and explodes as a supernova, leaving a normal pulsar at its core. The explosion may disrupt the binary, leaving the pulsar as one of the ‘normal’ population. But if there is no disruption, the second star eventually evolves, its atmosphere expands, accretion onto the first neutron star starts, and a rapidly rotating x-ray pulsar is born. Finally the second star completes its evolution and explodes, leaving a second neutron star, which may itself become a pulsar. The first star is now a millisecond pulsar in a double neutron star system, while the second rotates at the slower rate of a normal pulsar.

Complete confirmation of this theory came in 2003, with the discovery of a binary pulsar (PSR J0737–3039A/B) in which both components are pulsars, with periods of 23 milliseconds and 2.8 seconds, respectively (Lyne *et al.* 2004). Although both masses in several double neutron star systems had previously been determined, this was the first in which both rotation periods could also be found. The orbital period of this pair is only 2.4 h, which is among the shortest known of any double neutron star system.

1.9 Clocks and Relativistic Physics

A pulsar regarded as an isolated spinning inert massive star should be a precise clock. Pulsars almost follow this description, and the timing of their pulses has become a major part of observational pulsar astronomy. In Chapter 5 we describe the techniques that provide consistent monitoring of pulse arrival times, with an accuracy that in many cases reaches 100 nanoseconds. Rotation periods may be quoted to 14 places of decimals consistently over some years, leading to very accurate positions and precise orbital parameters of binary pulsars. The behaviour of close binary systems, involving strong gravitational fields, provides the most accurate tests of general relativity. The precise timing of pulsar rotation is the major basis of research in many observatories around the world.

1.10 The Growth of Pulsar Astronomy

The half century following the discovery of pulsars saw a spectacular expansion into many branches of astrophysics, as will be evident throughout this book. Here we give a brief outline of the main topics, with a guide to the chapters in which we deal with each subject.

1.10.1 Search and Discovery

The advent and growth of massive computer power has enabled the development of three vital aspects of radio search techniques: broad bandwidth, pattern recognition, and telescope multi-beaming. These are essential elements of the Square Kilometre Array (SKA), but they are already yielding new discoveries of pulsars at low levels of flux density and covering large solid angles of the sky. Chapter 2 describes the very different techniques in x-ray, gamma-ray and TeV (Cerenkov) photon detection. Chapter 3 describes the new receiver systems and massive data analysis that have become possible through digital technology.

1.10.2 The Source of the Radiation

Extensive descriptions and analyses of the complex characteristics of the radio pulses, and of the somewhat simpler high energy pulses, have been made, with the intention of unravelling the physical processes of particle acceleration and beamed radiation. We describe the individual radio pulses, and the profiles obtained by integration over some hundreds of pulses, in Chapter 8. The very high brightness of the radio emission is only explicable as coherent emission from an assembly of many charged particles in a small space, possibly with dimensions of only a few metres. In contrast, the high energy emission (x-ray and gamma-ray) is accounted for as the incoherent sum of radiation from high energy particles in a different, more extended region (Chapters 16 and 17).

These emitting regions are located in an extended atmosphere, the magnetosphere, driven by the magnetic field of the neutron star to co-rotate with the neutron star. The configuration of the magnetosphere is understood in broad outline, although the details are only accessible through a complex computation (Chapters 13 and 16).

1.10.3 Positions: The Earth's Orbital Motion

Remarkably accurate positions are available for most pulsars, from their unique quality of emitting a precise timing signal. The orbital motion of the Earth causes a

roughly sinusoidal annual modulation of pulse arrival times, with amplitude reaching eight minutes for a pulsar near the Ecliptic plane. The amplitude and phase of this variation provides a measurement of pulsar position, as described in Section 5.1. Several astrometric results have followed from pulsar timing: proper motion is often measurable, giving transverse velocities; small effects on the Earth's orbit due to the planets and even to an asteroid can be measured; the combination of positions derived from timing with positions measured by long baseline interferometry has provided an accurate link between the two fundamental celestial coordinate systems.

Interpretation of these results requires a detailed geometrical analysis, allowing for the rotation of the Earth and its orbital motion. This is achieved in a complex analysis program which is used in common by observatories worldwide.

1.10.4 Relativistic Effects

Pulsars act as ideal clocks, providing unique tests of relativistic theory. Most notably, there are substantial relativistic effects in the tightly bound binary orbits of millisecond pulsars, including the loss of orbital momentum through gravitational radiation; the classic example is PSR B1913+16, which has a highly elliptical orbit with a period of $7\frac{3}{4}$ h (Weisberg & Taylor 1984; see Chapter 5). The loss of orbital energy, which is observed as a decrease in orbital period, gives a remarkably accurate value for the total mass of the system.

A further observable relativistic effect in binary systems is the delay in pulse travel time, known as the Shapiro delay, that occurs in the gravitational field of the pulsar's companion. The delay depends on the mass of the companion; provided the geometry of the orbit can be found from pulse timing through the orbit, both the companion mass and that of the pulsar itself can be found.

Relativistic effects measurable in the orbit of a binary pulsar system often provide more than one independent measurement of the component masses, and the agreement of the results is in effect a rigorous test of relativistic theory. No departure from standard general relativity has yet been found.

Gravitational waves originating in the early Universe are expected to be measurable as a small effect on large scale distances within the Galaxy. The consequent effect on pulse arrival times is expected to be correlated over a group of pulsars. Observations of this effect are very demanding, requiring timing accuracies measured in nanoseconds and extending over several years. Several international timing networks are engaged in the search for this effect.

1.10.5 The Interstellar Medium

Interstellar scintillation, discovered in the first observations of pulsars, was later joined by three other phenomena that have revolutionised our understanding of the

ionised interstellar plasma. These are pulse lengthening, dispersive pulse delay, and Faraday rotation, all of which can be observed on the lines of sight to all radio pulsars. Dispersive delay is valuable in determining pulsar distances; if a model is available for the distribution of electron density along the line of sight to a pulsar, then the delay, measured by comparing pulse arrival times at different radio frequencies, gives a direct measurement of distance, since there is a linear relation between the integrated electron content along the line of sight and the so-called dispersion measure (DM). On the other hand, the distance of the pulsar may be known by other means, in which case the DM values of a set of pulsars may be used as a means of determining the electron density distribution in the Galaxy. In Chapter 19 we outline the theory of scintillation due to diffraction and refraction in the ionised interstellar medium (ISM) and describe observations of the dynamics, scale and dependence on radio frequency of scintillation.

Faraday rotation is also a dispersive phenomenon. Pulsar radio signals are often highly linearly polarised, and Faraday rotation is observed as a frequency dependence of the plane of polarisation. The rotation is related to the product of the line of sight component of the interstellar magnetic field and the electron density, so that the combination of measurements of Faraday rotation and dispersion measure give a direct measurement of the magnetic field (Chapter 20).

There are, of course, complications. The distribution of electrons in the interstellar medium is far from uniform, and interpretation of dispersion measures and Faraday rotations has proved to be complicated and challenging. Nevertheless it can be regarded as a happy chance that the scintillation phenomenon that led to the original pulsar discovery has proved to be our most valuable tool in investigating the interstellar plasma.

1.10.6 The Population of Pulsars

Understanding the relationship between pulsars and the other stellar populations of the Galaxy requires surveys with known and consistent sensitivity limits covering most of the sky. Determining distance has proved difficult, and limited sensitivity has largely confined population studies to distances less than the distance of the centre of the Galaxy. The distance of some pulsars within about 1 kpc² of the Sun can be measured by conventional astrometry, extended in the radio regime by very long baseling interferometry (VLBI). Larger distances can be estimated by observing the dispersive propagation delay of radio pulses in the ionised interstellar medium and using a model of the distribution of electron density.

Although the pulsar surveys are necessarily limited by sensitivity and various selection effects, a useful model of the distribution of pulsars within the Galaxy has

² 1 kiloparsec (kpc) = 3.08×10^{19} m. At this distance, a star has a parallax of 1 milliarcsecond.

been constructed. There is a total population of between 10^5 and 10^6 active pulsars in the Galaxy. Most of them are concentrated in the plane of the Galaxy within a layer about 1 kiloparsec thick and within a radial distance of about 10 kiloparsecs from the centre. Measurements of their motion show that they have high velocities, presumably originating in their violent births, and are mostly moving away from the plane at a rate of order $200\text{--}300 \text{ km s}^{-1}$, so that the distribution is consistent with an origin within 100 parsecs of the galactic plane; this is to be expected if they represent the end product of the evolution of massive stars.

The millisecond pulsars (Chapter 10) represent a smaller population of older pulsars. Re-cycling by spin-up in binaries occurs much less frequently than the birth of normal pulsars, and re-cycled pulsars are only observable as a considerable population because of their long life. They are found throughout the Galaxy but much less concentrated towards the plane than are the younger pulsars. Many millisecond pulsars are also found in globular clusters, where the spin-up process is also seen at work in a concentration of x-ray binaries.

The first pulsar to be found in a globular cluster was PSR B1821–24 (period 3 milliseconds), in the cluster M28 (Lyne *et al.* 1987). Several other globular clusters were later found to be rich fields of millisecond pulsars (Chapter 8). Using the 20 pulsars then known in the globular cluster 47 Tucanae, Freire *et al.* (2001c) analysed their dynamics and their dispersion measures to delineate the distribution of masses and ionised gas within the cluster (Freire *et al.* 2001a).

Many observers have speculated on the possibility of observing a pulsar in a distant galaxy such as the Andromeda Nebula M31, which presumably has a similar population to our Galaxy; this may prove to be within reach of the largest radio telescopes, such as FAST. Such an observation would provide a measurement of the electron density in inter-galactic space. There are already several pulsars known in the Magellanic Clouds; the first of these, PSR B0540–69, was found as an x-ray pulsar and is now observed over a wide spectral range (de Plaa *et al.* 2003).

1.10.7 Fast Radio Bursts

The detection of weak radio signals from pulsars requires integration, which tends to smooth out and lose any short impulsive signals. The advent of fast sampling and digital recording preserved impulsive signals, although even then these were often rejected as man-made interference. In 2007, Duncan Lorimer was reanalysing recordings from a Parkes pulsar survey, and found an intensive isolated burst that showed the frequency dispersion characteristic of interstellar propagation (Lorimer *et al.* 2007).

A few hundred such fast radio bursts (FRBs) have been observed, most of which have large dispersion measures, indicating a location at cosmological distances.

The nature of their source is unknown, although a magnetar (Chapter 11) located in our Galaxy has been observed as a repeating source of FRBs. The energy in an FRB, which is usually only a few milliseconds long, is phenomenal; a single burst from a distant galaxy, if radiated isotropically, represents an energy output of 10^{43-45} ergs, comparable to the total energy released by the Sun in 1000 years.

The relation between pulsars and FRBs is as yet unproven, although the link with a magnetar is tantalising. There are properties of the radio emission in young pulsars that are reminiscent of the rotating radio transients (RRATs) and radio emission from magnetars, but there are important differences too. We will consider the growing field of variability in pulsars in Chapter 9, including the relation to FRBs and gamma-ray bursts.

2

Telescope Techniques, Radio to TeV

Observations of neutron stars and pulsars extend over 20 decades of the electromagnetic spectrum, from low radio frequencies (around 30 MHz) to TeV gamma-ray energies. The techniques used in telescopes between these extremes range from the coherent detection of radio waves in large arrays of receptors to photon detection techniques more usually associated with nuclear physics. There are, nevertheless, elements in common over the whole range: the need for sensitivity and for accurate positions. We will refer to these essentials in this and the following chapter on receiver techniques. These requirements are familiar in optical astronomy, where studies of individual faint objects may require the new 40 m class of telescopes, while surveys covering large areas of sky necessarily must use smaller telescopes. For radio, x-ray and gamma-ray astronomy, the essential technology is less familiar and will be the subject of this chapter. Massive advances in computer power have made possible most of modern pulsar observations; radio in particular now depends on digitisation, multichannel receivers and telescope arrays, which we describe in the next chapter. Techniques for pulsar searches, and for pulse timing and the astrometry that follows, have much in common at all wavelengths. We describe the available surveys and their catalogues in Chapter 4 and timing techniques in Chapter 5.

The terrestrial atmosphere is transparent to radio waves (except at short millimetric wavelengths where molecular absorption occurs and at long metric wavelengths where ionospheric refraction and reflection occur). Radio telescope arrays can therefore operate at ground level and can extend in size almost indefinitely, giving both high sensitivity and high angular resolution, with multiple beams. X-rays and gamma rays are absorbed in the atmosphere, and direct detection of such high energy photons can only be achieved using space-based telescopes, where telescope apertures are limited by the capabilities of launch vehicles to a few metres in diameter. Over most of this range, radiation is detected as individual photons, whose direction and time of arrival must be individually recorded. Pulse

repetition rates and shapes are only obtained after integration over observations that may extend over long times, which for gamma-rays may even be several years.

At the highest gamma-ray energies, however, individual photons can be detected at ground level through their creation of showers of energetic particles in the atmosphere; this is the basis of the Cerenkov air-shower arrays, which extend observations of pulsars and their wind nebulae up to 300 GeV and beyond.

2.1 Radio Telescopes and Arrays

Radio observations, which provide most of our knowledge and understanding of pulsars, require large radio telescopes to detect the signals from all but the strongest pulsars. The 1967 discovery by Antony Hewish and Jocelyn Bell was made using a dipole array at 3.7 m wavelength. Although this array covered the large area of 16,000 m², it was only able to detect single pulses from some of the brightest pulsars. Observations of single pulses are still important, but greater sensitivity is now achieved by integrating pulses over long times, requiring a telescope beam to track sidereal motion by steering, either physically or electronically in a phased array (which has the advantage of allowing the simultaneous use of multiple beams). Observations require the recording of the whole broadband signal in a telescope beam tracking a single area of sky and subsequently analysing the recorded data for periodic pulsar signals; the analysis techniques are described in Chapter 3. The largest reflector telescopes, namely Arecibo,¹ Effelsberg, Green Bank, the Lovell Telescope and Parkes, have been used in this way; most of the known 2500 pulsars have been found and studied by these telescopes. FAST,² the recently commissioned 500 meter-diameter telescope, is extending the possibilities of this technique.

Larger collecting areas, allowing greater sensitivity, are achieved by the coherent addition of signals from an array of individual radio telescopes.³ This has been achieved with the GMRT,⁴ an array of 30 dishes each of 45 m in diameter with a longest baseline of 25 km. It operates (in its upgraded format) from around 150 MHz up to 1.4 GHz. Several such arrays are in operation, covering the available wavelength range from several metres (LOFAR⁵ and MWA⁶) to shorter than 1 millimetre (ALMA⁷). The SKA⁸ will surpass all these arrays in collecting area. A large international effort is being devoted to the SKA, which will eventually provide

¹ The Arecibo radio telescope sadly collapsed in December 2020.

² Five hundred metre Aperture Spherical Telescope.

³ See An Introduction to Radio Astronomy, 4th ed. Burke, Graham-Smith and Wilkinson. CUP. 2019.

⁴ Great Metrewave Radio Telescope.

⁵ Low Frequency Array for Radioastronomy.

⁶ Murchison Widefield Array.

⁷ Atacama Large Millimetre Array.

⁸ Square Kilometre Array.

a collecting area 100 times larger than the present steerable reflector telescopes. Since the beamwidth θ of an individual antenna with diameter d is approximately λ/d radians, the comparatively small individual array elements have a wide primary beam, allowing multiple beams to be synthesised in the array, restricted only by the available computer power. The MeerKAT in South Africa, comprising 64 reflector telescopes, is a fore-runner of SKA and is already demonstrating its potential for discovering pulsars.

The large collecting areas necessary in searching for new pulsars imply narrow telescope beamwidths; for example, the Parkes 64 m radio telescope has a beamwidth of 14 arcminutes at the wavelength of 21 cm, at which its major surveys have been conducted. Surveying the whole of the sky that this telescope can reach requires at least 200,000 pointings, each typically lasting half an hour, which would take over 10 years to complete. The solution is to equip such reflector telescopes with multiple-feed systems, producing a cluster of adjacent beams. The Parkes telescope used a cluster of 13 individual feeds; a similar seven-beam receiver was used for the PALFA survey at the Arecibo telescope. In the near future, the approach will be to use a *phased array* at the focus, comprising a larger number of adjacent receiver elements whose signals can be combined electronically to produce multiple independent beams. The extent of sky coverage possible in these multiple-beam systems is limited by the aberrations inherent in the formation of off-axis beams.

The individual elements of large arrays are usually smaller than the single-aperture telescopes, allowing multi-beaming techniques to extend to wider fields of view. At the longer wavelengths, in telescopes such as LOFAR, the phasing of the array elements also allows the formation of multiple primary beams. The phased array feeds on the ASKAP telescope, also an SKA precursor, has been vital for FRB studies.

Radio frequencies of 1 GHz and above are used in the most sensitive searches for weak and distant pulsars, since at lower frequencies the pulses may be obscured or lost through scattering and dispersion in the interstellar medium; at the same time, the radio spectra of most pulsars fall rapidly with increasing frequency, so that observations become difficult above around 3 GHz. Most searches use frequencies around the reserved H I and OH bands at 1420 and 1667 MHz, often using a wider frequency band when interfering radio signals allow.

Observations at lower radio frequencies are usually directed at extending the spectral information on known pulsars and investigating scattering in the interstellar medium. New opportunities are provided by the low-frequency arrays LOFAR and MWA; the high angular resolution for which these arrays are designed is not needed for pulsars, but the antenna elements can be used in phase to give a large effective area. The large beams of these low-frequency instruments also means that they are efficient at surveying the sky.

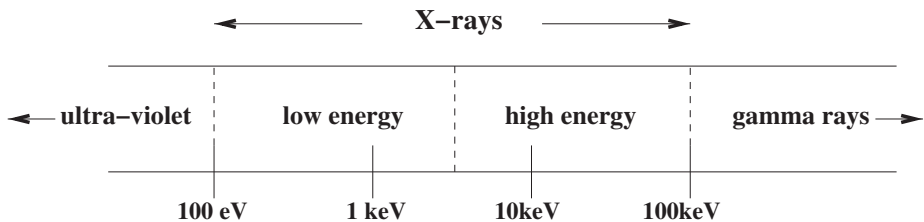


Figure 2.1 X-ray energies and wavelengths.

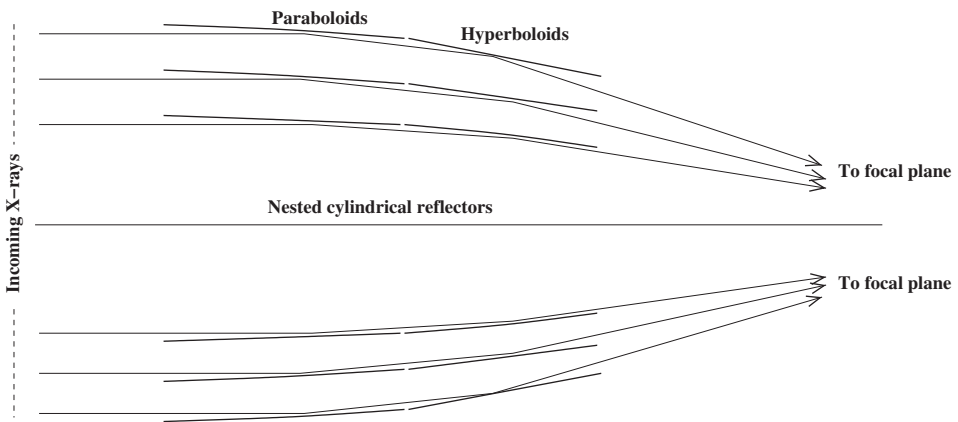


Figure 2.2 The Wolter x-ray telescope. The grazing incidence cylindrical reflecting elements are sections of paraboloids followed by sections of hyperboloids.

2.2 Focussing X-ray Telescopes

Early exploratory x-ray observations were made with sounding rockets designed to detect solar x-rays, with minimal angular resolution and short observations. The discovery of bright x-ray sources in the Galaxy prompted the design and construction of space-based telescopes with large collecting areas and with angular resolutions approaching that of most optical ground-based telescopes.

Two decades of the x-ray spectrum (Figure 2.1), from about 0.1 keV to 10 keV (or in terms of wavelength, from 12 nm to 0.12 nm), are accessible to imaging x-ray telescopes orbiting above the Earth's atmosphere. In this energy region, it is possible to focus x-rays by reflection at grazing incidence on highly polished metal surfaces. The basic geometric arrangement of a Wolter x-ray telescope is shown in Figure 2.2. The cylindrical mirror has two successive grazing-incidence reflecting surfaces, which are sections of a paraboloid and a hyperboloid; this brings rays to a focus at a distance from these components of several times their diameter, while

Table 2.1. *X-ray telescopes*

Dates	Telescope	Energy (keV)	Detector	Main Achievements
1970–3	UHURU	2–20	Proportional counters	4U catalogue
1978–81	Einstein	0.2–20	Wolter telescope	1st x-ray source catalogue
1990–99	ROSAT	0.1–2	Wolter telescope	1RXS catalogue
1995–2012	Rossi RXTE	0.1–2	NaI/CsI scintillators	8 μ s timing, 1 deg fov
1999–	Chandra	0.1–10	Wolter telescope, CCDs	16 μ s timing, 0.5'' resoln.
1999–	XMM Newton	0.2–12	Wolter telescope, CCDs	XMMS catalogue
2002–	INTEGRAL	15–10,000	Mask + CsI tiles	GRB location
2004–	Swift	15–250	Mask + CdZnTe tiles	GRB location
2012–	Nustar	3–79	Wolter, 133 shells	Timing, spectrum
2015–	ASTROSAT	0.3–8	41 shells	Timing, spectrum
2017–	HXMT	1–250	Slat collimators, 3 bands	Survey, imaging, timing
2017–	NICER	0.2–12	Multiple shells	Timing, spectrum
2019–	e-ROSITA	0.2–10	7 Wolter, 54 shells	Timing, spectrum
2019–	ART-XC	0.3–10	7 Wolter, 28 shells	Timing, spectrum

the use of the two profiles gives a larger field of view than a simple paraboloid. A set of mirrors may be nested inside one another to increase the effective area of the telescope.

The first imaging x-ray telescope was HEAO-2 (Einstein), launched in 1978. At present (2021), x-ray astronomy relies mainly on two orbiting imaging telescopes, both launched in 1999. The mirror system in Chandra has four nested elements, giving images with angular resolution of 0.5 arcseconds. The effective collecting area is 400 cm^2 . XMM-Newton has three telescopes, each with no fewer than 58 nested mirrors only 0.5 to 1 mm thick, giving a larger effective aperture (4000 cm^2) than Chandra, but with less angular resolution. Both have provision for spectroscopy: transmission gratings can be switched into the beam of Chandra, while reflection gratings are placed in two of the XMM-Newton telescope beams. Both telescopes are in highly elliptical Earth orbits, allowing long periods of integration away from perigee, avoiding contaminating signals from the radiation belts close to Earth.

Table 2.1 lists the x-ray telescopes that are of particular interest in pulsar astronomy. A succession of earlier x-ray satellite telescopes in the 1970s and 1980s contributed many fundamental discoveries, some of which are referred to in Chapter 12 of this book. ROSAT, operating from 1990 to 1999, imaged a large number of point sources and provided accurate timing for pulsars. Similarly Rossi

RXTE (1995–2012) provided timing observations that also contributed to the x-ray astronomy we discuss in Chapter 12.

Grazing incidence reflectors necessarily have a large focal ratio. Single or nested mirrors require a large focal length: both XMM-Newton and Chandra are mounted in spacecraft over 10 m long: Nustar was launched in a more compact form and when in orbit extended a 10 m mast to carry the detector array. Nustar has a Wolter reflector with 133 concentric shells, with multilayer coatings that extend the energy range to 79 keV.

A new technique – silicon pore optics – is under development for x-ray telescopes. This uses a close-packed array of small Wolter elements each only a millimetre across, built into a silicon disk by fusing together a stack of corrugated sheets. Using this technique, the ESA telescope ATHENA is planned to have a large collecting area of 1.4 m^2 while avoiding the difficulty of fabricating the large reflecting surfaces of the present generation of x-ray telescopes.

2.3 Gamma-ray Telescopes

2.3.1 *Gamma-ray Space-Based Telescopes*

Gamma-ray telescopes are mainly sensitive above 1 MeV, exploring a sky in which young pulsars outshine all other sources. The first high-energy maps were made by SAS-2 (Fichtel *et al.* 1975) and COS-B (Mayer-Hasselwander *et al.* 1982), detecting the Crab and Vela Pulsars and the Geminga source (in which the pulsations were not yet resolved). The Compton Gamma-Ray Observatory (CGRO) added at least four more pulsars among a total of around 200 detected discrete sources.

Gamma-ray photons can only be observed directly from above the terrestrial atmosphere. Only small apertures, at present less than one square metre, are available in space-based telescopes, and the photon flux received from individual sources is usually much less than one per minute. Furthermore, gamma-ray photons must be distinguished from a much greater flux of cosmic-ray particles. Nevertheless a series of telescopes (SAS-2, COS-B, Hakucho, GINGA), using spark chamber detectors, showed that gamma ray sources exist at energies of at least 1 GeV, leading to the development of telescopes with sensitivity to gamma rays with energies up to 300 GeV, angular resolution better than one degree, good energy discrimination and effective rejection of cosmic ray particle events. Gamma rays cannot be focussed by refraction or reflection, so detection of the direction of arrival is achieved by tracking individual photons. In the INTEGRAL spacecraft, a telescope operating up to 10 MeV uses a coded array of 95×95 tungsten tiles at the telescope aperture, casting a shadowgram on an array detector 3.2 m below, giving a resolution of 2 deg over a field of 16 deg (other instruments on the INTEGRAL spacecraft cover a

Table 2.2. *Gamma-ray space-based telescopes*

Operation Dates	Telescope	Energy range	Detector
1972–3	SAS-2	20 MeV–1 GeV	Spark chamber
1975–82	COS-B	2 MeV–5 GeV	Spark chamber
1987–91	GINGA	2 keV–5 GeV	Wire matrix spark chamber
1991–2000	CGRO Comptel	0.75–30 MeV	NaI scintillator
1991–2000	CGRO Egret	20 MeV–30 GeV	Pair conversion
1991–2000	CGRO BATSE	20 keV–2 MeV	NaI scintillator
2002–	INTEGRAL	15 keV–10 MeV	CdTe and CsI tile array
2007–	AGILE	30 MeV–50 GeV	Pair conversion
2008–	Fermi LAT	30 MeV–300 GeV	Pair conversion

wide optical and x-ray energy range). At higher energies (AGILE, Fermi LAT), the direction of arrival of photons is achieved by tracking the electron and positron pairs created by the passage of individual photons through thin sheets of heavy atomic material. Photon energy is measured by the scintillation of the ensemble of created particles in a large cesium iodide crystal.

Table 2.2 lists the space-based gamma-ray telescopes that are of particular interest in pulsar astronomy. The first major gamma-ray observatory, in operation 1991–2000, was the Compton Gamma-Ray Observatory (CGRO), carrying four instruments, of which the most important for pulsar astronomy was the gamma-ray telescope EGRET. Two gamma-ray telescopes at present (2020) in low-earth orbit and using the same principles are AGILE (launched 2007; Tavani *et al.* 2008) and Fermi (launched 2008, known earlier as GLAST) carrying the Large Area Telescope (LAT) (Atwood *et al.* 2009). Their essential components are shown in Figure 2.3. The tracker is made up of several such units, close-packed and forming a cube. Each separate layer in the tracker comprises a thin tungsten foil, the site of pair conversion, above two detector layers of parallel silicon strips. The strips in these two layers are at right angles, giving *x* and *y* coordinates for any ionising event within an accuracy of around 300 microns, the spacing between strips. The task of reducing the signals from around a million strips, to produce tracks and calculate the original direction of the gamma-ray, seems formidable to most astronomers but is of course familiar in high-energy particle physics.

Below the tracker is the calorimeter, which measures the total energy in each event. This is an assembly of CsI scintillator crystals, each with its own photodiode detector. The calorimeter is thick enough to absorb and detect all particles resulting from a photon event. The telescope must distinguish gamma-ray photons from a large flux of cosmic-ray particles. This is achieved by covering the tracker and calorimeter units with a blanket of plastic scintillator material, which responds to all

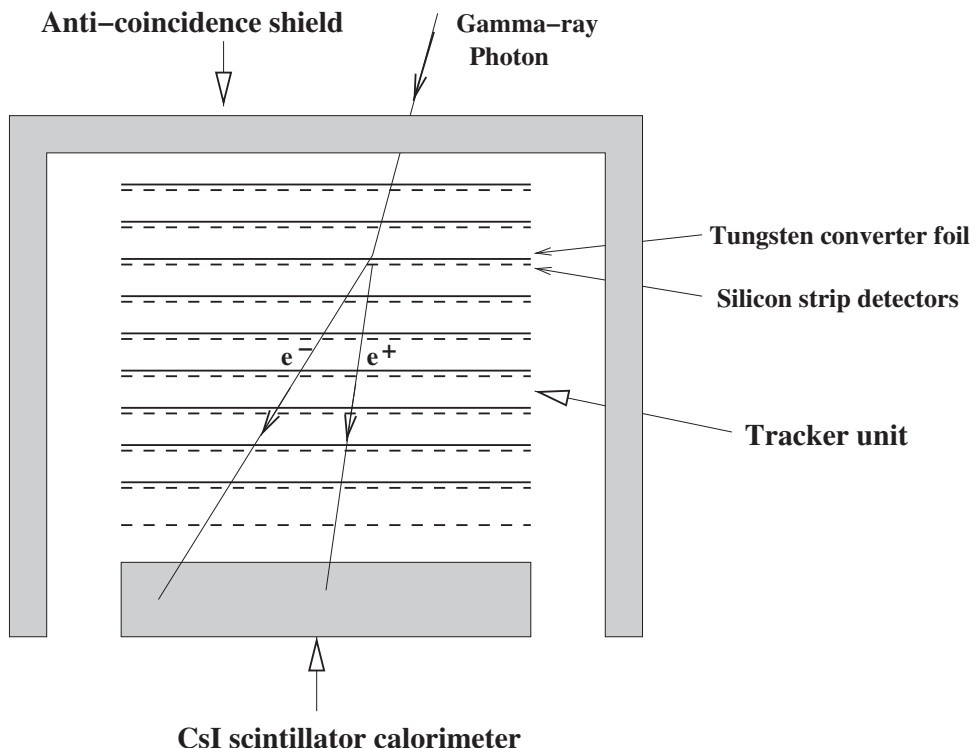


Figure 2.3 The essential components of a gamma-ray telescope. The tracker is a stack of units spaced several centimetres apart, each comprising a thin tungsten converter foil, in which electron–photon pairs are generated, above a double layer of silicon strip detectors. The total energy in each photon event is obtained in a scintillator calorimeter below the tracker. The anti-coincidence shield allows the rejection of cosmic ray particles.

high-energy particles but is almost transparent to gamma rays. Any event recorded in both the shield and the tracker is rejected.

The small aperture of these telescopes is compensated for by the large solid angle over which they are sensitive. Gamma rays from any sources within a solid angle of over two steradians will be detected, and the whole sky can be covered in a slow scan as the spacecraft rotates. The angular accuracy is best for photons arriving nearly centrally and pair-creating near the top of the tracker; depending on the geometry, a source may be located to around one arcminute.

AGILE and Fermi LAT have been successful in detecting pulsed gamma rays from many pulsars. This involves timing the arrival of photons to an accuracy approaching 5 microseconds, which is achieved by the use of GPS navigation systems.

2.3.2 Imaging Atmospheric Cerenkov Telescopes

The flux of gamma-ray photons with energies above 100 GeV is so small that they rarely cross the less than 1 m² aperture of the orbiting telescopes. Fortunately, another technique is available for the very highest energy photons, up to 1 TeV and beyond. The terrestrial atmosphere itself is the detector. A shower of charged particles is created by a multiplicity of interactions when a gamma ray reaches the upper atmosphere, and these particles continue in the direction of the gamma ray, as a disk spreading to make a shower with width of some 100 metres and only some few centimetres thick. Charged particles moving with velocities near to the velocity of light within the atmosphere are moving faster than the velocity of light in air, and they consequently radiate Cerenkov radiation in a narrow beam centred on the direction of travel. An air-shower telescope detects this radiation in an array of photomultiplier tubes mounted at the focus of a large optical telescope. The telescope does not need an accurate surface, like a conventional telescope; it is required only to image the shower as it develops and decays in the atmosphere, with an angular resolution of a fraction of a degree and with high time resolution. The image is elliptical, the long axis pointing along the direction of the gamma ray. Two or more such telescopes are used simultaneously, separated by a distance of around 100 metres, comparable to the sizes of typical showers. The stereoscopic view from two telescopes allows the direction of the shower to be determined to an accuracy of better than one degree.

The main difficulty with this technique is the almost overwhelming flux of cosmic ray particles, which also create air showers when they enter the atmosphere. However, the shape of the shower is recognisably different: at any given energy, a particle-initiated shower is longer and wider than a gamma ray photon shower. Using stereoscopic telescopes measuring the width and length of every shower allows a gamma-ray to be distinguished among around 10⁴ unwanted cosmic rays – a truly remarkable feat.

Imaging atmospheric Cerenkov telescopes can operate over three orders of magnitude of photon energy, from 100 GeV to 100 TeV. A typical 1 TeV shower produces of order 100 Cerenkov photons m⁻² on the ground, so that a telescope with a diameter of around 10 m collects sufficient photons for an effective discrimination against cosmic rays. A group of several such reflectors can provide both increased sensitivity and a stereoscopic view of a shower leading to more accurate source location. HESS (High Energy Stereoscopic System), located in the clear skies of Namibia at 1800 m elevation, comprises four reflectors, each 12 m diameter, 120 m apart on the corners of a square. Each reflector surface is made of 380 facets. At the focus is an array of 960 photomultipliers, covering a 5 deg field of view. Referring back to our basic criteria, we note that this system has both a large

collecting area and large field of view (but comparatively poor positional accuracy), excellent spectral coverage, good time resolution and remarkable discrimination against the ‘noise’ of interfering cosmic rays. Among notable discoveries by HESS is the detection of pulsar wind nebulae, which we discuss in Chapter 18. The technique of Cerenkov air shower telescopes is well established, with several systems in operation, including MAGIC, CANGAROO-III, and VERITAS (consult their websites for details). A large international project, the CTA (Cerenkov Telescope Array), consisting of more than 100 imaging Cerenkov telescopes covering the energy range 20 GeV to 300 TeV, is under construction on sites in Chile and La Palma (Canary Islands).

3

Receiver Techniques and Data Analysis

Although the development of large telescopes with high sensitivities has been vital for advances in radio pulsar astronomy, the field has always been limited by the technology available to the observers for processing the data that flowed from the telescopes. In this chapter, we explain the reasons for those limitations and describe how they have been progressively overcome as the available technology has developed.

Pulsar astronomy was born at the dawn of the digital age and at a time when astronomers studying time-varying phenomena could simply reduce thermal noise by an elementary integration of a signal, usually in an analogue circuit, with pen recording on a paper chart. Two main features of pulsar astronomy are the very short timescales (typically measured in microseconds) needed to resolve the detailed phenomena and the dispersive nature of the interstellar medium through which the signals travel. Dispersion delays pulses more at lower frequencies, so that narrow pulses are broadened in the wide receiver bandwidths required for high sensitivity. The removal of this undesirable effect is referred to as *de-dispersion*.

In this chapter, we describe firstly how radio pulsars are observed and then discuss the techniques required to discover them and study their properties.

3.1 Frequency Dispersion of Pulsed Signals

Although the basic characteristic of the pulsar signal that facilitates its recognition is the precise periodicity, the frequency dispersion in arrival time must be allowed for in any radio observation. We first analyse the propagation delay due to the ionised interstellar medium.

The refractive index n of ionised gas with electron density n_e for a wave with frequency ν is most simply expressed in terms of the resonant frequency ν_p of the plasma:

$$n = (1 - \nu_p^2/\nu^2)^{1/2}, \quad (3.1)$$

where

$$\nu_p^2 = \frac{n_e e^2}{\pi m} \text{ (Gaussian units)}, \quad (3.2)$$

in which e and m are the electronic charge and mass.¹ To a good approximation, $\nu_p = 9.0 \times n_e^{1/2}$ Hz, where n_e is in m^{-3} . For interstellar space, the electron density is usually quoted in cm^{-3} , giving the same numerical result in kHz. A typical interstellar electron density is 0.03 cm^{-3} , corresponding to a plasma frequency of 1.5 kHz; the refractivity ($n - 1$) for a 100-MHz radio wave is then -2.4×10^{-10} . The phase velocity is $v_p = c/n$, while the group velocity at which the pulses travel is $v_g = cn$. Note that the product $v_p v_g = c^2$. For small electron densities,

$$v_g = c \left(1 - \frac{n_e e^2}{2\pi m v^2} \right). \quad (3.3)$$

Hence the travel time T over distance L is

$$T = \int_0^L \frac{dl}{v_g} = \frac{L}{c} + \frac{e^2 \int_0^L n_e dl}{2\pi m c v^2} = \frac{L}{c} + 1.345 \times 10^{-3} v^{-2} \int_0^L n_e dl \text{ s}. \quad (3.4)$$

The first term here is just the free space travel time, and the second is the additional dispersive delay t . Customary units in astrophysics are parsecs (3×10^{18} cm) for distance and cm^{-3} for density: the integral $\int_0^L n_e dl$, which measures the total electron content between the pulsar and the observer, is known as the *dispersion measure*, DM, with units cm^{-3}pc . Observers usually quote radio frequencies in megahertz, so that the delay t becomes

$$t = \mathcal{D} \times \frac{\text{DM}}{v^2}, \quad (3.5)$$

where \mathcal{D} is the *dispersion constant*

$$\mathcal{D} = \frac{e^2}{2\pi m c} = 4.1488 \times 10^3 \text{ MHz}^2 \text{ pc}^{-1} \text{ cm}^3 \text{ s}. \quad (3.6)$$

The frequency dependence of this delay, seen in Figure 3.1, has a very important effect on observations of radio pulses. A short broad-band pulse at the pulsar will arrive earlier at higher frequencies, traversing the radio spectrum at a rate

$$\dot{\nu} = -1.205 \times 10^{-4} \frac{\nu_{\text{MHz}}^3}{\text{DM}} \text{ MHz s}^{-1}; \quad (3.7)$$

¹ We follow the convention in observational radio astronomy of using Gaussian units. As an example, this equation expressed in SI units would be $\nu_p^2 = (1/2\pi\epsilon_0)(n_e e^2/m)$.

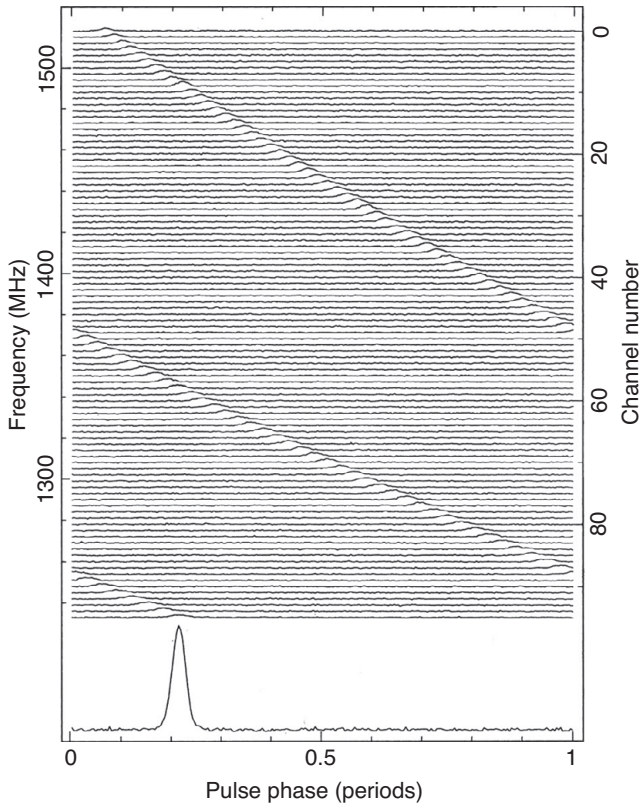


Figure 3.1 Frequency dispersion in pulses from PSR B1641–45. The data were folded at the pulsar period in 96 adjacent frequency channels, each 3 MHz wide.

correspondingly, a receiver with bandwidth B (MHz) will stretch out a short pulse to a length

$$\Delta t = 8.3 \times 10^3 \text{DM} \nu_{\text{MHz}}^{-3} B \text{ s}. \quad (3.8)$$

As a useful guide, $\Delta t = (202/\nu_{\text{MHz}})^3$ DM milliseconds per MHz bandwidth.

3.2 De-dispersion

If a pulsar with high dispersion measure is observed with a receiver having a wide bandwidth, its pulse is stretched so that the intrinsic pulse shape is lost, and the peak intensity is reduced. The lost time resolution and sensitivity may, however, be recovered by dividing a wide receiver bandwidth into separate bands and using separate detectors on each. The output of these several bands, collectively known as a filter bank, can then be added with appropriate delays so that the pulse components

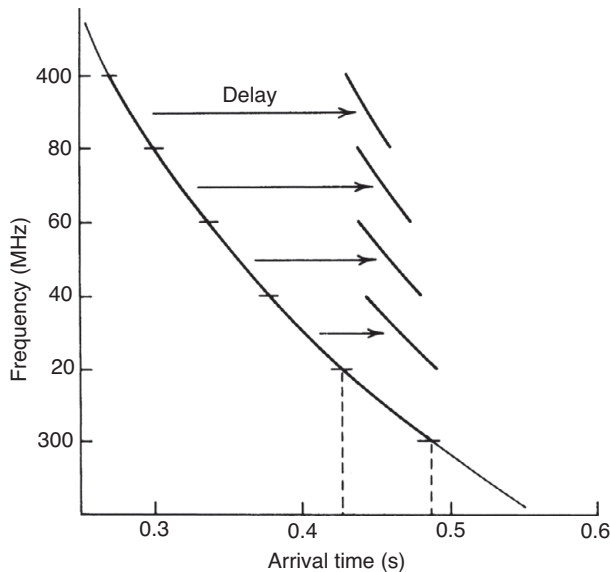


Figure 3.2 De-dispersion, achieved by sequential sampling and delay of adjacent frequency channels.

are properly superposed. This process of *incoherent de-dispersion* is shown in Figure 3.2. (We later describe a *coherent dispersion process*.)

The technique first used for de-dispersion involved a mechanically-driven sequential sampling of the separate receiver outputs (Large & Vaughan 1971). Digital techniques are now universally in use, either setting the individual delays to match the known DM of a given pulsar, or using a series of different delays in an off-line search through recorded data. In the latter case, each set of delays then allows the detection of pulsars in a definite range of DM.

Such de-dispersion by adding signals separately detected in contiguous bands, with appropriate delays, is referred to as *incoherent de-dispersion*. Incoherent de-dispersion is limited in the time resolution that it can achieve by the time taken for the signal to pass through a single filterbank channel. This can be combatted by the use of increasingly small bands δf but is ultimately limited by the time response $1/\delta f$ of the filters. Applying Eq. (3.8), we find that the maximum time resolution is thus when $1/\delta f = \delta t = 3\sqrt{(DM/v_{GHz}^3)} \mu s$. However, there is no such limit in the more sophisticated technique of *coherent de-dispersion*, in which the full bandwidth signal is processed before detection, totally removing the dispersion effect of the interstellar medium (Hankins & Rickett 1975; Stairs *et al.* 2000a; Stairs 2002). To achieve this, the signal is passed through a filter that delays the phase by an amount depending on frequency; such a filter, is

known as a *chirp* filter in radar technology. This was first applied to pulsar signal processing by Hankins (1971). To realise such a filter, the signal is digitised before detection, requiring high-speed sampling. A sequence of samples is then Fourier transformed, preserving the phase of each discrete component of the spectrum; a computed phase delay is then applied to each component, and a reverse Fourier transformation then recovers the signal without the dispersion delay. This technique is widely used in high-time-resolution measurements, particularly of millisecond pulsars.

Digitising involves sampling at a rate at least twice the highest frequency present in the signal. This frequency can be reduced by mixing the signal with an appropriate local oscillator, which moves the signal frequency down to *baseband*, that is a band from zero to a maximum equal to the bandwidth of the original signal, often some hundreds of MHz. The data rate is still very high, and it is common to split the receiver band using a set of filters before transforming each to baseband, followed by coherent de-dispersion using separate computers. The length of each sequence to be de-dispersed is critical; the processing time for each sequence increases as the cube of its length. In modern systems, the whole band is digitised by a fast sampler, and subsequent processing is conducted in powerful digital computers.

Precise de-dispersion is only possible when the dispersion measure is already known. In a blind search for pulsars in which the value is unknown, the analysis system must be open to a wide range of dispersion measures. The search in the domain of dispersion measure is usually carried out by adding the outputs of a filterbank with a series of different sets of delays, prior to a search for single pulses or periodicity. Recently, particularly at lower frequencies, a hybrid approach has been implemented where the data are coherently de-dispersed at discrete values of DM and incoherently de-dispersed at intermediate DM values (Bassa *et al.* 2018). This gives significantly improved sensitivity to millisecond pulsars.

Very long data sequences must be handled in searches in the domains of period and dispersion measure, and it is essential to use efficient computing processes, such as sequential folding algorithms for periodogram analysis and an analogous process, the fast fourier transform (FFT) for spectral analysis. These were introduced for de-dispersion analysis by Taylor (1974) and for searches in period by Staelin (1969). The effects on detectability of the various computational processes, such as sampling rate, digitisation and the inclusion of harmonics, have been analysed by Ransom *et al.* (2002).

Terrestrial impulsive interference is often a limitation on the sensitivity of searches, especially for transient radio sources, such as the RRATs and FRBs (Chapter 9). Unwanted impulses, however, usually occur without dispersion, and when this is detected, an analysis system can be devised to excise them from the signal (Eatough, Keane & Lyne 2009).

3.3 Interstellar Multipath Scattering

Unfortunately for the observer looking for the detailed structure of radio pulses, the electron density in the interstellar medium is not uniform, and the irregularities scatter the radio waves out of the direct line of sight. This has two main effects: point sources appear to have a finite angular diameter, and multiple radio waves arrive at the observer with increased ray path, delaying and broadening a pulse (Chapter 19). Such scattering can have a severe effect on the shape of a radio pulse, even to the extent of smearing out the whole profile and disguising the periodicity. Scattering is non-dispersive and cannot be recognised or compensated for by using an array of adjacent frequency channels. The extent of scattering is, however, strongly frequency dependent. The effect may be assessed by using the relation found empirically by Slee *et al.* (1980) between DM and pulse lengthening τ_{scatt} :

$$\tau_{\text{scatt}} = \left(\frac{\text{DM}}{1000} \right)^{3.5} \left(\frac{400}{\nu_{\text{MHz}}} \right)^4 \text{ s.} \quad (3.9)$$

Although there is a wide spread of actual values about this simple relation (see Bhat *et al.* 2004), the 4th power law in Eqn. (3.9) indicates the advantage of observing at high radio frequencies. For example, a pulsar at the Galactic centre would be practically undetectable due to interstellar scattering; at frequency ν (GHz), the pulse would be lengthened to approximately $350\nu^{-4}$ seconds. Searches for such sources must regard them as continuum emitters, to be detected as any other point source by large radio telescopes such as the VLA or MeerKAT.

3.4 Searching for Single Pulses

The original Cambridge discovery of pulsars depended on an unusual combination of radio telescope parameters, viz. long wavelength, short integration time, very large collecting area and regularly repeated observations. The first surveys, at Cambridge and at Molonglo (Australia), essentially scanned the northern and southern skies respectively for pulsars strong enough to be detected by the appearance of single pulses on pen chart recordings. The Molonglo radio telescope proved to be particularly suitable for pulsar search, and 28 pulsars were found by inspection of survey recordings (Vaughan & Large 1969).

It is still important to search for dispersed isolated radio pulses: the Crab Pulsar and the radio transients known as RRATs were discovered through individual pulses, and in gamma-ray astronomy all signals arrive as isolated photons. The Fast Radio Bursts (FRBs) are isolated single pulses that have anomalously high dispersion measures, consistent with an extragalactic origin. Cordes and McLaughlin (2003) estimate that about 1/3 of pulsars are detectable through their single pulses,

particularly the long-period pulsars. These are, however, the exceptions; surveys and searches for pulsars generally rely on the recognition of a precise periodicity in a radio signal that is deeply buried in noise.

3.5 Searching for Periodic Pulses

Hidden within the apparently random noise at the detector output of a radio telescope pointing at an arbitrary region of the sky, there may be a low-level, precisely periodic signal of unknown pulse width and unknown period. The detected signal can be sampled and digitised at an arbitrary rate, and an arbitrary length of record can be searched by computer for the periodic signal. The principle of the search may be to look either directly for a train of regularly spaced pulses (a periodogram analysis) or for their spectrum within the Fourier transform of the data stream. The two approaches are closely related (time domain and frequency domain are Fourier pairs), but the Fourier transform method is the more widely used in modern searches because it is more economical of computer resources.

The periodogram analysis is conceptually easy to follow. The data stream of N equispaced samples is folded at a series of N different values of period P , each operation providing a profile that may contain a pulsar signal. Each profile then has to be searched for pulses of different widths and phases, by scanning with a window function of variable width, since the width W may be anywhere between 1% and 50% of the period. The sensitivity depends on the pulse width W ; a narrow pulse can be detected with a signal-to-noise ratio increased by a factor of about $(P/2W)^{1/2}$ over a sinusoidal waveform with the same mean flux density. This dependency of sensitivity on pulse width is fundamental in all search processes.

An efficient implementation of a periodogram analysis involves taking the Fourier transform of the time series and inspecting the resultant spectrum for signals together with any associated harmonics. Figure 3.3 shows a sketch of the Fourier relationship between the time and frequency; the amplitudes and phases of the individual harmonics are determined by the average pulse profile in the time domain. For a nearly sinusoidal pulse, there will be a large fundamental spectral feature with small harmonics, while for a narrow pulse width W , there will be approximately $P/2W$ harmonics with amplitude comparable to the fundamental. Individually, these components may not be distinguishable from noise, and they must be combined in some way to maximise the detectability of the signal. This is achieved by an incoherent addition of the harmonics, that is by adding their amplitudes only, in a process introduced by Taylor and Huguenin (see Cordes 2002).

Figure 3.4 shows a spectrum containing several harmonics, and the same spectrum expanded by a factor of two so that the expanded fundamental coincides with

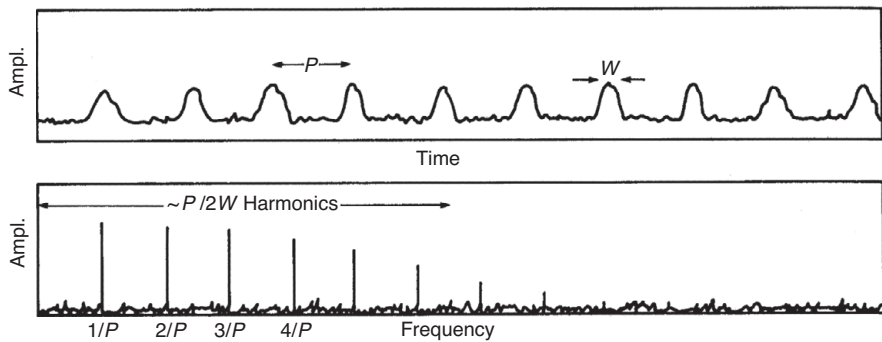


Figure 3.3 The Fourier relationship between the time and frequency domains for a pulse train with period P and pulse width W . The falling envelope of the frequency spectrum represents the Fourier transform of the mean temporal pulse profile.

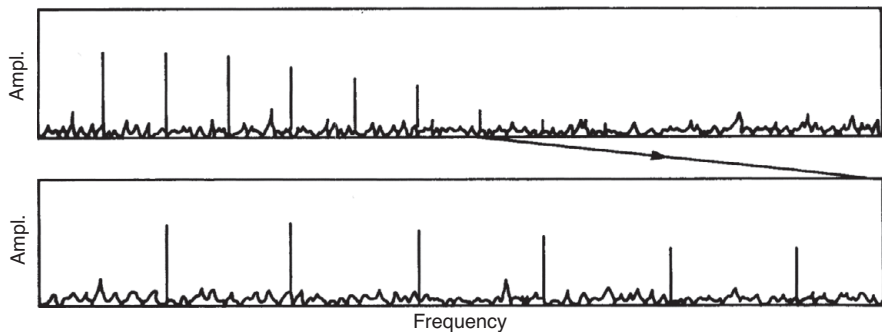


Figure 3.4 The first half of the power spectrum is expanded by a factor of two and added to the unexpanded spectrum so that each fundamental is added to its second harmonic.

its second harmonic. For a large signal with a narrow pulse, the sum of these two components is almost double the fundamental, while the noise increases by only $2^{1/2}$, giving a net gain in signal-to-noise ratio. In a spectrum with many elements, say 10^5 , this may greatly increase the significance of a suspected spectrum component. For example, a fundamental might appear with a signal-to-noise ratio of 4, a value occurring frequently by chance; in the combined spectrum this would be increased to 5.7, a value unlikely to occur by chance. The process of expansion and addition may be repeated several times, resulting in the summation of more and more harmonics and providing good sensitivity to narrower pulses. Since there are of order $P/2W$ harmonics, the signal-to-noise ratio is improved by a factor of about $(P/2W)^{1/2}$, the same improvement over a sinusoidal waveform as in the periodogram analysis. As many as 16 or 32 harmonics could be added in this way, giving good sensitivity to many small-duty-cycle pulsars.

Gamma-ray sources are recorded as a wide-spaced and apparently random series of pulse arrival times, which may contain an underlying periodicity at a much shorter interval. Searching for such a periodicity using standard Fourier transforms is inefficient. Atwood *et al.* (2006) introduced a technique that considered the Fourier transform of the intervals between arrival times of successive photons. Abdo *et al.* (2009a) found 16 pulsars through such a blind search of the photons detected with the Fermi LAT. The long intervals inherent in gamma-ray search observations may require a very accurate knowledge of pulsar position, even better than the improved angular resolution of the Fermi LAT, so that secular changes in apparent pulse period can be avoided (Saz Parkinson *et al.* 2010). Further improvements to the search methods using sliding windows and extending to include the possible pulsar spin-down resulted in further discoveries, although they still required significant computing resources. Subsequent inclusion of binary parameters resulted in the first ever detection of a binary millisecond pulsar through its gamma-ray emission (Pletsch *et al.* 2012). The computational cost of these searches resulted in the development of the distributed volunteer computing scheme, called Einstein@Home (Allen *et al.* 2013), which enabled the discovery of many more gamma-ray-only-emitting sources and radio pulsars.

3.6 Searches for Pulsars

For the first 20 years of pulsar astronomy, most surveys were conducted at frequencies of 400 MHz or below, where it appeared that there were advantages in signal-to-noise ratio and in the comparatively large telescope beamwidths. Higher frequencies, mainly around 1400 MHz, were used in later surveys, to take advantage of new low-noise receivers and the larger available bandwidths. Higher frequencies also involve less interstellar dispersion and scatter-broadening; furthermore, Galactic radiation, which determines the system temperature near the Galactic plane at low frequencies, is much smaller. The smaller beamwidths meant, however, that the searches were painfully slow; this was eventually overcome by using multiple telescope beams, each with its own receiver.

In Chapter 4, we list the main surveys in which a substantial part of the sky was searched and in which 10 or more pulsars were discovered. Notable surveys at 400 MHz were conducted at the Molonglo Cross telescope near Canberra, at Jodrell Bank with the Lovell telescope, at Greenbank with the 90-metre transit telescope, and at Arecibo with the 300-metre telescope. A total of around 350 pulsars were found up to 1986 in these surveys. Of these, 155 were found in the second Molonglo survey, which introduced several features now routinely used in modern surveys, notably multiple telescope beams and multiple receiver channels. The east-west arm of the Mills Cross telescope, used in this survey, is 1.6 km long by 11 m wide,

with area 18,000 m². At 408 MHz it has a wide beam (4.3 deg) in the declination direction, which is advantageous in covering the sky, but only 1.4 arcminutes in hour angle, so that the transit time for a source on the celestial equator was only 5.5 seconds, giving an inadequate integration time. In the survey, separate elements of the telescope were coupled to produce eight contiguous beams in hour angle, which were fed to separate receivers; in addition, the frequency band was split into four, each of 0.8 MHz width, providing some resolution in dispersion measure. These improvements required the installation of 88 low-noise amplifiers in the telescope feed system and a total of 32 separate receiver channels.

It has so far been a challenge to cover the whole sky in the more sensitive surveys at higher frequencies, on account of the narrow telescope beamwidths; surveys such as the second Molonglo survey, which covered a large solid angle, are therefore still of considerable importance in evaluating the galactic population of pulsars.

The first surveys at 1400 MHz were by Clifton and Lyne (1986) at Jodrell Bank and Johnston *et al.* (1992) at Parkes in Australia; between them they discovered about 100 pulsars lying close to the Galactic plane. These surveys showed that higher frequencies enabled the discovery of more distant and younger pulsars. A further decisive factor in the subsequent choice of higher frequencies was the discovery by Backer *et al.* in 1982 of the millisecond pulsar B1937+21. The realisation that a search for millisecond pulsars should cover the whole sky dictated the selection of parameters for further surveys (Camilo *et al.* 1996b), leading in particular to the major survey of the southern sky at the Parkes radiotelescope.

The major surveys and their parameters are listed in Chapter 4, with references that may be consulted for further details. New and more sensitive multibeam surveys, which between them will cover the whole of the sky, are in progress at Parkes (Australia) and Effelsberg (Germany). These use 1024 frequency channels covering 400 MHz centred on about 1400 MHz, sampled at the short interval of 64 µs, and together form the High Time Resolution Universe (HTRU) survey (Keith *et al.* 2010). A survey at the lower frequency of 350 MHz, the Green Bank N Celestial Cap (GBNCC), will extend to cover the sky to declination $\delta - 40^\circ$ (Stovall *et al.* 2014). A number of multi-element synthesis telescopes have started to have a large impact in this area, notably the LOFAR and MeerKat arrays (Section 2.1).

3.7 The Detection of Binary Pulsar Systems

The extreme sensitivity required in searches for all but the strongest pulsars requires long integration times, allowing a precisely periodic pulse train to appear as a coherent signal above the inherent system noise. However, when a pulsar is in a binary system with another star, the varying line-of-sight velocity results in a periodically changing Doppler shift of the pulsar rotational frequency. The standard approach of

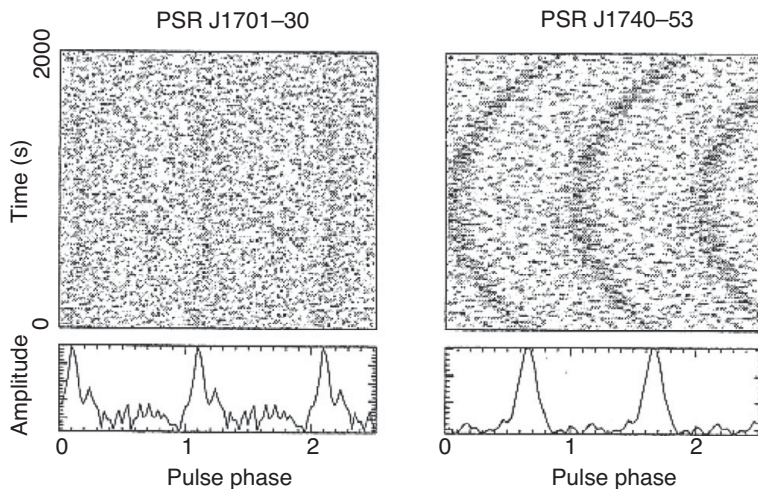


Figure 3.5 Discovery observations of two millisecond binary pulsars observed for 2100 s. Individual integrations over 16 s at a fixed periodicity show a barely recognisable signal, but successive observations show the slowly varying period due to changing Doppler shift in a binary orbit (d'Amico *et al.* 2001).

simple Fourier analysis may still apply to a pulsar in a binary system with an orbital period of several days, since the Doppler shift will usually be nearly constant in an integration lasting only a few minutes; even so, the recognition of a newly detected pulsar will be confused by the different pulse periods that are found when it is observed at widely different times. For short orbital periods, in which the period will change appreciably within the observation time, the integration technique must be modified to match the changing period as closely as possible. Figure 3.5 shows an example of two millisecond binaries that show typical changing periods (d'Amico *et al.* 2001). Unfortunately, the period and the other orbital parameters are initially unknown and can fall within wide limits. A ‘matched filter’ approach might be adopted, in which a multi-dimensional search attempts sequentially to cover a wide range of possible orbital parameters, or simultaneously in parallel multiple computing elements. Extending this approach rapidly becomes impracticable, and a limited search tactic is essential.

The first move is to limit the length of individual integrations, so that the period can be assumed to be approximately constant for each integration, and repeat the process at short intervals of time. The sensitivity of each integration is, of course, reduced, but the successive time-resolved pulse profiles can be examined to find a signal at a slowly changing frequency.

If the pulsar period P can be regarded as changing linearly with time during a longer observation due to a constant gravitational acceleration a of a pulsar over part

of its orbit, this can be allowed for in the analysis, so that a full coherent Fourier analysis can still be achieved. The analysis must now include a new parameter, the period first derivative $\dot{P} = aP/c$. The signal, which is recorded as a sequence of digital samples at uniform time intervals, is ‘re-binned’ at stretched time intervals, so that an arbitrarily chosen rate of change of pulsar period will be cancelled out to produce a constant periodicity, and the normal Fourier analysis can be applied at full sensitivity. The process must, of course, be repeated to accommodate a series of values of the acceleration. This first step in a multi-parameter search is already very demanding on computer capacity; nevertheless, more than 100 pulsars have been discovered in ‘acceleration searches’. An analysis including the next frequency derivative, the ‘jerk’ analysis, has been demonstrated by Andersen and Ransom (2018) and has already discovered a highly accelerated binary pulsar in the globular cluster Terzan 5.

The recognition of an orbital period from occasional widely spaced observations adds a new feature to a long-established classical process applied to optical binaries, in which the Doppler shift of an optical spectrum is the analogy of the shift of pulsar period. In pulsar searches it may be difficult to construct the orbital curve when the period is very short compared with the spacing of the observations; the precision of the individual observations is, however, often sufficient to allow measurement of the rate of change of period \dot{P} . This extra information can be used by plotting \dot{P} against P , that is acceleration against velocity in the orbit, as in Figure 3.6. A pattern characteristic of the orbit will appear after only a small number of observations, even if they are spaced many orbital periods apart (Freire *et al.* 2001b). In the

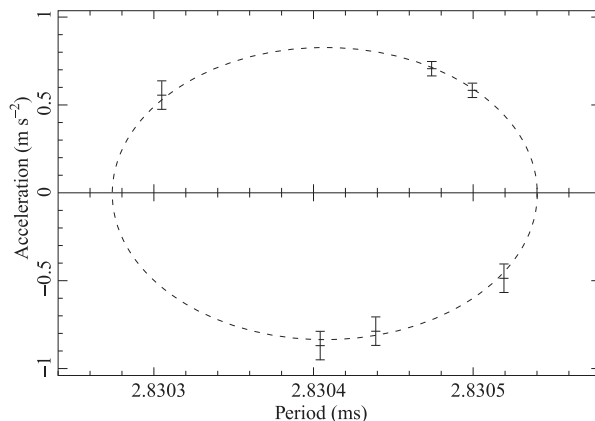


Figure 3.6 Discovery observations of the binary pulsar 47 Tucanae S, which has an orbital period of 1.202 days. Individual widely spaced integrations allowed both P and \dot{P} to be measured, and the locus of the measured points gives the essential characteristics of the binary orbit (Freire *et al.* 2001b).

case shown in Figure 3.6, the orbit is circular, and the locus of the P/\dot{P} plot is an ellipse. The figure shows the discovery observations for the binary millisecond pulsar 47 Tuc S, one of the binary systems within the globular cluster 47 Tuc. The observations were spread over 475 days; the strength of the pulsar signal was very variable due to interstellar scintillation, so that measurements were only possible on six occasions during this time, which covered 1.4×10^{10} pulsar rotations and 375 orbital periods.

The limitations on sensitivity in searching for binary pulsars were analysed by Johnston and Kulkarni (1991).

3.8 Searches for Millisecond Pulsars

Historically, the most interesting pulsars, which probably account for as much published work as all the others put together, are the Crab Pulsar, the binary pulsar PSR B1913+16 and the double pulsar PSR J0737–3039. Of these, the binary PSR B1913+16 was the only millisecond pulsar with a signal large enough and of a long enough period (8 hrs) to have been discovered in any of the main surveys up to the mid-1980s; even this pulsar might have been overlooked in a large-scale survey because of its varying period arising from its orbital motion. The main reason for the relative inadequacy of these surveys was the lack of rapid data recording and computing resources. The problem is particularly acute for millisecond pulsars because, for a given dispersion measure, the amount of data to be recorded and processed depends on the inverse square of the minimum period of the search. For instance, a doubling of the sampling rate to detect shorter period pulsars has to be matched by a doubling of the number of frequency channels to be sampled within the total receiver bandwidth, so that dispersion broadening in a single channel can be halved and remain the same fraction of the period. Thus, for example, the move from the searches of the 1970s, with sample rates of typically 10 ms, to the millisecond pulsar surveys of the 1980s, with sample rates of 0.3 ms, required increases of about three orders of magnitude in data storage and computer capacity.

In 1982, the pulsar B1937+21 was discovered by Backer and collaborators (Backer *et al.* 1982). This resulted from a search directed at a radio source that had the steep spectrum and high linear polarisation properties that were characteristic of many pulsars. The 1.557 ms period of this pulsar was discovered at Arecibo as an alias in a search that sampled the data every 4 milliseconds. Fortunately, the pulsar was so strong that a very narrow receiver bandwidth could be used to avoid the smearing affects of dispersion. However, large-scale searches for other such millisecond periodicities were not really practical at that time, and, in spite of many efforts, only two others in the galactic plane (PSR B1953+29 and PSR B1855+09) were found before the end of the decade (Boriakoff *et al.* 1983;

Segelstein *et al.* 1986). The problem was that, as remarked above, for a given dispersion measure, observation time and bandwidth, the number of data points that need to be sampled and processed is proportional to the inverse square of the required time resolution. Because of this, most further searches for millisecond pulsars in the 1980s were carried out by using continuum searches using large aperture synthesis telescopes to identify small-diameter, steep-spectrum sources that might be pulsars. Once identified, targeted radio searches of these candidate sources were performed to seek the characteristic periodicity of a pulsar. Targetted searches are again productive, directed at gamma-ray sources detected by Fermi LAT but not yet identified as pulsars (Camilo *et al.* 2009b); this is proving to be a very productive source of new millisecond pulsars, and a consortium of radio observatories (the Fermi Pulsar Search Consortium) has been organised to search the LAT sources.

In 1968, digital computers were a very young technology, and a sampling rate of 100 samples/second was just about possible. In 1982, with the discovery of PSR B1937+21, approximately 10,000 samples/second were required on each of about 100 channels. At a sampling resolution of 4 bits/sample, a data rate of about 0.5 MB/second was required, and this was impossible at the time. The data handling requirements can be dramatically reduced by the use of single-bit sampling, which for small signals reduces the sensitivity by a factor of only $\sqrt{2/\pi} = 0.80$ compared with multi-bit sampling. Single-bit sampling is also very robust in the presence of strong impulsive radio-frequency interference.

With such advances and the availability of inexpensive computing power, by the early to mid '90s, large-scale surveys for millisecond pulsars became possible. Arecibo and Parkes were particularly successful, and, for example, the 64-m telescope at Parkes surveyed 2/3 of the celestial sphere at around 436 MHz and discovered 100 new pulsars of which 17 were millisecond pulsars, more than doubling the number of such pulsars known in the Galaxy at that time (Lyne *et al.* 1998) and providing the first major uniform sample of millisecond pulsars. The number of millisecond pulsars has now been increased by an order of magnitude by surveys such as the Parkes Multibeam Surveys, PALFA, HTRU, and the aforementioned gamma-ray source searches.

3.9 Searches of Supernova Remnants and Globular Clusters

Very deep searches of individual locations such as supernova remnants may be performed by making long observations of single positions with high time resolution. Such searches have become progressively more sensitive with the development of large computer storage.

The initial discovery of pulsars in globular clusters in 1987 (Lyne *et al.* 1987) and other early searches in these objects involved aperture synthesis mapping of

clusters, followed by long FFTs on those candidate clusters, which showed the presence of small-diameter, steep spectrum sources. Only later was it possible to conduct deep searches in period and dispersion measure carried out on clusters without synthesis mapping. After one pulsar had been detected in a cluster, the range of dispersion measures searched could be restricted, hence releasing available computer capacity for acceleration searches. In some cases, such as the cluster 47 Tucanae, interstellar scintillation often focusses the pulsar radiation, occasionally causing the instantaneous flux density to be many times the mean value, so increasing the effective sensitivity. The Green Bank Telescope GBT has been especially successful in searches for pulsars in globular clusters, using a multi-channel receiver giving 600 MHz bandwidth at 2 GHz (Kaplan *et al.* 2005).

These searches have been very successful and have found many pulsars in globular clusters, including many millisecond pulsars in binary systems. A catalogue is maintained by P. Freire;² in 2021 there were 221 pulsars listed as members of 36 clusters.

3.10 Sensitivity: Selection Effects

Apart from the hope of discovering interesting individual pulsars, the main object of a survey is to measure the population of pulsars as a function of parameters such as period, flux density, spectrum and location within the Galaxy. The limits of sensitivity within each search must therefore be carefully delineated. For example, a high sensitivity can only be achieved by using a long integration time, while the shortest periodicity requires a rapid sampling rate; the two together determine the total number of samples in an integration, which is limited by available possibilities of data processing, since the observations commonly require multimillion-point Fourier transforms as part of the processing. The background noise level in a typical large radio telescope operating at 20 cm wavelength corresponds to a flux density of order 20 Jy ($1 \text{ Jy} = 1 \text{ Jansky} = 10^{-26} \text{ W m}^{-2} \text{ Hz}^{-1}$). Observable pulsar flux densities are of order 10^5 smaller. Reaching such a small fraction of the receiver noise level is commonly achieved in radio astronomical observations by using a wide receiver bandwidth B and averaging the signal over an integration time τ . The smallest detectable signal is then a fraction $(B\tau)^{-1/2}$ of the total noise level; this is at 1 sigma of the integrated noise, while a level of 5 or even 7 sigma may be appropriate for a large survey. For instance, a modern receiver might have a bandwidth of 1000 MHz,

² www.naic.edu/~pfreire/GCpsr.html

and it may be required to detect a single pulse 1 ms long; the 1 sigma level would then be 10^{-3} of the input noise, or about 10 mJy in a large radio telescope. Single pulses are rarely as strong as 1 Jy, and weaker pulses would be lost in noise. However a series of 10,000 pulses, suitably added together, would provide a further factor of 10^2 in sensitivity, giving a more useful sensitivity of 0.1 mJy within the averaged pulse; the mean flux density of a detectable pulsar will be lower than this, depending on the ratio of pulse width to period.

In large surveys, the signal-to-noise ratio S/N for a significant detection must be set high enough to avoid too many false detections. In a system with total noise temperature T_{sys} and antenna gain G , using N_p polarisation channels ($N_p = 1$ or 2), the minimum flux density S_{\min} is given by:

$$S_{\min} = \frac{\alpha\beta}{(N_p \Delta v t_{\text{int}})^{1/2}} \left(\frac{W}{P - W} \right)^{1/2} \frac{T_{\text{sys}}}{G}. \quad (3.10)$$

Here α is the threshold signal-to-noise ratio, β is a factor due to digitisation and other processing losses, W is the effective pulse width and P is the pulse period (Dewey *et al.* 1985). The effective pulse width P must take account of interstellar pulse smearing; it is given by

$$W^2 = W_0^2 + t_{\text{samp}}^2 + t_{\text{DM}}^2 + t_{\text{scatt}}^2, \quad (3.11)$$

where W_0 is the intrinsic pulse width, t_{samp} is the sampling interval, t_{DM} is the dispersion smearing across one frequency channel and t_{scatt} is the broadening of the pulse due to interstellar scattering.

The necessary sampling rate is determined by the range of dispersion measure to be covered. Furthermore, even when the receiver bandwidth is divided into separately detected bands to avoid the effects of dispersion, a procedure that considerably increases the amount of data recording and computation, there is a fundamental limit due to interstellar scattering (Section 3.1), which stretches pulses so that the periodicity may be smoothed out, particularly for distant pulsars close to the Galactic plane. Such pulsars are also difficult to detect because of the contribution of galactic background radiation, which can increase the value of T_{sys} by an order of magnitude at frequencies around 400 MHz.

Figure 3.7 shows the limitations due to these factors of an early survey at 0.4 GHz and of later surveys at 1.4 GHz (the recent surveys at Parkes and Arecibo have similar characteristics). Although the main population of pulsars probably lies within the area at the upper left of this diagram, with comparatively long periods and small dispersion measures, the limitations of the earlier periodicity searches are obvious. For example, the Crab Pulsar ($P = 33$ ms, $\text{DM} = 57 \text{ cm}^{-3} \text{ pc}$) would not have been

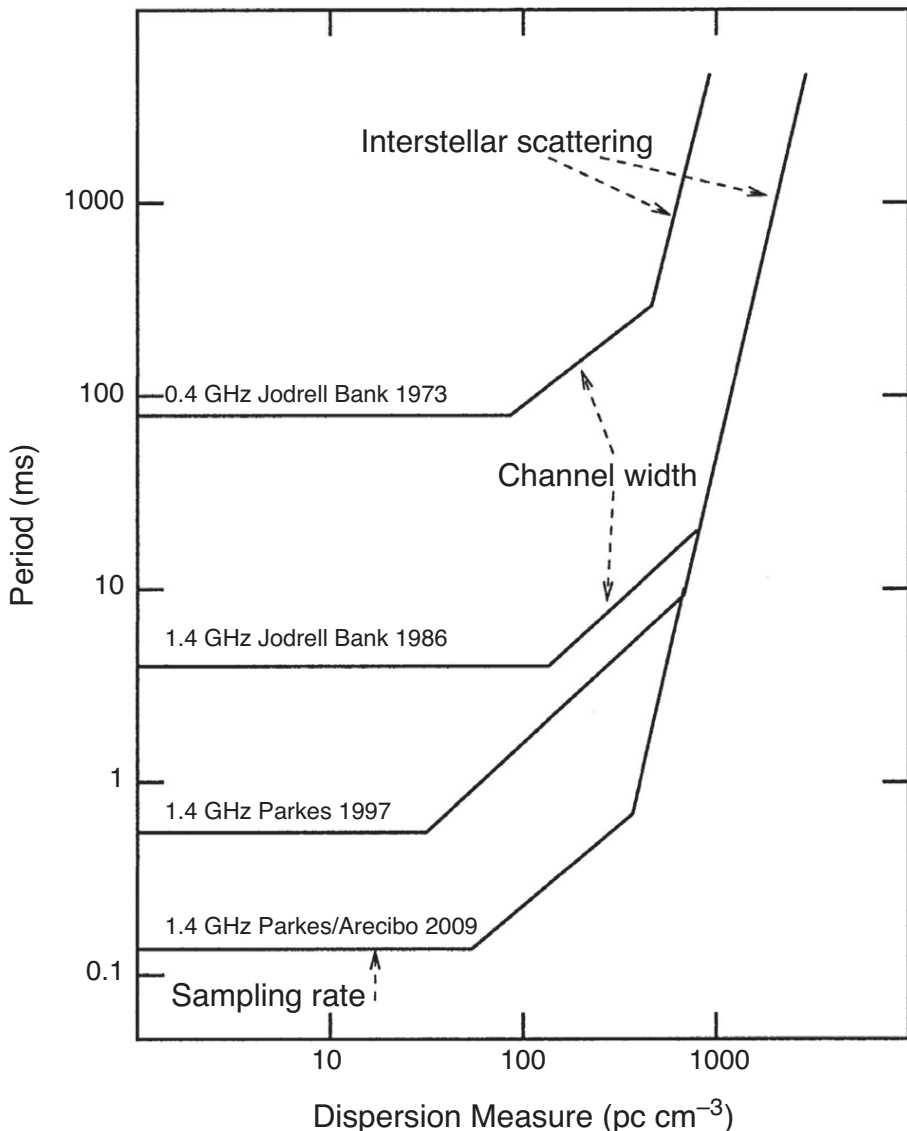


Figure 3.7 The evolution of the range of period and dispersion measure covered by four representative pulsar surveys. The surveys had little sensitivity below the indicated lines. The horizontal lines are determined by the sampling rate, the next sloping segment by dispersion broadening in the filterbank channel bandwidth and the steep lines by the broadening due to multipath scattering in the interstellar medium.

found by its periodicity alone, while the millisecond pulsar PSR B1937+21 has such a short period (1.6 ms) that it would not be found even in the 1986 survey.

In searches for longer-period pulsars, the sampling rate can be low, and a long integration time then becomes possible. For example, the first pulsar discovered

in the Small Magellanic Cloud (PSR J0045–7319, McConnell *et al.* 1991) has a mean flux density of only 1.3 mJy; the long period of 0.926 seconds allowed a total integration time of 87 minutes to be used in the search. On the other hand, a pulsar with a very long period may be missed because the analysis technique is biased towards the normal range of periods: the long period pulsar PSR J2144–3933, which has a period of 8.51 s, was missed in this way, but the third harmonic of the periodicity was detected, and the pulsar was listed for some years with a period of 2.84 s (Young *et al.* 2000). In 2018, the longest period known, 23.5 s in PSR J0250+5854, was discovered in LOFAR data by a machine-learning analysis (Tan *et al.* 2018).

3.11 Current and Future Surveys

The requirement to search over a large solid angle of sky in a reasonable observing time dominates the choice of parameters for major radio pulsar surveys. The need for high sensitivity and the avoidance of interstellar scattering dictate the use of the mid-range frequency of \sim 1400 MHz, where very low noise and large bandwidth receivers are available. Only the largest radio telescopes are sufficiently sensitive, but large apertures at small wavelengths bring a penalty of small beam width, with the prospect that many years might be needed to complete a survey. This is now being overcome by the use of multiple beams, either with a cluster of feeds at a reflecting telescope focus or multiple beams of a synthesis array telescope (see Section 2.1).

The major survey at the Parkes 64-m telescope (Manchester *et al.* 2001) illustrates the demanding nature of the problem. Thirteen feeds were used, each with two low-noise amplifiers for the two polarisations, all mounted together in one large cooling system. The multiple feeds allowed much more time to be spent on searching each area of sky, so providing very high sensitivity. The bandwidth was 288 MHz in two separate polarisations, each split into 96 bands of 3 MHz to allow for interstellar dispersion. The sampling rate was 4 kHz. Compared with the Johnston *et al.* (1992) survey using the Parkes telescope at the same frequency (see Section 3.5), the narrow channels and the rapid sampling effectively doubled the distance limit set by dispersion and scattering; for example, at $DM = 100 \text{ cm}^{-3} \text{ pc}$, a pulse is smeared by only 0.9 ms.

Analysis of such a survey is very demanding. A single survey observation involving an integration time of 35 min produced 2.3×10^{10} data samples, which had to be stored and processed repeatedly to cover a large range of dispersion measure; further, the search for pulsars that are accelerated in close binary systems required some tens or hundreds of times more processing. This huge task was shared among several participating institutes, each mobilising an array of computing workstations.

The history and the future of pulsar searches is discussed by Lorimer (2010). The key to effective surveys must lie in the use of broadband multibeam systems, following the lead of the Parkes system (Keith *et al.* 2010) and a 1400-MHz multi-beam system, known as PALFA, at Arecibo (Cordes *et al.* 2006a). The large collecting areas of FAST and of the Arecibo telescope not only provide very good sensitivity, but the required dwell time on a position on the sky is small so that it retains good sensitivity to highly accelerated pulsars. LOFAR has demonstrated the possibilities of surveys at low radio frequencies for steep spectrum pulsars. Apart from incremental improvements to these systems, the next major advance is expected to be the international Square Kilometre Array, comprising arrays at several frequencies, each with a very large collecting area. This is designed to provide massive multibeaming capability within large primary telescope beams and will be ideally suited to pulsar searches. However, the large number of beams (greater than 1500) to be received at once to give a reasonable field-of-view and thus a reasonable survey time, mean that the data stream needs to be processed in real time. This is a huge computational challenge as a wide-ranging search for systems in binaries (see Section 3.7) will also be undertaken, resulting in total compute requirements of at least 10 petaops.³

3.12 Combatting Radio Interference

Radio astronomy observations have a severe problem not shared by x-rays and gamma rays: other users of the radio spectrum produce signals that may be overwhelmingly large compared with any astronomical signals and which, even if weak, may be pulsed and thereby confuse the analysis system. There are frequency bands internationally and nationally allocated to radio astronomy, and some long-term programmes that monitor known pulsars use only these protected bands. But wider bandwidths are essential for the most sensitive observations, especially searches and surveys. Radio observatories are sited, whenever possible, in geographic areas of low activity, but they cannot escape the increasing presence of spacecraft that use radio for communication and navigation services; for example in L-band 1–2 GHz, the Global Navigation Satellites (GNSS) GPS, GLONASS, GALILEO and China’s BeiDou constellation. Although radio telescope feeds are designed to minimise sensitivity to signals from outside the main reception beam, no observatory can entirely avoid radio frequency interference (RFI). Receiver techniques now include low noise amplifiers with bandwidths of some hundreds of MHz, and it is inevitable that several strong RFI signals will be included in such a band.

³ 10^{16} operations per second.

RFI signals can be removed, or at least reduced, by using radio frequency filters at the input amplifiers of the telescope. Filters with low insertion loss and sharply defined pass bands are available using cold components; these are commonly used to mitigate the effects of strong signals at or just beyond the edge of the receiver band. At a later stage in the receiver, the wide frequency band is split into a number of narrow channels, using analogue filters or digitally using polyphase filters. These separate channels are independently detected and processed; this is the technique used to remove the effect of dispersion (Section 3.2). The outputs from any one or more frequency channels containing an RFI signal may then be excised without serious loss of sensitivity.

Impulsive RFI signals are usually broadband and cannot be removed by frequency filtering techniques. Removing intense spikes after detection can seriously distort the wanted signal; searches for new pulsars, and especially for intermittent pulsars (RRATs and FRBs; see Chapter 9), are particularly vulnerable. Impulsive RFI may, however, be distinguishable from pulsar signals since it does not display a dispersed signature and appears simultaneously in all channels of a multi-channel receiver. The RFI pulse can therefore be removed by calculating the mean of all frequency channels in each time sample and subtracting this from each individual channel. Eatough *et al.* (2009) applied this technique to archived data from the Parkes PMPS survey (Section 3.6) and discovered four pulsars whose signals had previously been obscured by impulsive RFI.

4

Surveys and Population

Over the first half century of pulsar research, the available techniques in telescopes and data handling advanced dramatically, as described in Chapters 2 and 3, providing catalogues of almost 3000 pulsars of several distinct varieties. This chapter describes the analysis of this database, giving an account of their population, life history and evolution. It should be recognised immediately that there are large selection effects in the available data. The outstanding limitation is overall sensitivity, which for example allows only a few powerful pulsars to be detected at distances beyond the centre of the Milky Way Galaxy; furthermore, the most sensitive surveys have only searched the sky in the vicinity of the plane of the Galaxy. Nevertheless the analysis now provides a coherent account of birth rate, development, transformation and eventual death of pulsars, analogous to demography translating a population census into a comprehensive account of the human race.

4.1 The Surveys

A glance through the catalogue of known pulsars shows at once that they are mostly found close to the plane of our Galaxy, the Milky Way. The normal (non-recycled) pulsars show the clearest concentration towards the plane, while the millisecond (recycled) pulsars, most of which can only be detected at smaller distances, are more nearly isotropically distributed. The normal pulsars must therefore be young Galactic objects, and it might be assumed that their distribution through the Galaxy is similar to that of young massive stars and supernovae. Although this is nearly correct, it can only be established by reading the catalogue in conjunction with a description of the surveys in which the pulsars were found; many of these surveys were, in fact, concentrated on the plane of the Galaxy, giving an obvious bias to the catalogue, while others show considerable variations of sensitivity over the sky.

The first surveys to cover large areas of the sky were comparatively insensitive and necessarily gave rather meagre evidence. For example, Large and Vaughan

(1971) found only 29 pulsars in 7 steradians of the southern sky. Nevertheless this catalogue, combined with a northern hemisphere catalogue covering low Galactic latitudes (Davies, Lyne & Seiradakis 1973) showed that there must be at least 10^5 active pulsars in the Galaxy.

There are now nearly 3000 known pulsars, over half of which have been discovered in surveys carried out at frequencies near 1.4 GHz. The entire sky has now been surveyed to a reasonably well-calibrated flux density limit, for normal and millisecond pulsars, and for x-ray and gamma-ray pulsars, while radio surveys with greater sensitivity cover low Galactic latitudes. Table 4.1 lists the main surveys that are available for studying the statistical properties of pulsars.

The table identifies the most important international efforts devoted to finding pulsars and where they exist in the Galaxy. The approximate dates of the start of each survey are given, together with the central observing frequency. The next columns give the total number of pulsars detected, N_{det} , the number of those that were new discoveries, N_{disc} , the number of millisecond and recycled pulsars, N_{rec} , and some of the more important papers describing the survey properties. The first section contains mostly large surveys with well-defined selection effects and suitable for statistical studies. The second section contains radio searches for pulsars in globular clusters, the Magellanic Clouds and in gamma rays, and all other smaller searches are gathered under the heading of ‘Other Searches’. Data are taken from the ATNF Pulsar Catalogue v1.61.

Distances of various precision are available for most pulsars, from geometric parallax for some of the nearest and more generally from optical identifications or, for radio pulsars, from dispersion measures (Chapter 7). In using a survey to determine the distribution of pulsars in luminosity and spatially, the sensitivity limits of the survey must be taken into account. The luminosity of each radio pulsar is defined as a *specific luminosity* at a standard frequency (usually 1.4 GHz). Then the luminosity $L_{1.4} = S_{1.4}d^2$, where d is the distance.

4.2 Analysis Methods

The canonical normal (non-recycled) radio pulsars constitute the major part of the total population of pulsars in the Galaxy. The surveys and catalogues are sufficiently comprehensive to allow a statistical analysis of their population and characteristics. Our first aim in this chapter is to characterise the population of normal radio pulsars in the Galaxy in terms of their distribution in galactocentric radial distance R , distance from the Galactic plane z , luminosity L and period P . Millisecond pulsars are analysed and discussed in Section 4.6. The evolutionary sequence from normal to millisecond (re-cycled) pulsars will be discussed in Chapter 10.

Table 4.1. *The main pulsar surveys.*

Survey	Date	Freq (MHz)	N _{det}	N _{disc}	N _{rec}	References
Molonglo I	1968	408	34	31	0	1
Jodrell Bank I	1969	408	51	37	0	2
Arecibo I	1974	430	49	40	1	3
Molonglo II	1977	408	224	154	0	4
Green Bank I	1978	400	50	31	1	5, 6
Green Bank II/III	1985	400	169	54	0	7, 8
Jodrell Bank II	1986	1400	61	40	0	9, 10
Parkes I	1990	1400	100	46	1	11
Parkes II	1993	436	298	101	19	12, 13
Arecibo III	1995	430	61	24	2	14
Arecibo IV	1995	430	139	92	16	15,16,17,18
Parkes Multibeam (PMBS)	1998	1400	1121	832	31	19,20
Parkes Swinburne	2000	1400	244	109	15	21,22
Parkes High-Lat	2000	1400	41	18	4	23
Parkes Perseus Arm	2004	1400	15	14	1	24
Arecibo PALFA	2004–	1400	256	125	24	25, 26
Parkes HTRU	2008	1400	1029	203	39	27, 28
Bonn HTRU	2013	1400	160	30	3	44
Green Bank Drift	2008	350	73	72	9	29
Arecibo Drift	2010–	327	50	48	9	30,31
Green Bank GBNCC	2014–	350	145	87	16	32, 33
LOFAR LOTAAS	2018–	135	311	73	2	34
Fermi	2009–	γ-ray	125	125	53	35
Parkes GC	1989–	1400	–	41	41	36,37
Arecibo GC	1989–	430	–	27	27	38, 39
Green Bank GC	2003–	?	–	74	74	40,41
Parkes LMC and SMC	2006–	1400	–	28	0	42,43
Other Searches	1968–	Various	–	280	24	
TOTAL			2806	409		

References:

- 1 Large *et al.* 1968a
 2 Davies *et al.* 1973
 3 Harrison and Tademaru 1975
 4 Manchester *et al.* 1978
 5 Damashek *et al.* 1978
 6 Damashek *et al.* 1982
 7 Dewey *et al.* 1985
 8 Stokes *et al.* 1985
 9 Clifton and Lyne 1986
 10 Clifton *et al.* 1992
 11 Johnston *et al.* 1992
 12 Manchester *et al.* 1996
 13 Lyne *et al.* 1998
 14 Nice *et al.* 1995
 15 Foster *et al.* 1995
 16 Camilo *et al.* 1996a
 17 Camilo *et al.* 1996b
 18 Ray *et al.* 1996
 19 Manchester *et al.* 2001
 20 Lorimer *et al.* 2006b
 21 Edwards *et al.* 2001
 22 Jacoby *et al.* 2009
 23 Burgay *et al.* 2006
 24 Burgay *et al.* 2013
 25 Cordes *et al.* 2006a
 26 Parent *et al.* 2019
 27 Keith *et al.* 2010
 28 Burgay *et al.* 2019
 29 Hessels *et al.* 2008b
 30 Deneva *et al.* 2013
 31 Martinez *et al.* 2019
 32 Stovall *et al.* 2014
 33 Lynch *et al.* 2018
 34 Sanidas *et al.* 2019
 35 Abdo *et al.* 2013
 36 Manchester *et al.* 1991
 37 Camilo *et al.* 2000
 38 Anderson 1993
 39 Hessels *et al.* 2007
 40 Ransom *et al.* 2005
 41 Freire *et al.* 2008
 42 Manchester *et al.* 2006
 43 Ridley *et al.* 2013
 44 Barr *et al.* 2013

The main principles of the analysis and the general features of the distributions have been established for several decades and have been refined as new surveys and modelling techniques have become available. The analysis for normal pulsars that follows was originally carried out by Lyne, Manchester and Taylor (1985). Progressive improvements were made by Lorimer *et al.* (1993) and Lyne *et al.* (1998), using the distance model of Taylor and Cordes (1993); more recent analyses, notably those of the Parkes multi-beam survey by Faucher-Gigu  re and Kaspi (2006) and Lorimer *et al.* (2006b) used the improved distance scale NE 2001 by Cordes and Lazio (2002). A new distance model YMW16 (Yao, Manchester & Wang 2017) has recently been introduced and is in use. Story, Gonthier and Harding (2007) extended the analysis to include millisecond pulsars, using data from 10 surveys. Further references can be found in Cieslar, Bulik and Oslowski (2018), who also include magnetic field evolution in their model.

The analysis proceeds by constructing a model distribution of pulsars in luminosity and location within the Galaxy and applying the sensitivity limits of the survey to produce a trial model of observable pulsars. This is then compared with the actual observed distributions, and adjustments are made to the trial model to improve the match between model and observed distributions; this is achieved by a random Monte Carlo process.

The distributions in age and location are initially treated as independent, although they may in fact be linked; for example, the younger and more luminous pulsars are mainly found near the Galactic plane, while older ones have had time to migrate away from the plane and fade in luminosity, so that the distribution in distance z from the plane may differ for different ranges of P and L . An initial trial model that ignores this evolution is clearly inadequate, and a second stage is necessary in which pulsars migrate from the plane as they age and decrease in luminosity. It will also be necessary to consider a possible evolution of magnetic field strength and inclination of the polar angle α . The model distributions derived in the first stage may be regarded as a snapshot of an evolving population. The later stages may be termed a dynamic model, which starts with the origin of neutron stars in a population of progenitor stars and their subsequent evolution, including the effect of their high spatial velocities. Chakraborty and Bagchi (2020) derive the population of normal pulsars in the Galaxy from such an analysis. These dynamic analyses incorporate further parameters beyond those in the snapshot model, enabling the analyses to achieve a close match with the observed population statistics. It should be noted, however, that the modelling and matching process is not a direct deduction from observations, and the statistical significance of derived parameters must be treated with caution. See further references to population synthesis in Popov *et al.* (2010).

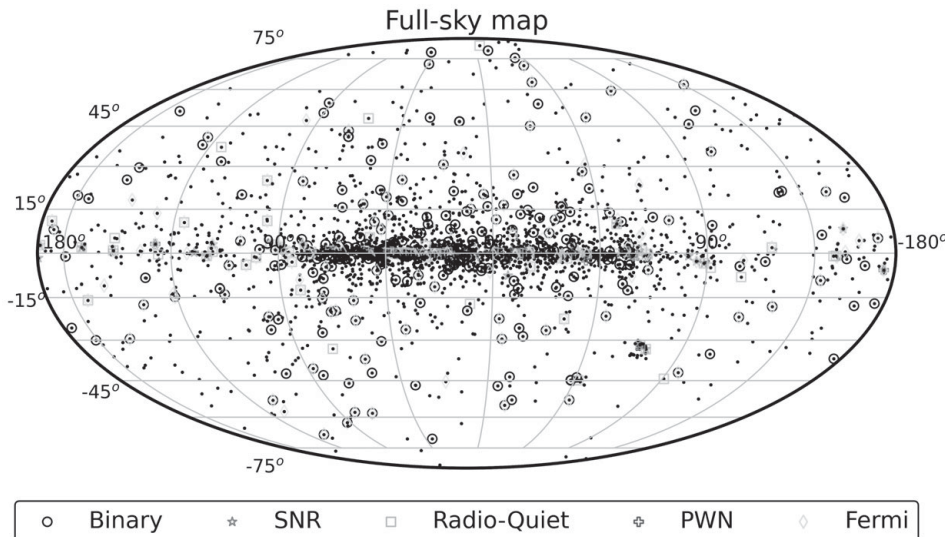


Figure 4.1 Distribution on the sky of all normal pulsars known in 2020, in Galactic coordinates l, b , showing the concentration along the plane of the Milky Way (based on a plot by L Vleeschouwer Calas).

4.3 The Observed Distribution of Normal Pulsars

Figure 4.1 shows the distribution on the sky of the 1600 normal pulsars detected in the various surveys. The plot is in Galactic coordinates, and the concentration of pulsars along the Galactic plane is clear. The depth of coverage is, however, far from uniform over the sky; in particular, the deep Parkes (PMBS, HTRU) and Arecibo (PALFA) surveys have been largely confined to low Galactic latitudes. The concentration of pulsars observed near Galactic longitude 50 deg is due to some deep Arecibo surveys, which covered a strip of sky crossing the Galactic plane at this longitude. In earlier surveys, pulsars towards the centre of the Galaxy were observed with reduced sensitivity due to the high Galactic background noise and interstellar scattering in this direction (Section 4.7); short period pulsars were particularly affected.

Given the distances, found primarily from their dispersion measures, we can explore the distribution of observed pulsars projected onto the Galactic plane. Figure 4.2 shows this projection for pulsars at low Galactic latitudes ($|b| < 20$ deg). As expected, the inverse square law has a very large effect on the apparent distribution on the plane; in particular, the true distribution towards the Galactic centre is very poorly sampled.

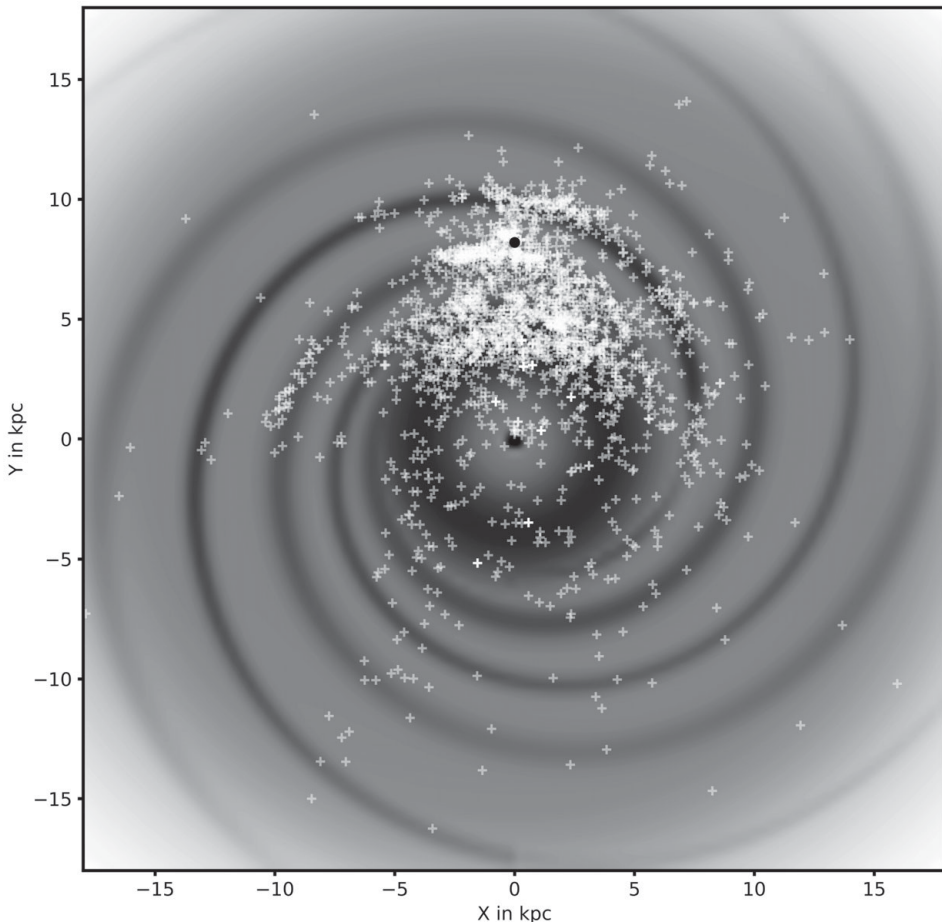


Figure 4.2 The positions of pulsars (known in 2020) at low Galactic latitude ($|b| < 20$ deg), projected onto the plane of the Galaxy. The Galactic centre is at the centre of the diagram. The observed pulsars are clustered round the Sun (black dot), assumed to be at a distance of 8.2 kpc from the centre, i.e. at $(0, 8.2)$ in this figure. The spiral structure underneath is from the YMW16 model for the distribution of electrons in our Galaxy (Based on a figure from A. Basu).

The concentration in the Galactic plane is seen in the distribution in z , the distance from the plane (Figure 4.3). Again, most of the pulsars in this plot are in the vicinity of the Sun, although there is no indication that the scale of the approximately exponential fall with z is different closer to the Galactic centre.

The true population must now be evaluated by taking into account the inverse square law and the other selection effects peculiar to the various surveys. Separate

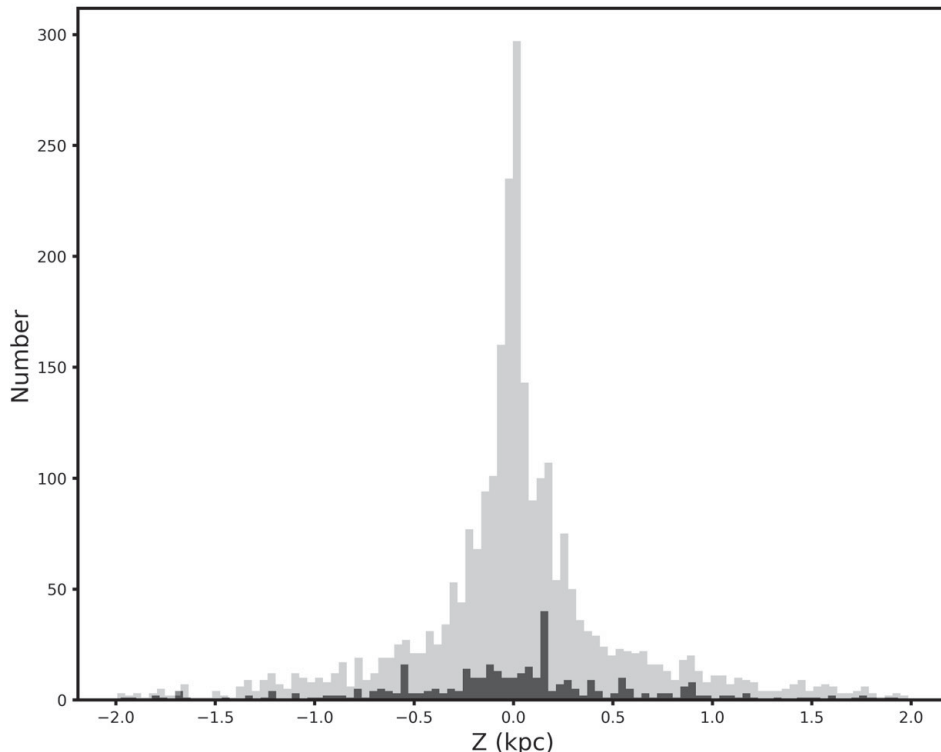


Figure 4.3 The distribution of observed pulsars located at a distance z from the Galactic plane. The darker bars show the millisecond pulsars.

analyses must be made for some different categories of pulsars; for example, millisecond pulsars have distinct distributions in velocity and distance from the Galactic plane.

The last, and richest, set of observed pulsar characteristics is the plot of pulse period P against its derivative \dot{P} , shown in Figure 4.4. The distinct group of millisecond pulsars require a separate analysis of location within the Galaxy, but their descent from the population of normal pulsars is understood and has been incorporated into several dynamic models, from Story, Gonthier and Harding (2007) onwards.

4.4 The Derived Luminosity and Spatial Distributions

In the trial model distributions in radial distance R , distance from the plane z and luminosity L , $\rho_R(R)$, $\rho_z(z)$ and $\rho_L(L)$ may initially take any simple form. Monte Carlo techniques are used to populate the models with individual pulsars, each of which must be subjected to the selection effects of the surveys. The resulting spatial

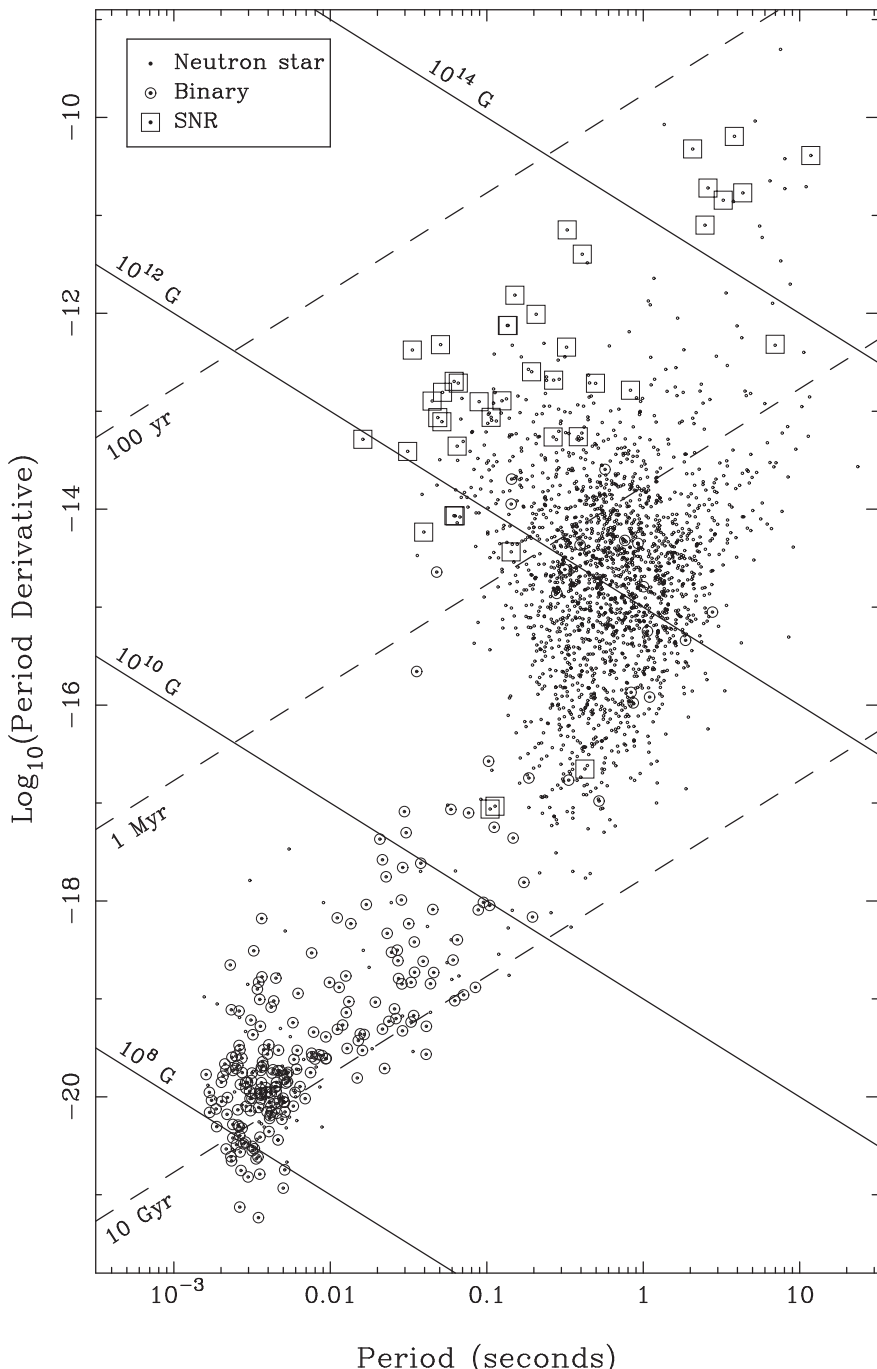


Figure 4.4 The $P - \dot{P}$ diagram for the known neutron-star population, showing those associated with supernova remnants (boxes) and those with binary companions (circles). Lines of constant magnetic dipole field strength (solid) and constant characteristic age (broken) are shown.

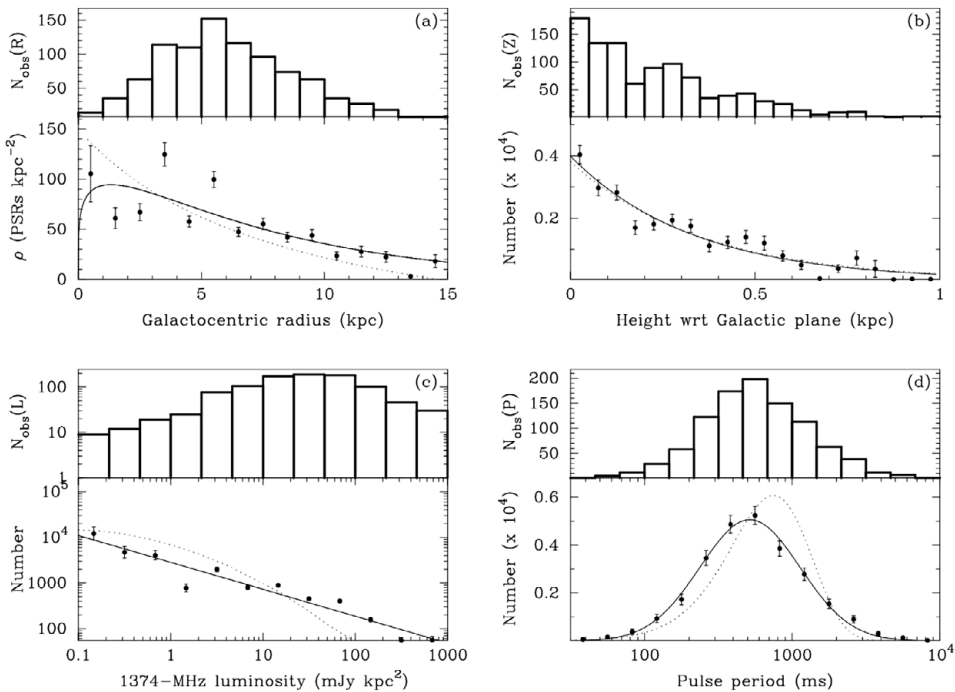


Figure 4.5 The derived distributions $\rho_R(R)$, $\rho_z(z)$, $\rho_L(L)$ and $\rho_P(P)$ in radial distance R , distance $|z|$ from the Galactic plane $\rho_R(R)$ from the Galactic centre, luminosity L and period P in units of number density kpc^{-3} . The distributions of the total numbers $N_R(R)$, $N_z(z)$, $N_L(L)$ and $N_P(P)$ actually observed at around 1.4 GHz are shown above (Lorimer *et al.* 2006b). The solid curves are smooth analytic functions fitted to the derived distributions. The dotted curves show: (a) the assumed radial density distribution of electrons from NE2001; (b) an exponential z distribution with scale height 180 pc; (c) a log-normal fit to the optimal population model derived by Faucher-Gigu  re and Kaspi (2006); (d) a parent period distribution used by Kolonko *et al.* (2004) in a study of pulse-width statistics.

and intensity distributions are compared with the observed distributions, and the parameters of the model are then progressively adjusted to find a best fit with the observations. The derived best-fitting distributions in R , z and L for normal pulsars (from Lorimer *et al.* 2006b) are shown in Figure 4.5 along with the distributions as observed. The distribution in period $\rho_P(P)$ is assumed to be the same as the observed distribution.

The radial distribution shows an increasing density towards the centre of the Galaxy (but see Section 4.7) and falling off towards the Galactic anticentre, as expected for supernova events and the massive Population I stars that are their likely progenitors. The large uncertainty and apparent lack of pulsars for $R < 4$ kpc arises

mainly because of the small number of pulsars detectable in that region (Figure 4.5), due to the large distance from the Earth as well as to other possible observational problems to which we will return in Section 4.7. The surface density, projected onto the Galactic plane at the radial distance of the Sun, is about 30 ± 6 observable pulsars per square kiloparsec with luminosity $L_{1.4}$ greater than 1 mJy kpc 2 (Lyne *et al.* 1998).

An empirical fit to the surface density is given by Lorimer *et al.* (2006b):

$$\rho(R) = A \left(\frac{R}{R_\odot} \right)^B \exp \left(-C \left[\frac{R - R_\odot}{R_\odot} \right] \right), \quad (4.1)$$

where R_\odot is the distance of the Sun from the Galactic centre, with values $A = 41(5)$ kpc $^{-2}$, $B = 1.9(3)$, $C = 5.0(6)$. The bracketted numbers are the statistical errors in the last digit; there may also be additional errors in distances due to the unknowns and irregularities in distances obtained from the model electron distribution NE2001 (see Chapter 7).

The z -distribution falls off approximately exponentially above and below the plane with scale height 330 pc. Lorimer *et al.* point out, however, that the scale height is very sensitive to the model electron distribution; a model that differs only slightly gave a value of 180 pc. The difference lies in the detailed description of electron density in the solar neighbourhood. At 330 pc, this is a wider distribution than those of most Galactic Population I objects, which have scale heights of order 50–100 pc; we see later that this is to be understood in terms of the high observed pulsar velocities.

The distribution in luminosity is shown in equal intervals of $\log L$. Over more than three decades, the distribution fits the empirical law

$$\log N = F \log L + G, \quad (4.2)$$

where $F = -0.77(7)$, $G = 3.5(1)$. The sensitivity of the surveys is as yet insufficient to show how the population falls below this law at low luminosities, as it must since the integration that gives the total population would otherwise be divergent for low luminosities. Even so, we have virtually no information on the underlying population of pulsars with luminosities below 0.1 mJy kpc 2 .

The result of integrating over the whole Galaxy gives an estimate of 30,000 observable pulsars with luminosity $L_{1.4} \geq 0.1$ mJy kpc 2 , within a statistical accuracy of 40%. The total number of active pulsars is larger than the total number observable by a factor depending on the angular width of the pulsar radio beam. An analysis by Tauris and Manchester (1998) shows that for normal pulsars this factor must be approximately five (see Chapter 16); we deduce that the total number of active pulsars is 150,000 for $L_{1.4} \geq 0.1$ mJy kpc 2 .

It should be noted that the pulsars actually observed from Earth consist mainly of high luminosity objects, having a mean luminosity about 10–100 times that of most of the Galactic population. Out of the large population of low luminosity pulsars, only a few that are close to Earth are observable. Overall only about 1% of pulsars with luminosity $L_{1.4} \geq 0.1$ mJy kpc² have been detected.

4.5 Pulsar Velocities and Ages

The large scale height in z -distance, which may be as much as 600 parsecs, as contrasted with much smaller values for massive stars and supernova remnants, was explained by Gunn and Ostriker (1970); they suggested that pulsars are runaway stars that have moved large distances since their birth. As described in Section 5.6, a large proper motion for PSR B1133+16 was found from timing observations by Manchester, Taylor and Van (1974), and direct interferometry measurements by Lyne, Anderson and Salter (1982) showed that transverse velocities between 100 and 200 km s⁻¹ were usual; an improved distance scale now gives even larger values (Lyne & Lorimer 1994).

Proper motions have been measured for over 250 pulsars by interferometry and by radio timing. Figure 4.6 shows the velocities of 52 pulsars plotted in Galactic coordinates. For the majority, the velocities are directed away from the plane, entirely confirming the Gunn and Ostriker suggestion. Pulsar speeds, that is the magnitude of the transverse component of velocity but not its direction, can also be measured by observing the speed of a scintillation pattern across the Earth, as described in Chapter 19. This was first achieved using spaced receiver observations (Galt & Lyne 1972) and later from scintillation rates observed at a single radio telescope (Lyne & Smith 1982). Although necessarily less accurate than the interferometer measurements, the results provide a useful extension of the data on velocities. The main problem in interpretation is that scintillation rates depend on the distribution of ionised clouds along the line of sight to the pulsar; Harrison and Lyne (1993) showed that the assumption of uniform distribution along the line of sight led to an underestimate of speeds for pulsars located away from the Galactic plane.

Lyne and Lorimer (1994) used interferometer measurements (Lyne *et al.* 1982; Bailes *et al.* 1990; Fomalont *et al.* 1992; Harrison *et al.* 1993) supplemented by scintillation data (Cordes 1986) to show that the mean space velocity at birth for a total sample of 99 pulsars was 450 km s⁻¹. Hobbs *et al.* (2005) compiled proper motion measurements for 233 pulsars and found an rms velocity of 400 ± 40 km s⁻¹ (these are three-dimensional velocities; most actual measurements are, of course, of two-dimensional velocities, and an isotropic distribution of velocities is assumed).

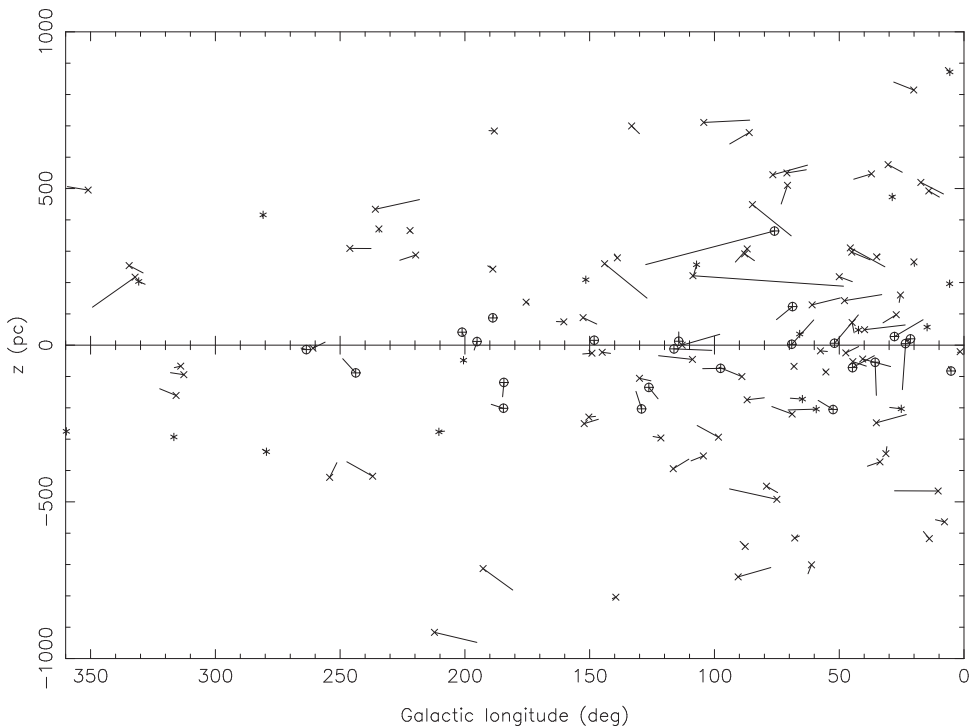


Figure 4.6 The measured velocities of pulsars, showing the general movement away from the Galactic plane. The symbols show the present position (in z -distance and Galactic longitude), and the tails show tracks of their motion in the last million years (Hobbs *et al.* 2005). With two exceptions, those outside the progenitor layer of Population I stars are predominately moving away from the plane with high velocity.

It is interesting that the velocities of about a quarter of the Galactic population of pulsars exceed 500 km s^{-1} , large enough to escape the gravitational field of the Galaxy and to end up in intergalactic space. Many of the others will end up in a large Galactic halo with a radius of several tens of kiloparsecs. At a velocity of 500 km s^{-1} , a pulsar will travel a distance of about 1 kpc in 2 Myr, the typical age of an active normal pulsar. The general migration seen in Figure 4.6 is consistent with this – we only see pulsars for a few million years, during the first part of their journey into the halo or into intergalactic space, after which time they fade and cease being detectable radio emitters.

If, as seems reasonable, all these pulsars were born close to the Galactic plane, their present ages can be found by extrapolating their velocities back to the plane. Such ‘kinetic ages’ can then be compared with the characteristic ages $\tau_c = P/2\dot{P}$ obtained from their present rate of slowdown. Figure 4.7 shows this comparison.

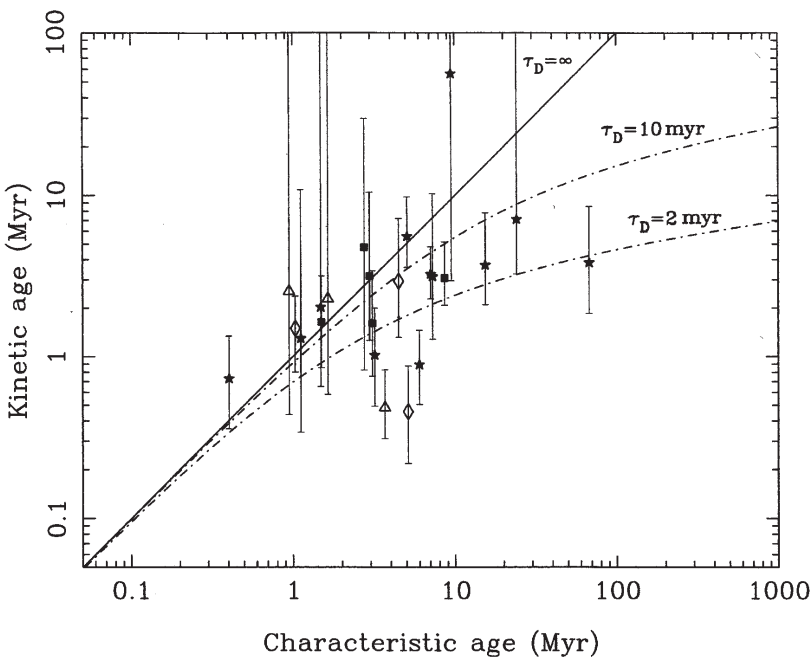


Figure 4.7 The characteristic ages of pulsars compared with their ‘kinetic’ ages derived from their velocities and distances from the Galactic plane. The solid line is the expected track of pulsars with constant magnetic dipolar field, while the broken lines indicate tracks if the magnetic field decays on timescales of 2 Myr and 10 Myr. (Harrison, Lyne & Anderson 1993).

The simple conclusion is that the agreement is satisfactory for young objects, but for the small number of observed older ones, the real ages are less than the characteristic ages, the discrepancy increasing with age. This effect has been the subject of much discussion. One possibility is that it is a result of the decay of the dipole magnetic field with age. This would cause a decrease in the slowdown rate, \dot{P} , with a corresponding increase in the measured characteristic age. It now appears, however, that the comparative lack of high velocity pulsars among the older population in Figure 4.7 may be the result of observational selection; such pulsars move away from the Galactic plane so fast that they soon become unobservable from the vicinity of the Sun (Harrison, Lyne & Anderson 1993; Lorimer, Bailes & Harrison 1997).

4.6 The Population of Millisecond Pulsars

The early surveys that were used in determining the pulsar population were unable to detect pulsars with periods of only a few milliseconds. Although the birthrates of millisecond pulsars are expected to be much lower than for normal pulsars, their

characteristic ages are typically much greater than the ages of the normal population; it is possible that a considerable population of millisecond pulsars might exist undetected. Recent surveys have addressed this problem, but the population data are still limited: most of the millisecond pulsars at present catalogued are either at a distance of less than 3 kpc or in globular clusters. The distribution on the sky of millisecond pulsars that lie outside the globular clusters shows only a mild concentration towards the Galactic plane, in contrast to the distribution of normal pulsars. It is, however, possible that many more millisecond pulsars (MSPs) exist away from the plane, but are not observable because they are older and their magnetic fields have either decayed or the dipole has become more closely aligned with the rotation axis (Rajwade *et al.* 2018).

Defining MSPs to have periods of less than 30 milliseconds, more than 300 have been discovered in radio and gamma-ray surveys, half of which are in globular clusters. An early analysis by Lyne *et al.* (1998) gave a projected density on the Galactic plane of $28 \pm 12 \text{ kpc}^{-2}$, to be compared with a projected density of $156 \pm 31 \text{ kpc}^{-2}$ for normal pulsars. The lower limit of luminosity in these analyses was 1.0 mJy kpc^2 at 430 MHz. The scale height found by Lyne *et al.* was $z_0 = 500 \text{ pc}$; but subsequent surveys have found more millisecond pulsars close to the Galactic plane, leading to a lower estimated scale height. Figure 4.2 shows the distribution in scale height; note, however that many surveys are biased towards the plane, and the scale height is not well established (see also Cordes & Chernoff 1997).

The observation that the velocities of MSPs are considerably lower than those of normal pulsars is consistent with this lower scale height. The analysis by Lyne *et al.* (1998) suggested that the total population of MSPs in the Galaxy is of order 30,000, remarkably similar to that of normal pulsars before any correction for beaming is applied. The beaming factor for MSPs is very uncertain; the best estimate is about 2 (Lorimer 2013), leading to a total number of active MSPs in the Galaxy of 60,000.

The characteristic ages of these MSPs are typically a few Gyr (10^9 years). The birthrate is likely therefore to be of order one per 10^4 – 10^5 years, very much less than for the normal pulsars. In Chapter 10, we consider the relation of this birthrate to the rate of formation of low mass x-ray binaries (LMXBs).

4.7 The Galactic Centre Region

The noise level in a radio telescope looking towards the Galactic plane is increased by the high level of the background radiation. This partly accounts for the poor statistics seen at small distances R from the Galactic centre in Figure 4.5. The population near the Galactic centre itself is hard to determine; the central region is comparatively small in volume and is at a large distance, so that only a small number

of pulsars will be above the limits of observability. Another important factor is the large effect of interstellar scattering. Many pulsars seen in the plane near the centre are expected to suffer from pulse broadening as well as high dispersion (Chapter 19). The test of this hypothesis was to observe at a higher frequency, since the length of pulse smearing varies inversely as approximately the fourth power of the frequency.

The survey carried out at Jodrell Bank, at 1.4 GHz, of the central regions of the Galactic plane (Clifton & Lyne 1986) showed that the hypothesis is correct. In a small area of only 200 deg² along the Galactic plane, defined by $0 < l < 100$ deg, $0 < |b| < 1$ deg, this survey discovered 40 new pulsars (Clifton *et al.* 1992), none of which had been found in the contemporary 400 MHz survey. A similar high radio frequency survey (Johnston *et al.* 1992) of the southern Galactic plane using the Parkes radio telescope discovered 45 new pulsars. The main penalty of observing at this higher frequency is that the area of sky surveyed by the single beam of a telescope is reduced by an order of magnitude compared with 400 MHz. These results led to the development of a multibeam system at 1400 MHz in the major Parkes Multibeam Surveys, which subsequently discovered over 1000 pulsars.

A cluster of pulsars has now been discovered within 15 arcminutes of the Galactic centre object Sag A* (Johnston *et al.* 2006; Deneva *et al.* 2009). This concentration of five pulsars is far in excess of the number expected in the general population, and it is evident that they are bound gravitationally to the super-massive black hole at this location. They all have long periods (four greater than 900 ms), and they were all detected at high frequencies (2–3 GHz). It is very likely that shorter period pulsars exist in this cluster, which would not have been found, especially at lower radio frequencies, because of interstellar scattering.

Although there is a known large concentration of stars within 30 arcseconds of Sag A*, no pulsars have yet been discovered in this very interesting location. Possible reasons, including scattering and free-free absorption, are discussed by Rajwade *et al.* (2017).

Further from the Galactic centre, but still within an angular distance of 2 deg, five pulsars have been studied by Perera *et al.* (2019a), four of which are short period pulsars in binary systems. Their measured period derivatives indicate that they are accelerating towards us in the Galactic gravitational field and hence are located beyond the centre. They have high dispersion measures, but not as high as expected from current models. There is evidently much remaining to be discovered about the centre and its surroundings.

4.8 The Pulsar Birthrate

The concentration of young pulsars towards the Galactic plane, and the high velocity of migration away from the plane, show that the distributions $\rho_R(R)$, $\rho_z(z)$ and $\rho_L(L)$ are not independent. The link between them is pulsar age; as pulsars move

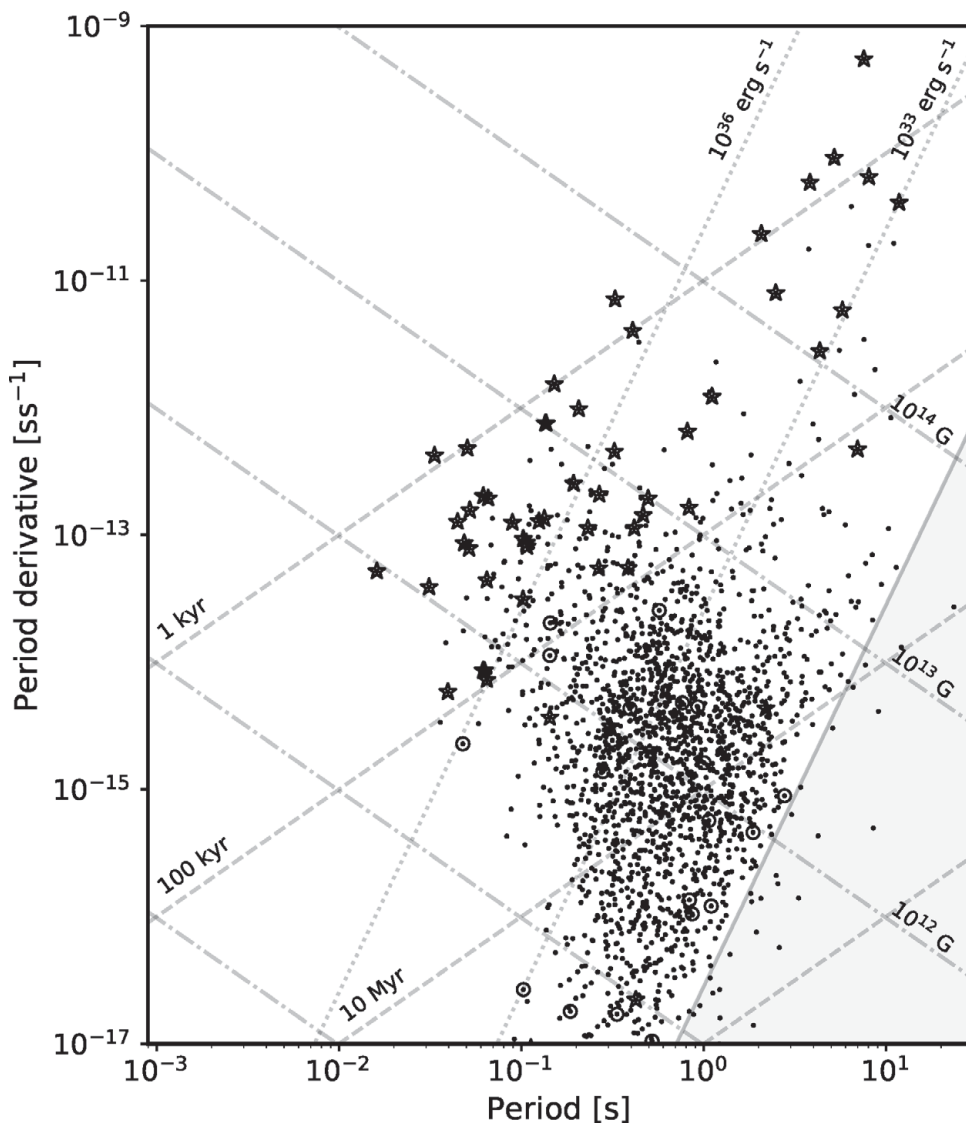


Figure 4.8 The $P - \dot{P}$ diagram for normal radio (non-millisecond) pulsars and magnetars. Young pulsars that are still associated with SNRs are encompassed by star symbols and binaries with circles. Lines of constant magnetic dipole field (dot-dashed), characteristic age (dashed) and spin-down energy (dotted) are shown. The solid line is a plausible death line from Ruderman and Sutherland (1975).

from a birthplace near the plane, their luminosities decay, so that the main link is between $\rho_z(z)$ and $\rho_L(L)$. Unfortunately, the relation between luminosity and age is not yet known in any detail, although the comparative lack of pulsars with long periods on the right-hand side of the $P - \dot{P}$ diagram (Figure 4.8) shows that there is a large decay, leading to extinction.

In the $P - \dot{P}$ diagram, individual pulsars migrate towards increasing P and decreasing \dot{P} ; assuming a constant magnetic dipole field, the migration will follow a line of constant $P\dot{P}$, as shown. If all pulsars start life with a small P , the density of pulsars along this path in the diagram depends primarily on the evolution of their luminosities. This evolution has been represented in several empirical analyses as an exponential decay, followed by a cut-off at a ‘death line’.

Without a clear understanding of the radio emission process, there can be no proper model of luminosity as a function of P and \dot{P} . Leaving aside a possible evolution of the dipole field strength B , the simplest assumption is that luminosity is related to the rate of loss \dot{E}_{rot} of rotational kinetic energy, that is to $P\dot{P}^{-3}$ or to BP^{-2} . The exact relation is unknown: in fact the result of the analysis may reveal or at least constrain the possible relationship. A death line given by a minimum value of $BP^{-2} = 0.17 \times 10^{12} \text{ G s}^{-2}$ (Ruderman & Sutherland 1975) is shown in Figure 4.8; this appears to be a boundary for observable pulsars, although it is not precise and categoric. The decay of luminosity from birth to the death line has been represented by empirical laws derived from the observations by Stollman (1986), in which $L \propto \dot{E}^{1/2}$, and by Narayan (1987) in which $L \propto \dot{E}^{2/3}$. These laws have been used, for example, by Bhattacharya *et al.* (1992), Wakatsuki *et al.* (1992), Hartman *et al.* (1997), Mukherjee and Kembhavi (1997), Tauris and Konar (2001) and by Gonthier *et al.* (2002) in constructing model populations with $P - \dot{P}$ diagrams for comparison with the observed distribution. Further consideration should also be given to the place of magnetars in the evolutionary sequence; in Section 11.5.2, we discuss the possibility of rapid changes in magnetic field in these very active young pulsars.

Although these analyses generally agree that the distribution can be represented by a luminosity that decays exponentially with BP^{-2} , reaching a cut-off that also depends on BP^{-2} , the exact law remains unknown. We note in Chapter 17 that a different law may be applicable to young pulsars up to an age of 10^5 years; for the youngest pulsars, the average luminosity is practically independent of age.

The lifetime of the main population of pulsars, of the order of 10 million years, is so small compared with the age of the Galaxy that we can assume a constant birthrate of pulsars, providing a steady population subject only to statistical fluctuations. The best way of determining their birthrate is to track their movement across the $P - \dot{P}$ diagram (Figure 4.8). Across each interval from P to $P + \delta P$, there is a ‘current’ of pulsars (Phinney & Blandford 1981) determined by their values of \dot{P} . The current $J(P)$ is defined as:

$$J(P) = \frac{1}{\delta P} \sum_{i=1}^{N_{\text{psr}}} \dot{P}_i. \quad (4.3)$$

If all pulsars start life with small periods, the current will be constant until pulsars drop out at the right of the diagram. The current is poorly determined in individual intervals, but it is reasonably constant for periods up to about 1 s. The current falls at longer periods, showing that most pulsars cease to radiate between here and $P = 4$ s. The analysis is complicated by the possibility that pulsars are not all born with short periods, and some are ‘injected’ into the diagram with longer periods. The current then depends on a combination of injection and the slowdown law, which may vary with P and \dot{P} (see Faucher-Gigu  re and Kaspi (2006) and Vranešević and Melrose (2011)). Bearing in mind this difficulty, we may take the results of the Parkes Multibeam Survey (Lorimer *et al.* 2006b) to obtain an average value of the current at short periods to give the birthrate of all pulsars.

The analysis is necessarily heavily weighted towards the pulsar population in the vicinity of the Sun, and it can only apply to pulsars with luminosity above a lower limit. Lyne *et al.* (1998) found a birthrate integrated through the Galaxy by assuming that the radial distribution is the same as that of Population I stars. Multiplying by five for the beaming factor, they found that to sustain the observed population with $L_{400} > 1$ mJy kpc² requires the birth of 1 pulsar every 60–300 years.

This result is comparable with the rate of supernovae in the Galaxy. Clark and Caswell (1976) surveyed the supernova remnants and their ages, concluding that they must have formed at the rate of 1 per 150 yr. From the historical records, Clark and Stephenson (1977) found a higher rate of supernovae, about 1 per 30 years. Blaauw (1985) points out that this is a high rate in relation to the evolution of the known population of stars; for example, the evolution of all stars with mass greater than $9M_{\odot}$ would provide a supernova rate of 1 per 50 years (see also a discussion in Chapter 18). Bearing in mind that not all supernovae may leave either a pulsar or an observable remnant, the statistics show that most if not all radio pulsars were born in supernova explosions. We consider the populations of other neutron stars, such as x-ray pulsars and magnetars, in Chapter 11.

4.9 Gamma-ray Pulsars

The first decade of Fermi LAT gave us a remarkable catalogue of pulsars that emit gamma rays. Some of these are also observed as TeV sources by Cerenkov shower telescopes, and there is a good prospect that many more of these will be discovered when the large Cerenkov telescope arrays come into operation. Are any of these high-energy (HE) pulsars a distinct population, which adds to the total of active neutron stars?

At the time of writing, about 250 pulsars have been detected as gamma-ray emitters, with the majority, around 80%, also known or subsequently discovered to be

radio emitters. A regularly updated catalogue¹ shows that the population currently (in 2020) consists of 135 young pulsars and 118 millisecond pulsars. In both cases, approximately 50% of them were identified by folding the gamma-ray photons with the known pulsar ephemerides. Approximately 60 of the young pulsars were discovered through searching for pulsations of sources identified in the gamma-ray images, and only a handful of those have subsequently been shown to be radio emitters. Many of the millisecond pulsars have been identified through radio searches of gamma-ray-identified targets, and some have subsequently been shown to exhibit pulsed gamma rays too. Remarkably, six millisecond pulsars were first detected as pulsed gamma-ray sources directly from their gamma rays (e.g. Clark *et al.* 2018) (some of these searches used computational power donated by volunteers through the Einstein@Home project), and two remain undetected as radio emitters. There remain quite a large number of unidentified gamma-ray sources that are likely to be pulsars, and searches are ongoing. It is also predicted that the gamma-ray excess seen towards the centre of the Galaxy is due to an as yet undiscovered population of gamma-ray-emitting millisecond pulsars.

There are evidently two gaps in the close relation between gamma and radio pulsars. First, among the normal pulsars, only the young pulsars emit gamma rays; this may simply be a consequence of the lower spin-down energy of older normal pulsars. Secondly, there is evidently a sizeable sample of gamma-ray pulsars that are not observable as radio pulsars; the famous example is Geminga (Jackson *et al.* 2002). This is explicable as a geometric effect of emission beamwidths, since the radio beams are often narrower and may be directed away from us. They have only a small effect on our estimates of pulsar population. In the case of millisecond pulsars, to date there are fewer systems which are undetected as radio emitters, and this is probably due to their lower beaming fraction – that is, they have wider beams.

¹ <https://confluence.slac.stanford.edu/display/GLAMCOG/Public+List+of+LAT-Detected+Gamma-Ray+Pulsars>

5

Pulsar Timing

Astrophysics provides many examples of rotating and orbiting bodies whose periods of rotation and revolution can be determined with great accuracy. Within the Solar System, the orbital motion of the planets can be timed to a small fraction of a second, while the rotation of the Earth is used as a clock that is reliable to about one part in 10^8 per day. Outside the Earth there is, however, no other clock with a precision approaching that of pulsar rotation.

The arrival times of the radio pulses from pulsars are easy to study, and a surprising amount can be learned from them. Not only do they provide information on the nature of the pulsed radio source; they can also give an accurate position for the source, and they can explore the propagation of the pulses through the interstellar medium. All three kinds of information were noted by Hewish and his collaborators in the discovery paper of 1968. They showed that the narrowness of the pulses, and their short and precise periodicity, implied that the source was small and that it might be a rotating neutron star. They showed also that the pulse period was varying because of the Doppler effect of the Earth's motion round the Sun; this annual variation implied that the source lay outside the Solar System. Finally, they showed that the arrival time of a single pulse depended on radio frequency; this dispersion effect was found to be in accord with the effect of a long journey through the ionised gas of interstellar space.

Arrival time measurements now provide precise information on rotational slowdown and on the orbits of binary pulsars; they have also made possible some fundamental tests of general relativity and gravitational radiation, and provided time standards with stabilities challenging that of the best atomic clocks.

The following sections are intended to provide an introduction and explanation of the main steps in relating the observed time of arrival (TOA) of a pulse to the time of emission at a pulsar. The accuracy of observations now demands a complex analysis involving parameters of Earth rotation, solar system dynamics, interstellar propagation and pulsar dynamics, including the characteristics of binary pulsars. A standard

analysis system, TEMPO, which has been developed and used by many observatories since 1972, incorporates all these, allowing a best fit to be made to the position and many other characteristics of the well-observed pulsars. The accuracy of this process of data reduction, and a similar comprehensive package TEMPO2,¹ must match an accuracy of timing observations approaching 10 nanoseconds, requiring an accuracy of 1 ns in all the geometric and relativistic aspects (Edwards, Hobbs & Manchester 2006).

5.1 Pulsar Positions and the Earth's Orbit

Since the time of Römer, who made observations of the motion of Jupiter's satellites when the Earth was at different positions in its orbit, it has been known that light takes about $8\frac{1}{2}$ minutes to travel from the Sun to the Earth. Pulses from a pulsar lying in the plane of the ecliptic will therefore arrive earlier at the Earth than at the Sun when the Earth is closest to the pulsar, that is, when it is at the same heliocentric longitude. Six months later, the pulses will arrive late by the same amount. Assuming for simplicity that the Earth's orbit is circular and centred on the Sun, the delay t_c is given by

$$t_c = A \cos(\omega t - \lambda) \cos \beta, \quad (5.1)$$

where A is the light travel time from Sun to Earth, ω is the angular velocity of the Earth in its orbit and λ, β are the ecliptic longitude and latitude of the pulsar (Figure 5.1a).

The observed arrival times of pulses emitted by a pulsar at equal time intervals throughout the year will therefore show a sinusoidal variation as in Figure 5.1b, where the phase of the sine wave is determined by the heliocentric longitude and the amplitude by the heliocentric latitude of the pulsar. The angular accuracy of the positions so determined is greatest near the pole of the ecliptic, since the ecliptic latitude β is poorly determined near $\beta = 0$. An error in the assumed coordinates $\delta\lambda, \delta\beta$ gives rise to periodic timing errors

$$\delta t_c = +A \cos \beta \delta \lambda \sin(\omega t - \lambda) - A \sin \beta \delta \beta \cos(\omega t - \lambda). \quad (5.2)$$

Fitting such a model to the variation of pulse arrival times through a year gives positions that are remarkably accurate. Depending on the pulse shape, it is usually possible to obtain an arrival time after a few minutes of integration to a precision of about one milliperiod; for example, a pulsar with a period of about 1 s can give a point on the timing curve with an accuracy of about 1 ms. At least four such observations through one year are needed to find the source position, but the result

¹ www.atnf.csiro.au/research/pulsar/tempo2.

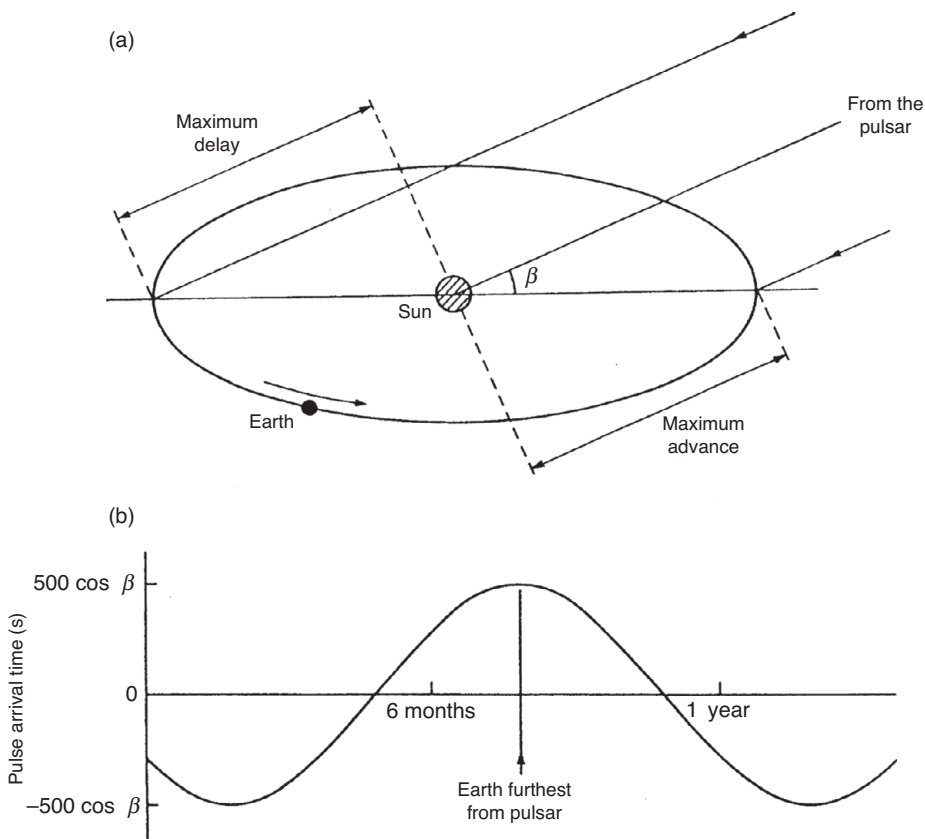


Figure 5.1 The Römer delay. (a) The annual variation in pulse arrival time due to the Earth's orbital motion round the Sun. (b) The amplitude of the variation is $500 \cos \beta$ s, where β is the ecliptic latitude of the pulsar. The phase of the sinusoid is used to determine longitude.

is a position accurate to better than 1 arc second, and positions have therefore been obtained from timing observations for most of the known pulsars. In the case of a 10 ms period pulsar, we can determine the position to 10 milliarcseconds or better, which allows one to identify optical companions and high energy counterparts even in the crowded regions of the Galactic plane. The application of the method requires consideration of the following details:

1. Rotation of the Earth introduces a variable time increment relative to the centre of the Earth of up to the light transit time over one Earth radius (21 ms).
2. The Earth's orbit is elliptical, not circular.
3. The Sun moves in relation to the centre of inertia of the Solar System, known as the *barycentre*, which moves essentially uniformly through space and is therefore a convenient inertial frame of reference. The Sun's motion around the barycentre

- depends upon the orbital motion of the planets, mainly the massive planet Jupiter; it is sufficiently large to place the barycentre just outside the surface of the Sun.
4. The gravitational potential at the Earth differs from the potential at a large distance from the Sun; furthermore, it varies annually through the ellipticity of the Earth's orbit. Einstein's general theory of relativity therefore predicts a small annual variation of Earth-bound clock rates, as compared with a reference clock in a circular orbit or outside the Solar System.
 5. The second-order Doppler effect, predicted by special relativity, varies as the square of the Earth's velocity: the variation of this effect due to the ellipticity of the orbit is in practice indistinguishable from the general relativistic effect in (4) above.
 6. There is a variable delay, predicted by general relativity, caused as the pulses pass through the gravitational potential well of the Sun; this *Shapiro delay* is the effect of the curvature of spacetime due to a massive object.
 7. The effective frequency of the radio receiver as observed in an inertial frame of reference varies through the year due to the Doppler effect of the Earth's motion. Since the arrival time depends on frequency, due to dispersion in the interstellar medium, a correction may be needed for timing observations of pulsars with high values of dispersion measure.

The task is to apply corrections to the observed times of arrival of pulses (TOAs) in order to give times that would have been observed at the barycentre of the solar system, so that they do not have the modulating effects arising from the Earth's motion. We can then study the intrinsic rotation of the pulsar and any effects of its orbital motion with a binary companion. Before corrections for these effects are considered, the local standard of time, usually a hydrogen maser, must be calibrated by reference to a standard set of caesium clocks. This is done using GPS satellite time transfer to an accuracy of about 10 ns. The time is then available on the uniform scale TAI (International Atomic Time).²

We group the components of the correction of pulse arrival times t to barycentric times t_b under four headings:³

$$t_b = t - \left(D \frac{DM}{v^2} + \Delta_{R\oplus} + \Delta_{E\oplus} + \Delta_{S\oplus} \right). \quad (5.3)$$

² The GPS provides Coordinated Universal Time (UTC), which differs from TAI by an integral number of seconds. Another time scale that may be encountered is Terrestrial Time (TT), which results from small retrospective corrections to TAI (Seidelmann & Fukushima 1992). Relevant resolutions by the International Astronomical Union are set out by Kaplan (2005). TEMPO2 uses TCB (Barycentric Coordinate Time); see Edwards *et al.* (2006).

³ In some papers, a fifth term $\Delta_{A\oplus}$ is added. This represents aberration due to the changing angular aspect of the rotating pulsar; it is, however, negligible in all practical circumstances.

Here $\mathcal{D}_{\nu^2}^{\text{DM}}$ is the dispersive propagation delay at radio frequency ν (see Section 3.1). $\Delta_{R\oplus}$ is the large geometrical term, which incorporates the classical geometry of the solar system; it may be termed the Römer delay, and it includes the effect of wavefront curvature, which can be used for determining parallax (Chapter 7). $\Delta_{E\oplus}$ is the Einstein delay due to gravitational redshift and time dilation, and $\Delta_{S\oplus}$ is the Shapiro delay due to the curvature of spacetime in the solar system. The subscript \oplus relates to the solar system; a similar set of terms without the subscript is used in relation to the orbits of binary pulsars (Chapter 6). In the next sections, we discuss these effects in more depth.

5.2 The Römer Correction to the Barycentre

In practice, the corrections incorporated in the Römer delay $\Delta_{R\oplus}$ are computed using an assumed pulsar position λ, β and an ephemeris that gives the vector distance \mathbf{r}_{ob} from the observer to the Solar System barycentre. This vector distance is the sum of the three vectors, \mathbf{r}_{oe} from the observer to the centre of the Earth, \mathbf{r}_{es} from the centre of the Earth to the centre of the Sun and \mathbf{r}_{sb} from the centre of the Sun to the barycentre:

$$\mathbf{r}_{\text{ob}} = \mathbf{r}_{\text{oe}} + \mathbf{r}_{\text{es}} + \mathbf{r}_{\text{sb}}. \quad (5.4)$$

Then the time t_c to be added to the observed time to give a barycentric arrival time is

$$t_c = -\frac{\mathbf{r}_{\text{ob}} \cdot \hat{\mathbf{s}}}{c}, \quad (5.5)$$

where $\hat{\mathbf{s}}$ is the unit position vector $(\cos \lambda \cos \beta, \sin \lambda \cos \beta, \sin \beta)$ of the source at λ, β , and c is the speed of light.

The three components of \mathbf{r}_{ob} are obtained separately. The vector \mathbf{r}_{es} is by far the largest and is available in terms of the astronomical unit; in practice it may be necessary to combine two ephemerides that give respectively the motion of the barycentre of the Earth–Moon system and the motion of the Earth within that system. The astronomical unit itself has been well determined as a light travel time from planetary radar observations and spacecraft transponders. The barycentric correction \mathbf{r}_{sb} is obtained from the vector positions \mathbf{r}_i and masses m_i of the Sun and planets (measured in units of the solar mass):

$$\mathbf{r}_{\text{sb}} = \frac{1}{1 + \sum m_i^{-1}} \Sigma (\mathbf{r}_i m_i^{-1}). \quad (5.6)$$

The Earth radius correction \mathbf{r}_{oe} may be computed directly as a light travel time, since it depends only on the radius of the Earth at the observatory and the source elevation E . At the mean radius of the Earth, the time correction is $21.2 \sin E$ ms.

The ephemerides of the planetary motions have been improved during the era of pulsar astrometry and continue to improve, mainly from observations of spacecraft on Mars and the Moon and from angular astrometry of the outer planets. The original radar measurements improved the accuracy of the astronomical unit by two orders of magnitude (Ash, Shapiro & Smith 1967), providing the ‘MIT’ ephemeris (named after the Massachusetts Institute of Technology), which was accurate to about 10 microseconds in planetary distances and 5 microseconds in the Earth–Sun distance. The astronomical unit was quoted as 499.004786 ± 0.000005 light seconds.

An independent and evolving ephemeris (Standish 1982), known as the DE 200 JPL ephemeris (named after the Jet Propulsion Laboratory), provided the planetary and lunar ephemeris for the Astronomical Almanac for the years 1984 to 2002. An improved version DE405 replaced it from 2003 (Standish 2004), and further improvements are incorporated in DE409. The best pulsar timing accuracies are in the region of 100 ns, which requires an accuracy of a few metres in the correction to the barycentre. At this level, the ephemerides can be expected to become out of date within only a few years, due mainly to the influence of the outer planets and minor solar system bodies. The improvement between DE200 and DE405 for pulsar timing was substantial, as first demonstrated by Splaver *et al.* (2005) in observations of the binary pulsar system PSR J1713+0747. The importance of up-to-date ephemerides in allowing for the detection of gravitational waves using pulsars has become very clear in recent years (see e.g. Lazio *et al.* 2018). A comprehensive review of astronomical reference systems by the International Astronomical Union has led to a series of resolutions in 1997 and 2000. These are explained by Kaplan (2005) in US Naval Observatory Circular 179, which includes discussions of relativity, time scales, precession and nutation, and Earth rotation.

5.3 The General Relativistic Corrections

General relativity gives rise to two components: time dilation, which affects the clock rate on Earth and the Shapiro delay $\Delta_{S\oplus}$ due to the passage of radiation through the curved spacetime in the Solar System.

The annual variation in the rate of an atomic clock on the surface of the Earth as it follows its elliptical orbit round the Sun was analysed by Clemence and Szebehely (1967). The differential relation between the time S shown by a clock on the Earth and coordinate time t shown by an identical clock at an infinite distance from the Sun is given by

$$\frac{dt}{dS} = 1 + \left(\frac{1}{r} - \frac{1}{4a} \right) \frac{2GM_\odot}{c^2}, \quad (5.7)$$

where r is the Earth–Sun distance, a is the semi-major axis of the Earth’s orbit, G is the gravitational constant and M_\odot is the mass of the Sun. The constant $2GM_\odot/c^2 = 2.95338$ km. (which is the Schwarzschild, or ‘event horizon’, radius

of a black hole of 1 solar mass). This equation takes account of the time-dilation of special relativity due to the Earth's orbital velocity and the gravitational redshift of general relativity, which depends on distance from the Sun. The major part of the difference from unity in Eqn. (5.7), amounting to a rate of 1.48×10^{-8} , is incorporated into the definition of atomic time, which refers to a standard clock in orbit at a constant distance a from the Sun. The variable part, due to the variation of r round the Earth's orbit, is a rate amounting to $3.3079 \times 10^{-10} \cos f$, where f is the 'true anomaly', that is, the angle between the least radius vector of the Earth's orbit (at perihelion) and the instantaneous vector. Since the orbit is elliptical, the true anomaly is slightly different from the 'mean anomaly' l , which increases uniformly with time. The integrated fractional difference between the atomic clock and the standard clock at any time is given by the integral

$$3.3079 \times 10^{-10} \int_0^l \cos f \, dl, \quad (5.8)$$

which contains a major term $\sin l$ and minor terms depending on the eccentricity e :

$$\int_0^l \cos f \, dl = \sin l + e \left(\frac{1}{2} \sin 2l - l \right) + \frac{3}{8} e^2 \left(\sin 3l - \frac{1}{3} \sin l \right). \quad (5.9)$$

The term $-el$ represents a constant rate error and is therefore absorbed into the definition of the standard clock; the result is a relativistic correction Δt_r , which is given to the nearest microsecond by:

$$\Delta t_r = 1.661 \sin l + 0.028 \sin 2l \text{ ms.} \quad (5.10)$$

The clock is correct on January 1, when $l = 0$ deg; the maximum error is approximately at $l = \pm 89$ deg, that is, on April 1, when the clock is slow, and on October 3, when the clock is fast. A more precise analysis by Blandford and Teukolsky (1976) gives the correction as

$$\Delta t_r = 1.66145 \left[\left(1 - \frac{e^2}{8} \right) \sin l + \frac{1}{2} e \sin 2l + \frac{3}{8} e^2 \sin 3l \right] \text{ ms.} \quad (5.11)$$

The effect of curved spacetime near the Sun was first pointed out by Shapiro (1964) as an angular deviation of a light ray. This also introduces a time delay, given to a good approximation by

$$\Delta_{S\oplus} = -\frac{2GM_{\odot}}{c^3} \ln(1 + \cos \theta), \quad (5.12)$$

where θ is the angle pulsar-Sun-Earth. This delay, known as the Shapiro delay, reaches a maximum of 120 microseconds when the line of sight is close to the Sun's limb (Hellings 1986). The effect of the planets is usually negligible: a line of sight

close to Jupiter would give a delay of only 200 ns. The Shapiro delay is important in binary pulsars (Chapter 6). A full discussion of this and other relativistic effects in pulsar timing is given by Backer and Hellings (1986).

5.4 Fundamental Positional Reference Frames

The two fundamental astrometric reference frames, ecliptic and equatorial, are based respectively on the Earth's orbit and on its rotation. The annual variation of pulse arrival times yields pulsar positions in ecliptic coordinates; conventional radio interferometer techniques and optical astrometry yield positions in equatorial coordinates. The poles of these two coordinate systems are inclined at the obliquity angle of $23\frac{1}{2}$ deg, and the intersection of their equatorial planes defines the direction of the vernal equinox. The relation between the Earth-rotation and the Earth-orbit frames has been known for some time to an accuracy of about 0.1 arcsecond; a comparison of interferometric and timing positions of pulsars now provides an independent measurement, with much improved accuracy.

This comparison was made initially for 59 pulsars with good timing positions and with interferometric positions measured on the VLA (the Very Large Array in New Mexico), with an accuracy of about 0.2 arcseconds (Fomalont *et al.* 1984); this confirmed the relation between the two systems. The dramatic improvements in timing accuracy achieved for millisecond pulsars (Kaspi 1995) give timing positions in ecliptic coordinates with an accuracy better than 0.1 milliarcseconds. This was matched in equatorial coordinates by VLBA interferometry on an individual millisecond pulsar (Bartel *et al.* 1996); such measurements have now been extended over the whole sky using VLBI, with an accuracy of around 40 microarcseconds (Ma *et al.* 2009). Similar accuracy is already achieved in radio astrometry on point-like extragalactic sources, providing a link between optical and radio coordinate systems; a further tie is now available using millisecond pulsars in binary systems with optically observable companions. A detailed discussion of the transformation between Earth-orbit (celestial) and Earth-rotation (terrestrial) systems can be found in IERS Technical Note 32 (McCarthy & Petit 2004) of the International Earth Rotation and Reference Systems Service. A comparison of pulsar positions measured in the two systems is given in Wang *et al.* (2017).

5.5 Periods and Period Changes

The analysis of the Römer delay and the effects of general relativity allow the observed times of arrival (TOAs) to be reduced to a time of arrival at the barycentre

of the Solar System. In order to model the arrival times, the period P and its rate of change \dot{P} are now required; these are conveniently obtained in terms of the pulsation frequency⁴ $\nu = P^{-1}$. Starting at a reference time t_0 , the expected pulse number N at an observed arrival time t is expressed as a Taylor series:

$$N = \nu_0(t - t_0) + \frac{1}{2}\dot{\nu}(t - t_0)^2 + \frac{1}{6}\ddot{\nu}(t - t_0)^3 + \dots \quad (5.13)$$

If the parameters in this Taylor series are correct, N is expected to be integral at the observed TOAs. The differences between observed and calculated values of N are usually expressed as differences in arrival times, when they are known as timing residuals; errors in the timing model or the assumed position will be revealed by systematic trends in the timing residuals. The forms of these residuals for various errors in the timing model are shown in Figure 5.2. It is then possible to employ a fitting process that involves the adjustment of the parameters to minimise the timing residuals over the whole run of observations using a least-squares fitting procedure.

All known pulsars, except the accreting x-ray pulsars, have the basic characteristics of an intrinsically precise period, modulated only by a slow monotonic increase in period due to a gradual loss of rotational energy. The change of period of the Crab Pulsar can be detected within a few hours, and the change for the Vela Pulsar within days, but generally the rate of change is so small that it can only be determined from observations over a period of a year or more. Furthermore, accurate positions of pulsars are usually only available from the timing observations themselves, so that an apparent change of period over a short observing time may be due only to an error in the assumed pulsar position. It may, alternatively, for a minority of pulsars be an indication that the pulsar is in a binary system. Careful analysis is required in order to decouple these competing effects. We note that the use of interferometers for searching (Chapter 4) will give more precise positions and thus can separate this covariance with position more rapidly.

The outstanding result from extended timing measurements on many pulsars is that the arrival times of the pulses are astonishingly regular. Discontinuities in frequency ν or its differential $\dot{\nu}$ are, however, commonly observed in young pulsars, notably the Vela Pulsar and the Crab Pulsar; many others show a low level of timing irregularity referred to as timing noise (Chapter 9). In contrast, the level of timing irregularities in many millisecond pulsars is so low that they approach the performance of the best available terrestrial time standards.

⁴ Note that pulsars are usually characterised by their periods P , while observers quote accurate values of rotation frequency $\nu = \frac{1}{P}$, and theorists often use angular velocities $\Omega = 2\pi\nu$. The following equations should provide the useful equivalents: $P = \frac{1}{\nu}$, $\dot{P} = -\frac{\dot{\nu}}{\nu^2}$, $\ddot{P} = \frac{2\dot{\nu}^2}{\nu^3} - \frac{\ddot{\nu}}{\nu^2}$, $\nu = \frac{1}{P}$, $\dot{\nu} = -\frac{\dot{P}}{P^2}$, $\ddot{\nu} = \frac{2\dot{P}^2}{P^3} - \frac{\ddot{P}}{P^2}$.

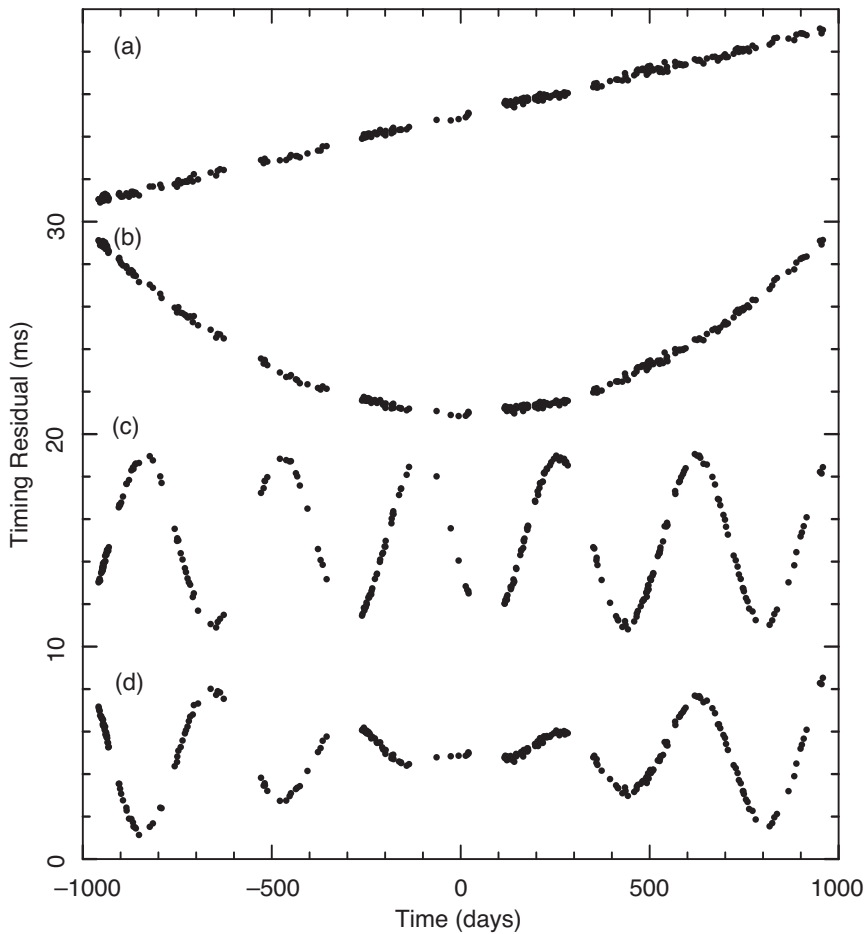


Figure 5.2 The form of residuals in pulse arrival times due to errors in the timing model (a) in period P , (b) in period derivative \dot{P} , (c) in position, (d) in proper motion.

5.6 Proper Motion

The proper motions of most pulsars are large enough to be measured by observing pulse arrival times over a period of several years (Hobbs *et al.* 2003). This was first achieved for PSR B1133+16 by Manchester *et al.* (1974), using timing observations over a four-year period. Figure 5.3 shows the progressively increasing residual in pulse arrival times due to the proper motion (Helfand *et al.* 1977b). This method of measuring proper motion has proved to be difficult for non-MSP pulsars because of the random timing noise observed in most pulsars (Chapter 9). A simple comparison between positions made in unrelated timing observations several years apart has proved to be as productive (Zou *et al.* 2005).

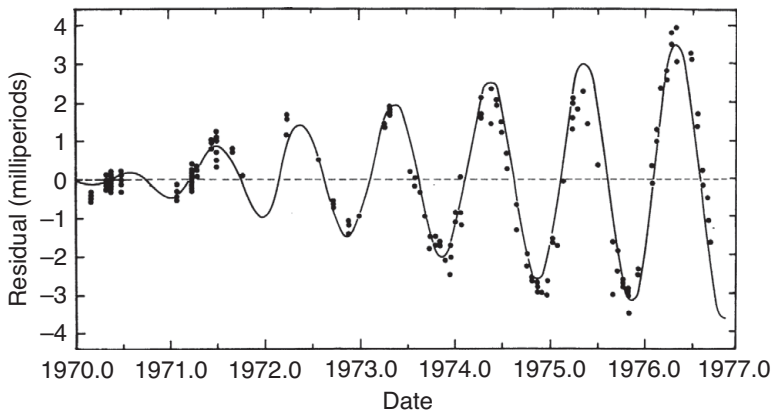


Figure 5.3 Proper motion of PSR B1133+16. The growing sinusoidal pattern of errors in pulse arrival time is due to an angular motion of about 1/3 arcsecond per year (Helfand *et al.* 1977b).

Direct interferometric measurements were originally made using the MERLIN interferometer network by Lyne, Anderson and Salter (1982); more recently, long base-line interferometers (VLBI) have been used to yield the most accurate values of proper motion and parallax (Brisken *et al.* 2002; Chatterjee *et al.* 2009; Deller *et al.* 2009; Verbunt, Igoshev & Cator 2017). See Deller *et al.* (2018) for measurements using VLBA and a comparison with the results of pulsar timing.

Part of the non-relativistic geometric term $\Delta_{R\oplus}$ in Eqn. (5.3) has special significance for a pulsar with a velocity transverse to the line of sight. As pointed out by Shklovsky (1970), a large transverse component of velocity gives rise to an appreciable increase in apparent period P even if the pulsar is not slowing down (see Section 4.2). This effect is the same as that of the ‘train-whistle’ effect, due to a changing Doppler shift in frequency. It is also closely related to the effect on pulse arrival time of the Earth’s orbital motion.

5.7 Gravitational Acceleration

The observed rotational period derivative may differ from its intrinsic value if the pulsar is accelerating in a gravitational field such as that of the Galaxy, a globular cluster or a companion star. If the pulsar experiences a component of acceleration a along the line of sight, the observed period derivative \dot{P}_{obs} is related to the intrinsic value \dot{P} by (Phinney 1992)

$$\dot{P}_{\text{obs}} = \dot{P} + \frac{a}{cP}. \quad (5.14)$$

The effect is largest for pulsars in a globular cluster, where it may dominate the observed value of \dot{P} . For example, in the globular cluster M15, two pulsars

that are closest to the centre, the millisecond PSRs 2127+11A and D, both have $\dot{P}/P \approx -2 \times 10^{-16} \text{ s}^{-1}$, indicating an acceleration away from the observer. The magnitude of the acceleration toward the centre of the cluster provides a useful measure of the total mass in the core of the cluster. In the globular cluster 47 Tucanae, 14 out of the 23 known pulsars with a measured \dot{P} have a negative value and must be located on the far side of the cluster (Freire *et al.* 2001c). They also have larger values of dispersion measure than those located on the near side, giving a measure of the total electron content of the ionised gas in the cluster (e.g. Freire *et al.* 2001a). Higher-order contributions to period derivative are also measured; Perera *et al.* (2017) argue that these are evidence for a massive black hole at the centre of NGC 6624. Prager *et al.* (2017) show that a number of the pulsars show up to the third derivative of frequency, which they attribute to interactions with other stars in this cluster.

5.8 Pulsar Ages and the Braking Index

According to classical electrodynamics, a magnetic dipole with moment M_\perp , rotating at angular velocity $\Omega = 2\pi\nu$ about an axis perpendicular to the dipole, radiates a wave at angular frequency Ω with a total power $\frac{2}{3}M_\perp^2\Omega^4c^{-3}$. The energy supply is the angular kinetic energy of the rotating body, $\frac{1}{2}I\Omega^2$, where I is the moment of inertia. In this simple model, the rate of change of rotational kinetic energy is

$$\frac{d\left(\frac{1}{2}I\Omega^2\right)}{dt} = I\Omega\dot{\Omega} = \frac{2}{3}M^2 \sin^2\alpha \Omega^4 c^{-3}, \quad (5.15)$$

where α is the angle between the dipole and rotation axes, and M is the dipole moment. The energy flow from a pulsar may be a combination of this dipole radiation and an outflow of particles. Even if the particles carry a large share of the energy, the total energy flow is expected to be approximately given by Eqn. (5.15), since the magnetic field dominates the physics of the outer magnetosphere. The combined outflow may be regarded as a flow of radiation and particles at velocity c through an area $4\pi r_c^2$, where r_c is the radius of the velocity-of-light cylinder. Provided that the total energy density at the velocity-of-light cylinder is approximately $B^2/8\pi$, where B is the magnetic field strength, the energy flow is given by Eqn. (5.15); we will see, however, that the observed slowdown law is often significantly different, so that this argument may be somewhat oversimplified.

Assuming that the slowdown follows Eqn. (5.15), and given that I is known within tight limits (Chapter 13), the orthogonal component of the dipole moment $M \sin \alpha$ can be derived from measured values of P and \dot{P} , its first derivative. A conventional value of the magnetic field strength at the surface, $B_s = MR^{-3}$, is often quoted: this assumes an orthogonal rotator with a radius 10 km and moment of inertia 10^{45} g cm^2 , giving

$$B_s = 3.2 \times 10^{19} (P \dot{P})^{1/2} \text{ gauss.} \quad (5.16)$$

Although most texts and tabulations use Eqn. (5.16), the field $B_s = MR^{-3}$ is actually the field at the magnetic equator; the polar field, which is more important in the behaviour of the magnetosphere, is $2B_s$ (see Shapiro & Teukolsky 1983, p. 278).

Integration of Eqn. (5.15) shows that, for a pulsar with initial period P_0 and constant dipole field B_s (G), the period evolves with time t (years) as

$$P(t) = (P_0^2 + 3.15 \times 10^{-32} B_s^2 t)^{1/2}. \quad (5.17)$$

The simple model of slowdown may not be correct, and it may be better to assume more generally that a pulsar is slowing down according to a power law

$$\dot{\Omega} = -\kappa \Omega^n, \quad (5.18)$$

where κ is a constant and n is referred to as the *braking index*, equal to 3 in the case of pure magnetic dipole braking (see Eqn. (5.15)).

If the pulsar is formed with a high angular velocity $\Omega_0 = \frac{2\pi}{P_0}$, integration of this equation gives the relation between Ω , $\dot{\Omega}$ and the age, t :

$$t = -\frac{\Omega}{(n-1)\dot{\Omega}} [1 - (\Omega/\Omega_0)^{n-1}]. \quad (5.19)$$

Provided $n \neq 1$ and $\Omega_i \gg \Omega$, we can approximate to a *characteristic age* τ_c given by

$$\tau_c = -\frac{1}{(n-1)} \frac{\Omega}{\dot{\Omega}} = \frac{1}{(n-1)} \frac{P}{\dot{P}}. \quad (5.20)$$

For magnetic dipole braking with $n = 3$, the characteristic age $\tau_c = -\Omega/2\dot{\Omega} = P/2\dot{P} = -v/2\dot{v}$. This is the accepted definition of characteristic age, even though the actual value of n may be observable and may differ from 3. The characteristic ages in the catalogues are calculated as:

$$\tau_c = \frac{P}{2\dot{P}} = 15.8 \left(\frac{P}{\text{s}} \right) \left(\frac{10^{-15}}{\dot{P}} \right) \text{ Myr.} \quad (5.21)$$

The actual ages of individual pulsars, from which their angular velocities at birth can in principle be found, are known only for those few pulsars that are clearly associated with a supernova event of known date. There are, however, some serious discrepancies between the characteristic and actual ages; for example, PSR J0205+6449 is a young energetic pulsar with characteristic age 5400 yr, which is associated with the SNR remnant 3C58, which is believed to be the remains of SN 1181, only 840 years ago (see references in Li *et al.* 2018). These discrepancies may be attributed either to a braking index $n \neq 3$ or to a significant initial angular velocity Ω_i .

Table 5.1. Measurements of long-term braking index

PSR	n	Reference
B0531+21	2.51(1)	Lyne <i>et al.</i> (1993)
J0537–6910	–1.5	Middleditch <i>et al.</i> (2006)
B0540–69	2.140(9)	Livingstone <i>et al.</i> (2007)
B0833–45	1.4(2)	Lyne <i>et al.</i> (1996)
J1119–6127	2.91(5)	Weltevrede <i>et al.</i> (2011)
B1509–58	2.839(1)	Livingstone <i>et al.</i> (2007)
B1727–33	1.8(3)	Espinoza <i>et al.</i> (2017)
J1734–3333	0.9(2)	Espinoza <i>et al.</i> (2011)
B1737–30	1(1)	Espinoza <i>et al.</i> (2017)
B1757–24	1.1(4)	Espinoza <i>et al.</i> (2017)
B1800–21	1.9(5)	Espinoza <i>et al.</i> (2017)
B1823–13	2.2(6)	Espinoza <i>et al.</i> (2017)
J1846–0258	2.65(1)	Livingstone <i>et al.</i> (2007)
J2229+6114	0(1)	Espinoza <i>et al.</i> (2017)

Differentiation of the spin-down law Eqn. (5.18) shows that a direct measurement of n is obtainable if the second differential can be found. In terms of angular velocity Ω , frequency $\nu = \Omega/2\pi$ or period P :

$$n = \frac{\Omega \ddot{\Omega}}{\dot{\Omega}^2} = \frac{\nu \ddot{\nu}}{\dot{\nu}^2} = 2 - \frac{P \ddot{P}}{\dot{P}^2}. \quad (5.22)$$

Using the timing data available, it was possible for Lyne and Manchester (1988) to measure the third derivative of Ω of the Crab Pulsar to an accuracy of about 10%. The value agrees tolerably well with the theoretical relation

$$\ddot{\Omega} = \frac{n(2n-1)\dot{\Omega}^3}{\Omega^2}. \quad (5.23)$$

It should be noted, however, that the rotational history of the Crab Pulsar shows some long-term variability; see a more comprehensive analysis of 45 years of measured rotation rates of the Crab Pulsar (Lyne *et al.* 2015).

Significant and consistent values of braking index, which describe the long-term rotational evolution, have been found for a small number of the youngest pulsars, as shown in Table 5.1.

The difficulty in extending this analysis to older pulsars is that the expected values of $\ddot{\Omega}$ are small, and the long-term effect is usually obscured by the effects of glitches or of timing noise (Chapter 15). In particular, the recoveries from many glitches result in large values of $\ddot{\Omega}$ between glitches and resultant braking indices as large as many tens. These are not representative of the long-term evolution of pulsar rotation.

For the Vela Pulsar, a run of 25 years of timing data allowed Lyne *et al.* (1996) to overcome the effects of a series of large glitches and obtain the remarkably small value of braking index $n = 1.4 \pm 0.2$. Using a similar technique, some further values of long-term braking index using typically 30 years of timing data to allow for the effects of glitches have been given by Espinoza, Lyne and Stappers (2017).

In the younger pulsars, the deviations from the value $n = 3$ expected for pure magnetic dipole radiation suggest that κ in Eqn. (5.18) may not be a constant, in which case the value n_{obs} of braking index found from a measurement of the second differential becomes

$$n_{\text{obs}} = \frac{\ddot{\nu}\nu}{\dot{\nu}^2} = n + \frac{\dot{\kappa}}{\kappa} \frac{\nu}{\dot{\nu}}. \quad (5.24)$$

Assuming that the magnetic dipole model is correct, the change in κ may be due to changes in I (moment of inertia), B (dipole field strength) or α (the angle of inclination between the magnetic and rotation axes):

$$n = n_{\text{obs}} + 2 \frac{\nu}{\dot{\nu}} \left(\frac{\dot{I}}{I} + 2 \frac{\dot{\alpha}}{\tan \alpha} + \frac{\dot{B}}{B} \right). \quad (5.25)$$

The required rates of change for both the Crab and Vela Pulsars is high; for the Crab it is a fractional increase of 10^{-4} per year. If this is sustained for a substantial fraction of the lifetime, it seems unlikely that it can be attributed to changes in I and α , and the above analysis suggests that the dipole field must be increasing.

The low values of n may alternatively indicate that the simple dipole model is inapplicable. If the torque from the outflow of particles does not conform to the same slowdown law as the magnetic dipole, an index as low as 1.0 may be accounted for. The outflow torque, which applies even for an aligned dipole and is therefore sometimes referred to as unipolar, is proportional to ν rather than ν^3 ; the frequently observed values $n \sim 2.5$ are then accounted for by assigning one quarter of the slowdown torque to the particle outflow.

Tong and Kou (2017) analysed the effect of a change in braking index during the lifetime of a pulsar due to changes in particle outflow and also to evolution of the inclination angle, suggesting that for the Crab Pulsar, the index may have been above 3 and is now in a monotonic decline due to the increasing effect of particle outflow.

5.9 Pulsars as Standard Clocks

The discovery of the millisecond pulsars (Chapter 10), all of which have very low values of \dot{P} and very low timing noise, opened up a new possibility for a standard of time. The present definition of Universal Time (UTC) is in terms of an ideal caesium

clock, but in practice it is realised as the average of a selected set of caesium clocks. A standard of time based on pulsars would have no link to a reproducible physical phenomenon such as the oscillation of a caesium atom, but it might nevertheless provide a smoothly running clock with a stability comparable with the present UTC. Verbiest *et al.* (2009) have shown that a timing accuracy better than 100 ns is attainable for several millisecond pulsars, in observations extending over several years. The number of pulsars timed to this precision (and better) has been extended and is summarised in the data releases associated with the International Pulsar Timing Array searches for gravitational waves (e.g. Perera *et al.* 2019b).

The smooth running of a clock is characterised by the Allan Frequency Deviation (also known as the Square Root Allan Variance) $\sigma_y(\tau)$ of its errors, which is a measure of its fractional deviation over a period of time τ . For a pulsar, allowance must be made for a uniform slowdown rate, which must be determined from the same set of timing observations; the residuals are then used to determine a derived measure of stability designated $\sigma_z(\tau)$ (Matsakis *et al.* 1997).

The stability of atomic clocks is measured by a sequence of frequency determinations. If the accuracy of these determinations is limited by white noise, then $\sigma_y(\tau)$ varies as $\tau^{-1/2}$. A pulsar clock measures a pulse arrival time; if the errors after all corrections are due only to white noise, then $\sigma_z(\tau)$ should vary as τ^{-1} . Figure 5.4 shows this dependence for four millisecond pulsars, two caesium clocks, a hydrogen maser and optical clocks (for details see Hartnett & Luiten 2010). The convergence of the pulsar and standard caesium clocks has led to speculation that pulsars might ultimately provide the smoothest running clocks in the universe, overtaking both caesium and hydrogen clocks. However, as pointed out by Hartnett and Luiten, the recently developed optical clocks, based on Hg^+ and Al^+ ions, appear to be set to overtake all others in the near future.

Figure 5.4 shows that the Allan variance typically decreases over a period of time during which the behaviour of the clock is predictable; for a standard caesium clock this is about one month, while for improved caesium clocks it is about one year. The hydrogen masers have better stability, but over a shorter period. The stability of optical clocks has already reached 10^{-16} . The millisecond pulsars shown in the Figure (PSRs B1937+21, J1909–3744, J0437–4715, J1713+0747, see references in Hartnett & Luiten 2011) have been observed for several years and have reached a stability of around 10^{-15} , improving approximately as $\tau^{-1/2}$. The extrapolation shown in Figure 5.4 suggests that pulsar clocks will only demonstrate a similar stability to the optical clocks after another 100 years.

A useful pulsar time scale can nevertheless be created through an extensive series of observations of several of the smoothest running pulsars, combining them to give a ‘mean pulsar clock’. Hobbs *et al.* (2020) have compared the best available pulsar time scale with terrestrial time scales, including TT/BIPM17 maintained at

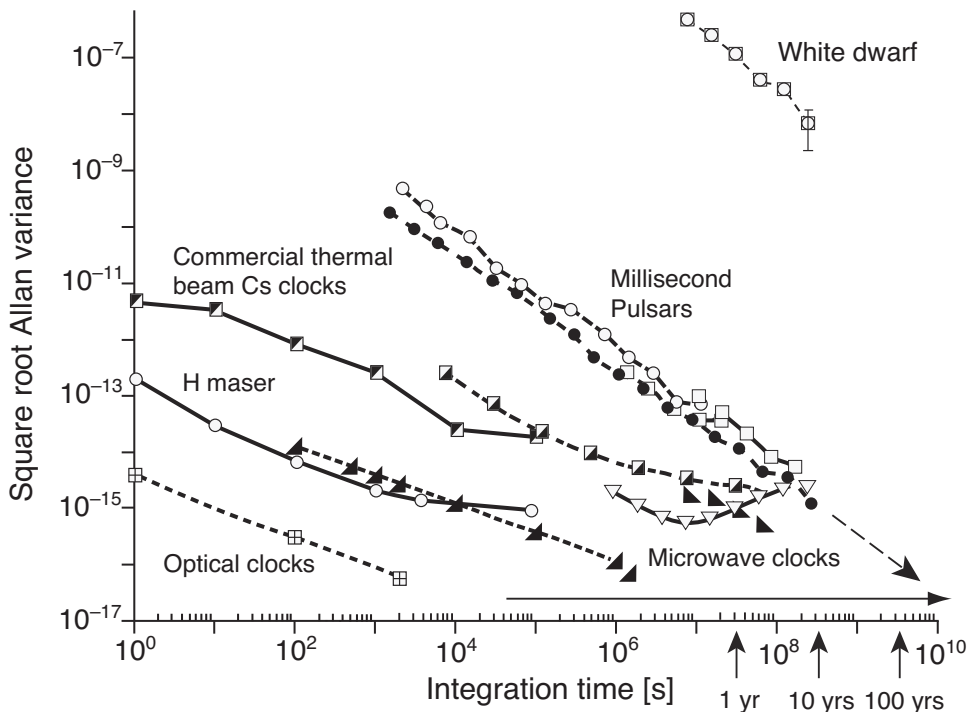


Figure 5.4 Measured square root Allan variances ($\sigma_y(\tau)$) for millisecond pulsars, $\sigma_z(\tau)$ for caesium, hydrogen and optical (Hg, Al) atomic clocks, against integration time τ (from Hartnett & Luiten 2011).

the Bureau International de Poids et Mesures and the time scale at the USA Naval Observatory based on four rubidium fountains, concluding that the pulsar time scale provides a useful comparison but is unlikely to supersede the terrestrial scales. The practical application of such a clock would initially be to search for gravitational waves that would be seen as differences between distant and local clocks, on time scales of order 10^7 s. The ultimate limitation on the pulsar scale is the uncertainty of corrections for the detailed dynamics of the Solar System.

6

Timing and Astrometry of Binary Pulsars

Millisecond pulsars are wonderfully accurate clocks, with narrow pulses marking rotational phase and with a generally smooth and uninterrupted long-term behaviour. Many are isolated, but the majority are in binary systems, with other condensed stars as companions. (In contrast, the so-called normal pulsars are almost all isolated individuals.)

The first binary pulsar to be discovered, PSR B1913+16, was found by Hulse and Taylor (1974) during a systematic search using the Arecibo radio telescope. It is still one of the most remarkable systems, and it is often known by name as the Hulse–Taylor Binary Pulsar. The orbit is highly eccentric ($e = 0.62$), with a major axis of only 6.4 light seconds and a minor axis of 5 light seconds (the orbit is only slightly larger than the Sun, whose diameter is 4.6 light seconds). The orbital period of $7\frac{3}{4}$ h is remarkably short – so short, in fact, that the rapid changes of period due to changing Doppler shift made its detection and confirmation particularly difficult. The period changes through a range of more than one part in a thousand during the orbit, so that successive observations showed changes in Doppler shift much greater than the accuracy of measurement even in the initial observations. Figure 6.1 shows the velocity curve obtained from early observations.

The orbits of the binary pulsars include extremes of high and low eccentricity. PSR J2032+4127 is a 143 ms pulsar in a 52-year orbit with eccentricity of 0.964 (Ho *et al.* 2017), while PSR J1909–3744 is a 2.9 ms pulsar in a 1.5-day orbit, which has an eccentricity of only 1.14×10^{-7} (Reardon *et al.* 2016). These extremes are related to the origins and evolution of the binary systems.

The orbits of millisecond binary pulsars encompass extremes of velocity and strong gravitational fields that require analysis by general relativity theory. Not only does this provide information on several otherwise inaccessible parameters, such as the individual masses of the two components, but it also provides some of the most stringent tests of relativity theory. For a full discussion of these tests, we refer

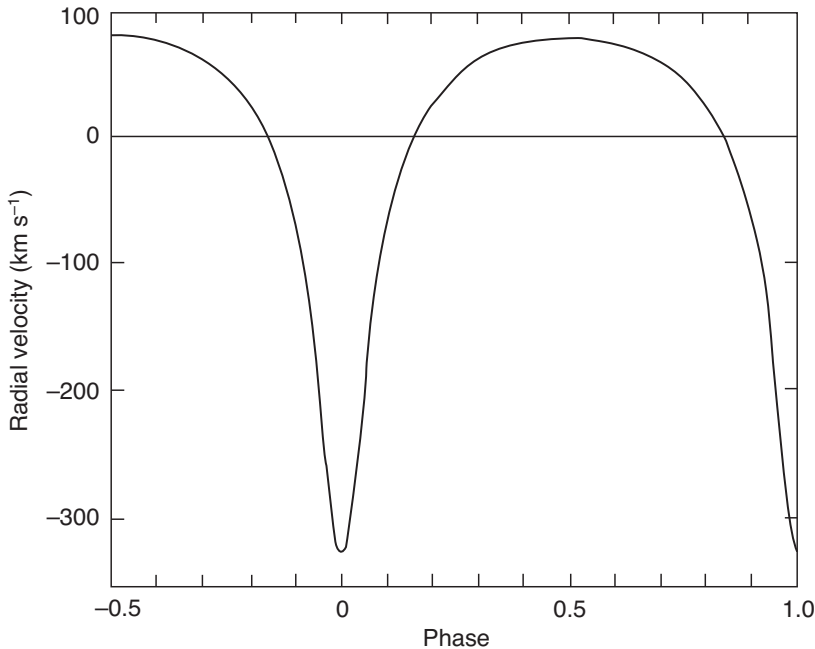


Figure 6.1 Radial velocity curve for the ‘relativistic’ Hulse–Taylor binary pulsar PSR B1913+16. The velocity is found from the modulation of the pulse period due to the Doppler effect. The curve is markedly non-sinusoidal, due to the large eccentricity of the orbit.

the reader to Lorimer and Kramer’s *Handbook of Pulsar Astronomy* (2005); in this chapter, we first summarise the Newtonian non-relativistic theory of binary orbits and then describe the main relativistic effects.

6.1 Parameters of a Binary Orbit

Large gravitational fields and high velocities in many binary pulsar systems require the use of general relativity (GR), but we first set out the classical Keplerian treatment and show separately the effects of post-Newtonian dynamics. Figure 6.2 is a face-on view of an elliptical orbit, showing the path of one of a binary pair of stars with comparable masses, as for example in the PSR B1913+16 binary system. Both stars move in ellipses that have a common focus, the centre of gravity, or *barycentre*, of the system. Seen from Earth, the plane of the orbit is inclined at angle i to the plane of the sky; the planes intersect on the *line of nodes*. For each star, the semi-minor axis b is related to the semi-major axis a by

$$b^2 = a^2(1 - e^2), \quad (6.1)$$

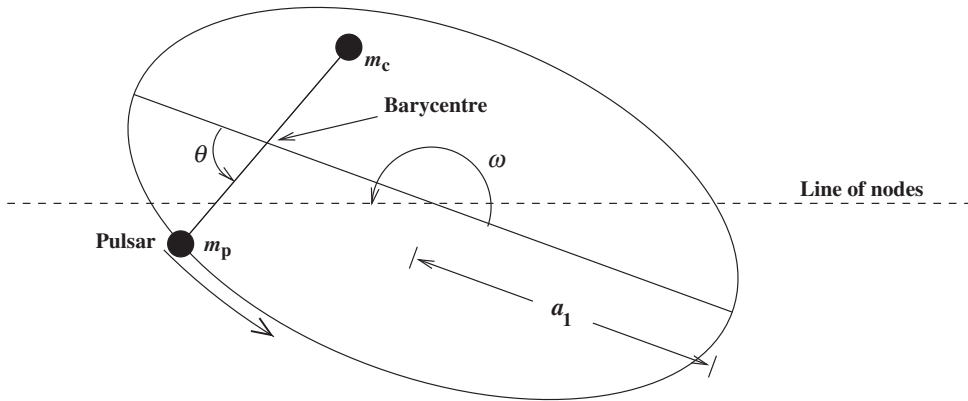


Figure 6.2 Geometrical parameters for an elliptical orbit seen face-on. The plane of the orbit intersects the plane of the sky along the line of nodes (the broken line) at the inclination angle i . The orbit is further defined by the semi-major axis a_p , the longitude of periastron ω and the eccentricity e .

where e is the eccentricity. *Periastron*, when the pulsar is closest to the barycentre and to its companion, is at longitude ω ; a reference time at which the pulsar passes this point is designated T_0 . The distance of the pulsar from the barycentre is a minimum of $a_p(1 - e)$ at periastron and a maximum of $a_p(1 + e)$ at *apastron*.

Kepler's third law, with Newton's law of gravity, relates the semi-major axis of the relative orbit, which is the sum of the semi-major axes a_p, a_c of the pulsar and its companion, to the mean angular velocity Ω_b and the total mass by

$$\Omega_b^2(a_p + a_c)^3 = G(m_p + m_c), \quad (6.2)$$

where m_p, m_c are the masses of the pulsar and its companion. The sizes of the two orbits are related to the masses by

$$\frac{a_p}{a_c} = \frac{m_c}{m_p}. \quad (6.3)$$

In a Keplerian analysis of a binary pulsar orbit, the masses m_p, m_c of the two components cannot be determined separately. The *mass function* $f(m_p, m_c)$ obtained from the orbital period P_b and the projected semi-major axis $x_p \equiv a_p \sin i$ (where i is the orbital inclination) is conveniently related to the two masses by

$$f(m_p, m_c) = \frac{4\pi^2 x_p^3}{P_b^2 T_\odot} = \frac{(m_c \sin i)^3}{(m_p + m_c)^2}, \quad (6.4)$$

where $T_\odot = GM_\odot c^{-3} = 4.9255 \times 10^{-6}$ s, P_b is in seconds and the masses are here expressed in units of the solar mass M_\odot . The mass function contains the unknown angle of inclination i ; this often remains unknown except when eclipses

are observed, which would indicate that the line of sight is nearly in the plane of the orbit, that is, i is close to 90 deg. As we will see, the individual masses and the orbital inclination may be separately determined from post-Keplerian parameters.

The first orbital parameter to emerge following a discovery observation is the orbital period P_b . The phase of the observed orbit, measured from the time elapsed from the time of periastron, is the *mean anomaly* M . The next stage of the analysis is to match the curve of the observed pulse period $P(t)$ to a model elliptical orbit. In terms of the *true anomaly* θ , which is the angular position in the orbit with respect to periastron (Figure 6.2), the line of sight velocity $v(\theta)$ is

$$v(\theta) = \frac{2\pi}{P_b} \frac{a_p \sin i}{\sqrt{1 - e^2}} [\cos(\omega + \theta) + e \cos \omega], \quad (6.5)$$

where ω is the longitude of periastron. The observed Doppler shifted period (for $v \ll c$) is $P_0(1 + \frac{v}{c})$. We require $v(t - T_0)$ as a function of time from periastron passage at time T_0 . This is achieved via the mean anomaly M and the *eccentric anomaly* E , which are related to θ by

$$M = \frac{2\pi}{P_b}(t - T_0) = E - e \sin E \quad (6.6)$$

$$\text{and } \tan \frac{\theta}{2} = \left(\frac{1+e}{1-e} \right)^{\frac{1}{2}} \tan \frac{E}{2}. \quad (6.7)$$

In general, orbital solutions are found by computer trial for the five observable Keplerian parameters $P_b, a_p \sin i, e, \omega, T_0$. The relation between the observed Doppler curve and the orbital parameters for small e is set out by Lange *et al.* (2001); for highly eccentric orbits, see Blandford and Teukolsky (1976). Note that the inclination i is not obtainable from this Keplerian analysis, since $a_p \sin i$ appears as a single parameter x_p . The separation of these two parameters may in some cases be achieved through classical orbital analysis, as described in the next section; it is more often achieved through the observation of Shapiro delay, the general relativistic effect which we describe later.

6.2 Annual Orbital Parallax

The orbit of Earth around the Sun, which leads to a parallactic change of apparent position (Section 5.1), also leads to a periodic change in the angle from which a binary system is observed. The effect, which is small and unmeasurable except for nearby systems, is an annual change in inclination angle i , allowing a separation of

a_p and $\sin i$. An analysis due to Kopeikin (1995) shows that the fractional change in $\sin i$ is proportional to $(\cot i)/d$, where d is the distance of the binary system. The parallax of a large sample of millisecond pulsars has now been measured as part of the gravitational wave searches (see Perera *et al.* 2019b and references therein).

An observable change in the projected semi-major axis can also occur through the proper motion of the whole binary system. This has been demonstrated in the neutron star–white dwarf system J1012+5307 by Lazaridis *et al.* (2009).

6.3 Relativistic Effects in Binary Orbits

The modulation of pulse arrival times from a pulsar in a binary orbit is closely analogous to the cyclic variation of arrival times due to the position of the observatory relative to the barycentre of the Solar System, and the simple Keplerian terms are similar to those introduced in Chapter 5. Many of the orbits are small compared with the Earth’s orbit, so that the propagation delays are smaller and the velocities are larger; the ‘relativistic’ or ‘post-Newtonian’ terms of order $(v/c)^2$ therefore become more important. Following the notation of Eqn. (5.3), the observed pulse arrival times t are related to barycentric times t_b within the orbit by

$$t = t_b + \Delta_R + \Delta_E + \Delta_S. \quad (6.8)$$

The classical Römer term Δ_R includes an acceleration term (the transverse Doppler, or Shklovsky effect, Section 5.6), whose magnitude depends on the proper motion of the binary system. The Einstein term Δ_E includes the delay due to gravitational redshift and time dilation. The Shapiro term Δ_S is the delay in propagation across the orbit due to curvature of spacetime in the vicinity of the binary companion. The analysis of pulse arrival times in a binary pulsar, taking account of these effects, is described by Backer and Hellings (1986), Bell (1998) and van Straten *et al.* (2001).

The Einstein term is only detectable through its variation with orbital phase (eccentric anomaly) in an elliptical orbit; a mean component is absorbed into the measured rotation rate of the pulsar. The variable part is expressed as a delay depending on pulsar mass m_p , companion mass m_c and eccentricity e as

$$\Delta_E = \gamma \sin E, \quad (6.9)$$

$$\text{where } \gamma = \frac{e P_b G m_c (m_p + 2m_c)}{2\pi c^2 a_R (m_p + m_c)}. \quad (6.10)$$

(Note the confusing nomenclature: γ is not the usual relativistic factor.)

The Shapiro delay for a binary pair of neutron stars depends on the mass m_c of the companion and on the angle pulsar-companion-observer.

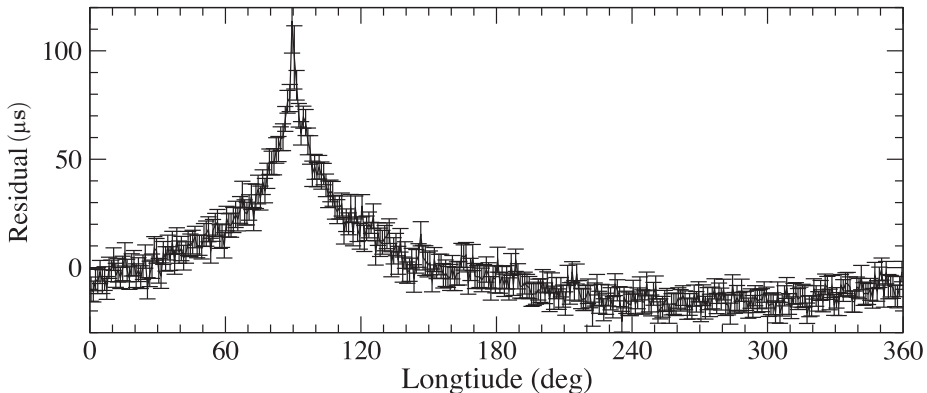


Figure 6.3 The Shapiro delay Δ_S of the binary pulsar J0737-3039A due to its companion (Kramer *et al.* 2006b). The orbit of this system is nearly edge-on, so that there is a large peak delay as the pulsar passes behind its companion.

For a low eccentricity, the Shapiro delay varies round the orbit as

$$\Delta_S = -2r \ln[1 - s \cos(\phi - \phi_0)], \quad (6.11)$$

where the two parameters r and s , known as the *range* and the *shape* of the curve, are

$$r = \frac{Gm_c}{c^3}, \quad s = \sin i, \quad (6.12)$$

where i is the inclination of the orbit, and $(\phi - \phi_0)$ is the orbital phase measured from the configuration when the pulsar appears closest to and behind its companion. The more general theory is presented by Damour and Taylor (1992). Freire and Wex (2010) show that the delay curve may be more conveniently presented as a harmonic analysis rather than the r, s parameters, especially for nearly circular orbits.

Figure 6.3 shows the Shapiro delay for the MSP in the binary system J0737–3039 (Kramer *et al.* 2006b), in which the peak delay is 100 μs. Similar measurements for other binary systems are reported by Stairs *et al.* (2002), Lyne *et al.* (2004) and Ferdman *et al.* (2010). As timing precision is improved and more millisecond pulsars are found, the Shapiro delay has been measured for a growing number of systems. These, when combined with other measurements (see below), can be used to measure neutron star masses.

6.4 The Relativistic Evolution of a Binary Orbit

In most millisecond pulsar binaries, the partner to the pulsar is also a condensed star, either another neutron star or a white dwarf. Provided that the system is

undisturbed by external influences, such as the gravitational attractions within a globular cluster, the two components can be regarded as point masses, constituting an ideal testbed for theories of relativistic gravity (Taylor 1992). Keplerian orbits, based on Newtonian gravity, should show no change in any of the orbital parameters, but for several binaries, including B1913+16, measurements over a period of some years have provided the rates of change \dot{P}_b , \dot{x}_p , $\dot{\omega}$, \dot{T}_0 of the orbital parameters. These would all be zero in a Keplerian analysis, but their magnitudes are predicted from relativistic theory; in fact their measurement provides some of the most stringent tests of general relativity, particularly in the strong-field regime.

The earliest classical test of general relativity was through accurate measurement of the precession of the orbit of the planet Mercury. The size of this effect depends on the strength of the solar gravitational field in the orbit. For Mercury, the component of the rate of advance of periastron $\dot{\omega}$ (i.e. the angular movement of major axis of the elliptical orbit) due to general relativity is 43 arcseconds per century (out of a total precession of 574 arcseconds per century). The crucial factor is the ratio between gravitational potential energy and rest mass energy; for PSR B1913+16, this factor (GM/c^2r) reaches 10^{-6} , and the precession rate is 4.2 degrees per year.

This measured value of the rate of advance of periastron ($\dot{\omega}$) is important, since it provides a measure of the total mass of the system. If m_p and m_c are the masses of the pulsar and its companion, then the rate expected from general relativity is

$$\dot{\omega}_{GR} = 3(P_b/2\pi)^{-5/3}G^{2/3}(m_p + m_c)^{2/3}c^{-2}(1 - e^2)^{-1}. \quad (6.13)$$

(See Stairs *et al.* (2002) for the origin of equations expressing the post-Keplerian parameters). For PSR 1913+16,

$$\dot{\omega} = 2.11 \left[\frac{(m_p + m_c)}{M_\odot} \right]^{2/3} \text{ deg yr}^{-1}, \quad (6.14)$$

where M_\odot is the solar mass. From the measured value of precession, the sum of the masses is found to be $m_p + m_c = 2.8M_\odot$ (provided that there is no contribution from tidal or rotation effects in the companion star; both components are evidently neutron stars, so that such effects are negligible).

The various effects on the pulse arrival time vary with orbital phase in different ways, so that a long series of precise timings can be used to find a consistent set of orbital parameters, including the orbital inclination. A series of 1000 observations spanning 4 years allowed Taylor and Weisberg (1982) to determine separately the masses m_p and m_c of PSR B1913+16 and its neutron star companion, since the different relativistic effects are proportional to different combinations of the masses. They were able to show that $m_p = m_c = 1.4M_\odot$, and $\sin i = 0.76 \pm 0.14$ (for more recent values, see Weisberg, Nice & Taylor 2010).

Two further effects predicted by general relativity are now measurable in observations of this and other binary systems. The orbital energy of the binary is expected

to diminish through quadrupolar gravitational radiation, giving a decrease of orbital period as the stars spiral in. The orbital period is expected to decrease as

$$\dot{P}_b = -\frac{192\pi}{5} \left(\frac{P_b}{2\pi}\right)^{-5/3} \left(1 + \frac{73}{24}e^2 + \frac{37}{96}e^4\right) (1-e^2)^{-7/2} G^{5/3} c^{-5} \left(\frac{m_p m_c}{(m_p + m_c)^{1/3}}\right). \quad (6.15)$$

For PSR B1913+16, the observations showed a cumulative effect of 35 seconds in the phase of the orbit over a period of 30 years (Figure 6.4), giving a rate of change of orbital period

$$\dot{P}_b = (-2.4184 \pm 0.0009) \times 10^{-12}. \quad (6.16)$$

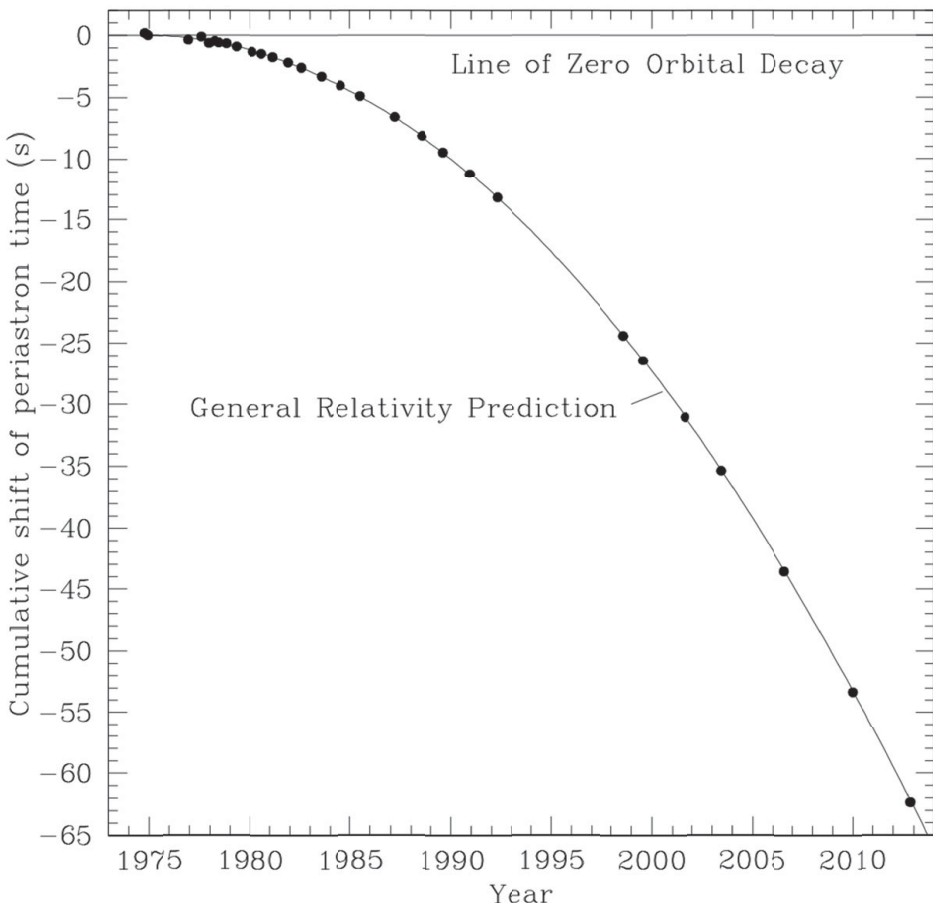


Figure 6.4 The effect of gravitational radiation on the orbit of the binary pulsar PSR B1913+16. The deviation from constant orbital period is apparent as a cumulative change of orbital phase (Weisberg & Huang 2016).

This is consistent with the expected rate of energy loss through gravitational radiation and constituted the first demonstration of the existence of such radiation.¹

Gravitational radiation from a binary system, according to general relativity, is quadrupolar, at twice the orbital frequency. An alternative post-Newtonian theory might allow dipolar radiation from a system such as a pulsar/white dwarf binary; direct observation of such a gravitational wave would provide a test of such theories (see the textbook by Will, 1993).

Damour and Taylor (1991) point out that the measured value of \dot{P}_b will be affected by any component of velocity transverse to the line of sight; this is the Shklovsky effect (Section 5.6), which is usually considered in relation to the pulsar period P . The orbital period is therefore affected by proper motion and acceleration in the Galactic gravitational field in addition to the effects of gravitational radiation. After correcting for proper motion, which was found from the series of accurate position measurements, Damour and Taylor showed that \dot{P}_b is within 0.8% of the theoretical value.

Since the effects of proper motion and gravitational radiation are similar and additive, it is now possible to reverse this procedure in other binary pulsars (Bell & Bailes 1996). A measured value of \dot{P}_b is the sum of the two effects. The component from gravitational radiation can be calculated and subtracted, leaving only the component due to transverse velocity. This has been achieved for PSR B1534+12, for which the proper motion was already known in angular measure; the outcome is a value of the pulsar distance (Fonseca, Stairs & Thorsett 2014).

The second effect predicted by general relativity, which was detected after several years of observation, is a precession of the rotation axis of the pulsar. This is due to a coupling of the angular momentum of the rotating pulsar with the angular momentum of the orbit. The interesting and observable consequence is that the observer's line of sight may make a progressively different cut across the beam of radiation. Changes in the integrated pulse shape that may be attributed to this geodetic precession have been clearly identified in PSR B1913+16 (Kramer 1998; Weisberg & Taylor 2002; Weisberg, Romani & Taylor 1989). Such a change in aspect raises the possibility not only of a full delineation of the shape of the beam in two dimensions but also that precession will take the beam direction so far from the line of sight that the pulsar becomes unobservable within a few decades of its discovery, possibly by the year 2025.

The accuracy of measurement of the orbital parameters is demonstrated in Table 6.1. These quantities are taken from Weisberg and Taylor (2005). The indications are that the behaviour of this binary system conforms very closely to

¹ A simple statistic: the major axis of the orbit of PSR 1913+16 is shrinking by approximately one centimetre per day.

Table 6.1. Orbital parameters of PSR B1913+16

Projected semi-major axis	$x_p = a_p \sin i$	2.3417725 (8) lt. s
Orbital eccentricity	e	0.6171338 (4)
Binary orbit period	P_b	0.322997448930 (4) days
Longitude of periastron	ω_0	292.54487 (8) deg
Rate of advance of periastron	$\dot{\omega}$	4.226595 (5) deg yr ⁻¹
Derivative of orbit period	\dot{P}_b	$-2.4184 (9) \times 10^{-12}$

Some of the accuracies quoted in this table reflect differences in systems of ephemerides rather than observational accuracy (see Weisberg & Taylor 2005).

Table 6.2. Neutron star–neutron star binaries

PSR	P ms	P_b h	$a_p \sin i$ lt. s	Ecc	Reference
J0453+1559	45.8	97.7	14.5	0.113	Martinez <i>et al.</i> (2015)
J0509+3801	76.6	9.11	2.05	0.586	Lynch (2018)
J0737–3039A/B	22.7/2770	2.45	1.42	0.088	Burgay <i>et al.</i> (2003)
J1518+4904	40.9	207	20.0	0.249	Nice <i>et al.</i> (1996)
B1534+12	37.9	10.1	3.73	0.274	Stairs <i>et al.</i> (2002)
J1753–2240	95	326	18.1	0.304	Keith <i>et al.</i> (2009)
J1756–2251	28.5	7.67	2.76	0.18	Faulkner <i>et al.</i> (2005)
J1757–1854	21.5	4.40	2.23	0.606	Cameron <i>et al.</i> (2018)
J1906+0746	144.1	3.98	1.42	0.085	Lorimer <i>et al.</i> (2006a)
J1811–1736	104	451	34.8	0.828	Lyne <i>et al.</i> (2000)
J1829+2456	41	28	7.2	0.14	Champion <i>et al.</i> (2004)
B1913+16	59.0	7.75	2.34	0.617	Weisberg, Nice and Taylor (2010)
B2127+11C	30.5	8.05	2.52	0.681	Jacoby <i>et al.</i> (2006)

the ideal of two point masses and that it is therefore providing the classic text-book test of the effects of special and general relativity on the orbit of a binary system.

The double-neutron-star binary systems known in 2020 are shown in Table 6.2.

Some of the binary systems with white dwarf companions are in orbits that are expected to show large relativistic effects; for example, PSR J1141–6545 is a pulsar with period $P = 394$ ms in a highly elliptical orbit with period $P_b = 4.8$ h and eccentricity $e = 0.17$ (Kaspi *et al.* 2000).

6.5 The Double Pulsar Binary J0737–3039A/B

The double-neutron-star binary with the shortest orbital period, 2.45 h, in J0737–3039, has an orbit that would fit inside the Sun (Burgay *et al.* 2003). Although the eccentricity is comparatively low ($e = 0.088$), the rate of periastron advance ($\dot{\omega} = 17$ deg yr⁻¹) is easily measured; it is four times that of the classic Hulse–Taylor

Pulsar B1913+16. This binary pair is rapidly losing energy through gravitational radiation and will merge in about 85 Myr, a much shorter time than for any other known double-neutron-star binary. The existence of such short-lived binaries is encouraging for the direct observation of the gravitational waves expected at the time of such mergers (see Section 6.7).

The binary system J0737–3039A/B by a happy chance is observed with the orbit nearly edge-on, so that the line of sight passes close to the neutron star companion. Furthermore, the neutron star companion has been found itself to be a pulsar (Lyne *et al.* 2004), whose orbit can be determined independently. The ratio of projected semi-major axes gives the ratio of the two masses m_A/m_B ; their sum is found from the precession of the orbit, so that their individual masses are obtained with remarkable precision (Section 6.6).

The two pulsars (A and B) have rotation periods 22.7 ms, and 2.77 s, respectively. The slower pulsar B has the much larger magnetosphere, occupying a significant fraction of the distance between them. Eclipses of A by B's magnetosphere are observed, and an energetic wind from A distorts B's magnetosphere, suppressing its pulses for a large part of the orbit. Nevertheless, observations over $2\frac{1}{2}$ years have given values for post-Kepler (PK) parameters for both pulsars, providing the best tests so far available for gravitational theory. The very rich range of phenomena, both in the orbits and in their interactions, is described in a comprehensive review by Kramer and Stairs (2008).

General Relativity theory also predicts observable effects of coupling between the angular momenta of the pulsar spin and the orbit. The application of such tests of strong-field gravitation is discussed by Damour and Esposito-Farese (1992) and by Esposito-Farese (1999). Spin-orbit coupling may already have been observed in the double neutron star PSR 0737–3039A/B; Breton *et al.* (2008) found that the eclipse of A by the large magnetosphere of B is changing, indicating precession of the rotation axis of B at the rate of 4.77 ± 0.65 deg yr $^{-1}$, consistent with theory. Subsequently B has faded from view, although it is not yet clear whether this is due to a change within its magnetosphere or to precession of the spin axis (Perera *et al.* 2010).

6.6 Tests of Gravitational Theory

The most precise tests of general relativity theory are based on lunar laser ranging and spacecraft penetrating deeper into the Solar system (Bertotti *et al.* 2003); these are, however, confined to regions of weak gravitation and low accelerations. Binary pulsars offer the only opportunity to extend tests into a regime of strong gravitational fields and large accelerations (Damour & Esposito-Farese 1998). Earlier sections of this chapter have shown how general relativity (GR) predicts values

of post-Keplerian (PK) parameters that agree remarkably well with observations. The strong equivalence principle (SEP), which is embedded in GR, is based on the equivalence of inertial and gravitational mass; in other gravitational theories that do not conform to the SEP, there may be differences that would lead to different values of the PK parameters. This would appear as discrepant values of masses obtained from the various PK parameters, which have not so far been found. Figure 6.5

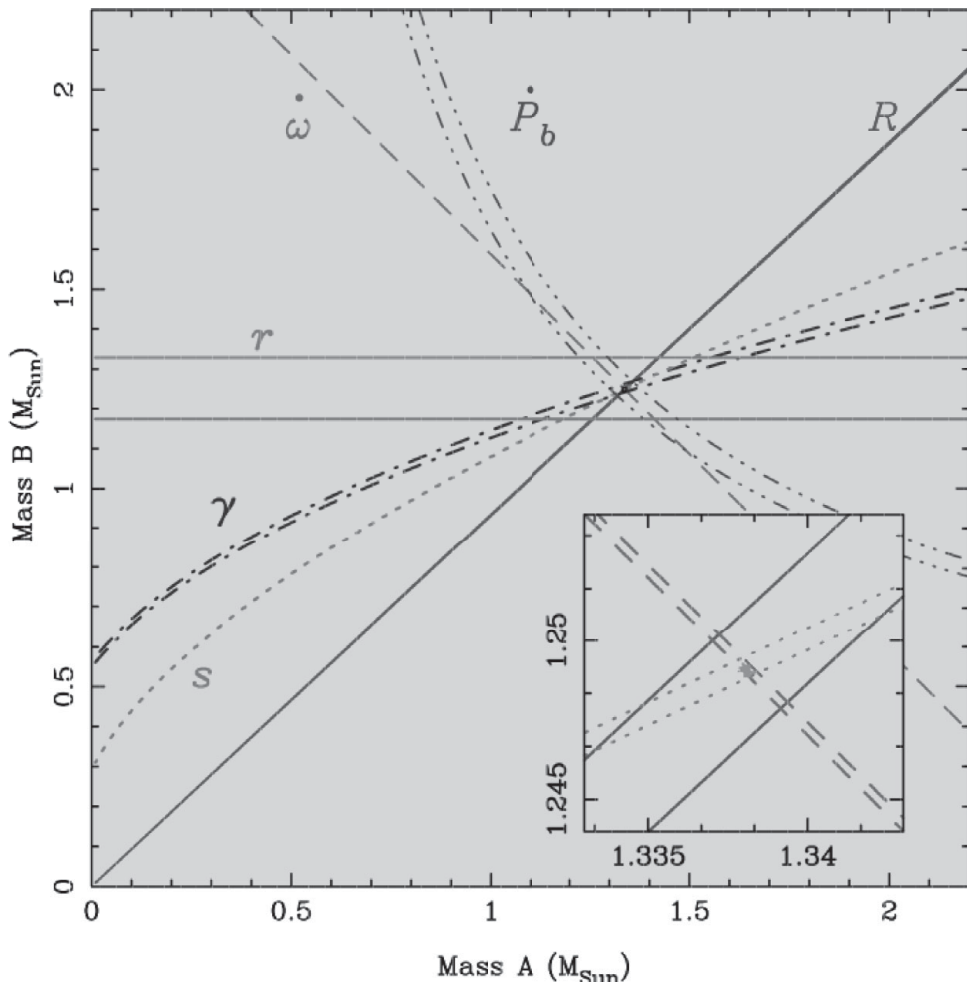


Figure 6.5 Mass-mass plot for the Double Pulsar J0737–3039A/B, showing the observational constraints on the masses m_A and m_B (Kramer *et al.* 2006b). The Keplerian mass functions allow only the unshaded region. Other constraints are shown as pairs of lines separated by the observational uncertainties: R is the mass ratio, $\dot{\omega}$ is the advance of periastron, γ is the Einstein redshift/time dilation parameter, r and s are Shapiro delay parameters, \dot{P}_b is orbital decay (gravitational radiation). The expanded view (inset) shows that all constraints are in agreement.

(from Kramer *et al.* 2006b) displays this agreement for the two masses of the Double Pulsar; here the mass m_B is plotted against m_A , showing the regions allowed (within their accuracies) by the measured values of the PK parameters in the context of GR. The accurately known ratio of the masses is shown by the line R . All allowed regions converge on the masses $m_A = 1.3381 \pm 0.0007$ and $m_B = 1.2489 \pm 0.0007$ solar masses.

6.7 Gravitational Waves

Gravitational wave theory was first established by the observations of orbital decay in the Hulse–Taylor binary; after heroic efforts, the direct detection of gravitational waves was achieved by ground-based detector systems. In these gravitational wave detectors, named LIGO, VIRGO, GEO 600 and TAMA 300, the lengths of two orthogonal arms are compared by sophisticated optical interferometry, aiming to detect a strain in space that amounts to less than one part in 10^{21} . These systems are only sensitive to gravitational wave frequencies greater than about 10 Hz and up to 10 kHz. A space-based system, LISA, is proposed comprising widely separated spacecraft, to provide a longer baseline detector that will be sensitive to frequencies as low as 10^{-4} Hz, that is, a period of some hours (see a review of interferometric detectors by Pitkin *et al.* 2011).

Within the Milky Way galaxy, the most likely source of gravitational waves giving a detectable signal is the coalescence of a double neutron star (DNS) system at the end of the slow decay of its orbit. Such an event would be observable throughout the Galaxy, and the probability of its observation as a characteristic burst of gravitational waves depends on the population of such DNS systems and their coalescence time τ_{GW} . Peters (1964) showed that τ_{GW} is obtainable from the orbital characteristics, and Champion *et al.* (2004) present a simplified relation due to Lorimer:

$$\tau_{\text{GW}} \approx 10^7 \text{ yr} \left(\frac{P_b}{h} \right)^{8/3} \left(\frac{\mu}{M_\odot} \right)^{-1} \left(\frac{(m_p + m_c)}{M_\odot} \right)^{-2/3} (1 - e^2)^{7/2}, \quad (6.17)$$

where the reduced mass $\mu = m_p m_c / (m_p + m_c)$. The smallest known value of τ_{GW} is for the DNS system J0737–3039A/B, which is expected to coalesce in about 85 Myr (Burgay *et al.* 2003). The first such event to be observed directly was in 2017 (Abbott *et al.* 2017).

Detweiler (1979) pointed out that pulsar timing observations are sensitive to very large scale strains in space, so that a consistent set of timing observations extending over some years would detect very long wavelength gravitational waves, with periods of order 1–10 years. To achieve this, the concept of a ‘Pulsar Timing Array’ was introduced (Foster & Backer 1990); this is an ensemble of pulsars

distributed throughout the sky, timed systematically with high precision over several decades. Gravitational waves are expected to create a specific signature in the correlated timing residuals of the pulsars forming the array (Hellings & Downs 1983). Bertotti, Carr and Rees (1983) suggested that such timing observations would detect a stochastic signal from a cosmic background of binary systems in the early universe. As the universe expanded, the wavelength of this background would expand with the horizon size, and the wave energy density would be a constant fraction of the total energy. Detection of gravitational waves by pulsar timing is a very demanding proposition. Extensive observations are under way in several major collaborations, the European Pulsar Timing Array (Janssen *et al.* 2008a), the Parkes Pulsar Timing Array (Hobbs *et al.* 2010) and the North American Nanohertz Observatory for Gravitational Waves; these collaborations have recently been joined by the Indian Pulsar Timing Array and a Chinese Pulsar Timing Array.

The intention is to obtain pulse arrival times from 40 or more pulsars to an accuracy of better than 100 ns, in a continuous series of weekly observations extending over 5 years (Siemens *et al.* 2013). The observing programme will be shared by several radio observatories in each array. Eventually an extensive programme will be undertaken by the planned Square Kilometre Array.

6.8 The Detection of Planetary Pulsar Systems

Only about 5% of the known pulsars are obviously in binary systems. Some of the companion stars have masses below $0.1M_{\odot}$, at the bottom of the range of stellar masses. Here we examine briefly the possibility that undetected orbiting companions with even lower masses may exist in some of the apparently solitary pulsars.

A heavy planet at a large distance from a pulsar should be detectable because of the periodic displacement of the pulsar from the barycentre of the system. Jupiter, for example, orbiting with a period of 11.9 years, causes the Sun to be displaced from the barycentre of the Solar System by 2.5 light seconds; an effect of this size would soon be seen in pulsar timing.

The first detected pulsar planetary system was PSR B1257+12, in which three orbiting planets were found, with periods 25.3, 66.6 and 98.2 days (Wolszczan & Frail 1992). The first has a very low mass, but the other two have masses comparable with the mass of the Earth (4.3 ± 0.2 , $3.9 \pm 0.2 M_{\text{Earth}}$ respectively; Konacki & Wolszczan 2003). Figure 6.6 shows the modulation of pulse arrival time due to these two planets. The orbital periods of these are almost in a harmonic ratio of 3/2, so that gravitational interactions are significant. Konacki and Wolszczan show that the configuration is stable, with small long-term perturbations.

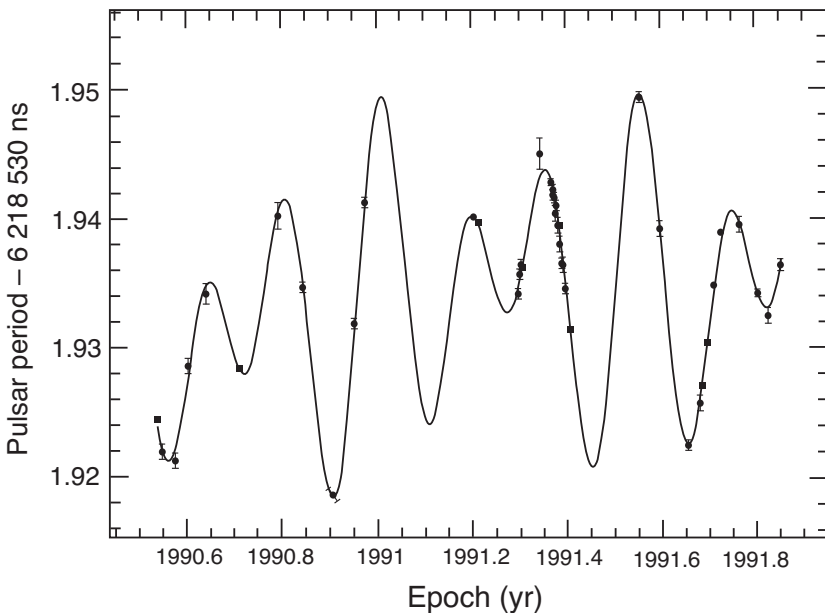


Figure 6.6 Modulation of the pulse periodicity in the planetary system PSR B1257+12 (Wolszczan & Frail 1992).

Although such systems are evidently rare, less massive planets at large distances from their host pulsar, causing a long period modulation of pulse arrival time, might easily go undetected for several years. Longer period binaries are certainly not common; if they were, at least some pulsars would be showing a negative value of \dot{P} . For example, a pulsar with $P = 1$ s and an intrinsic $\dot{P} = 10^{-15}$ would appear to have a negative value of \dot{P} if the orbital acceleration were greater than 3×10^{-7} m s $^{-2}$. Since the maximum line of sight acceleration is $1.6x_p P_b^{-2}$ m s $^{-2}$ (where x_p is measured in light seconds and P_b in days), the limiting orbital period is $2309x_p^{1/2}$ days. Limits on possible numbers of long term binaries are hard to establish, and undetected binary systems with periods of several decades may indeed exist, although the range of possibilities is diminishing as timing observations extend over longer intervals. A likely candidate is a proposed third member of the binary system containing PSR B1620–26, an 11 ms pulsar in the globular cluster M4. The main companion is a white dwarf with orbital period 191 days, but the precise determination of the characteristics of this system is confused by large values of the second and third differentials of the pulsar period. The analysis suggests the existence of a third member, less massive and with a considerably longer orbital period (Arzoumanian *et al.* 1996; Sigurdsson & Thorsett 2005). Extensive searches have taken place for planets around other pulsars, and even with the greatly improved timing precision, none have been definitively identified.

7

The Distances of the Pulsars

Unlike traditional optical astronomy, pulsar distances cannot be determined from assumed values of intrinsic luminosity, since this is chaotically variable both from time to time and from pulsar to pulsar. Pulsar distances are instead uniquely available in the radio domain from the frequency dispersion due to propagation delay in the interstellar medium.

We saw in Chapter 3 that for every pulsar observed in the radio domain, the frequency dispersion in pulse arrival time provides a dispersion measure (DM), which is a measure of the total electron content along the line of sight to the pulsar. Given a model of the electron distribution in the Galaxy, the DM provides a measurement of distance. For the majority of pulsars this is the only way to determine distance, which is vitally necessary in determining luminosity and the distribution of pulsars in the Galaxy. For some pulsars an optical identification provides a distance; the DM then gives a value for the integrated electron content and hence the average electron density over that line of sight. For example, the Crab Nebula is known from optical measurements to be at a distance of 2 kpc, with an uncertainty of about 20%. The dispersion measure of the Crab Pulsar is 56.8 cm^{-3} pc; neglecting the small part of this that may be attributable to ionised gas within the nebula, we obtain a value of 0.03 cm^{-3} for the mean electron density along the line of sight. In the absence of a detailed model of electron distribution, this value of electron density within the Galaxy, with a measured DM, is a useful first indicator of distance for a pulsar. Other optically identified objects with known distances give further values for integrated electron content, contributing to a model of the electron distribution throughout the Galaxy.

Apart from associations with optically identified objects, an increasing number of distances are available purely from radio observations. In optical astronomy the distances of stars can be obtained from their *trigonometric parallax*, which is the apparent annual cyclic movement of position due to the Earth's orbital motion round the Sun. The distances of many of the closest pulsars may similarly be obtained from

very-long-baseline interferometry (VLBI) measurements of parallax, with accuracies better than the best optical measurements of other stars. Parallax is observed in two ways, either from annual variation of position or from six-monthly variation of pulse arrival time. A related and remarkably accurate measurement of *kinematic* or *dynamical* distances is available from the accurate timing of pulses from some millisecond pulsars and also from the orbital motion of some binary pulsars (see Chapter 6).

Distances that have been determined in the several ways that we describe in this chapter are used with measured DMs to construct a model distribution of electron density n_e in the Galaxy; this model is then available to estimate distances of other pulsars for which only the DM is known.

7.1 Pulsar Distances from Parallax

The distances of a number of pulsars within about 2 kpc of the Sun have been obtained from measurements of their annual parallactic motion. This technique may be regarded as a measurement of the curvature in a wavefront arriving from the pulsar (Figure 7.1). The curvature can be measured as the Earth moves in its orbit round the Sun, either as a change in apparent position of the pulsar or by the small cyclic change of pulse arrival times. The measurements must be spread through a complete cycle: annual for position changes; six-monthly for pulse arrival times. The astrometric positional measurements, using VLBI, require an angular

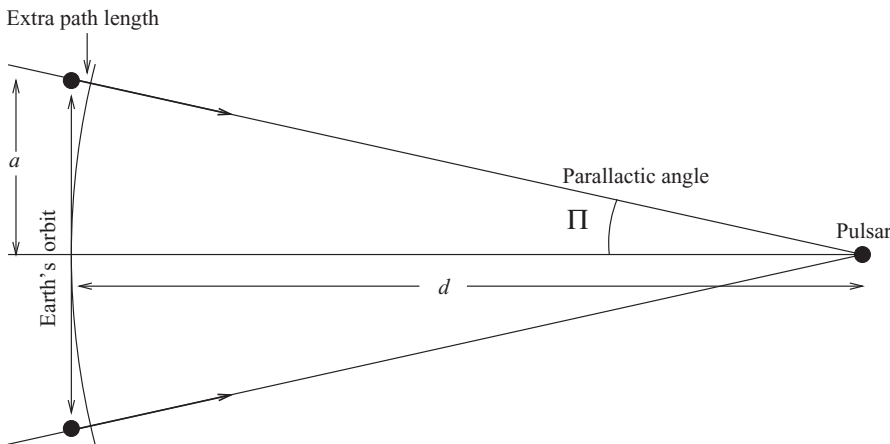


Figure 7.1 Parallax. The Earth's orbital motion carries the observer across a notional wavefront whose radius of curvature is the distance d to the pulsar. The curvature is measured either as an annual periodic change in apparent direction (trigonometric parallax) or as a six-monthly periodicity in pulse arrival time due to the changing path length from the pulsar to the Earth.

accuracy better than 10 microarcseconds, while the timing measurements require an accuracy better than about 1 microsecond.

The trigonometric parallax is defined as the angle $\Pi = a/d$, where a is the radius of the Earth's orbit, and d is the distance of the star. A star with a parallax of one arcsecond is at a distance of 1 parsec, i.e. 3.085×10^{16} m. The parallactic movement through the year depends on the ecliptic coordinates (λ, β) of the star; the displacements x, y parallel and perpendicular to the ecliptic follow an ellipse (Smart 1977, p. 220):

$$x = \Pi \sin(\odot - \lambda) \quad \text{and} \quad y = \Pi \sin \beta \cos(\odot - \lambda), \quad (7.1)$$

$$\frac{x^2}{\Pi^2} + \frac{y^2}{\Pi^2 \sin^2 \beta} = 1, \quad (7.2)$$

where \odot is the Sun's longitude. The motions $\Delta\alpha$ in right ascension and $\Delta\delta$ in declination depend also on ϵ , the obliquity of the ecliptic to the celestial equator:

$$\Delta\alpha \cos \delta = \Pi(\cos \alpha \cos \epsilon \sin \odot - \sin \alpha \cos \odot) \quad (7.3)$$

$$\begin{aligned} \Delta\delta = & \Pi(\cos \delta \sin \epsilon \sin \odot - \cos \alpha \sin \delta \cos \odot \\ & - \sin \alpha \sin \delta \cos \epsilon \sin \odot). \end{aligned} \quad (7.4)$$

The required angular accuracy of around 10 microarcseconds can only be achieved with long baseline interferometer arrays, using a differential technique to measure changes in position relative to a distant reference radio source situated within a few degrees of the pulsar. Corrections for path differences in the ionosphere are required; these may be computed from models of the ionospheric electron content and its lateral gradient, or they may be determined from their differential effects over a wide receiver bandwidth. The differential method was introduced by Lyne *et al.* (1982) for measurements of proper motion and developed to a fine degree for parallax by Brisken *et al.* (2002) and Chatterjee *et al.* (2009), using the Very Long Baseline Array (VLBA). Early interferometric parallaxes are listed by Brisken *et al.* (2002). Deller *et al.* (2019) measured parallaxes of 57 pulsars, achieving a precision of 4.5 microarcseconds and extending measured distances beyond 2 kpc. The precision achieved depends on the intensity of the pulsar. These results show that measurements can be extended to luminous pulsars up to the distance of the Galactic Centre, so covering half the Galaxy.

Figure 7.2 shows two examples from Brisken *et al.* (2002). Five positions of PSR B1929+10 ($\Pi = 3.0$ mas, $d = 330$ pc) spread through a year fall precisely on an ellipse, as expected from parallactic motion. The positions of PSR B0950+08 ($\Pi = 3.8$ mas, $d = 262$ pc) show a large proper motion with the annual parallactic motion superposed.

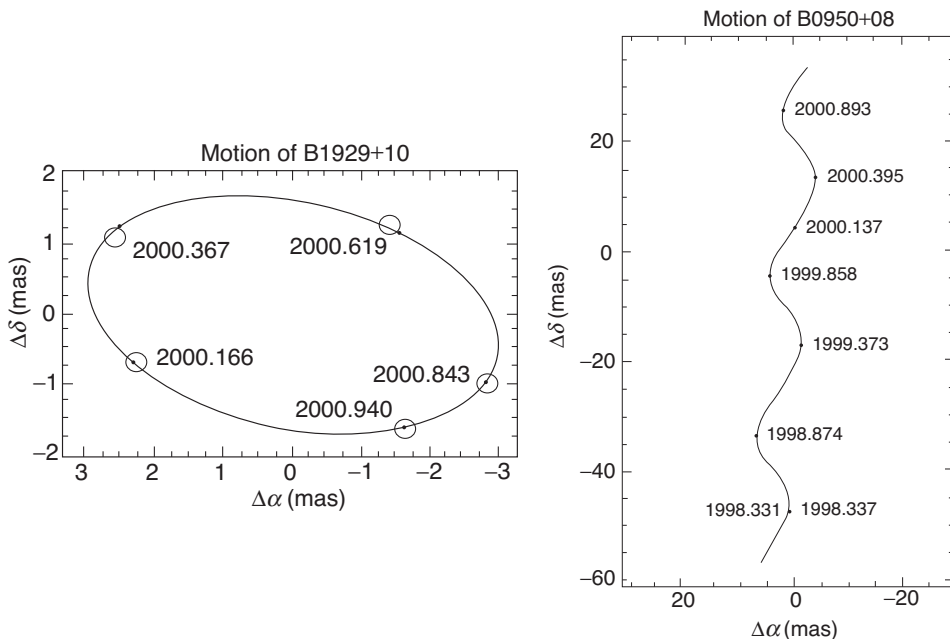


Figure 7.2 Parallactic motion of two pulsars (Brisken *et al.* 2002). PSR B1929+10 shows the classical parallactic ellipse; PSR B0950+08 has in addition a large proper motion that leads to the combined sinusoidal and linear motion across the sky.

7.1.1 Parallax from Timing

The effect on pulse arrival time is a delay with six-month periodicity. Figure 7.1 shows the maximum extra path, amounting to $a^2 \cos^2 \beta / 2cd = \Pi a \cos^2 \beta / 2c$.

The timing precision needed to detect parallax in this way is high but is achievable for millisecond pulsars. The pulsar timing array programs attempting to detect gravitational waves are resulting in large and improved timing data sets that are now allowing dozens of timing parallaxes to be measured for millisecond pulsars. In some cases this is allowing parallaxes as small as 0.3 mas to be measured (e.g. Alam *et al.* 2020).

7.2 Kinematic Distances

A component of velocity transverse to the line of sight gives rise to an increasing pulse delay, which we introduced in Section 5.6 as an increase in apparent period derivative \dot{P} (the Shklovsky effect). Using Figure 7.1 for a pulsar at distance d moving transverse to the line of sight with velocity V , the pulse delay τ is given by

$$\tau = \frac{a^2}{2dc} = \frac{V^2 t^2}{2dc}. \quad (7.5)$$

This applies equally for a transverse movement of the observer or the pulsar. It is observed as a rate of change \dot{P} in period P , given by

$$\dot{P}/P = \frac{1}{c} \frac{V^2}{d}. \quad (7.6)$$

For example, a pulsar at distance $d = 1$ kpc with a transverse velocity of 100 km s^{-1} has $\dot{P}/P = 3.4 \times 10^{-11} \text{ y}^{-1}$ due to the Shklovsky effect. For most long period pulsars, the effect is an unimportant contribution to \dot{P} ; even for PSR B1133+16, which has a large proper motion and is at a small distance, it amounts to only 5% of the measured value of the characteristic age $P/2\dot{P}$. Since the intrinsic slowdown rate is necessarily unknown, the magnitude of the Shklovsky effect cannot usually be determined. Most millisecond pulsars, however, have very low intrinsic values of \dot{P} , and this kinematic effect may be the dominant contribution to the observed slowdown rate (Camilo, Thorsett & Kulkarni 1994).

The Shklovsky effect applies to all periodic phenomena, including the orbital period P_b of a binary pulsar (Bell & Bailes 1996). Except in those systems where the emission of gravitational waves is important, or in eclipsing binary systems with low-mass companions, there is not expected to be a significant intrinsic rate of decrease, and the Shklovsky effect is predominant.

This was first demonstrated in the millisecond binary pulsar PSR J0437–4715, which has now been timed with sufficient accuracy over a period of ten years to give both a proper motion and a kinematic distance (Verbist *et al.* 2008). The observed value of \dot{P}_b is $(3.73 \pm 0.06) \times 10^{-12}$. At this level of accuracy, correction must be made for acceleration of both the pulsar and the Solar System in the gravitational field of the Galaxy. The distance obtained is 157.0 ± 2.4 pc, in satisfactory agreement with the value of 156.3 ± 3 pc obtained from trigonometric parallax.

For the binary B1534+12, the observed rate of slowdown in orbital period can be attributed mainly to gravitational radiation (see Chapter 6); this can, however, be calculated from theory, leaving a well-determined residual due to the transverse velocity. For this pulsar the proper motion but not the parallax was known, so that it was possible to find the distance from the observed slowdown (Stairs *et al.* 2002). An independent accurate measurement of the distance would provide a check on the calculated rate of gravitational slowdown in this system.

Some remarkably accurate distances are becoming available from kinematic distances for pulsars at distances less than 1 kpc. Table 7.1 shows three early determinations. The table includes ratios of the kinematic distance to distances derived from the measured DM and the then-current knowledge of the electron density

Table 7.1. *Kinematic distances and DM distances*

PSR	l°	b°	DM (pc cm $^{-3}$)	D _K (kpc)	D _K /D _{DM}	Ref
J0437–4715	69	14	2.6	0.1570 ± 0.0024	1.1	1.
J1012+5307	133	39	9.0	0.84 ± 0.09	2.1	2.
J2145–0750	326	5	9.0	0.5 ± 0.2	1.0	3.

References 1. Verbiest *et al.* (2008); 2. Lazaridis *et al.* (2009); 3. Löhmer *et al.* (2004a).

distribution. Note that this is a factor of two for PSR J1012+5307, indicating the need for further improvement in the model electron density distribution.

7.3 Pulsar Distances from Neutral Hydrogen Absorption

Interstellar matter, which comprises a large proportion of the mass of the Galaxy, is most obvious in the form of dust clouds, which obscure the distant regions of the Milky Way. The more diffuse gas, which pervades the whole Galaxy, is observable optically through the absorption lines of ions such as Ca II, Na I, etc., which appear in stellar spectra. The most abundant element in the interstellar medium is hydrogen. Neutral hydrogen is observed through its radio spectral line emission at 21 cm wavelength, the Doppler frequency shifts giving a dynamical picture of its distribution throughout the Galaxy.

Pulsars at low Galactic latitudes may be observed through the spiral arm structure of the Galaxy, and their spectra will then show absorption at 21 cm wavelength by neutral hydrogen in clouds along the line of sight. The spin-flip transition responsible for the absorption is inherently narrow-band, and the hydrogen is at a low enough temperature (below 100 K) that most of the structure in the observed spectral line is due to Doppler shifts that are related to the bulk velocity of gas relative to the velocity at the Earth. The absorption relates to structure in front of, but not behind, the pulsar. Using a dynamical rotation model of the Galaxy, the velocity structure of the absorption can thus be interpreted as distance.

The pulsating nature of the source is a great advantage in these measurements. The spectrum of the 21-cm line as observed in the direction of any pulsar includes the emission spectrum of all the hydrogen in the telescope beam, and the superposed absorption spectrum of the pulsar is only a small perturbation. The pulsation means, however, that the perturbation is detectable by comparing the spectrum during the pulses with the spectrum between the pulses. A typical observation integrates this difference over some thousands of pulses. The first observations to be made in this way were of PSR B0329+54 (de Jager *et al.* 1968). Figure 7.3 shows a comparison

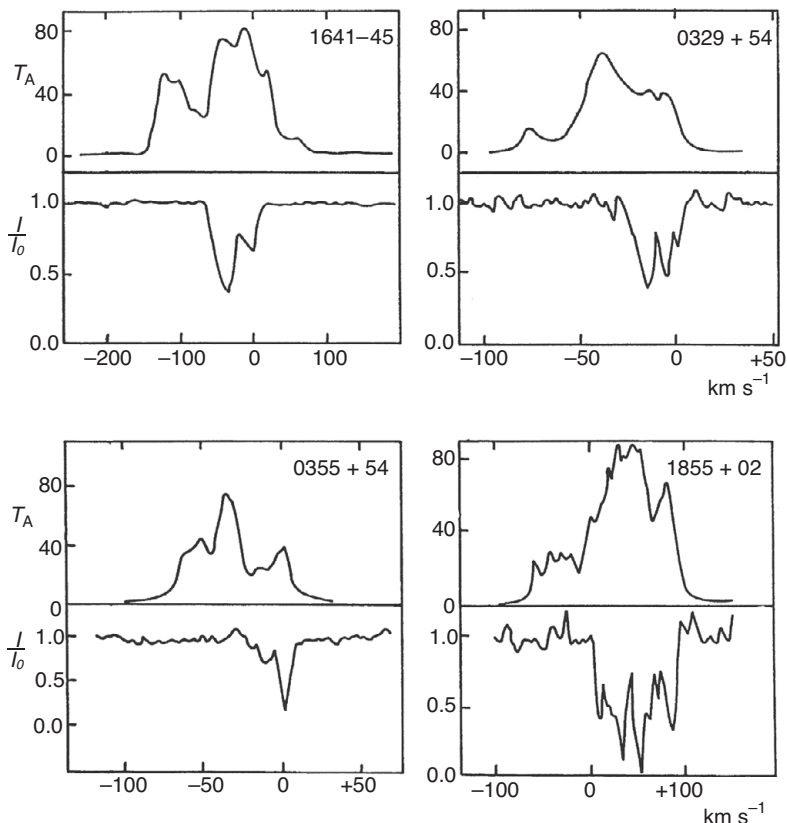


Figure 7.3 Hydrogen-line absorption spectra in pulsars. In each panel, the lower trace shows the absorption spectrum and the upper trace the hydrogen emission spectrum from the same direction. Spectral features that are seen in both absorption and emission correspond to hydrogen gas in front of the pulsar (Graham *et al.* 1974; Caswell *et al.* 1975).

of the emission and absorption spectra for pulsars recorded by Graham *et al.* (1974) and by Caswell *et al.* (1975). In these observations the pulsar is clearly located between HI components, giving a useful measurement of distance.

There is, however, an inherent problem in the interpretation of absorption spectra in terms of distance, which applies to lines of sight within 90 deg longitude from the Galactic centre, i.e. inside the solar circle. At ± 90 deg, the line of sight is tangential to Galactic rotation, and there is no differential velocity in the nearby spiral structure. Closer to the centre there are two distances corresponding to the same velocity. The problem is shown in Figure 7.4, where the lower curve shows the relation between velocity and distance in the direction of PSR J1401-6357; here the main absorbing features could be at either of two widely separated locations.

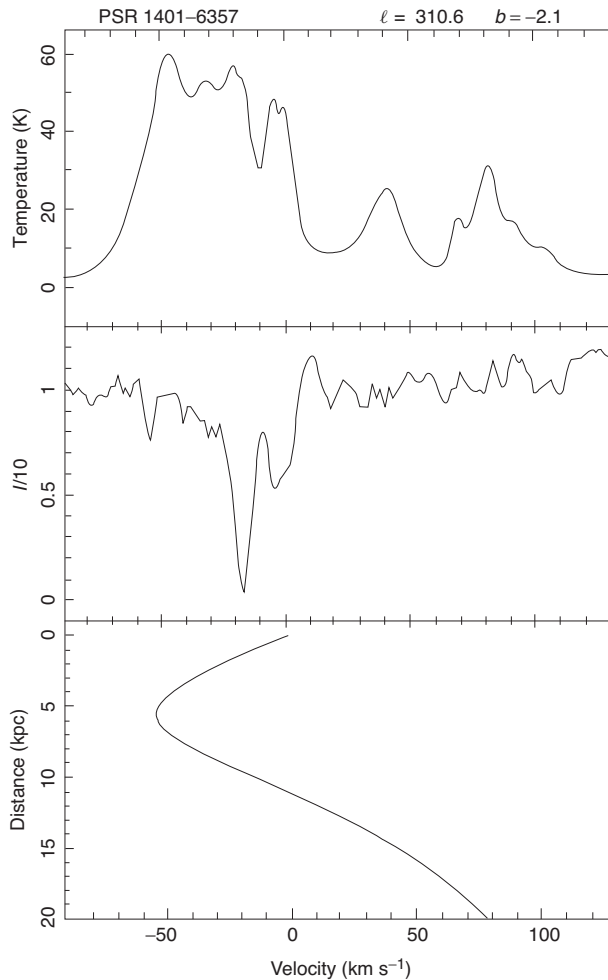


Figure 7.4 The interpretation of HI absorption spectra. The lower trace shows the relation between velocity and distance for PSR J1401–6357; in this example the line of sight crosses the Galactic plane within the solar distance (Johnston *et al.* 1996).

Although these distances obtained from hydrogen line absorption are important in constructing a model of electron density distribution, they are inevitably inaccurate and often give only upper or lower limits; nevertheless, they provide the main calibration of the pulsar distance scale at large distances. Compilations of observations of distances measured by hydrogen line absorption may be found in Manchester and Taylor (1981), Frail and Weisberg (1990), Koribalski *et al.* (1995), Johnston *et al.* (1996) and Johnston *et al.* (2001). See also a discussion of the accuracy of these determinations by Verbiest *et al.* (2012).

7.4 Pulsar Distances from Optical Identifications

7.4.1 Supernova Remnants (SNR)

Since the original observations of the Crab Pulsar and its surrounding nebula, several such associations of pulsars with supernova remnants have provided some useful measurements of pulsar distances. These supernova remnants are mainly close to the Galactic plane; they provide a major calibration of electron density in the disk of the Galaxy. Searches in pulsar wind nebulae, some of which were found by X-ray telescopes, have yielded further identifications useful in establishing the model; for example Murray *et al.* (2002) discovered PSR J0205+6449 in the remnant 3C58, and Camilo *et al.* (2006a) found PSR J1833–1034 in SNR G21.5 at a distance estimated from HI line absorption in the remnant emission as 5 kpc. References to well-established associations between pulsars and supernova remnants may be found in Lorimer *et al.* (1998). Camilo *et al.* (2009a) reported the discovery of PSR J1747–2809 in a nebula close to the Galactic plane, possibly at a distance of 13 kpc; they note that fewer than 20 such associations have been firmly established. Higher-sensitivity surveys of the Galactic plane with telescopes such as the Murchison Widefield Array and MeerKAT are revealing a large number of new supernova remnants (see e.g. Hurley-Walker *et al.* 2019a,b), which may result in many more associations. However, associations are difficult when the remnants are large as there may then be a number of unassociated pulsars lying within the remnant.

7.4.2 Globular Clusters

Several hundred pulsars, mostly MSPs, have been identified in the globular clusters, which are distributed in a roughly spherical halo extending well outside the disk of the Galaxy. The dispersion measures of these pulsars located within globular clusters are particularly useful in extending the measurements outside the plane of the Galaxy and to large distances; this is possible because the distances to the clusters are usually well-established by optical distance methods of astrometry and photometry.

7.4.3 White Dwarf Binaries

Binary systems in which a pulsar is associated with a visible white dwarf star may in some cases yield accurate distances. The companion of PSR J1012+5307 was identified as a white dwarf by Lorimer *et al.* (1995). By following the Doppler shift of optical spectral lines, Lange *et al.* (2001) found a distance of 840 ± 90 parsecs and also the mass of the companion.

Although white dwarf stars are generally faint optically, many of the nearer ones are within range of the astrometric satellite GAIA. The parallax of the white dwarf companion of PSR J1012+5307 is among these, giving a distance of 0.94 ± 0.03 kpc (Jennings *et al.* 2018). It is even possible to get distances to pulsars where no timing or interferometric distance is known. For example, Jennings *et al.* (2018) found the distances to PSR J1227–4853 and PSR J1431–4715 using the GAIA parallaxes for their white dwarf companions. More measurements will be possible as the GAIA data set expands. Obtaining accurate distances from radio and optical interferometric methods and also through radio pulsar timing allow the two important reference frames to be tied together (see Section 5.4).

7.5 Radio Interstellar Scattering

In addition to the dispersive delay, which is the main effect on radio waves propagating in the ionised interstellar medium, there are scattering processes that are observed as intensity fluctuations (scintillation), angular broadening (corresponding to optical ‘seeing’) and pulse broadening, all due to multi-path propagation. These effects are mainly observed in pulsars, as described in Chapter 19, but they are also occasionally observable in point-like extragalactic radio sources. We note here that they depend primarily on the square of the fluctuations in electron density and also to some extent on the distribution of irregularities along the line of sight to the radio source. If there is a close relation between the total electron content and its fluctuations, the radio scattering measurements can give information on the distribution of electron density. The relation seems to be close enough for scattering observations to be useful in constructing the model electron distribution, especially for extragalactic sources at high Galactic latitude, when they relate to the integrated electron density through the whole of the disk of the Galaxy. It should be emphasised that the model is concerned with an integrated electron content; on a shorter scale, radio scintillation observations described in Chapter 19 show that the distribution of electron density along the line of sight to most pulsars is very uneven.

Using long-baseline interferometers, the angular diameters of small-diameter extragalactic radio sources have been observed to be increased by scattering in our Galaxy; this provides a probe of the whole line of sight through the Galaxy and has been used to measure the electron content away from the plane. Readhead and Duffett-Smith (1975) used observations of diffraction in extragalactic radio sources to show that the scale height of the extended thick disk of ionisation is around 500 pc; this value is consistent with the observation that the largest values of DM for pulsars at high Galactic latitudes are about 20 cm^{-3} pc. Further measurements have been made in the anti-centre direction by Lazio and Cordes (1998).

7.6 The H II Regions

A first-order model of the distribution of electron density through the Galaxy consists of two components: a thick disk, extending to large Galactic radial distances, and a thin disk more closely confined to the Galactic plane, extending to around the solar radius and containing most of the spiral arm structure. Any such model must take account of large perturbations, reflecting the presence of both voids and concentrations. The most prominent are the discrete ionised clouds, known as H II regions, surrounding the very hot O and B type stars, whose ultraviolet light is responsible for their ionisation. A classical analysis by Strömgren (1939) showed that the ultraviolet light from a hot star ionises a spherical region whose radius S_0 (pc) depends on the density N (cm^{-3}) of the interstellar hydrogen gas, and the radius R (in solar radii) and temperature T (K) of the star, according to

$$\log_{10}(S_0 N^{2/3}) = -0.44 - 4.51 \frac{5040}{T} + \frac{1}{2} \log_{10} T + \frac{2}{3} \log_{10} R. \quad (7.7)$$

Within this *Strömgren sphere*, the ionisation is complete. The density N is somewhat uncertain and may vary considerably from one H II region to another. It is generally taken to be about 10 cm^{-3} .

An individual H II region near the Sun may contribute significantly to the dispersion measure of any pulsar whose line of sight passes through the region. Typically a line of sight through an H II region may add up to 100 pc cm^{-3} to the DM of a distant pulsar. The most prominent H II region, the Gum Nebula, centred roughly on the direction of the Vela Pulsar, covers an angular diameter of about 35 degrees.

Prentice and ter Haar (1969) and Grewing and Warmsley (1971) listed these individual regions in the neighbourhood of the Sun and estimated their effect on apparent distances of pulsars. They also estimated the combined effect of the more numerous smaller H II regions; these may be regarded as a minor contribution to the thin disk.

7.7 The Model Electron Distribution

A simple model of the electron distribution was constructed by Lyne, Manchester and Taylor (1985). This ‘LMT’ model aggregated the whole of the thin disk, including all but one of the H II regions, into a single disk component with a density on the plane that decreases with distance R from the centre of the Galaxy. The distribution with height z above the plane was exponential, with a scale height of 70 pc. It also included a more extended disk with scale height 1000 pc. The Gum Nebula was treated separately. This model was developed further by Taylor and Cordes (1993), who distinguished a separate spiral arm component; many published pulsar distances have been derived from their model. Gomez, Benjamin and Cox (2001)

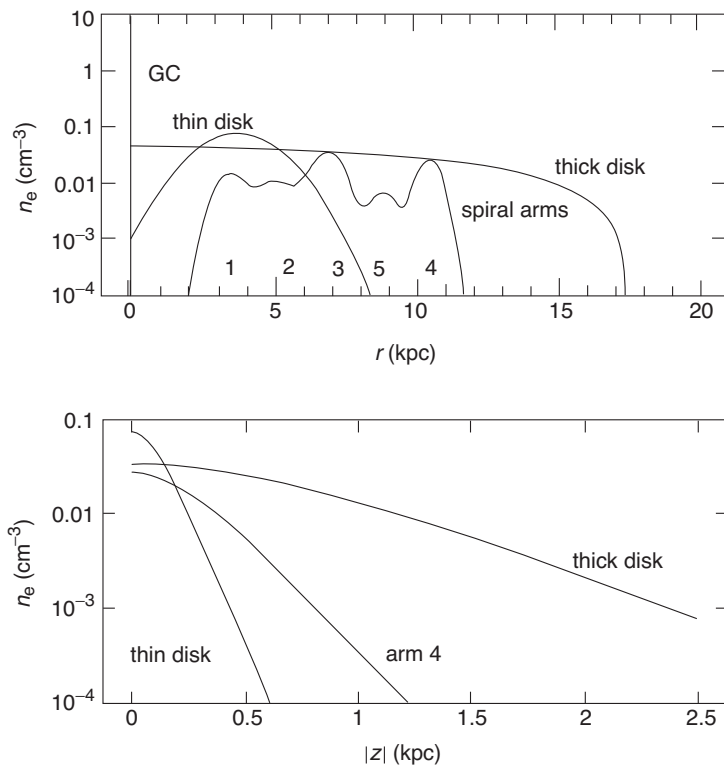


Figure 7.5 The disk and spiral arm components of the electron density distribution n_e , in the model by Cordes and Lazio (Cordes 2004). Top: n_e plotted against Galactocentric radius in the direction from the centre through the Sun. Bottom: n_e plotted against $|z|$, the distance from the Galactic plane. For the thin disk component, the cut is for Galactocentric radius 3.5 kpc; for the thick disk it is at the solar Galactocentric distance, and for the spiral arm component it is at 10.6 kpc.

used more recent data to refine this model, showing that a smoothed distribution accounted well for most pulsar distances.

Subsequently Cordes and Lazio (Cordes 2004) constructed a more elaborate model, designated NE2001, which includes the effect of a number of discrete ionised clouds and some large perturbations of electron density close to the Sun. The parallax measurements of pulsars within about 1 kpc of the Sun show low values of density (except in the direction of the Gum Nebula); this is due to a local hot bubble of gas centred on the Sun. This and other low-density regions are incorporated into the model. The large-scale components defined by Cordes and Lazio are shown in Figure 7.5.

The z distribution of the ionised component shown in Figure 7.5 is close to an exponential $\exp(-|z|/H)$. It is, however, plotted as $\text{sech}^2(|z|/H)$ rather than an

exponential, as this avoids a discontinuity at $z = 0$. The integrated total electron content is the same for both functions, and the $1/e$ heights are nearly the same.

The shape of the disk is approximately that of the neutral hydrogen disk. Kerr (1969) characterised the broad distribution of neutral hydrogen in the Galactic plane as a thin disk with a density n_{H} , which varies exponentially with distance z from the plane as

$$n_{\text{H}} = n_{\text{H}_0} \exp\left(-\frac{|z|}{z_0}\right). \quad (7.8)$$

The parameters n_{H_0} (central density) and z_0 (scale height) vary with Galactic radial distance R . According to Kerr, the scale height is reasonably constant at 150 pc for $R = 4\text{--}10$ kpc, decreasing to 85 pc at the 4-kpc spiral arm and increasing to 500 pc in the outer arms in the vicinity of $R = 15$ kpc. The central density is about 0.7 cm^{-3} for $R = 7\text{--}11$ kpc, decreasing to 0.3 cm^{-3} at $R = 4$ kpc and 0.1 cm^{-3} at $R = 15$ kpc.

The model electron density distribution is progressively under improvement as further parallax and kinetic parallax measurements become available. Yao, Manchester and Wang (2017) presented a model that uses 189 independently determined distances, including 70 from VLBI parallax and 30 from timing parallax measurements. The main component in their model is the thick disk, with scale height 1.2–2.0 kpc and extending to a Galactic radius 15 kpc, and a higher density thin disk, scale height 50–70 pc, peaking in density at Galactic radius 4–5 kpc. Spiral arm components are located within the thin disk, and individual regions of high and low density are located and parametrised in their model, which is designated YMW16.

7.8 The Accuracy of the Electron Density Model

The use of Dispersion Measure as the sole indicator of distance should be treated with some caution. It is intended as a broad-brush treatment of the whole sky, using a model that takes in only the major departures from a simple symmetrical electron distribution. An increasing number of new individual measurements of distance are now available to test its accuracy. Chatterjee *et al.* (2009) obtained the geometric parallax of a number of pulsars distributed over the sky to test the model and compared the parallax distances D_{π} with the distances D_{DM} obtained from dispersion measures using the Lazio and Cordes model NE2001. Observations of seven parallaxes at southern latitudes, by Deller *et al.* (2009) using the Australian Long Baseline Array, found differences up to a factor of two between D_{π} and D_{DM} , the largest ratios occurring for the most distant pulsars.

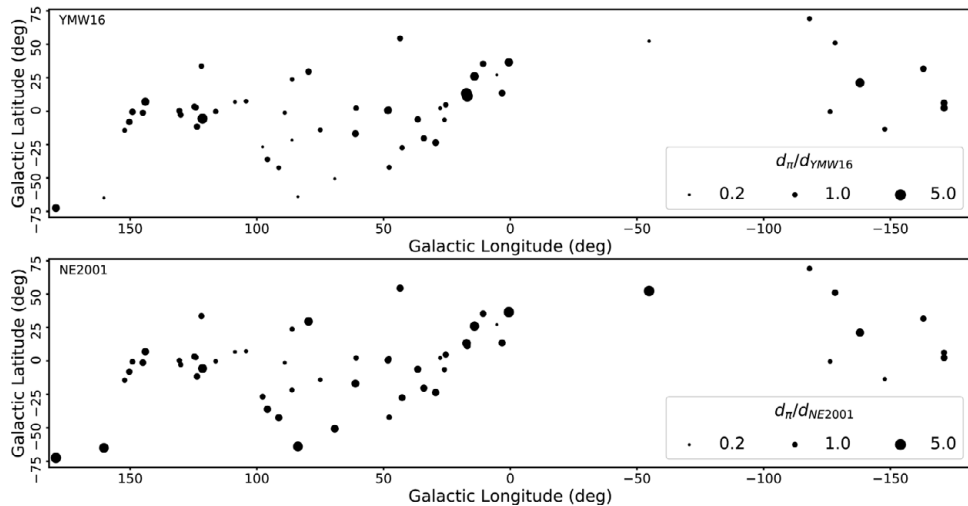


Figure 7.6 Comparison of distances obtained from parallax measurements (D_π) with those obtained from the YMW16 and NE 2001 distance models. The dot size is proportional to the ratio of the parallax distance to that predicted by the distance model (Deller *et al.* 2019).

The situation is steadily improving. Yao, Manchester and Wang (2017) showed that the model YMW16 yields distances that differ by less than 40% from independently determined distances for at least half those for which such distances are available. The most recent sample of interferometric parallaxes determined by Deller *et al.* (2019) are compared to the measurements from both the NE2001 and YMW16 models in Figure 7.6. It appears that the model DM distances are underestimates for pulsars located at large distances from the Galactic plane, often by a factor of two. An analysis by Gaensler *et al.* (2008) of 34 high Galactic latitude pulsars with well-determined distances, suggested that the scale height of electron density used in NE2001 should be increased to 1820^{+250}_{-120} pc. It seems also that more locally the electron density within about 1 kpc of the Sun is also considerably overestimated for some pulsars.

Part II

Observed Physical Characteristics

8

Pulse Profiles

Over the whole electromagnetic spectrum from radio to the very high energy gamma rays, pulsar radiation forms pulse profiles that are unique signatures differing from pulsar to pulsar. For some individual pulsars, notably the Crab Pulsar, very similar profiles are observed over the whole spectrum. The majority of pulsars are observable only in radio; here the individual pulses are often very variable, and it is only by averaging many hundreds or thousands of pulses that the characteristic shape is seen.

Observations of gamma-ray pulses from six pulsars by EGRET in the late 1990s, and the advent of the Fermi satellite (launched in 2008) with its Large Area Telescope (LAT) and the air shower Cerenkov detectors HESS, MAGIC and VERITAS, opened a new window for observing the high energy beamed radiation from pulsars and the continuum emission from some associated nebulae energised by pulsars, the *wind nebulae*. Many young pulsars, and especially those with large spin-down energy, are observable with the LAT, along with many of the millisecond pulsars. In the high-energy regimes, the radiation is detected as individual photons, arriving so infrequently that typically integration over many millions of pulse periods is needed before the profile emerges.

These integrated profiles are the key to understanding the geometry and the physical processes within the magnetosphere surrounding the neutron star (Chapters 13 and 16). We distinguish two general categories, high-energy (HE) and radio, which are believed to originate in different regions of the magnetosphere and are generated by different mechanisms; there is, however, some overlap between these two categories, as for example in the Crab Pulsar (Figure 8.1), where the radio profile has components falling into both categories.

In this chapter, we start with the gamma-ray profiles, which have proved to be the key to understanding the structure of the outer magnetosphere (Chapter 16). We then describe the radio pulses, which display an astonishingly wide range of phenomena, both in their detailed shapes and in their variations over various time scales.

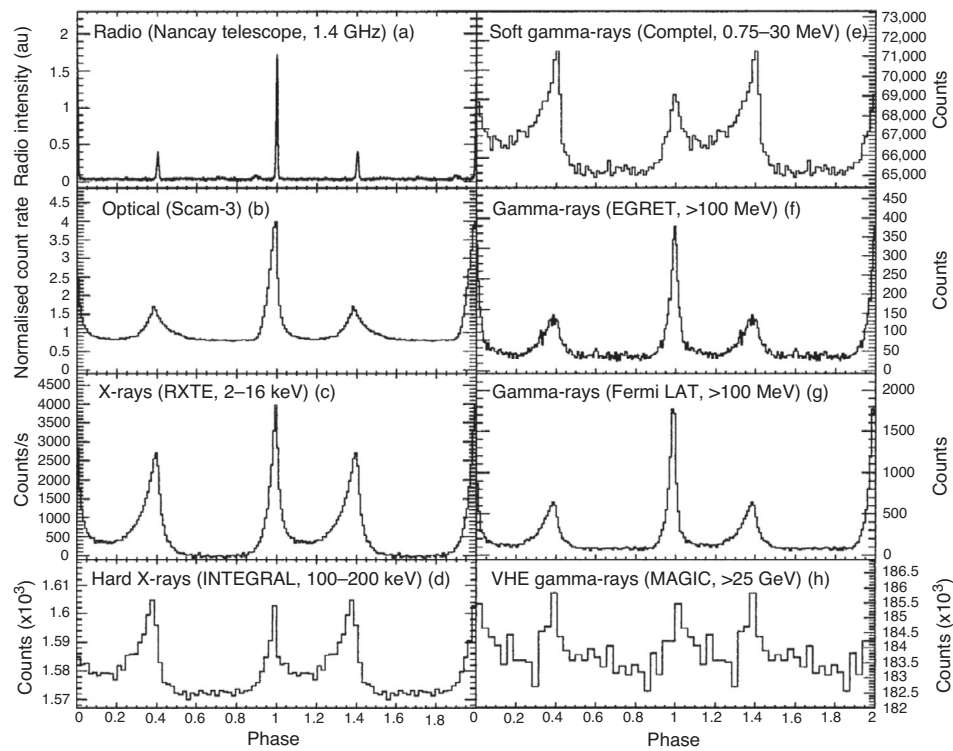


Figure 8.1 Pulse profile for the Crab Pulsar from radio wavelengths to gamma rays (Abdo *et al.* 2010b).

8.1 High-Energy Profiles

Apart from ground-based Cerenkov shower detectors (Chapter 2), high energy photon (x-ray and gamma-ray) observations can only be made from above the atmosphere. The construction of a light curve from observations of individual photons as they arrive at a distant and rapidly moving satellite, requiring measurements of angular positions to a fraction of an arcminute and timing to a fraction of a millisecond, is a demanding technological challenge. Nevertheless, there is now a growing catalogue of pulsars with published gamma-ray pulse profiles, more than double the 117 listed in the second Fermi LAT catalogue (Abdo *et al.* 2013). These cover a wide range of pulse shapes, as well as different categories of pulse period and spectrum (Smith *et al.* 2017).

The archetypical integrated pulse profile is that of the strongest and first pulsar to be observed at gamma-ray energies, the Crab Pulsar, shown in Figure 8.1. The twin

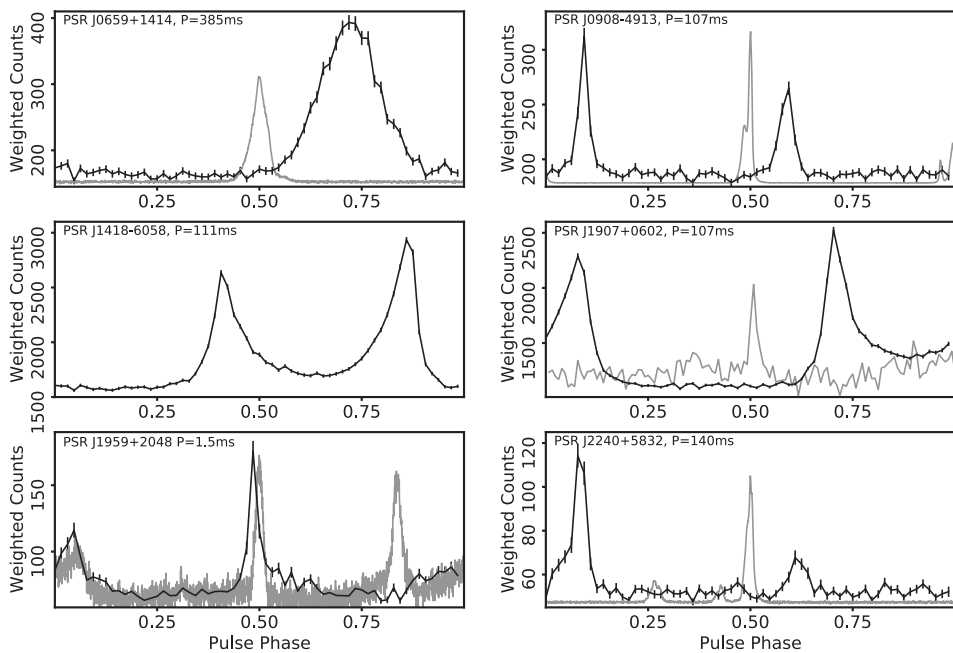


Figure 8.2 A collection of gamma-ray profiles (black line) and radio profiles (grey line) spanning the diversity of phenomena including the radio quiet source PSR J1418–6058 (Data kindly provided by D. Smith).

peaks of these profiles, separated by nearly half the pulse period and with some wider components between, are found in the majority of gamma-ray profiles. There are a whole range of different gamma-ray profiles (Figure 8.2), which range from narrow single peaks to broad connected double peaks and more complex profiles. Most gamma ray pulsars are also detected in the radio, and the radio pulses are typically offset from the gamma rays, reflecting their origin in different regions of the magnetosphere. In some cases, such as PSR J1418–6058 in Figure 8.2, there is no radio detected at all.

8.2 X-ray Pulse Profiles

Imaging x-ray telescopes mainly operate at photon energies of between 1 and 10 keV, corresponding to black-body temperatures of order 10^6 K. Thermal radiation from the surfaces of neutron stars, or from the accretion material in a binary system, is in a similar temperature range, and most x-ray pulsars are

observed as thermal sources, as described in Chapter 12. In this chapter, we are concerned with *rotation powered* pulsars, in contrast to the *accretion powered* thermally radiating x-ray pulsars. The x-ray pulse profiles of the rotation powered pulsars are generally similar to their gamma-ray counterparts.

Figure 8.3 shows the pulse profiles at x-ray, gamma-ray and radio for PSR 0540–69 (Mignani *et al.* 2019). This energetic young pulsar, located in the Large Magellanic Cloud, was the first extragalactic pulsar to be detected.

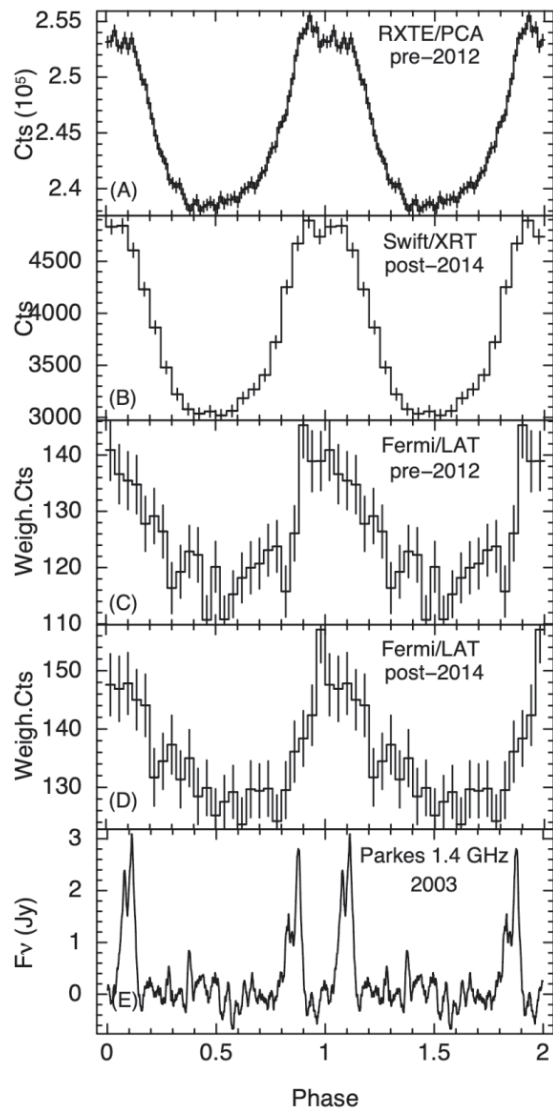


Figure 8.3 Pulse profiles of PSR B0540–69 at radio, x-ray and gamma-ray wavelengths (Mignani *et al.* 2019).

8.3 Optical and UV Pulse Profiles

The Crab Pulsar, which was first detected optically by Cocke, Disney and Taylor in 1969, is among a small group of pulsars detected in the optical and UV bands. Its twin-peaked pulse profile, shown in Figure 8.1, is remarkably similar over the whole available spectrum from radio to gamma rays (Spolon *et al.* 2019); at low

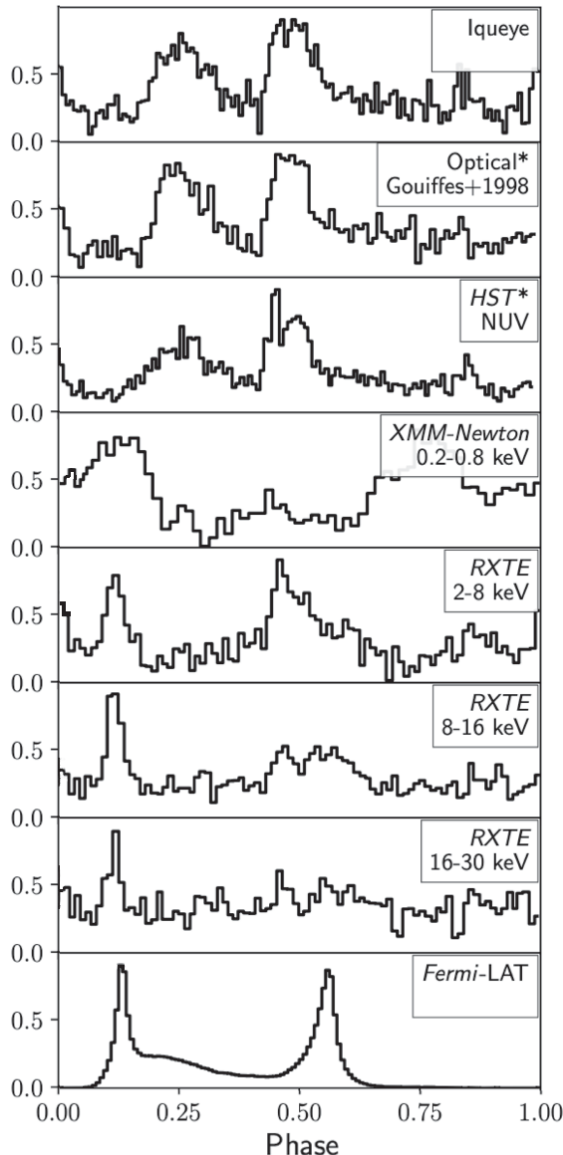


Figure 8.4 Profiles of the Vela Pulsar at optical, UV, x-ray and gamma-ray wavelengths, relative to the narrow radio pulse that lies at phase zero (Spolon *et al.* 2019).

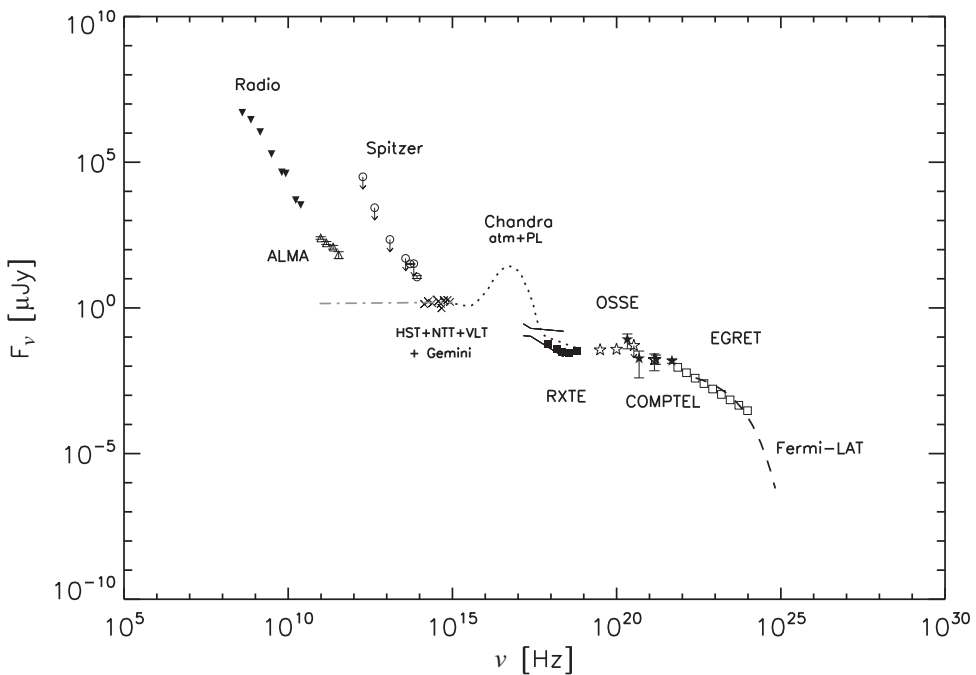


Figure 8.5 The Vela Pulsar: spectral energy distribution from radio to gamma wavelengths (Mignani *et al.* 2017).

radio frequencies, below 1 GHz, there is, however, an extra component with a steep spectrum. This component, known as the precursor, dominates the profile at frequencies below 100 MHz. We interpret this precursor as similar to the radio profile of normal pulsars, while the twin-peaked component is similar to the high-energy profiles at optical, UV and x-ray.

The Vela Pulsar, one of the brightest radio pulsars, is also observable optically and in the UV but is much fainter (Wallace *et al.* 1977). Figure 8.4 shows the double pulse profile at optical/UV, x-ray and gamma-ray wavelengths, relative to the narrow radio pulse. This pulsar has also been detected at millimetre wavelengths by ALMA (Liu *et al.* 2019). The spectrum appears to be continuous from radio to TeV (Figure 8.5), but this hides an intrinsic difference between radio and high energy radiation for this pulsar. As with the Crab Pulsar, it appears that two different sources are involved; the radio pulse resembles that of normal pulsars, while the optical/UV profile is a typical high-energy (HE) profile.

The ultraviolet (UV) brightness of the small number so far observed depends strongly on their ages, as seen in Figure 8.6 (Mignani *et al.* 2017). Apart from the Crab and Vela Pulsars, only three others have been seen to pulsate optically (PSR B0540–69 (Middleditch & Pennypacker 1985); B0656+14 (Shearer *et al.* 1997); Geminga (Shearer *et al.* 1998)). Their optical/UV pulse profiles are similar to their gamma-ray profiles.

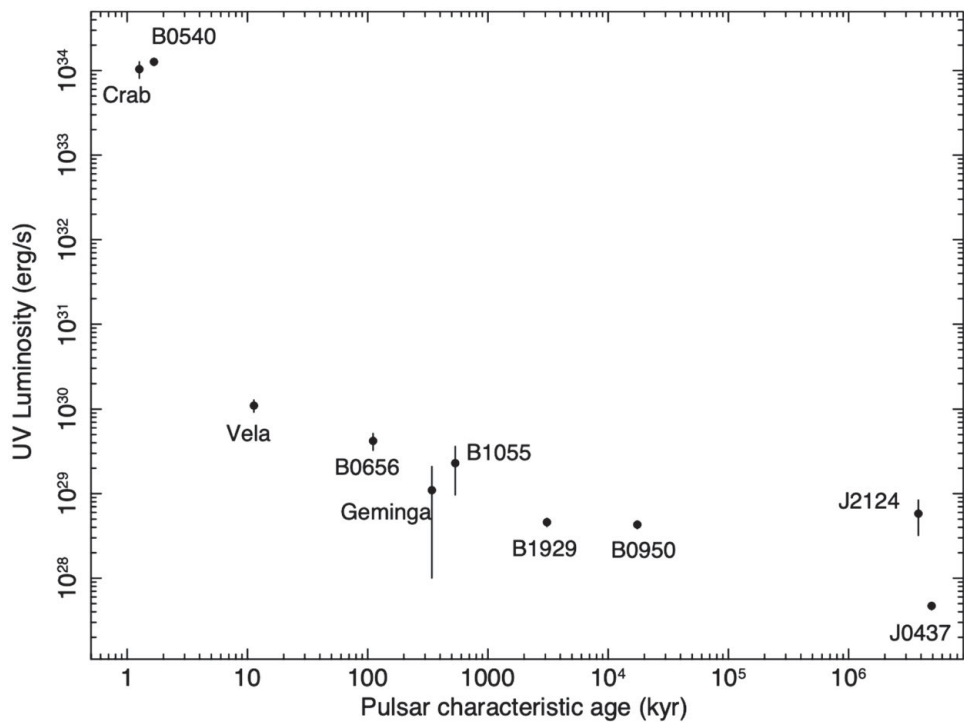


Figure 8.6 The UV luminosity as a function of characteristic age (Mignani *et al.* 2019).

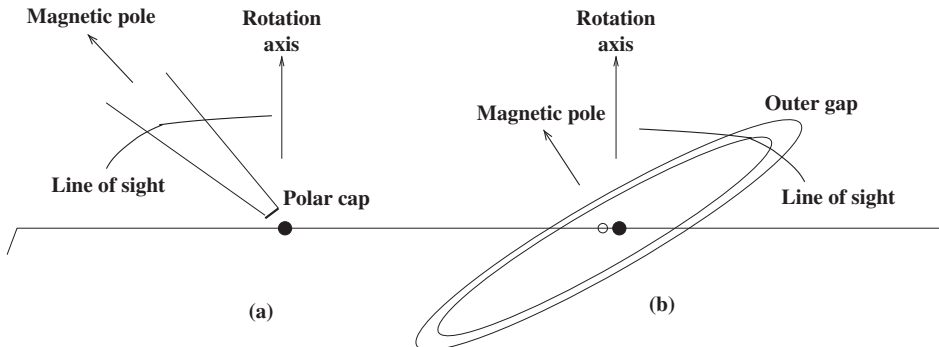


Figure 8.7 The locations of (a) polar cap and (b) outer gap emitting regions. The double peaks of high-energy pulses are attributed to the line of sight crossing the source in the outer gap, which forms a ring round the magnetic pole.

8.4 Polar Cap and Outer Gap

The radio pulse profiles from normal pulsars and the high-energy profiles (gamma, x-ray, optical) are evidently in distinct categories. We will explore their interpretation in Chapter 16, but a preliminary discussion may be helpful. Figure 8.7 shows in outline the ways in which the radiation beams from the two categories are

intersected by the line of sight as the star rotates. In each case, the magnetic axis is inclined at an angle to the rotation axis. In (a), a beam is radiated from a region of the magnetosphere above a magnetic pole, while in (b), the radiation originates in an outer gap located far out in the magnetosphere, in an extended region forming a ring or halo. A typical pulse originating in the polar gap has a single profile (albeit with internal structure), while the outer gap produces a double pulse with two components that are separated by up to half a rotation.

8.5 The Radio Profiles

In this section, we are concerned with the integrated pulse profiles of the majority of normal (non-recycled) radio pulsars, in which the emission is associated with the polar cap. In contrast, the high-energy (HE) profiles are generally attributed to sources in the outer magnetosphere.

Integrated radio pulse profiles are available for all the known pulsars. They typically cover about 10–20 deg of rotational phase; some are as short as 1 deg, and others extend almost up to 360 deg. Examples are shown in Figure 8.8.

Most integrated profiles comprise several components, each with a width of several rotation degrees. There are usually between one and five such components, although more, but less prominent, components may be seen in some very precisely measured profiles. These are often identified by fitting with gaussians, allowing their positions, widths and intensities to be quantified; the von Mises function is also used in fitting profiles of components (Weltevrede & Johnston 2008).

8.6 Integrated Pulse Widths

Outside the main radio pulse profile, the flux density usually falls rapidly to an undetectable level, indicating that radiation is typically emitted in a narrow beam and that the emitting region has a limited extent within the magnetosphere. Defining the angular width of an observed profile against a background of random noise requires setting an arbitrary level, usually 50% or 10% of the peak intensity. Figure 8.9 shows W_{10} (the width at 10% of the peak intensity) plotted against pulse period P . Although there is a wide scatter, there is a trend towards smaller angular width in the integrated profiles of longer period pulsars (see also Johnston & Karastergiou 2019). The lower bound to the wide scatter in this plot in this plot shows width roughly proportional to $P^{-0.3}$.

For a small minority of pulsars, an *interpulse* is observed approximately half-way through the cycle. An example is shown in Figure 8.10. In most cases this is interpreted as an oppositely directed beam of radiation, originating in the opposite magnetic pole and observable when the magnetic dipole axis is nearly perpendicular to the rotation axis. Manchester and Lyne (1977) and Maciesiak *et al.* (2011) point

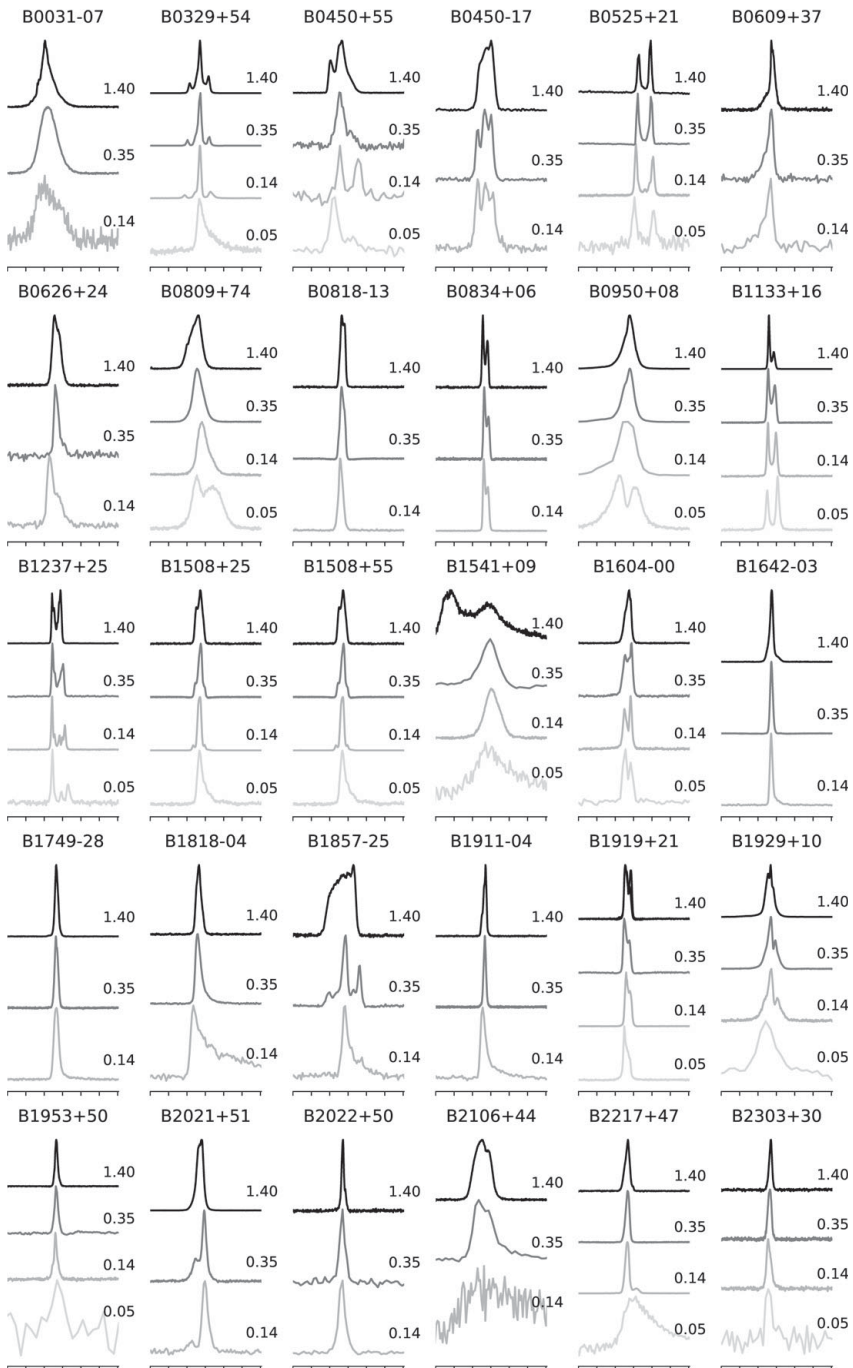


Figure 8.8 Pulse profiles (Pilia *et al.* 2016) of normal pulsars at a range of frequencies (as labelled in GHz). The pulse profile spans 120 degrees, and the tick marks are at 20 degree intervals. In some cases only part of the pulse is visible due to scatter broadening.

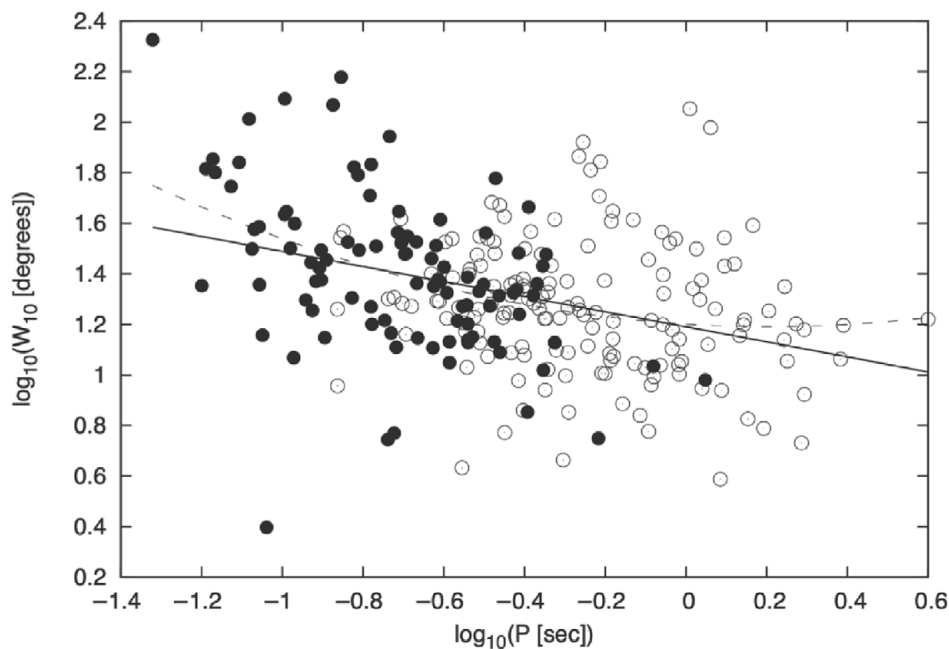


Figure 8.9 The measured profile 10% widths versus period P . The solid line is the power-law fit through the data, which has a slope of -0.30 . The dashed line indicates the fit of a second order polynomial through the data points (which is statistically no better than the power-law fit). The filled points are pulsars with $E > 10^{34}$ erg/s, and the open points have a lower E . All the observations shown were made at a wavelength of 20 cm (Weltevrede & Johnston 2008).

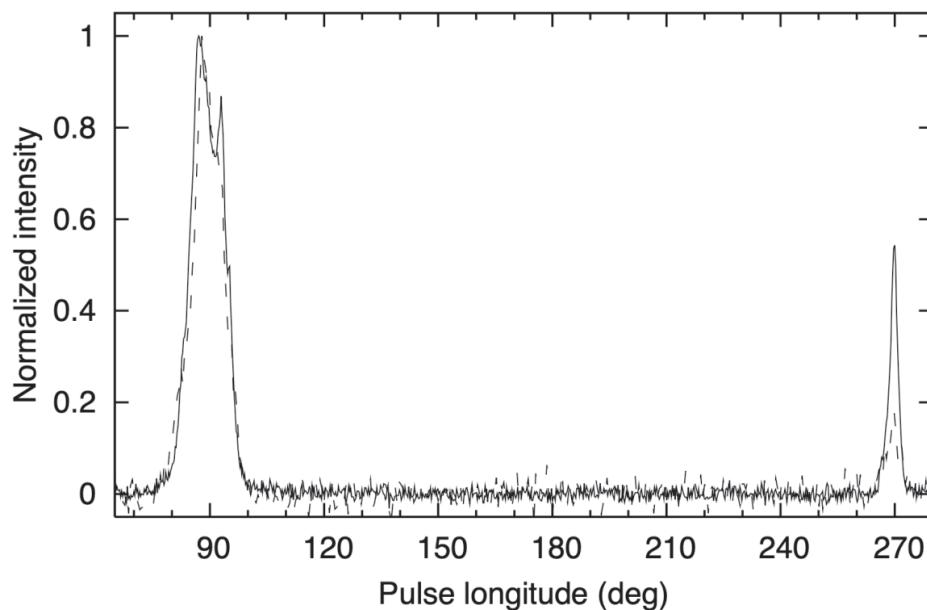


Figure 8.10 Interpulse in PSR B1702–19. The intensity profiles are nearly identical at 1380 MHz (solid line) and at 328 MHz (dashed line). The two profiles are normalised to their peak intensity (Weltevrede *et al.* 2007).

out that this occurs mainly in young pulsars, suggesting that magnetic alignment occurs in older pulsars.

8.7 Radio Frequency Dependence

Although the components of an integrated pulse profile may have appreciably different spectra, they are usually recognisable over a very wide frequency range. The spacing between them, and with it the whole profile width, usually expands at low radio frequencies, as shown in Figure 8.11. This progressive increase can often be fitted by a power law (Figure 8.12), in which the separation of individual components varies as $\nu^{-0.25}$ or thereabouts (Thorsett 1991). Xilouris *et al.* (1996) extended the measurements of profile widths to 32 GHz (Figure 8.13), where they were able to measure widths at half intensity (W_{50}) for 8 pulsars. Combining their measurements with published values at lower frequencies shows that a better fit is obtained by adding a constant to the power law, as

$$W_{50} = a_0 + a_1 \nu^{-\gamma}, \quad (8.1)$$

with $0.3 < \gamma < 0.9$.

Observations of a large sample of pulsars with good temporal resolution at frequencies below 240 MHz have shown that the behaviour can be more complex, with new components appearing. In some cases the narrowest pulse features are

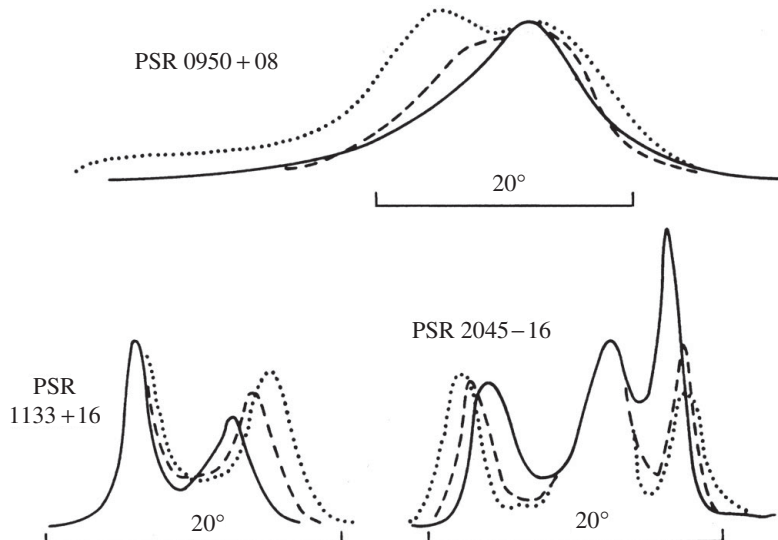


Figure 8.11 Integrated profiles of PSR B0950+08, PSR B1133+16 and PSR B2045–16 at 610 (solid line), 240 (dashed line) and 150(dotted line) MHz.

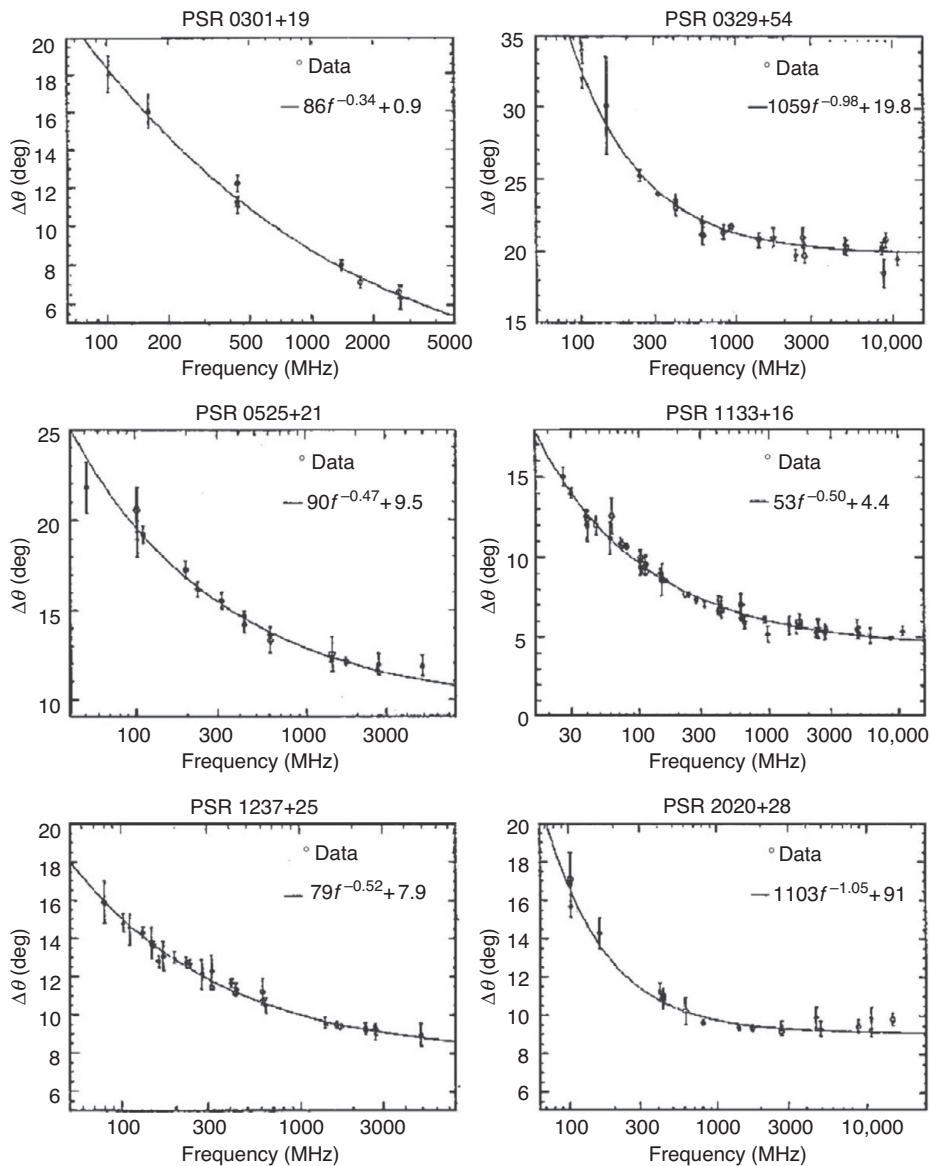


Figure 8.12 Component separations versus frequency for six pulsars, showing best fit curves following a power law plus a constant (Thorsett 1991).

seen at the lower frequencies (Pilia *et al.* 2016). Chen and Wang (2014) extended the analysis of profile widths to a higher range of frequencies, from 0.4 to 32 GHz, where they found that only half of their sample of normal pulsars continued the expansion with decreasing frequency, while some actually showed a contraction.

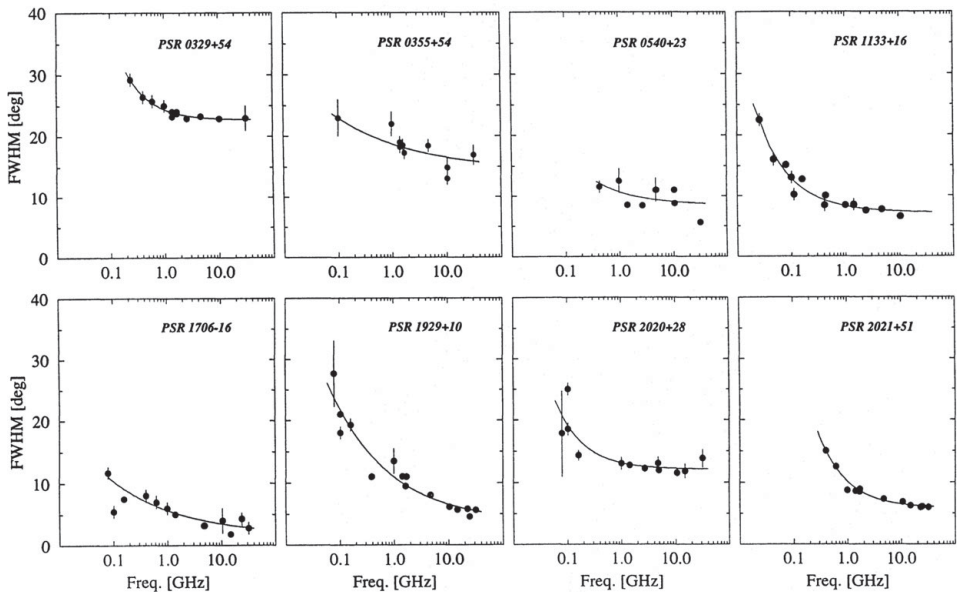


Figure 8.13 Profile widths W_{50} measured at a 50% intensity level versus frequency for six pulsars detected at frequencies up to 32 GHz (Xilouris *et al.* 1996).

8.8 Beam Components, Core and Cone

The symmetry displayed in profiles such as PSR B0329+54 in Figure 8.8 leads naturally to a classification in which a central component is called a *core* while the outer components are regarded as part of a hollow *cone* (Gil, Kijak & Seiradakis 1993). These are not separate entities, although there is a gradation in properties with radial distance from the beam centre: the core components have larger widths and steeper spectra (Lyne & Manchester 1988).

The angular radiated width of the individual components within the beam is usually found by fitting gaussian curves.¹ As we noted for the overall profile widths, the distribution of widths of the components shows a well defined lower bound; this is to be expected since the width must depend on the angle between the rotation axis and the magnetic pole. The shortest pulses should be observed from pulsars where this inclination angle α is near 90 deg; the scatter of points above this lower limit corresponds to pulsars with smaller values of α . From this lower bound, the half-power widths w_{50} (in degrees, at 1.4 GHz) of conal and core components are found to be

$$w_{50,\text{conal}} = 2.5 P^{-\frac{1}{2}} / \sin \alpha \quad (8.2)$$

$$w_{50,\text{core}} = 1.75 P^{-\frac{1}{2}} / \sin \alpha. \quad (8.3)$$

¹ The analyses in this section were derived from observations at frequencies around 1 GHz.

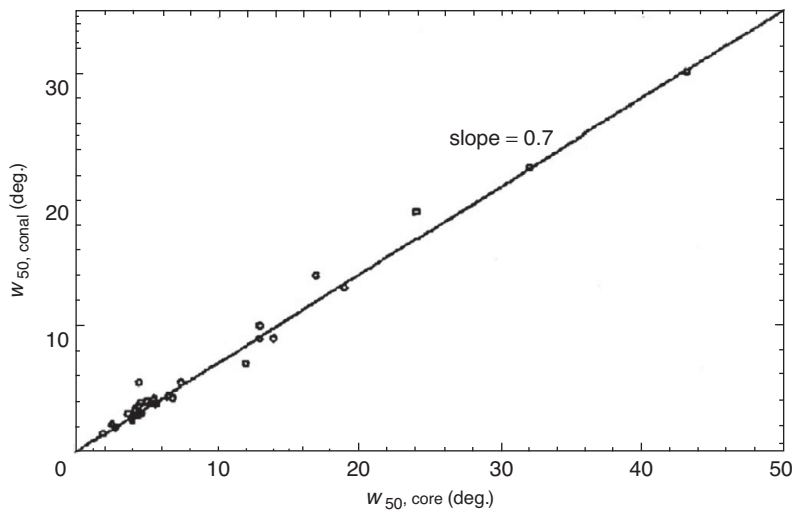


Figure 8.14 The relation of core component width $w_{50,\text{core}}$ to conal component width $w_{50,\text{conal}}$.

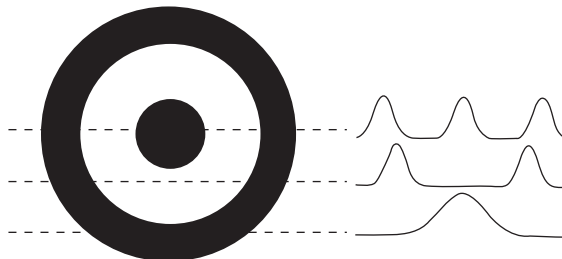


Figure 8.15 A model of core and conal beams, with various types of symmetrical profiles generated by lines of sight crossing at different impact parameters.

The difference in width between core and conal components is confirmed in practically all individual pulsars. The relation of core component width to conal component width, where both can be clearly distinguished, is shown in Figure 8.14; the conal components include both three- and five-component pulsars. The remarkably close relationship shows that the widths of core components are consistently about 1.4 times greater than the widths of conal components.

The apparent symmetry of many integrated profiles with two or more components suggests that they might be arranged as a discrete central core surrounded by a hollow cone of emission (Figure 8.15) (Komesaroff, Morris & Cooke 1970; Backer 1976). This model was developed by Rankin (1993), who made the further suggestion that the occurrence of five-component profiles indicated an arrangement in a double hollow cone.

Locating the component beams within an overall beam requires some knowledge of the beam geometry and the line of sight. Lyne and Manchester (1988) used estimates of these angles for some hundreds of pulsars, following models outlined in Chapter 16, and found no preference for components to be located within discrete cones. Han and Manchester (2001) followed the same geometric procedure to construct a two-dimensional image of the mean radio beam shape for 87 pulsars. They again found a smooth distribution over the polar cap but with some enhanced emission at the core and at around 0.7 of the polar cap radius.

8.9 The Overall Beam Shape

The geometry of the dipole field lines (Chapter 12) leads to a suggestion that the overall beam of polar cap radio emission may not be circular in cross-section. This remains as an area of uncertainty, although a circular beam has been assumed in this chapter. Narayan and Vivekanand (1983) suggested that the beam was elliptical, extended in latitude, while Biggs (1990) suggested the opposite, with a compression in latitude. Most investigations of normal pulsars (e.g. Lyne & Manchester 1988; Gil & Han 1996; Björnsson 1998) favour circular beams. There is some evidence that the overall beam shapes of millisecond pulsars may be compressed meridionally, that is, extended in latitude (see Chapter 16).

An actual observation of beam shape becomes possible in the rare circumstance that the spin axis of a pulsar precesses, so that the line of observation makes a progressively different cut across the radiated beam. The precession of the binary pulsar B1913+16 due to spin-orbit coupling revealed that the beam of this pulsar may have an hour glass-shape (Weisberg & Taylor 2002). The binary pulsar PSR J1906+0746 also precesses due to spin-orbit coupling, and over 13 years, the cuts across the beam are spread by 29° (Desvignes *et al.* 2019); in this case, the beam shape is found to be more complex.

Pulsars are only observable if the beam crosses the observer's line of sight. The total number of pulsars is therefore greater than the population deducible from the pulsar surveys (Chapter 4) by a *beaming factor*; the beam widths and alignments found in this chapter suggest that this factor varies from about two or three for the short period pulsars to about four or five for the long period pulsars. (Note that the beaming factor is smaller for gamma-ray pulsars, in which the emission covers wider solid angles.)

8.10 Polarisation

Radio pulses from all types of pulsars are characterised by very high degrees of linear and circular polarisation, reaching 100% in many cases. An example is the

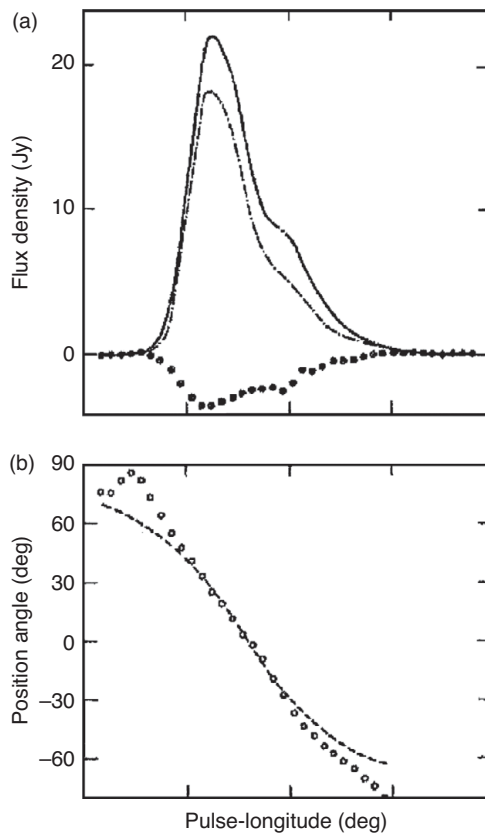


Figure 8.16 The integrated pulse profile of the Vela Pulsar, PSR B0833–45, showing the smooth sweep of polarisation position angle. (a) Solid line, total intensity; broken line, linearly polarised intensity; circles, circularly polarised intensity. (b) Position angle: circles measured values; dashed line, model for $\alpha = 60$ deg and $\beta = 6.2$ deg (Krishnamohan & Downs 1983).

Vela Pulsar, Figure 8.16, in which the integrated profile is fully linearly polarised through the whole of the profile, with a small circularly polarised component in part of the profile. The position angle of linear polarisation varies smoothly and monotonically through the profile, forming an S-shape curve extending almost to 180 deg. This pattern is substantially independent of radio frequency, apart from a rotation of the plane of polarisation due to Faraday rotation in the interstellar medium. In Chapter 16, we interpret this smooth position angle curve in the integrated profile as a spatial distribution of linearly polarised emitters.

The polarisation of all normal pulsars is available from routine measurements at or soon after their discovery. Examples are shown in Figure 8.17. It is remarkable that in many profiles, the position angle of polarisation follows a smooth continuous curve even when the profile contains several distinct sub-pulse components; there

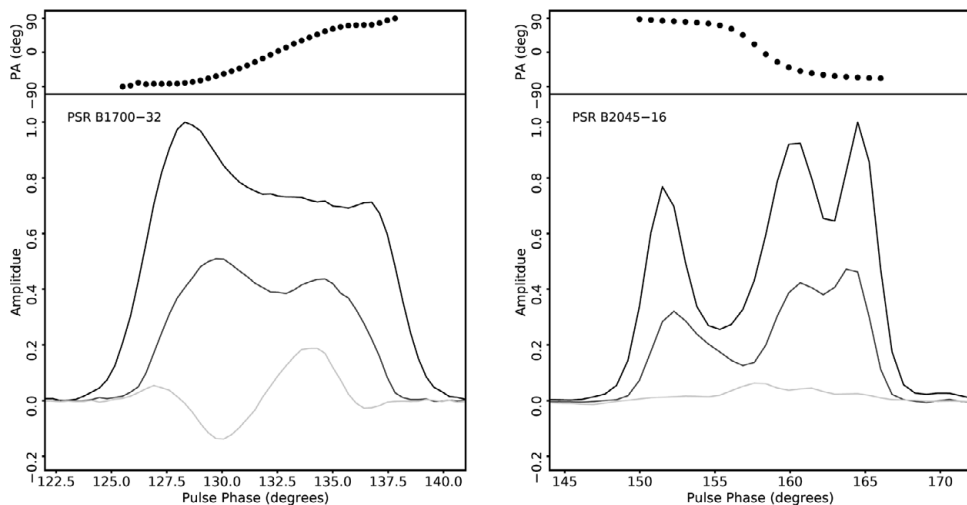


Figure 8.17 Integrated profiles of two pulsars, showing their polarisation characteristics.

are, however, profiles in which the position angle steps by 90 deg. Circular polarisation amounting to about 20% is often seen, reversing in hand near the centre of the profile. In some pulsars for which the profiles show less than full polarisation, individual pulses are observed with polarisation different from that of the integrated polarisation, accounting for the reduced polarisation in the integrated profile.

The geometry of observed polarisation is intimately related to the configuration of the magnetic field in the magnetosphere. We explore this relationship in Chapter 9 (Section 9.8).

8.10.1 Polarisation – Optical and UV

Although the integrated radiation of the few known optical/UV pulsars is observed to be polarised, the polarisation properties of their phase-resolved profiles are known only for the Crab Pulsar, for which there are detailed observations in both the UV and optical (Graham-Smith *et al.* 1996; Slowikowska *et al.* 2009). The maximum linear polarisation, up to 30%, is observed between the two peaks (main and interpulse); at both peaks there is a rapid swing of position angle similar to that observed in radio emission from normal pulsars, but less highly polarised. As yet no polarisation can be measured in x-rays or gamma rays.

8.11 Millisecond Pulsars

It might be expected that the radiation from millisecond pulsars (MSPs) would be very different from that of normal pulsars, since the scale of the magnetosphere and

the strength of the magnetic field are both many orders of magnitude smaller. In both the radio and the high-energy regimes, however, the observed integrated pulse profiles are not obviously different from those of normal pulsars. Examples may be found in Xilouris *et al.* (1998), Ord *et al.* (2004) and Han *et al.* (2009). There are, however, some characteristics of radio emission from MSPs that are significant in our later discussion of the location of the emitting regions:

1. The integrated profiles of MSPs below 240 MHz reveal that the separations and widths of the pulse components do not show the strong variation with frequency typical of normal pulsars (Kondratiev *et al.* 2016).
2. On average, the degree of polarisation in the integrated pulse profiles at 1.4 GHz is greater in the MSPs, although observations at higher frequencies show that, as for normal pulsars, the polarisation decreases rapidly (as shown in Figure 16.17).
3. The position angle curves are generally shallower than for normal pulsars (Yan, Manchester & van Straten 2011).

9

The Variability of Pulsar Emission

The well-organised radio pulse profiles obtained by integrating some hundreds of individual pulses conceal a rich diversity of behaviour among the individual pulses. The integrated radio profiles are made up of very varied individual pulses, each of which may have more than one distinct component: it is the distribution of these components over a range of pulse longitude, combined with their characteristic width and the probability distribution of their intensities, that determine the repeatable shape of the integrated profiles (Figure 9.1). Even the integrated profiles for many pulsars have two, or sometimes three, different stable forms and switch from one to another at intervals ranging from minutes to months; this effect is known as *mode changing*.

Although it may exist, no such complexity and variability has been observed in optical or other high-energy pulses, possibly because detection is severely restricted by low photon rates. Some pulsars, notably the Crab Pulsar, have radio pulses apparently originating in the same location in the outer magnetosphere as high-energy pulses; these do contain some very complex structure both in time and radio frequency, which we consider in Sections 9.9 and 9.10. This chapter is mainly concerned with pulses from the bulk of the known radio pulsars, the so-called normal pulsars. These are pulses believed to originate in the polar cap. The detailed behaviour of these pulsars is very revealing of the nature and location of the emitting sources, as considered in Chapters 16 and 17.

9.1 Subpulses

The components of an individual pulse are often identifiable as characteristic *subpulses*, with a typical width in longitude of a few degrees (as compared with the typical width of some tens of degrees for the integrated profiles). These sub-pulses may occur apparently at random longitudes within the ‘window’ defined by the

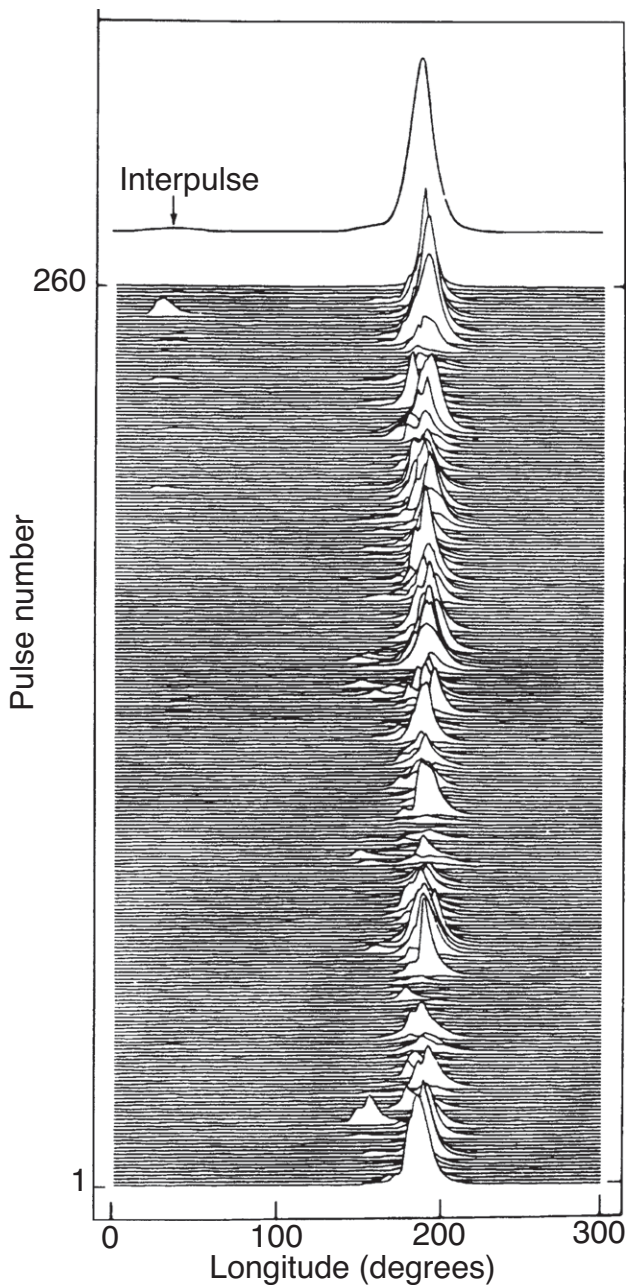


Figure 9.1 A sequence of pulses from PSR B0950+08 with the integrated profile obtained by adding together the sequence of individual pulses (Hankins & Cordes 1981).

Table 9.1. Examples of mean sub-pulse widths and full integrated pulse widths.

PSR	w_{50} (deg)	W_{10} (deg)	PSR	w_{50} (deg)	W_{10} (deg)
B0031–07	5.5	36	B1642–03	2.7	7
B0138+59	2.0	28	B1706–16	1.2	12
B0301+19	2.6	19	B1749–28	2.9	8
B0320+39	1.1	9	B1818–04	4.6	11
B0329+54	1.9	16	B1821+05	2.7	20
B0355+54	2.7	30	B1831–03	4.6	34
B0450–18	2.9	40	B1857–26	4.1	42
B0525+21	1.7	20	B1900+01	6.4	13
B0540+23	2.6	28	B1907+10	6.3	14
B0628–28	4.1	38	B1911–04	3.1	6
B0740–28	9.7	19	B1919+21	1.6	11
B0809+74	3.8	26	B1920+21	2.9	13
B0818–13	1.5	12	B1929+10	2.0	24
B0820+02	1.9	17	B1933+16	1.9	12
B0823+26	2.4	10	B1944+17	6.5	37
B0826–34	4.4	190	B1946+35	6.4	24
B0834+06	1.1	9	B2002+31	1.9	5
B0919+06	2.4	20	B2016+28	2.4	14
B0943+10	2.5	21	B2020+28	2.9	18
B0950+08	5.2	31	B2021+51	2.4	22
B1112+50	1.1	9	B2045–16	1.1	17
B1133+16	0.8	12	B2111+46	9.1	11
B1237+25	0.8	15	B2154+40	3.3	26
B1508+55	3.0	7	B2217+47	3.1	11
B1540–06	1.1	10	B2303+30	1.3	8
B1541+09	13.7	24	B2310+42	1.4	16
B1604–00	2.7	17	B2319+60	2.4	25

Notes: Sub-pulse widths are between half-intensity points (w_{50}); integrated pulse widths are between 10% intensity points (W_{10}). Both are in degrees of rotation and are measured at 408 MHz. The sub-pulse data were compiled by M. Ashworth at Jodrell Bank.

integrated profile, or they may show a preference for certain longitudes at which the integrated profile shows a peak, or again they may ‘drift’ across the window, appearing at a longitude which changes slowly from pulse to pulse.

The sub-pulse width is almost independent of radio frequency. Table 9.1 shows the full width to half intensity of typical sub-pulses, together with the full width of the integrated profile (quoted here between 10% intensity points so as to avoid ambiguities in some of the more complex profiles). For some pulsars, such as PSR B1911–04, the individual pulses recur remarkably regularly at nearly the

same longitude and with nearly the same shape. For others, such as PSR B0950+08 (see Figure 9.1), the sub-pulses are mostly much narrower than the integrated profile. In PSR B1133+16, which has a double-peaked profile, they occur preferentially at or near the longitudes of the peaks; the widths of these peaks are largely determined by the widths of the sub-pulses.

The sub-pulses are regarded as basic components of the pulse profile; an individual sub-pulse then represents the radiation from a discrete location within the physically extended emission region covered by the integrated profile.

There is also structure on a much shorter time scale, known as the *microstructure*. This appears to be a modulation of sub-pulse radiation rather than a distinct component of radiation, taking the form of isolated short and intense *micropulses*. Groups of several micropulses, often spaced approximately periodically, may occur within a single pulse.

All components, whether they are sub-pulses or micropulses, usually show a very high degree of polarisation. The polarisation characteristics of sub-pulses are organised in a simple manner, but the changes through a single sub-pulse, and the variations from one sub-pulse to the next, are often sufficient to dilute the polarisation in the integrated profile.

In this chapter, we describe these phenomena in the light of the geometric description of the source of the radio emission of normal pulsars, which we set out briefly in Chapter 8: that is, a pattern of emission from within a cone above a magnetic pole. The emission is not uniform over the cone; sources in the outer ring may be more powerful, so that a cut across the cone can give a double pulse. The inner *core* and outer *conal* components often have different spectral indices, so that the inner components become more prominent at lower frequencies. The emissivity is also patchy, so that a cut across the polar cone may give a series of apparently discrete components.

9.2 Single Pulse Intensities and Pulse Nulling

The quoted mean intensity of a pulsar conceals an interesting distribution of total pulse power among the individual pulses (Figure 9.2). Many pulsars, such as PSR B1642–03, show a distribution of total pulse power that resembles a normal distribution about a mean value. Others, such as PSR B0950+08, show an asymmetric distribution with a high probability of low values and a long tail towards high values of pulse power; in some cases this fits a lognormal distribution (Cairns, Johnston & Das 2004). PSR B0834+06 shows a bimodal distribution; there is a finite probability of zero power and a separate distribution of values about a mean. The zeroes occur in groups of pulses; they represent a switching off to a level well

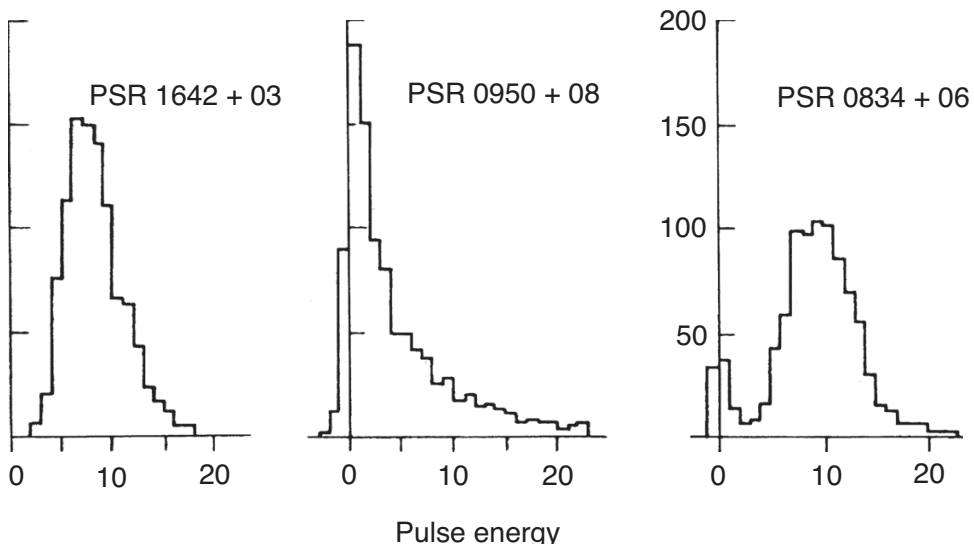


Figure 9.2 The distribution of pulse power among the individual pulses from three pulsars, recorded at 408 MHz (Smith 1973). PSR B1642–03 shows a smooth distribution about a single peak. PSR B0950+08 shows a smooth continuous distribution with a long tail, indicative of rarer bright pulses, with a peak near zero. PSR B0834+06 shows a smooth main distribution with a small distinct peak at zero intensity (the null pulses).

below 1% of the mean pulse power. The phenomenon is known as *pulse nulling*; it was first reported by Backer (1970). It usually occurs simultaneously over the whole radio band, although some works have suggested a frequency dependence (e.g. Bhat *et al.* 2007). The high intensity pulses may involve the addition of *microstructure* (see Section 9.9). In some high-energy pulsars, such as the Crab Pulsar (PSR B0531+21), we see a further and more extreme example of large pulses, the *giant pulses* (Section 9.10); these occur at preferred longitudes, often within the integrated profile of the normal pulses, and may originate in the same locations.

The lengths of the nulls and the intervals between their occurrences vary randomly about values that are characteristic of each pulsar that displays the phenomenon. For some pulsars, nulls of 1, 2 or 3 pulses duration may occur at intervals of order 100 pulses (Backer 1970), while for others the null state may last for minutes to months and occupy more than half the total time. The switch between the two states is very rapid. Some examples – including PSR J1502–5653, where the nulls occupy more than half the time and occur roughly periodically – are shown in Figure 9.3 (Wang, Manchester & Johnston 2007). Nulling on a very short time scale, comparable with the rotation rate of the star, has been observed in several pulsars.

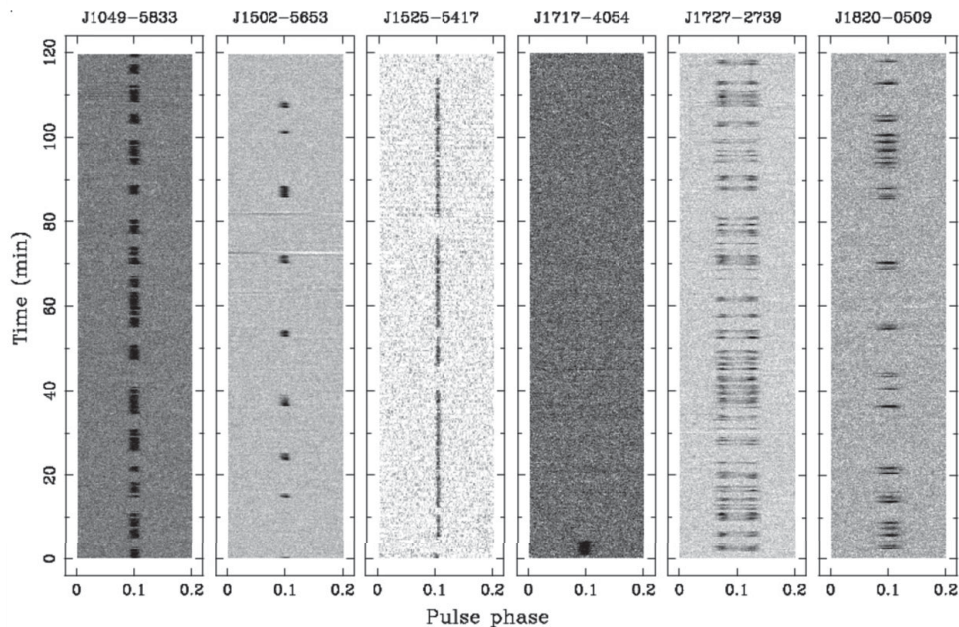


Figure 9.3 Nulling in six pulsars. Short bursts of pulses occur at various intervals (Wang *et al.* 2007).

An example is PSR B0818–13, in which Janssen and van Leeuwen (2004) found nulls lasting several pulse periods, where there appears to be a coincidence between an underlying periodic null lasting 0.2 periods and the main pulse periodicity. Short nulls may, of course, be missed in observations of weak pulsars that can only be detected after integration of many pulses.

An example of long nulls is found in PSR B0826–34, whose discovery was very difficult to confirm because the pulsar proved to be in the null state for 90% of the time, with nulls extending for periods of over seven hours (Durbin *et al.* 1979).

More recently, the phenomenon has been found to extend to even greater timescales. Kramer *et al.* (2006a) reported the discovery of the intermittent pulsar B1931+24, which is typically a normal pulsar for about a week followed by a period of about a month with no detectable emission, the switching occurring almost instantaneously. PSR J1841–0500 displays emitting and null states that are about one year and several years respectively (Camilo *et al.* 2012). PSR J1929+1357 was initially detected in less than 1% of observations but subsequently switched to a mode where it was seen in about 16% of observations (Lyne *et al.* 2017). Although only a small number of such long-term intermittent pulsars have so far

Table 9.2. *Pulsars with long-term nulls and switching slowdown rates*

PSR	ν Hz	T days	f_{ON}	$\dot{\nu}_{ON}/\dot{\nu}_{OFF}$
J1832+0029	1.873	2000	0.6	1.7
J1841–0500	1.095	800	0.5	2.5
J1910+0517	3.246	1	0.3	...
J1929+1357	1.153	1–10	0.01–0.17	1.8
B1931+24	1.229	40	0.2	1.5

Notes: T is the time for a complete on/off cycle. f_{ON} is the fraction of time when the pulsar is on. For accuracies and more details, see Lyne *et al.* 2017.

been discovered, they are unlikely to be detected and very difficult to confirm, so that there is undoubtedly a large population of such pulsars remaining undiscovered.

For some long-term intermittent pulsars, the slowdown rate has been shown to be different in the on and off states, as seen by extrapolating the timing sequence through the null. Table 9.2 (from Lyne *et al.* 2017) shows five examples in which the slowdown rate in the on state is substantially greater than that in the off state. These pulsars are located in the P/\dot{P} diagram of Figure 9.4.

There now appears to be a continuum of time scales associated with nulling and intermittency, so that they should be regarded as manifestations of the same phenomenon. The process that determines the time scales is not understood.

The occurrence of nulling appears to be a characteristic of the older pulsars. The most obviously nulling pulsars are found in the P/\dot{P} diagram (Figure 9.4) close to the boundary known as the *death line*; pulsars approaching this line from the left side are nearing the end of their active lives. A natural interpretation would be that pulsar emission ceases abruptly at this stage by the same process as is involved in nulling; possibly the cessation takes place through stages of nulling in which the proportion of time spent in the nulled state becomes progressively larger. It is, however, clear that the total radiated power decreases with age, whether or not nulling occurs; this decrease is probably directly related to the rotation rate and possibly also to a decay of the dipole magnetic field.

9.3 Mode Changing

In the phenomenon of *mode changing* or *moding*, the integrated profile switches between two different forms, each of which is stable for a long sequence of

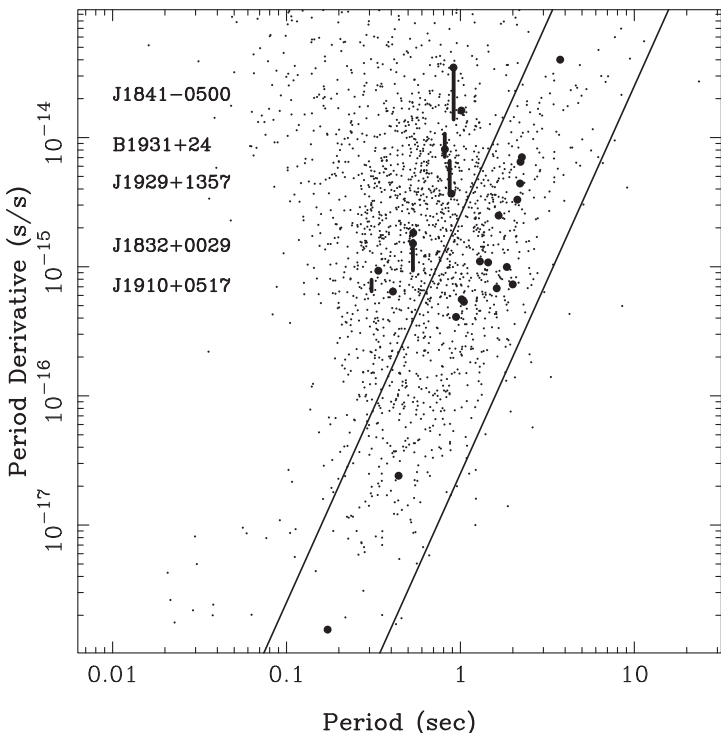


Figure 9.4 The position of pulsars showing nulling in a logarithmic plot of period P against its derivative \dot{P} . Pulsars showing null fractions of at least 15% are shown as filled circles; they are found mostly at low values of \dot{P} and towards the cut-off line where radio emission ceases. The five long-term intermittent pulsars listed in Table 8.2 are shown as vertical lines between the two different values of \dot{P} found in the ON (top) and OFF (bottom) states. The sloping lines are the lines along which the rate of loss of rotational kinetic energy are $\dot{E} = 10^{32} \text{ erg s}^{-1}$ (upper) and $\dot{E} = 10^{30} \text{ erg s}^{-1}$ (lower) (Lyne *et al.* 2017).

individual pulses before switching instantaneously to the other form. Examples of the profiles in two pulsars are shown in Figure 9.5. Individual components of the two profiles may occur in both modes, but with different intensities. Mode changing is closely related to pulse nulling, in which the radio emission suddenly cuts off completely; these two phenomena occur in approximately the same population of older pulsars and on similar time scales. A null may be regarded as a mode change in which all components have disappeared or switched to a very low intensity; in PSR B0826–34, an apparent null state was found after many years to be a mode change in which the intensity had fallen to below 1% of the normal intensity (Esamdin *et al.* 2004).

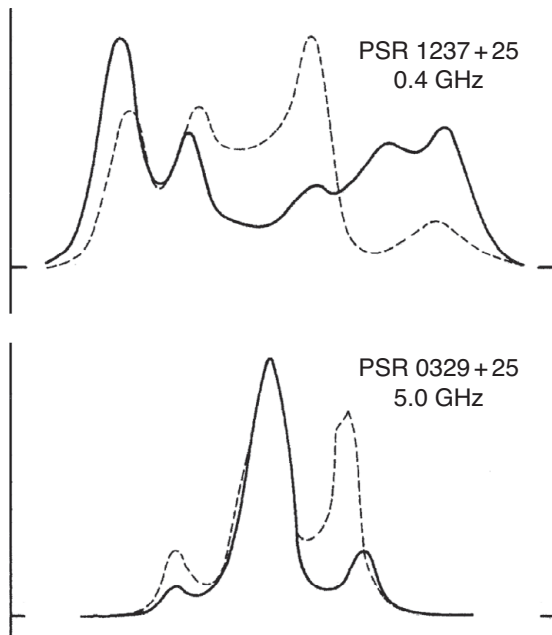


Figure 9.5 Changes in the integrated profiles due to mode changes in the pulsars PSR B1237+25 and PSR B0329+54 (Bartel *et al.* 1982).

9.4 Drifting and Modulation

While some pulsars, such as PSR B0329+54, show apparently random occurrences of sub-pulses through their integrated profiles, in other pulsars, such as PSR B0809+74 and PSR B0031–07 (Figure 9.6), successive pulses contain sub-pulses that appear at progressively changing longitudes. This marching of the sub-pulses across the window of the integrated profile, which may be in either direction, is shown in the idealised diagram of Figure 9.7. The normal pulse periodicity is labelled P_1 , and P_2 is the spacing between sub-pulses within a single pulse. The drift brings successive sub-pulses to the same longitude at intervals P_3 , so that the drift rate $D = P_2/P_3$. The drift periodicity P_3 is usually expressed in terms of P_1 .

The drifting sub-pulse phenomenon appears to be an integral part of the emission mechanism as it has been shown to be very common, occurring in at least a third of the pulsar population (Weltevrede *et al.* 2006, 2007; Basu *et al.* 2016, 2019). Drifting and nulling both occur predominantly in older pulsars.

Figure 9.6 shows both types of behaviour together. Redman *et al.* (2005) also found an association of drifting with moding in PSR B2303+30; in this pulsar, nulls occur only in one mode with its specific drift rate, and not in another mode that has a

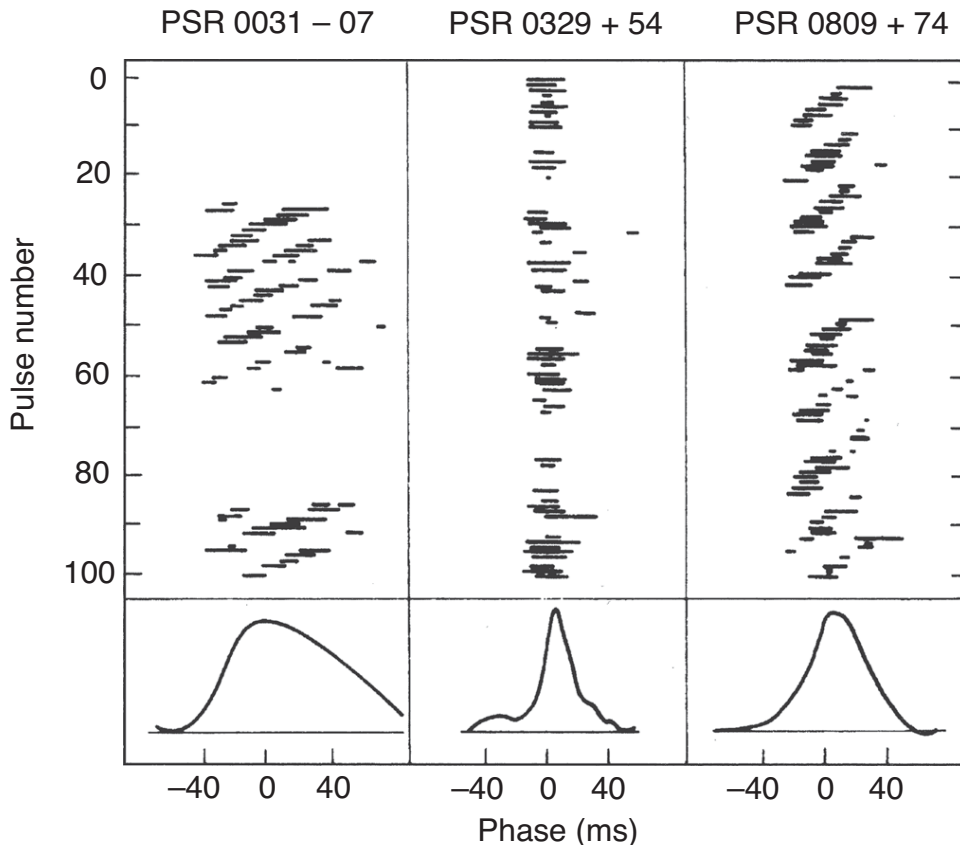


Figure 9.6 Drifting and nulling. Each horizontal line is centred on the expected arrival time, with time increasing downwards and to the right. The positions of each sub-pulse are shown. PSR B0329+54 shows a random pattern of sub-pulses, while PSR B0031-07 and PSR B0809+74 are typical drifters. PSR B0031-07 shows large nulls, missing about 20 pulses (Taylor & Huguenin 1971).

different drift rate. These phenomena are clearly linked, although their explanation is still elusive.

The cycle of repetition at interval P_3 may be observed as a modulation of the integrated pulse power. In Figure 9.8, we show a series of longitude resolved fluctuation spectra (RFS, middle panel), which show the strong modulation at P_1/P_3 . The corresponding values of P_3 are approximately $6P_1$, $2.7P_1$ and $11P_1$ for PSRs B0031-07, B2043-04 and B0809+74, respectively. The lower panels of Figure 9.8 show the two-dimensional fluctuation spectrum (2DFS; Edwards & Stappers 2002),

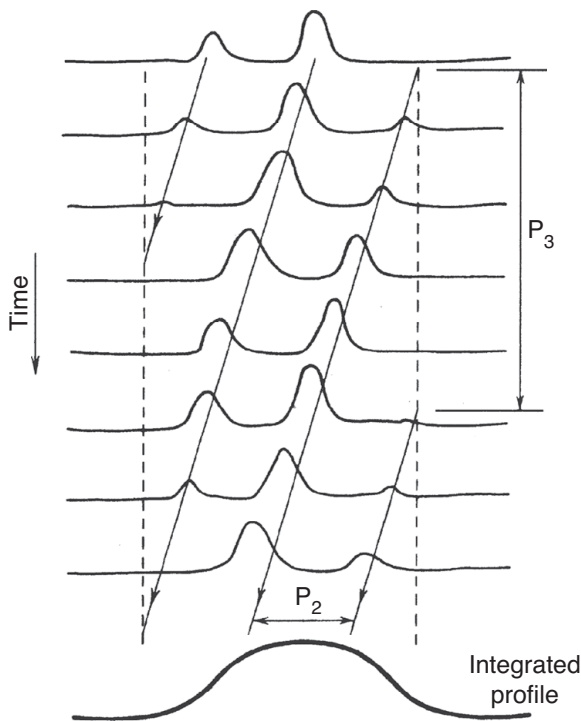


Figure 9.7 An idealised pattern of drifting sub-pulses. Successive pulses appear at the fundamental period P_1 . The pattern repeats at interval P_3 . Sub-pulses are separated by a typical interval P_2 . Drifting may occur either earlier or later in direction.

where the offset in the y-axis indicates that the sub-pulses are drifting, and the offset from zero gives P_1/P_2 , where P_2 is the separation between subpulses. In two of the sources in the figure we see that the pulsars are sufficiently strong, and the drifting so periodic, that higher harmonics can be seen in both the LRFS and the 2DFS. This modulation is often more obvious if a restricted range of longitude is analysed. Figure 9.9 shows the result of a Fourier analysis, at five discrete longitude intervals, of a long train of pulses from PSR B1237+25. Here the characteristic periodicity $P_3 \simeq 3P_1$ shows a modulation frequency of 0.35 cycles per period P_1 . The drift is, however, only seen in the outer parts of the pulse window, indicating that the phenomenon is located in the outer cone of emitting regions.

There are several examples of pulsars in which P_3 is close to $2P_1$, with the result that pulses are alternately strong and weak. A Fourier analysis of the total pulse power of PSR B0943+10, for example, shows a dominant modulation at 0.473

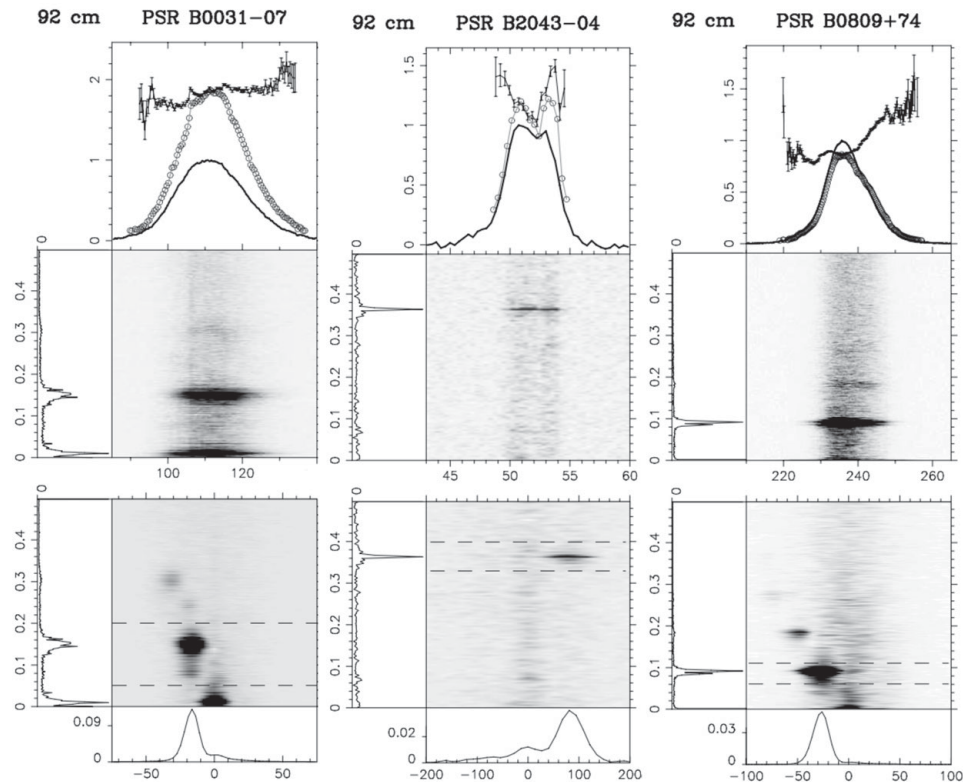


Figure 9.8 Examples of pulsars with drifting subpulses. The top panel shows the integrated pulse profile (solid line), the longitude-resolved modulation index of the individual pulse intensity (solid line with error bars) and the longitude-resolved standard deviation of the individual pulse intensity (open circles). The greyscale plots below the top panels correspond to the LRFS and the 2DFS respectively. The panels to the left of the greyscales are horizontally integrated, while the panel below the 2DFS is vertically integrated between the dashed lines shown. The x-axis of the top two plots gives the pulse longitude in degrees and that of the 2DFS is P_1/P_2 . The y-axis of the LRFS and 2DFS are the fluctuation frequency of the drifting subpulses given as P_1/P_3 . Data are taken from Weltevrede *et al.* (2007).

cycles per P_1 . In such cases it is difficult to distinguish this frequency from the alias frequency 0.527 cycles per P_1 ; the two possibilities correspond to drifting in different directions at slightly different rates. (This example provides a more general warning that observed modulation frequencies may be the result of aliasing and may not represent the true value of P_3 .)

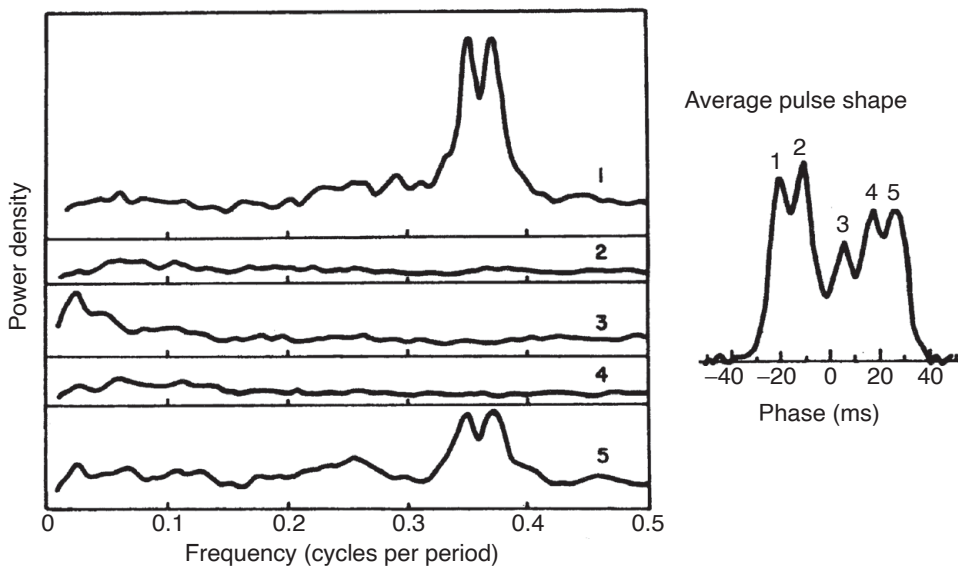


Figure 9.9 Periodic modulation of intensity in a pulsar with no apparent simple drifting. In a series of pulses from PSR B1237+25, the outer components of the pulse vary with a cycle of 0.36 pulse periods (Taylor & Huguenin 1971). The inner components show few fluctuations.

9.5 Drift Rates

Table 9.3 presents the drift rate D , in units of degrees of longitude per rotation, for a typical selection of pulsars in which drifting is observed. The table also shows the data for P_1 , P_2 and P_3 . The overall accuracy for D is about 10% for most of these pulsars. Some pulsars display more than one drift rate: in these cases the component spacing P_2 does not change, and the change in P_3 is inversely proportional to the drift rate. PSR B0031–07 and PSR B2319+60 are examples of pulsars that show three distinct values of drift rate corresponding to three different modes. The three rates for PSR B0031–07 are almost harmonically related, suggesting the name ‘The Harmonic Pulsar’; this may be coincidental, but it is remarkable that the same ratios of drift rate are also found, within rather wider limits of observational error, in PSR B2319+60. In both pulsars, the succession of the modes tends to follow a complex but definite pattern, examples of which are seen for PSR B0031–07 in Figure 9.6. Recently, Ilie *et al.* (2020) showed that in this pulsar there is a corresponding switch between orthogonal polarisation modes (see Chapter 16) when the drift mode changes.

Table 9.3. *Typical drift parameters*

PSR	P_1 (s)	P_2 (ms)	P_3 (periods)	D (deg/ P_1)	Ref
B0031–07	0.94	21	12.5	-1.7 ± 0.2	1
			6.8	-3.2 ± 0.6	
			4.0	-5.3 ± 1.1	
B0148–06	1.46	32	14	-0.57	2
			7	-0.30	
B0301+19	1.39	24	6.4	-0.96	3
B0320+39	3.03	22	8.5	$+0.3 \pm 0.2$	4
B0525+21	3.75	27	4	-0.7 ± 0.2	4
B0809+74	1.29	47	11.1	-1.2 ± 0.2	5
B0818–13	1.24	14.5	4.4	-3.0 ± 0.1	4
B0820+02	0.87	16	4.9	$+1.2 \pm 0.4$	4
B0834+06	1.27	3.5	2.16	$+0.25 \pm 0.16$	4
B0943+10	1.10	25	2.11	$+4.0 \pm 0.1$	7
B1237+25	1.38	41(C 1)	2.8	$+3.8 \pm 1.0$	8
		85(C 2)	2.8	$+7.3 \pm 1.5$	
B1540–06	0.71	4.6	3.07	$+0.8 \pm 0.15$	4
B2303+30	1.58	22	2.0	-2.4 ± 0.1	4
B2310+42	0.35	3.9	2.05	$+1.8 \pm 0.3$ (or -2.1 ± 0.3)	4
B2319+60	2.26	38	8	$+0.8 \pm 0.2$	8
			4	$+1.3 \pm 0.6$	
			3	$+2.0 \pm 0.7$	

$$D = \frac{P_2}{P_3 P_1} \times 0.36 \text{ deg}/P_1. \quad (9.1)$$

- | | |
|-------------------------------|------------------------------|
| 1. Wright and Fowler 1981 | 5. Unwin <i>et al.</i> 1978 |
| 2. Biggs <i>et al.</i> 1985a | 6. Biggs <i>et al.</i> 1985b |
| 3. Schonhardt and Sieber 1973 | 7. Sieber and Oster 1975 |
| 4 Ashworth 1982 | 8. Bartel <i>et al.</i> 1980 |

In several pulsars, the drift rate varies significantly through the range of longitudes covered by the integrated profile. In Table 9.3, two distinct rates are quoted for two of the inner components (C 1 and C 2) of PSR B1237+25; this is an extreme example, and it is more usual to find a variation of order 20% in drift rate across the profile. Drifting is most commonly seen in the outer components of the profile, which correspond in the polar cone model to the outer cone of emitting regions. The drift rate is often appreciably higher at lower radio frequencies. According to the ‘radius-to-frequency’ model (Chapter 16), the emission at lower frequencies is from higher up in the diverging cone, resulting in an increased P_2 ; the periodicity P_3 is, however, the same, as would be expected if the emitting regions are connected

along magnetic field lines. The drift rate in the inner cone, if it appears at all, is often lower than in the outer, and it may appear only as a slow fluctuation of intensity. The direction of drift is indicated by the sign in the table, where + means a drift from the leading to the trailing edge of the profile. PSR B1839–04 is an example of a pulsar with a complex profile that exhibits bi-drifting, which is where the drifting is seen to be in opposite directions in the leading pulse components compared to the trailing pulse components (e.g. Szary *et al.* 2020). These systems might provide clues to the conditions in the magnetospheres of pulsars.

The integrated profile of PSR B0826–34 is remarkable in that it extends through the whole of the period; this is attributed to a near alignment of rotation axis, magnetic axis and line of sight to Earth. In this pulsar, a pattern of drifting sub-pulses can be seen through the whole period, and it appears that a complete ring of about 13 discrete sources of emission is distributed evenly round a cone with about 8 deg radius. The whole pattern drifts together at an irregular rate (Esamdin *et al.* 2004). A similar pattern is found for PSR B0943+10 (Deshpande & Rankin 1999); here a more regular drift pattern in this pulsar indicates the existence of 20 separate beams at 5 deg radius.

9.6 Drifting after Nulling

The close connection between drifting and nulling is illustrated by their relation at the time of a null. As noted above, some pulsars show multiple drift modes that are separated by nulls. Cole (1970) showed that even when a new drift mode is not invoked after a null, the subpulses restart at a pulse longitude ‘remembered’ from the point when the null started. Directly before a null in PSR B0809+74, the drift rate appears to change, while directly after the null, the drift rate is lower and increases exponentially to the previous value (Figure 9.10, from Lyne & Ashworth 1983). The time constant for this increase depends on the length of the null. Van Leeuwen *et al.* (2003) showed that this rate of change of the drift rate allows one to solve the aforementioned aliasing problem (Section 9.4) for this pulsar. It also appears that at least the first pulse after the null is brighter than the normal pulses.

Continuity of drift phase across an extended null implies the continued existence of an identifiable source, even when its emission is temporarily suppressed or absent. An attractive model for such a source is presented by Filippenko and Radhakrishnan (1982), who suggest that the spark discharge across the gap at the magnetic pole is confined to discrete magnetic flux tubes, each of which has a continuous flow of energetic particles. The emission from a flux tube depends on the energy distribution and the bunching of electrons or positrons in the flow; the flux tube and the continuous stream may therefore remain in place even if the radiation

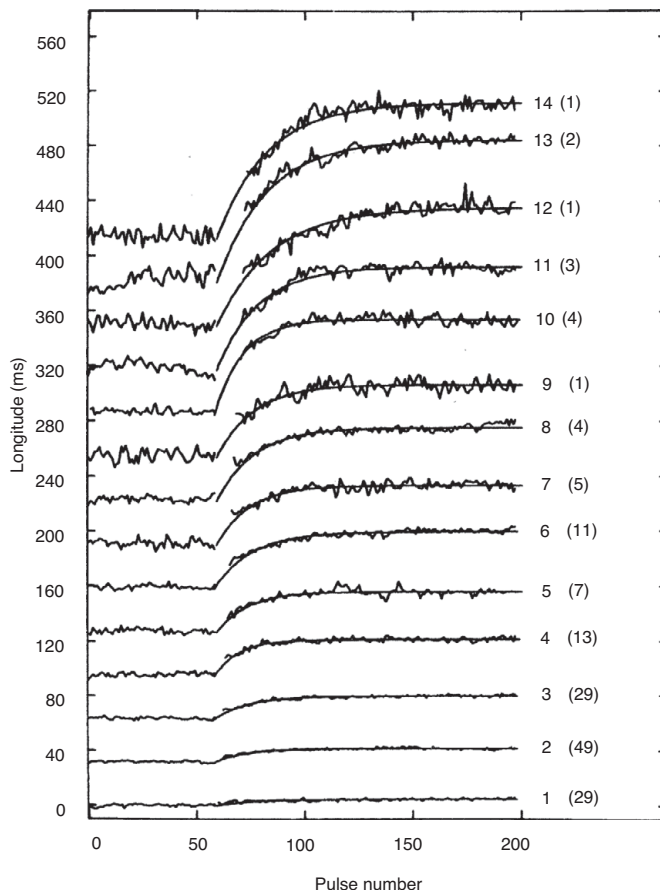


Figure 9.10 The phase of the drifting sub-pulses at nulls of various lengths in PSR B0809+74. The nulls start at around pulse number 60, and the null length is shown at the right of each track, followed in parentheses by the number of tracks in each average. The curves are exponential relaxations (Lyne & Ashworth 1983).

has stopped. The radiation starts again when the flow again becomes bunched. Ruderman and Sutherland (1975) showed that a localised discharge across the polar gap would tend to move sideways; this drift would depend on the component of electric field E along the direction of the magnetic field B in the gap, giving a small $E \times B$ drift relative to the surface of the star. The change in emission at the time of the null, and the change in drift rate, would then both be due to a change in the discharge across the gap. However, the drift rates and the number of sub-beams are challenging for this original model, and many modifications have been proposed to ‘slowdown’ this drift (Faber & Rasio 2002).

9.7 Isolated Pulses: RRATs and FRBs

For many years, searches for radio pulsars relied on recognising a precisely periodic signal against a background of noise. The discovery of extreme cases of nulling suggested that some pulsars were evading detection by producing only occasional isolated pulses, and prompted searches for single pulses. Despite the inevitable lower sensitivity, this led to the remarkable discovery in data already recorded in the Parkes Multibeam Pulsar Survey (Chapter 2) of 11 isolated sources of single pulses. These were distinguished from terrestrial impulsive interference by their similarity to pulses from normal pulsars; notably, they showed a similar frequency dispersion. After prolonged observations most sources were found to show pulses repeating at long intervals, from 4 minutes to 3 h, and eventually underlying periods of order a few seconds could be found. They were in fact extreme examples of nulling pulsars, in which there was no detectable pulse for many hundreds or thousands of rotations, followed by a single detectable pulse. They were named rotating radio transients (RRATs) by their discoverers McLaughlin *et al.* (2006).

Surveys aimed at the discovery of transient radio sources require high sensitivity, achieved by using telescopes with large collecting areas, large receiver bandwidths and large fields of view, combined with a receiver system that can search through a wide range of dispersion measures. Current examples are the High Time Resolution Universe (HTRU) surveys at Parkes and at Bonn, and formerly PALFA at Arecibo, which were designed to detect pulsars with large null fractions. The first results from these surveys fully support the interpretation that RRATs should be regarded as extreme examples of the nulling phenomenon.

9.7.1 Fast Radio Bursts (FRBs)

It was while undertaking a search for sources like RRATs in archival data taken with the Parkes radio telescope in the direction of the Magellanic Clouds that the first fast radio burst (FRB) was found (Lorimer *et al.* 2007). Originally dubbed a Lorimer burst, there was a long period of time when no similar source was discovered, and so there was some uncertainty as to its astrophysical nature. The burst was considered exceptional not only because of its brevity, but also because of its implied distance: the dispersion measure not only placed it well outside our Galaxy but also well beyond the Magellanic Clouds. It was only with the discovery of a further four FRBs by Thornton *et al.* (2013) that they were established as an astrophysical population of sources, and it was generally accepted that they were extragalactic in origin. It appeared that there might be a few thousand of these bursts occurring across the sky every day.

The sky locations of these initial FRBs were extensively followed up, but no further FRBs were detected from these sources. It was initially believed that they

might be associated with a catastrophic event that marked, for example, the merging of neutron stars or the collapse of a rapidly spinning neutron star to a black hole. However, there were also models that suggested they might be extreme versions of the giant pulses from radio pulsars, or associated with young magnetars (see Chapter 11). These latter two origins gained further attention when a burst FRB 121102 was shown to repeat (Spitler *et al.* 2014). To date there is still a possible dichotomy between repeating and non-repeating FRBs, and it is unclear whether they are from separate origins or part of a continuum of giant bursts.

The repeating nature of FRB 121102 allowed it to be localised using an interferometer, and thus its host galaxy could be identified, thereby confirming its extragalactic nature (Tendulkar *et al.* 2017). Since then, a number of host galaxies have been identified for FRBs, for both repeating and non-repeating sources (e.g. Bhandari *et al.* 2020); they seem to form a diverse sample, so a much larger sample is needed to distinguish between different FRB origins and also potentially between repeating and non-repeating sources.

The radio emission from FRBs is characterised by very narrow pulses, typically less than a few milliseconds wide. A number of sources show a complex frequency dependence, either of the intensity or of the pulse shape. In the former case, this is sometimes consistent with expectations from scintillation (see Chapter 19) but not always. Some of the sources (and this is best studied in the repeaters) show evidence for pulse components that drift with frequency (Hessels *et al.* 2019) in a way that is not consistent with dispersion delay and is sometimes attributed to plasma lensing, perhaps related to what is sometimes seen for giant pulses from the Crab Pulsar. The bursts are often polarised, In most cases the rotation measure (RM) is low, but for FRB 121102 it is as extreme as that for the magnetar near our Galactic centre (Chapter 11).

The association with magnetars was boosted with the detection of a bright burst of radio emission from the Galactic magnetar SGR J1935+2154 (Andersen *et al.* 2020; Bochenek *et al.* 2020), which were the most luminous bursts of radio emission from a neutron star in our Galaxy (although still about two orders of magnitude less luminous than even the faintest FRBs detected so far).

As well as potentially significantly expanding the nature of radio emission from neutron stars, which spans 10 orders of magnitude in luminosity from pulsars to magnetars, RRATs and FRBs, the FRBs are also useful as cosmological tools. Identifying FRB host galaxies and measuring their redshifts combined with the dispersion measure allows one to map out the electron content of the Universe in much the same way as we map the electron distribution in our own Galaxy. This has already been done to confirm that the missing baryons in the Universe are most likely located in the intergalactic medium (Macquart *et al.* 2020) and may in the future allow us to determine the other important features in the ionisation history

of the Universe. For more on the theories of FRBs, see Platts *et al.* (2019); and for more on the phenomenology, see Cordes and Chatterjee (2019) and Petroff, Hessels and Lorimer (2019).

9.8 The Polarisation of Sub-pulses

Sub-pulses are generally more highly polarised than integrated profiles; the difference is accounted for by the variability of polarisation of successive sub-pulses and by variations within individual sub-pulses. Recordings of the polarisation of individual sub-pulses by Manchester, Taylor and Huguenin (1975, Figure 9.11), demonstrated these effects clearly. Figure 9.11(a) shows a highly polarised pulsar, PSR B1929+10. Here the individual pulses are fully elliptically polarised, with little change through the duration of the sub-pulse. Figure 9.11(b) shows a similar situation in PSR B0031–07, in which there is an organised drifting. Here the polarisation varies across the window of the integrated profile, as expected, but there are also some additional variations within the sub-pulses. These variations are often accounted for by switches between orthogonal modes (Ilie *et al.* 2020).

Taylor *et al.* (1971) found that there is an organised sweep of position angle within individual pulses in addition to the sweep expected from the polarisation of the integrated profile. It seems that the total swing within a single sub-pulse is typically less than about 30 deg, in this and in other pulsars.

Finally, Figure 9.11(d) shows PSR B1919+21, which demonstrates the confusion that arises from the superposition of several different sub-pulses in a single pulse. It is a reasonable assumption that the individual sub-pulses that contribute to such a pulse are highly polarised in a simple manner, and that a number of different sources are observed simultaneously. Note that the fluctuations in both linear and circular polarisation at any one longitude give rise to substantial depolarisation, resulting in the low polarisation seen in the integrated profiles of Figure 9.11.

9.9 Microstructure

At the highest possible time resolution, and over a wide range of observing frequencies, the individual pulses of many pulsars are seen to contain structure on a considerably shorter time scale than the sub-pulses. This is referred to as *microstructure*. Detailed observations are only possible for the brightest pulsars; even for these, there is some difficulty in resolving the shortest pulse components, or *micropulses*, which may be only a few microseconds wide.

Simultaneous observations at widely separated frequencies show that micropulses have a wide bandwidth. Rickett, Hankins and Cordes (1975), for example, showed

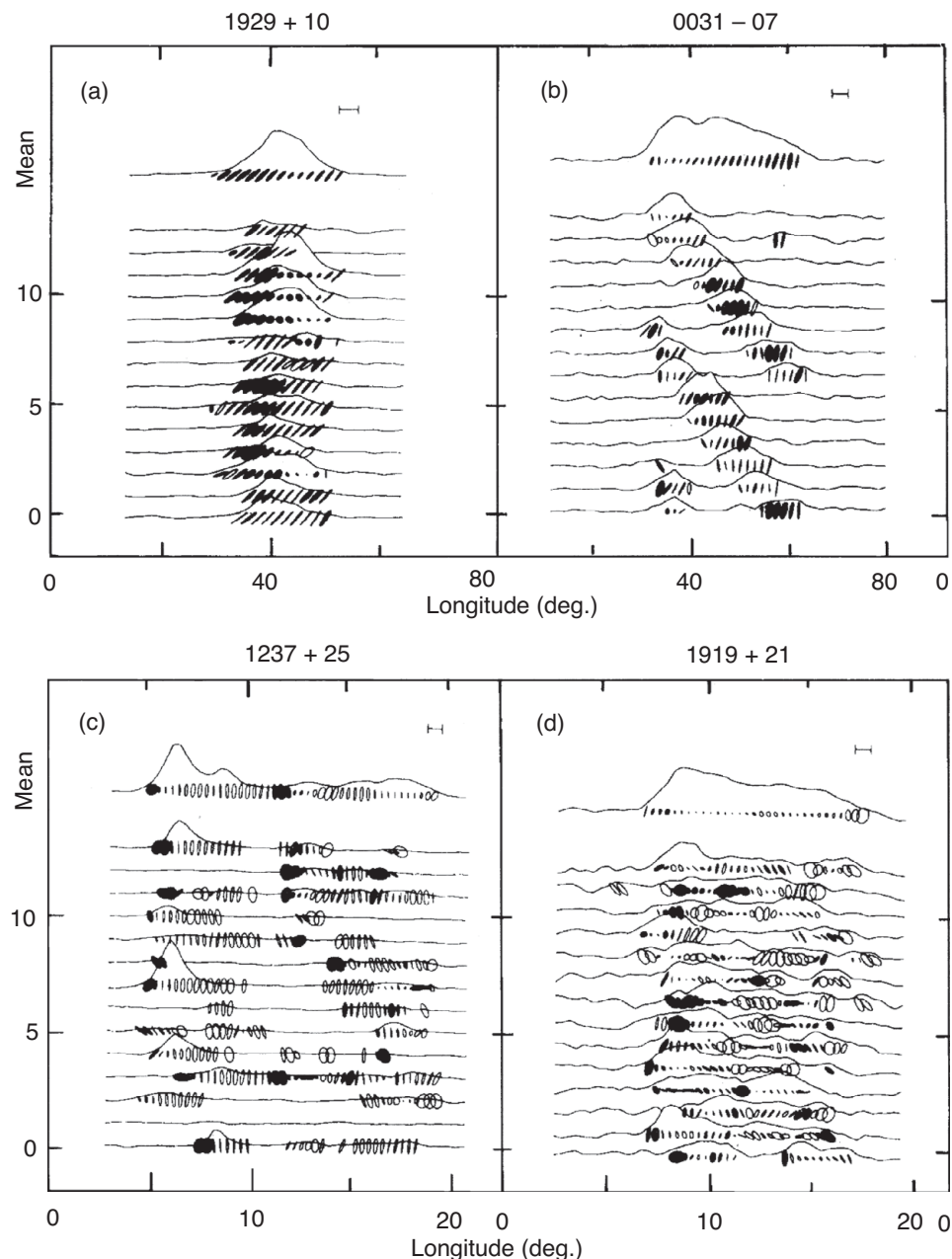


Figure 9.11 The polarisation of individual sub-pulses from four pulsars, compared with their integrated profiles: (a) PSR B1929+10, (b) PSR B0031-07, (c) PSR B1237+25, (d) PSR B1919+21. The major axes of the polarisation ellipses represent the fractional linear polarisation and the position angle; left-hand polarisation is represented by filled ellipses (Manchester, Taylor & Huguenin 1975).

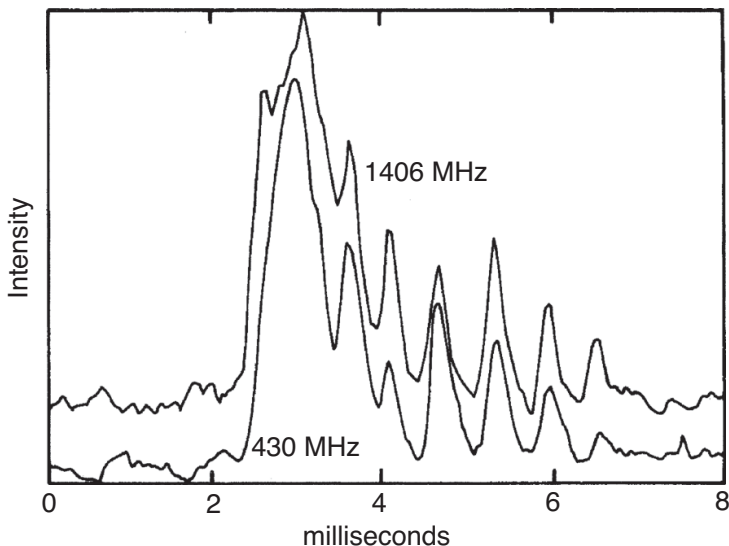


Figure 9.12 A periodic train of micropulses in a single pulse from PSR B0950+08, recorded simultaneously at 430 MHz and 1406 MHz (Boriakoff, Ferguson & Slater 1981).

that micropulses observed at 111 MHz and 318 MHz from PSR B0950+08 and from PSR B1133+16 occasionally contained structure shorter than 10 microseconds that was correlated at the two frequencies. In some pulsars, including the Vela Pulsar, the flux density of individual isolated micropulses may be over 50 times the mean flux density in the pulse. Kuzmin *et al.* (2003) showed that microstructure is present at the low radio frequency of 102 MHz. The polarisation of micropulses is generally similar to that of the underlying sub-pulse.

Micropulses are often observed to occur in short quasi-periodic groups, with a periodicity of order half to one millisecond for normal pulsars and shorter in MSPs (in proportion to the pulse period). It is significant that this periodicity is found to be independent of the observing frequency, as may be seen in the example of Figure 9.12, showing a single pulse of PSR B0950+08 at 430 MHz and 1406 MHz (Boriakoff, Ferguson & Slater 1981). It appears that micropulses are an enhancement of normal polar cap emission due to an increase in excitation below the emitting region.

Single pulses from the Crab Pulsar have been observed with high time resolution at frequencies up to 43 GHz by Hankins, Eilek and Jones (2016). There appear to be several distinct and physically separate sources in this astonishing and intriguing pulsar, some located in the polar cap and some associated with high-energy emission from the outer magnetosphere. The main components consist of broad-band

microstructure, which contains narrower bandwidth structure with width only a nanosecond or less, referred to as ‘nanoshots’.

Kramer *et al.* (2002) described the micropulse structure in the Vela Pulsar and list observations of microstructure in 13 others. It appears to be a common phenomenon: Mitra, Arjunwadkarar and Rankin (2015) found that microstructure is usually present at a low level in most normal pulsars, while De, Gupta and Sharma (2016) detected microstructure in two millisecond pulsars. As a matter for speculation, it seems possible that all radio pulses are in fact an assembly of unresolved microstructure.

9.10 Giant Pulses

Short and extremely intense radio pulses, known as *giant pulses*, were first observed in the Crab Pulsar; (they are sufficiently intense that they enabled the original discovery in 1968 by Staelin and Reifenstein). Mickaliger *et al.* (2012) observed a large sample of these pulsars, showing that individual pulses covered a wide frequency band (0.3, 1.2 and 8 GHz), although with some differences of pulse shape. It is not clear whether this microsecond structure continues to lower radio frequencies, since the time resolution of observations is usually limited by interstellar scattering. Karuppusamy *et al.* (2010) used a multiband system covering 1.31–1.45 GHz to determine the statistical distribution of giant pulse energies in the Crab Pulsar; they found that the rate of occurrence of giant pulses depends strongly on their energy; over a range of 1000 in energy, the rate varied from one per second to one per three hours. There is a difference between the two pulse components; the rate is $\times 10$ greater in the main pulse, while above 5 GHz, more are observed at the interpulse.

Giant pulses are also known to occur in several other pulsars associated with high-energy, outer gap sources, including the Vela Pulsar (Kramer *et al.* 2002) and some millisecond pulsars, notably PSR B1937+21 the first to be discovered and still (in 2020) the second fastest ($P = 1.56$ ms). McKee *et al.* (2019) used the combination of European radio telescopes (LEAP) to find the intensity distribution of single pulses at 1.4 GHz from PSR B1937+21 and confirmed that they occur in narrow longitude regions on the trailing edge of both the main pulse and the interpulse.

It may be significant that these pulsars have high magnetic fields at the radius of the light cylinder; for example, in B1821–24A this is almost the largest known at 7×10^5 G (Bilous *et al.* 2015). The brightness temperature in these short pulses is extremely high, exceeding 10^{36} K for the Crab Pulsar (Kostyuk *et al.* 2003).

The energy contained in these very short pulses is astonishing. Hankins and Eilek (2007) showed that individual pulses were as short as 0.4 nanoseconds and with

intensities of 2 MJy. They are highly polarised. The source of these giant pulses can be no more than a metre in any dimension (depending on an unknown Doppler shift), so that a large proportion of the energy contained in that part of the magnetosphere must be converted into radio emission practically instantaneously (Chapter 15). No analog to these bright pulses has been seen in the gamma-ray or X-ray emission from the Crab Pulsar to date (e.g. Lundgren *et al.* 1995). However, Shearer *et al.* (2003) showed that there was a 3% enhancement in the optical emission whenever a radio giant pulse occurred, indicating a link between the coherent radio emission and the incoherent optical emission.

10

Millisecond Pulsars

The majority of pulsars are following a simple course of evolution, from birth in a supernova, through a slowdown from a rotational period at birth of some tens of milliseconds to a death at a few seconds when the radiation ceases or becomes undetectable after about 10 million years. The millisecond pulsars constitute a separate and much longer-lived population, which originates from this general population of normal pulsars as the result of gravitational interactions with binary partners, in which their rotation is spun up to millisecond periods. In this *recycling* process, most retain their companions, but some have lost them, or are possibly in the process of losing them, thus becoming solitary millisecond pulsars.

Most millisecond pulsars have rotational periods less than 10 ms, although a useful definition includes periods up to 30 ms. Figure 10.1 shows their position in the $P - \dot{P}$ diagram, which also shows all known binary systems as circles. Although there is a distinct gap between normal and binary pulsars in this diagram, there are some pulsars within the gap; most of these have the characteristics of millisecond pulsars, such as a comparatively small slowdown rate, and they have probably experienced the same binary interactions. These systems are likely to have had higher mass companions; as a result, they have accreted less material and so have not been spun up as much.

10.1 The Discoveries

The discovery of millisecond pulsars was a severe technical challenge for many decades. As described in Chapter 3, searches for short period pulsars not only required an increase in sampling rate but also required a similar increase in the number of frequency channels needed to combat broadening of the pulse due to interstellar dispersion. Hence a search for a 1-ms pulsar required a 10,000-fold increase in data storage and computation over that required for a 0.1 second pulsar,

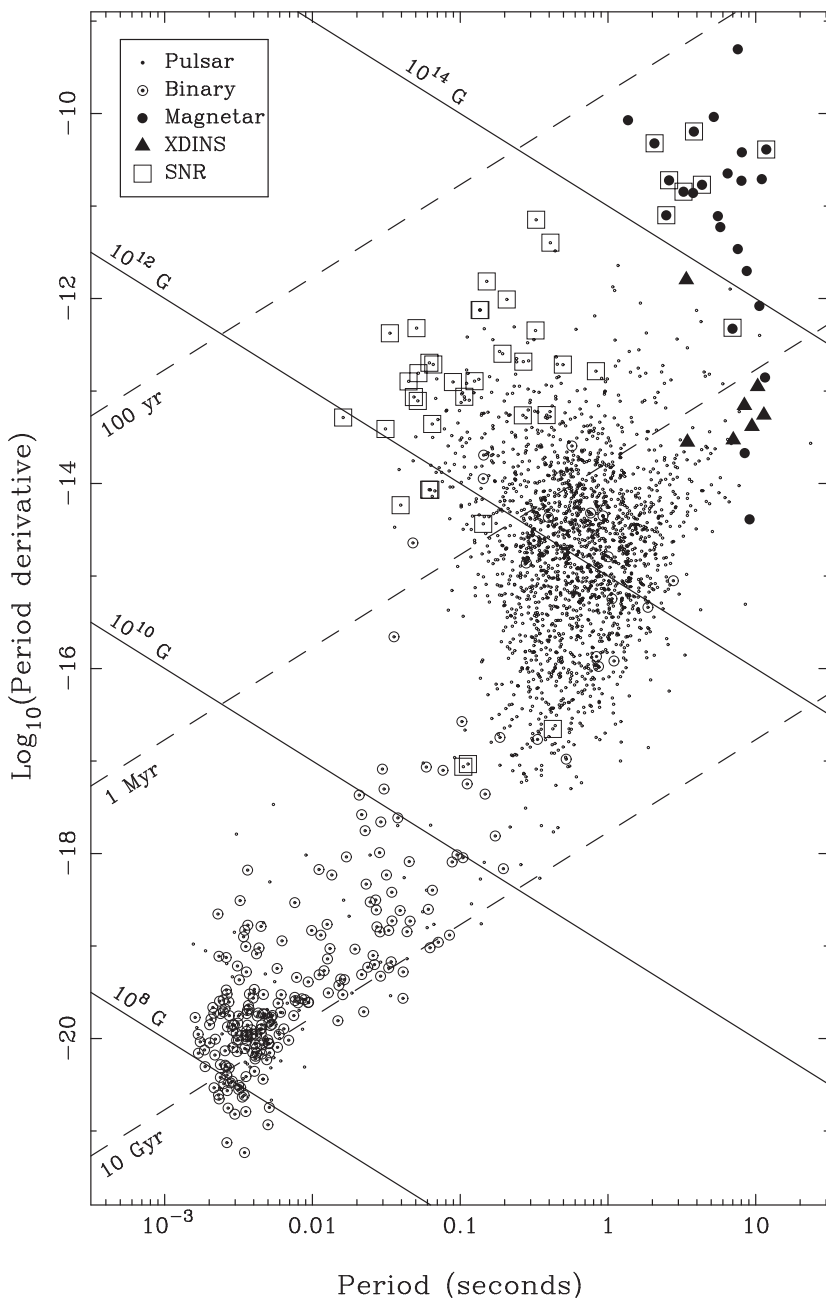


Figure 10.1 The millisecond and binary pulsars are mostly located in the lower left of the $P - \dot{P}$ diagram. Young pulsars still associated with supernova remnants are shown encompassed by square symbols. The binaries are shown as circles. Lines of constant characteristic age and dipole magnetic field are shown.

a real challenge at the time. Furthermore, in contrast to the solitary nature of most normal pulsars, most millisecond pulsars are in binary systems with consequential variation of the pulse period due to the Doppler effect of their motion (Chapter 6), limiting the length of data in which a simple coherent periodicity search can be made. Searches for millisecond pulsars now additionally require searching in acceleration space, with a first period derivative, and even in ‘jerk’ space including a second derivative.

The first pulsar to be found in a binary system, PSR B1913+16 (Hulse & Taylor 1974), has an orbital period of $7\frac{3}{4}$ h and a pulse period of 59 ms, longer than the general run of millisecond pulsar periods but among the shortest known at the time. The binary nature was discovered by the unexpected differences in period observed in a series of short integrations.

The first discovery of a millisecond pulsar (Backer *et al.* 1982) was an equally momentous occasion in pulsar astronomy. It had been suspected for some time that the discrete radio source 4C21.53 might be a pulsar, because of its steep spectrum and high degree of linear polarisation, but no periodic pulses could be found in the range of periods encountered up to that time. After many attempts with progressively higher sampling rates and shorter receiver time constants, the periodicity of 1.6 ms appeared in the recordings, and the source became known as the solitary pulsar PSR B1937+21. Not only did this discovery extend the range of known pulsar periods by a factor of 20; it soon appeared that the rate of change of period was very small, indicating a weak effective dipolar magnetic field. Only after 30 years of searching was a pulsar found with a shorter period: PSR J1748–2446ad, in the globular cluster Terzan 5, has a spin period of 1.396 ms (Hessels *et al.* 2006).

A further surprise was the discovery that many of the millisecond pulsars are strong gamma-ray emitters, radiating a substantial proportion of their slowdown energy in this band. Some have been discovered as gamma-ray pulsars that have no detectable radio emission. Like many of the young pulsars, they radiate from the outer part of their magnetospheres, and they provide a valuable insight into magnetospheric physics (see Chapter 16).

10.2 The Evolution of Binary Systems

The millisecond pulsars have opened a rich field of astrophysics. It turns out that most (about 80%) are in binary systems, usually with white dwarf stars, but a few are in double neutron star systems (DNS), as in PSR B1913+16, or have main-sequence stars as companions. We include in the main-sequence category the so-called spider pulsars, black-widows and redbacks (see Section 10.3), which have companion masses of about 0.025 and $0.2M_{\odot}$ respectively. There is an evolutionary sequence

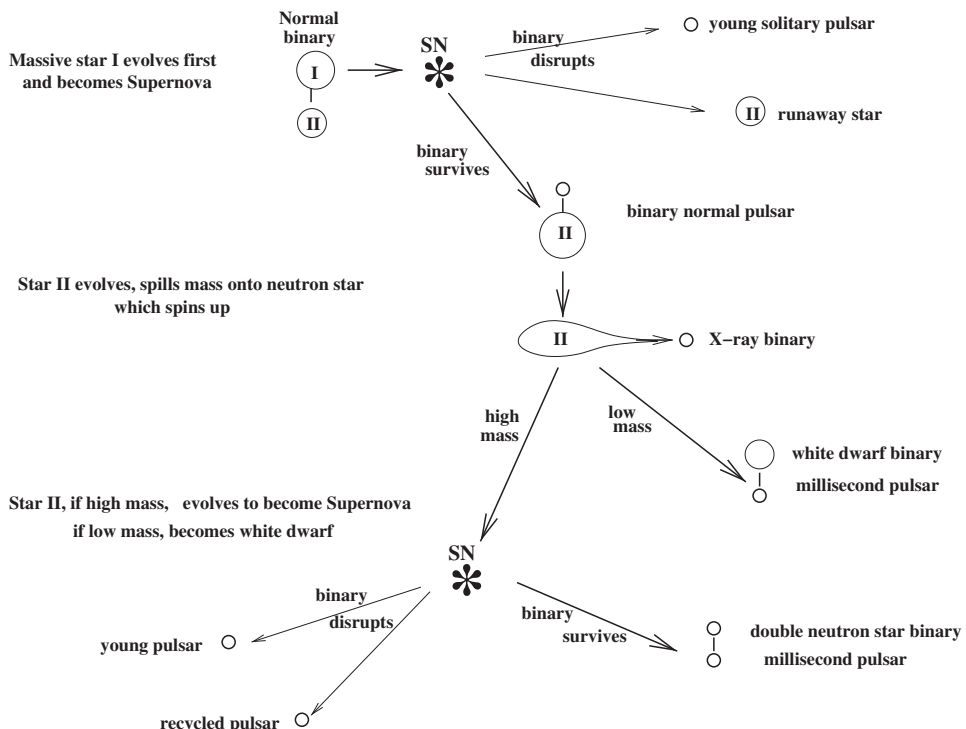


Figure 10.2 Evolutionary sequence for binary millisecond pulsars.

connecting normal binary stars with masses greater than $\sim 8 M_{\odot}$ to several distinct families of binary and millisecond pulsars, which is firmly established and forms the basis of our classification in later sections. This may be followed in Figure 10.2.

1. Starting with a main sequence binary, the more massive component (Star I) evolves faster, and its core collapses to a neutron star in a supernova explosion. The binary may disrupt, either through orbital dynamics or because the neutron star acquires a large velocity due to asymmetry in the collapse; if it disrupts, the outcome is a solitary normal pulsar and a runaway massive star (these are the high velocity OB stars that have been known for many years).

2. If the binary survives, the normal young neutron star may be observed as a binary pulsar in an eccentric orbit with a main-sequence star as its companion. Several examples are known: for instance PSR B1259–63.

3. The binary companion (Star II) evolves into a red giant, having a white dwarf core with an extended atmosphere that expands until it starts to be accreted onto the neutron star by its gravity. The gravitational energy released in the transfer heats the neutron star and a halo around it; this becomes a source of x-rays. Many such x-ray binaries have been discovered (Chapter 12).

4. The orbital angular momentum of the accreted matter is also transferred to the neutron star, which spins up to a millisecond periodicity. The accretion process and tidal effects result in the circularisation of the orbit. After the atmosphere is removed and the transfer is complete, the condensed core of Star II remains; a recycled millisecond pulsar may then be observed in a circular orbit with a white dwarf companion.

5. If Star II is sufficiently massive, it may in its turn collapse in a supernova explosion. Again there are two possibilities: the binary may disrupt or survive.

6. Disruption leads to a solitary neutron star that may be a new young pulsar, and a solitary ‘old’ millisecond pulsar.

7. Survival leads to a double neutron star binary in an elliptical orbit, with one young and one recycled component. In the fortunate case of the Double Pulsar PSR J0737–3039, both components were observable as pulsars;¹ in other neutron star binaries, the young pulsar fades rapidly, and only the recycled pulsar is observable, as for instance in the case of PSR B1913+16.

Among the remarkable products of this complex sequence are the double neutron star binaries (DNSs), a family of at least thirteen known as of 2020 (see Table 6.2) with closely similar characteristics. The masses of both stars in such binaries and their orbital parameters can be measured with remarkable precision, leading to the most searching tests of general relativity (Chapter 6). Other products along the evolutionary sequence are young pulsars with main-sequence companions, solitary pulsars and white dwarf binaries with a range of properties, depending mostly on the mass of the white dwarf star.

A white dwarf companion may in many cases be identified from optical observations; the first example was PSR B0655+64, which was identified with a magnitude 22 white dwarf (Kulkarni 1986). The absence of an optical identification, however, is not sufficient to identify a companion as a neutron star. The usual distinguishing characteristics of the two families are the total mass of the system, which for the DNSs must be greater than about $2.5M_{\odot}$, and the high eccentricity of the orbit in a DNS. The high eccentricity of the DNS arises from a supernova event in a binary, while in a white dwarf binary, gravitational interaction, in the form of tidal effects and mass transfer, reduces eccentricity, in some cases to the smallest eccentricities known in any astronomical orbits.

10.2.1 Double Neutron Star Binaries

The DNS systems have followed the full series of events illustrated in Figure 10.2, starting with a pair of stars both with masses $> 8 M_{\odot}$ and surviving the second

¹ In 2010 the B component of PSR J0737–3039 faded and became unobservable a few years after discovery (Perera *et al.* 2010)

supernova event without disruption but with an enduring highly eccentric orbit. Of the 13 DNSs known in 2020 (Table 6.2), in one both components are pulsars, PSR J0737–3039A and B; one is a recycled pulsar with short rotation period; and the other is a normal pulsar with longer rotation period and a smaller age. Another DNS system, PSR J1906+0746, comprises a 144 ms pulsar with mass $1.25M_{\odot}$ and an unseen neutron star companion with mass $1.37M_{\odot}$. In this binary the pulsar has a characteristic age of only 10^5 yr ((Lorimer *et al.* 2006a) and is apparently the result of the second supernova event.

The DNS systems present outstanding opportunities for observing post-Newtonian relativistic effects, as outlined in Chapter 6. Several are close binary systems in which the orbits are shrinking at an observable rate due to energy loss through gravitational radiation, leading to merging on a time scale considerably shorter than the age of the Universe. Such events are expected to produce bursts of gravitational radiation, which have been detected by the interferometric systems such as LIGO and VIRGO.

10.2.2 Binaries with White Dwarf Companions

If only one of the progenitor stars of the binary has a mass $> 8 M_{\odot}$, some time after the first supernova event the binary will comprise a normal pulsar and a star expanding into a red giant. The development now depends on the mass of the giant. Overflow of mass onto the neutron star increases its rotation rate and may create a heated accretion disk that radiates x-rays; this occurs if the companion mass is $\sim 1 M_{\odot}$ and is the ‘low-mass’ scenario, which produces an observable x-ray binary (an LMXB, see Chapter 12). Through the slow transfer of angular momentum from the orbit to the neutron star, the pulsar period is reduced to below 10 ms, and the orbit becomes circular, with very small eccentricity. Once the atmosphere of the red giant star has been removed in this process, the condensed core remains as a white dwarf. The majority of known binary pulsar systems are in this category.

10.3 Solitary Millisecond Pulsars and Widows

In the standard evolutionary scenario outlined above, one would expect that at the end of the LMXB phase we would end up with recycled pulsars spinning with periods of a few to tens of milliseconds in binary systems with low-mass companion stars. However, like the original millisecond pulsar B1937+21, approximately 35% of all millisecond pulsars are isolated, and thus they must have somehow lost their companions. As PSR B1937+21 is not in a globular cluster, the very small density of stars in the galactic plane makes it unlikely that a companion has been lost

through a stellar interaction. Instead it was proposed (e.g. Alpar *et al.* 1982) that the companion star may have been evaporated by radiation and a wind of particles from the pulsar itself, once the accretion phase had ceased. Support for this evolutionary route came from the discovery of PSR B1957+20 (Fruchter, Stinebring & Taylor 1988a, Fruchter, Gunn, Lauer & Dressler 1988b), which has a spin period of just 1.6 ms and is in a 9.2 h orbit with a companion with a mass of only $0.035M_{\odot}$. Not only did this system have an astonishingly low mass companion, but it exhibited eclipses (Section 10.4) due to material being ablated from the companion star. This interaction led to the name *black widow* pulsar.²

This evolutionary phase is thought to be short lived, and so the discovery of another system outside of a globular cluster, PSR J2051-0827 (Stappers *et al.* 1996), was unexpected. It was also found that the rate at which material was being ablated in these systems was insufficient to evaporate a companion on a reasonable timescale, so that this process was unlikely to be responsible for the formation of isolated millisecond pulsars.

A number of these eclipsing binary systems with low-mass companions were also found in globular clusters. Their origin is likely to be different and lies in the high density of stars within the clusters, where near collisions are frequent, and exchange interactions can result in a pulsar exchanging a white dwarf companion for a low-mass main sequence star. The new binary orbit then shrinks by tidal friction, creating a black widow system. Eclipsing systems with heavier mass companions, for example PSR B1744-24A (Lyne *et al.* 1990), were also discovered in globular clusters, and these were thought to be the result of more recent capture events. The discovery of the millisecond pulsar J1023+0038 (Archibald *et al.* 2009), which is in a 4.8 h orbit, is eclipsed by its approximately $0.2M_{\odot}$ companion and is not located in a globular cluster, led to the identification of these heavier-mass companion-eclipsing binary millisecond pulsar systems as a separate class called *redbacks* (Roberts 2011).

In recent years there has been a significant increase in the population of both black widows and redbacks enabled by deep searches of globular clusters (Chapter 3) and through the follow-up of gamma-ray sources identified by the Fermi-LAT telescope (Ray *et al.* 2012; Grenier & Harding 2015). The LAT has been particularly successful because of the rapid spin of these pulsars, resulting in a high spin-down energy, which is converted into gamma-ray emission and/or interacts with the companion wind to make a gamma-ray-bright source. There are around 20 black widow pulsars and 30 redback pulsars (known or candidates), and these large numbers allow us to better delineate their properties. The black widow pulsars are characterised by companion masses in the range 0.01 – $0.05M_{\odot}$, and they are thought to

² Black widow spiders comprise several species known for their potent venom. Among these are the redbacks, in which the females devour the males after mating.

be semi-degenerate stars that might be similar to brown dwarfs. The companions in redback systems have masses in the range $0.1\text{--}0.5M_{\odot}$ and are thought to be a combination of main sequence and He white dwarf stars. The observations of the light curves and radial velocities of the optical companions in these systems suggests that the neutron stars are probably heavier (e.g. van Kerkwijk *et al.* 2011) than those that are found in the double neutron star systems (Chapter 14).

The discovery of the first black widow PSR B1957+20 lent support to the model in which millisecond pulsars were spun-up to their rapid rotation rates in binary systems, but this was even more emphatically shown with the discovery of SAX J1808.4–3658. This was the first of the accreting millisecond pulsars and was found to exhibit x-ray pulsations at a period of 2.5 ms during an x-ray outburst (Wijnands & van der Klis 1998; Chakrabarty & Morgan 1998). This showed that the neutron stars in LMXBs were indeed spinning at millisecond periods, and around 16 of these sources are now known. The discovery of two intriguing redbacks has further strengthened this connection and will also provide important details on the transition from the accreting to non-accreting phase in the evolution of millisecond pulsars. PSR J1023+0038 is a 1.7 ms pulsar, and shortly after its discovery as a radio pulsar (Archibald *et al.* 2009), it was recognised that it was coincident with an object that had previously been classified as an LMXB with an accretion disk. That source had subsequently been shown to have lost its accretion disk and so it was established that this pulsar had recently transitioned from an LMXB to a radio pulsar. In 2013, PSR J1023+0038 was seen to transition back the other way as radio emission ceased to be detectable (Stappers *et al.* 2013). The globular cluster pulsar PSR J1824–2452I (Papitto *et al.* 2013) has been seen to transition in this direction too, with the same periodicity detected in the x-ray and radio emissions. Such objects are now called *transitioning* millisecond pulsars (tMSPs), and the class at present consists of three confirmed and four candidate systems.

10.4 The Eclipsing Cloud in the Millisecond Binaries

There is only a small chance that the orbital plane of a binary pulsar would be close enough to the line of sight for the pulsar to be occulted by the disk of a white dwarf companion, whose diameter of around 10^4 km is much smaller than the typical orbit diameter of, say, 10^7 km. However, the first known of the eclipsing millisecond pulsars PSR B1957+20, is occulted by its $0.02M_{\odot}$ companion for approximately one tenth of its binary orbit. The duration of the occultation shows that the occulting region is in fact larger than the Sun.

Immediately before and after the occultation, there is a large increase in the dispersion measure of the pulsar, showing that the line of sight is passing through ionised gas. This ionised gas cloud is more than 10^6 km ($1.5 R_{\odot}$) across. It must

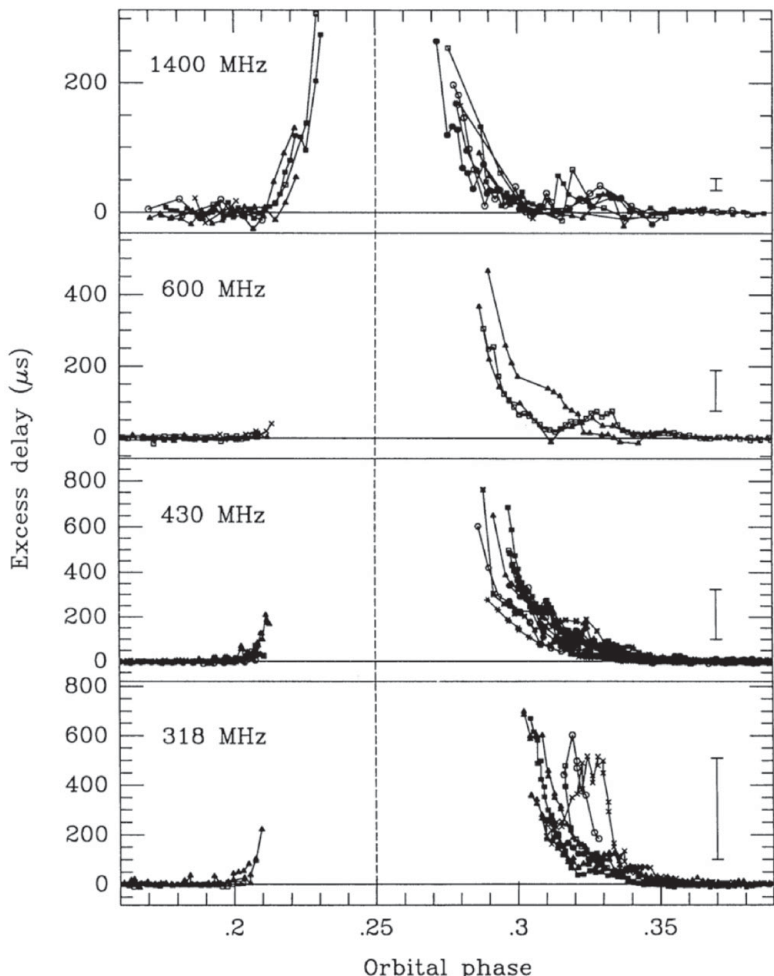


Figure 10.3 Pulse delays in the periodic eclipse of PSR B1957+20 at four frequencies from 318 to 1400 MHz. The vertical bars represent an increase in dispersion measure DM of $0.01 \text{ cm}^{-3} \text{ pc}$ (Ryba & Taylor 1991).

therefore be an outward flowing wind, since a stable atmosphere would be confined within the Roche lobe, whose diameter is only $\sim 0.5 R_{\odot}$. The average free electron density can be found by combining observations at several wavelengths from a series of eclipses, giving the remarkable plot of Figure 10.3 (Ryba & Taylor 1991). The asymmetry in the average electron density between ingress and egress from eclipse is likely due to a cometary-like tail of material trailing the companion in its orbit. The discovery of a large number of black widows has allowed for a range of eclipse phenomena to be observed. Eclipse durations are typically around 10% of the orbital period, centred on inferior conjunction, when the pulsar is on the far side of the companion, but in some systems they can be much longer. The durations of the

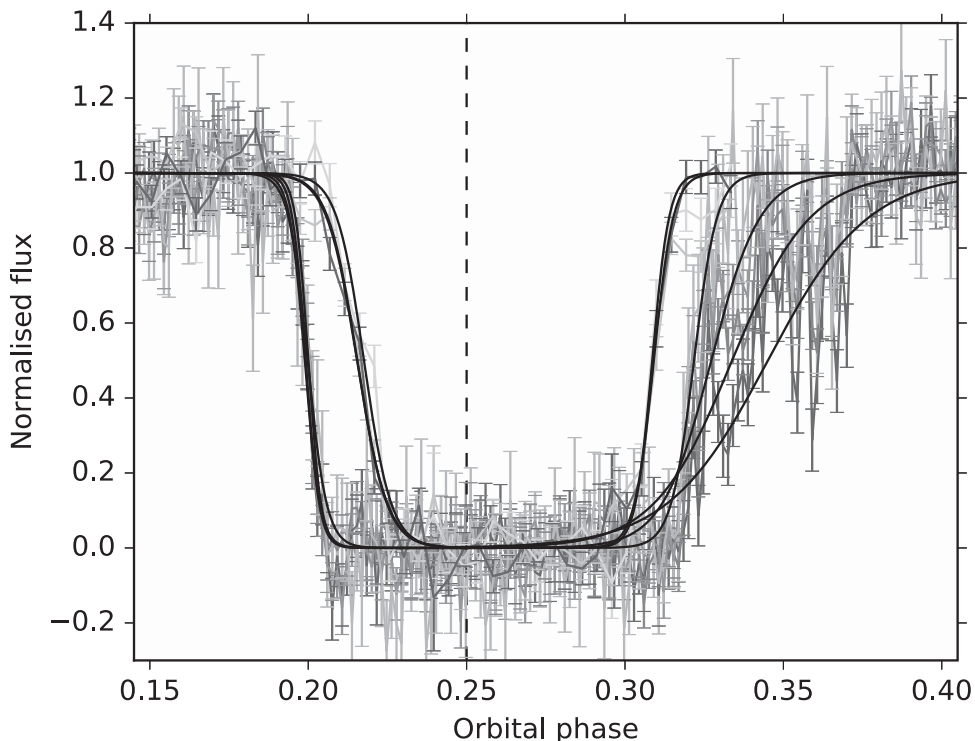


Figure 10.4 Eclipse in the black widow binary PSR J1810+1744, observed at 150 MHz (longer eclipse) and 350 MHz (shorter) (Polzin *et al.* 2018).

eclipses are frequency dependent, and in some cases pulses are seen at frequencies above 1 GHz throughout the eclipse region, but they are delayed compared to the expected arrival time. In some cases these delayed pulses exhibit structure that might be associated with magnetically constrained regions in the companion wind. Some systems, in particular the redbacks and tMSPs, show strongly variable eclipse durations and eclipses at other orbital phases (e.g. PSR B1744-24A, Lyne *et al.* 1990) which are likely related to complex mass loss in the system.

There are several different eclipse mechanisms proposed; these are reviewed in detail in Thompson *et al.* (1994). Although the increased electron column density seen at the eclipse edges suggests that increased dispersion and/or scattering may be responsible, if they can exceed the pulse period, it appears that this is not the primary mechanism of the loss of pulsations. One of the favoured mechanisms is cyclotron/synchrotron absorption in a magnetised plasma. Polzin *et al.* (2018) observed the eclipse of the black widow binary PSR J1810+1744 at frequencies of 150 MHz and 359 MHz (Figure 10.4) and attribute it to cyclotron/synchrotron absorption.

The interaction between the pulsar wind and that of the companion star can result in the formation of an intra-binary shock. In this shock region, particles may be accelerated sufficiently that the source is visible as a gamma-ray and x-ray source, and that x-ray emission may have an orbital phase dependence that depends on the relative strength of the winds. In some of these systems, the energy density of the companion wind is sufficiently high that the shock forms around the pulsar rather than the companion. This can lead to larger eclipse regions in the radio and also to enhanced x-rays at orbital phases close to inferior conjunction.

As mentioned in Section 10.2, the companions in these systems are often detectable optically. They are in tidally locked orbits where one side is continually irradiated by radiation from the pulsar and/or from the intra-binary shock. This manifests in optical light curves, which often exhibit differences of many magnitudes between the irradiated and dark side of the companion. Modelling of these light curves can provide crucial information on whether the companion is filling its Roche lobe, and the orbital inclination.

While the majority of redbacks and black widows are known to be eclipsed by their companions, there are some comparable systems that do not exhibit eclipses. In cases such as PSR J0610–2100 and J2234+0944, this is probably because their companion stars are significantly smaller than their Roche lobe, and thus material is more tightly bound. In some systems it may also be the case that the inclination angle of the binary is sufficiently high for our line of sight to miss the companion and the associated wind.

The presence of these shocks and the associated emission indicates the presence of magnetic fields. However, whether these are due only to the pulsar or there is a contribution from a companion magnetosphere is of interest as it may affect the internal properties of the companion star. There is growing evidence that the companions in some systems do show magnetic activity through their asymmetric light curves (e.g. Sanchez & Romani 2017).

10.4.1 Mildly Recycled Pulsars

In a ‘high-mass’ scenario, the giant companion has a mass of several M_{\odot} ; now the evolving giant expands and develops a common envelope containing the neutron star and the condensed core of the evolving star, a concept introduced by Thorne and Zytkow (1977) and often referred to by their names. The neutron star and the condensed core spiral in and expel the envelope of the companion. This occurs more rapidly than in the low-mass scenario; the result is a longer periodicity pulsar in an orbit that, although nearly circular, has a larger eccentricity. In the $P - \dot{P}$ diagram (Figure 10.1) these binaries populate the gap between the main groups of normal and millisecond pulsars. This group includes the Hulse–Taylor Binary B1913+16;

in this case the companion star has evolved and collapsed to form a second neutron star. There are also some (eight known in 2021) isolated pulsars with periods of 28–60 ms in this gap region. Each of these appears to be the product of a binary that was disrupted during an explosion of the secondary after a mild recycling of the neutron star (Lorimer *et al.* 2004); they may be regarded as ‘failed double neutron star binaries’ (Lorimer 2008).

10.4.2 Solitary Millisecond Pulsars

Of the 170 millisecond pulsars known in 2020, 64 are solitary. These must at some stage have been recycled in a binary system. Their escape from binary systems can occur by ablating their companions, as in the black widow systems, or dynamically in the supernova explosion of the companion star after it has spun up the neutron star, as in Figure 10.2 (see also Section 10.4.1). A supernova explosion of one binary component is likely to disrupt the binary if the component is the more massive of the two at the time of the explosion; the pulsar velocities expected from this are generally below 100 km s^{-1} . In addition, there may be an asymmetry in the explosion, which gives an extra kick to the pulsar; this would account for some of the largest velocities (see Section 4.5).

The general conclusion is that the probabilities of disruption match the observed proportion of solitary systems among the millisecond pulsars reasonably well.

10.5 The Globular Cluster Pulsars

At the time of the discovery of the first millisecond pulsar, it was already known that about 20% of all low mass x-ray binaries (LMXBs) were located in globular clusters, and the theory of accretion and spin-up of neutron stars in binaries was already current. Globular clusters therefore became the targets of several intensive searches for millisecond pulsars.

A pulsar PSR B1821–24, with a 3-ms period, was eventually found in the globular cluster M28. This cluster was known to contain a radio source with the steep spectrum and high polarisation characteristic of pulsars (Hamilton, Helfand & Becker 1985), but the source was comparatively weak, and it was only after an extensive search that the periodicity was discovered (Lyne *et al.* 1987). A few months later another millisecond pulsar, PSR B1620–26, with a period of 11 ms, was found in the globular cluster M4 (Lyne *et al.* 1988b). This pulsar is in a binary system with a comparatively long period (191 days); the orbit is nearly circular; it is now believed that this system is also orbited by a planet in an orbit of period around 100 years.

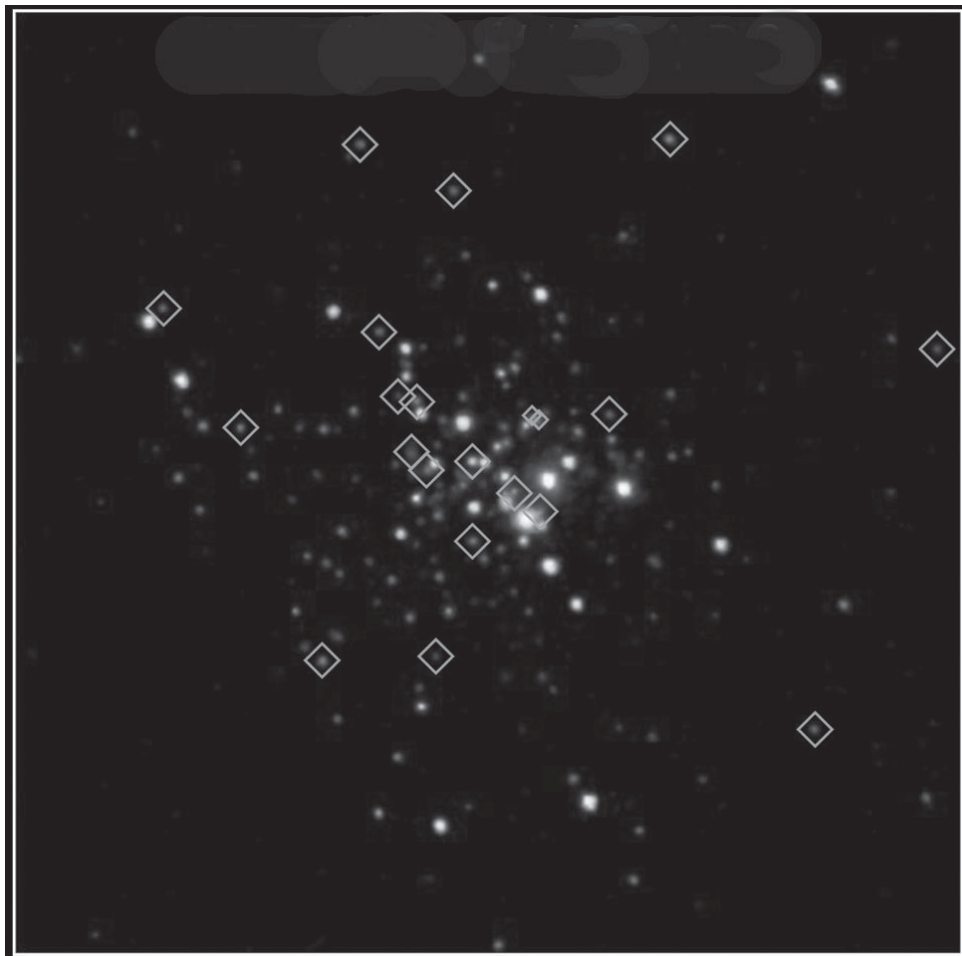


Figure 10.5 Pulsars in 47 Tucanae. At least 21 of the known millisecond pulsars in the globular cluster 47 Tucanae are coincident with x-ray sources (indicated by the diamond symbols) seen with the Chandra x-ray telescope (credit Craig Heinke).

Although these millisecond pulsars were near the limit of detection, the first to be discovered in a particular cluster helps the process of finding further pulsars by removing the need for searches in dispersion measure; since globular clusters contain little gas, the dispersion measure is nearly the same for all members of the cluster. Searches using the Parkes and Green Bank telescopes have been particularly productive (e.g. Lynch *et al.* 2011). Three clusters have a notably large population: 47 Tucanae has a group of 27 pulsars (Figure 10.5), all with periods between 2 and 6 ms (Freire *et al.* 2003); in M28 there are 14 pulsars known with a wide range of properties, including one that is a known gamma-ray source and six that are

either redbacks or black widows; Terzan 5 has the record number of 39 pulsars. After the revolution in globular cluster discoveries brought about by the Green Bank telescope, many new discoveries are coming from the FAST and MeerKAT telescopes, with more than three dozen new pulsars discovered since 2019, including some in clusters with no previously known pulsars. A catalogue maintained by Freire³ contained (March 2021) 223 pulsars in 36 globular clusters. See Cadelano *et al.* (2018) for references to recent searches in globular clusters.

Until the advent of the x-ray telescopes Chandra and XMM Newton, all the globular cluster pulsars were only observable in the radio, although most have been detected subsequently in x-rays; the radiated flux is then found to be greatest in x-rays. In 47 Tucanae, most x-ray sources are thermal, with $T_{\text{eff}} = 1 - 3 \times 10^6$ K. In NGC 6397 there are 27 x-ray sources and only two radio pulsars. These discoveries showed that LMXBs and millisecond pulsars are both common in globular clusters, giving strong support to the theory that they are associated in an evolutionary sequence.

Many of the globular cluster binary pulsars are related to normal Galactic disk pulsars, with white dwarf companions in two apparently distinct groups. The lowest mass companions have mass $M_c \leq 0.04M_\odot$; they are helium white dwarfs. The second group have high mass companions $M_c > 0.1M_\odot$; these companions have evolved to become CO and ONeMg white dwarfs. Others are unique to globular clusters: some have main sequence companions, and of these, several undergo eclipses by their companions. Others are in highly eccentric orbits, with $e > 0.1$; their evolutionary histories must be related to the high probability of interactions between pulsars and the other stars of a densely packed globular cluster.

On the large scale, the central mass concentration of the cluster itself can accelerate a pulsar and affect the measured values of the period derivative: for example, PSRs B2127+11A, D in M15 both have negative observed values of \dot{P} . On a small scale there are near collisions with passing stars, which will affect the observed \dot{P} and also possibly disturb the circular orbits of white dwarf binaries: this is seen as the explanation of the highly eccentric orbits of some binaries in the more densely populated clusters.

Millisecond pulsars in globular clusters have proved to be valuable both in revealing the gravitational field in a cluster by their values of \dot{P} , which are dominated by acceleration in the cluster gravitational field, and in the first demonstration of the existence of low density ionised interstellar gas from small differences in dispersion measure between pulsars located in the near and far sides of the cluster 47 Tucanae (Freire *et al.* 2001a).

³ www.naic.edu/~pfreire/GCpsr.html

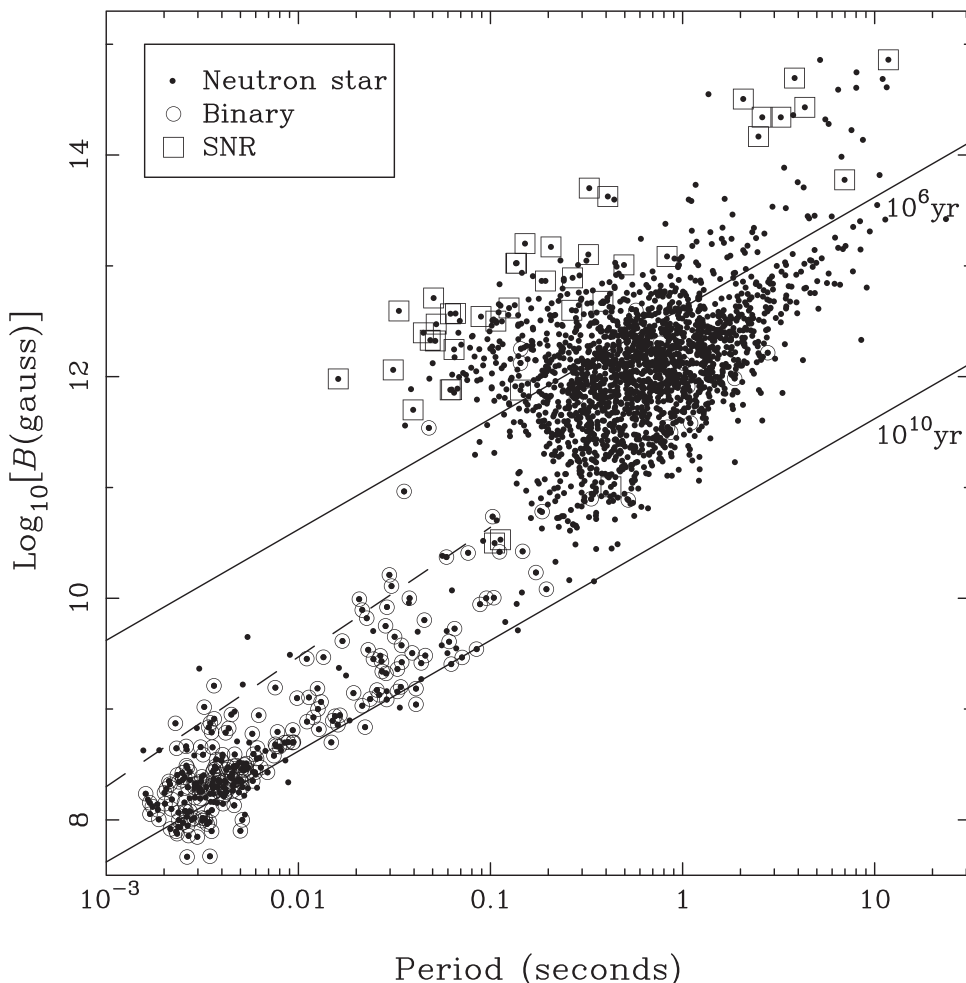


Figure 10.6 The position of the millisecond and binary pulsars in the $P - B$ diagram. The binaries are shown as circles, representing their orbits.

10.6 The Magnetic Fields of the Millisecond Pulsars

The surface magnetic dipole field B deduced for the millisecond pulsars from their slowdown rates is between 10^8 and 10^9 G, in contrast to the 10^{12} G fields typical of the normal pulsars. Figure 10.6 shows the clear distinction between these two groups. It seems that the process of accretion must involve a reduction in dipole field by a factor of around 1000. Intermediate values, around 10^{10} – 10^{11} G, are found in other binaries, including the double neutron star binaries.

Explanations are still needed for the following main features of the pulsars' magnetic fields:

1. the original fields of around 10^{12} G;
2. the process that reduces the field during accretion;
3. why the process of reduction appears to stop at about 10^8 G, with little or no decay during the long lifetime of millisecond pulsars.

Two possibilities have been discussed for the reduction process: ohmic decay and field advection. The first appears not to apply in the population of normal pulsars, where there is no clear relation between field strength and age (see Figure 10.6, although it should be noted that the youngest pulsars have values of B on average three times those of the main population). The second postulates the trapping of the field in a dense plasma that is accreting onto the surface of the neutron star, so that the magnetic flux is carried beneath the surface (Muslimov & Page 1996).

10.7 The Velocities of Millisecond Pulsars

The proper motions of pulsars are measured both by timing observations and by interferometric observations extending over several years (Section 4.5). Hobbs *et al.* (2005) catalogued 233 measured velocities, obtained from proper motions combined with distances either measured astrometrically or calculated from dispersion measures (Chapter 7). Line of sight velocities are not obtainable, so the quoted results are velocities on the plane of the sky, or 2-D velocities. Millisecond pulsars are comparatively easy to measure through timing observations because of their very stable periods and sharp pulses.

Hobbs *et al.* found 2-D speeds ranging from 12 km s^{-1} for PSR B1706–16 to 1625 km s^{-1} for PSR B2011+38. The mean for young ($<3\text{Myr}$) normal pulsars is $307 \pm 37 \text{ km s}^{-1}$, and for older non-recycled pulsars, the mean is $209 \pm 19 \text{ km s}^{-1}$. The recycled pulsars have a much lower 2-D velocity: the mean is $87 \pm 13 \text{ km s}^{-1}$. In each case, the measured velocities follow a Maxwellian distribution.

These velocities are consistent with a mean birth velocity (3-D) of $400 \pm 40 \text{ km s}^{-1}$ imparted to pulsars in the violence of the supernova explosion. The lower average speed of the older normal pulsars is attributable to the loss over time of high velocity pulsars from the gravitational potential well of the Galaxy. The much lower speed of the recycled millisecond pulsars is related to the complex sequence of events with which this chapter has been concerned; roughly speaking, a binary system will only survive the formation of a neutron star, which can subsequently be recycled, if the supernova kick is small. A full analysis, producing a model of velocities and the distribution of pulsars with distance from the Galactic plane (the z -distance), requires consideration of the distribution of the progenitor binaries and the effects of the supernovae, including the dynamical effects in binary orbits and the kick velocity at birth. This complex analysis has been developed by several authors, most recently by Kiel and Hurley (2009).

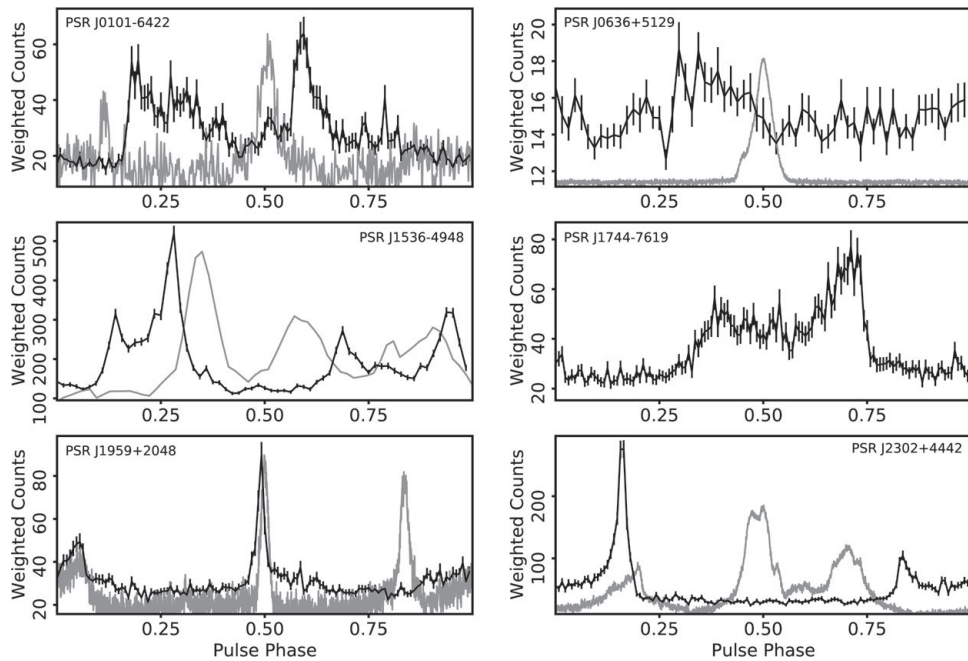


Figure 10.7 Gamma-ray (Fermi-LAT) and radio profiles for a range of MSPs. The dark lines are the gamma-ray profiles, and the radio profiles are in grey. In the case of PSR J1744–7619, there is no detected radio emission from this source (thanks to David Smith for the data).

10.8 Pulse Profiles of Millisecond Pulsars

In Chapter 8, we displayed a wide variety of pulse profiles from many pulsars and introduced two broad categories, those originating over the polar cap (designated PC) and those originating in a vacuum gap far out in the magnetosphere (designated OG). Many the pulse profiles of millisecond pulsars all fall into the OG category. Within this category there is a wide variety of form and width, as shown in Figure 10.7, which is generally accounted for by a variety in the geometry of angle between rotation axis and magnetic axis, and the angle at which the pulsar is viewed. We explore these geometries in Chapter 16.

10.9 Gamma-ray MSPs

Gamma-ray observations of MSPs by Fermi LAT are presented by Abdo *et al.* (2013), including an analysis of their properties and the distribution over the sky of the then known 171 gamma-ray pulsars (there are now, in 2020, over 200 known gamma-ray pulsars). Of these, about half are young normal pulsars; the other half

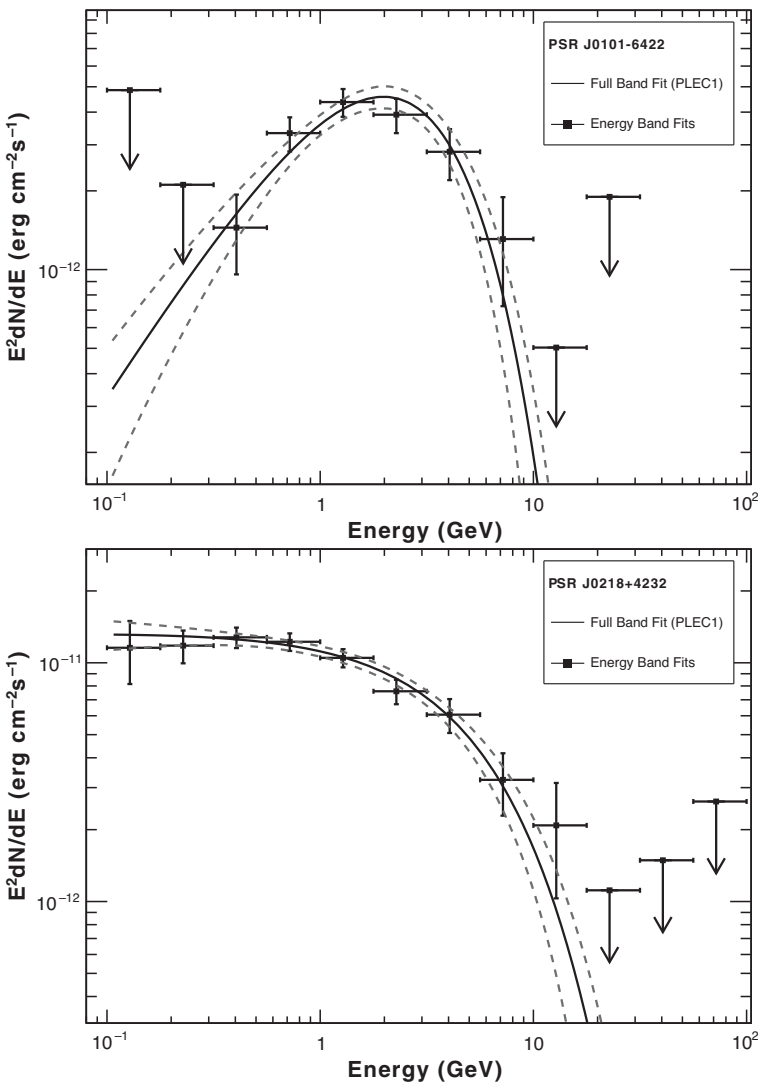


Figure 10.8 Typical gamma-ray spectra (Abdo *et al.* 2013).

are MSPs divided roughly equally between those known to be radio pulsars and the others that were discovered in searches for periodicities in gamma-ray sources. As can be seen in Figure 10.7, the beam widths indicated by the gamma-ray pulse profiles are generally wider than the radio profiles, which probably accounts for those seen as gamma-ray but not radio pulsars.

Figure 10.8 shows a typical spectrum over the HE range (x-ray to TeV), from Abdo *et al.* (2013). There are fewer observations at the ends of the HE spectra; conveniently for observations with Fermi LAT, most spectra peak near 1 GeV, while

the x-ray and TeV observations are less sensitive and cover smaller areas of sky. Malov and Timirkeeva (2019) list a total of 61 rotation-powered x-ray radio pulsars that are identified with radio pulsars; of these, only 21 are MSPs, with the typical characteristics of large spin-down energy and large magnetic field at the light cylinder.

Radio observations of pulse profiles are available for most gamma-ray MSPs. There is no need for a separate discussion of those that are visible in gamma-rays but not radio, since this is presumably due to radiated beams that are wider in gamma-ray than in radio.

11

Magnetars

The magnetars are a small group of young, energetic and very variable rotating neutron stars, with extremely high effective dipole magnetic fields. They are mostly observed at x-ray and gamma-ray wavelengths. Originally comprising soft gamma-ray repeaters (SGRs) and anomalous x-ray pulsars (AXPs), they now include some erratic radio pulsars. In all of these categories the rotation periods are long, and the slowdown rates are high, consistent with a high magnetic field and a short lifetime. The radiated energy in x-rays and gamma rays is far higher than the rate of loss of rotational energy, and it is commonly assumed that the energy for the radiated x-rays and gamma rays is derived from a decay of the magnetic field stored in the interior of the neutron star. For many years, SGRs, AXPs and normal radio pulsars were regarded as distinct populations, but it now appears that they may better be regarded as the extremes of a continuum.

11.1 The Soft Gamma-ray Repeaters (SGRs)

Cosmic gamma-ray bursts (GRBs) are single short bursts of emission that were first detected by satellites equipped with gamma-ray detectors, which were intended to monitor man-made nuclear explosions. Since then some thousands of GRBs have been observed; many of these were measured from several satellites simultaneously, allowing positions to be determined from relative times of arrival. The GRBs were found to be distributed isotropically over the sky, with no concentration towards the Milky Way, and they are thought to be extragalactic in origin.

Among the thousands of GRBs, a small number showed repeated bursts from the same location. This small class of soft gamma-ray repeaters (SGRs) is apparently entirely distinct from the majority of GRBs; they were distinguished originally as sources with a particularly soft gamma-ray spectrum. Multiple very energetic gamma-ray bursts were recorded in 1979 from three separate sources. On 5 March

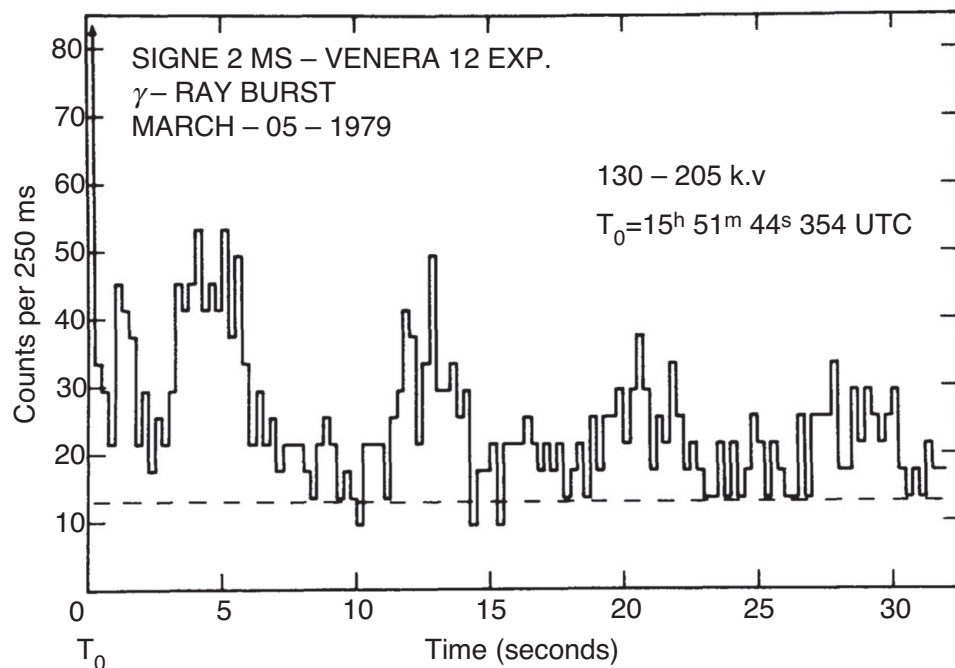


Figure 11.1 The discovery of periodicity in an SGR giant flare. An 8 s period is seen in the decay of the flare 1979 March 5, from SGR 0526–66, recorded by the Venera 12 Venus probe in the 130–205 keV energy range (Barat *et al.* 1979).

1979, SGR 1900+14 produced three bursts (Mazets, Golenetskii & Gur'yan 1979), including the most energetic ever recorded. The first recorded SGR burst was from SGR 1806–20 on 7 January 1979; over 100 repeated bursts from this source were recorded in the following 7 years (Laros *et al.* 1987). Recurrent bursts in SGR 0526–66 were discovered by Golenetskii, Ilyinskii and Mazets (1984) from observations with the spacecraft Venera 13 and 14.

The structure of the largest bursts, known as giant flares, has been recorded in detail by several spacecraft. An initial spike with a rapid rise, lasting less than a second, is followed by a decay lasting several minutes. Barat *et al.* (1979) discovered a periodicity of 8 s in the decay of a burst in SGR 0526–66 (Figure 11.1), and Figure 11.2 shows the giant flare of 27 August 1998 in SGR 1900+14 with a 5-second periodicity (Hurley *et al.* 1999). Periodicities of 2–9 s are found in all SGRs, either in the gamma-ray or x-ray observations; these are interpreted unequivocally as the rotation rate of a neutron star.

Table 11.1 lists the rotation periods and characteristic ages of all magnetars, including the SGRs and AXPs, known in April 2020.

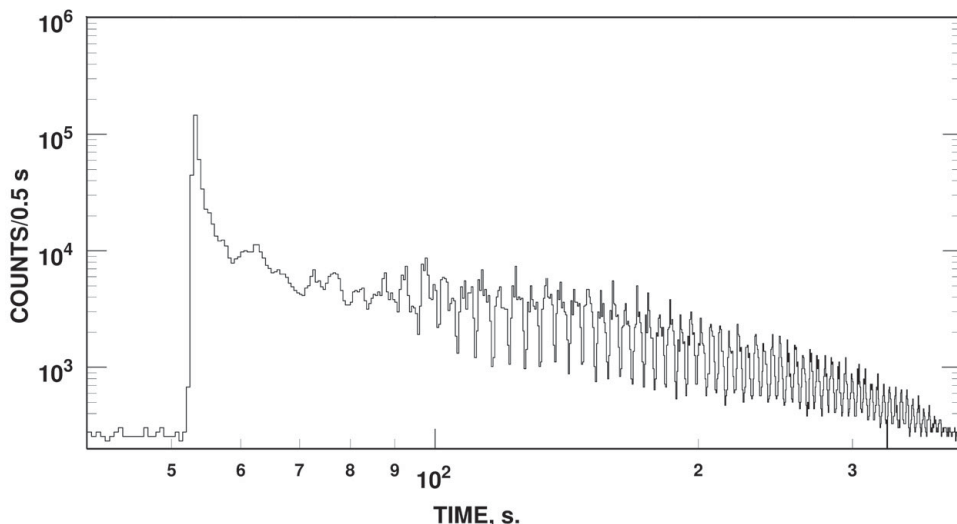


Figure 11.2 The giant flare from SGR 1900+14, 27 August 1998, recorded in the energy range 20–150 keV by the Ulysses spacecraft, showing the 5-s modulation due to the neutron star rotation (after Hurley *et al.* 1999).

The giant gamma-ray flares that revealed these hitherto unknown SGRs were observed by several spacecraft, and the discoveries were reported in a plethora of papers and IAU Circulars, for which references may be found in reviews by Rea and Esposito (2011) and by Kaspi and Beloborodov (2017). The 1979 flare in SGR 0526–66 was detected by no fewer than 12 detectors in 9 spacecraft; the relative times of arrival in their locations distributed in space gave a source position accurate to one arc minute (Evans *et al.* 1980). Faint optical and infrared counterparts have been found for only a few SGRs, notably SGR 1806–20 (Israel *et al.* 2005; Kosugi, Ogasawara & Terada 2005).

Despite the very high intensity of the bursts, intensive searches with several spacecraft had revealed only four SGRs by 2000 (see a review by Hurley (2000)). A catalogue of magnetars (Olausen & Kaspi 2014) maintained at McGill University¹ now contains (in April 2020) nine confirmed SGRs. Two SGRs are clearly associated with the supernova remnants remaining from the formation event. A number of other such suggested associations are now believed to be incorrect (Gaensler *et al.* 2001); however, an association with young stellar clusters is suggested by Klose *et al.* (2004), consistent with an origin in the supernovae of massive young stars whose remnants may have faded by now.

¹ www.physics.mcgill.ca/~pulsar/magnetar/main.html

Table 11.1. Magnetars

	Period P (s)	\dot{P} 10^{-12} s/s	Age τ_c kyr	M 10^{14} G	Notes
CXOU J0100–72	8.02	18.8	6.8	3.9	—
4U 0142+61	8.69	2.0	7.0	1.4	O
SGR 0418+5729	9.08	0.004	36000	0.06	—
SGR 0501+45	5.76	5.9	15	1.9	O
SGR 0526–66	8.05	38.0	3.4	5.6	—
IE 1048–5937	6.16	22.5	4.5	3.9	O
IE 1547.0–5408	2.07	47.7	0.69	3.2	RS
PSR J1622–4950	4.33	17.0	4.0	2.7	RS
SGR 1627–41	2.59	19.0	2.2	2.2	S
CXOU J164710.2–455216	10.6	0.8	>420	< 0.66	—
IRXS J170849.0–400910	11.01	19.6	9.0	4.7	—
CXOU J171405.7–381031	3.82	64.0	0.95	5.0	S
SGR J1745–2900	3.76	13.8	4.3	2.3	R
SGR 1806–20	7.55	495.	0.24	20	O
XTE J1810–197	5.54	7.8	11	2.1	O,R
Swift J1818–1607	1.36	84.6	0.25	3.5	R
Swift J1822.3–1606	8.44	0.021	6300	0.14	—
SGR 1833–0832	7.56	3.4	34	1.6	—
Swift J1834.9–0846	2.48	8.0	4.9	1.4	S
1E 1841–045	11.79	40.9	4.6	7.0	S
3XMM J185246.6+003317	11.56	0.14	>1300	< 9.41	—
SGR 1900+14	5.20	92.0	0.90	7.0	—
SGR 1935+2154	3.24	14.3	3.6	2.2	S
1E 2259+586	6.98	0.47	230	0.59	OS

O = optical or infrared;

R = radio;

S = SNR Association.

11.2 The Anomalous X-ray Pulsars (AXPs)

The AXPs are a small class of x-ray pulsars showing pulsations having long rotation periods (6–12 seconds), short spin-down times ($\tau_c \sim 10^3 - 10^5$ years) and soft x-ray spectra. They are very variable, and their discovery usually depends on occasional intense bursts picked up by wide-angle telescopes such as SWIFT. Despite their sporadic behaviour, their rotation can be monitored continuously, allowing coherent timing solutions between separate observing sessions. Glitches occur that are similar to those of normal radio pulsars (Dib, Kaspi & Gavriil 2009). Their magnetic fields, as deduced from their spindown rates as $B = 3.2 \times 10^{19} (P \dot{P})^{1/2}$ G, are the highest known, reaching 10^{14-15} G; the energy stored in these fields is the source that heats the star and keeps the surface at an observable temperature. Table 11.1 includes 15 members of this class.

The first, 1E2295+586, was discovered in Einstein HEAO-2 observations of the supernova remnant CTB 109 by Fahlman and Gregory (1981), who pointed out that the x-ray luminosity was more than 1000 times the spindown luminosity. Six are clearly associated with supernova remnants (SNRs), showing that they are comparatively young, probably less than 10^{4-5} years old; this is supported by the low characteristic ages τ_c in Table 11.1. There is no sign of binary companions or immediately surrounding nebulae (Olausen & Kaspi 2014).

The AXPs have soft x-ray spectra corresponding to a thermal energy of $\sim 0.2\text{--}0.7$ keV. An extension of the spectra into higher energies, following a power law, is probably generated by Compton scattering of thermal surface radiation in an energetic magnetosphere (Morii *et al.* 2003). The power radiated in the x-ray region is $10^{34\text{--}35}$ erg s $^{-1}$. A broad spectral line at 12.6–14 keV has been observed in several AXPs; this is interpreted as a proton cyclotron resonance in a field of $\sim 10^{14}$ G (Ibrahim, Swank & Parke 2003).

Around the turn of the century, following a suggestion by Thompson and Duncan (1996), it became clear that SGRs and AXPs were closely related. Kouveliotou *et al.* (1998, 1999) found that the SGRs 1806–20 and 1900+14 were also x-ray sources, with long rotation periods like those of the AXPs. Furthermore, the slowdown rates are also similar; assuming that the slowdown is entirely due to magnetic braking, the surface dipole magnetic fields are respectively 8×10^{14} G and 6×10^{14} G. This link with SGRs was further strengthened by the observation of x-ray bursts from the AXP 1E1048.1–5937 that were similar to the bursts from SGRs (Gavriil, Kaspi & Woods 2002).

The measured values of spin period and slowdown show that the SGRs and AXPs co-exist in an extreme region of the $P - \dot{P}$ diagram, shown in Figure 11.3. Their high magnetic field places them in the category of magnetars, and it is widely accepted that SGRs and AXPs are different manifestations of the same phenomenon. (See e.g. a review by Woods and Thompson (2006)).

11.3 Other Emission from Magnetars

Although defined by their extreme high-energy emission, some magnetars also emit detectable radiation in other parts of the electromagnetic spectrum.

Optical pulsations have been seen from three magnetars (references may be found in Olausen and Kaspi (2014)). The pulses are broad and similar to the x-ray profiles, with high pulsed fractions. Three other magnetars show emission in the optical and/or infrared bands but so far with no detectable pulsations.

The radio detection of the transient AXP XTE J1810–197 (Camilo *et al.* 2006b) initiated a new era in which the distinction between magnetars and normal radio pulsars became blurred. An increase in x-ray intensity by a factor of 100 in 2003

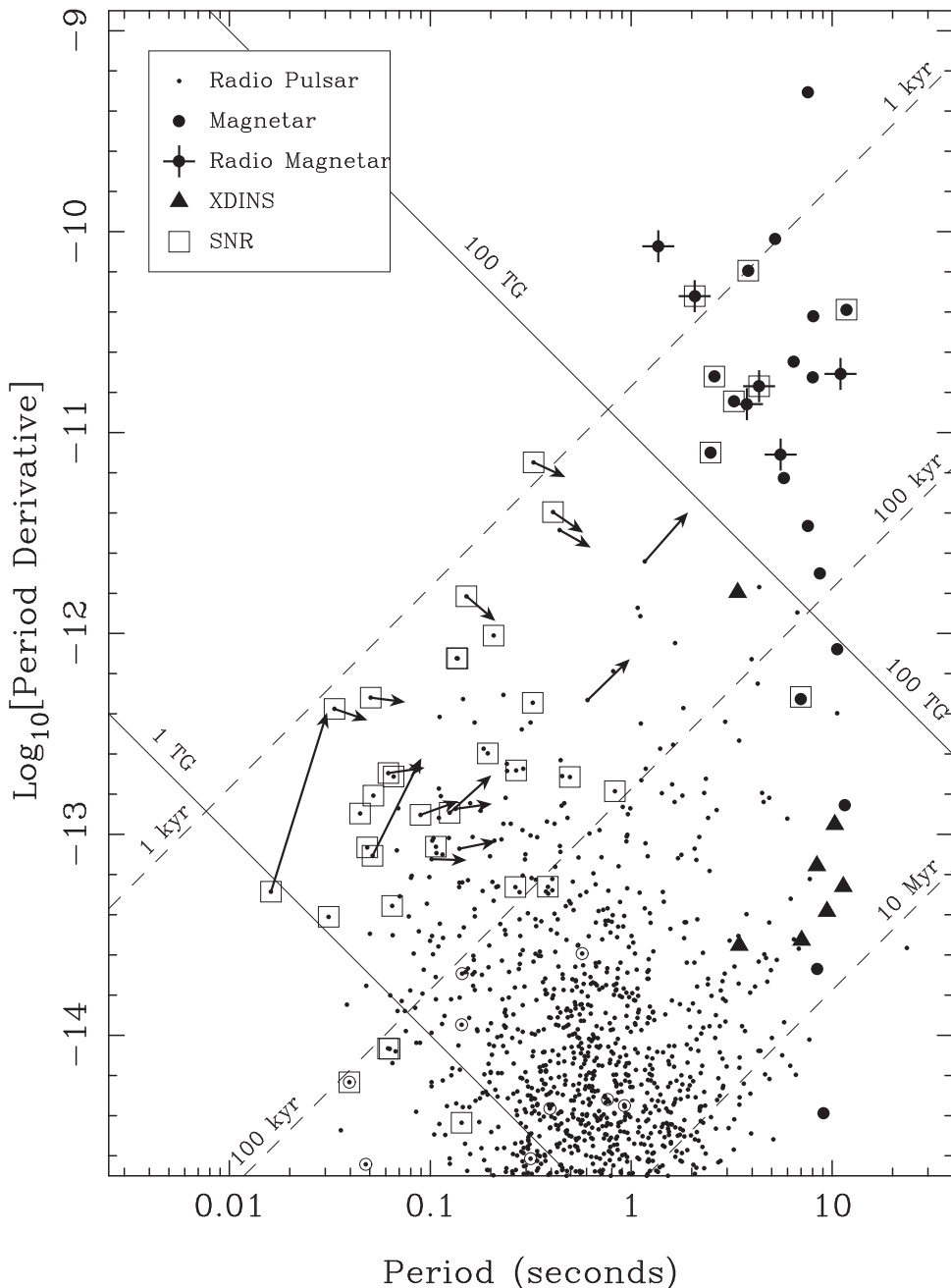


Figure 11.3 The magnetars, together with normal pulsars, are shown in the upper region of the $P - P$ diagram. The arrows indicate the direction of movement of some pulsars as determined by the measurement of their long-term braking indices (after Espinoza, Lyne & Stappers 2017). The lengths of the arrows indicate the approximate distance of travel after time τ_c , their present characteristic age.

(Ibrahim *et al.* 2004) was followed a year later by its appearance as a radio pulsar, emitting bright narrow pulses. The radio spectrum is flat and, at 20 GHz, this became the brightest radio emission from any neutron star (Camilo *et al.* 2006b). The radio emission ceased in 2008, but intense radio pulsations were redetected 10 years later (Lyne *et al.* 2018), coincident with an x-ray outburst.

By 2020, four other magnetars had been found to be radio emitters, all of which were transient, very bright, highly linearly polarised and very variable in radio flux density and profile shape. These four were 1E 1547.0-5408 (Camilo *et al.* 2008), PSR J1622-4950 (Levin *et al.* 2010) – which was the first magnetar to be discovered at radio wavelengths before the x-ray counterpart was discovered – SGR J1745-2900 (Eatough *et al.* 2013) – which is located close to the Galactic centre – and J1818-1607 – which has a period of only 1.36 seconds and a characteristic age of only 250 years. SGR 1935+2154 recently gave off the brightest burst of radio emission from a neutron star ever detected. The same pulse was seen by the wide field instruments CHIME (Andersen *et al.* 2020) and STARE2 (Bochenek *et al.* 2020). These bright bursts have been followed by a number of fainter bursts, which show that the radio bursts from this source span some seven orders of magnitude.

11.4 Other Possible Magnetar Manifestations

Following the realisation that several magnetars also emit strong radio pulsations, it would not be entirely surprising if some high-magnetic-field rotation-powered normal pulsars were to exhibit magnetar-like high-energy emission. Indeed, one such high-B pulsar, PSR J1846-0258, in the centre of the supernova remnant Kes 75, was discovered to have a characteristic age of about 700 years and a magnetic field of 5×10^{13} G (Gotthelf *et al.* 2000). Although seen only in x-rays, it showed weak steady pulsation for several years until it was detected to emit a sudden six-week-long intense x-ray outburst (Gavriil *et al.* 2008), which included several short magnetar-like bursts as well as a large glitch, before returning to a more normal state (Kuiper & Hermsen 2009; Livingstone *et al.* 2010).

More recently, the normal rotation-powered young radio pulsar, PSR J1119-6127, which has a characteristic age of about 1500 years and a magnetic field of 4×10^{13} G, showed a similar intense x-ray outburst, preceded by magnetar-like bursts and a large glitch (Archibald *et al.* 2016). In Chapter 9, we noted that the bright radio pulses mean that the Galactic magnetar SGR J1935+2154 may be a source of fast radio bursts (FRBs) (Andersen *et al.* 2020; Bochenek *et al.* 2020).

These discoveries further show that the dividing line between normal pulsars and magnetars is blurred, and there may be a continuum of properties between them.

Additionally, there are two other classes of neutron star that may be related to magnetars, namely the RRATs and XDINSs.

Some of the rotating radio transients (RRATs), described in Chapter 9, may be related to magnetars. There are now at least 29 known RRATs (Keane *et al.* 2010), with locations determined by timing and dispersion measure. Their rotation periods range from 0.125 to nearly 8 seconds. They are mostly located in the right-hand side of the $P - \dot{P}$ diagram (Figure 11.3), where old pulsars are expected to be found, but they mostly have large magnetic dipole fields around 10^{13} G.

The x-ray isolated neutron stars (XDINSs) were discovered by the ROSAT satellite during the 1990s as thermal x-ray sources without radio counterparts. Although these seven objects emit only thermal x-rays, temperature variations across their surfaces result in quasi-sinusoidal modulation at their rotation period. Their long spin periods and rapid spin-down indicate that they all lie immediately below the magnetars in Figure 11.3. Their high surface magnetic fields are in the range 10^{13-14} G, possibly identifying them as related to magnetars (Haberl 2007; van Kerkwijk & Kaplan 2007), perhaps later in their life cycle. Originally called ‘The Magnificent Seven’, no more were found until it was recently discovered that the 3.4-second radio pulsar J0726–2612 also showed thermal x-rays, which placed it in this group (Rigoselli *et al.* 2019).

11.5 Demography and Origin of the Magnetars

The magnetars appear to be a young and short-lived class among the wider variety of neutron stars. Their youth is most clearly indicated by their location close to the Galactic plane; Olausen and Kaspi (2014) find their z -distances fit an exponential with scale height of only 20–30 pc, even though their velocities are typically ~ 200 km s $^{-1}$ (Tendulkar *et al.* 2012). They are all slowing down rapidly, with positive \dot{P} ; their characteristic ages are small, although this is an unreliable indication of their actual age, as their braking indices are unknown. Estimates of size of their population depend on distances, which are reasonably accurately known from x-ray absorption in magnetars, and from dispersion measure for the RRATs.

As might be expected for short-lived stars, the population of magnetars in the Galaxy is small. The SGR bursts are so intense that they would be detected from anywhere in the Galaxy. On the basis of the small sample known so far, it appears that no more than a few dozen magnetars exist in the Galaxy. The populations of RRATs and the XDINSs are much larger; both may be closer to the population of normal pulsars, and they may be part of a normal evolutionary sequence.

It is generally believed that normal pulsars originate in supernova collapse, rotating with periods of some tens of milliseconds, and may be seen surrounded by supernova remnants. As they slow down, they migrate from left to right of the $P - \dot{P}$

diagram. This migration is shown in Figure 11.3; if the dipole magnetic field is constant, pulsars ideally follow a track downwards at an angle of 45° , parallel to the lines of constant magnetic field. If magnetars have evolved with a constant magnetic field from part of the normal population, we would expect to see several precursors in the empty top left of the diagram, even though their evolution would be rapid. Two possibilities must be considered: a different origin, or an evolution with an increasing magnetic field.

11.5.1 A Separate Origin for Magnetars?

As noted in Sections 11.1 and 11.2, and seen in Figure 11.3, there are only a few supernova remnants associated with magnetars. This small number is somewhat surprising since the apparent youthful age of the magnetars is likely to be less than the time expected for any associated remnants to decay. There is also a possible association with star clusters containing very massive stars. It is thought that the magnetars may have originated in the supernova collapse of stars with very high mass, perhaps of $50M_\odot$, although this is contrary to the accepted theory that the collapse of such massive stars would produce black holes rather than neutron stars.

11.5.2 An Increasing Magnetic Dipole Field?

Although magnetars were at first regarded as a distinct and separate population to the normal pulsars, we saw in Sections 11.3 and 11.4 that there was a continuum of rotational properties near the interface. Moreover, there is an overlap in some of the emission properties, with some magnetars showing radio-pulsar-like behaviour and some rotation-powered pulsars exhibiting magnetar-like high-energy bursts.

As remarked in Chapter 5, it has been suggested for many years that the low braking index of most young pulsars might be due to an increasing dipole magnetic field. We now explore the possibility that there is an evolutionary route from these young rotation-powered pulsars to the magnetars. The young pulsars with well-established and enduring values of braking index are indicated in the $P - \dot{P}$ diagram (Figure 11.3) by arrows, showing the direction and speed of their progress across the diagram. The possibility that some or all of these might evolve into magnetars remained a speculation; as can be seen, there are few objects lying between the young pulsars and the magnetars. That gap has been bridged by a key observation of a rapidly-increasing dipole field in a pulsar, PSR J1734–3333, midway between the two groups.

PSR J1734–3333 was discovered as a radio pulsar in the Parkes Multibeam Pulsar Survey and tentatively associated with the supernova remnant G 354.8–0.8

(Manchester *et al.* 2002). The rotation period is 1.17 s, and the characteristic age is 8.1 kyr. A measurement of the second derivative of the rotation rate has been obtained, showing that the braking index is $n = 0.9 \pm 0.2$ (Espinoza *et al.* 2011).² It is reported to be an x-ray source (Olausen *et al.* 2010). If the progress of this pulsar in the $P - \dot{P}$ diagram continues without change, the rotation will slow to a period of 8 s in only about 30 kyr, and the pulsar will then be in the centre of the magnetars. Remarkably, the characteristic age will be unchanged at 8 kyr.

Such a link between the young pulsars and the magnetars provides a possible explanation for several of the mysteries that appear in the earlier part of this chapter. If the magnetars do indeed evolve through a normal young pulsar phase, then:

- There is no need to invoke an origin of magnetars in a different kind of supernova collapse of a massive star.
- The large dipole magnetic fields of the magnetars originate within the young pulsars.
- The ages of the magnetars are unrelated to their present characteristic ages, and may be of order 10^4 – 10^5 years.
- At that age the remains of any supernovae in which they were born may have decayed, and only a few magnetars will still be associated with visible SNRs.

We note in passing that it is unfortunate that magnetars are very unstable in their rotation properties, making it unlikely that reliable values of their braking index will ever be determined, which would indicate their motion in the $P - \dot{P}$ diagram (Figure 11.3), as is possible for some young normal pulsars.

An evolutionary sequence from radio pulsars to magnetars, including RRATs and XDINSs, is consistent with a birthrate for neutron stars expected from the observed rate of supernovae (Keane & Kramer 2008). The single problem that remains is the growth of the dipole field by two orders of magnitude over a period of 10^3 – 10^4 years in a process that appears not to apply to all neutron stars.

Duncan and Thompson (1992) showed that a dynamo action within a newly collapsed neutron star could generate a magnetic field of 10^{14} – 10^{15} G. The dynamo would be powered by convection, which would occur within the first few seconds after collapse and would only occur in a rapid rotator with period of around 1 ms or less. The magnetic field would constitute a vast reservoir of energy, which would dominate the behaviour of the star. In a later paper (Thompson & Duncan 1995), they showed that such a high field would account for several features of SGRs, including the energy required for the outbursts and the confinement of plasma after

² An analysis of 21 years of observations now gives $n = 1.2 \pm 0.1$.

the outburst as observed in the tail of the outburst. They also showed (Thompson & Duncan 1996) that as the strong magnetic field diffused outwards, it would fracture the crust on small and large scales, accounting for the onset of the outbursts.

A further key element of the early history of the magnetic field is described by Geppert, Page and Zannias (1999). Shortly after the formation of the neutron star, a considerable part of the supernova remains may collapse onto the neutron star. The ram pressure in this rapid accretion may overcome the magnetic field pressure even for the strongest magnetar fields. At this stage the accretion can be described as a simple hydrodynamical process, which builds up a layer around 100 m thick on the surface. The field eventually diffuses out through this accreted layer and establishes the familiar dipole field. Accretion of $0.01 M_{\odot}$ material is sufficient to suppress the field, which may diffuse out over a time of some 10^3 years. A larger accretion, of say $0.1 M_{\odot}$, might confine the magnetic field for much longer, and the star may never become a pulsar.

The growing dipole field due to this break-out process might account for the development of magnetars from part of the normal population of pulsars. It might also account for the low braking index observed in the young pulsars.

12

Thermal X-rays from Neutron Stars

Pulsed x-rays have been discovered from some of the youngest and some of the oldest of the radio pulsars. The wide spectrum observed for the young pulsars, such as Crab and Vela, and the older recycled millisecond pulsars, extends from long radio wavelengths to gamma rays; in these sources the x-rays are powered by rotational slowdown and originate in the outer magnetosphere. In this chapter, we concentrate on thermal radiation originating from the surface and, in binary systems, from accreting gas clouds.

The spectrum of thermal radiation from a neutron star with surface temperature of order 10^6 K peaks in the x-ray spectrum at a photon energy around 1 keV. Only the largest x-ray telescopes can detect the thermal radiation from the surface of an isolated neutron star. The first observation of an x-ray source outside the solar system, made in 1962 using a rocket-borne instrument (Giacconi *et al.* 1962), revealed an unexpected and powerful source, designated Sco X-1. The explanation of this source was given by Shklovsky (1967); it is indeed a thermal source associated with a neutron star, but the thermal x-rays are from matter in a hot circumstellar disk surrounding the neutron star, accreted from a companion star in a binary system. Sco X-1 is now the prototype of a class of binary x-ray sources known as low mass x-ray binaries (LMXBs).

Confirmation of the nature of Sco X-1 and other x-ray sources in the Galaxy revealed by the first x-ray astronomy satellite UHURU (launched in 1970) came when the source Cen X-3 was shown to be pulsating with a period of 4.8 seconds. Following the same arguments as in the interpretation of the binary radio pulsars, it soon became clear that the source must be a rapidly rotating neutron star in a binary system. The orbital periods are typically several days, indicating that the stars in the binary systems are close enough for mass transfer to occur. In many cases the companion star can be seen optically, so that a complete resolution of the characteristics of the system, including the masses of the separate components, can be made; in Sco X-1, the neutron star mass is $1.4M_\odot$, and the companion mass

is $0.42M_{\odot}$ (Mirabel & Rodrigues 2003). The companions are often more massive young stars, whose evolution is expected to lead to a rapid expansion and overflow onto the surface of the neutron star; these are the high mass x-ray binaries (HMXBs). The energy supply is derived from the gravitational potential drop through which the overflowing matter falls. These pulsars are thermal emitters; they are classified as *accretion-powered* pulsars, distinguishing them from the isolated *rotation-powered* pulsars.

By 1984, there were over 100 known compact x-ray sources with accurate enough positions for many of them to be identified with optically detectable objects. More than half of the identified sources turned out to be accretion-powered binaries. The others were supernova remnants, isolated hot white dwarfs, some non-degenerate stars and some globular clusters; the globular clusters are now known to be rich concentrations of x-ray sources. A comprehensive account of the optical identifications at this time was given by Bradt and McClintock (1983).

Subsequent observations by ROSAT and other orbiting telescopes detected x-ray pulsations from a substantial number of isolated radio pulsars (Becker & Trümper 1997; Voges *et al.* 1999), where the energy source is the rotation of the neutron star rather than accretion in a binary system. Becker and Trümper found a remarkably close relation between the x-ray luminosity and the rate of loss of rotational kinetic energy $I\Omega\dot{\Omega}$; this was extended to 41 rotation-powered sources by Possenti *et al.* (2002) (Figure 12.1). The figure shows five different types of x-ray source that derive their energy from rotational slowdown; the values of L_X refer to the total energy in the range 1–10 keV, including the radiation from any nearby nebulae apparently powered by the discrete source. At the highest levels the filled stars represent the Crab and other young pulsars; at the lowest level are the pulsars with the lowest spindown rates, including several millisecond pulsars.

Beyond the range of these rotation-powered x-ray sources lie the *magnetars*, in which the rate of loss of rotational kinetic energy is too small to account for their very high x-ray luminosity (Chapter 11).

At the lowest end of the range of intensities, it has been possible to detect thermal x-rays from the surface of isolated neutron stars. The thermal radiation from an isolated neutron star has a ‘soft’ spectrum (photon energy ~ 1 keV); this is within the energy range of x-ray telescopes, but the total intensity from the small area of a neutron star ($\sim 10^3 \text{ km}^2$) is often too low to be detected, even though the surface temperature might be around 10^{6-7} K. Thermal x-ray emission from an isolated non-accreting neutron star was discovered by Pons *et al.* (2002); the observed spectrum is that of a black body at 35 eV, which has presumably been reduced from ~ 50 eV by the surface gravitational redshift $z \sim 0.3$.

X-ray astronomy has grown through a series of orbiting telescopes whose performances now compare well with their optical ground-based counterparts. The first

all-sky survey for objects such as supernova remnants was achieved by ROSAT, launched in 1990, which had an angular resolution of $1\frac{1}{2}$ arcminutes. Three x-ray telescopes, Chandra, XMM-Newton and NuStar, now produce images with 1 arc-second resolution and also provide spectra; these are grazing incidence reflector telescopes, working at photon energies of a few keV (Chapter 2). Accurate pulse timing was first achieved by the Rossi X-ray Timing Explorer (RXTE) and later by NICER; sufficient time resolution is now available to detect x-ray pulses in several millisecond pulsars. The sensitivity is sufficient to allow detection of thermal radiation from the surface of nearby neutron stars (Section 12.11). AstroSat is a multi-purpose instrument undertaking both imaging and timing studies. eROSITA is currently undertaking an all-sky survey in X-rays that will ultimately be 25 times more sensitive than that undertaken by ROSAT, revealing more SNRs and XDINS,

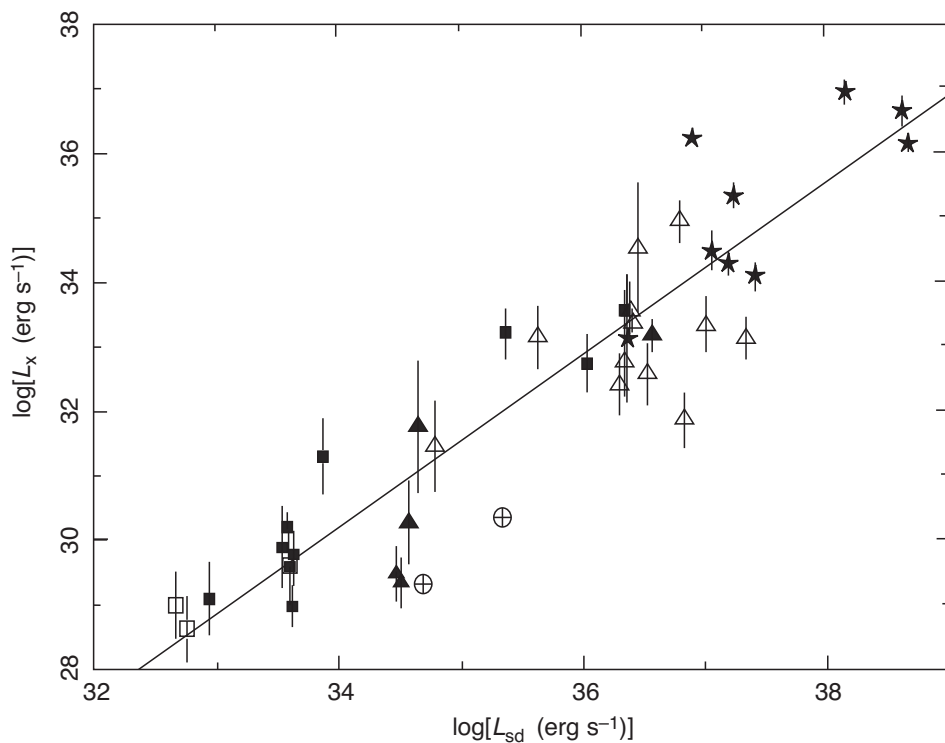


Figure 12.1 X-ray luminosity L_X vs. spin-down luminosity L_{sd} for 39 rotation-powered pulsars (Possenti *et al.* 2002). The five groups of objects are: millisecond pulsars (filled squares), Geminga-like (filled triangles), Vela-like (empty triangles), Crab-like (filled stars), older normal pulsars (empty squares). The line is an empirical fit.

amongst other things. INTEGRAL has been observing profiles of XRBs and their variability at high energies and transient sources since 2002. HXMT is operating in the higher energy band of 20–250 keV and amongst other things is looking at the possibility of using X-ray observations of pulsars for space craft navigation.

12.1 Binary X-ray Light Curves

In contrast to the narrowly-beamed radiation of rotationally powered pulsars, the light curves of the accretion-powered binary x-ray sources are interpreted as thermal radiation from a hot patch either on the surface or on an accretion disk orbiting the star. The x-ray ‘light curve’ seen as the neutron star rotates is, to first approximation, the variation in the visible projected area of the hot spot. There are, however, many complications, as can be seen from the light curves of Figure 12.2. In particular, there are large differences between low- and high-energy x-rays; these differences are not consistent between different classes of x-ray sources, although they can be explained by more complex models of optical depth within the emitting region. In these models, the polar cap may emit either a pencil beam or a fan beam, depending on the energy range (White *et al.* 1983).

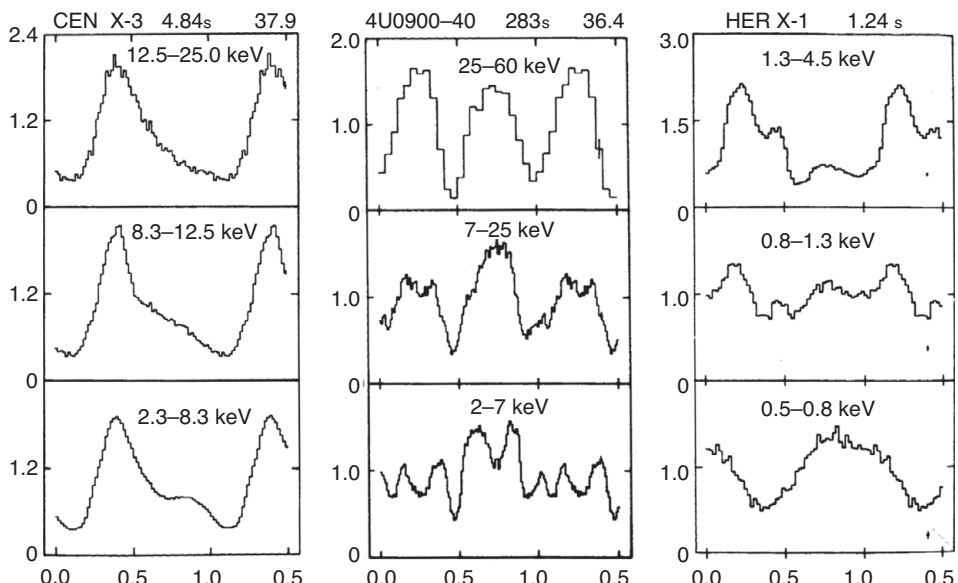


Figure 12.2 X-ray light curves at various wavelengths for Cen X-3, 4U 0900–40 and Her X-1 (from White *et al.* 1983).

12.2 Orbits and Companion Masses

When the companion can be observed optically, it is often possible to combine optical spectroscopy with pulse timing to measure the orbital velocities of both components. As for radio pulsars, the Doppler shifts of pulse period give values for the mass function (Chapter 6). Where the velocity of the companion can also be followed through the orbit by observation of optical absorption lines, the ratio of the observed peak-to-peak velocity ranges V_c of the companion and V_n of the neutron star gives the ratio of the masses m_c , m_n directly:

$$\frac{m_c}{m_n} = \frac{V_n}{V_c}. \quad (12.1)$$

For a circular orbit, the total mass is given by the period P_b , apart from the unknown inclination angle i of the orbit from the plane of the sky, since from Kepler's laws:

$$G(m_c + m_n) = (P_b/2\pi) \left(\frac{V_c + V_n}{\sin i} \right)^3, \quad (12.2)$$

where G is the gravitational constant.

Only the inclination i now needs to be determined; fortunately this is often available when the companion star has an expanded envelope that may eclipse the neutron star. Figure 12.3 shows the effect for Her X-1. In this case the observer's line of sight must lie almost in the plane of the orbit, so that $i \sim 90^\circ$. If the occulting

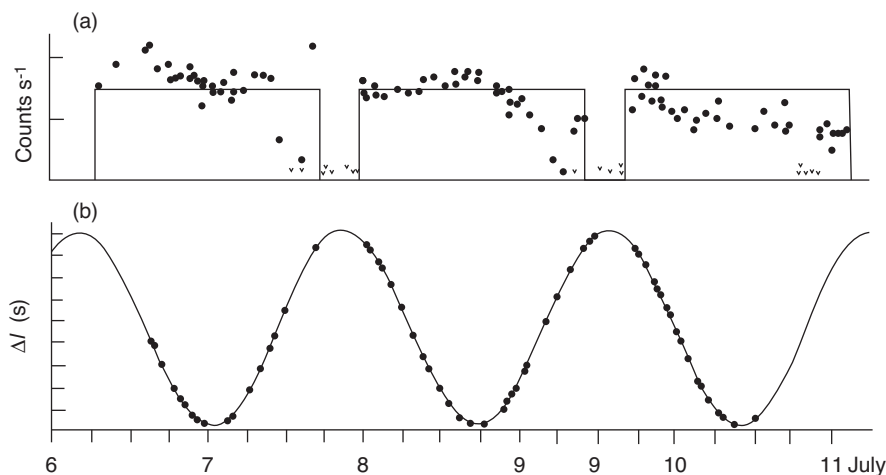


Figure 12.3 The x-ray source Her X-1. (a) The cycle of x-ray intensity (the x-ray 'light-curve'), showing the periodic occultation; (b) sinusoidal variation of pulse arrival time (Giacconi 1974).

star fills its critical potential lobe (the ‘Roche lobe’), the size of this occulting envelope is known, and the length of the eclipse then gives a more accurate value for the inclination i . Generally, the existence of an eclipse allows a statement that $i > 45^\circ$ approximately, so that errors in the precise geometry are not serious. An example is 4U 0900–40, with period 8.96 days, inclination $i = 76^\circ \pm 10^\circ$, in which $m_n = 1.9 \pm 0.3 M_\odot$ and $m_c = 24.0 \pm 2.5 M_\odot$ (Joss & Rappaport 1984). Here the companion is evidently a massive young star. All binary systems yield similar masses for the neutron star (Chapter 14), while the companion masses fall mainly into two classes: the HMXBs as in the above example and the LMXBs with companion masses in the range $0.2\text{--}0.4 M_\odot$. The LMXBs are more difficult to analyse, since they show little or no pulsation, are fainter optically and show less detail spectroscopically; they are, however, the parents of the majority of the millisecond pulsars and deserve our close attention.

Examples of both categories are listed in Table 12.1. A more comprehensive list of neutron star x-ray sources is given by Seward and Charles (1995). X-ray observations have proliferated in recent years; catalogues of HMXBs by

Table 12.1. *Some typical binary X-ray systems*

		Companion type	P_0 sec	P_b day
Massive Systems $m_c \geq 20 M_\odot$				
4U0532–66	LMC X-4	O7	14	1.4
4U1119–60	Cen X-3	O6.5	4.8	2.1
4U0115–73	SMC X-1	B0	0.7	3.9
4U0900–40	Vela X-1	B0.5	283	9.0
4U0538+26	V725 Tau	O9.7	104	111
Low-mass Systems $m_c \leq M_\odot$				
4U1626–67	KZ TrA		7.7	0.029
4U1755–33	V4134 Sgr			0.186
A0620–00 (transient)	V616 Mon(BH)			0.323
4U1456–32 (transient)	Cen X-4			0.629
4U2142+38	Cyg X-2			9.843
Peculiar Systems				
4U1656+35	HerX-1	A9	1.2	1.7
4U1956+35	Cyg X-1(BH)	WR		0.2
4U1516–56 (transient)	Cir X-1			16.6
4U1909+05	SS 433			13.2

Liu *et al.* (2005, 2006) contain 114 entries for the Galaxy and 112 for the Magellanic Clouds, with some thousands of references. Many x-ray sources observed in extragalactic nebulae, for example M81 (Swartz *et al.* 2003), are believed to be HMXBs.

12.3 The High-Mass X-ray Binaries (HMXBs)

Massive main sequence stars in a binary system are expected to evolve as suggested in Chapter 10, with the more massive star evolving more rapidly and expanding to overflow onto the less massive star, losing a large part of its original mass. When it eventually undergoes a supernova explosion, it then has less mass than its companion; as a consequence the binary is unlikely to be disrupted, and the result is a neutron star with a high-mass companion. The second star now evolves and transfers mass onto the neutron star, which is then observed as a high mass x-ray binary (HMXB). The companion typically is an evolved star with mass $\geq 18 - 20M_{\odot}$, near the end of hydrogen burning.

The orbital periods P_b of the HMXBs range from 0.2 to 187 days, and the rotation periods P_0 of the neutron star from 69 ms to 835 seconds. The rotational periods are much less stable than those of the radio pulsars and usually show a spin-up rather than a spin-down. Figure 12.4 shows the history of the rotation period for four x-ray pulsars. The rate of spin-up is found to be related to the x-ray luminosity, since both depend on the rate of accretion onto the neutron star. The spin-up timescale varies from 100 to 100,000 years.

Although an HMXB is a normal stage in the evolution of high-mass binaries, the short lifetimes of massive stars make it a comparatively short-lived phenomenon. Thus high-mass stars represent a small proportion of the total stellar population, and HMXBs are rare; van den Heuvel (1992) estimates a total population of 40,000 in the Galaxy.

The massive companions in these systems are supergiant stars or Be stars. In both, the neutron star is immersed in a wind flowing out from the star; especially in the supergiant systems, the x-ray emission is randomly variable, presumably as the neutron star ploughs through irregularities in the wind. The supergiant systems have large companion masses and short orbital periods $P_b = 1.4 - 10$ days. The companion is an evolved star, near the end of hydrogen burning, and is filling its Roche lobe. The Be systems have more elliptical orbits and longer orbital periods $P_b = 15$ days to several years; the rotation period P_0 is usually greater for large values of P_b . The companion is a main sequence star that is not filling its Roche lobe: the wind from Be stars is known to be very erratic, and several of these sources are transient with long quiescent periods.

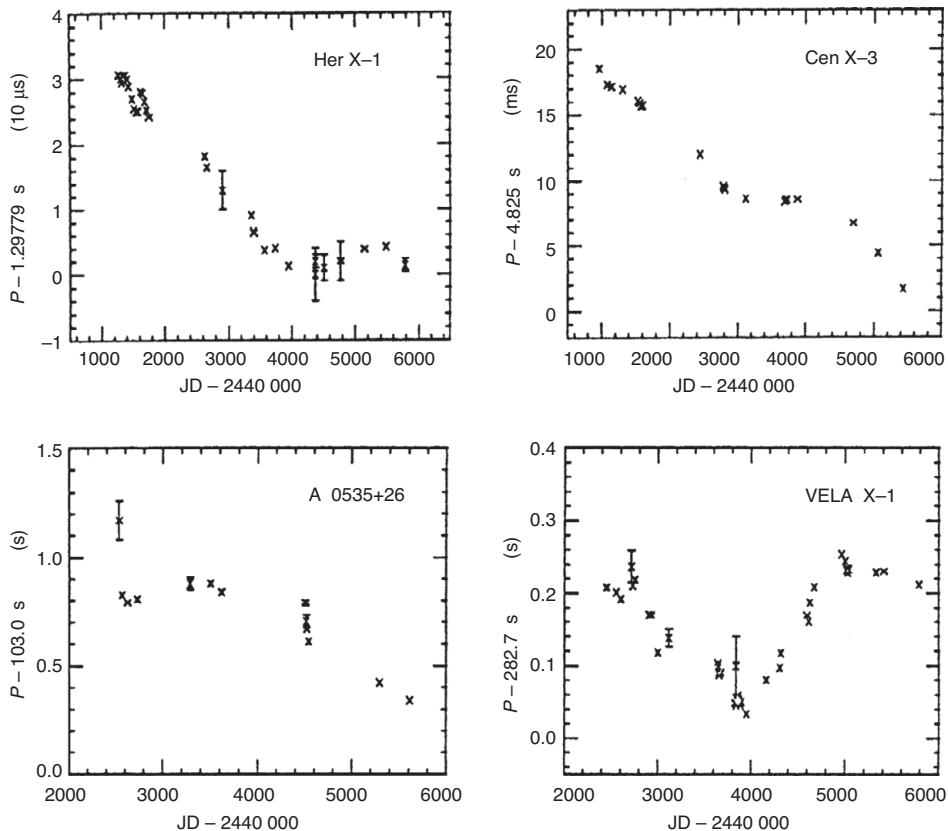


Figure 12.4 The spin history of four x-ray pulsars (White, Nagase & Parmar 1995).

12.4 The Low-Mass X-ray Binaries (LMXBs)

The low-mass companions of the second main group of x-ray binaries (the LMXBs) are more difficult to study, because little if any light can be observed directly from the star, and there may be no spectral lines from which to measure Doppler shifts. The main source of light is often not the star itself but the gas in an accretion disk. Orbital periods (P_b) have been obtained for some from variations in optical brightness, but for most the only information on P_b is derived from variations in x-ray intensity. The orbital periods are mostly less than one day.

The orbital parameters cannot be obtained in the same detail as for the massive systems, but some progress can be made by assuming that the companion star fills its Roche lobe and adopting a model relating the size of that lobe to the diameter of the orbit. Unfortunately, the model depends on the relation between the mass of the companion and its radius, and this relation depends on the type of the companion, which is usually unknown. Nevertheless, if the companion is assumed to be on the

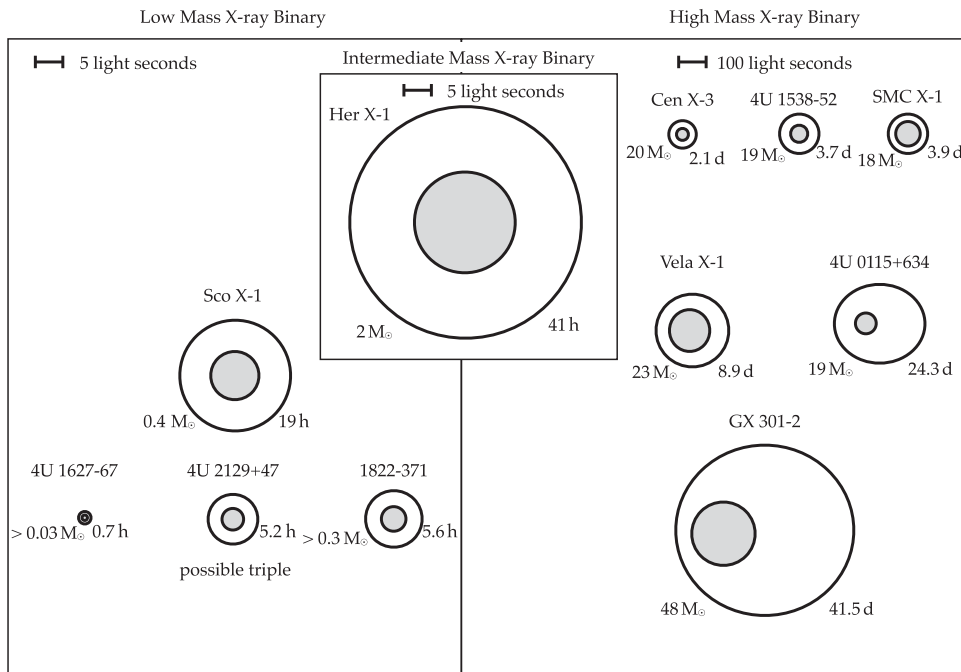


Figure 12.5 The geometry of binary x-ray systems, showing the relative diameters and separations of low-mass and high-mass systems. The masses of the companions and the orbital periods are indicated (after Bradt & McClintock 1983).

main sequence, the model gives its mass; assuming further that the mass of the neutron star is $\sim 1.4 M_{\odot}$ as in most massive binaries, we can obtain reasonable values for all the orbital parameters. Some typical values have been used in Figure 12.5 to illustrate the geometry of high- and low-mass systems.

We should not assume that all companions of the low-mass binaries are of the same type. There are several K-type main sequence stars clearly identified among them, including the companion of Cen X-4, whose companion apparently has a mass of only $0.1 M_{\odot}$. This identification is certain because there are large and related variations in the optical and x-ray emissions from this system.

The low-mass binaries are often referred to as Galactic bulge or late-type x-ray binaries, since their distribution over the sky shows a concentration towards the centre of the Galaxy, following the distribution of the old stars of Population II. It seems likely that the x-ray sources in Galactic clusters are of the same type. Although many of the Galactic bulge x-ray sources show neither the precisely periodic pulsations that directly indicate the presence of a neutron star, nor the clear spectrum of a late-type star as companion, there is good reason for believing that all these Galactic bulge sources are actually low-mass binary systems.

Identification of many more of the low-mass binaries will be difficult. Many are found at low Galactic latitude ($|b| < 2^\circ$), where optical absorption is very heavy. Their spectral characteristics are varied, although most have a large ultra-violet excess, by up to one magnitude over normal main sequence stars. Their spectra include emission lines from He II (468.6 nm) and N III (464.0 nm), both generated by the x-rays from the neutron star. These line emissions, and the continuum, are notably variable from day to day.

A catalogue by Liu *et al.* (2007) lists 187 LMXBs in the Galaxy and the Magellanic Clouds. Their slowdown rates indicate magnetic fields of order 10^{7-9} G. The evolution of the LMXBs is slow: their characteristic ages are of order 10^9 years. The population of LMXBs in the Galaxy is nevertheless lower than that of the short-lived HMXBs (van den Heuvel 1992).

12.5 Peculiar Systems, Black Holes and Transients

A simple classification into low- and high-mass systems should not be allowed to obscure the rich variety of binary x-ray sources. Table 12.1 therefore includes a note (BH) beside two examples where the compact object is too massive to be a neutron star and is therefore believed to be a black hole. Many systems are transients, including especially those with Be companions. Finally, Table 12.1 includes Peculiar systems, which fit into neither main category. Her X-1, for example, has a companion, HZ Her, with intermediate mass $2.35M_\odot$; unusually for an A9 star, it is located 3 kpc above the Galactic plane and is believed to have been ejected from the plane. The remaining three objects in the table are strong and variable synchrotron radio emitters; SS433 is characterised by twin jets ejected in opposite directions from the compact object with velocity $\sim 0.26c$.

12.6 Spin-Up, Accretion and Inertia

The rapid decrease of rotational periods in most of the pulsating x-ray sources shows that the torque responsible for this spin-up must be more than three orders of magnitude greater than the magnetic torque on the pulsars, and in the opposite sense. This torque is provided by the accretion of material from the companion star. In the HMXBs this occurs as the neutron star ploughs through a powerful outward stellar wind, but for the K stars of the LMXBs, there is a much smaller outflow, which is the overflow from an extended atmosphere filling the star's Roche lobe; here the whole of the outflow is concentrated on the neutron star via an accretion disk. The angular momentum transferred to the neutron star is derived from the orbital momentum of the binary system. This is the process that is the source of the population of rapidly rotating millisecond pulsars.

The maximum rate of accretion and the x-ray luminosity are linked by a simple relation due to Eddington. The accreting plasma consists of electrons and protons held together electrostatically. The outward flux of radiation from the hot gas exerts a pressure mainly on the electrons, and the opposing force of gravity acts mainly on the protons. The plasma can only accrete if the radiation pressure is less than the gravitational force, that is, is less than the *Eddington Limit* L_E given by

$$L_E = \frac{4\pi GMm_p c}{\sigma_T}, \quad (12.3)$$

where M is the stellar mass, m_p is the mass of the proton and σ_T is the Thomson cross-section of the electron. In numerical terms,

$$L_E = 1.3 \times 10^{38} \frac{M}{M_\odot} \text{erg s}^{-1}. \quad (12.4)$$

We therefore expect the total x-ray luminosity for an accreting neutron star to reach but not exceed about 2×10^{38} erg s $^{-1}$. This agrees well with observation; some exceptionally high luminosities may be either transient or associated with anisotropies in the stellar atmosphere.

The energy supply from the infalling material is related to the flow rate and the gravitational potential at the surface. A greater rate of accretion cannot give a greater luminosity, as the radiation would halt the accretion. As pointed out by Lynden-Bell in 1969, the gravitational energy given up by a particle falling onto the surface of a neutron star is up to 10% of its rest mass and is several orders of magnitude greater than might be available in nuclear fusion.

The accreting material is ionised. As it falls towards the neutron star, it encounters an important boundary, the magnetospheric boundary or Alfvén surface, outside which the magnetic field of the neutron star is not felt and within which the plasma can only flow along the magnetic field lines. From the point of view of spin-up torque, the flow becomes attached to the pulsar at the Alfvén surface. Outside the Alfvén surface, the material is in Keplerian orbit round the neutron star, so that the accelerating torque on the star depends only on the rate of mass transfer and the radius of the Alfvén surface. The observed speed-up rates agree well with this theory, using the standard value of moment of inertia and a surface dipolar field of at least 3×10^{12} G.

The rotational speed-up of the neutron star continues until it reaches the Keplerian angular velocity at the Alfvén surface, whose height depends on the strength of the magnetic field and the accretion rate \dot{M} . This sets a lower limit P_{\lim} to the rotation period, which becomes the lower limit for the millisecond pulsars. It is given by

$$P_{\text{lim}} = 1.9(B_9)^{6/7} \frac{\dot{M}}{M_E} \text{ milliseconds}, \quad (12.5)$$

where B_9 is the magnetic field in units of 10^9 G, and \dot{M}_E is the accretion rate at the Eddington limit.

The irregular nature of the spin-up seen in Figure 12.4 must correspond to irregularities in the rate of mass transfer. There are also large fluctuations in the x-ray output, which may also be due to the same irregularities, although this is difficult to establish. An actual reversal of torque, causing a spin-down episode such as that of 10 September 1972 in Cen X–3, requires a drastic change in the flow pattern and probably a temporary ejection of matter from the neutron star.

12.7 Magnetic Field Strength

There is a very interesting observation in several HMXBs of an x-ray spectral line that appears to be a cyclotron resonance absorption in the emitting region. The first example was found at 35 keV in Her X–1 by Trümper *et al.* (1978); several others were found by Mazets *et al.* (1981), while in GB880205, Murakami *et al.* (1988) found a line and its second harmonic at 20 keV and 40 keV.

The photon energy of an electron cyclotron resonance is $E_c \sim 11.6 B_{12}$ keV, where B_{12} is the magnetic field in units of 10^{12} G. The observed line is gravitationally redshifted by a factor $(1+z)^{-1}$, where $z \sim 0.3$ at the surface of a neutron star. The observed absorption lines therefore indicate values for the magnetic field in or above the emitting region in the range $(1-3) \times 10^{12}$ G.

There is, however, a possibility that the lines are in some cases due to a proton rather than an electron cyclotron resonance. The proton cyclotron resonance is at $0.0063 B_{12}$ keV. Three harmonically related lines were found by Bignami *et al.* (2003) at 0.7, 1.4 and 2.1 keV in 1E1207–52A. Here it is unclear whether this indicates an electron or a proton cyclotron resonance; for electrons this would mean a remarkably low field of $\sim 0.8 \times 10^{11}$ G, or for protons a remarkably high field of $\sim 1.6 \times 10^{14}$ G.

The magnetic fields of AXPs and other magnetars, as measured by their periods and slowdown rates, apparently are of order 10^{14} G. This is above a quantum level at which the separation of Landau levels for an electron exceeds the electron rest mass. This quantum critical field is

$$B_c = \frac{2\pi m_e^2 c^3}{e h} = 4.4 \times 10^{13} \text{ G}. \quad (12.6)$$

Such high fields could in principle be generated by a dynamo mechanism in the first few seconds after the birth of a neutron star (Duncan & Thompson 1992), and there is no reason to regard the quantum level B_c as a fundamental limit.

12.8 The X-ray Bursters

The category of x-ray objects known as the Galactic bulge sources are characterised by high intensity (total radiation $\sim 10^{34}$ erg sec $^{-1}$), soft spectra ($T \sim 3 \times 10^7$ K as compared with $T \sim 10^8$ K for the massive binaries), no pulsations and no eclipses. A subset of the Galactic bulge sources also show x-ray bursts, usually lasting some tens of seconds and recurring at intervals of some hours or days. These are the x-ray bursters. Their distribution in the sky is shown in Figure 12.6, together with the known binary sources.

With some exceptions, the x-ray bursts are believed to be flashes of energy liberated in thermonuclear explosions in material accreted onto the surface of neutron stars. Although every astrophysicist readily accepts the concept of a controlled release of nuclear energy in the interior of normally evolving stars, it is a novel and startling concept to interpret the bursts as a sequence of catastrophic nuclear explosions on the stellar surface. The evidence, both observational and theoretical, is nevertheless very strong.

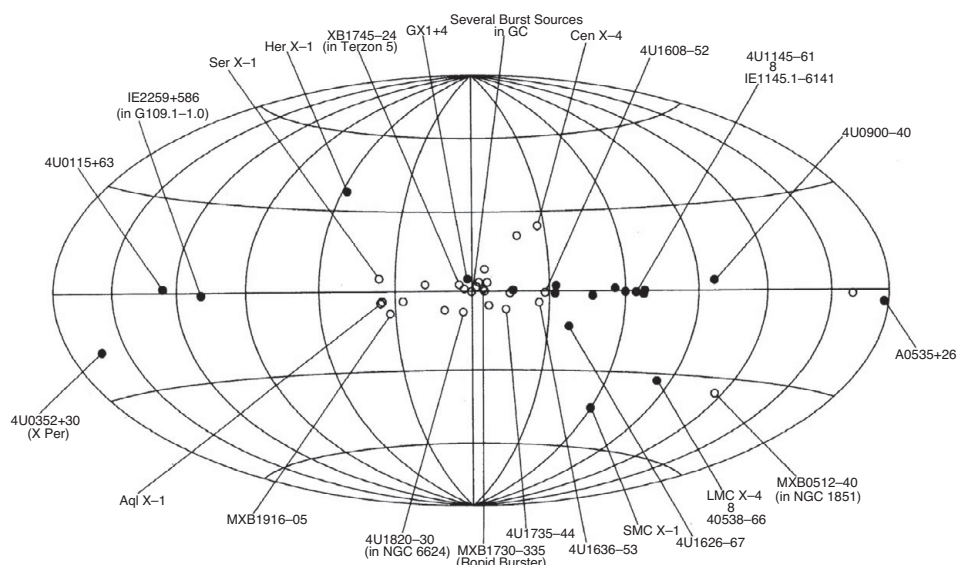


Figure 12.6 Sky map of some well known binary x-ray pulsars (filled circles) and burst sources (open circles) (After Joss & Rappaport 1984).

The observed x-rays from a burst have a spectrum that fits well to a thermal source. The temperature of this source, however, falls during the burst, as seen by the progressive softening of the spectrum: typically 20-keV x-rays last for 20 seconds. The total energy, together with the temperature obtained from the spectrum, gives a measure of the area of the source, which is found to have a radius of about 7 km, corresponding to most or possibly all of the area of a neutron star. The temperature of this whole area is raised within a few seconds to about 3×10^7 K, cooling with a time constant of order 10 seconds. Some hours or days later, the process is repeated.

The theory follows naturally from the known structure of neutron stars. The surface, shown in detail in Figure 12.7, starts with a layer of order one metre thick, consisting of condensed hydrogen formed from the accreting plasma. As more hydrogen accretes on the surface, so must the hydrogen at the bottom of the layer fuse to form successively helium, carbon and iron, releasing energy as it progresses. There will therefore be a hydrogen burning region, followed by a helium layer also perhaps one metre thick, followed again by a helium burning layer. These thin burning layers, or shells, may be unstable if hydrogen is fed to the surface at a sufficient rate. The instability depends on the temperature coefficient of the fusion reaction.

The hydrogen burning shell appears not to be the source of the instability, since hydrogen burning involves several intermediate stages of beta-decay from nuclei such as ^{13}N and ^{14}O , which have time constants of 100 seconds or more. No such restraint exists in helium burning, and it is the helium burning layer one or two metres below the surface that is the origin of the explosions.

The overall statistics of the energy release are simple. About 10^{21} grams of hydrogen accrete for each flash, corresponding to a million tonnes per square metre accreting over a time of about 10^4 seconds. The flash releases up to 10^{39} ergs, which raises the temperature of the surface to 3×10^7 K in about 0.1 second. Radiation then cools the surface to below 10^7 K in about 10 seconds. Averaged over the cycle, the mean

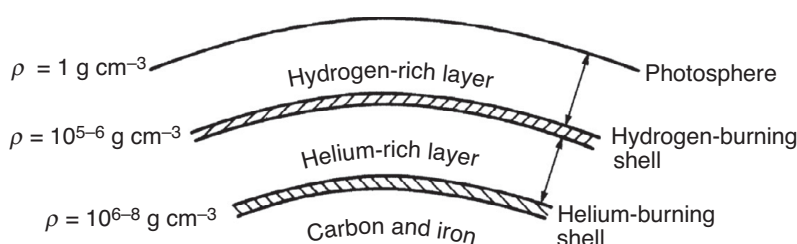


Figure 12.7 The surface structure of an accreting neutron star (after Lewin & Joss 1981).

power is 50 times that of the Sun: concentrated into a fraction of a second and into a small area, the event is seen as a thermonuclear explosion of truly awesome proportions.

12.9 The Rapid Burster

X-ray bursters were discovered independently by Grindlay *et al.* (1976) using the Netherlands Astronomical Satellite and by Belian, Conner and Evans (1976) using records made several years previously by the Vela 5B satellite, which had been launched to monitor man-made nuclear explosions rather than the unexpected celestial bursts. A new type of bursting behaviour was discovered soon afterwards (Lewin *et al.* 1976), with the extraordinary property of a rapid succession on various time scales of the order of seconds to minutes from an x-ray source known as the Rapid Burster.

These rapid bursts represent an instability in the accretion rate rather than thermonuclear flashes. Both types of burst can be seen from the Rapid Burster. The rapid bursts, known as Type II, also represent very large releases of energy, but the source is gravitational rather than nuclear. About one tenth of the energy released per proton in the thermonuclear explosion of the slower Type I bursts is gravitational energy released in falling on to the surface.

Another transient x-ray source, GRO J1744–28, has a hard spectrum like that of the Rapid Burster, but uniquely among the bursters it shows a persistent modulation that appears to be due to the rotation of a neutron star (Finger *et al.* 1996). The period of 467 ms is decreasing, indicating spin-up by accretion, and a periodic Doppler shift shows a binary orbital period of 11.8 days. This x-ray source provided valuable confirmation of the neutron binary nature of the hard x-ray sources. Other examples of periodic modulation of the burst signal are given by van der Klis (2000).

12.10 Quasi-periodic (QPO) and Kilohertz Oscillations

The idea that mass transfer in binary systems, such as the LMXBs, would speed up the rotation of a neutron star component received powerful support from the discovery of PSR B1953+29, which is a binary radio pulsar with a rotation period of 6 ms (Boriakoff *et al.* 1983). The possibility that some of the LMXBs might contain such a rapidly rotating neutron star led to renewed efforts to detect short-period fluctuations in the flux of known x-ray sources. A periodicity relating to the rotation of the neutron star was eventually discovered by high timing resolution observations with the Rossi X-ray Timing Explorer, but the first attempts found instead a totally different quasi-periodic fluctuation in several of the LMXBs.

This discovery is described in a review by Lewin and van Paradijs (1986). The quasi-periodic oscillations were found in intense x-ray sources including Sco X-1, Cyg X-2 and the Rapid Burster. The periodicity is variable; for Sco X-1 it varies between 6 Hz and 30 Hz, and in all sources this variation is strongly correlated with x-ray intensity. The periodicity is not precise; it is best described as a broad peak in a noise spectrum. The accepted explanation of the quasi-periodic oscillations is that the period is determined by the Keplerian orbit period at the inner edge of the accretion disk. The diameter of the disk depends on the rate of accretion, which also affects the x-ray luminosity. High luminosity corresponds with a smaller diameter and hence a shorter orbital period. Modulation of the x-ray luminosity must occur in the interaction of the rotation of the neutron star itself and the orbiting accretion disk, so that the observed frequency may be a beat between the periods of these two.

Higher frequency oscillations, as revealed by observations with RXTE, are known as millisecond or kilohertz oscillations. In a comprehensive review of such short period oscillations in x-ray binaries, van der Klis (2000) distinguishes three categories:

1. QPO's similar to those with longer periods, described above: these are due to orbital motion, but in an inner accretion disk where the Keplerian rotation is at higher frequencies.
2. Bursts of periodic signal at a frequency slightly below the neutron star rotation frequency: these are from an atmosphere in near co-rotation with the star.
3. Modulation within an x-ray burst at the true rotation frequency of the neutron star: this is due to thermal radiation from the surface, with surface temperature differences round the star.

The last of these have become known as the millisecond X-ray binaries (msXRBs); the periods range from 1.6 to 3.7 ms. The identity of the burst modulation period with the rotation period was established by Chakrabarty *et al.* (2003). An outstanding example is the binary J1751–305, with $P = 2.3$ ms and the very short orbital period $P_b = 24$ min (Markwardt *et al.* 2002); the binary companion is a very low mass helium dwarf.

12.11 Thermal X-rays from Isolated Neutron Stars

Apart from the high-energy radiation from some young pulsars such as the Crab and Vela and the magnetars, which originates in the outer magnetosphere, x-ray emission from isolated rotation-powered pulsars originates in heated patches of the surface within the polar caps. These patches are heated by a back-flow of electrons or positrons from pairs created by high-energy gamma rays in the magnetosphere.

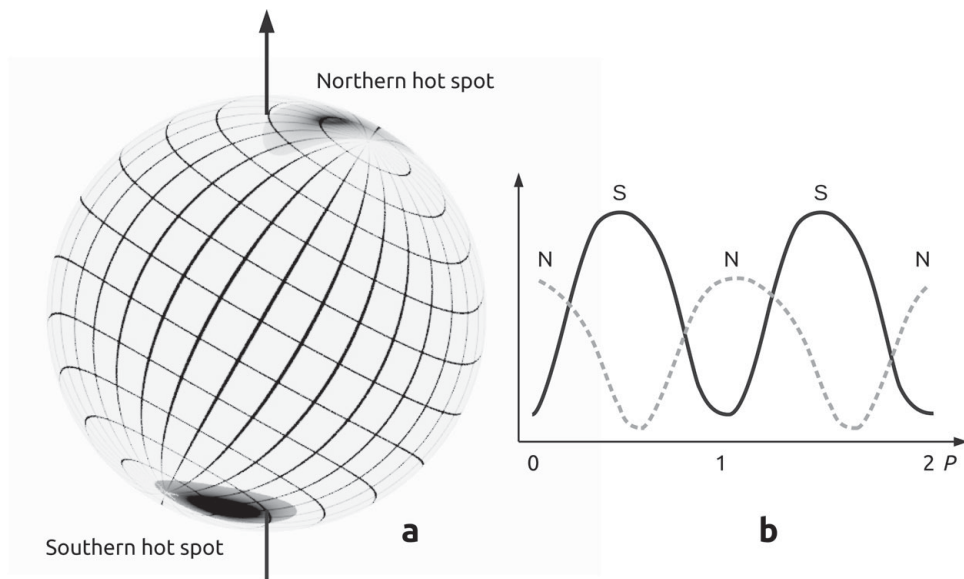


Figure 12.8 Thermal radiation from polarcap hotspots (a). Self-lensing allows both poles to be seen simultaneously resulting in the lightcurve components shown in (b). Credit: Anna Bilous and Thomas Riley, University of Amsterdam.

The spectrum is thermal, indicating a temperature of order 10^6 K, conveniently matching the spectral sensitivity of most x-ray telescopes (centered on 1 keV). As the star rotates, the hot patches sweep across the visible hemisphere, modulating the observed emission at the rotation rate. The two polar caps are seen 180° apart, at different angles with correspondingly different intensities. Sophisticated models of the pulse shapes expected have now been developed and used to show that the emission deviates significantly from being antipodal for PSR J0030+0451 (Bilous *et al.* 2019). A simplified version of such a model and associated light curve is shown in Figure 12.8. The analysis of such pulse shapes can reveal the angle between the rotation and magnetic axes, and the line of sight.

The observed x-ray light curves confirm the general concept, but with substantial differences due to;

1. Self-lensing. Pechenick, Ftaclas and Cohen (1983) pointed out that general relativity (GR) requires ray paths to be curved in the vicinity of the massive star (Figure 12.9), so that more than 75% of the surface is visible at any time. The effect is to smooth out the modulation.
2. General Relativity also requires the spectrum to be redshifted, reducing the apparent temperature.
3. Doppler and time delays near the limb of the disk may introduce skewness in the pulse profile.

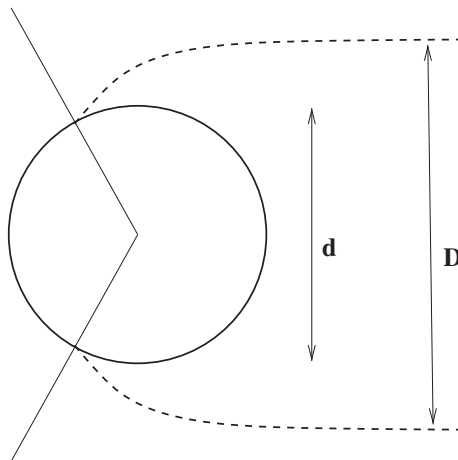


Figure 12.9 Self-lensing. Rays may be observed which originate from behind the neutron star, giving an increased apparent diameter D .

4. The temperature is expected to vary over the hot patch, which may not fill the polar cap.
5. The magnetic field may not be a simple dipole, modifying the shape of the polar cap.

The basic geometric and GR effects were set out by Bogdanov, Rybicki and Grindley (2007). The construction of a profile modelling the observed profile of the well-observed pulsar J0437–4715 and incorporating all these effects is described by Lockhart *et al.* (2019).

12.12 Ultra-luminous X-ray Sources

It has been proposed that ultra-luminous x-ray sources (ULXs), located outside galactic nuclei and with x-ray emission exceeding that possible through accretion at the Eddington rate onto a stellar-mass black hole, are due to accretion onto supermassive or intermediate mass black holes. However, the discovery of x-ray pulsations with a period of 1.37 seconds in a ULX near the centre of the galaxy M82, and with a binary period of 2.5 days (Bachetti *et al.* 2014), was followed by a handful of others with periods between 0.4 and 30 seconds, showing that they are actually neutron stars. These sources appear to be accreting at super-Eddington rates, but this can be interpreted instead as a result of beaming, which would require very high magnetic field strengths. It remains to be seen whether all ULXs are neutron stars, but at least some of these sources are, showing the wide range of manifestations of neutron stars and how they emit.

Part III

Neutron Star Physics

13

Neutron Stars

Broadly speaking, when a normal star has exhausted its sources of energy, it collapses under its own gravity. A star with the density of normal matter then ends up in one of three possible states: white dwarf, neutron star or black hole. The extent of the collapse depends on the mass of the progenitor star; the most massive become black holes, and the least massive become white dwarfs. The progenitors of neutron stars have a limited intermediate range of mass, about $8\text{--}20M_{\odot}$. The large number of supernovae now discovered in the search for standard candles for cosmology, amongst other reasons, has resulted in a number of cases where the progenitor star can be identified in archival observations. The masses of these progenitor stars are consistent with the expected range for the formation of neutron stars.

It follows from the statistical distribution of stellar masses that more than 95% of stars end their lives as white dwarfs without further collapse. The formation of a white dwarf is a smooth and continuous process; as nuclear fuel becomes exhausted, a core grows within an expanding outer shell, the total gravitational collapse of the core being prevented by the pressure of electron degeneracy. If and when the mass of the core exceeds $1.4M_{\odot}$ (see discussion below), this pressure is insufficient to resist the increasing force of self-gravity and to prevent the further collapse of such a degenerate core to a neutron star. The collapse to a neutron star is catastrophic; within a few seconds, a large proportion of the gravitational potential energy of the star is released, and the event is observed as a supernova. Most of the original mass of the star lies outside the collapsing core and is expelled and lost in the process, but the remainder of the star still has a mass of order one M_{\odot} .

The steps in density between normal stars and white dwarfs, and between white dwarfs and neutron stars, are both greater than a million. The neutron star, however, is not far from a black hole: for a mass of $1.4M_{\odot}$, the ratio of diameters is less than a factor of 3. The density of a stellar mass black hole, calculated from its total mass and nominal diameter (event horizon), is only 10 times greater than that of

a neutron star. Supermassive black holes with masses $\sim 10^8 M_\odot$, as found in the centres of galaxies, have a density comparable to that of water.

The majority of massive stars are in binary or multiple star systems. The supernova explosion of a member of a binary pair will most frequently disrupt the system; those binaries that survive evolve to form a wide array of systems in which a neutron star is paired with a compact object or a non-degenerate star (see Chapter 6). Another way in which a neutron star can be formed is when a white dwarf in a binary system with a normal star accretes matter from the companion, and this extra mass pushes the white dwarf above a limiting stable mass (see Chandrasekhar limit below), leading to its collapse to a neutron star. Recently it has been recognised that at the low end of the progenitor mass range for neutron star formation, $8\text{--}10 M_\odot$, the star is unable to ignite Ne, and the $1.34 M_\odot$ core of the star undergoes an electron capture supernova in which the explosion is much weaker. The Crab Pulsar and associated remnant are thought to be the results of such a supernova.

13.1 White Dwarf Stars

Although white dwarf stars are common, they are hard to observe because they are small – typically only the size of planet Earth – although with a mass of a normal star such as the Sun (see Fantin *et al.* (2017) for a recent survey). Since they have no intrinsic source of energy, they all must cool down with age. They radiate a thermal spectrum, approximately black-body at the surface temperature but with absorption lines due to a thin envelope of cooler gas. The surface temperature may still be 10,000 K or more – hence the name white dwarf. Colder stars are fainter, although the spectrum is not as red as might be expected, due to selective absorption of longer wavelengths in the envelope. The envelope, which contains less than 1% of the mass, is non-degenerate, composed predominately of hydrogen and helium. The spectral classification of white dwarf stars depends on the absorption lines due to this envelope. The commonest type, DA, shows the Balmer series of a hydrogen atmosphere; these are among the hottest white dwarf stars.

The composition of the main body depends on the mass of the progenitor star. The majority are composed of carbon and oxygen; lower-mass progenitors lead to helium white dwarfs, while in those from higher-mass progenitors, the carbon is fused into neon and magnesium.

The structure of a white dwarf was famously analysed by Chandrasekhar (1931). The star consists of tightly packed atomic nuclei with a sea of degenerate electrons, whose quantum mechanical pressure supports the star against gravitational collapse. The mass cannot exceed the so-called Chandrasekhar limit of $1.46 M_\odot$, above which

the star will collapse to a neutron star. The observed mass distribution, consisting mainly of DA stars, is largely confined to between 0.4 and $1.0M_{\odot}$, with a sharp peak at $0.6M_{\odot}$. Evidence from pulsar binaries (see Chapter 6) suggests that the mass distribution may extend down to below $0.1M_{\odot}$.

The population of white dwarf stars is of great interest in understanding the structure and evolution of the Galaxy. The lack of any internal source of energy results in the surface temperature of a white dwarf falling monotonically with time, so that colour gives a good indication of age (see a discussion by Fontaine *et al.* 2001); the time constant is around 10 Gyr, comparable to the age of the Universe. The distribution of white dwarfs in luminosity in a region of the Galaxy, such as the disk, or the halo, or within a globular cluster, therefore indicates the age of that region. The population in globular clusters, where pulsar–white dwarf pairs are found, is of particular interest in pulsar astronomy; these white dwarfs are, however, only detectable in observations reaching very faint magnitudes, both by the Hubble Space Telescope (Zoccali *et al.* 2001) and by large ground-based telescopes (Moehler & Bono 2008). They are distinguishable from normal stars by their location in a colour–magnitude (Hertzsprung–Russell) diagram.

A small proportion of white dwarfs are highly magnetic, as evidenced by Zeeman splitting of spectral lines in the envelope. Field strengths from 1 to 700 MG have been observed (see a review by Putney 1999). Kemp (1970) pointed out that conservation of magnetic flux in the collapse of a normal star could account for such high field strength, as indeed might be the case for neutron stars. One magnetic white dwarf (AR Sco) has been observed to behave as a pulsar (Marsh *et al.* 2016).

Reviews by Koester (2002) and by Bergeron *et al.* (2019) provide further details and references to fill out our brief discussion of white dwarf stars.

13.2 Neutron Stars: The Equation of State

A suggestion by Landau in 1932 led Baade and Zwicky in 1934 to the first proposal that a neutron star might be the end product of the supernova collapse of a normal star. Oppenheimer and Volkoff in 1939 analysed the structure of a star consisting of a degenerate neutron gas, showing that the degeneracy was so complete that temperature has no effect and the only important relationship is between pressure and density, independent of temperature, and is well known as the equation of state (EoS). The relation between mass and radius is found by integration through the star, the large gravitational fields requiring an equation taking account of general relativity (the Tolman–Oppenheimer–Volkoff equation).

Since then the problem has been to improve the EoS,¹ in a regime where laboratory measurements of particle interactions are inadequate and in addition the necessary theories of multibody interactions are still incomplete. Given the EoS, a unique relation between mass and radius can be deduced; it is theoretically possible to work back from observed parameters and constrain the EoS itself.

The neutron star is like a gigantic nucleus, with density similar to that of nuclear matter. For a commonly assumed model, a neutron star with radius 10 km and mass $1.4M_{\odot}$ would have a mean density of $6.7 \times 10^{14} \text{ g cm}^{-3}$, higher than the density of nuclear matter $\rho_0 = 2.7 \times 10^{14} \text{ g cm}^{-3}$. The corresponding mean number density of neutrons² is 0.4 fm^{-3} , compared with the nuclear number density of neutrons and protons $n_0 = 0.16 \text{ fm}^{-3}$ in normal nuclei. The main bulk of the star is a neutron fluid, in equilibrium with about 5% protons and electrons; the proportion is determined by a balance between the rates of neutron decay and proton/electron association. The combination may be termed a hadron fluid. In the centre of the star, where the densities are highest, the hadron fluid may include a hyperon or quark component. It is possible that one ends up with different types of compact star, for example a quark or strange star, depending on the nature of the constituents of the central region. An outer crust, about 1 km thick, is a crystalline solid lattice, made of heavy nuclei: iron near the surface, with increasingly neutron-rich heavy nuclei below.

The EoS of the neutron fluid, which is the main component of the overall mass, is found from free scattering measurements, which must be augmented to incorporate multi-component interactions in a relativistic field theory (e.g. Gandolfi *et al.* 2019). Integration through the star gives relationships between density and radial distance from the centre, and between mass and radius. Leaving aside the effects of the crust and the core, the relation between mass and radius may be represented by Figure 13.1(a). This shows the main features of the many versions in an extensive literature:

1. The radius is almost the same for a range of masses between around 1 and $2M_{\odot}$.
2. Most of the various EoS's give this radius as between 10 and 11 km.
3. The maximum mass is around $2\text{--}2.5M_{\odot}$, above which the star must collapse into a black hole.

A core of quark matter, which may exist at the highest densities, would have a ‘softer’ EoS, that is, it would be more compressible than the neutron fluid, with the effect that the maximum mass before collapse is reduced. Baym *et al.* (2018) show that the transition between the hadronic and quark states is not abrupt, with

¹ The EoS is often specified as a relation between pressure and *energy density* (which includes mass energy).

² 1 femtometre (fm) = 10^{-15} m .

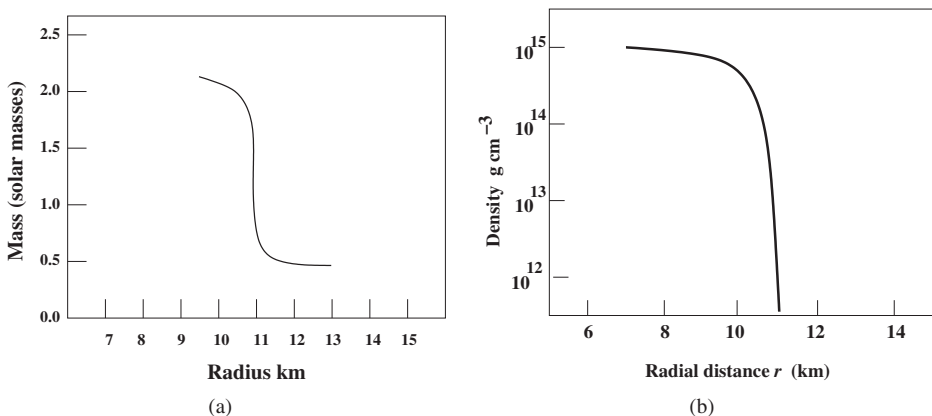


Figure 13.1 Indicative diagrams of the mass and density of a neutron star, using a typical equation of state. (a) The relation between mass and radius (b) The density distribution with radius from the centre. Detailed versions may be found in, for example, Lattimer (2012) and Zdunik *et al.* (2017).

quarks pervading the hadronic fluid from a density of around $5\rho_0$ upwards. Baym and Furusawa (2019) find a maximum possible mass of $2.35M_\odot$.

The physics involved in the EoS is reviewed by Glendenning (2000) and by Baldo and Burgio (2012). More recent references may be found in Özal and Freire (2016), who survey the theories and observations; see also Zdunik *et al.* (2017), who unify the EoS of the core and the crust at their interface, and Baym *et al.* (2018).

In Chapter 14, we compare the theoretical relationships between mass and radius with an increasing number of observations of these quantities, some of them remarkably accurate (See [Özel & Freire 2016](#)).

13.3 The Crust and the Neutron Fluid

Figure 13.2 shows a slice through the interior of a model neutron star. The transition between the liquid interior and the 1 km thick crystalline solid crust is at a density near $\rho_0 = 10^{14}$ g cm⁻³, approaching the density of nuclear matter (see Steiner *et al.* 2015). At the base of the crustal region there is a region, sometimes called the pasta phase, where the nuclei become very deformed.

The density of the crust covers a range of about eight orders of magnitude, from 10^6 to 10^{14} g cm $^{-3}$. The total mass of the crust is only 1% of the total mass of the star. The outer part of the crust is a very rigid and strong crystalline lattice, primarily of iron nuclei. At higher densities it becomes energetically favourable for electrons to penetrate the nuclei and combine with protons to form neutrons, resulting in nuclei with unusually high numbers of neutrons. Compared with the

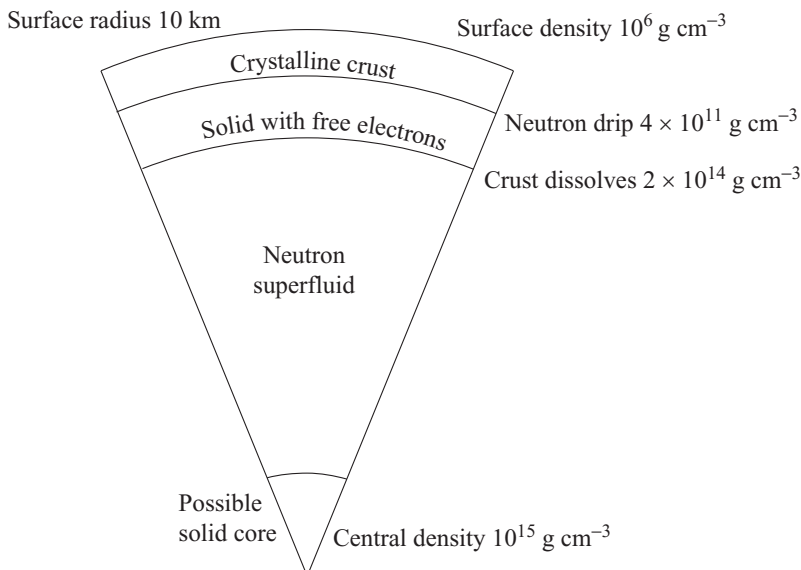


Figure 13.2 Typical cross-section of a neutron star. Exotic matter in the core is currently believed to be quark fluid.

nuclei of normal matter, in which the neutron number N and the atomic number Z are approximately equal, in the heavy nuclei N approaches $2Z$, creating species unknown in the laboratory, such as ^{118}Kr , a remarkable nucleus with 82 neutrons and 36 protons (Baym, Pethick & Sutherland 1971; Pethick & Ravenhall 1995). The basic physics of this crustal region, with density up to the nuclear density $\rho_0 = 6.7 \times 10^{14} \text{ g cm}^{-3}$, was discussed by Pethick and Ravenhall (1991). Up to a density of $4 \times 10^{11} \text{ g cm}^{-3}$, there are almost no neutrons outside the nuclei. Above this density, referred to as the neutron drip point, the most massive nuclei become unstable, and the inner part of the crust is pervaded by a neutron fluid.

The whole of the neutron fluid, including the component in the inner crust, is superfluid, with no viscosity. (The proton component of the hadronic liquid is also superfluid; the electrons, which interact more weakly, are not superfluid and play little part in the structure of a neutron star). As well as the neutron superfluid, one might expect superconducting phases of quark matter. A crustal component of the neutron superfluid interpenetrates the inner part of the solid crust and can move independently. The angular momentum of this crustal superfluid may be decoupled from the rest of the star, and it may rotate at a different rate; this is important in the explanation of irregularities of pulsar timing (Chapter 15). The rotation of a superfluid is in the form of discrete vortices, each carrying a quantum of angular momentum. The density of vortices is proportional to the angular velocity; for a

pulsar with rotation period P seconds, the area density is $10^4 P^{-1} \text{ cm}^{-2}$. The angular velocity of the superfluid can only change if these vortices move; they must move radially outwards if the angular velocity of this component is to reduce along with the slow-down of the rest of the star. Their movement is, however, impeded by interaction with the crystal structure of the crust; if the vortices are pinned to the solid crust, their area density is fixed and hence their angular velocity cannot change. A glitch in observed rotation rate occurs when part or all of the crustal superfluid uncouples catastrophically from the solid crust.

13.4 Moments of Inertia

The distribution of density with radius, as outlined in Figure 13.1(b), allows the moment of inertia I to be calculated. For a sphere with uniform density, the ratio $I/MR^2 = 0.4$; although the density of neutron stars does vary with radial distance, the same ratio is approximately correct; see Lattimer and Prakash (2001) for results using various EoS's and masses. The moment of inertia is of order $3 \times 10^{44} \text{ g cm}^2$; this value³ is conventionally used in calculations of rotational slowdown; see Chapter 5. Steiner *et al.* (2015) find I for a $1.4M_\odot$ star to be between 61 and $73M_\odot \text{ km}^2$, with 2–4% in the crust (the fraction in the crust is larger for lower masses). A direct measurement of I may become possible for one component of the double pulsar PSR J0737–3039, through the relativistic effect of spin–orbit coupling (Chapter 6).

13.5 Rotation Rate: An Upper Limit

The very large rotation speed of the fastest pulsars gives an upper limit for the radius. Consider the balance between centrifugal force and gravity for a mass on the equator of a sphere of mass M and radius R , rotating with angular velocity ω ; this is the same condition as for a satellite orbit grazing the surface:

$$\omega^2 R = \frac{GM}{R^2}. \quad (13.1)$$

For period $P = 2\pi/\omega$, the radius is

$$R = 1.5 \times 10^3 \left(\frac{M}{M_\odot} \right)^{\frac{1}{3}} P^{\frac{2}{3}} \text{ km}. \quad (13.2)$$

This is an upper limit to the radius. The shortest known periods are close to 1.4 ms (see Chapter 4); assuming a mass of $1.35M_\odot$, this gives an upper limit of 21.5 km

³ Coincidentally, this is nearly the same as the moment of inertia of planet Earth.

for the radius. This upper limit may be reduced, since any rapidly rotating star may be unstable to large scale distortions before the centrifugal limit is reached; if these develop, the star will radiate gravitational waves, and the rotation will be slowed down. The modes of instability for a neutron star have been analysed by Haensel, Salgado and Bonazzola (1995) and by Morsink, Stergioulas and Blattnig (1999); see also a wider review of instabilities in relativistic rotating stars by Paschalidis and Stergioulas (2017). These analyses suggest that the apparent lower limit of pulsar period at 1.4 ms indicates an upper limit of radius of about 18 km. It would be interesting to find any pulsars with shorter periods; if none are found it may indicate that rotational instability is indeed limiting the possible rotation rate.

13.6 The Magnetic Fields of Neutron Stars

Pulsars are very strongly magnetised neutron stars. Their dipole field strengths are consistent with the collapse of a normal star with a polar field of order 100 G (10^{-2} tesla), the magnetic flux being conserved in the collapsing stellar material. The dipole axis is usually substantially misaligned with the rotation axis. Since the proton component of the neutron fluid is superconducting, the decay time of the magnetic field is long compared with the life of a pulsar. Polar field strengths of order 10^{10} – 10^{12} G are found in the main body of pulsars; while in the very energetic x-ray sources known as magnetars (Chapter 11), the fields reach more than 10^{14} G, the highest fields known anywhere. In contrast, the magnetic field in the older, evolved millisecond pulsars may be as low as 10^8 G ('low' is a comparative term: this is still thousands of times larger than fields attainable in the laboratory).

Despite the intensity of the magnetic field, it has very little effect on the overall structure of the star. The magnetic energy density is very high; converted to an equivalent mass density, this is a matter density of order 1 kg cm^{-3} , but much smaller than the typical matter density of $10^{12} \text{ kg cm}^{-3}$, so that the only effect of the magnetic field on the structure is a modification of the crystal structure near the surface (Ruderman 1974; Lai 2001).

The magnetic field does, however, exert a powerful dynamical influence on the interior of a pulsar. The core neutron fluid contains a small proportion of electrons and protons; this charged component couples the fluid strongly with the magnetic field. The part of the fluid core that penetrates the inner solid crust is not, however, completely coupled, so that the rotation of the neutron star comprises a solid-body rotation and a fluid rotation, the coupling between these components being variable. The coupling can in fact change discontinuously; the rotation rate then shows a step, observed as a *glitch*. These glitches prove to be valuable indicators of conditions inside neutron stars.

The magnetic field in the superconducting interior is in the form of quantised flux tubes. The area density of these flux tubes is proportional to the field: for a field of $B_{12} \times 10^{12}$ G, the area density is $5 \times 10^{18} B_{12}$ cm $^{-2}$.

A direct measurement of magnetic field strength at the surface of some neutron stars may be available from absorption lines in x-ray spectra, due to cyclotron resonance in a thin hydrogen atmosphere. Both electron- and proton-cyclotron resonances may be observable in the band 0.1–1.0 keV, corresponding to fields of 10^{10} – 10^{11} G and 2×10^{13} – 2×10^{14} G respectively: for example, an absorption line at 5 keV observed in SGR 1806–20 was attributed to a proton-cyclotron resonance in a field of 1.0×10^{15} G (Ibrahim *et al.* 2002).

The most obvious effect of the strong magnetic fields of pulsars is the slowdown in rotation rate. This occurs through the loss of angular momentum in electromagnetic radiation at the rotation frequency of the magnetic dipole; the slowdown rate has conventionally and usually been used as a measure of the dipolar field. (Note however that an unknown, and possibly variable, part of the slowdown may be due to particle outflow; see Section 15.14 in Chapter 15.) In some younger pulsars, where it has been possible to measure the rate of change of slowdown rate, it appears that the dipole field itself may not be constant, but increasing.

X-ray binaries (Chapter 12) also contribute to our knowledge of the magnetic field of neutron stars. The matter accreted from the binary companion onto the neutron star is constrained to fall on restricted regions at the magnetic poles; these heated regions are responsible for the x-ray emission.

13.7 The Magnetosphere

Without a magnetic field, a neutron star would be cold and inert, unobservable and exerting no influence on its surroundings (except gravitation). There would be no atmosphere; any such would collapse under gravity. The existence of pulsar wind nebulae (PWNe), such as the Crab Nebula, and powerful gamma-ray emission demonstrate that there is instead a very energetic atmosphere, generating a high-energy particle stream and radiation observable over the whole electromagnetic spectrum. This is entirely due to the very strong dipole magnetic field.

Outside the star, that the magnetic field B completely dominates all physical processes, outweighing gravitation by a very large factor. The ratio

$$\frac{GMm}{r^2} / \frac{e\Omega rB}{c} \quad (13.3)$$

between the gravitational and induced electrostatic forces on an electron near the surface of the Crab Pulsar is of order 10^{-12} .

The dipole axis is usually substantially misaligned with the rotation axis. The orthogonal component generates a radiating electromagnetic wave at the rotation

frequency; the angular momentum carried by this wave accounts for the loss of rotational energy and the observed slowdown (Chapter 5). The aligned component generates a field that can accelerate a stream of particles, which contributes to the loss of angular momentum.

Within the magnetosphere, a local electric field is induced at the surface of the neutron star by the rotating magnetic field, strong enough to overcome any surface work function and populate an atmosphere of charged particles. At the crustal surface, the work function is believed to be negligible for electrons but may be significant for ions (Ruderman 1974). Detailed calculations of the work function (Medin & Lai 2007) show that the typical temperatures of pulsars provide sufficient surface emission of ions, which are extracted by the electric field and lifted to the magnetosphere. The magnetic field sweeps this ionised atmosphere, the *magnetosphere*, into co-rotation with the star. The magnetosphere extends from the pulsar surface out to a radial distance $R_{lc} = \frac{c}{\Omega}$, that is, the distance where a co-rotating extension of the pulsar, with angular velocity Ω , would have a speed equal to the velocity of light c . This radial distance defines the *velocity of light cylinder*. It is within this magnetosphere that the beam or beams of radiation originate and the stream of high-energy particles energising pulsar wind nebulae (PNWe) is generated.

Goldreich and Julian (1969) analysed the fields and charge densities expected to be built up in the magnetosphere for the simplest case, in which the magnetic field is aligned with the rotation axis (Figure 13.3). The magnetosphere is highly conducting along (but not perpendicular to) the magnetic field lines. This condition in the magnetosphere is similar to the high conductivity of the stellar interior, where there can be no net electric field. This *force-free* condition applies in most of the magnetosphere plasma, where the induced electric field is cancelled by a static field, so that

$$\mathbf{E} + \frac{1}{c}(\Omega \times \mathbf{r}) \times \mathbf{B} = 0. \quad (13.4)$$

In this fully conducting situation, there must be a charge density equal to $(1/4\pi) \operatorname{div} \mathbf{E}$; a simple analysis then shows that the difference in number density of positive and negative charges is given by

$$n_- - n_+ = \frac{\Omega \cdot \mathbf{B}}{2\pi ec}. \quad (13.5)$$

As a useful guide, the particle density is given approximately by

$$n_- - n_+ = 7 \times 10^{-2} B_z P^{-1} \text{ cm}^{-3}, \quad (13.6)$$

where B_z is the axial component of the field in gauss, and P is the period in seconds. Opposite signs of net charge are found in an equatorial torus and the polar regions, divided by a null charge surface.

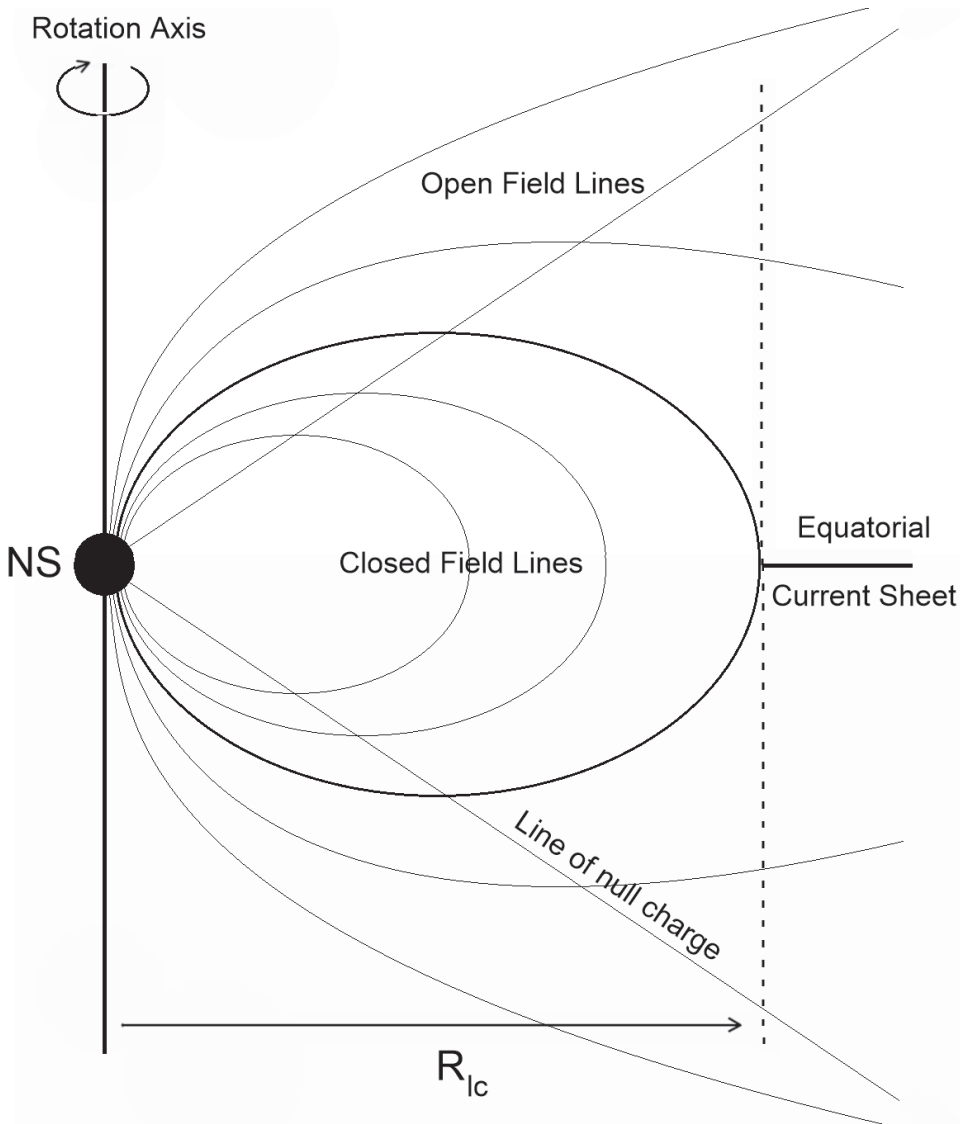


Figure 13.3 The essential features of a pulsar magnetosphere in which the magnetic dipole and rotation axes are aligned. Within a radial distance $R_{lc} = c/\Omega$ of the rotation axis, there is a charge-separated, co-rotating magnetosphere. Since charged particles are constrained to move only along the field lines, there is a closed toroidal region within the field lines that touch the velocity-of-light cylinder, and only particles on the open field lines outside this region can flow out from the magnetosphere. The return flow occurs in an equatorial current sheet that extends outside the light cylinder.

In such a force-free plasma, the inertia of particles is negligible. It does not account for the acceleration of particles to high energies and the stream of plasma to the pulsar wind nebula. Nevertheless, the particle density obtained by Golreich and Julian still applies in most of the magnetosphere and is often referred to as ρ_{GJ} .

The boundary between the equatorial torus and the polar cap region (between the closed and the open field lines in Figure 13.3) is defined by those magnetic field lines that reach but do not cross the light cylinder. Charged particles are trapped within the equatorial region but can flow out along open field lines in the polar regions. A return flow of charged particles from outside the light cylinder is confined to a current sheet where the force-free condition does not apply since the magnetic field reverses, going through zero. At the light cylinder the current sheet divides, flowing down the boundary of the equatorial torus.

The force-free condition does not apply in three regions of the co-rotating magnetosphere, where large unshielded electric fields allow the acceleration of particles to very high energies; these are the so-called *vacuum gaps* and the equatorial current sheet. The field in the *polar gap* lifts particles from the stellar surface, populating the polar cap and providing the polar outflow. The *slot gap* extends from the surface to the light cylinder, following the boundary of the equatorial torus; inner and outer regions are divided where the sign of the space charge reverses. In these gaps electrons and positrons reach such high energies that they emit gamma-ray photons when they are accelerated in the dipole magnetic field. These photons then create electron–positron pairs, again in the dipole field, resulting in an e^\pm cascade. This cascade is the source of the polar gap outflow and also the seat of the beamed radiation in radio and gamma rays. We discuss the location of these radiation processes in Chapter 16.

This description of the magnetosphere so far is obviously incomplete, since an aligned and symmetric rotator cannot produce the rotating beams that we observe as pulses. The next stages of analysis must consider the effect of non-aligned dipole and rotation axes. This has been the subject of many papers; see a summary with a list of references by Cerutti and Beloborodov (2017).

At the velocity-of-light cylinder, a radial field line is swept back by 45 deg, becoming the perpendicular field of the outward flowing electromagnetic field at the rotation frequency, which carries away angular momentum from the rotating star. The general case of the non-aligned rotator has been tackled only by numerical methods, introduced by Spitkovsky (2006), in which individual particles are traced through an array of cells (the PIC, or particle in cell analysis), involving a huge computation. Recent analyses, for example by Brambilla *et al.* (2018) and Kalapotharakos *et al.* (2018), show, however, that the general description and terminology of the aligned rotator are still applicable. For example, the return current sheet shown in Figure 13.3 continues with a wave-like distortion that has been

described as like a pirouetting ballerina's skirt. We have presented neutron star magnetospheres as stable and static. The occurrence of nulling and moding indicate that abrupt changes evidently occur on time scales from seconds to years, while evidence is accumulating of a slow evolution of magnetic field strength and polar angle on an evolutionary timescale.

13.7.1 The Energy Outflow

For a young pulsar, the outward energy flow from the polar cap is sufficient to generate a *pulsar wind nebula* (Chapter 18), such as the Crab Nebula. Collimation of the jet is due to the rotation of the pulsar, which twists the dipole field and creates a toroidal field (Komissarov & Lyubarsky 2004). The energy in this outflow may represent a substantial part of the total rotational energy loss (Harding, Contopoulos & Kazanas 1999). The detailed analyses cited above provide an estimate of the total energy outflow, suggesting a simple dependence between total luminosity L_* and the polar angle χ between the rotation and dipole axes (Cerutti & Beloborodov 2017):

$$L_* \propto (1 + \sin^2 \chi). \quad (13.7)$$

This relation is important in understanding the lifetime of a pulsar, but as yet we are uncertain how the polar angle evolves during this lifetime.

14

Radius and Mass

In 1966, before any neutron star had been observed, John Wheeler reviewed the concept of highly condensed stars (Wheeler 1966), concluding that stable neutron stars could exist only within the approximate ranges of mass $1\text{--}3M_{\odot}$ and radius 9–12 km. There seemed at the time little prospect of measurements to check the prediction, apart from the possibility of measuring an x-ray brightness and spectrum, for which there was at the time no sufficiently sensitive telescope. The discovery of binary millisecond pulsars was a transformation, eventually providing measurements of mass that were more accurate than for any other object outside the solar system. Less accurate measurements of radius are also achieved for some solitary pulsars as well as binaries; Wheeler’s 1966 predictions of mass and radius have been found to be completely correct.

In this chapter, we review the methods of measuring mass and radius of pulsars (and for binaries the mass of the companion). We then assemble the known masses, noting the present observational limitations, and consider any implications for the evolution of the pulsar population.

14.1 Radii of Neutron Stars: Luminosity and Redshift

14.1.1 Thermal Radiation

Stellar diameters are classically calculated from measured luminosities, assuming that they radiate as black bodies and that their surface temperature and distance have been determined. Before any neutron star had been observed, Chiu and Salpeter (1964) pointed out that the thermal radiation from a neutron star with a surface temperature of 10^6 K should be measurable at x-ray wavelengths. This offered

the possibility of measuring the radius R of a neutron star, given the distance D and a temperature T (found from the spectrum), using the classical relation for the flux F :

$$F = \sigma T^4 \left(\frac{R}{D} \right)^2, \quad (14.1)$$

where σ is the Stefan–Boltzmann constant.

The many attempts to apply this to isolated neutron stars and quiescent low mass x-ray binaries (LMXBs) were reviewed by Miller and Lamb (2016). The distance D is found either from trigonometric parallax, measured interferometrically, or from an optical identification, as for example a neutron star within a globular cluster. Distances may also be deduced from measured values of DM, although this relies on a model of the electron distribution in the interstellar medium. Disentangling the mass and the radius is made more difficult because the apparent radius of the star is considerably increased by self-lensing (Chapter 12), which extends the visible disk to part of the back of the star; the extent of lensing depends on the mass of the star.

Another feature of x-ray emission that affects the estimation of radius is the substantial gravitational redshift expected for radiation from the surface of a neutron star. The redshift z at the surface of a star with radius R_\star and mass M is given by

$$1 + z = \left(1 - 2 \frac{GM}{R_\star c^2} \right)^{-1/2} \quad (14.2)$$

$$= \left(1 - \frac{R_g}{R_\star} \right)^{-1/2}, \quad (14.3)$$

where $R_g = 2 \frac{GM}{c^2}$ is the Schwarzschild radius (approximately $2.94 \frac{M}{M_\odot}$ km). As observed from a large distance, the bolometric luminosity L_∞ and the equivalent temperature T_∞ of a blackbody are related to these quantities at the star (L_\star, T_\star) by

$$L_\infty = L_\star (1 + z)^{-2} \quad (14.4)$$

$$\text{and } T_\infty = T_\star (1 + z)^{-1}, \quad (14.5)$$

and the radius R_∞ deduced from the luminosity becomes

$$R_\infty = R_\star (1 + z). \quad (14.6)$$

This is a substantial correction: for models based on any reasonable EoS, the redshift is greater than $z = 0.3$. For a full account of general relativistic effects, see Psaltis *et al.* (2014).

Although thermal radiation has been observed from several of the nearest neutron stars (see Chapter 12), it turns out that distinguishing between thermal and non-thermal radiation is difficult. Furthermore, the surface of the star may be heated

unevenly, either by particles in a return flux from the magnetosphere or, in a binary system, by an x-ray flare caused by accretion from the companion (Section 14.1.2). There have been many observations of such higher-temperature regions, allowing many more estimations of temperature and radius, although with considerable difficulties of interpretation.

14.1.2 Radii: Hot Spots and X-ray Bursts

X-ray flares occur on a neutron star in a binary system when a slow accretion of hydrogen or helium from the companion star accumulates sufficient material for a thermonuclear reaction to occur on the surface, involving fusion of hydrogen, helium and possibly carbon. For a comprehensive review of x-ray bursts, see Galloway and Keek (2017).

Thermal photon energies of several keV are reached, giving bursts of x-rays lasting several minutes. As described above, if the whole surface of the star was at the same high temperature, which could be found from the x-ray spectrum, the intensity and the distance would give a measurement of the radius R . Unfortunately the burst temperature is uneven over the surface; furthermore, there may be an additional component of non-thermal radiation. The two components may in principle be distinguished by the overall spectrum, which consists of a power-law spectrum in addition to the blackbody.

A non-uniform distribution of brightness may appear as a periodic modulation of x-ray intensity at the stellar rotation period; this may not, however, reveal the extent of the surface differences, as the hot regions may be close to the rotation axis and will not show up as the star rotates.

X-ray bursts often contain complex structure, including quasi-periodic oscillations (QPOs) at frequencies of 100 Hz to 1 kHz (Section 12.10). In some cases the frequency has been found to be close to, or identical with, the rotation rate of the star, indicating an origin on the surface or in accreting material orbiting close to the surface of the star. This orbital frequency must be lower than the Keplerian frequency at the surface; if the mass is known, which it often is, the observed frequency of a QPO provides an upper limit to the radius (Miller & Lamb 1998). See a review by Watts (2012).

14.1.3 Radii: Relativistic Effects

Attempts have been made to attribute structure in the x-ray spectra of bursts to absorption or emission lines from heavy nuclei such as atomic iron or oxygen on the surface. Such atoms would be in a hydrogen-like state, that is, almost completely stripped of electrons. If such lines can be found and identified, their wavelengths

would be found to be shifted by factors of around $1 + z = 1.3$; if the mass of the star is known, this would yield a measurement of radius.

The modulation waveform from a single isolated hot spot offers another possibility for determining radius: this is a further consequence of general relativity. A combination of self-lensing, gravitational redshift and differential Doppler between the approaching and receding limbs has been shown to produce observable effects on the x-ray waveform.

Despite the diversity of methods available for estimating radius, none has confidently yielded values of radius accurate to better than 10%; see a comprehensive review by Degenaar and Suleimanov (2018).

14.2 Masses: The Dynamics of Binaries

In Chapter 6, we set out the basic Keplerian analysis, which relates the observations of binary systems to their physical parameters, and the post-Newtonian effects, which provide further access to their component masses. We briefly recapitulate the analyses and review the available measurements of mass in LMXBs and MSPs.

The observed orbital motion of a binary component is described in Newtonian gravity by five parameters: orbital period P_b , eccentricity e , semi-major axis a_p (observed as $x_p = a_p \sin i$, where i is the angle between the observer's line of sight and the normal of the orbit), T_0 the time of periastron and ω , the longitude of periastron. These are all obtained from timing observations of pulsars but not usually for x-ray binaries, where only a periodic variation of intensity is observed and not range from timing pulse arrival times.

The masses m_p and m_c of pulsar and companion stars are only available at this stage combined in the mass function $f(m_p, m_c)$ (repeated from Eqn. 6.4):

$$f(m_p, m_c) = \frac{4\pi^2 x_p^3}{P_b^2 T_\odot} = \frac{(m_c \sin i)^3}{(m_p + m_c)^2}, \quad (14.7)$$

where $T_\odot = GM_\odot c^{-3} = 4.9255 \times 10^{-6}$ s, P_b is in seconds and the masses are here expressed in units of the solar mass M_\odot .

Separating m_p and m_c requires either measurement of post-Newtonian effects (Section 14.4) in the pulsar orbit or a measurement of the companion's orbit, if it is visible. If it is a white dwarf or main sequence star, the orbit may be followed through the Doppler shift of spectral lines, giving the projected semi-major axis x_c , and the ratio of masses follows:

$$\frac{m_c}{m_p} = \frac{x_p}{x_c}. \quad (14.8)$$

In some systems the companion mass is known from its spectral type, and Eqn. 14.8 then gives m_p . Otherwise $\sin i$ is required.

14.3 Masses of Neutron Stars in X-ray Binaries

The masses of neutron stars in binary systems with high- and low-mass companions (HMXBs and LMXBs) may be found from a combination of x-ray and optical observations, as described in Chapter 12.

In several eclipsing HMXBs, the full set of orbital parameters is available from x-ray measurements, including the eclipse duration. Observations of optical spectral lines through the binary orbit then give values for m_{ns} and m_c . Figure 14.1 shows the results for a dozen HMXBs; the accuracies are of order 10%, in contrast to the high accuracies obtained in pulsar timing observations (Özel & Freire 2016; Section 14.4).

Masses of the components of LMXBs have been obtained from the spectra of thermonuclear bursts, as described in Section 14.1.2. Seven such systems are included in Figure 14.1. Although the accuracies are low, they are sufficient to make comparisons between the different categories of neutron stars.

14.4 Masses of Binary MSPs

In many neutron star binaries, the masses of both individual components are available, and in the case of double neutron star binaries, the masses have been determined with great accuracy. This is because the deep gravitational potential associated with these systems allows for the measurement of general-relativistic effects (PK, or post-Keplerian; see Chapter 6), in particular:

- decrease of orbital period P_b through gravitational radiation;
- precession of the major axis of the binary orbit due to the finite travel time of gravitational influence; and
- Shapiro delay, due to propagation along a line of sight through the gravitational potential of the companion star.

The first two are related to the total mass $m_p + m_c$ of the two neutron stars; using the mass function (Eqn. 14.7), this provides a value of $m_c \sin i$. The Shapiro delay is crucial: it provides the PK parameter r , which is directly proportional to the mass m_c of the companion, and s , which is directly related to $\sin i$.

14.5 Double Neutron Star Binaries

At present (2020) the total number of known Galactic double neutron star binaries is 19. The masses of both the neutron stars are known in 11 systems, and for a further 5, the total masses have been measured. In their review, Özel and Freire (2016) updated the analysis of the mass distribution for the component neutron

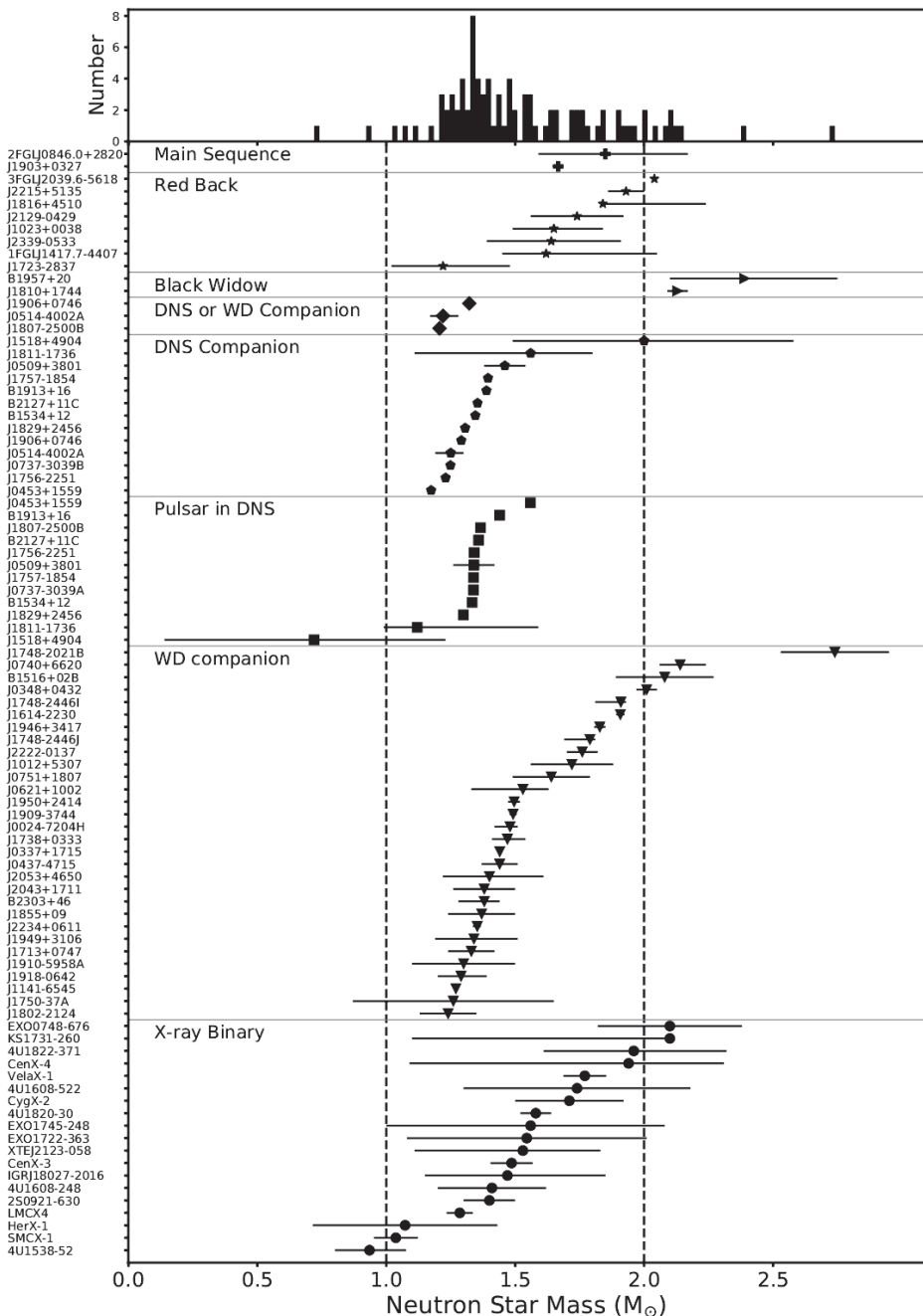


Figure 14.1 The masses of neutron stars in a range of different systems from x-ray binaries to double neutron star systems. Data compiled by John Antoniadis.

stars assuming a single Gaussian model and found a mean mass of $1.33M_{\odot}$ and a dispersion of only $0.09M_{\odot}$. The discovery by LIGO of the double neutron star merger event (GW 170817) and the recent discovery of three new double neutron star binaries have prompted new studies of the mass distribution. Zhu *et al.* (2019), for example, found that there is marginal evidence for the spun-up neutron stars to have a different mass distribution from those that have not been spun-up. They argued that precise neutron star mass measurements from 20 systems are needed to test this hypothesis and that a total of 60 systems are required to determine the shape of the mass distribution. The mass distribution for the double neutron star systems is narrower than for the other neutron star masses (see Figure 14.1) and likely points to a specific evolutionary mechanism or progenitors. We note that analysis of the gravitational waves from GW 170817 showed that the component masses are in the range 1.17 – $1.60M_{\odot}$ and that the total binary mass is $2.74^{+0.04}_{-0.01}M_{\odot}$ (Abbott *et al.* 2018).

14.6 White Dwarf Binaries

Although neutron star/white dwarf binaries are the most numerous, those that contain millisecond pulsars are typically in orbits with very low eccentricity. Thus, despite the very high timing precision, allowing their orbits to be very well determined, it is very difficult, or even impossible, to measure the precession of the binary orbit or the Einstein delay. The decrease of the orbital period will eventually give the total masses, but another PK term is required to give the individual masses. The exception to these circular systems are those in globular clusters, where gravitational interactions may result in a system with a significant eccentricity and thus allow a measurement of the orbital precession. The masses of millisecond pulsars in these systems gave an early indication that there was a population of more massive neutron stars than was suggested by the double neutron star binaries.

One of the other ways to find the masses in these systems is to measure the Shapiro delay. The majority of the white dwarf companions are, however, low-mass He white dwarfs and so require high timing precision and/or favourable orbital inclination for a measurement to be possible. This has been achieved for systems like PSR J1909–3744, where the neutron star has a mass of $M = 1.44 \pm 0.03M_{\odot}$ (Jacoby *et al.* 2003). As more masses of neutron stars in white dwarf binaries are found, it appears that they can be heavy – PSR J1614–2230 with $M = 1.928 \pm 0.007M_{\odot}$ (Demorest *et al.* 2010) – or light – PSR J1802–2124 with $M = 1.24 \pm 0.11M_{\odot}$ (Ferdman *et al.* 2010). The high-mass white dwarf companion to PSR J2222–0137 is thought to be so massive that there was very little chance for accretion, and thus the mass of the pulsar of $M = 1.76 \pm 0.06M_{\odot}$

(Cognard *et al.* 2017) is believed to be very close to its mass at formation. Those systems with measured masses are included in Figure 14.1.

If the white dwarf companion is sufficiently bright, then it is possible to measure its spectrum and determine both the changes in the line-of-sight velocity and also the broadening of the lines due to gravity. When combined with the knowledge of the orbital velocity of the pulsar, the former allows the mass ratio to be determined. If the latter can also be measured, then white dwarf models can be used to determine the mass and the radius and combined with the mass ratio to get the mass of the neutron star. The massive ($M = 2.04 \pm 0.04 M_{\odot}$ (Antoniadis *et al.* 2013)) neutron star in the PSR J0348+0432 system was identified using this method.

14.7 Black Widow and Redback Binaries

Optical spectroscopy can also be used to obtain the radial velocities of the companions in the black widow and redback systems, and therefore derive their mass functions. When combined with the mass function from the pulsar timing, it is possible to get the mass ratio of the pulsar and the companion, leaving only the inclination as an unknown. In these systems the interaction between the pulsar wind and the companion cause it to be heated, leading to ellipsoidal modulations, which can be modelled to determine the inclination with modest to good precision. The original eclipsing binary PSR B1957+20 was the first source for which this was done, and a large, although somewhat uncertain, pulsar mass was derived: $M = 2.40 \pm 0.12 M_{\odot}$ (van Kerkwijk *et al.* 2011). Since then, similar techniques have been used to determine the masses, or lower limits on the masses, of 14 neutron stars in redback systems, and an analysis of this sample by Strader *et al.* (2019) finds that they have a median mass of $1.78 \pm 0.09 M_{\odot}$, with two systems appearing to have neutron star masses greater than $2M_{\odot}$. Ten of the systems with the smallest errors in the mass measurements are included in Figure 14.1.

Although there are difficulties associated with modelling the heating of the low mass companion, the masses of the neutron stars in these systems appear to be significantly different from those in the double neutron stars and the normal MSP population, and there is a hint of a population of neutron stars more massive than $2M_{\odot}$. Distances to some of the optical companions will be determined from the measurements of parallax by the astrometric spacecraft GAIA, which will allow improvements in the optical light curve modelling.

14.8 Neutron Stars in X-ray Binaries

Some of the techniques described above can also be used to determine the masses of neutron stars that are in x-ray binary systems. In those systems where x-ray

pulsations are detected, it is possible to determine the orbit of the neutron star. If the orbital velocity of the companion star can also be measured using spectroscopy, either in the optical or the near infrared, then one can again get the mass ratio. In some cases the mass ratio may also be determined from the rotational velocity of the companion star. As with the eclipsing millisecond radio pulsar systems, it may also be possible to model the ellipsoidal modulations of the companion light curve. Similarly, some of the x-ray systems are seen to exhibit eclipses, and so the inclination angle of the orbit can be constrained. As discussed in more detail in Degenaar and Suleimanov (2018), it is also possible to use thermonuclear bursts on the neutron stars in low-mass x-ray binaries to constrain the mass and radius of the neutron star. Presently there are neutron star masses measured for around 10 high-mass x-ray binaries and 7 low-mass x-ray binaries.

14.9 Summary

In Figure 14.1, we show the current neutron star mass measurements over a range of system types. It can be seen that the narrowest distribution is for those neutron stars that are members of double neutron star binaries. The widest ranges are seen in the MSP-WD systems and in the high-mass x-ray binaries, while the low-mass x-ray binaries seem to show a narrow distribution.

Some high-mass neutron stars might be expected in the MSP-WD systems, following the accretion of significant matter, but this is unusual, possibly because the neutron star birth masses were low. The highest-mass neutron star systems appear to be those in the eclipsing binary systems, which often contain the most rapidly spinning pulsars. As discussed by Linares (2019), there are more than 9 NS measurements now with masses $> 2M_{\odot}$. Although not all of them are well constrained, this is compelling evidence that there is a significant population of massive neutron stars, and the maximum neutron star mass could be at least $2.5M_{\odot}$. This has important consequences for the neutron star equation of state (see Chapter 13).

15

Glitches, Timing Noise, Nudot Switching

On a time scale of some days, all pulsars show a remarkably uniform rotation rate. This is not surprising, since uniform rotation is exactly what is expected of a spinning body isolated in space. The angular momentum of the star can only change through the slowdown torque of its magnetic dipole radiation or an associated material outflow, or, for the accretion-powered binary x-ray pulsars, the accelerating torque of in-falling material. The effects on the radio pulsar are usually smooth and predictable; however, sporadic step changes in pulsar rotation are observed in many young pulsars, which are related to remarkable events within the interior of the neutron star. These are the *glitches*, which we describe and analyse in this chapter. At a lower level, an apparently unrelated irregularity observed in most pulsars is *timing noise*, slow quasi-random changes in rotation rate. This phenomenon is primarily understood as switching between two rates of rotational slowdown related to changes in the magnetosphere, which result in the moding that we described in Chapter 9.

15.1 Glitches

A glitch is a discontinuous step increase in rotation rate. The most spectacular glitches, and the first to be discovered, are those of the Vela Pulsar PSR B0833–45. Figure 15.1 shows a well-observed example (McCulloch *et al.* 1983). This pulsar has a period $P = 89$ ms (rotation rate $\nu = 11$ Hz), and the normal rate of change of period \dot{P} is an increase of 10.7 ns/day ($\dot{\nu} = -1.57 \times 10^{-11}$ s $^{-2}$). At typical glitches, which in the Vela Pulsar occur at intervals of around three years, the period decreases catastrophically by up to 200 ns (Figure 15.1a), subsequently recovering over several weeks to a period close to, but not identical with, that expected by extrapolation from pre-glitch observations. The sudden period change is usually observed as a

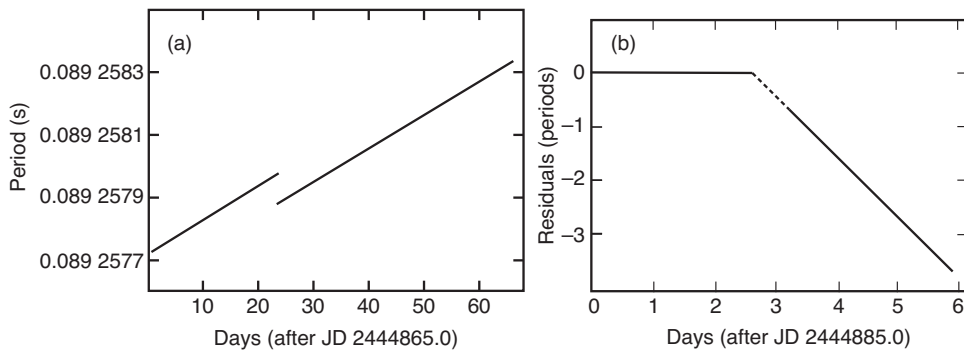


Figure 15.1 The glitch in the Vela Pulsar, October 1981 (McCulloch *et al.* 1983). (a) The mean period of the pulsar from daily observations. (b) Timing residuals (in units of one period) using a period obtained from the three days immediately preceding the glitch.

discontinuous downward change in the timing residuals (Figure 15.1b). In these large glitches, the step change in rotational frequency typically amounts to a fraction change of one or two parts in 10^6 ; the largest in Vela, in January 2000, amounted to a step of $\Delta\nu/\nu = 3.1 \times 10^{-6}$ (Dodson *et al.* 2002). Smaller glitches are observed in other pulsars down to the limit of detectability with steps of $\sim 10^{-9}$.

Glitches are widely understood to arise from the spasmodic transfer of angular momentum from a superfluid component in the interior of a neutron star to the solid crust, whose rotation we observe. A step change in the coupling of this component causes a change in the effective moment of inertia, observed as a change in slow-down rate. A partial relaxation to pre-glitch conditions may follow over a peiod of some hours or days.

Glitches may occur in all pulsars (although only extremely rarely in millisecond pulsars), but as they occur at intervals of several years, they are only noticed in long series of monitoring observations. A catalogue of glitches is maintained at Jodrell Bank Observatory¹ and at the Australia Telescope National Facility.² In 2020 these catalogues contained over 600 glitches in 200 pulsars.

An analysis of observations spanning 30 years by Espinoza *et al.* (2011), which was extended by Fuentes *et al.* (2017), provides the material for our discussion of the occurrence and properties of glitches in all types of pulsars. The phenomenon is surprisingly variable, both between different pulsars and even within individuals,

¹ www.jb.man.ac.uk/pulsar/glitches/gTable.html

² www.atnf.csiro.au/research/pulsar/psrcat/glitchTbl.html

so that large numbers of glitches are required for statistical studies to establish any different categories of behaviour.

15.2 Occurrence Rate

Glitches occur more frequently in the younger pulsars; almost a quarter of all those observed so far have been in three young pulsars: the Crab, Vela and J0537–6910. These are among a group of glitching pulsars seen in the familiar $P - \dot{P}$ diagram, Figure 15.2, in which all pulsars known to glitch are identified. This grouping shows that in normal pulsars, glitch activity peaks at an age of around 10 kyr, disappearing for ages above about 2 Myr. Only two glitches have been observed in any millisecond pulsars – PSR B1821–24 – (Cognard *et al.* 1996) and PSR J0613–0200 (McKee *et al.* 2016) – possibly because their rotational evolution is much slower than the majority of pulsars and they glitch very infrequently.

15.3 Glitch Size

Glitch size, as measured by the fractional step change in rotation frequency $\Delta\nu/\nu$, covers a wide range between 10^{-10} and 10^{-5} . Within this range there appear to be two distinct groups, as seen in the histogram of Figure 15.3. The larger group comprises the Vela-like glitches, a categorisation that is well substantiated by further observations of their characteristics, as seen in the following sections.

15.4 Intervals between Glitches

The most frequent regular series of Vela-like glitches is seen in the young PSR J0537–6910, discovered as an x-ray pulsar, in which a series of 23 glitches were observed in 7 years (Middleditch *et al.* 2006). The interval between glitches varies between 50 and 200 days; unusually in this pulsar, there is a clear relation between interval and glitch size: longer intervals are observed to be followed by larger glitches (Antonopoulou *et al.* 2018; Ferdman *et al.* 2018). A clear quasi-periodic repetition behaviour is seen in the Vela Pulsar (Figure 15.7) and in PSRs B1800–21 and B1737–30 (Figure 15.4).

Figure 15.5 shows the glitches in the Crab Pulsar. These are smaller than the Vela glitches and only show in detail after removing the long-term trend in rotation rate and expanding the scale. The intervals between glitches show no regular pattern.

For the majority of pulsars, there is no preferred time scale for the interval between glitches, and the probability distribution of intervals between glitches

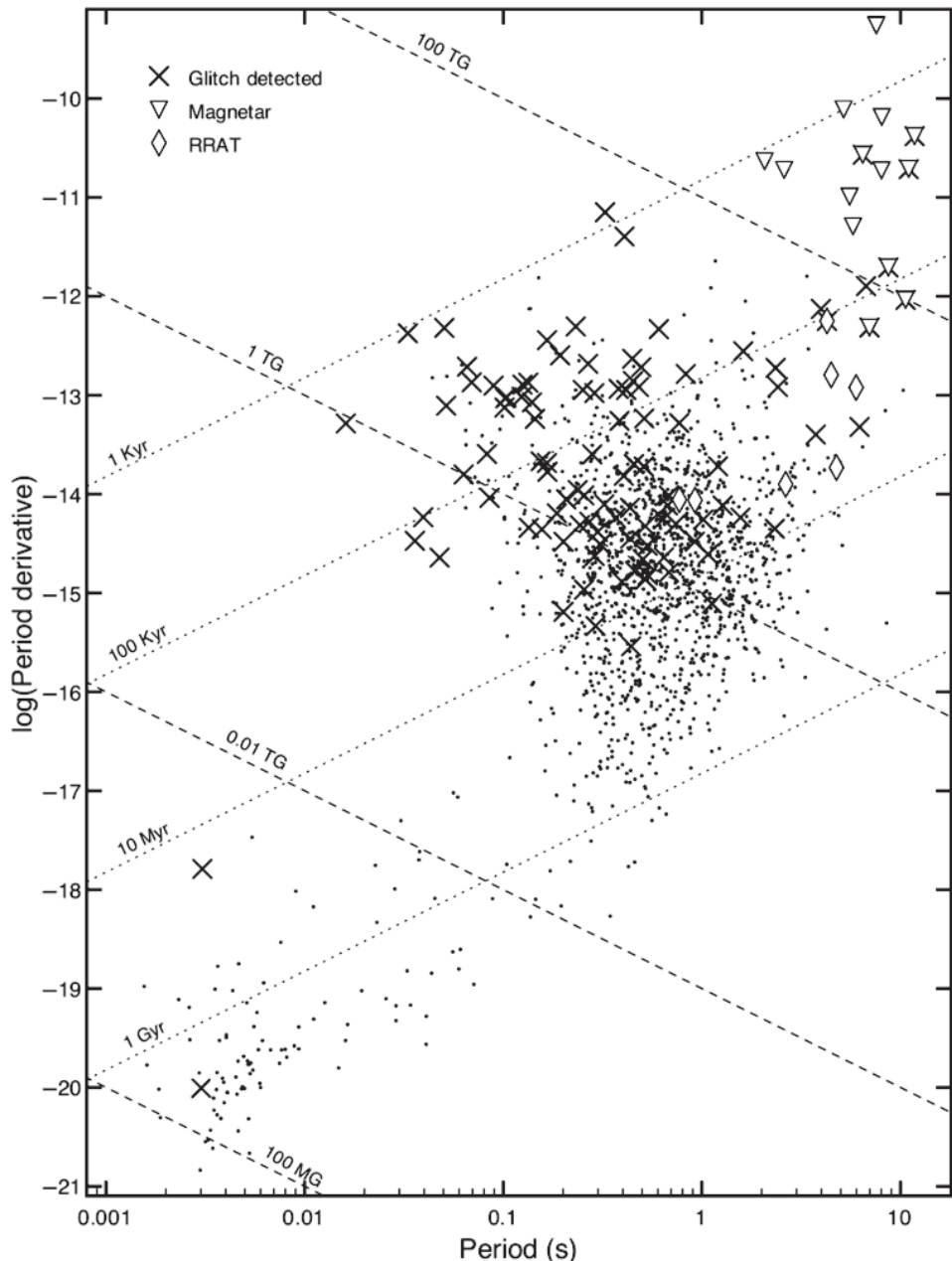


Figure 15.2 The location of glitching pulsars in the $P - \dot{P}$ diagram based upon a figure from Espinoza *et al.* (2011).

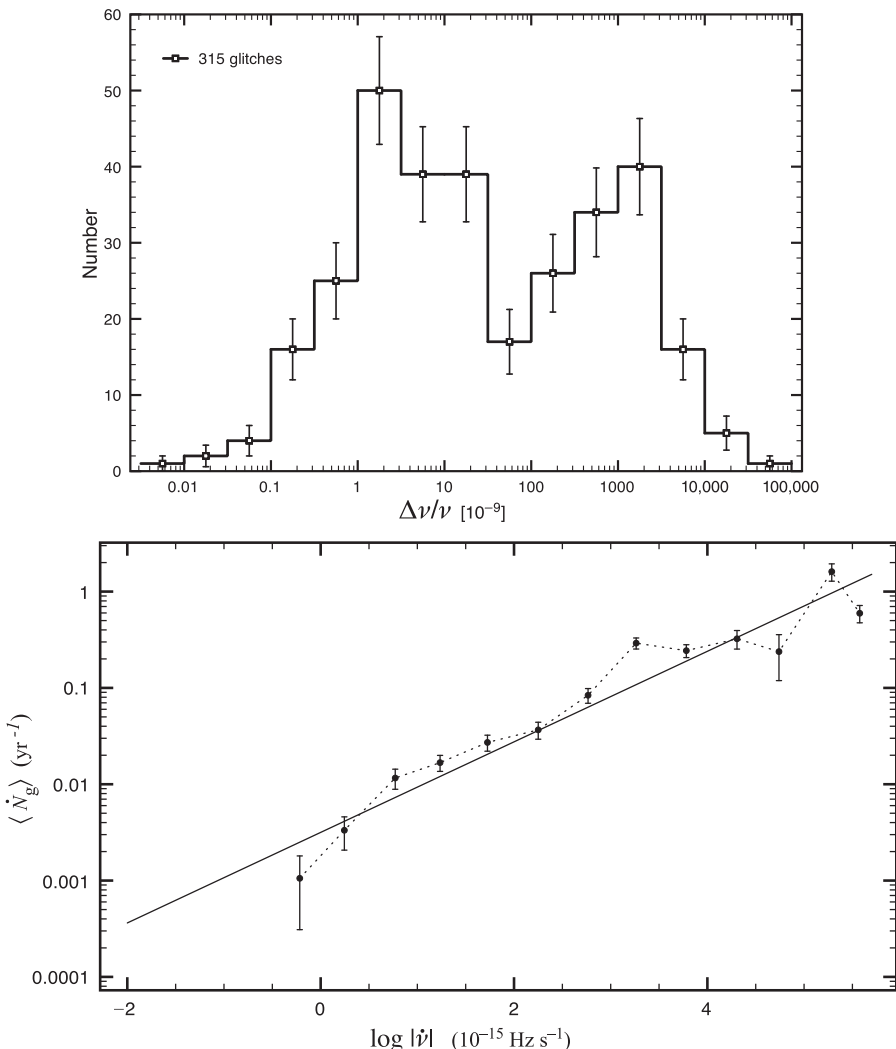


Figure 15.3 (a) Histogram of occurrence of glitch sizes; (b) frequency of occurrence of glitches as a function of size (Espinoza *et al.* 2011).

follows a Poisson-like statistic. If the mean glitch rate is λ , the probability of an interval Δt between glitches should follow the Poisson distribution

$$p(\lambda, \Delta t) = \lambda \exp(-\lambda \Delta t). \quad (15.1)$$

For the small number of pulsars where a sufficient number of glitches have been recorded for the statistics to be meaningful, Melatos and Drummond (2019) show that the distribution of interval for most pulsars follows an exponential

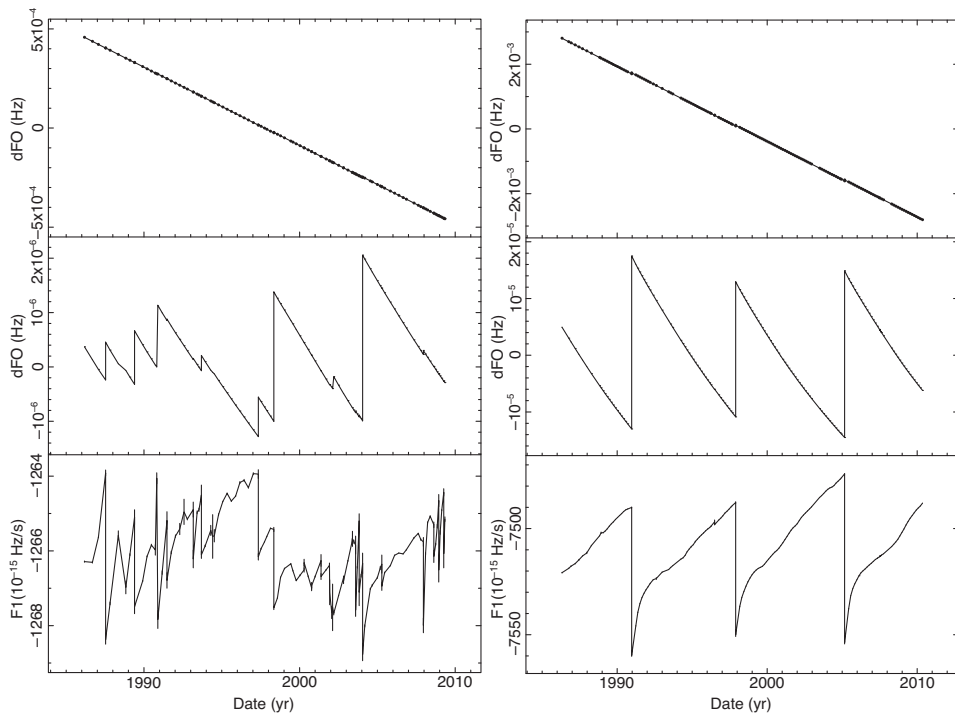


Figure 15.4 Glitches in two young pulsars, PSRs B1737–30 and B1800–21. Both plots show (in the top panels) the long-term decreasing rotational frequency. The glitches are revealed in the second panels after subtracting a uniform slope. The frequency derivative is shown in the bottom panels.

law, in contrast to the Vela-like pulsars where the intervals are in a Gaussian distribution around a mean value.

15.5 Slowdown Rate after a Glitch

Although the long-term slowdown rate of a pulsar may conform to a power law with a definite braking index (Chapter 5), the short-term behaviour after a glitch may be very different. The recovery from a glitch may be slow and may not be complete before the next glitch occurs; a braking index measured during the recovery time may then differ greatly from the long-term average.

The recovery from an individual glitch may occur on several time scales. In young pulsars, a substantial proportion of the step in rotation rate may be reversed on a time scale of seconds or minutes; Figure 15.6 shows this effect on the pulse arrival times for a glitch in the Vela Pulsar. Following this transient, a quasi-steady state is

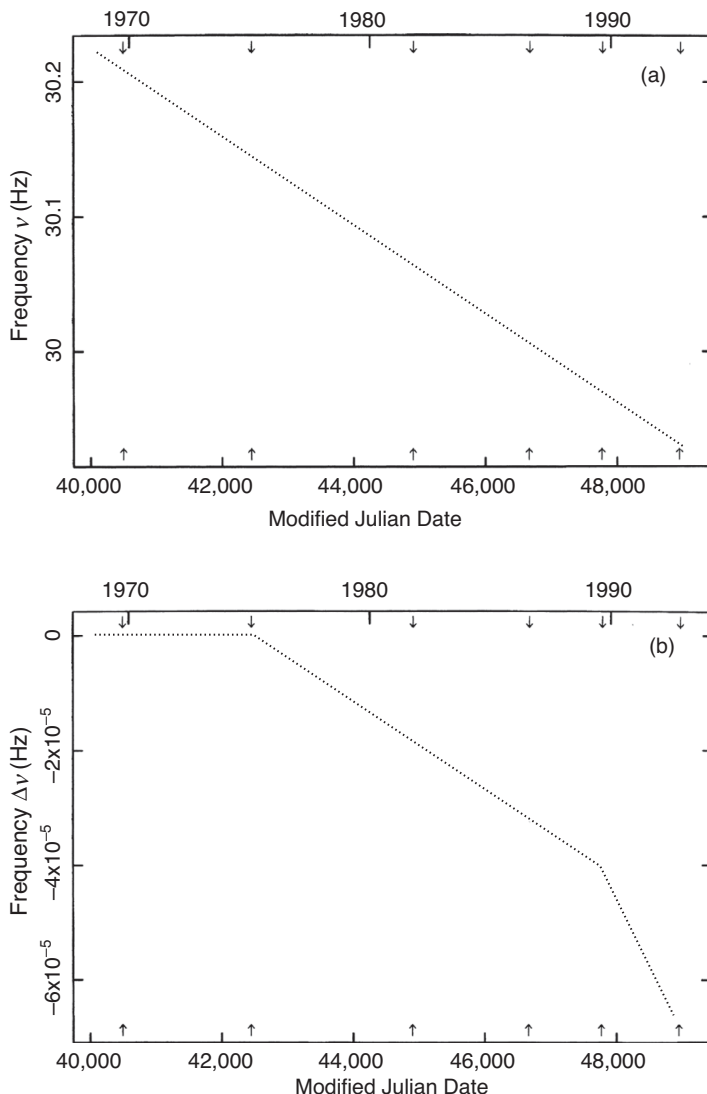


Figure 15.5 Glitches in the Crab Pulsar. (a) The slowdown observed over 25 years. (b) On an expanded scale, after subtracting the initial slowdown rate, the glitches show as steps in the slope, corresponding to increases in the slowdown rate. The transient steps in frequency at the glitches are difficult to discern on this scale (Lyne, Pritchard & Smith 1993).

established. Figure 15.7 shows the slowdown rate for the Vela Pulsar over 25 years, including the effect of 9 glitches. The steep slope between glitches corresponds to a large and varying braking index, while the average slope gives a low braking index of 1.4 (Lyne *et al.* 1996).

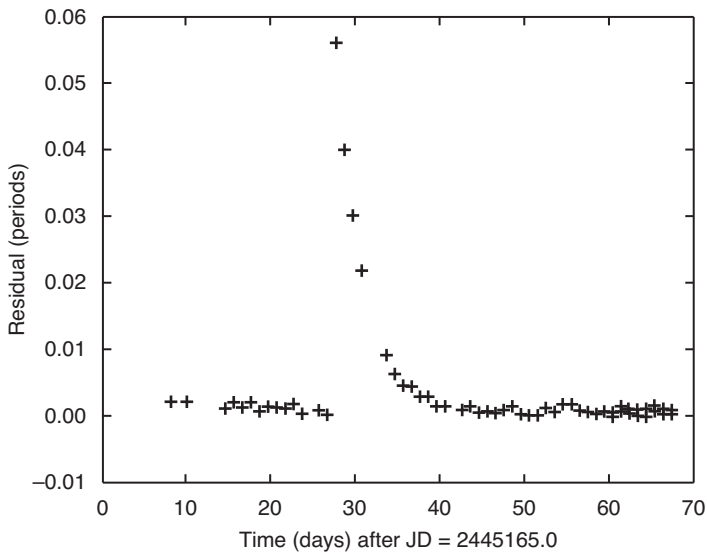


Figure 15.6 The exponential recovery from a glitch in the Vela Pulsar (McCulloch *et al.* 1983).

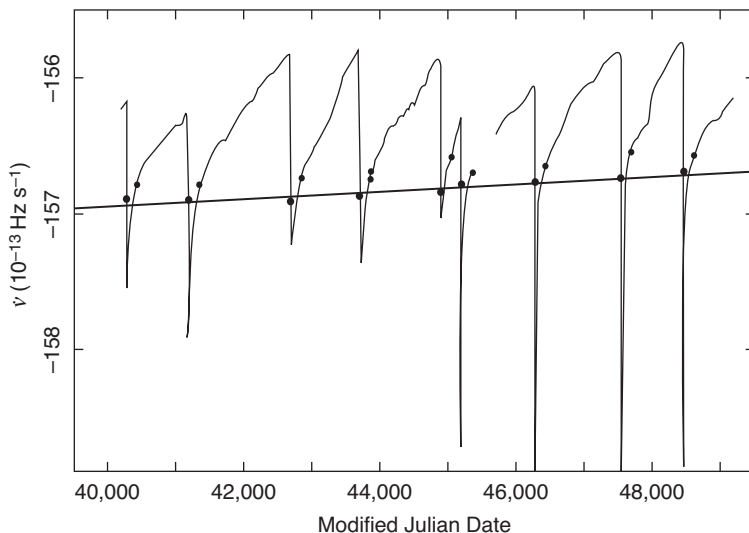


Figure 15.7 The slowdown rate of the Vela Pulsar over 25 years (Lyne *et al.* 1996).

In some young pulsars, notably the Crab, there is a change in slowdown rate that does not decay. Figure 15.5 shows the slowdown of the Crab Pulsar over 25 years. Monitoring was continued over 45 years, during which there were 24 glitches (Lyne *et al.* 2015). Here most of the glitches are small; as measured by $(\Delta\nu/\nu)$, the

largest glitches were of order 10^{-7} . There is, however, a large change in slowdown rate ($\Delta\dot{\nu}/\dot{\nu}$) due to glitches of order 10^{-4} per annum, which accumulates and has amounted to a total increase of 0.3% over 45 years of observation.

15.6 The Exponential Recoveries

Observations of the actual step in rotation properties and the short-term subsequent transients are rare; it is impossible to keep a continuous watch on every pulsar that might glitch at intervals of several years. Only the Vela and Crab Pulsars are under daily observation, although several hundred are monitored for timing irregularities at intervals of some weeks or months. The data for the Vela Pulsar glitch shown in Figure 15.1 were obtained from daily measurements of period from Hobart, Tasmania, supplemented by weekly measurements from the NASA Deep Space Tracking Station at Tidbinbilla in Australia (McCulloch *et al.* 1983). (The nearly continuous monitoring at Hobart had started only two days before a large glitch occurred; this must have been very gratifying for the observers, since the interval between steps is randomly spread between two and three years.)

The increase in rotation rate at a glitch in the Vela Pulsar corresponds to about one extra rotation per day. Timing observations can be made to an accuracy of about 10^{-4} of the period, so that the progress of the recovery from the step can be very precisely monitored. After allowing for the pre-step rotation rate and the normal slowdown rate, the short-term transient effects on pulse arrival time appear as approximately exponential recoveries. In a later glitch, Flanagan (1990) observed three distinct components, which are well fitted by exponentials with time constants of 32, 3.2 and 0.4 days. Dodson, McCulloch and Lewis (2002) observed four exponential recoveries in the glitch of Jan 2000, with time constants of 60 seconds, 0.56 days, 3.33 days and 19.1 days. Ashton *et al.* (2019) report a rise time of less than 12.6 seconds; they also observed a slowdown for a few seconds *before* the glitch.

Recoveries from glitches in other pulsars usually appear as single exponentials, although they are less well observed. In these longer period pulsars, the recovery usually amounts to a smaller proportion of the initial step in rotation rate. A large recovery was observed after a glitch in PSR B0355+54 ($P = 197$ ms) (Lyne 1987). The glitch was followed by a transient with decay time constant of 40 days, recovering 10% of the step; there was also a small permanent change in slowdown rate, amounting to $\Delta\dot{\nu}/\dot{\nu} = 0.5\%$. The initial change in $\dot{\nu}$, immediately after the glitch, was about 10%; the precise value depends on the date of the glitch, which is only known within about one month. This fractional change $\dot{\nu}$ is among the largest observed in any pulsar.

A different pattern of transient is seen in the Crab Pulsar glitches. Figure 15.8 shows a plot of rotation rate after the 1975 and 1989 glitches (Lyne, Pritchard &

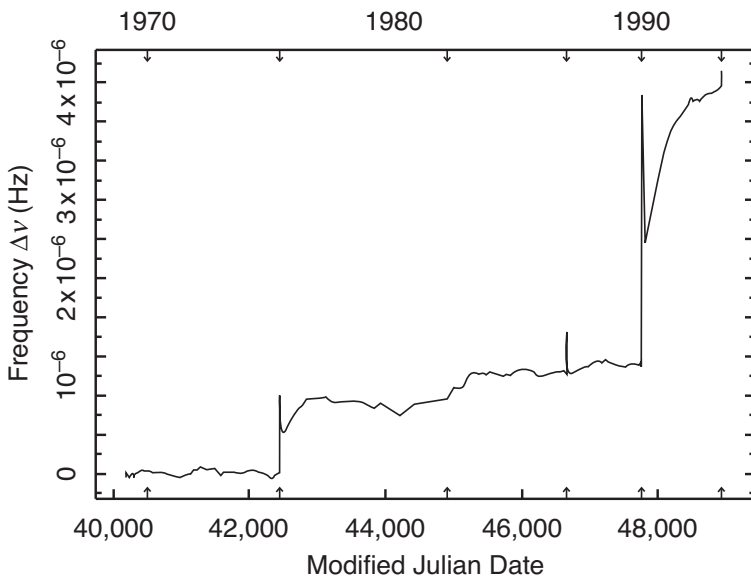


Figure 15.8 Transients at the Crab glitches, after subtracting the steps in slowdown rate seen in Figure 15.5 (Lyne, Pritchard & Smith 1993).

Smith 1993). This plot shows the transient changes in rotation rate after removing the major persistent step at the glitches. There are three components in the 1989 glitch: a decay with time constant of approximately 20 days and two positive-going asymptotic exponentials, with time constants 1 day and 200 days. A complete sequence of timing obsevations spanning 45 years is available for the Crab Pulsar (Lyne, Jordan, Graham-Smith *et al.* 2015).

In most pulsars, these various transients decay over timescales short compared with the interval between glitches; they should perhaps be regarded as responses to the step changes at a glitch rather than an intrinsic part of the glitch itself. There is, however, another component of the recovery that extends through the whole of the interval between glitches in the Vela Pulsar and that also appears to be inherent in the glitch process in several other pulsars. Figure 15.7 shows the slowdown rate, that is, the differential of the rotation rate, of the Vela Pulsar over 25 years. Apart from the glitches, the slowdown rate is expected to be nearly constant, showing only the short-term effects of the steps and the transient recoveries. The main effect is, however, an approximately linear sawtooth change in slowdown rate. We discuss the possible explanation later; here we note that Figure 15.7 also shows a slow monotonic change over the 25 years (Lyne *et al.* 1996), giving the value for the second differential $\ddot{\nu}$ that we used in Chapter 5 for deriving the braking index (Eqn. 5.24).

15.7 Catastrophe Theories

Glitches constitute a sequence of adjustments towards a slowly changing equilibrium state. Two processes are invoked to describe the steps: *crust cracking* and *superfluid vortex unpinning*. Both describe a relaxation of stress, which builds as spin-down takes the equilibrium state away from a frozen physical state, either the ellipticity of the rigid crystalline crust or the quantised rotation of the interior. In either case, the sequence of glitches might occur as a quasi-periodic relaxation or as the random phenomenon of *self-organised criticality* (Jensen 1998).

15.7.1 Crust Cracking

Given that the causes of glitches are internal to the neutron star, the conservation of angular momentum $I\Omega$ means that the small changes in ν observed at a glitch imply correspondingly small changes in moment of inertia I . The sensitivity of these observations is demonstrated by considering the small change Δr in radius r , which, if the neutron star shrank uniformly, would give an observed speed-up $\Delta\nu/\nu$ of one part in 10^9 (corresponding to the typical discontinuity in the Crab Pulsar). The corresponding change in moment of inertia I is given by

$$\frac{\Delta I}{I} = \frac{2\Delta r}{r} = -\frac{\Delta\nu}{\nu}. \quad (15.2)$$

For a star of uniform density and a radius of 10 km, the change would be only 5 μm , a remarkably small quantity to be detectable in an object at a distance of several kiloparsecs.

A more realistic explanation is in terms of a change in ellipticity ϵ as the pulsar rotation rate slows, accompanied by a sudden cracking of the solid crust to adjust to the new, more nearly spherical shape; again the change $\Delta\epsilon$ must be small in the observed Crab glitches, since the moment of inertia is $I_0(1 + \epsilon)$, where I_0 is the value for a spherical body. The equilibrium oblate form of a rotating body has ellipticity ϵ determined by the ratio of angular kinetic energy to gravitational energy, so that

$$\epsilon = \frac{2\pi^2 I \nu^2}{GM^2/r}. \quad (15.3)$$

If, in adjusting to a reduction in ν , the ellipticity changes by $\Delta\epsilon$, the strain energy released is proportional to $\mu V(\Delta\epsilon)^2$, where μ is the shear modulus of the crust and V its volume. The crust has a very strong crystal structure, with a high value of shear modulus. The energy released in a typical Crab glitch is about 4×10^{39} erg, as compared with a total stored oblateness gravitational energy of 2×10^{42} erg. A similar glitch could therefore be expected to occur every few years during a lifetime of 10^3 years, much as observed.

For the Vela Pulsar, the results of this calculation are totally different. If the much larger timing discontinuities are to be such ‘crust quakes’, the ellipticity would have to change by over 3% in a single step, while the energy released would be so great that such events would necessarily be separated by hundreds of years instead of the observed two or three years.

Although crust cracking may be part of the phenomenon in the Crab-like glitches, a different explanation involving differential rotation between the liquid and solid components of the neutron star is necessary.

15.8 Two-Component Models: Crust and Superfluid

Both the step and the exponential recovery after a typical glitch indicate that the pulsar does not rotate as a single rigid body but that it has two components that are only loosely or intermittently coupled together. The component with the majority of the moment of inertia comprises the solid crust and most of the interior neutron superfluid. The minor component is part of the superfluid that can rotate independently but is loosely or intermittently coupled to the solid crust. The steady slowdown of rotation resulting from the external electromagnetic torque on the crust may leave the minor component rotating faster than the crust, by a differential amount depending on the frictional forces coupling the two components. Alternatively, the liquid component may be completely decoupled from the spindown, continuing to rotate at a fixed rate between glitches; in this case, the moment of inertia of the decoupled liquid is effectively removed, and the observed spindown rate is increased. The step increase in rotation rate at a glitch results from a sudden increase in coupling between the two components, which speeds up the crust and slows down the liquid. In other words, during slowdown, the angular momentum of the minor component is not transferred steadily to the crust but is released spasmodically.

The solid component, to which the dipole magnetic field and the radio beam are attached, consists of the crust and all those parts of the fluid that are tightly coupled to it. This must include the electron and proton components of the inner neutron fluid, which are coupled to the crust by the magnetic field (Alpar *et al.* 1981). The separately rotating component is to be identified with that part of the neutron superfluid that co-exists with the crystal lattice in the inner part of the solid crust (see Figure 13.2). The process of coupling and uncoupling between the crust and the superfluid is an unfamiliar concept that we now describe.

15.9 Vorticity in the Neutron Fluid

We recall that the outer crust of a typical neutron star is about one kilometre thick, the total radius being about 11 km. The inner part of the crust is a crystal lattice

of neutron-rich nuclei, permeated by a free neutron fluid. Further inside the star, the liquid interior is composed mostly of neutrons, in equilibrium with a small fraction of electrons and protons. These two neutron fluid regions are in different states of superfluidity. As in the Bardeen, Cooper and Shrieffer (BCS) theory of superconductivity, the attractive force between neutrons with energies close to the Fermi energy leads to pairing, and their energy spectrum then shows a gap of order 1 MeV wide. The superfluid within the crust involves 1S_0 pairing; at the greater densities of the interior, the pairing is 3P_2 , giving an anisotropic superfluid.

Rotation in a superfluid is not a uniform co-rotation of the whole volume; instead it is in the form of vortices. Each vortex carries a quantum of angular momentum, so that the angular velocity of the superfluid core is measured by the area density n_v of the vortices (Ruderman, Zhu & Chen 1998):

$$n_v = 2m_n\Omega/\pi\hbar \sim 10^8/P_{\text{sec}} \text{ m}^{-2}, \quad (15.4)$$

where m_n is the neutron mass.

For the Crab Pulsar, with angular frequency 200 rad s^{-1} , there are about 3000 vortices per square millimetre. Each vortex is very small: the core of a vortex is of order 10^{-11} mm across. As the pulsar slows down, the rotation of the superfluid can only keep pace by a reduction in the density of vortices, that is, by an outward migration of the vortices at radius r from the rotation axis at a velocity $r\dot{\nu}/\nu$; for the Crab Pulsar, the vortices near the equator move outward at $3 \times 10^{-7} \text{ m s}^{-1}$.

The rotation of the main bulk of the superfluid is tightly coupled to the rotation of the crust. This occurs through the small population of electrons and protons in the neutron fluid: the electrons are coupled to the magnetic field of the crust, and they are also coupled to the vortices through magnetic forces. In this interior superfluid, there is therefore a steady outward migration of vortices to keep pace with the pulsar's rotational slowdown.

A different regime is found in that part of the superfluid that penetrates the inner parts of the crystalline crust. Here the nuclei themselves contain superfluid neutrons, and there is an interaction between the vortices and the nuclei. As pointed out by Anderson and Itoh (1975), the vortices may become pinned to the nuclei, and so are unable to migrate outwards. The angular momentum of this superfluid component is then fixed, and this component is then effectively decoupled from the crust and makes no contribution to the moment of inertia of the neutron star. The glitch is understood as the catastrophic breakdown of this pinning, when the vortices become free to move outwards, and angular momentum stored in the pinned vortices is suddenly shared with that of the rest of the neutron star, giving the observed speed-up. Pinning and unpinning may occur in several discrete regions, which are spatially isolated and act independently, giving a variety of glitching patterns within individuals and between different pulsars.

The equilibrium state is not a complete pinning in all regions but a steady outward creep of vortices through the crystal lattice. The rate depends on the energetics of the pinning, on the temperature and on the differential rotation rate between the creep region and the crust. Immediately after a glitch, the vortex density is close to that required by the rotation rate of the crust, and the vortices may become completely pinned. As the crust slows down, the differential rotation increases, and a force (the *Magnus force*) develops to break the pinning. A combination of thermal excitation and the Magnus force may then establish a steady creep of vortices, with an averaged lag of angular velocity, or there may instead be a catastrophic unpinning, giving another glitch.

The transient recoveries after a glitch are interpreted in terms of the re-establishment of vortex creep in a reservoir that has been discharged at a glitch. The recovery restores the differential velocity exponentially, with a time constant depending on the pinning energy and the temperature (Alpar, Cheng & Pines 1989). The energy dissipation in post-glitch relaxation has been discussed by Jones (2002).

Averaged over a long period, both the periodic and the random glitches involve around 1–2% of the total moment of inertia of the neutron star. At a periodic glitch, the whole or the majority of this component becomes unpinned, while in the smaller random glitches, only part is unpinned. A glitch may involve only a small number, possibly only one, of discrete regions of pinning; these are referred to as *reservoirs*.

Both the intervals between glitches and their sizes may extend over a range of several decades in a single pulsar; within this range the phenomenon is *scale invariant*. This behaviour is often described as analogous to the ‘sandpile effect’, in which a continuous trickle of sand causes an erratic series of avalanches with similarly random characteristics. Such systems are known as self-organised critical systems (Jensen 1998). In a system of self-organised criticality, an overall driving force (in this case the rotational slowdown) is balanced in the long term by the average effect of local relaxations, while on a shorter time scale, the random effects depend on the detail of the reservoirs and their collective unpinning behaviour.

15.10 Pinning and Unpinning

An individual vortex unpins when the pinning force is overcome by the Magnus force plus thermal excitation. The unpinned vortex then disturbs the local superfluid velocity field and with it the local Magnus force, leading to further unpinning of neighbouring vortices and the avalanche discharge of a reservoir. A very large number of vortices unpin at a glitch: a step of 1 μHz in rotation rate corresponds to about 10^{10} unpinning together. The discharge of an individual reservoir leaves a legacy in the pattern of the Magnus force, affecting the pattern of subsequent

glitches. Warszawski and Melatos (2008) model this interaction as an example of self-organised criticality.

The sites of pinning in the crystal lattice of the crust may be mechanical defects or quantum wells in a smooth structure. The defects may be related to crust cracking, in which case the pinned vortices in the reservoirs may be closely spaced. If they are quantum wells, there may be many more sites than vortices, so that pinned vortices may be separated by 10 or more possible sites; it is then not clear how neighbouring vortices are influenced to act collectively. An alternative to the interaction of neighbouring vortices in the latter case is presented by Melatos and Warszawski (2009): they show that thermal noise combined with a statistical variation in pinning force can produce the same collective behaviour.

For further details of glitch models, consult a review by Haskell and Melatos (2015).

15.11 Summary of Glitch Theory

We can now interpret the step changes at the various types of glitch in terms of vortex pinning as follows:

1. Quasi-periodic glitches, as in the young pulsars PSR J0537–6910 and the Vela Pulsar. Here the whole, or a large proportion, of the pinned vortices unpin and move outward together. The detailed observations of Vela (Figure 15.7) show a slowdown rate that increases catastrophically at the glitch and decreases steadily between glitches. Here the steady decrease in slowdown rate represents a progressive increase in coupled superfluid, corresponding to a progressive unpinning as the differential in angular velocity increases.
2. Old pulsars, where there is only a step in rotation rate, with no recovery and no long-term change in slowdown rate. Here the glitch involves superfluid pinned in a random selection of one or more discrete reservoirs. At the glitch, the vortices are completely released from pinning at the glitch, moving outwards to reduce the area density of vortices until the superfluid rotation rate is reduced to that of the crust and then completely repins. It remains pinned between glitches. About 1–2% of the total moment of inertia is involved in this stepping behaviour.
3. Crab-like glitches, where the main effect is a cumulative increase in slowdown rate at each glitch. Here the theory requires a progressive increase in the quantity of pinned superfluid, decreasing the effective moment of inertia at the mean rate of about 7×10^{-5} per year. This must be a short-lived phase, related to the youth of this pulsar; if it progresses at the same rate for only about 100 years, 1% of the total moment of inertia will be locked up in pinned superfluid, and there will be a large store of angular momentum waiting to be released in a later phase. Similar behaviour is observed in PSRs B0540–69, B1119–6127 and B1509–58.

15.12 Alternative Glitch Theories

As we noted earlier, the cumulative increase of slowdown rate at the glitches in the Crab Pulsar would lead, on the vortex pinning theory, to a build-up of pinned vortices that are not released at later glitches. These regions of accumulating pinned glitches would be domains with high angular velocity, which must remain frozen without release at the glitches. Alternatively, the increase of slowdown rate might be accounted for by an increase in external torque, that is, an increase in the strength or a change in configuration of the external magnetic field, to account for these changes in slowdown rate, as suggested originally by Link, Epstein and Baym (1992) and by Alpar *et al.* (1996). This suggestion is supported by analysis of the long-term slowdown of the younger pulsars and speculation on the origin of the magnetars (Chapter 11).

Since the magnetic field is firmly attached to the crust, an increase in field strength points to a crust cracking theory introduced by Ruderman (1991), in which the configuration of the external magnetic field is changed by movements of surface plates. Such movements might be in response to changes in ellipticity as the rotation slows down, or in response to internal stresses. As already noted, the interval between glitches in the Crab Pulsar is close to the calculated interval between crust crackings, and the theory does provide some overall simplification.

Crust cracking cannot, however, provide an explanation for the interval between glitches in older pulsars. The stepping behaviour shown in Figure 15.9 is simply

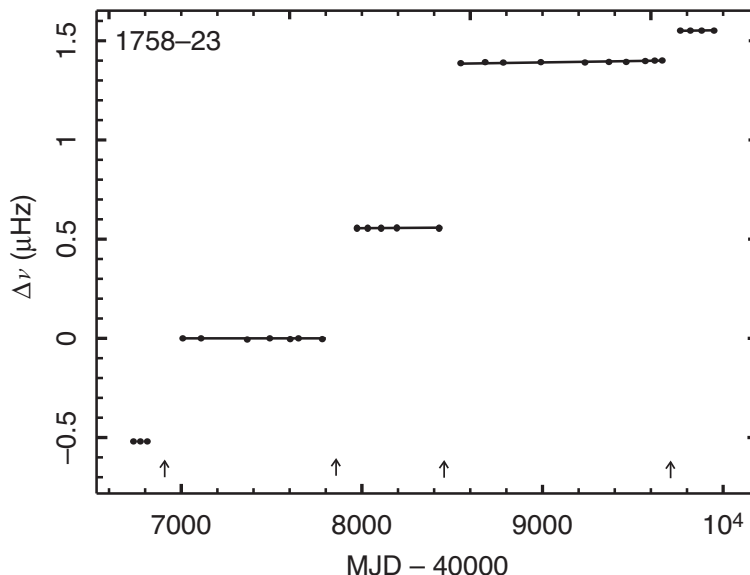


Figure 15.9 A series of glitches in PSR B1758–23 (Shemar & Lyne 1996).

explained as a catastrophic breakdown of pinning when a sufficient differential velocity has built up. The situation in the Vela Pulsar (Figure 15.7) is not as easily understood: the sawtooth effect in slowdown rate indicates only that the glitch occurs when progressive unpinning has reached a limit that triggers the catastrophe.

The two interacting components in most models are the neutron superfluid within the solid crust and the crust itself. An alternative possibility is to identify them with the two quantised structures within the fluid core, that is, the rotational vortices and the lattice of magnetic flux tubes. Chau, Cheng and Ding (1992) point out that the neutrons in the core form a 3P_2 paired superfluid, while the protons form a 1S_0 superconductor. The two systems, vortex and field lines, interact. The effect is similar to the pinning within the crust: the flux tubes are fixed to the solid crust, so that the outward flow of the rotational vortices is impeded by the interaction between the two systems. Jahan-Miri (2010) shows that the differential rotation between the vortices and the field lines can grow to a critical level at which there is a catastrophic breakdown, when the vortices transfer angular momentum to the crustal system and a glitch is observed.

The glitch phenomenon is evidently very rich, and the interpretation in terms of changes in the interior structure is correspondingly complex.

15.13 Timing Noise

Pulsars, and especially millisecond pulsars, are very good clocks. Even the normal pulsars are stable to an accuracy of one part in 10^{11} or better (after allowing for the steady increase in period as they slow down), apart from the rare discontinuities described earlier in this chapter. At this accuracy, however, there are often clearly discernible and apparently random irregularities in the periods. These are measured as phase deviations in the rotation of the pulsars, on the assumption that pulse timing is exactly synchronised to pulsar rotation.

Timing noise is a general term for fluctuations in time of arrival of pulsar signals remaining after full account of all known astrometric factors, as in Chapters 5 and 6. Apart from components introduced by the receiver, timing noise originates both in the pulsar itself and in propagation through the ionised interstellar medium (the ISM). Propagation noise is recognisable by its frequency dependence, which in principle allows its removal in multi-frequency observations. Timing noise originating in the star itself is referred to as *spin noise*. It is observed on a wide range of time scales but is usually characterised as ‘red noise’ (Shannon & Cordes 2010). The exact shape of the residual curves in plots such as Figure 15.10 depends on the way the fit is made and the length of the sequence under analysis. Unfortunately, as can be seen from the figure, the noise often appears to have a component with a periodicity close to the duration of the observations, and only more prolonged

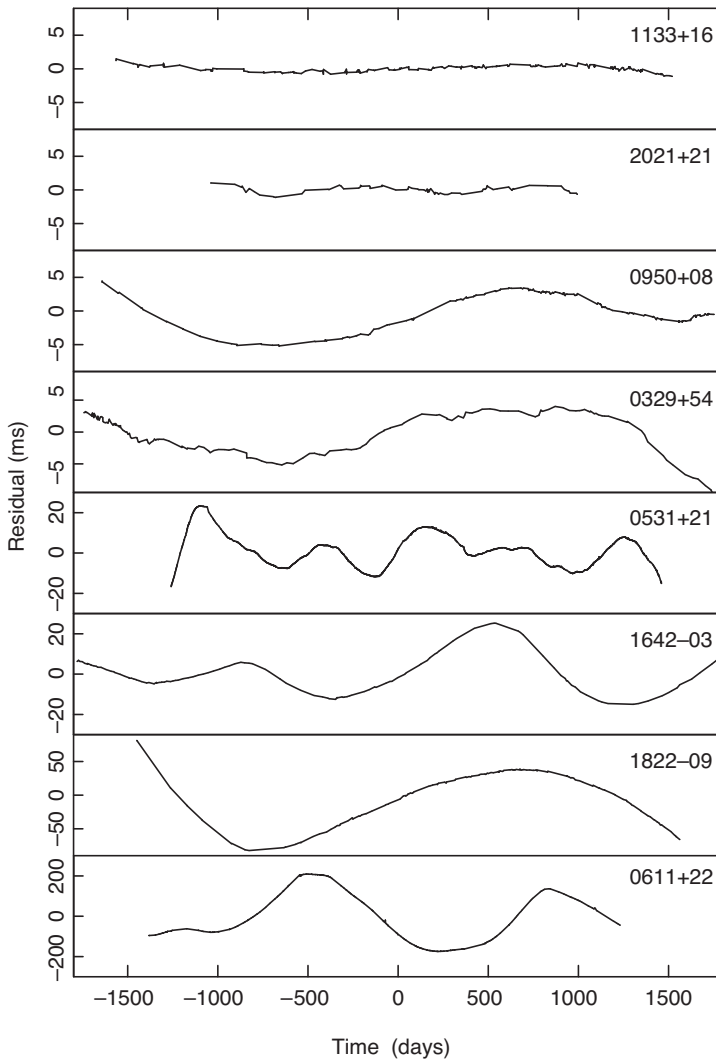


Figure 15.10 Timing noise from observations of eight pulsars at Jodrell Bank Observatory.

observations can reveal its true nature. An activity parameter Δ_8 introduced by Arzoumanian *et al.* (1994), which represents the noise as a variation in slowdown rate, is a useful representation; it is defined in terms of the differential \ddot{v} in the Taylor series

$$\phi = \phi_0 + vt + \frac{1}{2}\dot{v}t^2 + \frac{1}{6}\ddot{v}t^3 + \dots, \quad (15.5)$$

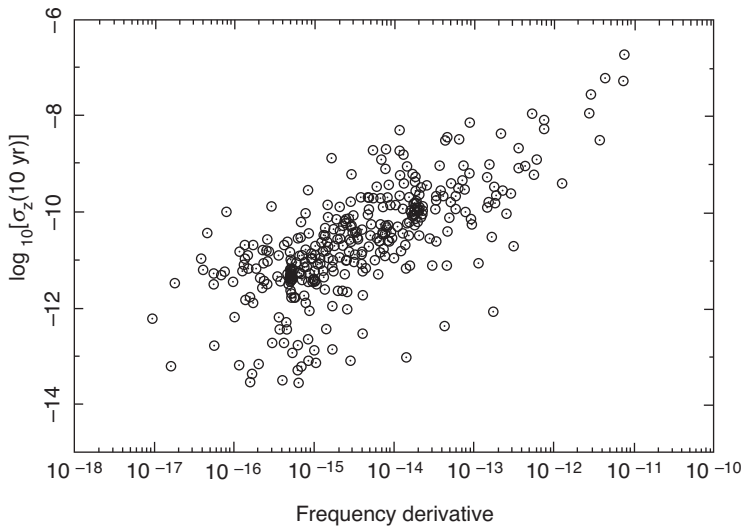


Figure 15.11 The relation between timing activity and the absolute value of the slowdown rate $\dot{\nu}$ (Hobbs, Lyne & Kramer 2010).

which is fitted to the observed pulse phase ϕ . The fourth term represents departures from the expected rotation and slowdown rates, averaged over a defined data span, usually 10^8 seconds. Then the activity parameter is defined as

$$\Delta_8 = \log_{10} \left(\frac{1}{6\nu} |\ddot{\nu}| t^3 \right). \quad (15.6)$$

The young pulsars are almost always the most active ones, and it is evident that noise activity, like glitch activity, is related either to the rate of slowdown or possibly to age. Hobbs *et al.* (2010) used the archive of timing data at Jodrell Bank, extending over 36 years and comprising over 6000 years of pulsar rotational history, to establish the relation between activity (measured over a 10 year span) and other parameters (rotation rate ν , slowdown rate $\dot{\nu}$, age $\propto \nu/\dot{\nu}$, dipole field $\propto \dot{\nu}^{1/2}\nu^{-3/2}$, rotational energy loss $\propto \nu\dot{\nu}$). They find a good correlation between activity and slowdown rate, as shown in Figure 15.11.

Dispersive timing noise due to the ISM, referred to as DM noise, may be due to random interstellar scattering or to multipath propagation in discrete clouds of ionisation. The frequency dependence of propagation time depends on the geometry, so compensation may be possible by observing on more than two separate frequencies. Keith *et al.* (2013) discuss the correction of pulse arrival times in recordings of MSPs to the high accuracies demanded by pulsar timing arrays (PTAs) using multi-channel receivers. It has been noted by Cordes *et al.* (2016) that chromatic effects

due to the different volumes of the ISM seen by the different frequencies might ultimately limit how well the dispersive effects can be corrected.

Major efforts are being made to characterise and correct for timing noise using PTAs to detect gravitational waves. Lentati *et al.* (2016) report on preliminary results of the international cooperation IPTA between three such arrays, which aim for accuracies down to 10 nanoseconds (a propagation distance of 3 metres). The results of 9 years of observations of 37 MSPs with the NANOGrav system indicate that 26 show timing noise in excess of the expected white noise (Lam *et al.* 2017).

The origins of spin noise might be within the star, possibly related to differential rotation of the superfluid, or in the magnetosphere, where instabilities in the radiation process may alter the radiation pattern, as described in the next section.

15.14 Slowdown Switching

A major component of timing noise in older normal pulsars is closely related to pulse nulling and mode changing (Chapter 8). Lyne *et al.* (2010) found that mode switching was also correlated with changes in slowdown rate. Figure 15.12 shows the effect for 17 pulsars observed over a period of several years. The implication is that a global change occurs in the configuration of the magnetosphere, including a switching of the dipole field responsible for the slowdown rate. The effect on precision timing may be important, requiring a recognition of the separate modes and allowance for the different values of \dot{v} .

Switching in slowdown rate was first observed in PSR B1931+24, a pulsar that switches between two modes of radio emission, normal pulses being observed for 5 to 10 days followed by a period of about 25 days in which no pulses can be detected. Kramer *et al.* (2006a) found that the slowdown rate differed by 50% between these two modes, the greater rate coinciding with the normal radiating mode. Lyne *et al.* (2010) then found that, for several older pulsars, timing noise is similarly not random but is characterised by an alternation between two or more slowdown rates, differing by around 1%. Lyne *et al.* also found that the integrated pulse profile switched between two slightly different shapes at the same time.

The origin of switching, and the varied time scales involved, are not understood, but the association between changes in pulse profile and slowdown rate suggests a step change in the magnetosphere, possibly originating as an alternation between two quasi-stable states of the magnetic field inside the neutron star, as suggested by Timokhin (2010).

It remains to be discovered whether all timing noise is attributable to such a switching process. If in any pulsar there are two distinct slowdown rates, and if these can be identified by distinguishing between two different pulse profiles, then

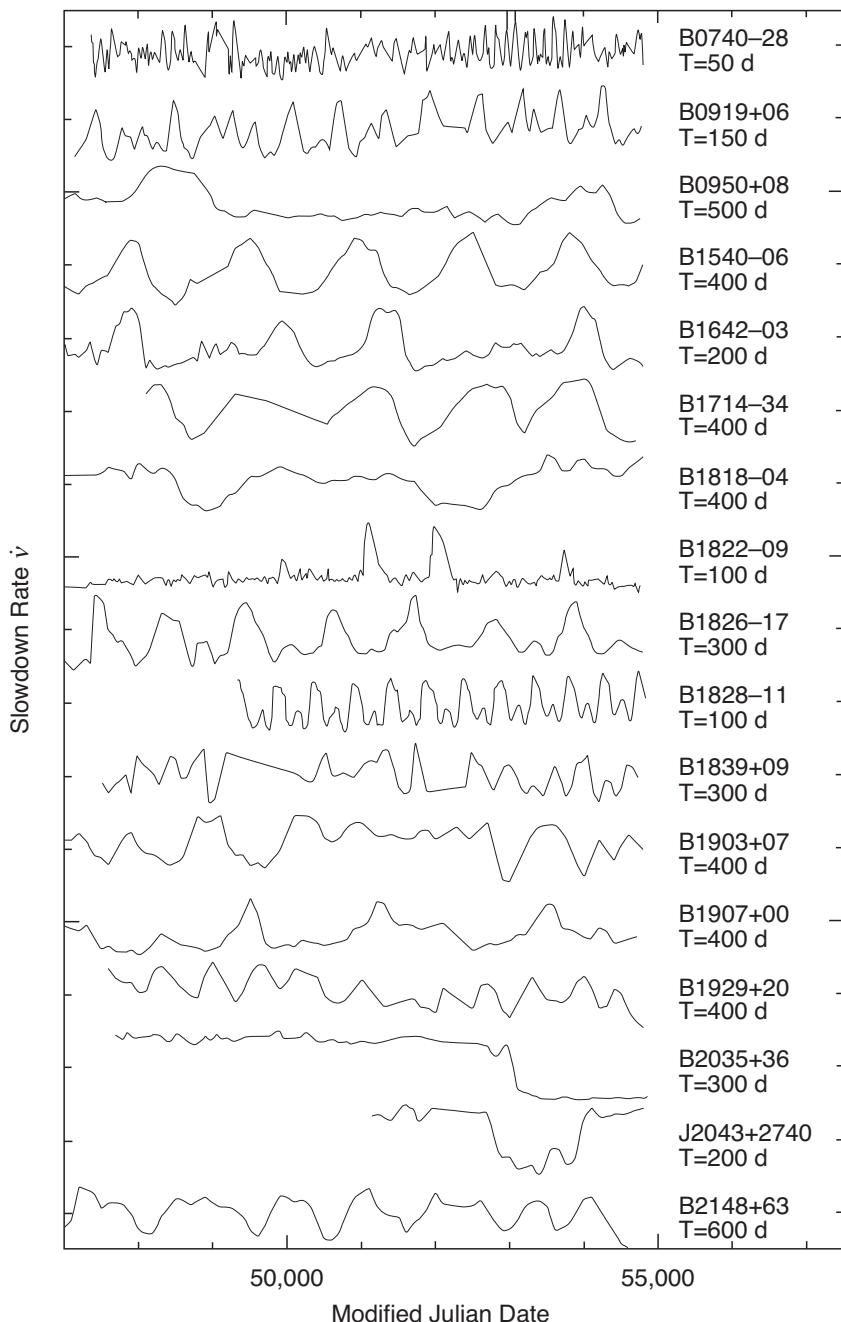


Figure 15.12 Quasi-periodic step changes in slowdown rate in 17 pulsars (Lyne *et al.* 2010).

the long term timing performance of the pulsar as a clock can be greatly improved. Although, as discussed in Chapter 5, pulsar clocks may never attain the performance of advanced atomic clocks, a network of regularly observed and corrected pulsar clocks has potential for the detection of very low frequency cosmic gravitational waves.

15.15 Precession

When all corrections have been made and the pulse times can be regarded as emission times at the pulsar, the differences between observed times and a smoothly running clock form a pattern that is characteristic of the pulsar itself. The main component is a uniform rotational slowdown; when the effect of this is removed, we see only irregularities in rotation. For some pulsars, and in particular PSR B1828–11, there is a quasi-periodic component in the timing noise, with a period of order one year or more, which was attributed to free precession by Stairs *et al.* (2000b). Although this attribution is now known to be incorrect (Section 15.14), any example of free precession that can be substantiated would be important because of its implications for the internal rotational dynamics of the star. We therefore briefly describe free precession, which is the behaviour of a spinning body, isolated from any external influence, which is perturbed so that the spin axis is not precisely aligned with its total angular momentum vector. We discuss separately geodetic precession of a pulsar in a binary system, which is a well-established relativistic effect (Chapter 6) with no implications for internal dynamics.

The equilibrium shape of a rotating neutron star is an oblate spheroid, with small eccentricity. The star may be rigid enough to preserve its shape even if the rotation axis does not coincide with the principal axis of its moment of inertia; in free precession, the rotation axis then traces a small circle centred on the total momentum direction. The main effect that this has on a pulsar timing signature is due to the periodic variation in the angle α between the magnetic dipole axis and the rotation axis, which is observable as a variation in slowdown rate. Precession may also be observed as a variation in pulse profile, since a wobble in rotation will cause the line of sight to cut across the radiated beam at a differing polar angle. For a biaxial rotator, the angular precession rate ω_p should be the rotation rate ω multiplied by the relative difference $\frac{\Delta I}{I}$ in moment of inertia in two orthogonal axes.

If the slowdown follows the standard theory of magnetic dipole radiation, then $\dot{v} \propto \sin^2 \alpha$, where α is the angle between the rotation axis and the magnetic dipole. If the amplitude θ of the precession is small, then $\sin \alpha$ becomes $\sin(\alpha + \Delta\alpha)$, where $\Delta\alpha = \theta \cos \omega_p t$. The ratio of slowdown rates with and without precession becomes

$$\frac{\Delta(\sin^2 \alpha)}{\sin^2 \alpha} \approx 2\theta \cos \omega_p t \cot \alpha, \quad (15.7)$$

giving a sinusoidal modulation of $\dot{\nu}$ with amplitude $2\theta \cot \alpha$. A second harmonic component would be expected in a nearly orthogonal alignment, with α close to 90 deg (Jones & Anderson 2001; Link & Epstein 2001). A necessarily more complex analysis of triaxial rotators has been presented by Akgun *et al.* (2006).

A serious difficulty in the theory of precession is the behaviour of the liquid components of the neutron star in the inner crust and the core. A normal viscous liquid would simply damp the precession; the liquid is, however, a superfluid in which the rotation is manifested as quantised vortices that may be pinned to the crystal lattice of the crust. Jones and Anderson (2001) and Link (2006) showed that slow precession can only occur if there are no pinned vortices: if the vortices are pinned, their reaction on the crust would mean that no slow precession would be possible. On the other hand, the vortices within the core are not free to realign during precession, since they would have to cut across a lattice of magnetic flux tubes.

Despite the difficulties in interpreting periodic timing effects as precession, the question is still open. Kerr *et al.* (2016) found 7 examples of long-period modulation among 151 young pulsars. They point out that the only plausible explanation for such long time scales (apart from the unlikely existence of similar planetary systems associated with each pulsar) is precession. Further, they suggest that other phenomena with similar time scales may be regulated in some way by precession.

16

Location and Geometry of Emitters

In this chapter, we bring together the observational evidence of pulse profiles from Chapter 8 and the theory of the magnetosphere from Chapter 13. The source of emission in the high-energy profiles, primarily observed in gamma rays, and also in some young pulsars with high spin-down energy, is located in the outer part of the magnetosphere, while the radio emission from the ‘normal’ radio pulsars, that is, excluding the youngest pulsars and those that have been spun up, or ‘recycled’, originates closer to the base of the magnetosphere, over the polar caps.

16.1 High-Energy Emission: The Outer Gap and Current Sheet

Among the 1451 entries in the first Fermi LAT catalogue of gamma-ray sources (1FGL; Abdo *et al.* 2010a) there were 8 MSPs. These are all known radio MSPs, and for some the main features of their integrated pulse profiles are remarkably similar between the radio and gamma-ray regimes (Abdo *et al.* 2009b).¹

Figure 16.1 shows two typical integrated gamma-ray profiles. The majority of gamma-ray profiles are double peaked, similar to the Crab Pulsar, but with peaks separated by between 0.15 and 0.5 pulse periods. A substantial proportion are single peaked. The total energy radiated from these young pulsars is predominantly in this high-energy regime; it is a considerable fraction of the spin-down energy \dot{E} . The relation of the gamma-ray luminosity to \dot{E} is shown in Figure 16.2. Part of the spread in this plot is due to uncertainties in the assumed distance, which is usually obtained from radio dispersion measures; part is due to poorly known beam shapes, which are wide but not isotropic. Allowing for these effects, the luminosity is remarkably closely proportional to between $\dot{E}^{1/3}$ and $\dot{E}^{1/2}$.

¹ The number of MSPs detected by LAT had increased to 118 by April 2020. <https://confluence.slac.stanford.edu/display/GLAMCOG/Public+List+of+LAT-Detected+Gamma-Ray+Pulsars>

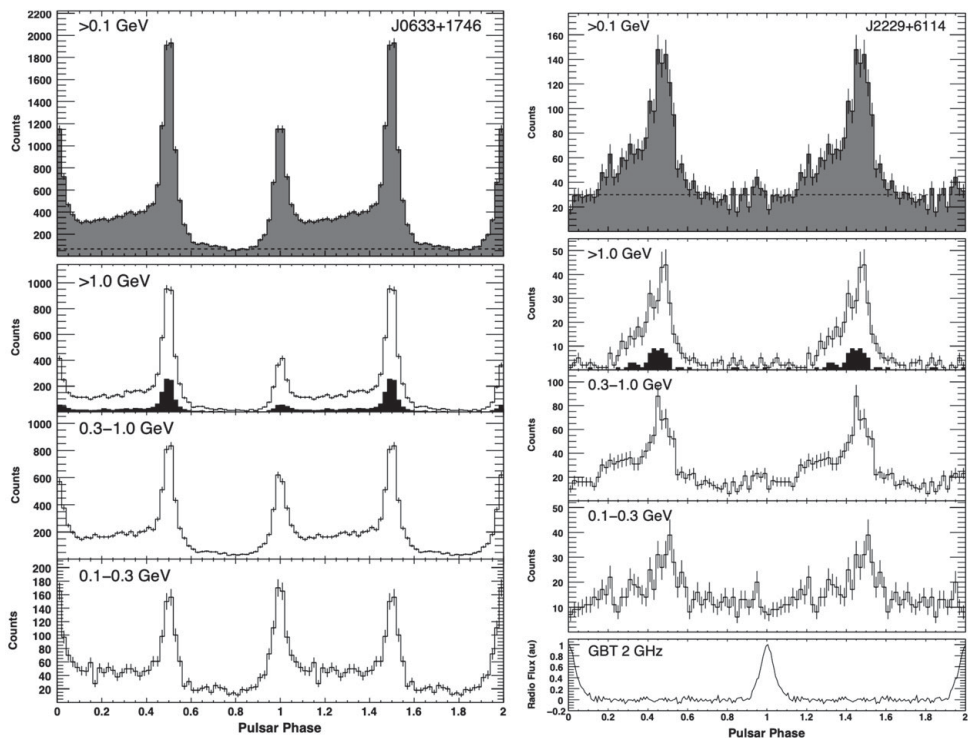


Figure 16.1 High-energy pulse profiles for J0633+1746 (Geminga) and J2229+6114, showing two complete periods. For J2229+6114 the radio pulse profile at 2 GHz is also shown (Abdo *et al.* 2010c).

In contrast to the radio polar cap emission, which is coherent, the high-energy emission is the incoherent sum of radiation from individual particles; this offers the prospect of comparing observed radiation patterns with models of energetic particle flow without the complication of coherent emission. Locating the expected site of the high-energy emission requires an analysis of currents and particle densities that extends beyond the initial 1969 model of Goldreich and Julian. In their model the magnetosphere was filled with sufficient charged plasma to cancel the large accelerating electric field E_{acc} induced by the rotating magnetic dipole. In this simple force-free (FF) model, there is no accelerating force to produce high-energy particles. Later models revealed two possible locations with low charge density, which would allow particle acceleration and consequent high-energy radiation; these are the polar cap (PC), and the slot gap (SG) at the boundary of the open field lines of the polar cap. The outer part of the latter, the outer gap (OG) between the neutral sheet (see Figure 16.3) and the velocity-of-light cylinder, appeared to be a possible

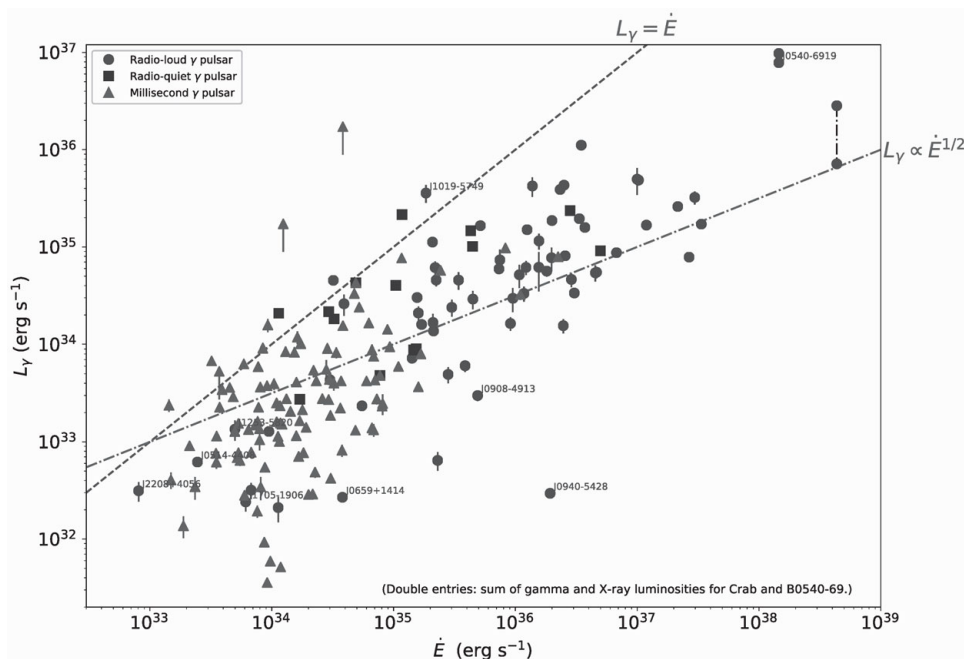


Figure 16.2 Gamma-ray luminosity versus spin-down energy. The dashed line shows $L_\gamma \propto \dot{E}$; pulsars on this line would have 100% efficiency of conversion of kinetic energy to gamma rays. The dot-dashed line represents $L_\gamma \propto \dot{E}^{1/2}$. Plot courtesy of D.A. Smith for the Fermi LAT collaboration.

location, while the PC was ruled out because high-energy radiation could not escape through the magnetosphere above it because of the pair creation process.

A full analytic model of the force-free magnetosphere does not exist, and advances on the Goldreich and Julian model instead required extensive computations tracing particle currents both within and beyond the light cylinder. These showed that the outward flow from the polar cap is balanced by a return current that is concentrated in an equatorial current sheet (ECS), which extends beyond the light cylinder. The sketch in Figure 16.3 shows the location of the ECS, which splits into a Y shape at the outer gap. The ECS is now regarded as the source of most of the high-energy radiation.

Extending the model to produce radiation patterns and intensities requires the injection of very high energy charged particles, which occurs throughout the magnetosphere by pair creation. Kalapotharakos *et al.* (2018) describe the development of the model (with useful references to earlier works) and show how the radiation depends on the rate of particle injection. Their models reproduce the observed gamma-ray pulse shapes and spectra, including models with several different

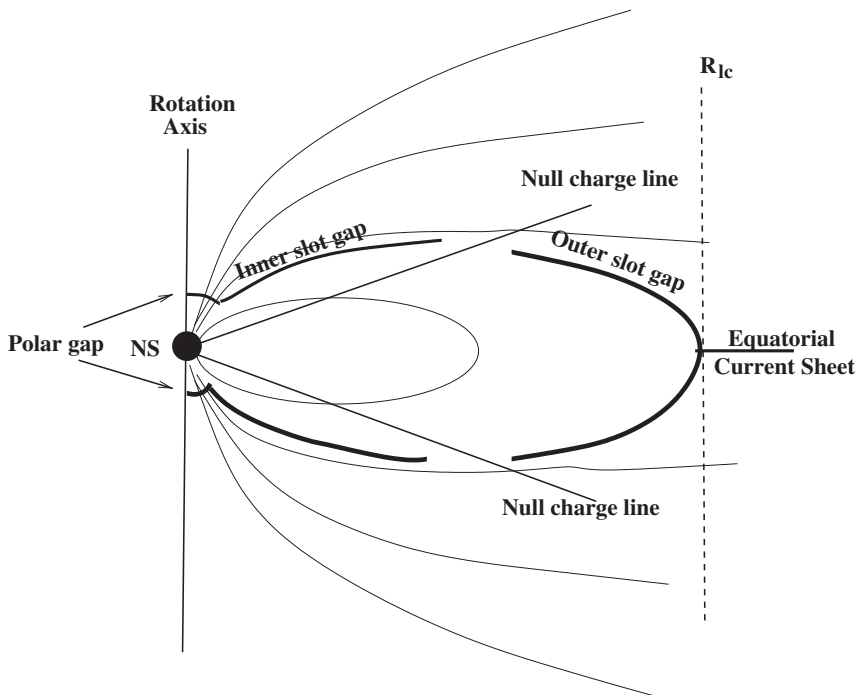


Figure 16.3 A sketch showing the locations of the polar cap, the inner and outer gaps, and the equatorial current sheet for a pulsar magnetosphere in which the magnetic dipole and rotation axes are aligned.

inclination angles α of the magnetic pole. Their analysis also applies to the gamma radiation from the Vela Pulsar, representing the young pulsars, in which they also account for the optical and infrared radiation (Harding *et al.* 2018).

A simple explanation of the typical high-energy double peak profile is in terms of radially outward-directed emission from the equatorial current sheet. If this extends round the magnetic equator, it forms a flattened torus at an angle to the rotation equator; this is the polar inclination angle α . As the pulsar rotates, the observer's line of sight then cuts the torus twice, giving a double peak with separation depending on α . At any phase of the pulse cycle, the emission comes from an extended source; it is often referred to as emission from a caustic.

16.2 Normal Radio Emission: The Polar Cap

An observed radio pulse profile depends on the way in which the radiation beam is cut by the line of sight to the observer as the pulsar rotates. The radiation beam from a normal pulsar is contained within a cone of field lines above a magnetic pole,

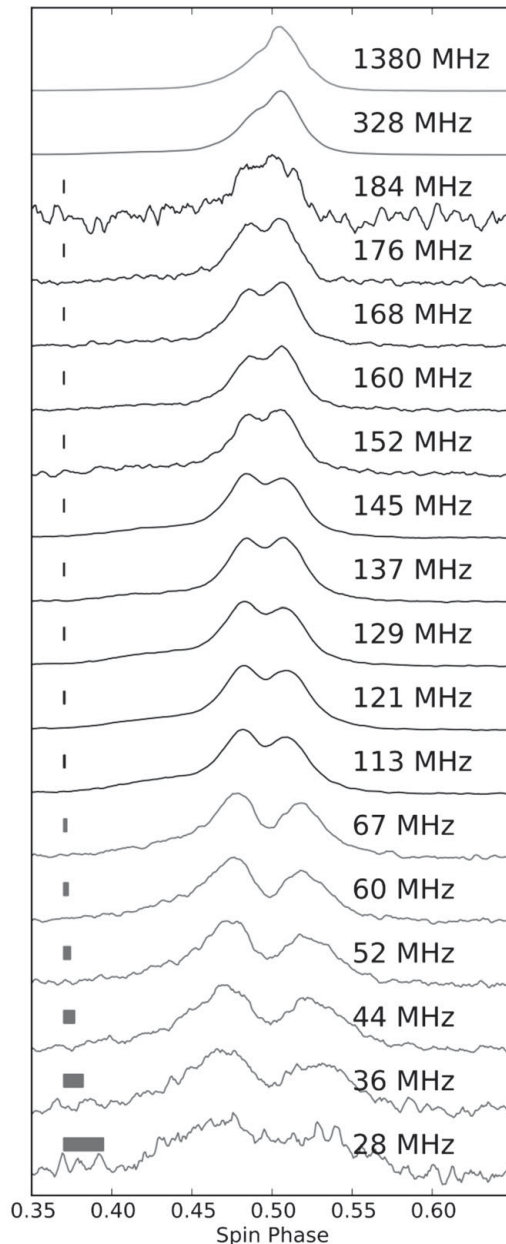


Figure 16.4 Pulse profiles of PSR B0950+08 from 28 to 1380 MHz (Pilia *et al.* 2016). Where present, the grey bar indicates the degree of broadening of the profile due to uncorrected dispersive effects.

although the emission is not distributed uniformly within the cone. Some profiles are notably symmetrical, suggesting a simple organisation of component beams within the cone; if this is universal, the unsymmetrical profiles observed in other pulsars are explained by weak or missing components.

The overall profile width is conventionally measured to 10% of the peak intensity; the angular width (expressed in degrees of pulsar rotation) is then designated W_{10} . The profiles of some pulsars have been measured at a range of frequencies from 20 MHz to 32 GHz; the most extensive sets of observations are at 0.4, 0.6 and 1.4 GHz. A library of profiles and references is maintained at the European Pulsar Network Archive.² The profile width is almost independent of radio frequency at frequencies above 1 GHz; at lower frequencies there is a progressive expansion of the profiles of many (not all) normal pulsars (see for example profiles of PSR B0950+08 from 28 to 1380 MHz in Figure 16.4). We relate this expansion to the location of the radio emission in Section 16.5.

16.3 The Beam Geometry

We first consider the geometrical relation between the overall width of the radiated beam and the observed profile. The geometry of the radiation beam is shown in Figure 16.5. Here the beam is shown as a cone with angular width 2ρ , at an *inclination angle* α to the rotation axis. The line of sight cuts the beam at an *impact angle* β to the centre of the cone. The cone is often assumed to be circularly symmetrical, although there have been suggestions of elongation either in latitude or longitude.

For a circular beam, the radius ρ of the radiating cone can be determined from the profile width W by the relation

$$\rho = 2 \sin^{-1} \left[\sin^2 \frac{W}{4} \sin \alpha \sin(\alpha + \beta) + \sin^2 \frac{\beta}{2} \right]^{\frac{1}{2}}. \quad (16.1)$$

This relation depends on both α and β ; the variation of these parameters accounts for a large part of the scatter in the observed widths. Fortunately, the impact parameter β may be found from the polarisation characteristics within the beam since, as we see in Section 16.7, the rate of swing of polarisation position angle depends mainly on β . (This gives only the modulus of β , since the cut may be across the upper or the lower half of the beam.) The inclination angle α is usually more difficult to determine. In some pulsars the inclination is known to be close to 90 deg, since an interpulse shows that beamed radiation is received from both magnetic poles. An analysis of six such pulsars by Johnston and Karastergiou (2019) has substantially elucidated the geometry and location of the radio emitting regions. In the absence of such direct knowledge of α , it is often useful to assume $\alpha = 90$ deg and find a

² www.epta.eu.org/epndb.

corresponding value, designated ρ_{90} , for the beam radius. These calculated values of ρ_{90} will then overestimate the actual beam width when α is small, so that the distributions of ρ_{90} for a number of pulsars will have a lower limit that is related to an average actual beam width.

Independently of the polarisation swing method, the observed widths of components within the profile may be used to determine the inclination angle α (Rankin 1990). This possibility arises because the individual component beams appear to be approximately circularly symmetrical Gaussians, so that the widths of the components do not depend on the way they are cut by the line of sight; furthermore, their widths, as determined for pulsars of a given period and at a particular frequency, are found to be fairly narrowly distributed. An observed width w is simply related to a component beam radius ρ_c by

$$2\rho_c = w \sin(\alpha + \beta). \quad (16.2)$$

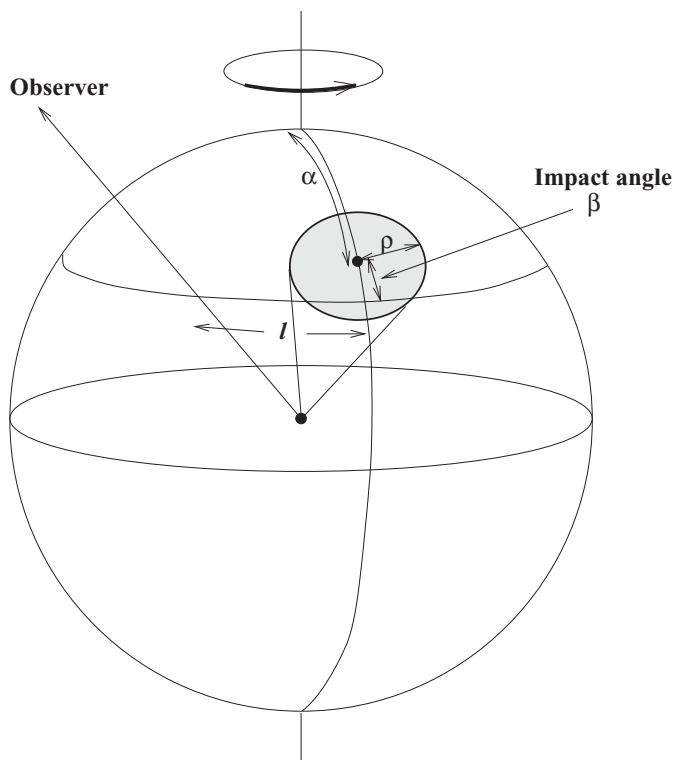


Figure 16.5 The relation of the observed profile width to the beam geometry. The radiation beam is shown as a symmetrical cone, angular width 2ρ , at inclination angle α to the rotation axis, cut by a line of sight with impact parameter β .

In most cases $\beta \ll \alpha$, so that Eqn. (16.2) can be used to determine α from the observed component widths.

16.4 Observed Profile Widths

There is remarkably little difference between the shapes of the profiles of pulsars with periods ranging from milliseconds to several seconds (although we will later distinguish two different locations for the emission from most MSPs and from normal pulsars).

There is, however, a progressive variation of angular width with period: the slowest rotator, with period 23.5 seconds, has one of the narrowest at 1 deg (Tan *et al.* 2018), while pulse profiles of short period pulsars may extend over half the period. The observed widths W_{10} , that is, without geometrical correction, are shown in Figure 16.6 for pulsars over the whole range of rotation periods, measured at a single radio frequency.

The wide scatter in Figure 16.6 is reduced in the plot of deduced beamwidths (Figure 16.7), and the clearly defined lower limit gives a beamwidth $13 \text{ deg } P^{-1/3}$ (Lyne & Manchester 1988). In similar analyses by Gil and Kijak (1993) and by Rankin (1993), the slope is found to be -0.5 , in sufficiently good agreement for our discussions. The distribution of points above the lower limit depends on the

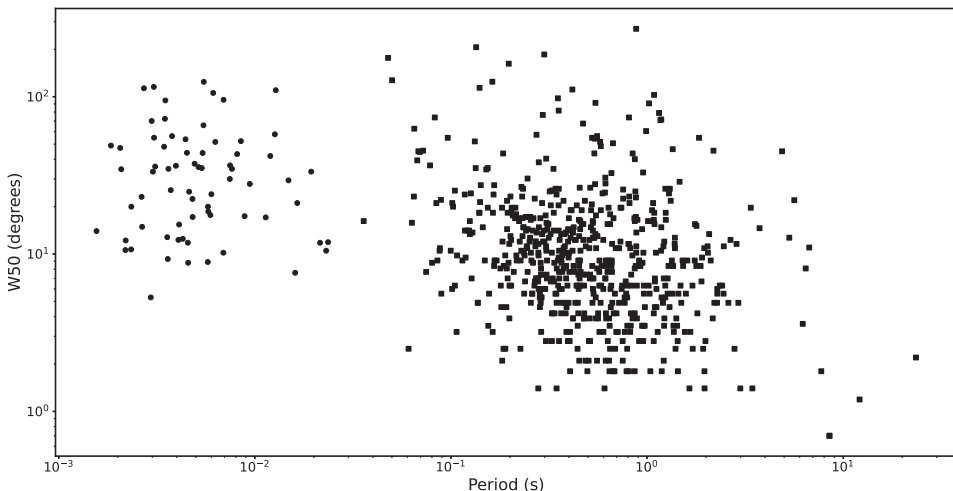


Figure 16.6 The pulse widths at 50% (W_{50}) of the maximum intensity for a selection of normal (squares) and millisecond (dots) pulsars observed at frequencies near 1.4 GHz.

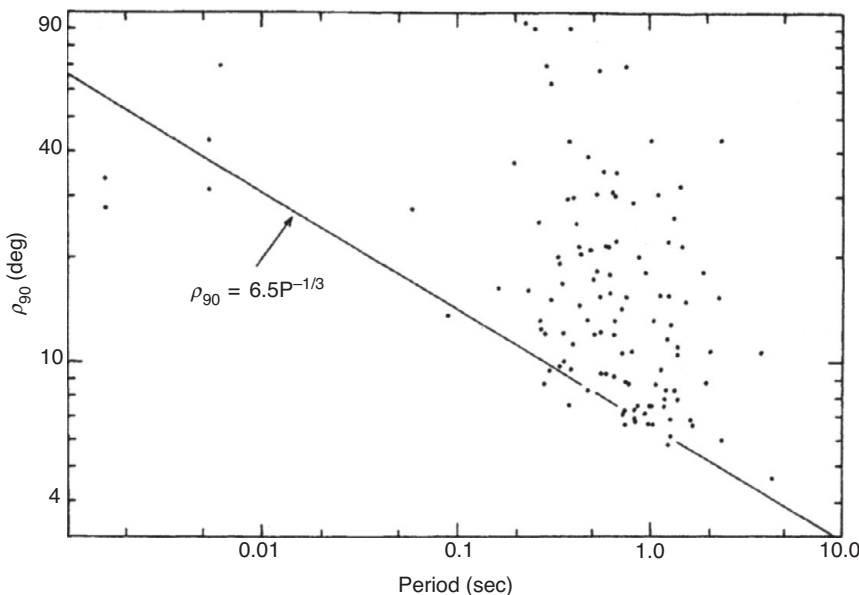


Figure 16.7 Deduced beam radii ρ_{90} as a function of period P (Lyne & Manchester 1988).

distribution of the inclination angle α . Lyne and Manchester (1988) suggest that the distribution of α shows a tendency for the rotation and magnetic axes to be more aligned in older pulsars; this is supported by Weltevrede and Johnston (2008), who remark that interpulses, which are characteristic of near orthogonality, are seldom observed in older pulsars.

16.5 Radio Frequency Dependence

The expansion of profile width at lower frequencies, as seen for example in Figure 16.4, is observed in many pulsars (but not all: see Chapter 8). It is usually interpreted as an increasing angular width of the cone of magnetic field lines containing the emitting region. The first suggestion was that the lower frequencies originated further out above the polar cap. The relation between location and frequency in this model is termed radius to frequency mapping (RFM). An alternative explanation is that the expansion at lower frequencies is due to refraction in the magnetosphere, with the emitting region being a broadband source at a single location. The location of the emitting region will be considered later in this chapter.

A third possibility is based on the concept that the pulse profile closely matches a lateral spread of the emitting region, which is confined to only a small region in height. In this case the changing profile width is due to an emission spectrum that

varies across the emitting region, the outer parts having a steeper spectrum, that is, greater intensity at lower frequencies. Large differences in spectrum would be required in this theory, but this could possibly occur, bearing in mind the non-linear coherent nature of the emission.

16.6 Sub-pulse Drifting

Sub-pulse drifting, as described in Chapter 9, is the organised movement of sub-pulses across a pulse profile. The geometry of pulse drifting is usually attributed to a carousel (Ruderman & Sutherland 1975), in which the emitting regions move in a closed track around the magnetic pole, as in Figure 16.8. As the pulsar rotates, the line of sight crosses the track either in the direction of drift or against it, giving the two opposite patterns commonly observed. No drifting would be observed if the line of sight cuts across the diameter of the track, but instead the pulse strength will be modulated as the emitters move across the line of sight.

The carousel track is usually depicted as circular as in Figure 16.8, although it might be elliptical with major or minor axis oriented on a meridian. The rare phenomenon of bi-drifting, in which opposite directions of drift are seen in two separate components of the same pulse profile, requires an interesting extension of this simple model. Bi-drifting may be attributed to an asymmetric carousel track such as an ellipse with tilted axis (Wright & Weltevrede 2017); since the magnetic field dominates the geometry of the magnetosphere, this would indicate the existence of multipole field components.

The emitting regions on the carousel were attributed by Ruderman and Sutherland to concentrations of the cascade discharge above the polar surface, referred to as *sparks*. The drift velocity is attributed to $E \times B$ forces. The location of the excitation close to the surface is supported by the observation of sub-pulse drifting in pulsars with multiple components. Drifting is often observed in several or all of the subpulse components of the more complex pulse profiles. These may often be attributed to two nested cones, each with its own carousel. Bhattacharya, Gupta and Gil (2009) show that the two drifts are phase-locked, demonstrating their common origin in the magnetic field at the polar surface.

16.7 Polarisation Geometry

An integrated pulse profile of the Vela Pulsar, one of the earliest to be discovered and now designated PSR B0833–45, is shown in Figure 8.16. This figure also shows the integrated polarisation, with the linearly and circularly polarised components shown as full and broken lines respectively. This pulsar is typical in its high degree of

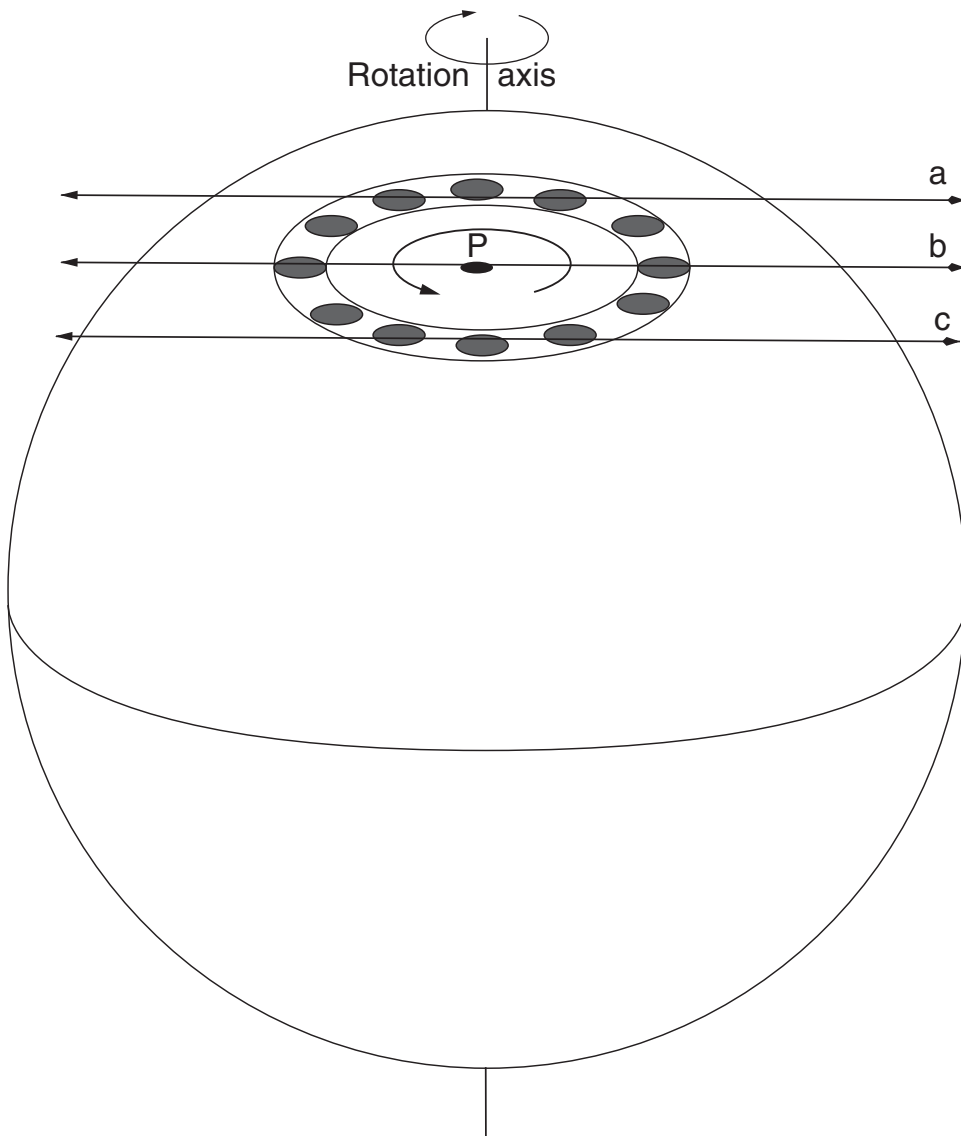


Figure 16.8 Carousel geometry, showing the circulation round the magnetic pole *P*. Lines of sight are shown crossing the track above (a), centrally (b) and below (c) the magnetic pole. Drifting will be observed in cases (a) and (c), and intensity fluctuations in (b).

linear polarisation, which approaches 100%, and in the monotonic sweep of position angle, which is shown in Figure 8.16.

The very high degree of polarisation of many pulsars is an important indicator of the physical processes in pulsar emission. The position angle of the linear

component appears to be closely linked to the orientation of the dipolar magnetic field at the emitter, and the changing position angle through the observed beam can be related to the changing aspect of the magnetic field direction in the emitting region as the pulsar rotates. The form of this change, and in particular the rate of change of position angle at the centre of the beam, is related by simple geometry to the angle of inclination α and the impact parameter β .

Radhakrishnan and Cooke (1969) showed that the sweep of position angle shown in Figure 8.16 could be fitted by a remarkably simple model, now generally known as the rotating vector model (RVM). This relates the polarisation vector to the position angle of a portion of a single magnetic field line, which is supposed to be the sole source of emission. As the single vector crosses the line of sight, its projected position angle changes smoothly in an S-shaped curve, by up to 180 deg. The rate of change at the centre of the curve depends mainly on the closest angular approach of the line of sight to the magnetic pole, providing an important indicator of the geometry of the rotating pulsar in relation to the line of sight.

The RVM assumes that the whole pulse profile originates in a single small source. The separate components of most pulse profiles appear, however, to be separate discrete sources that appear in sequence as they cross the line of sight, each on their own field line. For example, the profile of PSR B0525+21 shown in Figure 16.9 has two distinct components, which are regarded as physically separate sources within the radiating cone; nevertheless, there is a single S-shaped curve of polarisation position angle. In this and in more complex profiles, the position angle curve evidently should be interpreted as the position angles of a succession of sources as they cross the observer's line of sight. Remarkably, apart from extreme conditions where either α or β is near zero, the form of the curve is almost the same in the two interpretations (Blaskiewicz, Cordes & Wasserman 1991), and the geometry of the original RVM still applies. It is also notable that the position angle curve is usually simple and monotonic, even when the total intensity profile shows several distinct components.

The geometry of the RVM is shown in Figure 16.10. This figure shows the position angle ψ of linearly polarised radiation from a single point P. The radiation is polarised parallel to the plane of curvature of the magnetic field line through P. As the pulsar rotates, P moves across the arc ST. The zero of longitude ϕ is defined as the meridian through the magnetic axis, and position angles ψ are measured with respect to the projected direction ψ_0 of the rotation axis.

A simple expression for ψ is obtained using the angle $\zeta = \alpha + \beta$, which is the inclination of the observer direction to the rotation axis:

$$\tan(\psi - \psi_o) = \frac{\sin \phi \sin \alpha}{\sin \zeta \cos \alpha - \cos \zeta \sin \alpha \cos \phi}. \quad (16.3)$$

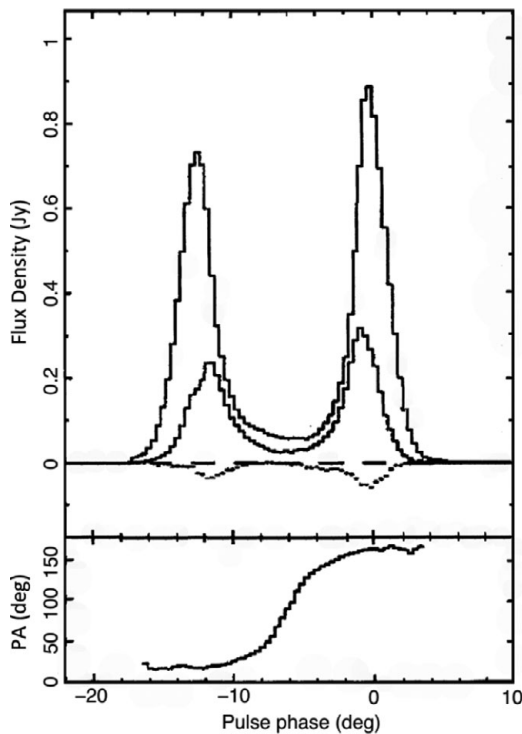


Figure 16.9 The integrated pulse profile of PSR B0525+21, showing two distinct components and a single smooth sweep of linear polarisation position angle (PA) (Weisberg *et al.* 1999).

The maximum rate of change of position angle occurs when the magnetic meridian crosses the line of sight, that is, when $\phi = 0$:

$$\left(\frac{d\psi}{d\phi} \right)_{\max} = \frac{\sin \alpha}{\sin \beta}. \quad (16.4)$$

These equations were obtained by Komesaroff (1970).

For some pulsars, unique values of α and β may be obtained from Eqn. (16.3) by fitting the full curve, but for most pulsars, the most useful quantity that can be measured is the maximum slope of the position angle curve, which is most closely related to the impact parameter β through Eqn. (16.4). Since $|\beta|$ can lie with equal probability between zero and the beam radius ρ , which is only a few degrees, while the average magnetic inclination α is expected to be 45 deg, the measured rate of swing is most sensitive to β ; indeed if there is no other information on α , it is convenient to set $\alpha = 90$ deg and $\sin \alpha = 1$. The maximum slope then gives a

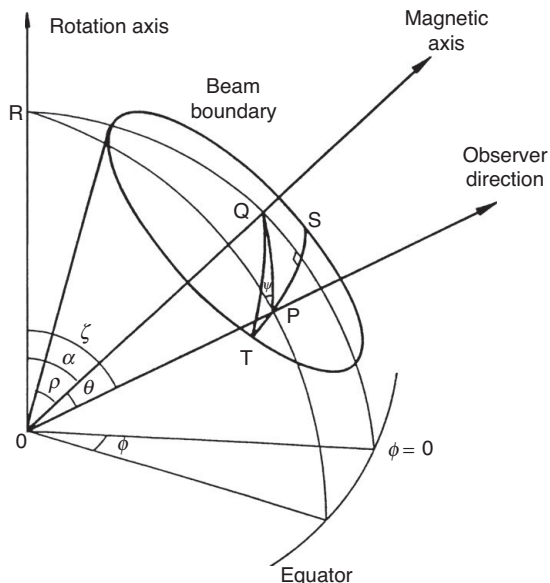


Figure 16.10 The geometrical model for polarisation position angle, showing the polarisation position angle ψ of linearly polarised radiation from a single point P that moves across the arc ST as the pulsar rotates. The zero of longitude ϕ is defined as the meridian through the magnetic axis, and position angles ψ are measured with respect to the projected direction of the rotation axis ψ_0 . The conical emission beam has an opening semi-angle ρ . The swing of polarisation position angle depends on the inclination angle α and the impact parameter $\beta = \zeta - \alpha$, which is the closest approach between the observer direction and the magnetic axis.

useful estimate of the impact parameter, which can be designated β_{90} . This estimate of the impact parameter may also be used in conjunction with measured values of the pulse width to obtain a value for the radius of the radiating beam; such a value is similarly designated ρ_{90} . The way the line of sight cuts across the radiating beam may then be specified by a normalised impact parameter, which is the ratio β_{90}/ρ_{90} .

Using the maximum slope in this way leaves an ambiguity in the sign of β ; the transit across the radiated beam may be on either side of centre. Transits respectively closer to the rotation axis and further from the rotation axis are referred to as inner and outer transits.

Compilations of beam parameters based on the analysis of component width and polarisation angles may be found in Lyne and Manchester (1988); Rankin (1990); Kijak and Gil (1997); Gould and Lyne (1998); Xilouris *et al.* (1998); Han *et al.* (2009).

16.8 Integrated Polarisation Profiles

The polarisation of the integrated profiles of most pulsars is predominately linear, and often with an S-shaped swing of position angle, but several also show considerable complexity, particularly when the degree of polarisation is small. There are steps in position angle, and usually there is also a considerable degree of circular polarisation. Both of these complexities are usually stable and broadband.

The majority of the available pulse profiles that include polarisation are from observations in the region of 0.4 GHz to 1.4 GHz. Figure 16.11 shows a selection of

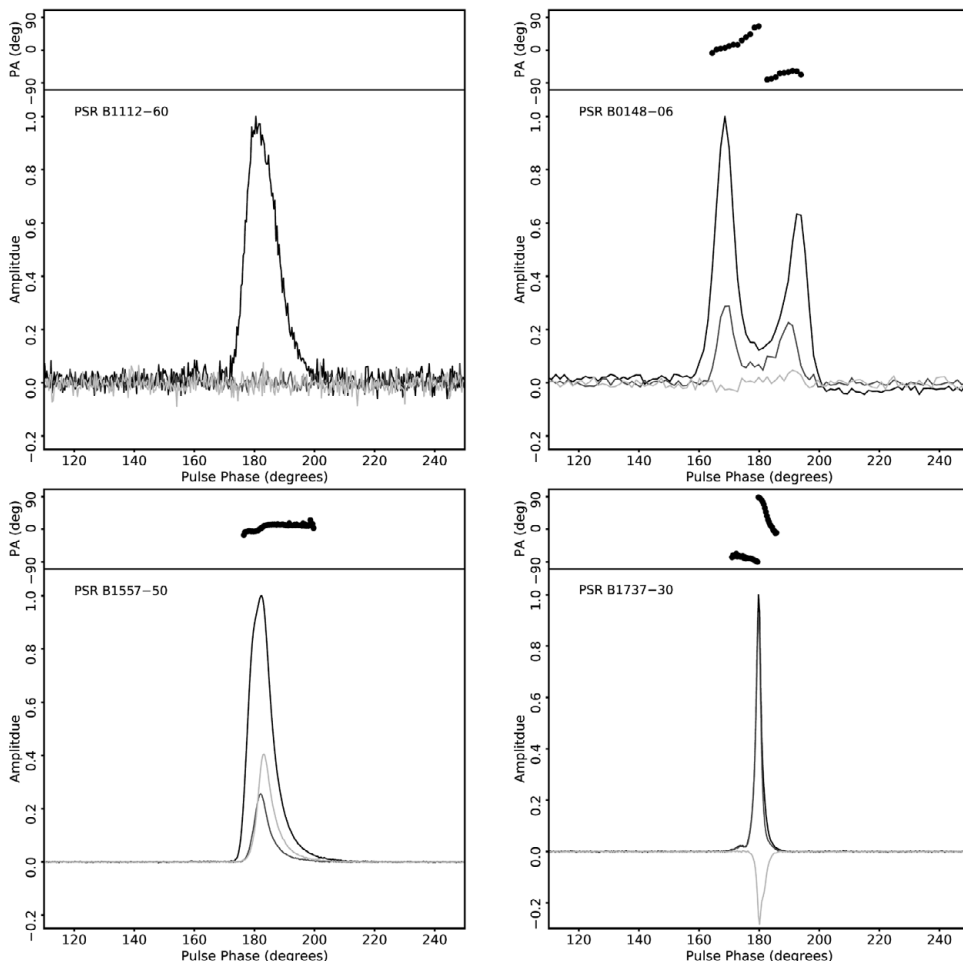


Figure 16.11 Examples of integrated profiles, showing the total intensity, the linear and circularly polarised components and the position angle of the linear component. Uses data from the EPN Pulsar data base.

integrated profiles, with linear and circular polarisation components and the position angle of the linear component. The examples are chosen to illustrate:

1. strong linear polarisation in two well separated components, with a continuous swing of position angle (PSR B0148–06);
2. polarisation less than a few percent (PSR B1112–60);
3. circular polarisation approaching 25% (PSR B1557–50);
4. polarisation approaching 100%, mostly linear but largely circular on the trailing edge (PSR B1737–30).

Observations of the swing of polarisation angle are becoming available over a wide range of frequencies for many pulsars; see for example broadband polarimetry covering 700 to 4000 MHz by Xilouris *et al.* (1996), and Oswald, Karastergiou and Johnston (2020), who included observations at frequencies up to 32 GHz. There are as yet no clear indications of any organised dependence of swing rate on radio frequency. Extending this study to lower frequencies may encounter the effects of scattering in the interstellar medium, which tends to smear all features in the pulse profile (Li & Han 2003). Noutsos *et al.* (2015) showed that some apparent reductions in swing rate observed by LOFAR are entirely accounted for as the effect of scattering. In most pulsars there is, however, a reduction of linear polarisation at frequencies above about 1 GHz; examples are shown in Figure 16.12 (see also Figure 16.16). In some pulsars there is also a corresponding increase in circular

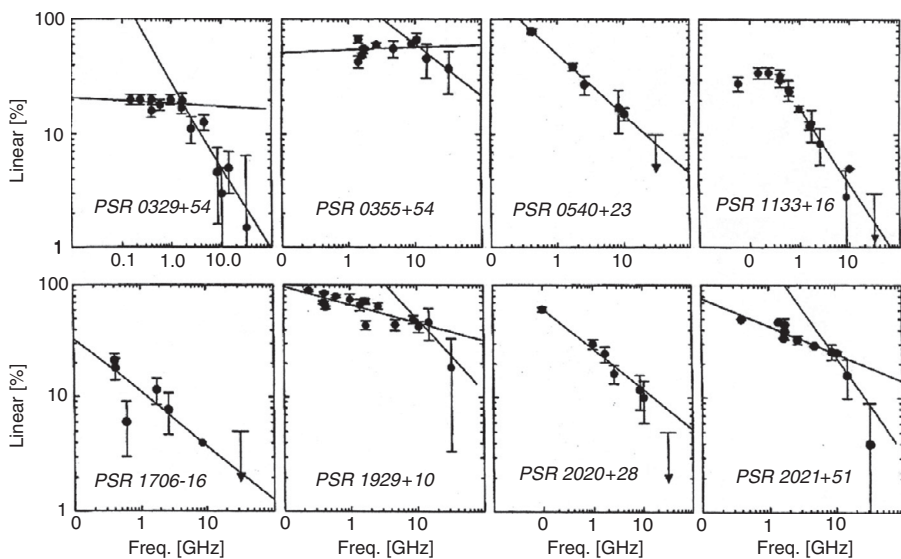


Figure 16.12 The percentage linear polarisation as a function of frequency for eight pulsars (Xilouris *et al.* 1996).

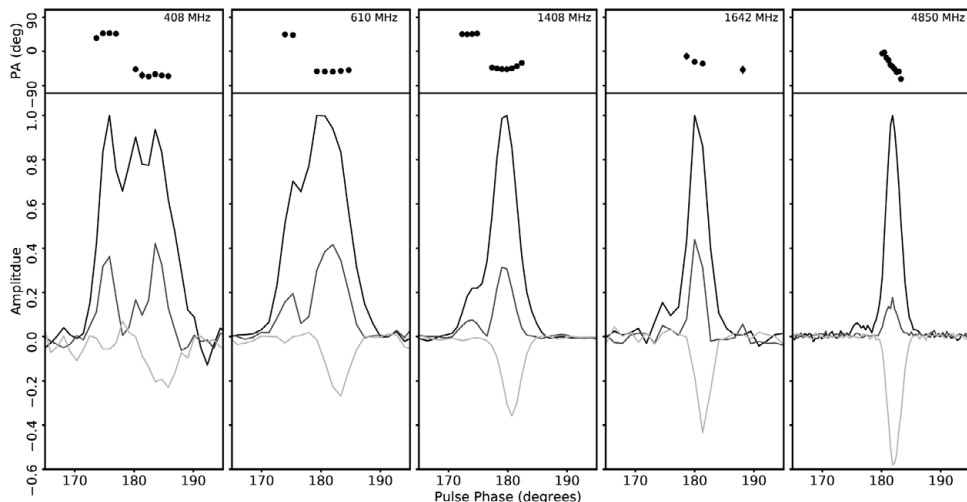


Figure 16.13 Integrated pulse profiles for PSR B0144+59 from 408 MHz to 4850 MHz. The increasing circular polarisation is shown in the lightly shaded areas (after von Hoensbroech *et al.* (1997), using data from the EPN Pulsar data base).

polarisation at these high frequencies (von Hoensbroech *et al.* 1997, 1998); an example is shown in Figure 16.13. There is, however, no clear pattern in circular polarisation. Johnston and Karastergiou (2019) show that the hand of circular polarisation is opposite in the two components of pulses in interpulse pulsars, as expected from the opposite magnetic poles of a dipolar magnetic field.

The observation of full linear polarisation in some pulsars suggests the possibility that the radiation mechanism is inherently completely polarised. Several observations support this possibility, demonstrating the existence of depolarisation mechanisms. It should be emphasised that the profiles discussed so far are integrated profiles and that there is considerable variation in the individual pulses. The individual pulses might be highly polarised, but with different patterns from pulse to pulse, often resulting in significant depolarisation in the integrated profile. The most potent effect is the phenomenon of switching between orthogonal polarisation modes, which we now describe.

16.9 Orthogonal Polarisation Modes

The profile of PSR B0355+54 in Figure 16.14 shows a region of low polarisation accompanied by a 90 deg step in position angle. As shown by Backer, Rankin and Campbell (1976), this is due to the simultaneous existence of two orthogonally polarised modes, in varying proportion. They found also that the two modes had

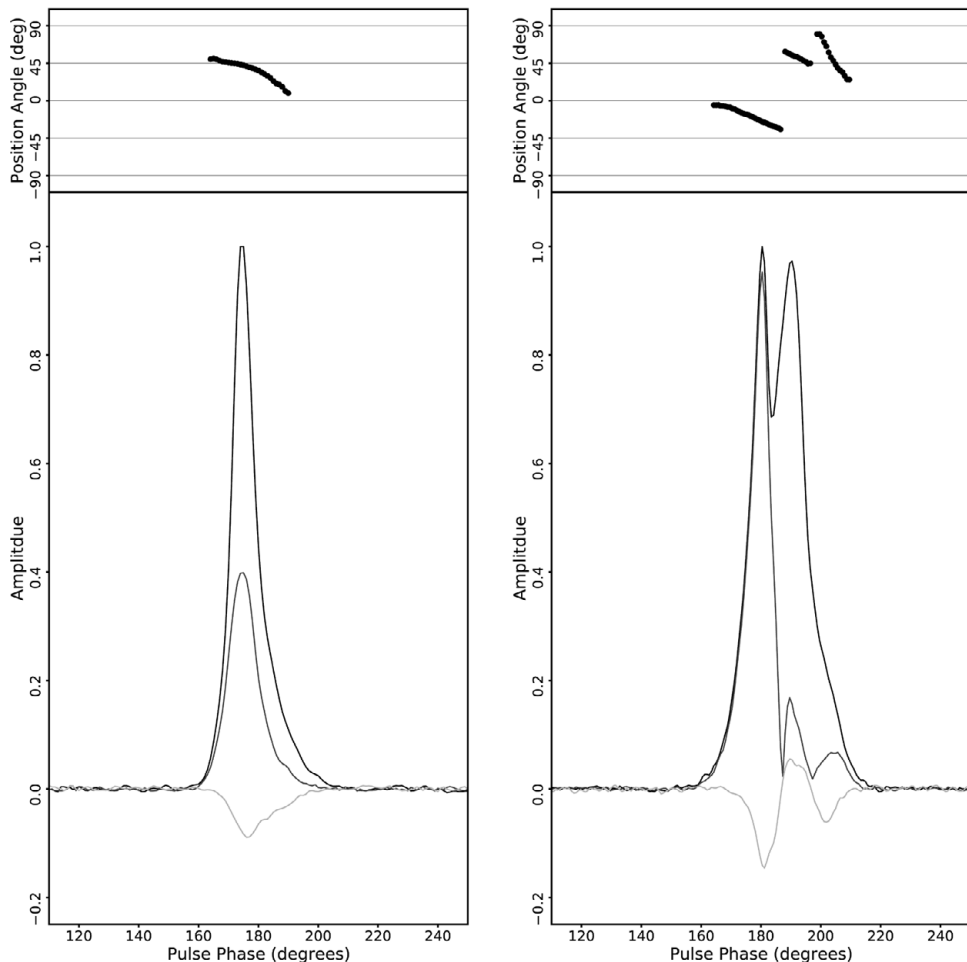


Figure 16.14 Polarised profiles for (a) PSR B0540+23, high polarisation with a smooth position angle curve; (b) PSR B0355+54, low linear polarisation with an orthogonally polarised section. Uses data from the EPN Pulsar data base.

opposite hands of circular polarisation, so that they could be represented by opposite points on a Poincaré polarisation sphere. The two modes might either occur independently or simultaneously but unrelated in phase, so that their sum is depolarised, with the position angle of the stronger mode. This is demonstrated in Figure 16.15, which shows a superposition of successive individual pulses of PSR B2020+28. The linear polarisation is least when the two orthogonal modes occur together (Stinebring *et al.* 1984). Switching between orthogonal modes appears to occur simultaneously over a wide frequency band, suggesting that it is inherent in the source rather than an effect of propagation in the magnetosphere above the source.

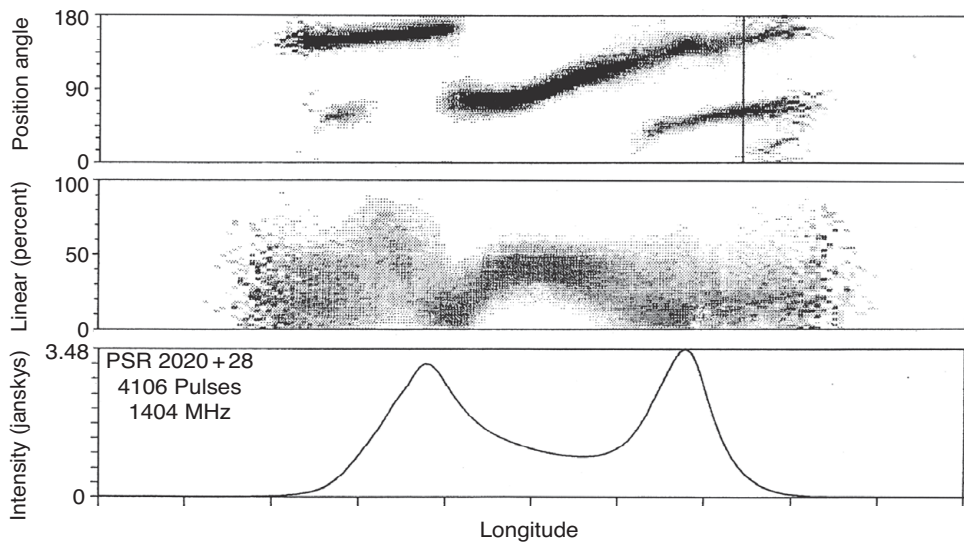


Figure 16.15 Superposition of polarisation characteristics of individual pulses from PSR PSR B2020+28: polarisation position angle (top); polarisation fraction (centre); integrated profile (bottom) (Stinebring *et al.* 1984).

High signal-to-noise recordings by Weisberg *et al.* (1999) show that orthogonal polarisation modes exist even in the most highly polarised pulsars, such as PSR B0525+21. Switching between polarisation modes is rapid and apparently random. McKinnon and Stinebring (2000) show that the two modes, which have different integrated profiles, can exist simultaneously, again suggesting that the emission mechanism is inherently highly polarised.

16.10 Position Angle Swing Rates

It will be recalled that the swing of position angle of linear polarisation through the profile is an important indicator of the impact parameter β , which measures the nearest approach of the line of sight to the centre of the emitting region. The rate of swing is assumed to be determined straightforwardly by the diverging geometry of the magnetic field lines above the polar cap. Observed values for the swing rate are tabulated for 75 pulsars by Lyne and Manchester (1988), and values may be found for many others from the catalogues of pulsar data (Chapter 4).

This geometric explanation of polarisation angle swing received a remarkable confirmation from the observation of precession in PSR J1906+0746, in which relativistic spin-orbit coupling over a period of 14 years showed a progressive change in the rate of swing of the polarisation position angle (Desvignes *et al.* 2019). This is attributed to a change in the impact parameter β as precession moves the rotation

axis, and with it the position of the magnetic pole in relation to the line of sight. The slope actually reverses, indicating that by good fortune the line of sight is now crossing on the opposite side of the magnetic pole. The demonstration of spin-orbit coupling is also a remarkable confirmation of a prediction of general relativity theory (Chapter 6).

In most analyses of the data, it is concluded that the rate of swing of position angle is independent of radio frequency. This is consistent with the polar cap theory, in which the height of emission has little effect; a small but interesting correction is needed, however, when the height becomes comparable with the radius of the magnetosphere, which can provide an estimate of emission height.

16.11 Emission Height

Ideally, for a pulse originating in a source distributed between the limiting open field lines, the inflection point at the centre of the S-shaped swing is not at the centre of the intensity profile, but is delayed due to retardation between the surface and the emitter and also by aberration (Dyks & Harding 2004; Chung & Melatos 2011). The combined effect is a delay observed as a shift in phase $\Delta\phi$ depending on height h_{em} :

$$\Delta\phi = 8\pi \frac{h_{\text{em}}}{P c}, \quad (16.5)$$

where P is the pulsar period. Rookyard, Weltevrede and Johnston (2015) applied this model to observations of 28 gamma-loud radio pulsars whose pulse profiles are reasonably nearly symmetric and for which the polarisation swing is well-defined. Despite the difficulty of determining the centre of the pulse profile, they were able to find emission heights mainly of order 100–300 km and to estimate the polar angles for each.

Gupta and Gangadhara (2003) showed that the height varies with longitude, increasing at the edges of the emitting region, that is, nearer the limit of the polar cap. In an analysis of interpulse pulsars at a frequency of 1.4 GHz, Johnston and Karastergiou (2019) found a range of heights from 0.025 to 0.04 of the light cylinder radius at the centre and edges of the beam, respectively. Yuen and Melrose (2014) accounted for this gradation in height in terms of the magnetic field configuration. The vertical extent of the emitting region is unknown; it may be restricted to a small volume of extremely intense broadband radiation.

16.12 Young Pulsars and Millisecond Pulsars

We have already remarked that the twin peak of the radio profile of the Crab Pulsar closely resembles the gamma-ray profile. This is characteristic of a small group of the youngest pulsars, including for example B0540–69, and it seems that in

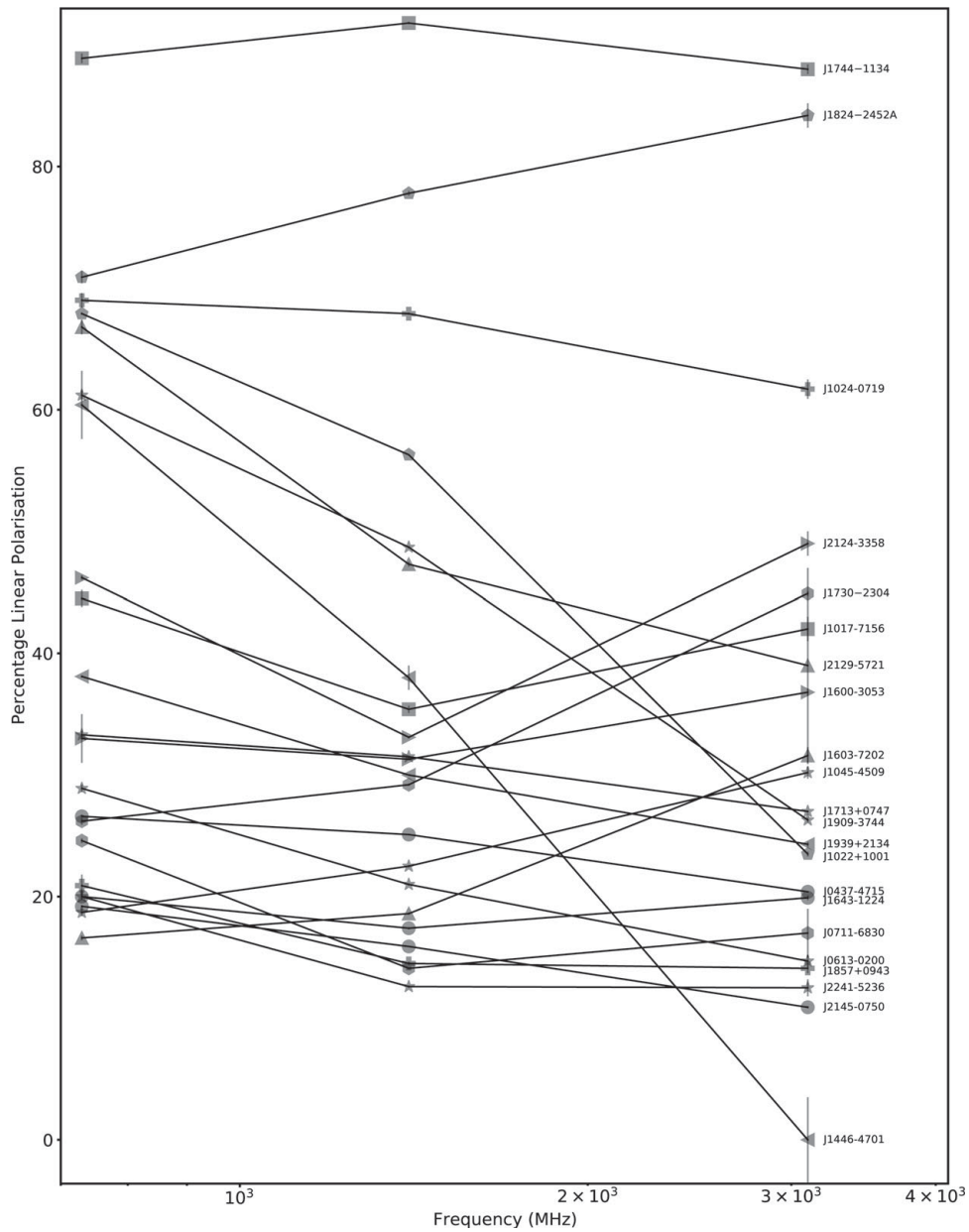


Figure 16.16 The fractional linear polarisation as a function of frequency for five millisecond pulsars (data from Dai *et al.* 2015).

these pulsars the main radio emission is co-located with the gamma emission in the outer gap of the magnetosphere (in the case of the Crab Pulsar, there is also a separate component, the ‘precursor’, which is similar to the polar cap emission of most normal pulsars). Among the catalogue of gamma-ray pulsars, a substantial

proportion are also normal radio pulsars. Johnston *et al.* (2020) found that these are distinguishable as those with spin-down energy greater than 10^{35} erg s $^{-1}$. Only the youngest and most energetic of these share the twin-peak profile of the typical gamma-ray pulsars. We conclude that all gamma-ray emission, from young and from millisecond pulsars, originates in the outer magnetosphere.

It might be expected that the radiation from millisecond pulsars would be very different from that of normal pulsars, since the scale of the magnetosphere and the strength of the magnetic field are both many orders of magnitude smaller. On the contrary, as pointed out by Kramer *et al.* (1999), the observed radio intensities and pulse profiles are not obviously different from those of a set of young pulsars. The majority of MSPs in the gamma-ray catalogue are identified as being radio MSPs, and those MSPs that are not observed as both radio- and gamma-loud are easily explicable in terms of limitations of observational sensitivity. Examples of radio profiles, with polarisation, are given by Dai *et al.* (2015).

On average, the degree of polarisation in the integrated pulse profiles at 1.4 GHz is greater in the MSPs, although observations at higher frequencies by Kramer *et al.* (1999) showed that as for normal pulsars, the polarisation decreases rapidly (Figure 16.16). It should be emphasised that this is the mean integrated polarisation; it is not yet clear whether individual pulses are more highly polarised. The position angle curves are generally shallower than for normal pulsars (Yan, Manchester & van Straten 2011). The shallow position angle curves may be inherent in the magnetospheric geometry of rapid rotators (Barnard 1986).

17

The Emission Mechanisms

More than 50 years after the discovery of pulsars, and despite many attempts to assemble and analyse the very detailed observational data, it is still not possible to give a clear exposition of the processes by which pulsars emit beams of radio waves. The later discovery of intense gamma-ray emission has proved more amenable to analysis, and the observed characteristics can be related to the particle energies and the geometry of the magnetosphere. In both radio and gamma emissions, the source of energy is the enormous electric field that is induced by the rapid rotation of the highly magnetised neutron star. This electric field accelerates electrons and positrons to high relativistic energies; this occurs in two emission regions, involving respectively the open field lines close to the polar cap and the outer gap (including the equatorial current sheet). The high-energy photons emitted from the outer source are curvature or synchrotron radiation from these relativistic particles; in contrast, the radio emission from both regions is coherent emission from a plasma created by the particle stream.

17.1 The Two Locations

The rapid rotation and strong dipole field of a typical pulsar give a maximum available potential of order 10^{14-15} volts. In a fully developed, co-rotating and static magnetosphere this would be shielded by the electrostatic field of the charged particle density n_{GJ} , as envisaged by Goldreich and Julian (1969). This only applies in the static equatorial region; in the polar regions where magnetic field lines cross the velocity of light cylinder, there is an outward flow, and an intense electric field develops over the magnetic pole, sufficient to accelerate electrons and positrons to high relativistic energies. The acceleration occurs in a vacuum gap, known as the *polar gap* or *polar slot gap*. Above the polar gap, the flux of high-energy particles is

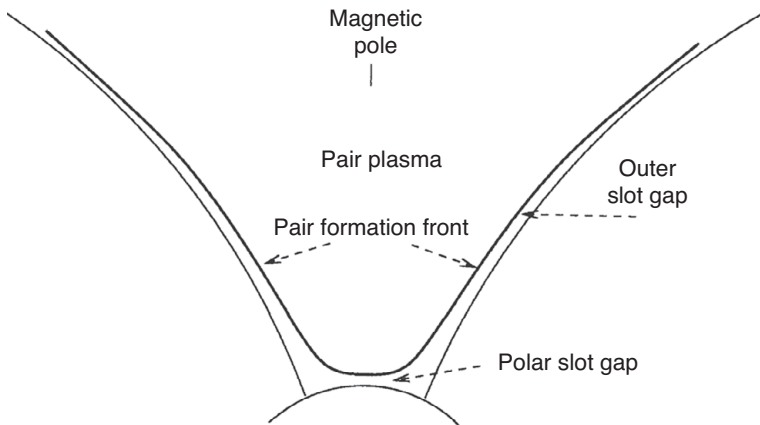


Figure 17.1 The slot gap over a magnetic pole.

multiplied in a cascade process. The magnetosphere above the polar gap consists of a plasma, probably like the Goldreich–Julian plasma but permeated with the outward flowing high-energy particles. This is the location of the radio emission from normal pulsars.

Another region of depleted charge density and high electric field develops further out in the magnetosphere, immediately outside the last defining field line of the equatorial region (Figure 13.3): this is the *outer gap* or *outer slot gap*. Although it is convenient to distinguish between the polar and outer gaps, they are actually joined, as in the sketch of Figure 17.1. Further out again, and possibly extending beyond the velocity-of-light cylinder, is the equatorial current sheet in which flows the return current from outside the light cylinder.

In both the polar gap and outer gap regions, the development of the electric field at the polar cap depends on the deficit of the charge density below n_{GJ} . Immediately above the surface of the star, the charge density may be maintained at n_{GJ} by several emission processes, which may be thermal, or field emission, or reaction from a reverse flow of particles with opposite charge (see a discussion by Hirschman & Arons 2001). Outward flow above this region reduces the charge density, and a slot gap develops, with a large electric field. A primary beam of particles with relativistic energies $\gamma \sim 10^{6-7}$ flows outwards along magnetic field lines above this accelerating region and, through a cascade process of pair production, creates a denser and less energetic secondary plasma. The charge density in this secondary plasma is again of order n_{GJ} , but the pairs increase the particle density by a large factor. The cascade is illustrated in Figure 17.2.

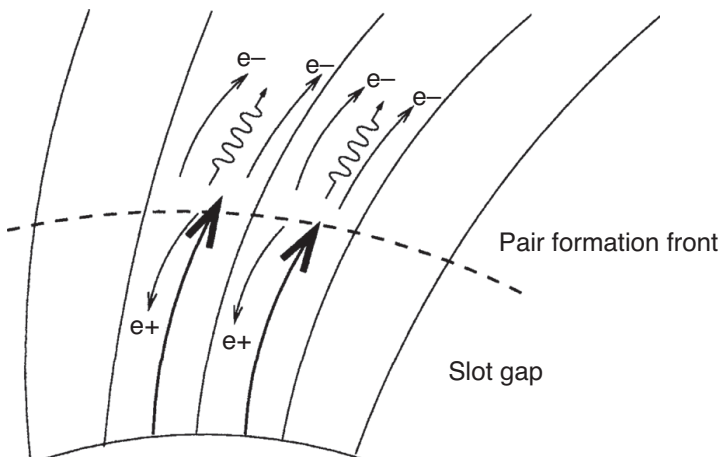


Figure 17.2 The cascade process within the polar gap.

In this diagram, the primary particles, shown as electrons, emit curvature radiation as gamma-ray photons. These interact with the magnetic field and create pairs of electrons and positrons, which in turn are accelerated in opposite directions by the intense electric field and emit further photons by curvature radiation. The final number density of the resulting secondary plasma above the polar gap may be $\sim 10^{3-4}$ greater than that of the primaries, and their energy will be correspondingly lower. The radio emission occurs within this secondary plasma.

A similar acceleration and cascade process occurs in the outer gap (Figure 17.3). Here, however, the accelerating electric field extends throughout a long charge-depleted region, and the electric field is not shorted out by a secondary plasma. Electrons and positrons are accelerated to extreme relativistic energies in the outer gap; there is then an energy balance between acceleration and loss by emission of gamma-ray photons through curvature and synchrotron radiation. The gamma-ray photons, which do not follow the curved magnetic field, may escape and are observed as a beam of radiation, or they may again create an electron-positron pair in an encounter with a lower-energy photon or with the transverse component of the magnetic field. A further process, Compton collisions with relativistic energy photons, may boost the energy of the newly created pair as part of the cascade. Note in Figure 17.3 the tendency for the photons to move out of the gap towards the magnetic polar region, injecting high-energy particles into the Goldreich–Julian plasma; this may be the seat of the radio emission in young pulsars such as the Crab Pulsar.

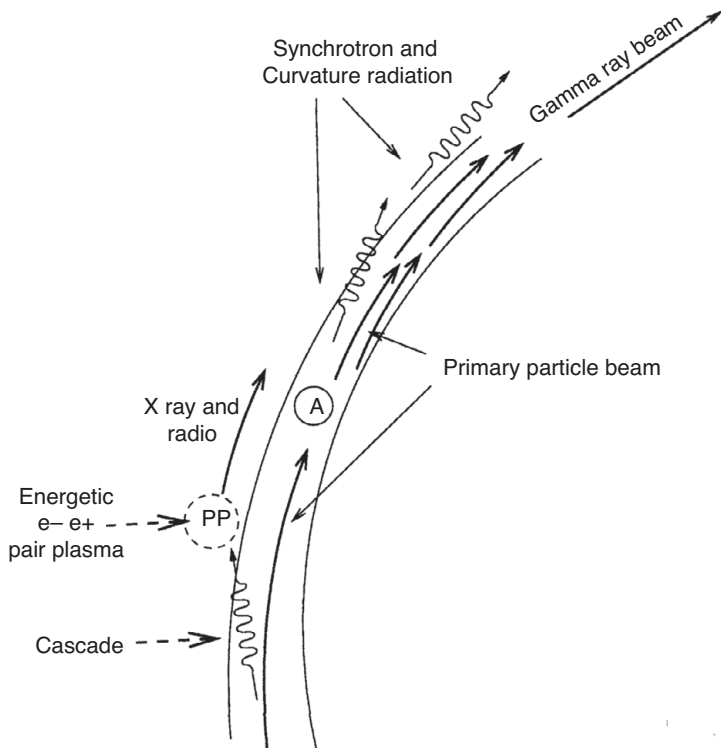


Figure 17.3 Particle acceleration and radiation in the outer gap.

17.2 Aberration, Retardation and Magnetic Field Sweep-Back

The various sources of radiation in the magnetosphere may be located at radial distances that are a considerable fraction of the light cylinder radius; hence, propagation time and relativistic aberration must then be taken into account. This is especially true for the gamma-ray and other high-energy radiation sources in the young pulsars, in which there can be a profound effect on the relation between the observed pulse and the geometry of the emitter; there can also be a smaller but appreciable effect on the polar cap sources of the radio emission. *Aberration* throws the radiation forwards in the direction of rotation, giving an earlier pulse than would correspond directly to the longitude of the source. Propagation time depends on the distance of sources distributed radially along the gap; this *retardation* means that at a given time, radiation is received from sources at a range of rotational phases. A further effect is the effect of rotation on the shape of the magnetic dipole field,

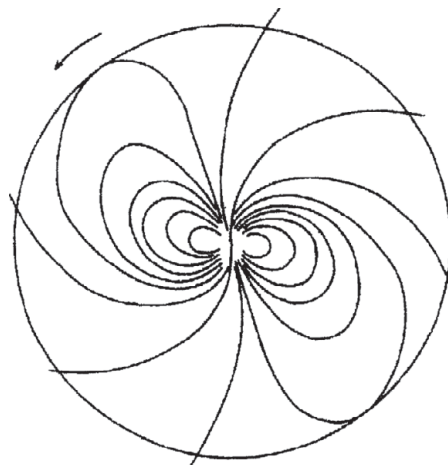


Figure 17.4 The swept-back equatorial magnetic field of a rapidly rotating dipole with orthogonal magnetic and rotation axes. The open field lines that cross the velocity-of-light cylinder develop further out into a propagating electromagnetic wave at the rotation frequency of the pulsar.

which is distorted and swept back by the order of a radian in longitude at the velocity of light cylinder, as in Figure 17.4.

These three effects on the arrival times of pulses from normal radio pulsars were considered by Phillips (1992). Pulses at two different radio frequencies ν_1 and ν_2 emitted at radii r_1 and r_2 suffer a relative delay due to retardation given by

$$\Delta t_r = \frac{P}{2\pi} \left(\frac{r_1 - r_2}{R_{LC}} \right). \quad (17.1)$$

Aberration bends the radiation beam forward by an angle θ_a , giving a relative delay

$$\Delta t_a = \frac{P}{2\pi} \left[\tan^{-1} \left(\frac{r_1 \sin \alpha}{R_{LC}} \right) - \tan^{-1} \left(\frac{r_2 \sin \alpha}{R_{LC}} \right) \right], \quad (17.2)$$

where α is the angle between the rotational and magnetic dipole axes.

Finally, the bending angle of the magnetic field for a spinning dipole in vacuo is $\theta_{mfs} \approx 1.2(r/R_{LC})^3 \sin^2 \alpha$ radians (Shitov 1983), giving a relative delay

$$\Delta t_{mfs} = 1.2 \sin^2 \alpha \frac{P}{2\pi} \left[\left(\frac{r_2}{R_{LC}} \right)^3 - \left(\frac{r_1}{R_{LC}} \right)^3 \right]. \quad (17.3)$$

Phillips found that for three normal pulsars observed at 430 and 1400 MHz, the sum of these three was less than 1 ms, allowing him to deduce that the difference in height $r_{430} - r_{1400}$ was less than about 200 km, in conformity with the heights found by arguments from beam widths.

Blaskiewicz, Cordes and Wasserman (1991) extended the analysis to the geometry of observed polarisation position angles and again found an upper limit to the effect of rotation, indicating an upper limit to the height of normal radio emission. As pointed out by Hirschman and Arons (2001), this geometrical analysis should take into account a small but possibly significant effect of current flow on the configuration of the magnetospheric magnetic field.

Further critical discussion of the determination of emission heights by such methods is given by Dyks, Rudak and Harding (2004).

17.3 The Outer Emission Regions: Curvature and Synchrotron Radiation

In the high-energy regime of optical to gamma-ray emission from the outer regions, there is no indication that the emission is coherent. The flow of individual particles can therefore be related to the observed flux density through the usual theory of curvature radiation.¹ For an electron with relativistic factor γ following a magnetic field line with radius of curvature ρ , the peak of the spectrum is near a critical frequency ν_c given by

$$\nu_c = \frac{3c}{4\pi\rho} \gamma^3. \quad (17.4)$$

The radius of curvature ρ of the last open field line is $\sim c/2\Omega$. Taking the Crab Pulsar ($\Omega \sim 200\text{rad s}^{-1}$) as an example, where the gamma-ray spectrum extends to 10^4 MeV, Eqn. (17.4) shows that the particle energy must extend to $\gamma \sim 10^7$, which is within the energy available from acceleration in an extended outer gap.

Romani (1996) showed that the whole of the high-photon-energy spectrum, from optical to gamma rays, can be accounted for as curvature radiation from individual particles with a spectrum of gamma-ray energies that varies through the outer gap. The energy of the gamma-ray particles is limited by the process of pair creation in the magnetic field; the maximum energy is inversely proportional to the field strength, so that the highest gamma-ray energies occur furthest out in the outer gap. For the same reason, high-energy curvature radiation cannot occur in the polar cap where the field strength is several orders of magnitude larger and the energy of gamma rays is restricted.

There may also be a component of synchrotron radiation from the same high-energy particles. Harding *et al.* (2008) showed that in the outer regions of the gap, beyond about halfway to the velocity-of-light cylinder, the particles of the primary beam may acquire considerable pitch angles and radiate synchrotron radiation.

¹ Introduction to Radio Astronomy (2019) Burke, Graham-Smith and Wilkinson.

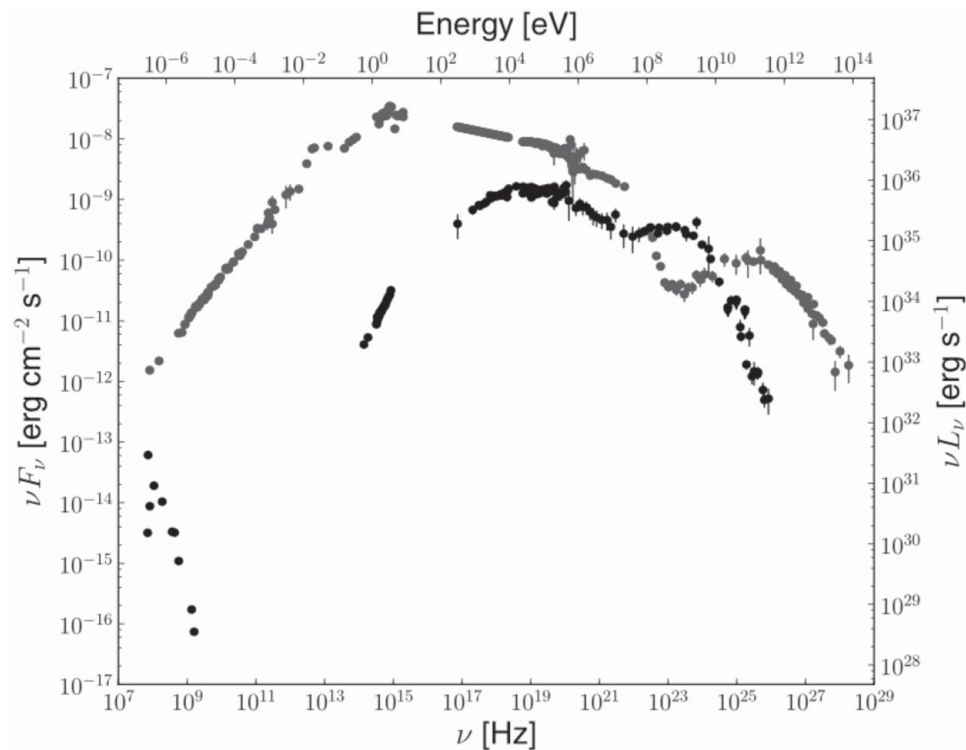


Figure 17.5 The integrated spectra of the Crab Pulsar (black) and the Crab Nebula (grey) (Bühler & Blandford 2014). The left-hand scale is the observed flux, while the right-hand scale is the estimated emitted luminosity assuming a distance of 2 kpc. The nebula dominates at all frequencies except around 10^{23} Hz. The radio data may be affected by scintillation.

The subsequent synchrotron radiation is at high harmonics of the cyclotron frequency, due to the high relativistic velocity.

The x-ray emission appears from the spectrum to be distinct from the gamma-ray emission. Figure 17.5 shows a dramatic break in the integrated spectrum of the Crab Pulsar at around 10 MeV; a similar break is found in the ratio of the two pulse components (Campana *et al.* 2009). The x-ray emission below this energy is from the lower half of the outer gap and is attributed to synchrotron radiation from a secondary pair plasma, on the polar cap side of the slot gap.

It seems inevitable that there are many different processes of particle acceleration and radiation all occurring in this slot gap, including curvature and synchrotron radiation, resonant cyclotron absorption and photon boosting by inverse Compton. Several papers discuss the particle energy spectrum within the outer gap and its relation to the observed gamma-ray, x-ray, optical and infrared spectra of the

high-energy pulsars. For example, Crusius-Waetzl and Lesch (2002) analysed the particle energy spectrum as a balance between acceleration and loss by radiation. Assuming a power-law distribution of particle numbers N with energy γ ,

$$N(\gamma) \propto \gamma^{-s}, \quad (17.5)$$

where the index s is related to the spectrum of the observed gamma-ray photon flux $F(\nu)$ (at the lower energies) by

$$F(\nu) \propto \nu^{-(s-2)/3}. \quad (17.6)$$

For a typical pulsar PSR B1706–44, they find an index $s = 2.75$.

The relation between the total high energy luminosity L_γ and the basic parameters B_s (the surface magnetic field) and P (the rotation period) can be found from this analysis as the product of the volume of the outer gap, the number density (assumed to be near n_{GJ}) and the power radiated by a single particle ($\propto \gamma^4$), giving $L_\gamma \propto B_s P^{-5/3}$. The observed relation (Chapter 15) to period P is close to $L_\gamma \propto P^{-3/2}$, in reasonable agreement with the theory. The spin-down luminosity \dot{E} is proportional to $B_s^2 P^{-4}$, so that L_γ is expected to be roughly proportional to $\dot{E}^{1/2}$, as observed.

The outer gaps form wide-angle cones round both poles, opening out and following the edge of the equatorial region. The high velocity of the emission regions and the propagation times across the magnetosphere have very large effects (aberration and retardation), and at the trailing edge of the gap, sources at all radial distances are observed nearly simultaneously. This may account for the two peaks of the Crab-like pulsars, which could be attributed to the trailing edges of two magnetic poles of a nearly orthogonal configuration; this is the two pole caustic (TPC) model due to Dyks and Rudak (2003) (but note the alternative theory of radiation from the equatorial current sheet, in Chapter 16). Chiang and Romani (1994) and Romani and Yadigaroglu (1995) trace the expected gamma-ray radiation pattern, projected on a cylinder aligned with the rotation axis, assuming that all parts of the outer gaps radiate along the magnetic field lines. Figure 17.6 shows this projection for an inclination angle $\alpha = 65$ deg, which is appropriate for the Vela Pulsar. The figure also shows the projection of the normal radiation patterns from the two polar caps.

Although the most detailed analysis has concentrated on the Crab and Vela Pulsars, for which there is a wealth of observational data, it appears that the millisecond pulsars detected by Fermi LAT conform to the same pattern. Ravi *et al.* (2010) found a close correspondence between the profiles of millisecond pulsars detected in the radio and gamma-ray surveys, and for several, the pulse profiles are strikingly similar to that of the Crab Pulsar (Abdo *et al.* 2010b). We return to this connection in Section 17.9.

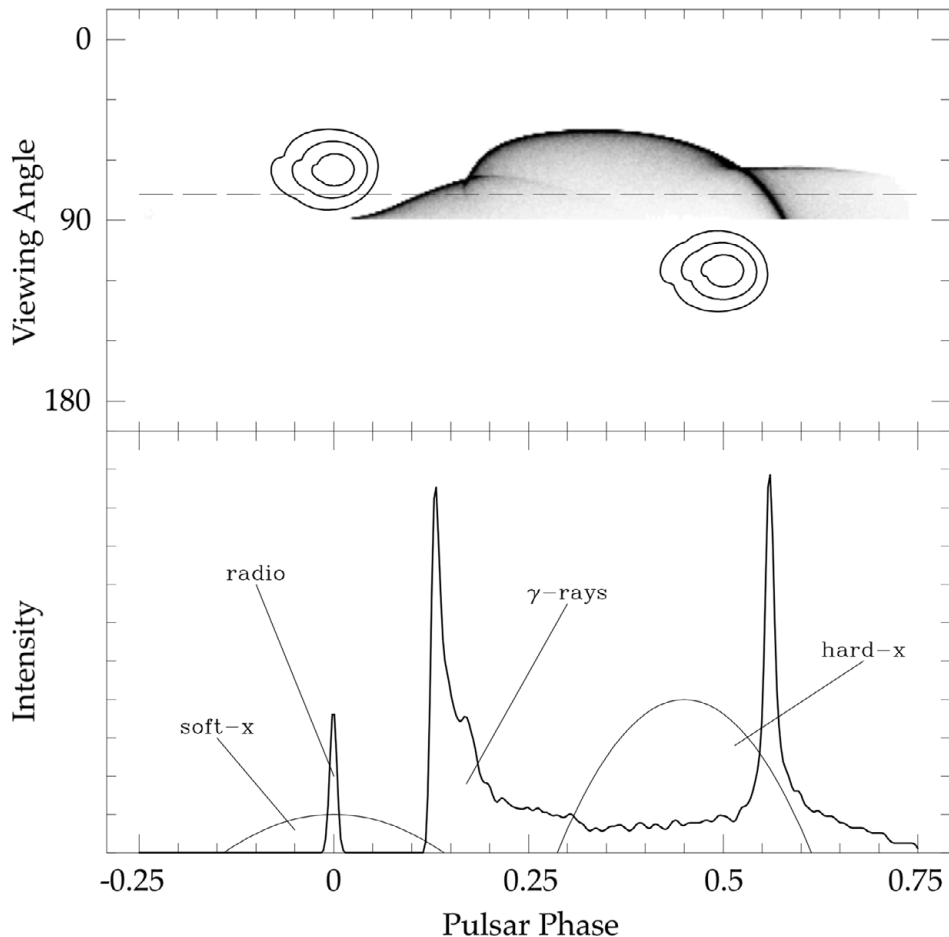


Figure 17.6 The radiation pattern for outer gap emission, projected onto a cylindrical surface aligned with the rotation axis. Only one hemisphere is shown; the radiation pattern surrounds the magnetic pole in the opposite hemisphere. The main parameter, the inclination α between the rotational and magnetic axes, is 65 deg, chosen to fit the Vela Pulsar. The broken line shows the cut across the pattern that produces the observed pulse profile in x-rays and gamma rays, shown in the lower panel. The two smaller patches show the radio radiation from the polar caps (Romani & Yadigaroglu 1995).

Despite the complexity of the competing physical processes at work in the outer gap, we consider that the process of high-energy radiation from the outer gap and equatorial current sheet is reasonably well understood. The similarity between the radio and the gamma-ray profiles of the Crab Pulsar suggests that both originate in the same stream of particles. However, the radio emission from the polar region is related to lower energy particles in a pair plasma, and if, as seems likely, the radio emission from the outer gap is emitted by a similar process, there must be a pair plasma at the edge of the outer gap, following a similar geometry.

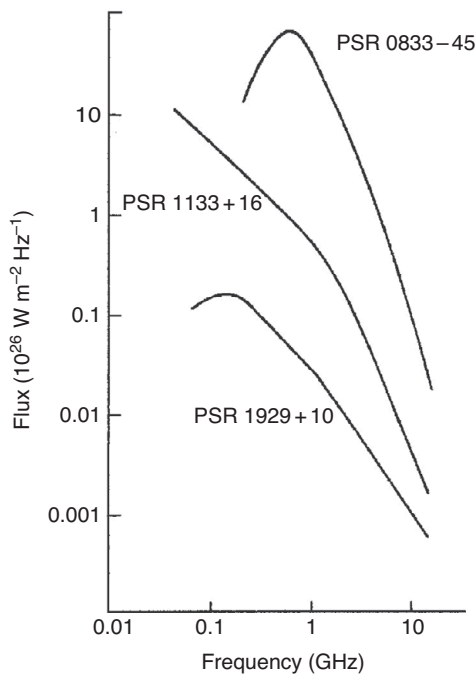


Figure 17.7 Typical radio spectra of pulsars. The spectra are generally curved and often show a low-frequency cut-off and a steepening at high frequency (the *gigahertz break*) (Sieber 1973).

17.4 Radio Spectra

The overall radio spectra of the total intensity are invariably steep, although they often flatten or turn over at lower frequencies (Figure 17.7). If the flux density S_ν varies with frequency according to the power law $S_\nu \propto \nu^\alpha$, the spectral index α for the upper part of the spectrum lies in the range -2 to -4 (Sieber 1973). This power law has been traced for some of the brightest pulsars as far as 35 GHz (Löhmer *et al.* 2008), and for the Vela Pulsar PSR B0833–45 to 343 GHz using ALMA (Mignani *et al.* 2017). The indices of the separate components in an individual pulsar may differ from one another, varying over a similarly wide range; this accounts for the evolution in profile shape with frequency. There is an organised difference in spectral index between the inner and outer components, so that outer components that are prominent at high frequencies may be practically lost at low frequencies.

These spectra cannot be directly related to the energy spectra of individual radiating particles, since the radio emission is due to the coherent motion of large groups of particles.

17.5 Power and Energy Density in the Polar Cap Radio Emitter

Consider first the power and energy density represented by the time-averaged radio emission from a model normal pulsar, with a rotation period $P = 1$ s and a peak flux density of 1 Jy² over a bandwidth of 1 GHz. The beam is taken to be contained within a solid angle of 0.1 steradian. At a distance of 1 kiloparsec (3×10^{19} m), the radiated power is $10^{-26} \times 9 \times 10^{38} \times 10^9 \times 0.1 \approx 10^{21}$ W. (This is much smaller than the rotational energy loss, or spin-down power, calculated from the slowdown rate, which is typically in the range $10^{24} - 10^{27}$ W for normal pulsars.) This is emitted from a region above the polar gap with a maximum radius limited by the locus of the last open field lines. At a radial distance R from the centre of the star, the radius of the bundle of open field lines is approximately $(2\pi R/cP)^{1/2}$. There is some uncertainty in the radial distance (see Chapter 15); here we set $R = 100$ km and obtain a radius 5 km. Assuming that the whole area is emitting, the irradiance is $\sim 10^{13}$ W m⁻²; the emission is normal to the surface, so this is the Poynting vector. For unity refractive index, the Poynting vector is related to the radiated electric field as $E^2/377$, giving a free space radiated field $E \sim 6 \times 10^7$ V m⁻¹. The energy density in the radiated field is 3×10^4 J m⁻³.

Such a high flux cannot be attributed to incoherent radiation in which the brightness temperature T_B of the source could be related to the energy \mathcal{E} of the individual particles by $kT_B \leq \mathcal{E}$. The observed brightness temperature (in the Rayleigh–Jeans regime, this is related to the flux density as $S = 2kT/\lambda^2$) is commonly greater than 10^{21} K.

These values are doubtless underestimates, since the separate pulse components are emitted from smaller regions than the whole polar cap, suggesting that the mean irradiance may be greater by a factor of 10. Much larger values of brightness temperature and energy density are observed in the giant pulses from the Crab and several other pulsars. It is abundantly clear that a non-relativistic linear theory of energy transfer from the particles accelerated in the polar gap and the radiation field will be totally inadequate for all observed radio emission.

17.6 Polar Cap Radio Emission

The high intensities of the radio emission from both the polar and outer gap regions, and the corresponding high brightness temperatures, require explanation as coherent radiation from bunches of particles moving in unison. The mechanism for radio

² 1 Jansky (Jy) = 10^{-26} W m⁻² Hz⁻¹.

emission from the polar cap might, for example, be coherent curvature radiation; but here there is a problem on geometrical grounds, since radio emission occurs over the whole of the polar cap including the central region over the pole itself where the dipole magnetic field lines are straight. Lesch *et al.* (1998) showed also that the curvature radiation model does not account for the luminosities or for radius-to-frequency mapping (Chapter 15). There is as yet no explanation for how coherent curvature radiation occurs, either in the radiation process itself or in subsequent amplification. Theory has therefore been directed to the growth of plasma waves and their coupling to radiation.

The physical parameters in the polar stream, both primary and secondary, have been considered in many papers; references may be found, for example, in Hibschman and Arons (2001). Two crucial parameters in the secondary pair plasma, which is regarded as the source of the radio emission, are the density and the particle energy distribution. The plasma density determines the resonant frequency, and the particle energy distribution mediates the growth of plasma waves (Arendt & Eilek 2002). The plasma resonant frequency is a serious difficulty; it is found to be too high to allow propagation of radio waves with frequencies below about 1 GHz. The suggested solution is to introduce spatial structure within the pair plasma (Gedalin *et al.* 2002). The growth of plasma waves is also difficult to explain in a stationary (i.e. steady) state and uniform model, but is understood as a non-stationary process (Usov 1987). Bearing in mind the fluctuations observed in radio pulses at all time scales from nanoseconds to hours, as described in earlier chapters, the introduction of spatial and temporal structure into the theory must be acceptable.

A solution to these problems has been presented by Philippov, Timokhin and Spitkovsky (2020), who simulated the pair-production process in a large-scale particle-in-box computation. They showed that the process is non-stationary, with a cyclic discharge leading to large amplitude fluctuations of electric field. These radiate as pulses, which couple to the ambient magnetic field and radiate outward. In this picture, the radio emission is broadband, with a spectrum determined by the pulse width of the instability. The radiation is guided along the magnetic field lines and breaks away at some point where its direction and polarisation become frozen. The model apparently favours radiation from the edges and centre of the discharge region, accounting for the observed core-cone structure. The same instability may be responsible for giant pulses and possibly also for fast radio bursts.

Understanding the coupling of oscillations in the pair plasma to the radio waves that we observe requires the theory of radio propagation in the magnetosphere, to which we now turn.

17.7 Radio Propagation in the Magnetosphere

Wave propagation in the plasma of the outer regions of the magnetosphere is remarkably simple, due to the very strong magnetic field. Electrons (and positrons) in the plasma cannot move transverse to the magnetic field; any transverse momentum is immediately lost by synchrotron radiation. Radio waves are emitted in the direction of the magnetic field and, to first approximation, travel outward in a straight line as though the magnetosphere did not exist. There are four normal wave modes in the one-dimensional plasma, two of which are Alfvén waves involving plasma oscillations. In the polar magnetosphere, the whole plasma is streaming outwards with relativistic velocity. Melrose and Stoneham (1977) showed that the same four normal modes can propagate along the direction of the magnetic field. The refractive indices at high angular frequencies ω of both non-Alfvén waves for a uniform outward velocity, with a single value of the relativistic factor γ , were shown to be

$$\mu = 1 - \frac{\omega_p^2}{2\gamma\omega^2}, \quad (17.7)$$

where ω_p is the angular frequency of the plasma resonance. Arons and Barnard (1986) give dispersion relations for these modes, including the effect of a large spread in γ . Beskin (1999) shows that this spread is accounted for by taking an average value of γ^{-3} , as in the following simplified expressions for refractive indices $n = kc/\omega$ applying to waves travelling at a small angle θ to the magnetic field wave:

$$n_1 = 1, \quad (17.8)$$

$$n_2 \approx 1 + \frac{\theta^2}{4} - \left(\frac{\omega_p^2}{\omega^2} \langle \gamma^{-3} \rangle + \frac{\theta^4}{16} \right)^{1/2}, \quad (17.9)$$

$$n_3 \approx 1 + \frac{\theta^2}{4} + \left(\frac{\omega_p^2}{\omega^2} \langle \gamma^{-3} \rangle + \frac{\theta^4}{16} \right)^{1/2}, \quad (17.10)$$

$$n_4 \approx 1 + \frac{\theta^2}{2}. \quad (17.11)$$

Exact expressions for these refractive indices and further references can be found in Beskin, Gurevich and Istomin (1993).

For propagation along the magnetic field ($\theta = 0$), the waves 1 and 4 are transverse waves with $n = 1$; when due to curvature of the field $\theta \neq 0$, they are differentiated into waves with electric vector respectively perpendicular to and in the plane of curvature of the field. Wave 1, designated an X wave, propagates linearly; wave 4, designated an O wave, follows the field line. Waves 2 and 3 are longitudinal

plasma waves, propagating at small angles to the plasma flow. They do not leave the magnetosphere, since they cannot propagate in the lower density plasma of the outer regions.

17.8 Polarisation

The orthogonal polarisation of the two propagating modes is naturally associated by many authors with the observed orthogonal polarisation mode (Chapter 9). The switch between modes may be inherent in the emission process, or it may be due to varying conditions in propagation, such as refraction in a lateral gradient of plasma density. There is a similar uncertainty about the origin of circular polarisation; if this is due to a propagation effect, it might result from coupling between modes (Melrose 1979). This would occur only below a polarisation limiting region, above which the separate modes, including circular polarisation, would propagate independently.

Arons and Barnard (1986) trace rays of the O and X modes through a pulsar magnetosphere. As shown in Figure 17.8, the O ray initially follows the magnetic field line but becomes disconnected after some distance. It therefore leaves the magnetosphere at a greater angle from the polar axis and if it is present must form the outer part of the integrated pulse profile. The height found from the opening angle is then the height of the disconnection rather than the emitting region.

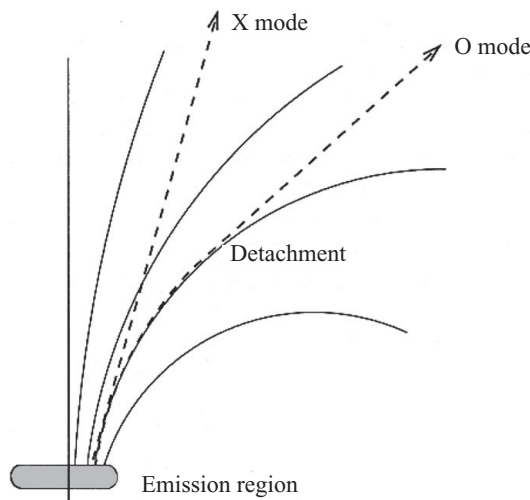


Figure 17.8 Propagation of the X and O waves in the magnetosphere. Both waves are emitted along the magnetic field lines; the X wave travels in a straight line, but the O wave follows the curved field line up to a disconnection point, which depends on the wave frequency.

McKinnon (1997) has suggested that this birefringence might be responsible for the whole of the frequency-dependent pulse broadening. If the broadening at low frequencies is due to propagation along a curved field line, as in Figure 17.8, it is possible that all radio frequencies might be emitted within a small range of heights, which would be around the minimum height discussed in Chapter 16. The separate ray paths of the two modes might also account for the switch between orthogonally polarised modes.

This interpretation remains to be tested. We noted in Chapter 8 that it is only the spacing between outer ‘conal’ components that increases at low frequencies, while the spacing and width of the inner ‘core’ components do not show the same angular spread. This suggests that the outer parts must be behaving as an O wave. The inner parts might be either X or O, but if they are O waves, the disconnection point must be close to the emitting region. It may be possible to distinguish the outer parts as pure O waves from their polarisation characteristics; this requires observations of orthogonal mode switching at low radio frequencies where the outer parts are well separated from the rest of the pulse profile.

The separation into four independent modes does not apply near the emission region itself, where there is some form of plasma resonance or instability leading to coherent emission. Outside the emission region, coupling between modes may continue to affect the polarisation. Barnard (1986) identified a radius R_{PL} as a *polarisation limiting radius* beyond which coupling does not occur; in shorter period pulsars this extends through a larger proportion of the magnetosphere. Mode coupling within this radius could account for circular polarisation, as suggested by Cheng and Ruderman (1979). Barnard showed also that it could account for the flattened polarisation swing in millisecond pulsars, where R_{PL} approaches the velocity of light radius R_{LC} .

17.9 The Radio Emission Mechanism

The parameters governing the emission process should be similar for all observed sources of radio, and especially should cover both normal and millisecond pulsars. If, as seems likely, the radio emission from the polar cap and the outer gap is by a similar process, we should also expect to find conditions at the boundary of the outer gap similar to those above the polar cap. Between these two regimes, the magnetic field strength differs by four orders of magnitude or more, so that it is unlikely that a cyclotron resonance frequency is involved; instead it is reasonable to consider only processes and propagating modes in which charged particles can only move parallel to a superstrong magnetic field. It is possible, however, that a local plasma frequency might be similar in these widely different sources. We note first that the Goldreich–Julian charge density ρ_{GJ} is similar in normal pulsars and

MSPs since it is proportional to field strength and inversely proportional to rotation period. This obviously does not apply to the outer gaps; however, we expect larger particle energies in these regions, and a combination of ρ_{GJ} and relativistic factor γ might be similar in all radio emitting regions, giving a similar plasma resonance frequency or a similar plasma instability.

The propagation modes considered in Section 17.7 are simply divided into the Langmuir waves, which can escape from the magnetosphere, and the Alfvèn or magnetohydrodynamic waves, which cannot escape. The Langmuir waves are in two orthogonally polarised modes and propagate almost as if in free space; the dispersion relation for the Alfvèn waves depends on charge density and magnetic field strength. A sequence of processes seems to be involved: an instability in the outflowing plasma excites the Alfvèn waves, which propagate outwards for some distance and couple to the escaping Langmuir waves. The mode coupling, which is crucial, is the least understood of this sequence; it is clear (Arons & Barnard 1986) that their refractive indices can coincide, but the coupling between these different types of wave is evidently highly non-linear and hard to analyse. The frequency at which their dispersion curves intersect is quoted as $\omega_p \langle \gamma \rangle^{1/2}$; although the definitions of both the plasma frequency ω_p and the suitably averaged relativistic factor $\langle \gamma \rangle$ are debatable, the combination might well be the parameter that is common to the various radio sources.

The excitation of the plasma instability is understandable in general terms. Any velocity dispersion in a streaming plasma that is not a normal thermal dispersion can give rise to an instability; a two-stream instability is the most familiar case. If the acceleration of the particles is a non-stationary process, so that particles leave the polar cap discharge in discrete bunches, the velocity dispersion results from faster particles in one bunch catching up with slower particles in a previous bunch (Asseo, Pellat & Sol 1983; Usov 1987).

There is, however, a serious problem in developing this theory: the calculated values of the critical frequency $\omega_p \langle \gamma \rangle^{1/2}$ are more than two orders of magnitude too high (Melrose & Gedalin 1999). The theory can only be rescued from this difficulty by introducing another parameter: a lateral filamentary structure in the plasma. This concept, which was introduced by Ruderman and Sutherland (1975), is consistent with the concept of discrete spark discharges in the polar gap; these will generate individual narrowly confined gamma-ray showers, which will persist as filaments throughout the radiating region. The lateral gradients in this filamentary structure then allow mode coupling to occur in a less dense region.

An alternative approach by Gedalin *et al.* (2002) proposes a non-resonant plasma instability in the outward-streaming pair plasma. This is a broad-band instability at frequencies below the resonant plasma waves. The growing waves flow outward with the pair plasma into regions with lower plasma density until the wave

frequency matches the resonant plasma frequency, where the plasma wave couples to the Langmuir-O wave and propagates out of the magnetosphere.

In a review of the problems of the ‘radio-loud plasma’, Eilek *et al.* (2002) suggested that there may be no satisfactory way of explaining the radio emission from pulsars as a simple, stationary process uniformly distributed over the defined regions of the polar cap and the outer gap. This is not surprising, in view of the complexities described in the earlier chapters of this review. Lateral structure on a large scale is a direct deduction from the multiple components of the pulse profiles; pulse drifting suggests the existence of a small scale spark discharge, moving within the polar gap. Rapid variations are seen in all pulsars, including some on a time scale of microseconds, again implying a small lateral structure. Moding, and particularly orthogonal polarisation moding, obviously implies both a local structure and an instability.

Finally, the giant pulses described in Chapter 9 are best described as a local impulsive collapse of a strong electric field rather than a plasma oscillation. Weatherall (1998) showed that the onset of plasma wave turbulence in a region of high electric field should be marked by such an explosive collapse and by bursts of radiation (see Section 17.5 above). In the Crab Pulsar, these giant pulses originate in the lower part of the outer gaps; the microstructure observed in double pulse components of millisecond pulsars may be from a similar location. Whether or not the emission mechanism for giant pulses is related to the normal radiation from pulsars is an open question, but it seems possible that all radio emission is made up of short impulses, of which only some large individuals are resolved in present receiver techniques. Such a chaotic behaviour is to be expected from coherent radiation with a very large gain factor, although it is remarkable that the mean luminosity (apart from nulling and moding) is essentially constant day by day and year by year.

Part IV

Environments and the Interstellar Medium

18

Supernovae and Their Remnants

Pulsar Wind Nebulae

18.1 The Nature of Supernovae

The obvious association between the Crab Pulsar and the remains of the supernova explosion of AD 1054 leads naturally to the suggestion that all pulsars originate in supernova explosions and even to the speculation that all supernovae might produce neutron stars, which could become pulsars. This turns out to be an oversimplification, and it is necessary to explore the nature of supernovae in some detail before their relation to pulsars can be pursued.

In 1921 Lundmark pointed out that the nova observed by Hartwig in 1885 in the constellation of Andromeda was probably within the Andromeda Nebula itself, and hence very distant and very bright (see a centenary review by de Vaucouleurs & Corwin 1985). He showed that there were many cases of these extremely powerful novae, and he was the first to associate the Crab Nebula with the Chinese records of the bright star that appeared in AD 1054. The physical significance of these enormous outbursts was appreciated by Baade and Zwicky, who first used the word ‘supernova’ in their publication of 1934. They made four very remarkable deductions from the observations:

1. The total energy released was in the range 10^{51} to 10^{55} ergs.
2. The remnant could form a neutron star.
3. Cosmic rays could have their origin in supernovae.
4. Supernova explosions could give rise to expanding shells of ionised gas.

These speculative deductions have been amply justified by later work, although the connection with cosmic rays was only firmly established in 2013 when an acceleration mechanism in an expanding supernova shell was identified by Ackermann *et al.* (2013). It is astonishing to reflect that the entirely new notion of neutron stars was correctly included in the list, even though it was a concept that remained unfamiliar to most astronomers up to, and even after, the time of the discovery of pulsars.

Zwicky devoted much effort to the systematic search for supernovae, using photographic techniques involving tedious comparisons of Schmidt plates from different epochs. Several hundred discoveries were made in this way, and the statistics have more recently been improved by the use of automated search techniques. On the basis of present statistics, it is reasonable to divide the observed characteristics into two main types, Type Ia and Type II (with less important sub-divisions such as Ib, Ic). The observed differences are mainly in the spectra: Type Ia spectra contain emission lines from many heavy elements, while Type II spectra are predominantly from hydrogen. The total output of energy, and the subsequent rate of decay, are similar in both types, and both are initiated by gravitational collapse of a stellar core, but the explosion processes are completely different: in Type II the energy is derived only from gravitational collapse after all nuclear burning has been exhausted, while in Type Ia the main source of energy is explosive nuclear burning resulting from the high density and temperature in the collapse. Only Type II can create a neutron star remnant. The differences are related to the mass of the progenitor stars: Type II originate from stars more massive than about $8M_{\odot}$, while Type Ia originate from white dwarf stars accreting mass from a binary companion and reaching a mass close to $1.4M_{\odot}$ (some models propose the merging of two white dwarfs in a binary system). The spectral differences arise from the extensive envelope of gas around Type II, which obscures the radiation from the exploding star itself.

Beyond the two main types, even more luminous supernovae are occasionally observed in distant galaxies, with luminosities 10 to 100 times that of a standard Type Ia. The nature and origin of these superluminal supernovae are unknown. We may be observing the collapse of very massive stars, or the result of a more normal supernova in a close binary system. Since the origin of magnetars is also unknown, there is some suggestion of a link between these two mysteries. See Jha, Maguire and Sullivan (2019) for a review of supernova types.

In both Types I and II, the rise to maximum light occurs very rapidly, usually within a few days (Figure 18.1). At maximum, the light is mainly in a continuum whose spectrum corresponds to a temperature of about 15,000 K. The total luminosity is about 10^{43} erg s⁻¹, mainly in the visible. A combination of these data gives a radius of about 10^{10} km at this stage, that is, about $10^4 R_{\odot}$. The subsequent decay can be observed for two years or more, following a monotonic decay which is approximately exponential with a time constant of between 50 and 100 days. The total energy emitted in the visible range is of order 10^{48} ergs.

Further details of the spectra, with references, are given by Filippenko (1997). Many other aspects of supernovae may be found in the proceedings of IAU Colloquium 145, ‘Supernovae and Supernova Remnants’, and in Weiler and Sramek (1988).

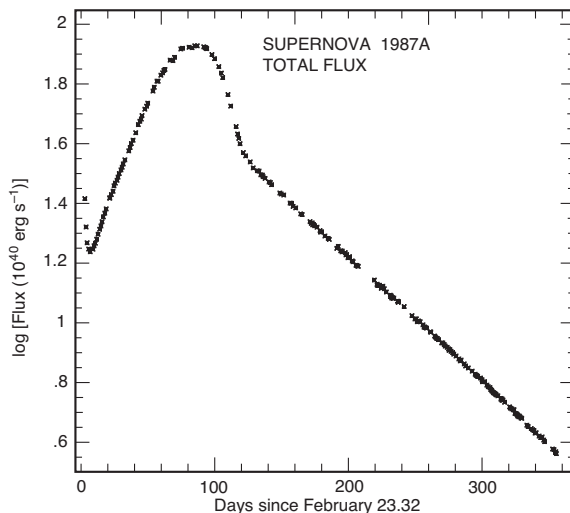


Figure 18.1 Bolometric light curve of SN 1987A (South African Astronomical Observatory).

18.2 Stellar Evolution and Stellar Collapse

The source of energy for a Type II supernova explosion is the gravitational energy released when the core of the star collapses. The collapse is a result of the exhaustion and failure of the central energy supply, which throughout the normal life of a star provides thermal pressure to balance the compressive forces of self-gravitation. The ‘main sequence’ consists of stars in which the balance is maintained through a steady nuclear burning of hydrogen to helium. Depletion of the hydrogen fuel occurs more rapidly for more massive stars: the hydrogen burning phase lasts for a time of approximately $10^{10}(M/M_{\odot})^{-3}$ years, so that for a star with the mass of the Sun ($M = 1M_{\odot}$), it lasts about 10^{10} years, while for a star with $M = 10M_{\odot}$, it lasts only 10^7 years. For stars less massive than about $4M_{\odot}$, this is the end of their evolution, and they end up as white dwarfs, which are condensed dead stars, supported by electron degeneracy pressure and with density of order 10^6 gm cm⁻³. For more massive stars, the depletion of hydrogen in the core is followed by helium burning. The central temperature then rises to 2×10^8 K, high enough to allow helium nuclei to fuse and form carbon, oxygen and other heavier elements, each stage releasing energy and heating the core. The hot core has a sufficiently high density that the gravitational force at its surface balances the large outward thermal pressure. The outer parts of the star expand, forming an opaque and comparatively cool envelope. The star is now a red giant; the proportion of mass in the envelope, and the overall diameter of the star, both increase with the total mass. The core itself

is now a compact star with the density of a white dwarf; its evolution now proceeds independently of the giant envelope surrounding it.

Progressive stages of nuclear burning can all be taking place at the same time in the core of a red giant, in a succession of shells. The energy available decreases at each stage, and each stage accordingly lasts a shorter time. Eventually the endpoint of iron is reached, beyond which no further energy is available from fusion. Collapse follows inevitably, the form of the collapse depending on the mass of the core. Within a small range of core masses, roughly from $1.9M_{\odot}$ to $2.5M_{\odot}$, it will collapse to form a neutron star, losing about $1M_{\odot}$ in the explosion that follows the collapse. This star is supported against further gravitational collapse by neutron degeneracy pressure and ends up with approximately nuclear density. A core mass of $1.9 M_{\odot}$ is the core size expected from the evolution of a main sequence star with mass of about $8 M_{\odot}$. A progenitor star more massive than about $15M_{\odot}$ will produce a more massive core, which will collapse to a black hole.

Further details of the physics of supernova collapse and explosions may be found, for example, in Woosley and Weaver (1986) and Janka (2012). We may summarise the discussion so far as follows:

1. Stars whose initial masses lie within a limited range evolve to produce cores that can collapse into neutron stars.
2. When the nuclear fuel in the core is exhausted, such progenitor stars will collapse under their own gravitation; this collapse is the origin of the energy of the supernova explosion.
3. The collapse to nuclear density, which takes place in a few seconds, is followed by a rebound, in which part of the core and all the outer parts of the star are blown away. The visible supernova results from this exploded material and from the excitation of the surrounding cloud by the radiation released in the collapse and rebound.
4. The core may disintegrate, collapse to a black hole or form a degenerate neutron star, according to its mass, which itself is determined by the mass of its parent star.

The masses of the progenitor stars whose evolution produces condensed cores following these various evolutionary tracks are only known approximately. Collapse to form a neutron star, via a Type II supernova, occurs for stars with initial mass between 8 and $15M_{\odot}$. From 2 to $8M_{\odot}$, a star may become a Type Ib or Ic supernova, leaving no neutron star. Above $15M_{\odot}$, the star will become a Type II supernova, but the core may either collapse to a black hole or disintegrate due to the photodisintegration of iron. (These mass limits are somewhat different for stars with binary companions; see Podsiadlowski *et al.* 2004.) The rate of occurrence of these three events depends on the distribution of the stellar population with mass

(the *initial mass function*); the population falls rapidly with increasing mass, so that neutron stars are more likely to originate from stars of $8M_{\odot}$ than of $15M_{\odot}$. On the other hand, stars with smaller masses evolve more slowly, so that the relative numbers reaching the three categories of collapse must depend on the age of the galaxy, or the part of the galaxy under consideration. This is borne out by observations of the locations of the two types: Type I events are found in all types of galaxy, while Type II are only found in spiral arms, where there is a large and rapidly evolving population of massive stars (Maza & van den Bergh 1976).

Cores with a mass smaller than $1.9 M_{\odot}$ may explode rather than collapse, because in these small cores the carbon burning phase occurs catastrophically, in a ‘carbon flash’ explosion, and the star is disrupted.

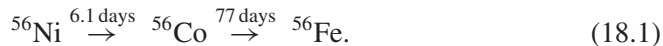
18.3 Accretion-Induced Supernova Collapse

Type I supernovae are more frequent than would be expected from the slow evolution of less massive stars, and it is now believed that some of them, Type Ia, follow a different route from stellar exhaustion to core supernova explosion. A partial collapse, to a white dwarf, is to be expected for many less massive stars, but the mass of the white dwarf is usually well below the critical level of $1.4M_{\odot}$ (the Chandrasekhar mass) above which there would be a further collapse to a neutron star. A collapse might however be induced by the accretion of sufficient matter to reach the critical mass; the most likely source of accreting material would be a close binary companion (Whelan & Iben 1973). The majority of stars are in binary systems; normal evolution may leave one star of a close binary as a white dwarf and the other as a red giant with an extended envelope. In a sufficiently close binary, mass will then be transferred to the white dwarf. A steady accretion may increase the mass above $1.4M_{\odot}$; above this limit, pressure in the centre of the star increases so much that the white dwarf becomes unstable and must either explode or collapse into a neutron star. Explosion is believed to be the most likely fate (Hillebrandt & Niemeyer 2000); this is the process associated with Type Ia supernovae.

18.4 Luminosity Decay of the Remnant

Most of the gravitational energy released in a supernova collapse is radiated away as a very high flux of neutrinos. Since these have very little interaction with other matter, they pass through and exert almost no outward pressure on the collapsing material, so that the collapse is unimpeded and is complete in a fraction of a second. The burst of neutrinos from the supernova SN 1987a, in the Large Magellanic Cloud, was observed on Earth some hours before the expanding cloud of the supernova became visible.

The spectrum of the expanding cloud of a Type Ia supernova contains traces of heavy elements synthesised in the disrupted core, while in Type II we see only the hydrogen that formed the pre-collapse outer envelope; all the heavy atoms remain in the neutron star. Earlier we remarked on the surprising similarity of the light curves of these two types. In both cases it is the events inside the supernova core that determine the initial release of energy; after the initial explosion, the main source of radiated energy is in-falling material energised and transmuted by the energy from the core. The decay of this radiation follows a remarkably simple pattern: it is governed by the exponential radioactive decay of nickel to iron. It happens that ^{56}Ni is an easily formed isotope, because it has atomic number Z equal to the neutron number N , while Z is also divisible by 4. It can therefore be synthesised directly from ^4He , and it has the highest binding energy per nucleon for $Z = N$. It decays according to the sequence:



The binding energy is released mainly as gamma rays and neutrinos, both of which transfer energy to the large expanding cloud. This is the source of the luminosity of both Type Ia and II. We now see that the decay of luminosity follows the 77 day time constant of the decay of ^{56}Co .

The peak luminosity and the exponential decay of all Type Ia supernovae both lie in a small range, because the mass of the collapsing core lies in a small range just below $1.4 M_{\odot}$. Since they are both bright and similar, they are used as ‘standard candles’ in cosmological studies. The peak luminosity of Type II supernovae cover a wider range and may be four or more magnitudes lower than that of Type Ia.

18.5 Frequency of Occurrence of Supernovae

Supernovae occur so rarely in any individual non-starburst galaxy that a measurement of the average frequency of occurrence requires continued observation of a large number of galaxies. Many observations have been directed at distant galaxies, particularly for discovering Type Ia supernovae for cosmological studies, and the extragalactic rate of occurrence (see for example van den Bergh & McClure 1994; Navasardyan *et al.* 2001) is better known than the rate for our own Galaxy. A remarkable feature of the observed rate of occurrence of supernovae is that the rates for Type Ia and II supernovae are comparable, despite the fact that they appear to be distinct categories originating in different types of star. The total rate is close to 1 per 100 years in a typical galaxy, Type II being about 3 times as frequent as Type Ia. Furthermore, although the total energy release for Type II is apparently much greater than for Type I, as demonstrated by the kinetic energy of the expanding remnants, the optical emission is not very different, so that the chances of

observation are similar. The ratio of kinetic energy to visible energy may be 10^3 times smaller for Type I than for Type II.

In our Galaxy, inevitably, the observations are far from complete, and some supernovae will be missed because of obscuration by dust clouds in the plane of the Galactic disk. The extent of this incompleteness is illustrated by the statistical work of Katgert and Oort (1967), who revised the previous estimate for the average frequency in our Galaxy from one per 450 years (Minkowski 1964) to one per 40 years (see also Tammann *et al.* 1994 and Maoz *et al.* 2011).

The assessment of completeness in the Galaxy requires some guesswork about the thoroughness of ancient observers. No supernovae have been observed since 1572 (Tycho) and 1604 (Kepler), but others may well have occurred in obscured regions of the Galaxy. The prime example is the intense radio source Cassiopeia A (Cas A), which must have exploded about the year 1700. There is good evidence that this was a Type II supernova. It was not reported from any observatory, even though the constellation Cassiopeia is circumpolar for most northern observers. The visible remnant, discovered after the source of the radio emission had been located with sufficient accuracy, is heavily obscured, to the extent of 10 visual magnitudes. The supernova explosion would then barely bring the star into the range of naked eye visibility.

The radio remains of other supernova explosions can be distinguished from other discrete Galactic radio sources by their size, shape and spectrum. Over 100 Galactic supernova remnants (SNR) were catalogued by Illovaisky and Lequeux (1972), Clark and Caswell (1976) and Weiler *et al.* (1996). A catalogue of Galactic SNRs (with 294 entries in 2019) is maintained by D.A.Green.¹ More are being discovered in GLEAM, a low frequency survey in the southern hemisphere (Hurley-Walker *et al.* 2019a) as well as with the sensitive radio surveys of the Galactic plane with MeerKAT and ASKAP and the all-sky x-ray surveys with eROSITA. Woltjer (1972) estimated the lifetime of the remnants, and, after allowing for the incompleteness of the catalogues, he found that they were formed at a rate between 1 per 60 years and 1 per 45 years. The typical age of a visible remnant is about 5×10^4 years (Clark & Stephenson 1977). These SNRs are mainly concentrated in a galactic disk with radius $R = 8$ kpc, with a surface density falling by a factor 10 at $R = 12$ kpc. Within $R = 6$ kpc, the z-distribution is close to an exponential with scale height 90 pc. The age and distribution of these remnants agree with an origin in Type II supernovae, which in turn are associated with young Population I stars. The youngest SNR so far observed in the Galaxy is G1.9+0.3, near the Galactic centre. Expansion of this SNR observed both by the VLA and Chandra after 22 years gave

¹ On line at www.mraocam.ac.uk/surveys/snrs

an age of 140 years. Reynolds *et al.* (2008) and the most recent ATCA data support this age (Luken *et al.* 2020).

A longer-term average rate of Type II supernovae is available from observations by the Comptel CGRO space telescope of 1.8 MeV gamma rays from radio active decay of ^{26}Al in the Galaxy. A well-known amount of ^{26}Al is formed in a core-collapse supernova, and the decay half-life is 7.2×10^5 years. The integrated brightness of the line indicates a Type II supernova rate of 1.9 ± 1.1 per century (Diehl *et al.* 2006).

18.6 Supernova Remnants

The appearance of a supernova remnant depends on: (i) its age, (ii) the type of supernova, (iii) whether it contains a pulsar that can provide a continued source of energy to all or a part of the remnant and (iv) the matter density of the medium into which it is expanding.

The expansion of the youngest SNRs, such as Cas A (Figure 18.2) and the Crab Nebula (Figure 18.4), has not yet been slowed significantly by the interstellar

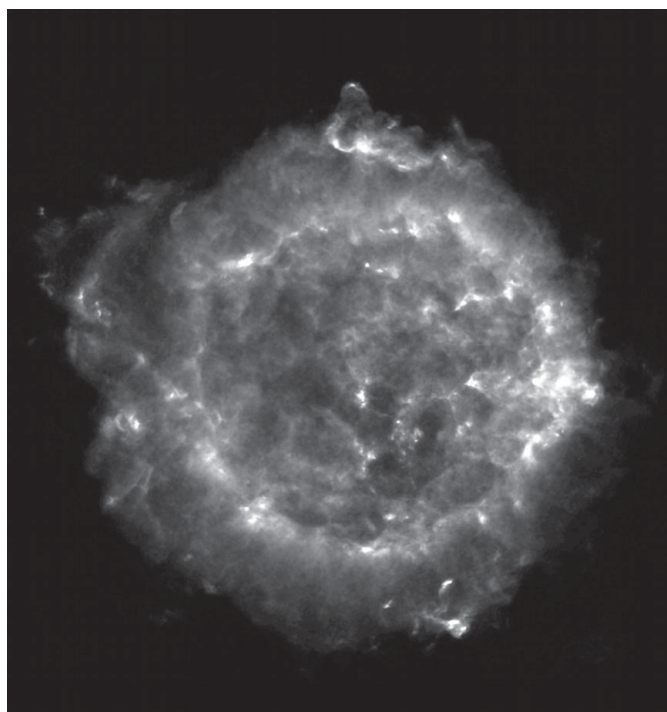


Figure 18.2 A Very Large Array radio image of the supernova remnant Cas A. (Credit: L. Rudnick, T. Delaney, J. Keohane and B. Koralesky, image composite by T. Rector).

medium; the expansion velocities can therefore be extrapolated back to the site and time of the original explosion. Cas A, one of the youngest known in our Galaxy, is a shell of hundreds of knot-like filaments, with velocities up to 6000 km s^{-1} . The radius is 1.6 pc, giving an apparent birth date of AD 1658 ± 3 years (Flamsteed may have observed the actual supernova at the later date of 1680, which suggests that the present-day velocities must be below the original expansion velocity). Cas A is still expanding essentially freely without appreciable resistance from the surrounding circumstellar medium, which is swept up by the expanding nebula. The initial blast wave velocity is believed to have been about 10^4 km s^{-1} . When some 1–5 times the total mass of the ejecta has been swept up, the expansion is slowed. This later phase, known as the Sedov phase, lasts typically 2×10^4 years; its progress as seen in radio maps of supernova remnants has been traced by Chevalier (1992). In remnants like the Cygnus Loop (Figure 18.3) and IC443, the expansion has almost stopped, and the visible remnant is composed largely of swept-up interstellar material.

The filaments of Cas A contain oxygen and other heavy elements, which must have originated from within the pre-supernova star. Optical spectra of the shells of the supernova remnants Tycho and Kepler, in contrast, are pure Balmer line emission from hydrogen; here the emission from the shells, including synchrotron radio and x-ray, is derived from the interaction of the expanding nebula with the interstellar medium. Most SNRs are shells, but some, like the Crab and the PSR B0540–69 nebula, are filled with emitting material at all wavelengths; these are called ‘plerions’.

Within the remnant there may be an extra supply of energy from a pulsar, which provides a wind of high-energy particles, accounting for the filled remnants. The interaction of the wind with colder material within the nebula may be seen as a distinct pulsar wind nebula (PWN); such PWNe are observed most clearly by their x-ray and gamma-ray emission.

The oldest observable supernova remnants are probably the extensive ‘loops’ of radio emission, such as the North Galactic spur. This may be an accumulation of nearly stationary shock fronts from several supernova in an OB association, which is a concentrated region of massive young stars. The expanding shell leaves behind a huge bubble containing hot gas at low density. The distribution over the sky of x-ray brightness indicates that the Sun may be contained inside such a cavity, known as the Local Bubble; if so, the local supernova that was responsible may also have left a nearby observable young pulsar, such as Geminga (Gehrels & Chen 1993).

Further descriptions and discussions of supernova remnants are given by Raymond (1984), van den Bergh (1988) and Dubner and Giacani (2015). We now concentrate on the most intensively studied of them all, the Crab Nebula.

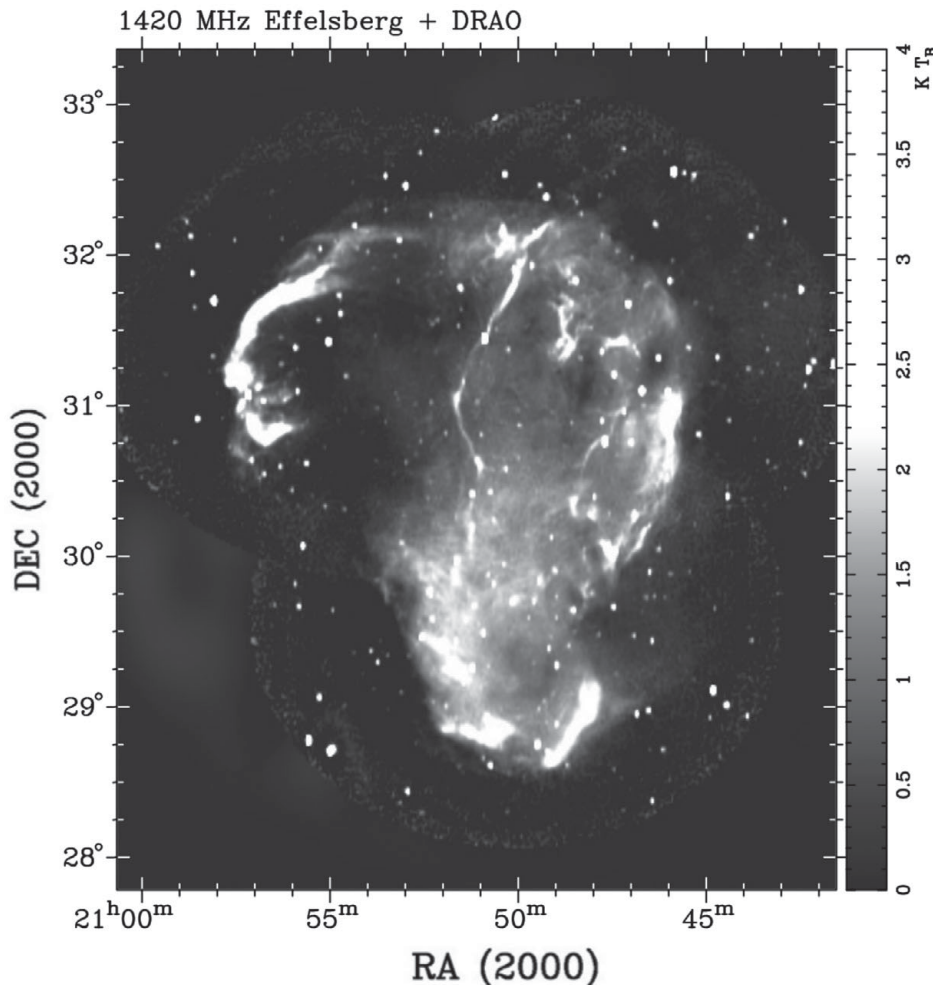


Figure 18.3 The Cygnus Loop, a supernova remnant, mapped at 1420 MHz using the Effelsberg and DRAO telescopes (Uyaniker *et al.* 2004).

18.7 The Crab Nebula

As a nebula, the Crab was first observed in 1731 by John Bevis, an English physicist and amateur astronomer. It took first place in the catalogue of nebulae compiled by Charles Messier in AD 1758, where it appeared as the nebula M1. The name ‘Crab Nebula’ was given to it about a hundred years later, when better telescopes revealed its tentacle-like structure (Figure 18.4). The present-day interest in the Crab Nebula dates mainly from the work by Baade in 1942, where he presented observations of its detailed structure and suggested that a prominent star near the centre of the



Figure 18.4 The Crab Nebula. NASA/ESA Hubble Space Telescope (Alison Loi/Jeff Hester, Arizona State University).

nebula might be related to its origin. Baade already knew that the nebula was very young (on an astronomical time scale). In 1939, Duncan had shown that the nebula was expanding at such a rate that it appeared to have originated in a point source only about 766 years earlier. But the most spectacular evidence of its youth was obtained from ancient Chinese and Japanese astronomical records.

The extensive material in ancient and mediaeval Chinese records of comets and novae is described by Ho Peng-Yoke (1962). Records of a nova in the year AD 1054 were noted by Lundmark (1921), but the association with the Crab Nebula seems to be due to Duyvendak (1942). The history of the Sung Dynasty (Sung Shih, completed in AD 1345) contains this record: ‘On a chi-chou day in the fifth month of the first year of the Chih-Ho reign-period a “guest star” appeared at the SE of Thien-Kuan (Taurus), measuring several inches. After more than a year it faded away.’ The date is well corroborated in other independent records. The new star was visible in the daytime for several days and remained as an object visible with the naked eye at night-time for nearly two years. There is no doubt that the ancient records describe a supernova explosion, and the near-coincidence of positions and

dates makes the identification with the present-day Crab Nebula certain. The discrepancy between the actual birth date of AD 1054 and the date obtained by projecting back the presently measured velocities, which now converge at AD 1140 ± 10 , is to be interpreted as a small but definite acceleration of the outward velocities, a fact of great significance in the question of the energy supply to the nebula.

Near the centre of expansion, there are two stars, of 15th and 16th magnitude, which show prominently on photographs of the nebula (Figure 1.2). Since there must be somewhere within the nebula a supply of energy to account for the continued emission of light, it was supposed that one of these two stars was the source of excitation. The one nearest to the centre of expansion was the south proceeding star of the pair; it was also a star with a most unusual spectrum. Baade suggested that this might be the parent star for the whole nebula, but he was unable to account for the excitation through the familiar process of ultraviolet light emission. The spectrum showed no emission or absorption lines, which suggested that the star had a very high temperature. At the same time there was no indication of the abnormally low colour index that would correspond to the strong ultraviolet emission of a hot star. We know now that this star is the Crab Pulsar, and that it feeds energy into the nebula not by light but through high-energy particles accelerated in a rotating magnetic field. We also know that the light from the pulsar is not from hot gas on the surface of a star, but is produced by these high-energy particles close to the pulsar.

The Crab Nebula (Figure 18.4) is contained within an ellipse 180×120 arcseconds across. The outer parts are filamentary, forming a network enclosing the more luminous central part. This is an amorphous mass concentrated towards the centre but extending over most of the major diameter and about two-thirds of the minor diameter. The light from these two components is totally different in character, so that in a colour photograph of the nebula the filaments show as predominantly red, while the centre is white or bluish-white. The red light from the filaments is spectral line radiation, mainly H α but including many other lines from heavier atoms such as helium, nitrogen, oxygen, sulphur and neon. The relative abundance of the elements is close to the standard solar composition, except for a rather higher helium abundance. The ionisation is due to the ultraviolet light from the nebula.

The line radiation from the centre of the nebula originates in filaments on the front and back, that is, the parts that approach and recede from the observer with maximum velocities. The Doppler shifts in these lines correspond to expansion velocities close to 1000 km s^{-1} . By combining this value for the expansion in the line of sight with the measured angular rate of expansion, and assuming that the expansion follows a simple elliptical form, the distance of the nebula may be obtained. This measurement and other estimates place the distance of the nebula in the range 1.5 to 2.5 kpc.

The white light from the central amorphous component has no spectral lines, and its origin was for a time a complete mystery. Although this component usually appears to be amorphous, under good seeing conditions it is found to be concentrated in fine filaments, like cotton wool. These fibrous concentrations run in organised directions, which are now known to be associated with a magnetic field within the nebula. The spectrum of this source of continuous radiation, and its high brightness, are incompatible with thermal radiation.

18.8 Continuum Radiation from the Crab Nebula

In 1949, the radio astronomers Bolton, Stanley and Slee (1949) identified the Crab Nebula as a radio source. This was the first identification of a discrete Galactic radio source. The radio flux density was far greater than expected from extrapolation of the spectrum of the visible light, so that the continuum radiation could not be explained in the familiar terms of thermal radiation from ionised gas.

The explanation of this bright continuum radiation was provided by I. Shklovsky in 1953. High-energy electrons moving in a magnetic field follow curved paths; this curved motion implies an acceleration, which leads to radiation. Previous analyses of energy loss in a synchrotron electron beam had already shown that this was an important effect, and it is generally called synchrotron radiation (it has also been referred to as magnetic braking radiation, or *magnetobremsstrahlung*). The main characteristics of synchrotron radiation are outlined in Chapter 16. The importance of this suggestion was that it provided the only known means for a very hot gas to radiate efficiently and over a wide range of wavelengths. Furthermore, it led to the prediction that the radiation at any wavelength would be at least partly linearly polarised.

Confirmation of the synchrotron proposal soon came from observations by two Soviet astronomers, Dombrovsky (1954) and Vashakidze (1954), who showed that there was indeed a large linear polarisation. A detailed investigation by Oort and Walraven was reported in a classic paper (1956). Photographs in this paper show that the degree of polarisation is so high that the appearance of the nebula varies dramatically according to the setting of a Polaroid filter on the telescope. The integrated light from the whole nebula is 9% polarised, while locally the polarisation may reach 60%. Oort and Walraven showed that the white radiation from the nebula must indeed be synchrotron radiation; their analysis showed that the magnetic field strength in the nebula must be about 10^{-3} G, and the electron energies must extend up to at least 10^{11} eV. The radiation mechanism was now understood, but the origin of the magnetic field and of the very high electron energy was to remain a mystery until the discovery of the Crab Pulsar.

Table 18.1. *The radio to x-ray spectrum of the Crab Nebula.*

Frequency range (Hz)	Flux density S_ν (Jansky)
$10^7 < \nu < 10^{12}$	$1040(\nu/10^9)^{-0.30}$
$2 \times 10^{13} < \nu < 3 \times 10^{15}$	$1.82(\nu/10^{15})^{-0.85}$
$10^{16} < \nu < 10^{19}$	$1.25 \times 10^{-3}(\nu/10^{13})^{-1.15}$

Radio observations of the Crab Nebula now extend over the wavelength range from 30 m to 3 mm. The optical observations have been extended into the infrared, covering 500 nm to 5000 nm. X-ray and gamma-ray observations are now made from satellites, over the energy range 0.5 keV to 500 keV, corresponding to a wavelength range 3 nm to 3 pm, and from air-shower arrays up to 100 TeV. The known spectrum therefore covers 21 decades, spanning frequencies from 10^7 to 10^{28} Hz. A review by Bühler and Blandford (2014) shows that the radio, optical and x-ray spectrum is probably continuous, with the spectral indices and flux densities in the three main parts of the spectrum as shown in Table 18.1 and Figure 17.5. The spectrum continues into the gamma-ray region; an enhancement above about 100 MeV is attributed to inverse Compton radiation.

18.9 The Energy Supply

The analysis by Oort and Walraven of the optical and radio emission led to a fairly precise definition of the energy spectrum and actual numbers of electrons within the nebula, as well as the average value of the magnetic field. The total energy of fast particles in the nebula was found to be of the order of 10^{49} erg, most of this being concentrated in particles with energy of order 10^{11} eV. This energy is about one-thousandth of the total energy that would be released if a solar mass burned from hydrogen into helium, which is the maximum amount of nuclear energy that could reasonably be expected from a supernova explosion. It would be remarkable, but not inconceivable, for the energy of the explosion to be so well concentrated into high-energy particles. But a further problem was pointed out by Oort and Walraven: the electrons must be radiating so efficiently that their energies would decay in a time of order only 100 years rather than 1000 years, so there must be another source of energy operating after the acceleration in the original explosion.

The lifetime of an electron emitting synchrotron radiation with a maximum spectral density at frequency ν (Hz) moving perpendicular to a field B_\perp (G) is expressed as a half-life:

$$\tau_{\frac{1}{2}} = 3 \times 10^4 \nu^{-1/2} B_\perp^{-3/2} \text{ years.} \quad (18.2)$$

The lifetime could only be extended for optical radiation at a fixed frequency by assuming a smaller value of the field B , which would imply a larger total electron energy to produce the observed emission. The total energy would then reach or exceed the total available from the supernova explosion. This dilemma was made worse by the observation of x-ray emission at energies in excess of 10 keV, where the synchrotron radiation must have come from electrons with energies of at least 10^{14} eV, which would have lifetimes of less than a year in any reasonable magnetic field.

An equally difficult problem was presented by the existence of the magnetic field itself, which contains the same order of magnitude of energy as the particles. Although there is no loss through radiation, it is impossible that this field is merely a remnant of a field that simply originated at the time of the supernova explosion. Any such field would have been reduced far below 10^{-3} G in an adiabatic expansion, transferring most of its energy into expansion energy of the nebula. There must be a means for the continued generation of a magnetic field throughout the nebula.

There was, therefore, even before the discovery of the Crab Pulsar, incontrovertible evidence that an energy source existed within the Crab Nebula that was providing both the high-energy particles and the magnetic field throughout the nebula. The location of this source was suspected to be at, or close to, Baade's star, both on account of its unusual spectrum and because of some remarkable activity in the nebula close to the star.

18.10 Associations between Pulsars and Supernovae

We now return to the question at the beginning of this chapter and propose the following guide to the relation between neutron stars and supernovae.

1. Core-collapse supernovae (Type II) all generate a neutron star.
2. Most (possibly all) accretion-induced supernovae (Type Ia) do not generate neutron stars.
3. Most (possibly all) neutron stars are generated in Type II supernovae.

The exceptions in propositions 2 and 3 refer to the possibility of accretion-induced collapse (AIC) in an accreting white dwarf star in a binary system producing a neutron star, rather than disruption in a thermonuclear explosion. AIC is believed to be less likely to occur, except in white dwarf stars with O/Ne cores (see a discussion by Hillebrandt & Niemeyer 2000).

Bearing in mind that only about 1 in 100 of the known pulsars appear to be convincingly associated directly with supernova remnants, the third proposal seems hard to prove. The reason is obvious: the lifetime of supernova remnants is only of order one hundredth that of pulsars. The first two proposals require concentrated

and sensitive searches for pulsars (or other neutron stars) within or close to observed supernova remnants, of which almost 300 are known already. Sensitive searches are now possible with the advent of the x-ray satellites Chandra and XMM Newton, and the use of the largest radio telescopes such as FAST and MeerKAT; they will be a prime target of the new synthesis arrays such as the SKA.

The SNRs resulting from the two types of supernovae are hard to distinguish. The presence of an active neutron star is, however, often indicated by a pulsar wind nebula (PWN), which may fill the observable SNR, as in the Crab Nebula, or part fill it, when the SNR is known as a *composite remnant*. A comprehensive discussion of the detection of pulsars in the various types of remnant is given by Kaspi and Helfand (2002). A prime example of an SNR containing a pulsar wind nebula and a pulsar is 3C58, discovered as a radio source and identified as the remnant of supernova SN1181. A compact x-ray source at the centre of the nebula was found in Chandra observations to be pulsating with a period of 65 ms (Murray *et al.* 2002); subsequently, radio observations showed it to be a normal but very weak pulsar J0205+6449 (Camilo *et al.* 2002c).

A similar example is PSR J1400–6325, a 31-ms pulsar found by RXTE at the centre of the x-ray source IGR J1403–6326 (Renaud *et al.* 2010). This is a central wind nebula inside a previously uncatalogued SNR ring; the pulsar is young, with an age of 12.7 kyr. A similar association is found between PSR J1747-2809 and the SNR remnant G0.9+0.1 (Camilo *et al.* 2009a). The association between PWNs and young pulsars is not, however, universal; for example PSR J1119–6127, with an age of only 1.6 kyr, is at the centre of an SNR shell, but with no discernable PWN (Pivovaroff *et al.* 2001).

Another essential parameter in this discussion is the age of the pulsar. If this considerably exceeds the lifetime of the visible supernova remnant, which is of the order of 10^5 years, then any apparent association is probably only a chance superposition. On the other hand, if the supernova remnant is no longer expanding, having encountered a sufficient mass of interstellar material to slow it down from an expansion velocity of 10,000 km s⁻¹ to 10 km s⁻¹, then a high velocity may have taken the pulsar outside the nebula. The observed associations confirm this view. The Crab Pulsar (age 10^3 years) is near the centre of the Crab Nebula. The Vela Pulsar (age 2×10^4 years) is well within a less well defined supernova remnant. PSR B1706–44 is less certainly associated with the remnant S343.1–2.3, as its position in relation to the nebula suggests that it must have had a velocity of at least 1000 km s⁻¹ over its lifetime (Frail *et al.* 1994).

In addition to the association between pulsars and supernova remnants, the Chandra x-ray telescope has detected thermal radiation from a neutron star in the centre of Cas A, the youngest known Galactic supernova remnant. Furthermore, changes in the spectrum over nine years show that the surface temperature has

fallen rapidly, from $2.12 \pm 0.01 \times 10^6$ K to $2.04 \pm 0.01 \times 10^6$ K (Heinke & Ho 2010); such rapid cooling may indicate a change of state in the interior.

Bearing in mind both the success in finding associations between Type II SNRs and radio pulsars and the difficulty of detecting the weakest such pulsars, it is not over-optimistic to assume that at least half of Type II remnants contain an observable neutron star and a PWN. The others may contain radio pulsars like Geminga, whose beams never pass over the Earth, or possibly some may contain black holes.

18.11 Pulsar Wind Nebulae

The activity close to Baade's star in the Crab Nebula had been noted in 1921 by Lampland. Later observations, especially by Scargle and Harlan (1970), confirmed his suggestion that some nebulous wisps about 10 arcseconds away from the star were moving and changing in brightness, sometimes even within periods of only a few months. X-ray and optical photographs by the Chandra telescope (Weisskopf *et al.* 2000) and the Hubble Space Telescope revealed the source of this activity in spectacular detail (Figure 18.5), showing a jet of high energy particles streaming from the pulsar, ending in a torus of hot gas at the location of the visible wisps. This is the prime example of a *pulsar wind nebula*, a PWN. The high energy material generating x-rays is short-lived, showing that the wind nebula is energised by a continuous flow from the pulsar. A similar x-ray image of the Vela Nebula

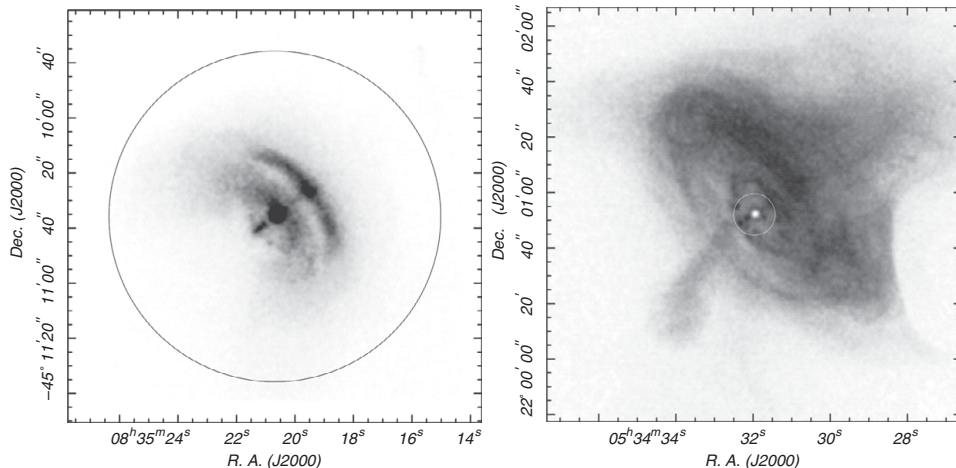


Figure 18.5 The wind nebulae formed by the Vela (left) and Crab (right) Pulsars, observed by the Chandra x-ray Observatory. The angular scale is the same for both; Vela is at a distance of 250 pc and the Crab is at 2 kpc, so that the Vela PWN is 16 times smaller than the Crab (Chandra images courtesy of NASA (Helfand *et al.* 2001)).

(Helfand *et al.* 2001) also shows a wind nebula within the supernova remnant, energised by the pulsar. As in the Crab Nebula, the jet is aligned in the direction of the rotation axis. We can now be certain that the Crab Pulsar itself is supplying energy to the nebula, sufficient to provide for the magnetic field, the particle energy and the accelerated expansion. The total energy required is about 10^{38} erg s $^{-1}$, which is close to the rate at which the pulsar is losing rotational energy.

Similar pulsar wind nebulae forming tori are observed in other young supernova remnants, primarily in x-rays but also in radio and optically. PSR J1856+0245, a young energetic pulsar ($P = 81$ ms, like the Vela Pulsar), coincides with a Hess gamma-ray source (Hessels *et al.* 2008a). Bamba *et al.* (2010) list 11 PWN tori observed by the x-ray telescope Chandra; they find a direct link between the radii of the tori and the spindown energy \dot{E} of the pulsars. In some remnants with wind nebulae, there may be a pulsar that is too weak to be detected in a normal survey; an example is the SNR G292.0+1.8, which was long known as a radio source and later as an x-ray source, but with no detected pulsar. A deep radio search eventually revealed PSR J1124–5916, a young but very weak pulsar at the centre of the nebula (Camilo *et al.* 2002b; Gaensler & Wallace 2003).

The spin-down energy of a pulsar is mainly radiated in the form of an electromagnetic wave at the rotation frequency, with some fraction as a stream or jet of particles from the polar regions. This energy is eventually absorbed, either in the surrounding remains of the supernova in which the pulsar was born or in the more diffuse interstellar medium. Close to the pulsar (but outside the magnetosphere), the wave and the particle stream excite charged particles to high energies, and they can radiate synchrotron radiation, which may be detectable over the whole spectrum from radio to gamma rays as a pulsar wind nebula. The particle energies may be high enough to scatter synchrotron photons to TeV gamma rays; this was first detected in the Crab Nebula (Weekes *et al.* 1989), and the HESS gamma-ray telescope has discovered many more examples. The radiated energy is roughly proportional to the slow-down energy \dot{E} , which varies with period P as $\dot{P}P^{-3}$, so that PWNs are generally associated with young pulsars.

The structure of a PWN depends mainly on the stage of development of the supernova remnant (SNR) in which it is embedded, but it may also depend on the velocity of the pulsar, which can take it outside the SNR itself. The SNR initially expands at a rate of thousands of km s $^{-1}$, while pulsar velocities are some hundreds of km s $^{-1}$ or less. At an early stage, the pulsar will be near the centre of the SNR, and the PWN may be formed entirely within the SNR, forming a distinct nebula at its centre. A young PWN expands supersonically into the unshocked SNR, with diameter increasing with age t as $t^{6/5}$ (Chevalier 1992). The Crab Nebula is a PWN today; no trace has been found of a surrounding SNR. The Nebula itself is referred to as an SNR but might properly be called a PWN, since it is entirely energised by the pulsar.

In an ideal case it may be possible to observe this early stage by detecting the pulsar itself, the expanding supernova shell and, within this, the PWN. An example is one of the youngest pulsars, PSR J1833–1034, which is probably only about 1000 years old (Camilo *et al.* 2006a). An x-ray image from Chandra shows an approximately circular supernova remnant, SNR G21.5–0.9, diameter 5 arcminutes, with the pulsar at its centre surrounded by a PWN (Matheson & Safi-Harb 2010).

At a later stage, the expanding SNR interacts with the surrounding ISM, sweeping up material in which kinetic energy is dissipated as thermal energy. The expansion slows, and a reverse shock develops, reacting back towards the centre of the SNR, and without an active pulsar, the whole SNR is filled with shocked material. If, however, the reverse shock meets an expanding PWN forward shock, the PWN will be compressed and heated, becoming more visible and detectable as a source of x-rays. An ideal, symmetrical example of this stage is unlikely to be found, for two reasons. First, the reverse shock is unsymmetrical due to irregularities in the ISM; second, after some 10,000 or more years, the high velocity of the pulsar itself may take it well away from the centre of the SNR and the PWN.

A PWN associated with the Vela Pulsar B0833–45, and the larger supernova remnant SNR G263.9-3.3 have been mapped in detail in radio and x-rays. Close to the pulsar, the Chandra x-ray picture shows axial emission and bright arcs ([Figure 18.5](#)), similar to those of the Crab Nebula shown in the same figure (Helfand *et al.* 2001). The PWN is, however, less well defined in Vela, and it appears that it is distorted by a reverse shock. The PWN is about 1 deg across, while the supernova remnant is about 4 deg across. The velocity of a pulsar may be sufficient to carry it outside its original PWN, so that it is moving at high speed through the shocked gas of the SNR. Its motion is at first subsonic, but the speed of sound drops towards the edge of the SNR, and the pulsar can be moving supersonically. In the ISM, the speed of sound depends on the temperature but is no greater than 100 km s^{-1} for the hot component; again the pulsar may move supersonically if it leaves the SNR completely. The PWN may now be observed as a bow shock. An example is the Guitar Nebula (Cordes *et al.* 1993). The bow shock here is very close to the pulsar, PSR B2224+65, but it leaves a visible trail 78 arcsec long ([Figure 18.6](#)). The beautiful bow shock created by the millisecond pulsar PSR J0437–4715 ([Figure 18.7](#)) is more clearly detached from the pulsar, forming about 10 arcsec in front of it. This pulsar has transverse velocity of around 100 km s^{-1} (Bell *et al.* 1995).

Another example of interaction between a high-velocity pulsar and the supernova remnant in which it was apparently born is shown in [Figure 18.8](#). Here the interaction is revealed in a radio image of the nebula G5.27–1.2, which is part of a larger nebula G5.4–1.2 (Frail & Kulkarni 1991). The pulsar PSR B1757–24 is located at the peak of the comet-like protrusion from the western edge of the nebula.



Figure 18.6 The Guitar Nebula created by PSR B2224+65, which lies at the top of the bullet-shaped structure (Chatterjee & Cordes 2002). The bow shock (upper left) is very close to the pulsar, but it leaves a faint expanding trail 78 arcsec long in the centre of the image.

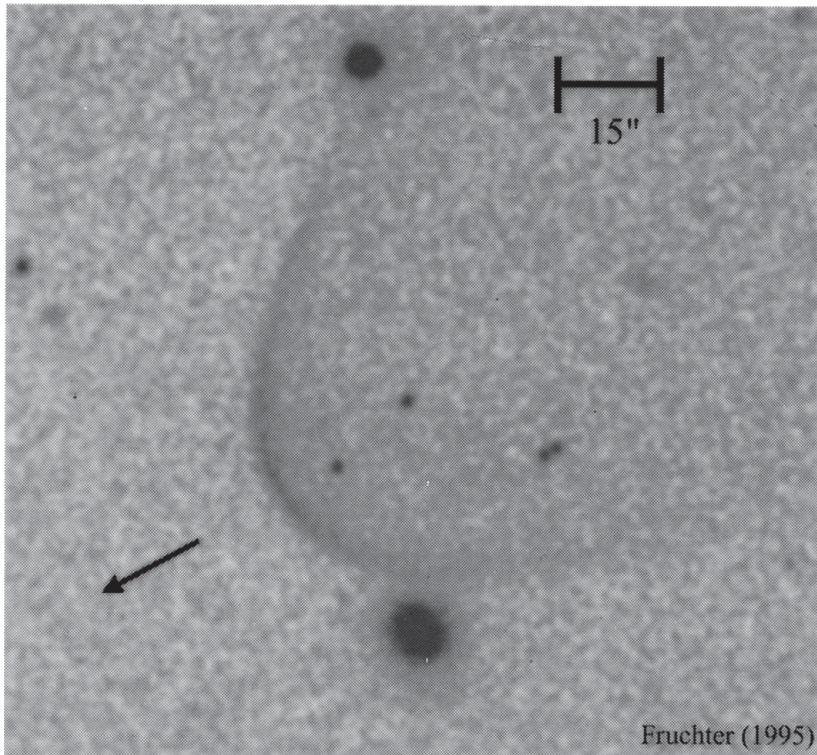


Figure 18.7 The bow shock created by PSR J0437–4715, a millisecond pulsar with transverse velocity of around 100 km s^{-1} . The binary companion star can be seen just inside the shell behind the arrow, which represents the direction of the motion of the system. Hubble Space Telescope photograph: courtesy of A. Fruchter.

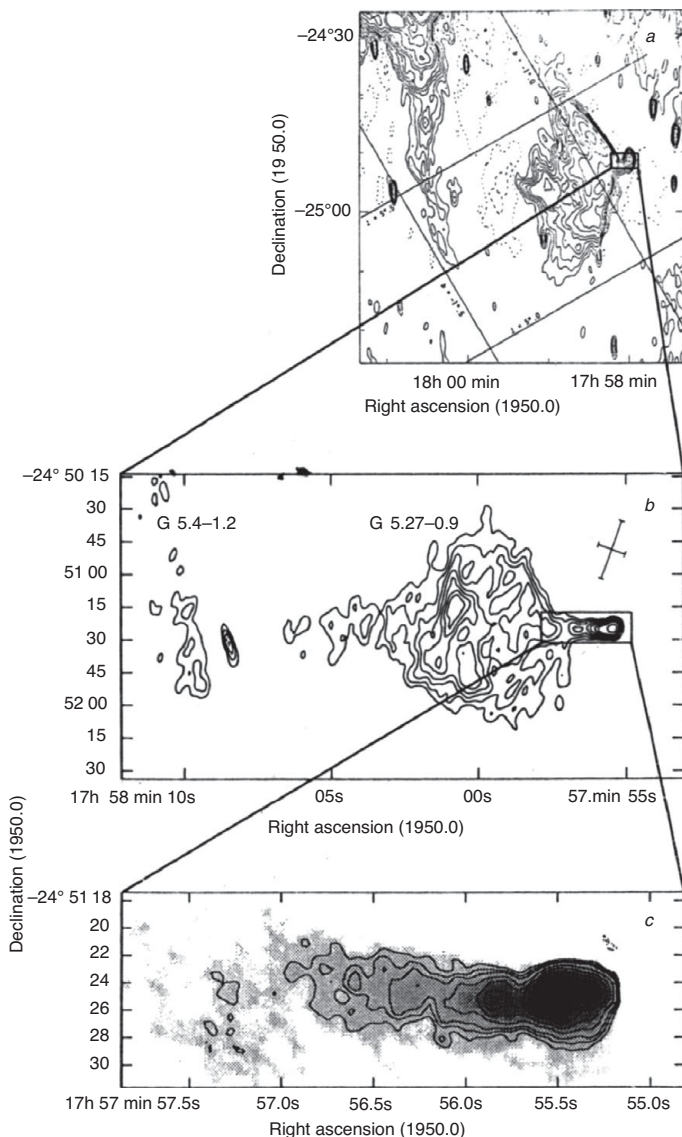


Figure 18.8 Radio image at 1.4 GHz of the nebula G5.27–1.2, showing the comet-like protrusion that contains PSR B1757–24 (Frail & Kulkarni 1991).

Both nebula and pulsar must be young, probably about 10^4 years old, so the location of the pulsar outside the main shell of the nebula suggests that it has a high velocity of around 1000 km s^{-1} and has overtaken the decelerating shell of the supernova remnant.

Table 18.2. Some typical pulsar wind nebulae.

PSR	SNR	PWN	Detections	Refs.
J0205+6449	3C58 SN1181	Plerion	R,X,O	1, 2
J0437–4715		Bow shock	R, O	3, 4
B0531+21	Crab SN1054	Plerion	R,X,O,G,T	
B0833–45	Vela	Plerion	X	5
B1509–58	MSH15–52	Plerion	R,X,G,T	6, 7, 8
J1718–3825	HESS survey		T	9
J1833–1034	G21.5–0.9	Plerion	X,R	10, 11
B1757–24	G5.4–1.2	Bow shock	R	12
B1929+10	G47.4–3.9	Bow shock	X	13
J1930+1852	G54.1+0.3	Plerion	R,X,T	14, 15, 16
J2124–3358		Bow shock	O	17
B2224+65	G108.6+6.8	Bow shock	O	18

Detections: R = radio, O = optical and infrared, X = x-ray, G = gamma-ray, T = terahertz

1 Murray <i>et al.</i> 2002	7 Gaensler <i>et al.</i> 2002a	13 Hui and Becker 2008
2 Bietenholz <i>et al.</i> 2002	8 Aharonian <i>et al.</i> 2005	14 Camilo <i>et al.</i> 2002a
3 Bell <i>et al.</i> 1995	9 Aharonian <i>et al.</i> 2007	15 Lu <i>et al.</i> 2002
4 Stappers <i>et al.</i> 2002	10 Safi-Harb <i>et al.</i> 2001	16 Acciari <i>et al.</i> 2010
5 Helfand <i>et al.</i> 2001	11 Camilo <i>et al.</i> 2006a	17 Gaensler <i>et al.</i> 2002b.
6 Seward and Harnden 1982	12 Frail and Kulkarni 1991	18 Cordes <i>et al.</i> 1993

A pulsar inside an SNR may be detectable by the effects of a stream of energetic particles from its poles, as seen in the moving wisps near the centre of the Crab Nebula (Figure 18.5). It is interesting to speculate that a pulsar whose radio emission cannot be detected because of its unfavourable geometrical orientation might nevertheless create a visible PWN that would reveal its presence. The nebula G328.4+0.2, for example, observed as a non-thermal radio and x-ray source, is probably a PWN energised by an un-detected pulsar (Gelfand *et al.* 2007), even though no SNR can be seen.

The typical spectrum of a PWN at radio frequencies is a flat power law, with index $\alpha \sim -0.3$. The spectrum is steeper at higher energies, especially in the outer regions. X-ray spectra have a typical index² of $\alpha \sim -1.0$. Emission in the TeV band, as detected by the Imaging Atmospheric Cerenkov telescopes, is probably generated by inverse Compton scattering of low-energy photons by very energetic electrons in the nebula (Aharonian *et al.* 2006). The *luminosity efficiency*, η , is the ratio of radiated power to spin-down energy \dot{E} , usually quoted separately for the radio and x-ray regimes. Typically, $\eta_R = L_R/\dot{E} \sim 10^{-4}$ and $\eta_X = L_X/\dot{E} \sim 10^{-3}$.

² In high energy wavebands, a photon index Γ is quoted, where the photon flux varies with energy as $F_E \propto E^{-\Gamma}$. The spectral index α is defined as $S_\nu \propto \nu^\alpha$. The two indices are related as $\Gamma = 1 - \alpha$.

Table 18.2 lists some typical PWNs, with references that may serve as an introduction to the many papers on this subject. A review of PWNs by Gaensler and Slane (2006) includes a comprehensive list of references. A catalogue of PWNs is maintained by M. S. E. Roberts.³

³ www.physics.mcgill.ca/pulsar/pwncat.html

19

Interstellar Scintillation and Scattering

Optical scintillation is familiar as the twinkling of stars and as the shimmer of distant objects seen through a heat haze. At radio wavelengths, scintillation is encountered in several different circumstances in which ray paths have differential time delays, giving rise to phase irregularities in a wavefront: the solar corona, for example, contains an irregular outflowing gas, which disturbs radio waves passing through it from distant objects to the Earth. The effects of this may be thought of either as refraction or as diffraction; in more general terms, the waves are scattered, giving rise to an angular spread of waves and to subsequent fluctuations in wave amplitude, which are seen as intensity variations as the Earth moves relative to a pattern of irregularities. Similar effects are observed in the passage of radio waves through the Earth's ionosphere.

At the time of discovery of pulsars, the known examples of radio scintillation gave a rapid fading pattern, not very different from the visible twinkling of stars. The comparatively slow, deep fading of radio signals from the pulsars was an entirely new phenomenon, which was first recognised as a form of scintillation by Lyne and Rickett (1968). The basic analysis of scintillation in terms of random refraction in the interstellar medium was presented by Scheuer (1968). He showed that the fluctuations should have a fairly narrow frequency structure, whose width should depend on the distance of the pulsar. Rickett (1969) obtained experimental proof of this and showed that fluctuations due to scintillation could be clearly distinguished from the various kinds of fluctuation that are intrinsic to pulsars. Interstellar scattering is also observed as a spread in travel time for pulses, seen as a broadening of sharp features; understanding and correcting for this is vital in accurate pulsar timing aimed at detecting gravitational waves.

The structure of the ionised interstellar medium along the line of sight to a pulsar is usually assumed to be turbulent, with a wide range of scale size. There are, however, situations where ray paths pass through individual discrete clouds; these

may contribute significantly to the structure of the diffraction pattern. We start our analysis with a simple model in which a random pattern of electron density irregularities is confined to a thin screen perpendicular to the line of sight, then extending this to a uniformly filled medium. The effect of discrete clouds follows in Section 19.3.

19.1 A Thin-Screen Model

A full theory must consider the development of a wavefront travelling through a turbulent interstellar medium that extends through the whole space between the source and the observer, and should include the effect of a wide spread of sizes of irregularities in the medium. The difficulty lies in the development with distance, since the effect of near and distant irregularities may be very different.

The simplest model is, however, useful for most of the analysis of pulsar scintillation. In Figure 19.1, random irregularities of refractive index found over the whole path between the source and the observer are concentrated into a thin screen roughly midway along the propagation path. The irregularities are all the same size, with typical dimension a . The average refractive index μ is close to unity, so that a variation $\delta\mu$ extending over a path length a changes the phase of a wave by an amount $\delta\phi \approx (2\pi/\lambda)a\delta\mu$. Since for μ close to unity

$$\mu - 1 \approx \frac{n_e e^2}{2\pi m v^2} = \frac{n_e e^2}{2\pi m c^2} \lambda^2, \quad (19.1)$$

where n_e is electron density in the medium, the phase change for a wave traversing a single irregularity is

$$\delta\phi = ar_e \Delta n_e \lambda, \quad (19.2)$$

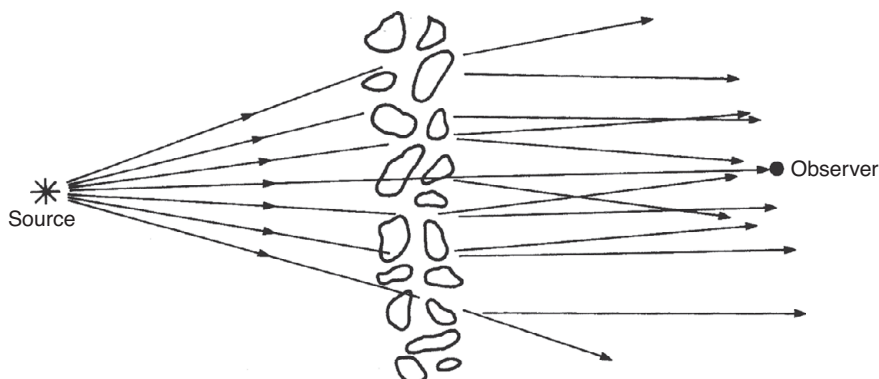


Figure 19.1 A thin-screen model of scintillation.

where $r_e = e^2/mc^2 = 2.82 \times 10^{-13}$ cm is the classical radius of the electron, and Δn_e is the fluctuation in electron density.

A ray traversing the whole path, length D , encounters on average D/a irregularities, randomly distributed, so that the phase changes concentrated into the thin screen must be

$$\Delta\phi \approx \left(\frac{D}{a}\right)^{1/2} \delta\phi = (Da)^{1/2} r_e \Delta n_e \lambda, \quad (19.3)$$

The lateral scale of the phase perturbations imposed by the thin screen is a , the size of the irregularities in the interstellar medium.

We may now employ either geometric optics to describe the angular spread of rays leaving the screen, or diffraction theory to describe the behaviour of a wave front with phase irregularities $\Delta\phi$ impressed upon it, varying with a lateral scale a . Geometrically, the tilt of the wavefront means that the rays are scattered through an angle

$$\theta_{\text{scat}} \approx \frac{\Delta\phi}{2\pi} \cdot \frac{\lambda}{a} = \frac{1}{2\pi} \left(\frac{D}{a}\right)^{1/2} r_e \Delta n_e \lambda^2, \quad (19.4)$$

and this, under conditions to be discussed later, is the apparent angular size of the source seen through the screen.

Immediately beyond the thin screen, there are phase variations but no amplitude variations across the wavefront. At increasing distance from the screen, the amplitude variations build up through interference between rays from various parts of the corrugated wavefront. The phase difference between separate rays reaching the observer from different parts of the screen will depend on their geometric path and on the different values of $\Delta\phi$ along their paths. The sum of the contributing rays will differ for observers more than a distance a apart. Hence, if the distance from screen to observer is L , and $L\theta_{\text{scat}} > a$, a randomly variable amplitude will be observed as the source, or the screen, or the observer, (or all three) move across the line of sight.

The ray paths will differ in length by $\frac{1}{2}\theta_{\text{scat}}^2 L$, which may be a difference of many wavelengths. Interference between rays will therefore differ at different wavelengths; the amplitude will vary over a wavelength difference $\Delta\lambda$, where

$$\frac{\Delta\lambda}{\lambda} \approx \frac{2\lambda}{\theta_{\text{scat}}^2 L}. \quad (19.5)$$

In practice, the screen may be extended along the line of sight so that $L \approx D$. The wavelength range $\Delta\lambda$ is more conveniently expressed as a frequency difference B_s , which for the simple model is given by

$$B_s \approx \frac{8\pi^2 ac}{D^2 r_e^2 (\Delta n_e)^2 \lambda^4}. \quad (19.6)$$

B_s is known as the bandwidth of this scintillation pattern. Note that the thin screen theory gives $B_s \propto v^4$.

These simple formulae contain the essential features of the scintillation phenomenon as observed. For example, the apparent angular size of pulsars can be measured by interferometry at long wavelengths, where it is confirmed that $\theta_{\text{scat}} \propto \lambda^2$; similarly Rickett (1969) found $B_s \propto \lambda^{-4}$ approximately, and decreasing with increasing dispersion measure, as expected if $B_s \propto D^{-2}(\Delta n_e)^{-2}$ and Δn_e was connected with the ionised gas along the line of sight. We will see later that the ionised interstellar medium (ISM) is, however, often found to be more complex, with large discrete clouds and anisotropic structure.

19.2 Diffraction Theory of Scintillation

The wave-front leaving the screen of Figure 19.1 may also be treated by diffraction theory. A wave-front with randomly distributed irregularities of phase $\Delta\phi$ may be constructed from a plane wave with constant phase, to which is added a range of other plane waves with a distribution of wave normals, forming an angular spectrum of plane waves (Figure 19.2). These are the scattered waves, covering an angle of $\frac{\lambda}{2\pi a} \Delta\phi$. The amplitude of the waves increases with $\Delta\phi$ until $\Delta\phi$ becomes large compared with 1 radian. The interference of these scattered waves at the observation point is responsible for the scintillation.

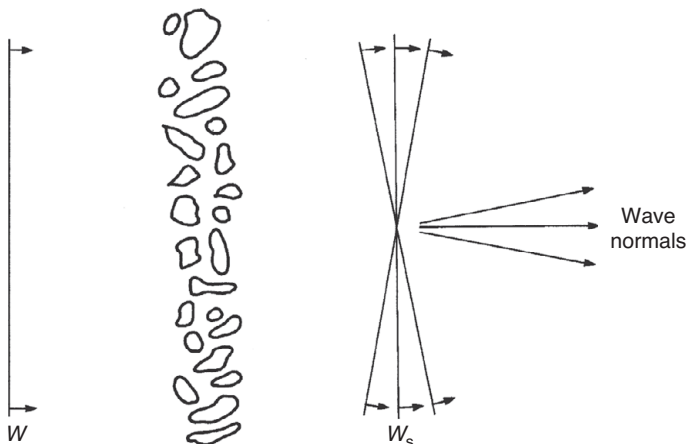


Figure 19.2 A wavefront W , scattered at a diffracting screen, emerges as a range of wavefronts W_s with a distribution of wave normals.

This diffraction analysis is particularly valuable in scintillation theory applying to screens that are extended along the line of sight (Section 19.3). Three simple results that emerge from the thin-screen model are still essentially valid in the full theory:

1. If $\Delta\phi \ll 1$, the wave emerging from the thin screen consists of an unscattered plane wave with smaller diffracted waves at angles θ_{scat} . A point source therefore appears to the observer as a point surrounded by a weak scattered halo. As $\Delta\phi$ increases, the point becomes weaker and the halo becomes stronger.
2. The lateral scale of the amplitude irregularities that develop in the wave-front is the same as the scale a of the phase irregularities provided that $\Delta\phi \ll 1$. When $\Delta\phi \gg 1$, the scale is reduced, and the typical scale S of the pattern becomes

$$S = \frac{a}{\Delta\phi} \approx \frac{\lambda}{2\pi\theta_{\text{scat}}}. \quad (19.7)$$

The lateral scale of the diffraction pattern may be observable directly by making simultaneous observations at widely spaced sites, or indirectly by observing the time scale τ_s of fluctuations at a single site and assuming that the scintillation pattern moves past the observer with a definite velocity V_s so that $S = V_s\tau_s$.

3. The amplitude of the wave at the observer is found from the addition of the scattered and unscattered waves with random phases. For strong scattering there is no unscattered wave, and the amplitude distribution approximates to a Rayleigh distribution. The addition of an unscattered wave changes this to a Rice distribution.¹

19.3 Thick (extended) Scattering Screen

The thin-screen analysis that has been used so far does not depend critically upon the location of the screen provided that it is not close either to the source or the observer. It is a reasonable deduction that a thick screen, occupying most of the space between the source and the observer, will behave similarly to a thin screen. The phase and amplitude modulations will, however, build up progressively, and in the early part of the path there will be an unscattered component that decays exponentially with distance z along the path, so that its relative intensity can be expressed as $\exp(-\beta z)$. Here, β is the coefficient of total scattering, given by Uscinski (1968) as

$$\beta = \pi^{1/2} r_e^2 (\Delta n_e)^2 a \lambda^2. \quad (19.8)$$

¹ A Rayleigh distribution of amplitude corresponds to an exponential distribution of intensity. The Rice distribution is discussed in connection with interplanetary scintillation by Cohen *et al.* (1967).

This refers to irregularities concentrated at scale a , which may be defined as the radial distance at which the autocorrelation function of Δn_e falls to $1/e$. Weak scattering corresponds to $\beta z \ll 1$ and strong scattering to $\beta z \gg 1$. Eqn. 19.8 must in practice be modified to take account of the actual distribution in size of the irregularities, as in Section 19.6. Following the simple case, the angular spectrum of plane waves emerging from a path z has a half-width θ_s (to amplitude $1/e$) given by

$$\theta_s = \frac{\lambda}{\pi a} \quad \text{for } \beta z \ll 1 \quad (19.9)$$

$$\theta_s = \frac{\lambda}{\pi a} (\beta z)^{1/2} \quad \text{for } \beta z \gg 1. \quad (19.10)$$

The full analysis for a Kolmogorov distribution of irregularities (see Section 19.6) is given by Lee (1976), and a more general review is given by Rickett (1990).

19.4 The Fresnel Distance

Close to the thin screen shown in Figure 19.1, there will only be variations of phase across the wavefront, since amplitude variations develop only beyond a distance z_0 where rays from different parts of the screen can cross. The transition to full scintillation is like the classical transition from Fresnel to Fraunhofer diffraction, and the distance at which it occurs is referred to as the Fresnel distance z_0 . It depends only on the scale size a and the wavelength λ , as

$$z_0 = \frac{\pi a^2}{2\lambda}. \quad (19.11)$$

Since the Fresnel distance depends on a , it may happen that for a given path only the small-scale irregularities will give rise to amplitude scintillation, while the larger scale irregularities are responsible only for refractive effects.

Coles *et al.* (2010) analysed scattering in an extended screen as a succession of thin screens, each of which produced a Fresnel diffraction field that was treated as the incident field on the next. A large computation is involved, but the authors were able to synthesise a complex scintillation pattern whose structure matched observed patterns.

19.5 Strong and Weak Scintillation

We noted in Section 19.2 the difference in diffraction when the phase modulation in the thin screen is greater or less than one radian. This may be thought of as a difference between *strong* and *weak* scintillation, but weak scintillation can also occur when the observer is close to the screen. A more general categorisation between strong and weak is obtained by isolating the part of the screen that contributes

most to the wave at the observer, that is, the first Fresnel zone, and considering the degree of phase modulation within this patch. We define a *coherence scale* s_0 in the wavefront as it leaves the screen; in a circular patch round the source with radius s_0 , the geometric phase differences are less than or equal to one radian. This scale is related to the scattering angle by $s_0 = \lambda/2\pi\theta_d$. The radius s_F of the first Fresnel zone at distance D is

$$s_F = (\lambda D)^{1/2} \approx 10^9 \text{ m} \left(\frac{d}{\text{kpc}} \right)^{1/2} \left(\frac{f}{\text{GHz}} \right)^{-1/2}. \quad (19.12)$$

The condition for strong scintillation is $s_0 < s_F$. Most pulsar observations are made in the strong scintillation regime; weak scintillation is expected only at high radio frequencies and for pulsars at small distances.

19.6 Distribution in Size of the Irregularities

Although the origin and the development of the fluctuations in electron density are not understood, it is reasonable to expect that they behave like other forms of turbulence, with energy fed into large-scale irregularities that degrade into smaller eddies. In such cases, provided that energy is fed in only at a large scale and is lost only at a small scale, the spectrum of irregularities is expected to follow a Kolmogorov power law. If we now define the spectrum $P(q)$ in terms of wave number q ,

$$P(q) = \int d^3r \langle n_e(x)n_e(x+r) \rangle e^{iqr}, \quad (19.13)$$

such a law has the form

$$P(q) = C_N^2(z)q^{-\alpha}, \quad (19.14)$$

where $C_N^2(z)$ is a measure of the mean square fluctuation at a point z along the path. The power index $\alpha = 11/3$ for Kolmogorov turbulence.

As we will see, observations of scintillation patterns in most pulsars show that the Kolmogorov spectrum applies over a wide range of scale size. The theory agrees remarkably closely with the thin screen model in most respects; for example, it predicts that the bandwidth of scintillation (Section 19.1) is proportional to $v^{4.4}$, close to v^4 as in the simple model.

Any particular example of scintillation arises principally from a limited range of scale sizes $a \approx 2\pi q^{-1}$. Figure 19.3 shows the angular scattering due to different scales of irregularity. Below and left of line A, the total phase deviation is less than a radian, and only weak scintillation can occur. To the right of B, interference between

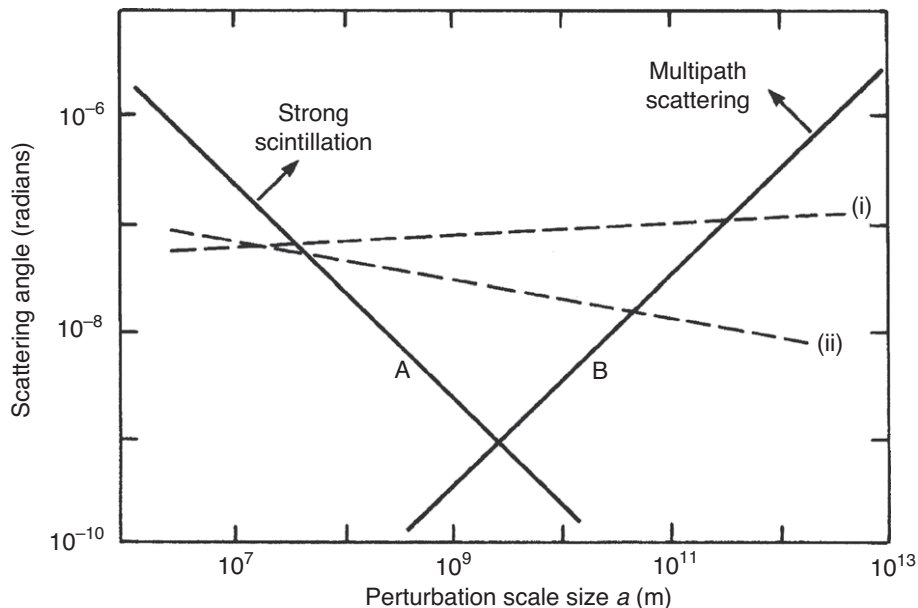


Figure 19.3 The limits of strong scintillation as a function of range of scale size and scattering angle. Weak scintillation occurs below the lines A and B. To the left of the line A (where $\phi = \pi$), the total phase deviation is less than one radian; to the right of the line B (where $z\theta = a$), the propagation path is less than the Fresnel distance. The broken lines (i) and (ii) represent respectively an interstellar medium with power-law index $\alpha > 4$ and one with index $\alpha < 4$. In this example, the source is placed at distance $z = 0.1$ kpc and the wavelength $\lambda = 1$ m.

the rays does not develop within the propagation path, as it is less than the Fresnel distance. These two limits depend on the wavelength of observation.

The broken lines in this figure represent power-law indices above and below the Kolmogorov spectrum, which would give a nearly horizontal line. The total angular scattering is found by integration over the relevant range of scale sizes. For longer radio wavelengths the range increases, while at a sufficiently short wavelength the range contracts to zero. Provided that $\alpha < 4$, the most important contributions to the integral come from the smaller scale sizes. The larger scale sizes, to the right of line B, cause an observable refraction effect, which is responsible for intensity variations on a much longer time scale.

19.7 Dynamic Scintillation Spectra

The intensity fluctuation pattern discussed above causes variations in received flux as it moves relative to the radio telescope with velocity V_s . The result can be seen in Figure 19.4, which shows the scintillation of a pulsar observed over a range of

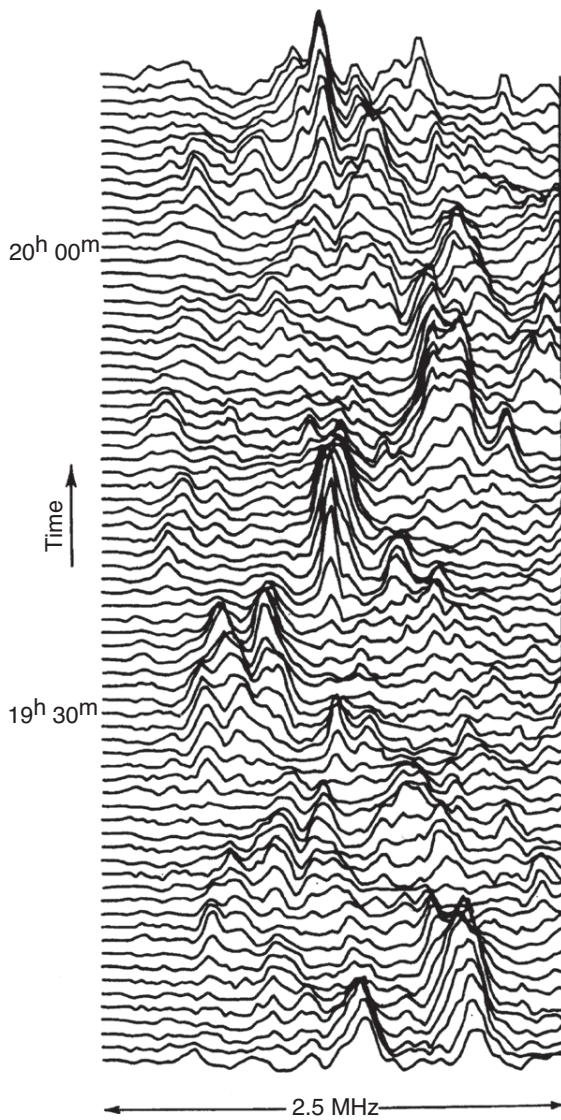


Figure 19.4 Scintillation of PSR B0329+54 observed simultaneously over a range of radio frequencies centred on 408 MHz.

radio frequencies; this is a *dynamic spectrum*. At any one frequency, a random fading pattern with lateral scale S is seen with a time scale $\tau_s = S/V_s$, while at any one time, the scintillation extends over a typical bandwidth B . Both τ_{rms} and B may be obtained from such a dynamic spectrum by an autocorrelation analysis. A typical form of the autocorrelation in time and frequency, giving a *secondary spectrum*, is shown in Figure 19.5. The variations in time are closely Gaussian

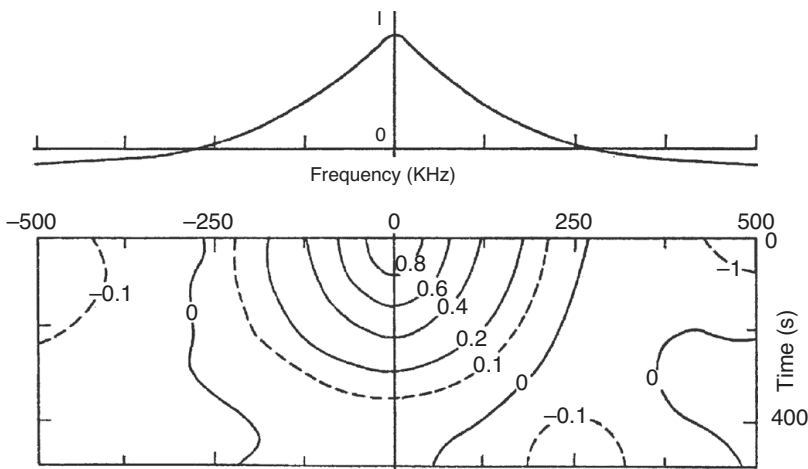


Figure 19.5 Autocorrelation of scintillation in time and in frequency: the two-dimensional autocorrelation function of the data in Figure 19.4. A section along the frequency axis at zero time delay is shown.

in form, but the variations in frequency depend on the distribution in size of the irregularities, as indicated in the previous section; the form of the autocorrelation function was used by Roberts and Ables (1982) and by Wolszczan (1982) to confirm the Kolmogorov spectrum. The time scale τ is usually measured as the time lag where the autocorrelation falls to e^{-1} , while B is usually measured to a frequency separation where the autocorrelation falls to 1/2.

The dynamic spectrum often shows organised structure, in which the features drift regularly across the observed frequency band, as in the upper two examples of Figure 19.6. This is the effect of refraction in large-scale irregularities. Refraction moves the whole scintillation pattern laterally; the refraction is greater at lower frequencies. As the pattern moves past the observer, this dispersive effect is seen as a frequency drift of scintillation features (Hewish 1980).

The rate of frequency drifting $d\nu/dt$ is expected to be related to the velocity V of the pattern, the angular spread of rays θ_r and the distance z of the pulsar by

$$\frac{d\nu}{dt} = \frac{\nu V}{\theta_r z} \sec \psi. \quad (19.15)$$

The term $\sec \psi$ takes account of the angle ψ between the velocity V and the direction of dispersion. This relation was shown by Cordes (1986) to hold for over 70 pulsars, and it can be used to find θ_r . Since this angle refers to refraction in large scale irregularities (to the right of the line marked B where $\theta_z = a$ in Figure 19.3), measurements of drift rate allow the spectrum of the irregularities to be extended over several orders of magnitude.

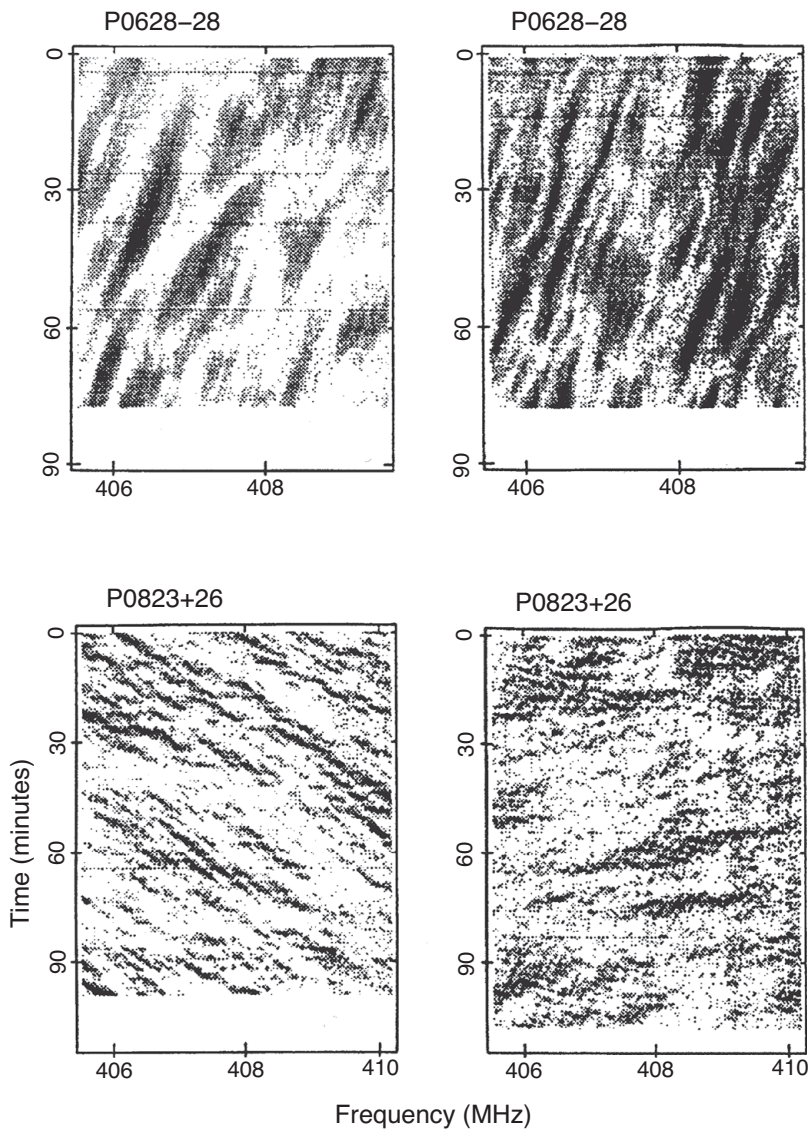


Figure 19.6 Examples of frequency drifting in the scintillation spectra of PSR B0628–28 and PSR B0823+26 (Gupta *et al.* 1994).

A comparison between the scattering angle θ_{scat} , obtained from the bandwidth and timescale of normal scintillation, and the refraction angle θ_r , showed that the Kolmogorov spectrum of irregularities usually applies over a range of sizes from 10^9 m to 10^{12} m (Smith & Wright 1985). Using additional evidence from fluctuations in dispersion measure and rotation measure, Armstrong, Rickett and Spangler (1995) showed that the same Kolmogorov law extends over the remarkably large range 2×10^6 m to 10^{13} m.

Table 19.1. Frequency dependencies in scintillation

		Gaussian	Kolmogorov
Scattering angle	θ_{scat}	-2	-2.2
Bandwidth	B_s	+4	+4.4
Time scale	τ	+1	+1.2

A further test of the spectrum is available through a detailed study of the variation with observing wavelength of the bandwidth and time scale of scintillation. As the wavelength changes, so does the range of scale sizes responsible for scintillation, and the simple laws of Eqns. 19.4 and 19.7 are modified. Lee and Jokipii (1976) contrasted a model in which sizes are concentrated round a single value, being spread only by a Gaussian distribution, and the power law distribution model with index α . They found that instead of $\theta_{\text{scat}} \propto v^{-2}$, as in Eqn. 19.4, the power law gave $\theta_{\text{scat}} \propto v^{-\alpha/(\alpha-2)}$. For index $\alpha = 11/3$, the frequency dependencies expected for the two spectra of irregularities are shown in Table 19.1.

19.8 Discrete Structures

Drifting patterns in dynamic spectra often contain organised structures on smaller scales of time and bandwidth. These resemble interference fringes (as in the lower two examples of Figure 19.6), and they are evidently due to the interference between a small number of predominant rays from the refractive regime (Rickett *et al.* 1997). The phenomenon is variable over a time scale of days or more, but when it is present, it indicates the existence of large scale irregularities that are more intense than those expected from the Kolmogorov law.

Stinebring *et al.* (2001) showed that the autocorrelation in time and frequency, which displays the two-dimensional ‘secondary’ spectrum of the dynamic spectrum (as in Figure 19.5 above), often displays some remarkably sharp features in the form of parabolic arcs (Hill *et al.* 2003). Figure 19.7 shows examples of such features in secondary spectra, with the dynamic spectra from which they were derived.

Scintillation arcs are related to large-scale features of a discrete refracting or reflecting plasma screen close to the line of sight. Individual arcs are observed over a wide frequency range, as much as five to one in some pulsars.

The parabolic form follows from a simple analysis of a thin screen, as in Section 19.1 but applied to a small number of discrete features. If there are two discrete sources separated by angle θ , we expect from Eqn. 19.5 that the frequency structure will depend on θ^2 , while the lateral scale will depend on θ . A point on a maximum in Figure 19.7 will therefore follow a parabolic relation $f_v = \rho f_t^2$. This effect is geometrical and does not involve any frequency dependence of

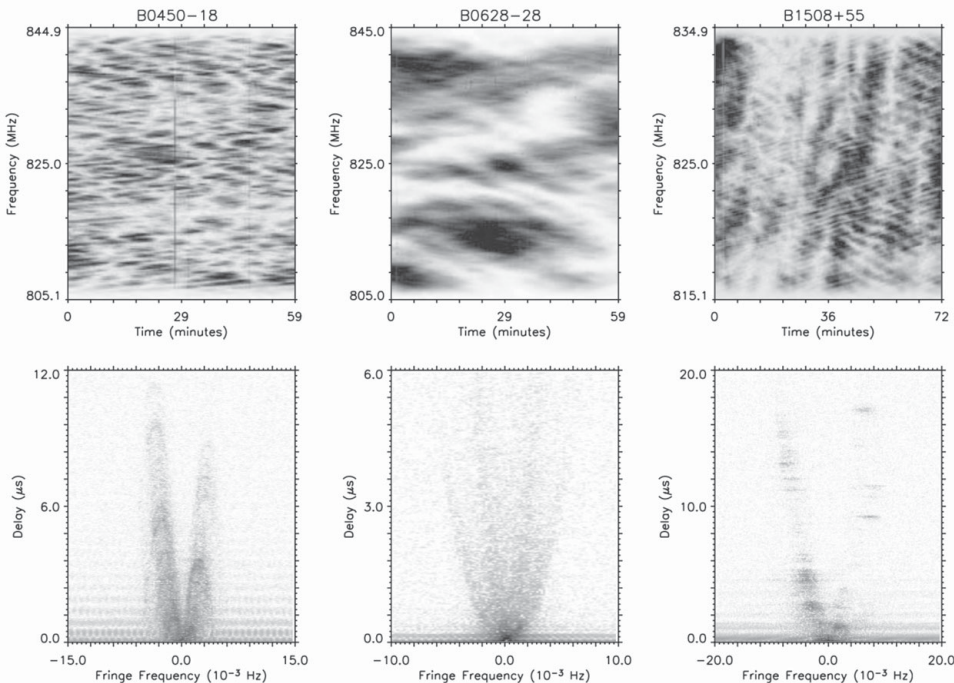


Figure 19.7 The dynamic spectrum and the secondary spectrum of scintillation in three pulsars, demonstrating the different effects of discrete structures in the ISM (Stinebring 2007).

refractive index. The curvature ρ of the paraboloid depends on the velocity V of the pattern and on the large-scale geometry as

$$\rho = \left(\frac{\sigma}{1 - \sigma} \right) \frac{D\lambda^2}{2cV^2}, \quad (19.16)$$

where D is the distance of the pulsar and σD is the distance of the diffracting screen from the observer.

Reardon *et al.* (2020) traced an annual variation of the curvature ρ in the binary MSP J0437–4715, superposed on a variation due to the lateral extent of the binary orbit. This pulsar is the nearest and brightest MSP, and their analysis shows that the scintillation is mainly due to two discrete scattering regions at distances 90 and 124 pc.

More generally, each point in the secondary spectrum corresponds to a sinusoidal pattern in the dynamic spectrum, whose period in delay time and frequency is related to the difference in arrival time between pairs of components in the scattered image. In weak scattering, one component of each pair is the unscattered direct wave, and

an analytical inversion can give the phase perturbations imposed by the scattering screen (Cordes *et al.* 2006b). The more general case of strong scattering is less amenable, although individual features that are prominent enough to give discrete arcs may be interpreted. These arcs are often related to scattering at angles much larger than the angles due to the scattering screen, revealing discrete features. An example is the well-developed interference pattern observed in PSR B0834+06, where a ray reflected or refracted at a glancing angle in a compact plasma sheet close to the line of sight interferes with the direct ray with delay up to 100 μ s (Walker *et al.* 2008).

A further elucidation of the scattered wavefront uses high angular resolution interferometry to isolate components of the secondary spectrum. Brisken *et al.* (2010) used VLBI at 327 MHz to resolve the two main components in the scattered image of PSR B0834+06. The wide separation of telescopes in a VLBI array may also be used to explore the pattern of intensity on the ground; the combination of these techniques provides a useful interpretation of the configuration of the scattering plasma in the ISM (Simard *et al.* 2019). Another possibility is suggested by the observation that scattering may affect different components of some pulse profiles independently; this could provide a measurement of the separation of the sources in the pulsar magnetosphere, with a linear resolution similar to the observed scale of the scintillation pattern on the surface of the Earth.

The large scattering and pulse delay effects found in pulsars such as PSR B0834+06 may, of course, occur on a smaller scale in other pulsars, including those for which very accurate timing has been attempted to detect the effects of gravitational waves. Dynamic scintillation spectra are observed to change significantly over periods of months, due to the transverse velocity in the source across the diffracting screen (Trang & Rickett 2007).

19.9 The Velocity of the Scintillation Pattern

The fluctuations of intensity due to scintillation may represent either a random turbulence in the scattering medium, which changes the configuration of the scintillation pattern over a plane containing the observer, or a relative velocity within the system of the observer, medium and source, so that the pattern drifts past the observer. (The two possibilities are familiar in the patterns of sunlight refracted onto the bottom of a swimming pool, when the waves on the surface are both travelling and changing shape.) Most pulsar scintillation is found to be due to pattern movement rather than pattern instability, so that the rate of the intensity changes is related to the pattern scale and the drift velocity. For example, a typical drift velocity might be 100 km s⁻¹, with a fading time scale of 10 min; the scale of an unchanging pattern would then be about 60,000 km – larger than the diameter of the Earth.

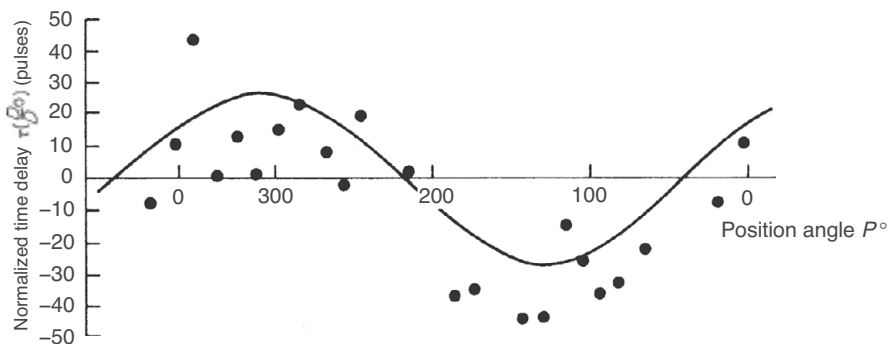


Figure 19.8 Time lag between scintillations of PSR B0329+54 recorded at Jodrell Bank and at Penticton. The time lag changes sinusoidally as the position angle P changes with the rotation of the Earth (after Galt & Lyne 1972).

A drifting and unchanging scintillation pattern was observed by Galt and Lyne (1972) for PSR B0329+54. Observations were made at 408 MHz simultaneously at Jodrell Bank and at Penticton, Canada, 6833 km apart. The orientation of this baseline changes as the Earth rotates; the pulsar is circumpolar so that a complete rotation of the baseline occurred during 24 h of observation. The scintillation fluctuations were highly correlated at the two observatories but with a varying time lag, as seen in Figure 19.8. A sinusoidal variation of this time lag, corresponding to the rotation of the baseline and with an amplitude of 18 s, is clearly present, corresponding to a velocity of 370 km s^{-1} . This is the velocity of the pattern moving over the baseline; presumably it is due to a large proper motion of the pulsar. There are also considerable random fluctuations, which may be due partly to pattern instability.

The velocity of the pattern can be deduced from measurements of B_s and τ_s at a single observing station. For a diffracting screen extending along the whole line of sight from a source at distance D ,

$$B_s = \frac{C}{\pi D \theta_s^2} \quad \text{and} \quad V_s = \frac{\lambda}{\sqrt{8\pi \theta_s \tau_s}}, \quad (19.17)$$

giving

$$V_s = (8\pi c)^{-1/2} (BD)^{-1/2} \lambda \tau_s^{-1}. \quad (19.18)$$

If we can regard the diffracting irregularities as stationary and unchanging, V_s measures the transverse velocity of the source, combined with a component of the Earth's orbital velocity, which is usually comparatively small. A comparison between values of V_s and the measured transverse velocities of pulsars obtained from their proper motions is shown in Figure 19.9 (Lyne & Smith 1982). This shows that it is acceptable to use values of V_s as a measure of pulsar velocity. The velocities

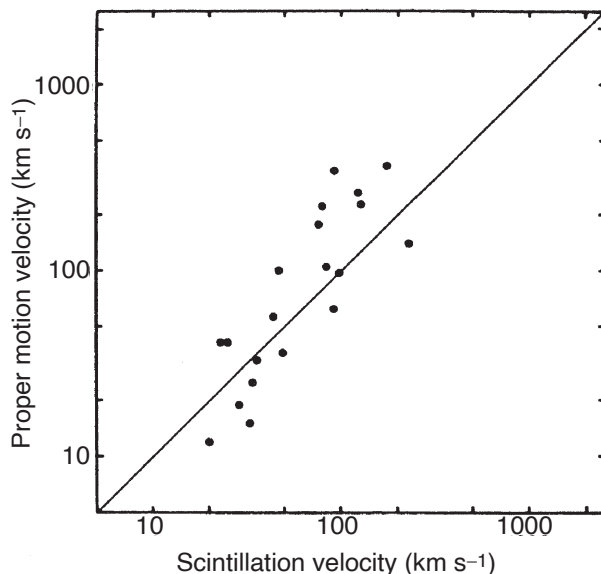


Figure 19.9 Correlation between transverse velocities of pulsars, deduced from their scintillation, and the transverse velocities obtained from their proper motions (Lyne & Smith 1982).

of pulsars outside the plane of the Galaxy are, however, often underestimated by this method; the concentration of the ISM close to the galactic plane gives a leverage effect that reduces the observed velocity V_s (Harrison & Lyne 1993).

The variation of fading speed as a pulsar moves in a binary orbit was used to measure the elements of the orbit of PSR B0655+64 by Lyne (1984). Reardon *et al.* (2019) used a six-year series of observations of scintillation of the millisecond binary PSR J1141–65 to establish the orbit in sufficient detail for a test of GR, as in Chapter 5. They also demonstrated the small effect of the Earth’s orbital velocity as an annual component of the variation in fading speed.

19.10 Pulse Lengthening

Scintillation is the most obvious, but not the only effect of propagation through irregularities in the ionised interstellar gas. Observations of distant pulsars, particularly at low radio frequencies, which may be expected to show greater effects of scintillation, also show the related phenomenon of pulse broadening. Figure 19.10 shows an example (Krishnakumar *et al.* 2019), in which a pulse is drawn out into a long tail at low frequencies. A further example is provided by the Crab Pulsar, which at frequencies below about 50 MHz shows as a continuous source, in which the pulses are almost completely smeared out by this lengthening process. Pulse

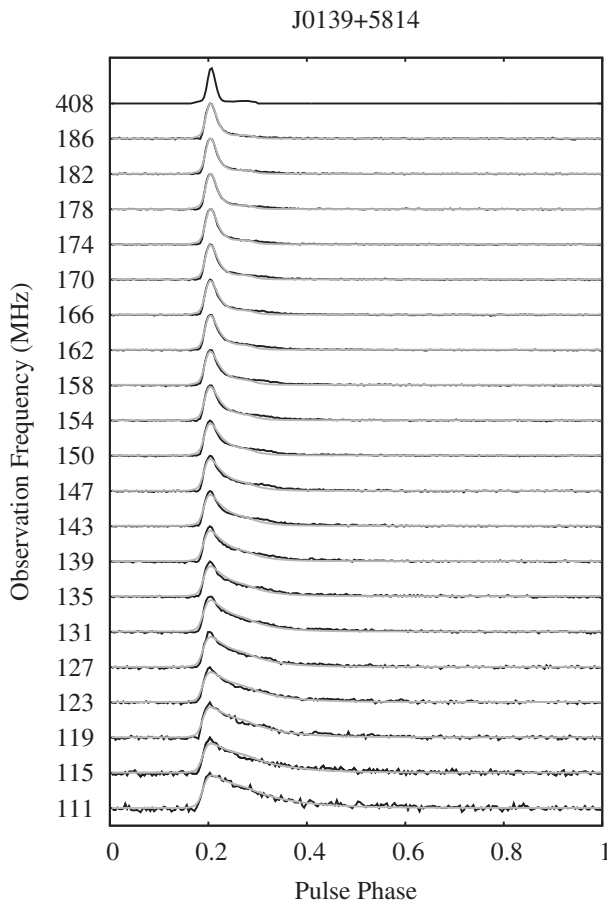


Figure 19.10 Pulse lengthening by scattering in the interstellar medium. Pulse profiles of PSR J0139+5814 ($P = 0.272$ s., $DM = 73.8 \text{ cm}^{-3}$ pc) from 111 to 408 MHz. (Krishnakumar *et al.* 2019).

lengthening is a severe limitation in radio searches for millisecond pulsars at low radio frequencies.

To understand the origin of pulse lengthening, consider first a thin slab of scattering material approximately halfway between the source and the observer, separated by distance L (Figure 19.11). If the slab behaves as a thick scatterer, in the sense that it introduces large random phase changes, then emergent rays are scattered with a Gaussian angular distribution, width θ_0 , with probability

$$P(\theta)d\theta \propto \exp(-\theta/\theta_0)^2 d\theta. \quad (19.19)$$

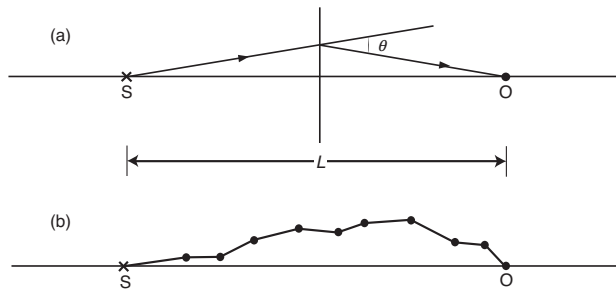


Figure 19.11 Geometry of multiple scattering: (a) single scattering; (b) multiple scattering. S, source; O, observer.

The delay t introduced into a ray deviated by angle θ is $(L/4c)\theta^2$. The probability of a ray deviated between θ and $\theta + d\theta$ reaching the observer is proportional to $\theta d\theta$, because of the solid angle subtended by an annulus of radius θ and width $d\theta$. The intensity of signals with deviation θ is therefore given by

$$I(\theta)d\theta \propto \theta \exp\left(\frac{\theta}{\theta_0}\right)^2 d\theta, \quad (19.20)$$

and hence the corresponding variation with delay t is

$$I(t)dt \propto \exp\left(-\frac{4c}{L\theta_0^2}\right) dt. \quad (19.21)$$

A narrow pulse will therefore be observed to have a sharp rise and an exponential decay, with time scale $\tau_s = L\theta_0^2/4c$. Since $\theta \propto v^{-2}$, the time scale is proportional to v^{-4} for a screen with a single scale size a . It is interesting to note that the apparent size of the source changes during the pulse; the sharp leading edge comes from a central point, while the exponential trail comes from an expanding halo of progressively more widely scattered rays. The close relation between scintillation and pulse lengthening is shown by the rough equality

$$2\pi B_s \tau_s \approx 1, \quad (19.22)$$

where B_s is the bandwidth of the scintillation, and τ_s is the pulse lengthening. This relation, discussed by Lang (1971), is proved experimentally for several pulsars, although in practice it can only be checked by using measurements of B_s and τ_s obtained at widely different frequencies, with an extrapolation using their known frequency dependence to bring them to the same frequency. The relation is easily understood: if ray paths reach the observer over distances differing

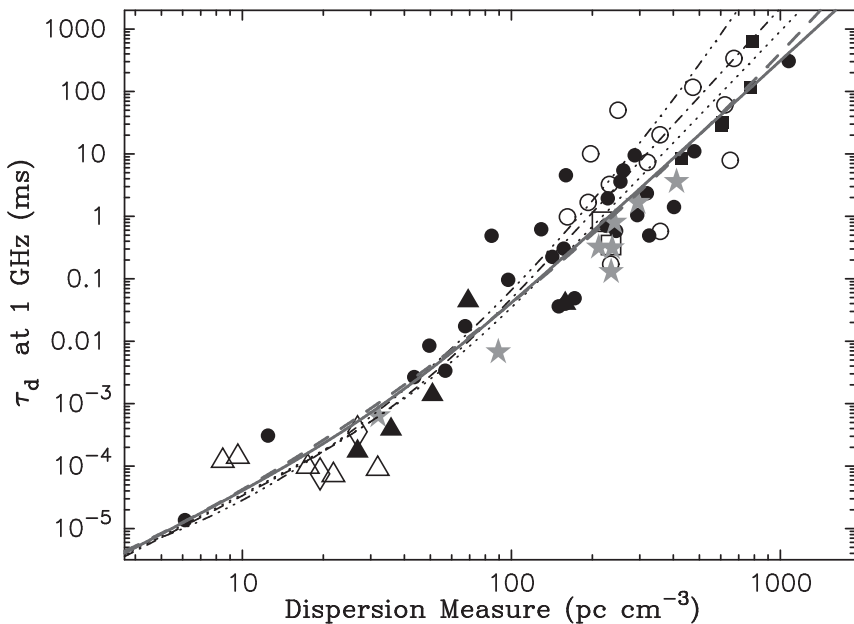


Figure 19.12 Logarithmic plot of pulse lengthening τ_s vs DM (from Lewandowski *et al.* 2015). Measured values of τ_s are reduced to a common frequency of 1 GHz using a power law with $\alpha = 4$. The solid and dashed lines correspond to τ_s versus DM relations proposed by Lewandowski *et al.* (2015). The other lines correspond to previously proposed relations: Ramachandran *et al.* (1997) – dash-dotted, Löhmer *et al.* (2004b) – dotted, and Bhat *et al.* (2004) – three-dot-dashed line.

by τ_s , then the relative phases of the various signal components will range over $(2\pi/\lambda)c\tau_s = 2\pi\nu\tau_s$, so that the relative phases of the interfering waves will change by the order of 1 radian over a band $B_s \approx (2\pi\tau_s)^{-1}$.

As expected, pulse lengthening τ_s increases with dispersion measure DM. Figure 19.12 (Lewandowski *et al.* 2015) shows a log-linear increase, with a wide scatter of values and significantly smaller values of τ_s at low values of DM, indicating large scale variations in the structure of the ionised ISM. Large dispersion may make a pulsar difficult or impossible to detect; for example, pulses from a pulsar at the Galactic centre, where high DM values are encountered, are expected to be lengthened to about $350\nu_{\text{GHz}}^{-4}$ seconds, so that a 30 Hz pulsar like the Crab would be undetectable at frequencies below 10 GHz. Note, however, that there may be considerably less dispersion and scattering on some sightlines, as shown by the magnetar PSR J1745–2900 near the Galactic centre (Section 19.12).

19.11 Multiple Scattering

Theoretical treatments of pulse broadening take either the geometrical or diffraction approaches to the problem. A geometric optics approach, involving ray theory, is appropriate for multiple scattering and greatly broadened pulses, while the diffraction approach may be needed for cases in which multiple scattering is not fully established. These two approaches were considered respectively by Williamson (1973) and Uscinski (1974).

The effect is similar for a screen located in a range of positions roughly midway between the source and observer, but if it is close to either source or observer, the time scale is shortened proportional to the shorter of the two distances. Extension of the analysis to a scattering medium filling the whole space involves a more complicated ray tracing problem (Figure 19.11b). Williamson (1973) obtained the delay distributions in Figure 19.13 from a random walk analysis, and Uscinski (1974) developed the diffraction analysis to produce similar although not identical results (see also Rickett 1990). Williamson (1974) showed the lengthened pulse shape for the Vela Pulsar conformed to case 3 in Figure 19.13, for scattering extending through the whole line of sight. Distinguishing between the various cases is not easy; Reardon *et al.* (2019) showed from their long series of observations of PSR J1141–65 that for this pulsar, scattering is best modelled

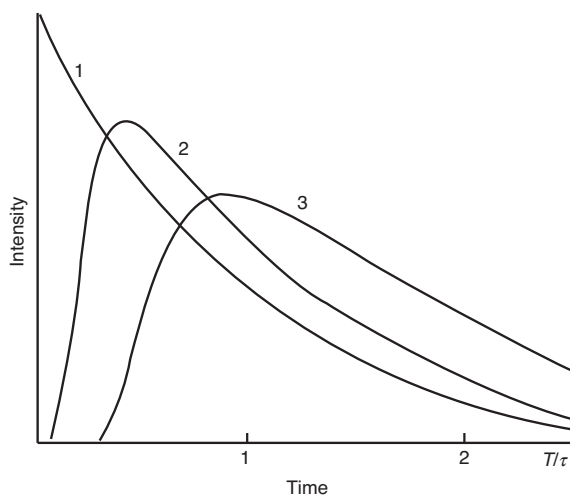


Figure 19.13 Pulse broadening functions. 1: Scattering from a thin slab; 2: scattering from a more extended region; 3: scattering from irregularities filling the whole line of sight (after Williamson 1973).

by a combination of a uniform spread over the line of sight with a concentration in a thin screen at 0.7 of the distance to the pulsar.

19.12 Observations of Pulse Lengthening

The ionised ISM is evidently more complicated than the uniformly turbulent medium we have assumed in the theory as presented above. Pulse profiles from many pulsars show evidence of large-scale clouds, and probably of anisotropy, in the structure of the ISM. Nevertheless, the simple theory does correctly predict the relations between pulse lengthening, frequency and dispersion measure. For any individual pulsar, τ_s is expected to vary with frequency as $\nu^{-\alpha}$, where $\alpha = 4$; Bhat *et al.* (2004) did indeed find $\alpha = 4$ for 98 pulsars at low Galactic latitudes. However, in more extensive observations at low radio frequencies, Geyer *et al.* (2017) found values of α ranging from 4.0 down to 1.5; they suggested that anisotropy and a patchy distribution of the ISM may be responsible. A large sample analysed by Oswald *et al.* (2021) yields a mean value of 4.0 ± 0.6 and indicates that some measurements may underestimate α .

Non-uniformity along the line of sight is clearly observed in pulse broadening in the Crab Pulsar. Here Sutton, Staelin and Price (1971) found that individual strong pulses, which are probably less than 1 ms long at the source, show a very sharp rise followed by an exponential decay with time constant $\tau_0 = 12.2$ ms at 115 MHz. The shape of this broadening is certainly not consistent with the uniform thick scatterer; it indicates instead that the scatterer is concentrated into a small fraction of the line of sight. As expected, the frequency dependence of the scattered pulse length is close to ν^{-4} (see Crossley *et al.* (2010) for a compilation of observations).

In 1974, the pulse broadening of the Crab Pulsar increased dramatically during a period of a few weeks (Lyne & Thorne 1975). At 408 MHz, the broadening pulse length increased to 4 ms (Figure 19.15); normally the broadening only lengthens the pulse by 50 μ s. Again the shape showed a sharp rise followed by a quasi-exponential decay, and again the interpretation must be that the scattering occurred in a concentrated region. The lengthened profile contained several discrete components, indicating that the scattering region contained a simple structure; it was almost certainly within the Crab Nebula itself. The movement of the region across the line of sight may be part of the expansion of the nebula, or it may be associated with the active ‘wisps’ near the line of sight to the pulsar. In another such dramatic event in 1997, the normal pulse profile disappeared for several days, during which time it was replaced by a similar profile delayed by 3 ms (Figure 19.14); this was interpreted as the effect of refraction in a discrete plasma within the Crab Nebula moving across the line of sight. Monitoring of these effects over many years at 610 MHz

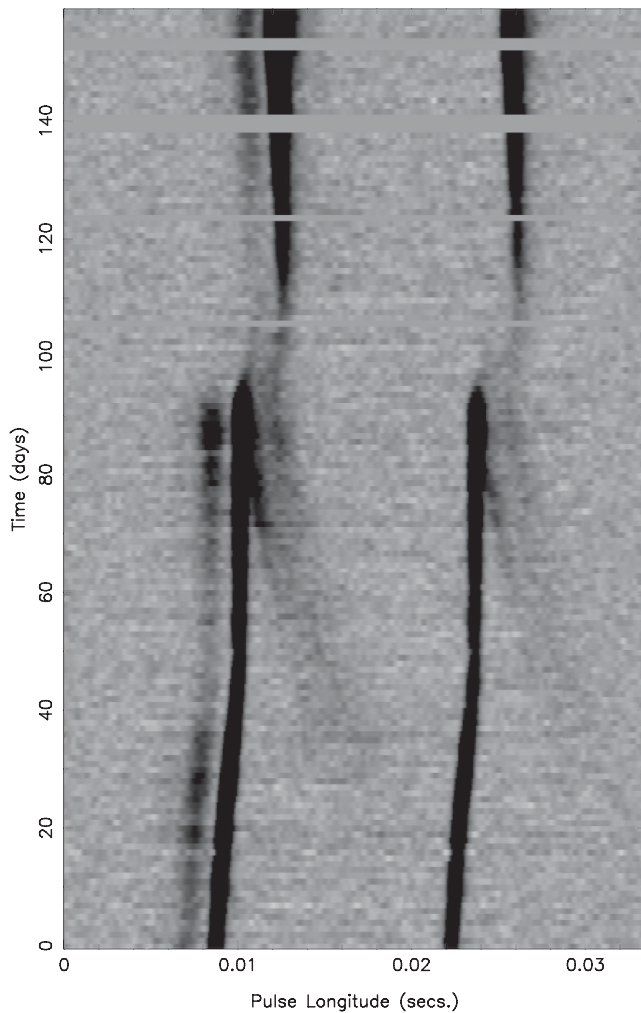


Figure 19.14 The dramatic scattering event in the Crab Pulsar in 1997 observed at 610 MHz (Lyne, Pritchard & Smith 2001). This greyscale plot shows the Crab precursor, main pulse and interpulse components over a 160-day period. Around day 30, a diffuse, delayed ‘echo’ from a plasma cloud close to the line of sight can be seen about 5 ms following the main components. This delay decreases to near zero at around day 90, at which point the pulses are almost obliterated by the scattering entity as it crosses in front of the pulsar.

(Lyne, Pritchard & Smith 2001, McKee *et al.* 2018), and at 350 MHz by Driessen *et al.* (2019), shows continued activity due to structure within the nebula (Figure 19.15). A similar, but weaker, effect has been observed in PSR B2217+47 at the lower frequency of 150 MHz; this is attributed to an echo from an isolated cloud in the ISM, halfway along the line of sight (Michilli *et al.* 2018).

Another indication that the scattering irregularities are not distributed uniformly is the difference between broadening observed in different pulsars with similar dispersion measures. Lyne (1971) pointed out, for example, that PSR B2002+31, with $\text{DM} = 235 \text{ cm}^{-3} \text{ pc}$, shows no detectable broadening at 408 MHz, while PSR B1946+35, with $\text{DM} = 129 \text{ cm}^{-3} \text{ pc}$, shows a large effect.

The variation with distance also deviates from an expected simple square law, which does, however, apply at low values of DM (Kuzmin 2001). Cordes and Lazio (2003) and Bhat *et al.* (2004) included scattering lengths deduced from scintillation bandwidths, and they found that the scattering over a wide range of DM is best fit by a parabolic curve.

In Figure 19.12 (Lewandowski *et al.* 2015), the values of τ (seconds, at 1 GHz) for the more distant pulsars (beyond $\text{DM} = 30 \text{ cm}^{-3} \text{ pc}$) are seen to be better fitted with an arbitrary line with slope 4.4, as

$$\log_{10} \tau = -13.8 + 4.4 \log_{10} \text{DM}. \quad (19.23)$$

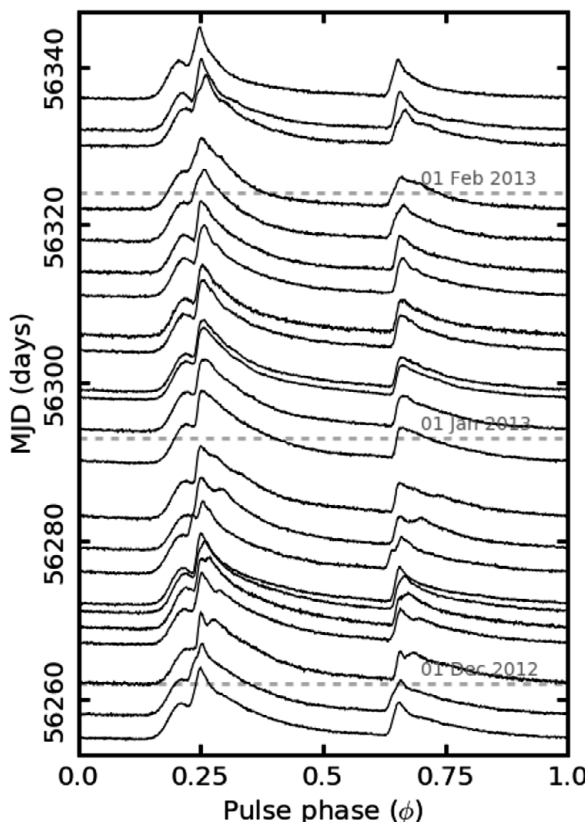


Figure 19.15 Variable scattering in the Crab Pulsar, observed at 350 MHz from 2012 November to 2015 June as a function of modified Julian date (MJD). Data from Driessen *et al.* (2019).

An extreme example is PSR J1745–2900, a magnetar within 3 arcseconds of the Galactic centre, with period 3.76 seconds. With $\text{DM} = 1778 \pm 3 \text{ pc.cm}^{-3}$, Eqn. 19.23 gives $\tau = 3.2$ s. The observed value is 1.3 s (Spitler *et al.* 2014), a low value that is encouraging for searches for further pulsars in the vicinity of the central black hole.

19.13 Apparent Source Diameters

As described in Section 20.9, the scattering in the interstellar medium, which is responsible for scintillation and pulse lengthening, also increases the apparent angular size of the source, as in the familiar examples of optical ‘seeing’ in telescopes and the radio diffraction in the solar corona. We now discuss the relation between scintillation and apparent angular diameter, in both theory and observation.

For the simple example of a physically thin screen halfway between the source and the observer (Figure 19.1), the source appears on average as a Gaussian disk with half-width θ_s . If the same screen is moved from the half-way position, the apparent angular size θ'_s varies according to the distance from the source, as in Figure 19.16, where $\theta'_s = \theta_s D / 2(D - d)$.

For multiple scattering in a medium filling the whole path, Williamson (1974) showed that the mean square image diameter of θ_s^2 is $\frac{1}{3}\phi^2 D$, where ϕ^2 is the mean square scattering angle per unit path length.

The angular size θ_s is small: for the Crab Pulsar, it is of the order of 100 milliarcseconds at 100 MHz, varying approximately as the square of the wavelength. The angular diameter of the pulsar itself is, of course, many orders of magnitude smaller at about 100 picoarcseconds. The scattered diameter can be resolved by very long baseline interferometry (VLBI). Using single baselines, Vandenberg *et al.* (1973) measured a diameter for the Crab Pulsar of $0''.07 \pm 0''.01$ at 115 MHz, and Mutel *et al.* (1974) measured a diameter of $1''.30^{+0.23}_{-0.13}$ at 26 MHz. Brisken (2010) used four telescopes of the global VLBI array to map the scattering disk of PSR B0834+06 at 327 MHz, showing that the disk was anisotropic; it also has a distinct component with a 1 ms delay, which appears to be due to refraction in a discrete cloud.

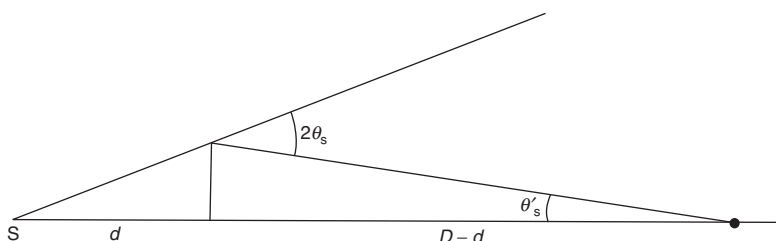


Figure 19.16 The apparent size θ'_s of a scattered source S , depending on the distance d of the screen in relation to the observer’s distance D .

Brisken *et al.* (2010) also included an analysis of the dynamic spectrum, which examines structure with resolution 100 μ arcsec. Simard *et al.* (2019) showed how VLBI can use a combination of auto- and cross-correlations to obtain high resolution of scattering discs. There is only a limited possibility of resolution by Earth-based interferometers; however, the Space Radio Telescope SRT, in combination with large ground-based telescopes, has been used to resolve scattering discs at 324 MHz of PSR B0329+54 (Popov *et al.* 2017) and PSR B1919+21 (Shishov *et al.* 2017), and the Vela pulsar PSR B0833–45 at 1668 MHz (Popov *et al.* 2019), using baselines up to 60,000 km. In all three, the disk is anisotropic. Pen and Levin (2014) showed that the milliarcsecond discrete components that appear in many scintillation discs are accounted for by reflection in a disk with a corrugated pattern of ionisation.

Interstellar scattering has been observed for extragalactic radio sources at 81 MHz by Duffet-Smith and Readhead (1976), continuing the pioneering work by Hewish that led to the discovery of pulsars. They found that no extragalactic source had an apparent diameter less than $0''.15 \pm 0''.05$. This result is reasonably consistent with the interferometer measurements. Finally, the observed pulse lengthening already discussed in Section 19.12 is simply related to θ_0 . For a uniformly filled path, the pulse lengthening τ is given by

$$\tau = \frac{L\theta_0^2}{4c}. \quad (19.24)$$

For the Crab Pulsar at 111.5 MHz, $\tau = 13$ ms, giving $\theta_s = 0''.1$, in good agreement with the interferometer measurements. The agreement is, in fact, good enough to exclude any configuration in which the main source of the scattering is concentrated near the pulsar. The variable component of lengthening observed for the Crab Pulsar must therefore have a different origin, since the speed of variability means that it is concentrated in a small volume, presumably within the Nebula itself.

19.14 Long-Term Intensity Variations

Soon after pulsars were discovered, it became apparent that their intensities varied over much longer time scales than those attributed to scintillation. It was at first unclear whether these long-term intensity variations were due to the radiation mechanism in the pulsar itself, or possibly to propagation conditions close to it.

The first clue to the origin came from Sieber (1982), who pointed out a close correlation between the time scale of the intensity fluctuations and the dispersion measures of a set of pulsars previously observed by Helfand *et al.* (1977a). This could only mean that the fluctuations were generated in the interstellar medium and must be regarded as another form of scintillation. The long time scale showed,

however, that very much larger linear scales of electron density fluctuations must be involved. Sieber also pointed out that the time scale seemed to decrease with increasing frequency, which was contrary to previous experience and to the conventional theory of scintillation.

The explanation came from Rickett, Coles and Bourgois (1984), who remarked that propagation of laser light through turbulent air had already shown a comparable effect, in which there were two coexisting regimes of angular scattering. They were then able to relate the dual nature of radio scintillation to the continuation of the spectrum of irregularities in the ISM to very large scales, possibly a power law spectrum conforming to the Kolmogorov law (Section 19.6). The slow variations are now known as refractive scintillation.

We noted that frequency drifting in the dynamic spectra of pulsars is related to refraction in large-scale irregularities, coexisting with scattering at small scales. The two scale sizes are each immediately to the right of the two limit lines in Figure 19.3; these correspond respectively to the limit of deep phase modulation and to the limit of multipath propagation. Significantly, the second of these varies as $(\lambda D)^{1/2}$, which is reasonably close to the observed dependence of the long-term time scale on wavelength and dispersion measure.

Rickett *et al.* (1984) were then able to attribute the long-term intensity variations to a focussing effect in electron clouds at about the Fresnel distance (Section 19.4). The form of the variations is assumed to be Gaussian, although focussing can produce occasional unexpectedly high peaks of intensity. The remarkable feature is that for a given pulsar, the two time scales t_s for conventional scintillation and t_c for refractive scintillation are related simply by

$$t_s t_c \simeq \text{constant.} \quad (19.25)$$

Refractive scintillation is also observed in extragalactic radio sources, provided that they have small enough angular diameters. The intensities of quasars and active galactic nuclei (AGN), with diameters less than a few milliarcseconds, will be modulated by focussing in the interstellar medium, either in our Galaxy or in a nebula surrounding the source. A wide range of timescales and intensities are observed: Bignall *et al.* (2003) found variations up to 40% within an hour in intensity at 4.8 and 8.6 GHz for PSR J1257–326.

The development of the understanding of scintillation in milliarcsecond AGN is given by Jauncey *et al.* (2016); for a concise exposition of the theory, see Rickett (2007).

Further evidence on the large-scale structure of the interstellar medium is provided by the observation of slow changes in the dispersion measure (DM) of closely monitored pulsars. The changes are small but easily measurable (Figure 19.17). Combined with measurements of proper motion, such observations may reveal

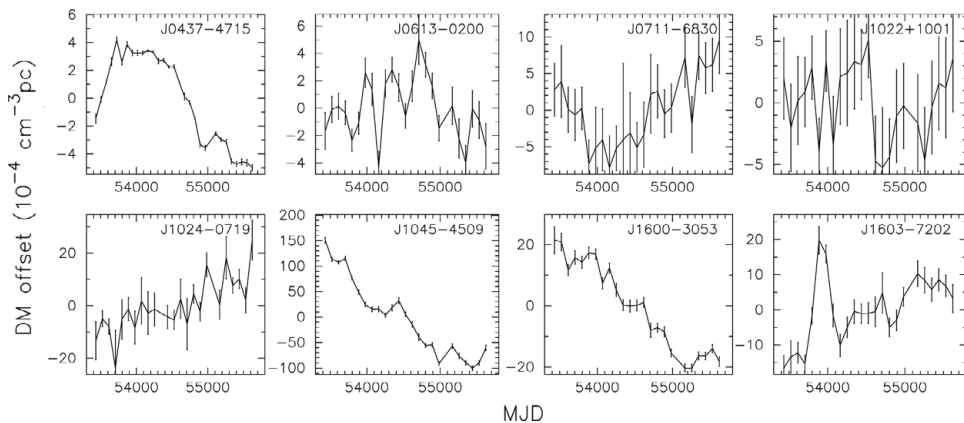


Figure 19.17 Variations in dispersion measure (DM) of two of the pulsars monitored by Keith *et al.* (2013). The DM scale is 10^{-4} ; the abscissa scale is days.

structure in electron distribution on a large scale. Precision timing, aimed at the detection of gravitational waves, must take account of these small variable delays (Keith *et al.* 2013).

Pulsars in a globular cluster are all at essentially the same distance and in principle offer the opportunity to measure transverse DM gradients; this has been achieved in the cluster Terzan 5, which contains 33 pulsars (Ransom 2007). However, some of such a gradient may be due to electrons within the cluster; Freire *et al.* (2001a) found that the cluster 47 Tucanae has a radial DM gradient due to an electron density within the cluster n_e of 0.067 cm^{-3} .

Scattering in interplanetary space, originally investigated by Hewish in observations that led to the discovery of pulsars, limits the angular resolution in mapping radio emissions from the surface of the Sun (Bastian 1994). The influence of the solar wind on more distant radio sources is also seen as an increased dispersion measure for lines of sight within several solar radii of the Sun (Tiburzi & Verbiest 2018), which again must be accounted for in precision timing.

20

The Interstellar Magnetic Field

The magnetic fields that are first brought to mind in any discussion of pulsars must surely be the enormous fields at the surface of the neutron star itself. These fields are of the order of 10^{12} G (10^8 tesla) for most pulsars, 10^{15} G for magnetars and 10^8 G for the older, millisecond pulsars. Pulsar radio waves may, however, be used as a means of measuring the magnetic field on the line of sight to the observer; this interstellar field is, by way of extreme contrast, of order 1 to 10 microgauss. The observational link between these extremes is simple: the high field of the pulsar is responsible for the linear polarisation of the radio emission, while the Faraday rotation of the plane of polarisation in interstellar space is a measure of the interstellar magnetic field along the line of sight.

20.1 Optical and Radio Observations

The existence of an interstellar magnetic field was first demonstrated by the observation of the polarisation of starlight, notably by Hiltner (1949) and by Hall and Mikesell (1950). A small degree of linear polarisation was found, which was common to several stars in the same general direction. The polarisation was due to scattering in interstellar space by particles that are elongated, so that they scatter anisotropically, and which are aligned with their long axes perpendicular to the Galactic magnetic field. This alignment occurs through an interaction between the particles and the magnetic field: any component of spin that brings the long axis periodically in and out of alignment with the field will decay. The plane of polarisation therefore provides a very useful measurement of the orientation of the field, but not of its strength.

Radio emission from the Galaxy was already known at the time of discovery of optical polarisation, but it was not until the synchrotron theory of its origin was developed by Shklovsky (1953) a few years later that the existence of radio emission

was used as evidence for a general magnetic field. The field strength was then estimated to be about 10 microgauss, although this value was derived on the basis of admittedly inadequate information on the flux of cosmic ray electrons. The most significant outcome of the theory was the realisation that the background radiation should be partially linearly polarised. The plane of polarisation should be related to the direction of the field, and the degree of polarisation should be related to the degree of organisation of the field.

Successful measurements of polarisation of the radio background radiation have been made over a range of wavelengths from 21 cm to 2 m. At the longer wavelengths there are severe effects from Faraday rotation between the source and the observer. Faraday rotation is best studied directly by the pulsar observations that are the main subject of this chapter, and we shall not therefore be concerned here with the long wavelength background polarisation. At short wavelengths, where Faraday rotation is small, the degree of polarisation exceeds 10% in several regions of the sky, indicating a well-aligned field over a considerable distance. The strongest polarisation is observed at galactic longitude $l = 140$ deg, where the line of sight appears to be nearly perpendicular to the field over a distance of several hundred parsecs.

The difficulty in constructing a model of the Galactic magnetic field from the synchrotron background polarisation is our location within the disk, where lines of sight may pass through several spiral arms. The situation is clearer for some spiral galaxies seen nearly face on, several of which are close enough for spiral arms to be resolved in some detail. Interpretation of polarised synchrotron radiation from the Milky Way and other galaxies is reviewed by Beck (2009).

A very direct measurement of the magnetic field in some localised regions is provided by the Zeeman effect. The 21-cm radio spectral line of neutral hydrogen is split in a magnetic field, giving two lines of opposite hands of circular polarisation separated by 2.8 Hz per microgauss. This has been observed in absorption, when the widths of some individual absorption components are small enough to allow the split to be observed. The field strengths measured in this way are often greater than 10 microgauss: they refer, of course, to individual absorbing clouds where the density is locally high, and the field strength is not typical of the interstellar medium.

In contrast to the localised Zeeman effect, Faraday rotation is observed as an integrated effect along a line of sight. This method of measuring the interstellar magnetic field was available before the discovery of pulsars, by observing extragalactic radio sources over the whole celestial sphere. The rotation is given by

$$\phi = R\lambda^2 \text{ radians}, \quad (20.1)$$

where R is the *rotation measure* of a particular source in units of rad m $^{-2}$, and λ is the wavelength of observation. R is determined by the electron density n_e and the component of field along the line of sight $B \cos \theta$, so that

$$R = 0.81 \int n_e B \cos \theta \, dL, \quad (20.2)$$

where B is measured in microgauss, n_e in cm $^{-3}$ and L in parsecs.

The most serious problem in interpreting the observations of Faraday rotation in extragalactic sources is in isolating the Galactic component, since there are large rotations intrinsic to some of the sources themselves. A clear pattern of variations of rotation measure over the sky does, however, emerge from surveys of a sufficient number of sources. Gardner, Morris and Whiteoak (1969) found that the average sign of R was opposite on either side of the Galactic centre, the division being perpendicular to the direction of the local spiral arm (known as the Sagittarius–Carina arm), indicating a field directed along the arm, approximately towards longitude $l = 80$ deg. A compilation of a larger body of data by Kronberg and Newton-McGee (2009) shows a remarkably clear symmetry about longitude $l = -11$ deg for extragalactic sources close to the Galactic plane, at latitude $|b| \leq 15$ deg, as expected from the local spiral arm. This pattern does not extend to higher latitudes, indicating that the field is closely associated with the spiral arm.

If the field were parallel to $l = 80$ deg at all distances, the pattern of R over the sky would be very simple, with a clear division of sign between the two hemispheres. The intrinsic rotations of the sources would obscure this pattern, but there are obviously also some large anomalies that indicate large-scale irregularities in the field pattern. The strength of the field was not obtainable directly from these Faraday rotation measurements, since the electron density n_e remained unknown; neither was it known whether the field direction was the same or reversed in adjacent spiral arms.

An account of the various pieces of evidence concerning the interstellar magnetic field, as they stood at the time of the discovery of the pulsars, was given by van der Hulst (1967). More recently, the availability of large databases of polarisation in extragalactic sources provided a more detailed model of the Galactic magnetic field (Jansson & Farrar 2012). This model included the following main features:

1. a large-scale field oriented along the spiral arms;
2. an oppositely directed field between the arms;
3. smaller scale striated structures within the spiral arm fields;
4. a field extending into the halo of the Galaxy.

Although the large database of extragalactic sources then available allowed the construction of a multi-component model, the observations were necessarily

addressing the integrated Faraday rotation along lines of sight extending through the whole Galaxy. As we will see, Faraday rotation in pulsars refers to shorter lines of sight, and, combined with dispersion measures, gives direct measurements of interstellar fields.

20.2 Faraday Rotation in Pulsars

The discovery of a high degree of linear polarisation in pulsar radio signals (Lyne & Smith 1968) led at once to the most direct way of measuring interstellar magnetic fields. Faraday rotation of the plane of polarisation can be measured, as for the extragalactic radio sources, by measuring the position angle of the polarisation at several radio frequencies. In contrast to the extragalactic radio sources, there is no rotation intrinsic to the pulsar, so that the uncertainty in the origin of the rotation is removed. The main advantage over the extragalactic sources is, however, the availability of the dispersion measure $DM = \int n_e dL$ at the same time as the rotation measure R . This removes most of the uncertainty in interpreting Eqn. 20.2, since it provides a value for the electron content in the line of sight and also provides the distance of the pulsar.

Thus the ratio

$$\frac{R}{DM} = 0.81 \frac{\int n_e B \cos \theta dL}{\int n_e dL} \quad (20.3)$$

gives a value of field $\langle B \cos \theta \rangle$, which is an average along the line of sight. A positive value of R indicates a mean field component directed towards us. The units in this equation are R in rad m⁻² and B in μ G (microgauss). The average is weighted by the electron density along the line; if, for instance, a large part of the dispersion measure in a particular pulsar is due to a single H II region, then the field in that region receives a heavy weighting. If a pulsar lies at a large distance above the galactic plane where the electron density may be small, its rotation measure does not depend much on the magnetic field in its immediate vicinity, but mostly on the field close to the Galactic plane; generally this means within about 1 kiloparsec, which is the approximate scale height of the electron density distribution. The method is obviously difficult to apply if the strength or direction of the field vary considerably along the line of sight; fortunately, the main structure of the field is on a large scale, and the average field $\langle B \cos \theta \rangle$ turns out to be a useful measure.

Faraday rotation is measured from the variation of polarisation position angle with radio frequency. This is usually obtained over a wide frequency range, although at low frequencies where the rotation is large it may be convenient to measure the small change in position angle $\Delta\phi$ between adjacent frequencies ν , $\nu + \Delta\nu$. If ν is in MHz,

$$\Delta\phi = -2R(300/\nu)^2 \Delta\nu/\nu \text{ radians.} \quad (20.4)$$

At frequencies near 300 MHz, a frequency separation $\Delta\nu$ of a few MHz is appropriate for most rotation measures; the more distant pulsars with large rotation measures may require observations at higher frequencies of order 1 GHz. There may be an ambiguity of $n\pi$ in measuring θ at two frequencies only, and three or more are often necessary.

The first measurements of pulsar Faraday rotation (Smith 1968) referred to PSR B0950+08, which had recently been found to be highly polarised. Unfortunately, the line of sight to PSR B0950+08 is nearly transverse to the local magnetic field, and this pulsar has almost the smallest known rotation measure; it is so small that the measured rotation could be accounted for by ionospheric rotation alone. Lyne, Smith and Graham (1971) subsequently obtained line of sight field values up to 3 microgauss for several pulsars. Data for over 500 pulsars are now available (Han *et al.* 2018); consult the ATNF pulsar catalogue for more recent values.

20.3 The Configuration of the Local Field

Close to the Galactic plane, the magnetic field is expected to follow, roughly, the spiral arm structure delineated by the 21-cm hydrogen line measurements. The local arm runs nearly azimuthally; it is inclined at an angle of about 80 deg to the radial direction from the centre. The nearest pulsars do show the expected pattern of a reversing sign of R on either side of this radial direction, but there are large non-conformities, especially in more distant pulsars. Figure 20.1 shows the magnetic field components deduced from a reasonably uniform set of RM measurements covering the whole sky (Sobey *et al.* 2019).

As can be seen in Figure 20.1, most of the known pulsars are close to the Galactic plane, and some are at distances of several kiloparsecs. Although this concentration may be exaggerated by a concentration of searches at low Galactic latitudes, this is helpful in allowing an exploration of the spiral arm structure beyond the local arm. The advent of sensitive low-frequency telescopes like LOFAR has allowed one to get values for R from nearby pulsars and more at high Galactic latitudes. Figure 20.2 shows the distribution of B -field values, projected on to the plane of the Galaxy. Distances are found from the values of dispersion measure, using the model electron distributions such as NE2001 and YMW16 (Chapter 7). The approximate locations of the spiral arms are indicated by the underlying grey scale, where the dark regions of high electron content come from the model of YMW16. The solar radial distance is taken as 8.2 kpc.

Dividing this plot into four quadrants centred on the Sun shows approximately the symmetry already found in the extragalactic measurements. Most values of B

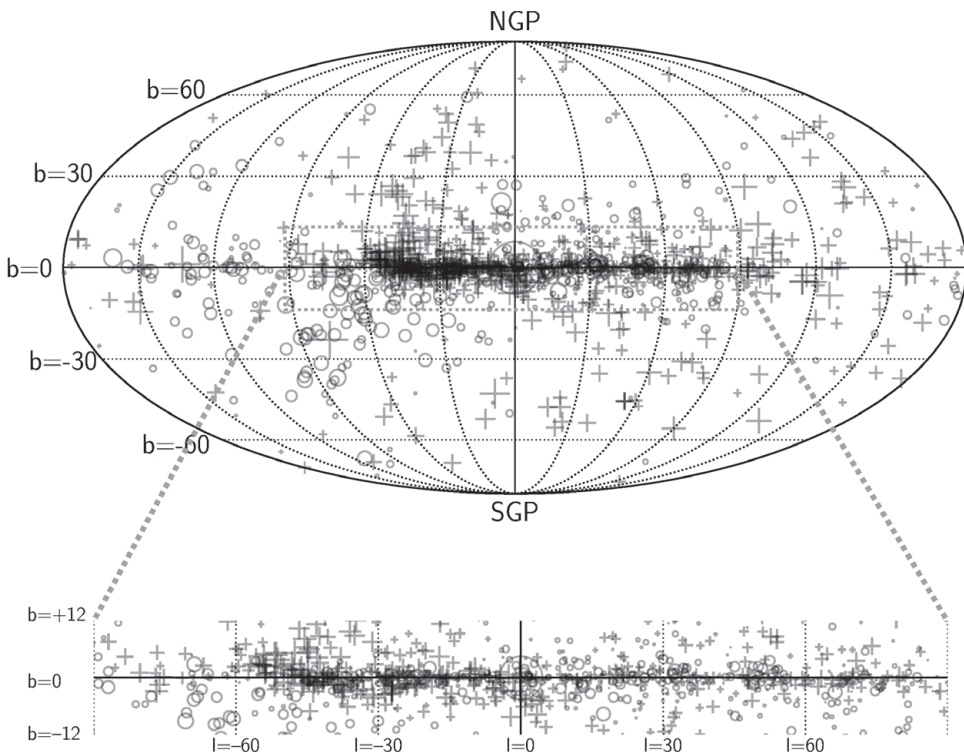


Figure 20.1 Hammer–Aitoff projection of the sky in Galactic coordinates, showing the magnetic field components obtained from pulsar Faraday rotation. The field is the weighted mean along the line of sight to all pulsars whose Faraday rotation had been measured in 2020. Plus signs and circles indicate respectively a field directed towards and away from us. The size of the symbols is proportional to the field strength. A zoom in showing the lower Galactic latitude parts of the Galaxy is shown below (Credit C. Sobey).

in the first and third quadrants ($l = 0 - 90$ deg, $l = 180 - 270$ deg) are positive, and those in the second and fourth quadrants are negative.

It is still not clear from this plot whether the direction of the field reverses in adjacent spiral arms. Part of the problem is the remaining uncertainty in distances, which can misplace a pulsar from the edge of one arm to the edge of another. Han *et al.* (1999) overcame this by selecting pulsars at the tangential points of each arm, where precise location is less important. They showed that the field is in the same direction in all arms, but reversed between the arms. This is a *bi-symmetric* pattern. The strength of this organised field is approximately 2 μG in the local arm and 4 μG closer to the Galactic centre.

The line of sight to a pulsar at Galactic latitude $|b|$ above about 8 deg would not intersect the more distant arms, and the magnetic field strengths of such pulsars

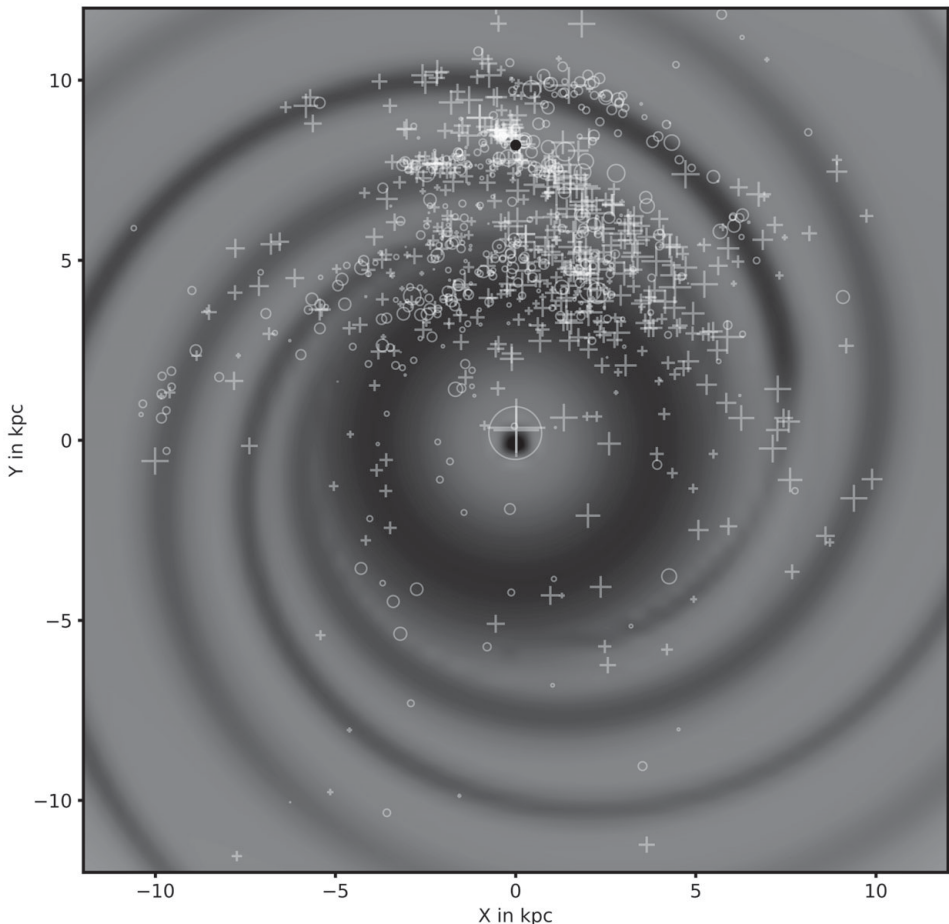


Figure 20.2 Magnetic field strength projected onto the plane of the Galaxy. The Galactic centre is at the centre of the diagram, and the black circle shows the position of the Sun. The spiral structure underneath is from the YMW16 model for the distribution of electrons in our Galaxy. The plus symbols and circle symbols indicate respectively fields directed towards and away from us. The size of the symbols is proportional to the field strength. The large value in the Galactic centre is due to the so-called Galactic-centre magnetar (Data provided by C. Sobey).

should show a clearer pattern relating only to the local arm. Figure 20.3 shows the field strength values for hundreds of pulsars with $|b| \geq 8$ deg. As expected, the division of positive and negative values is clearer than in Figure 20.2; there remain, however, some apparently random variations of strength and even of polarity on a range of spatial scales. Jaffe *et al.* (2010) used all available values of R , both pulsar and extragalactic (Figure 20.4), together with polarised synchrotron radiation, to

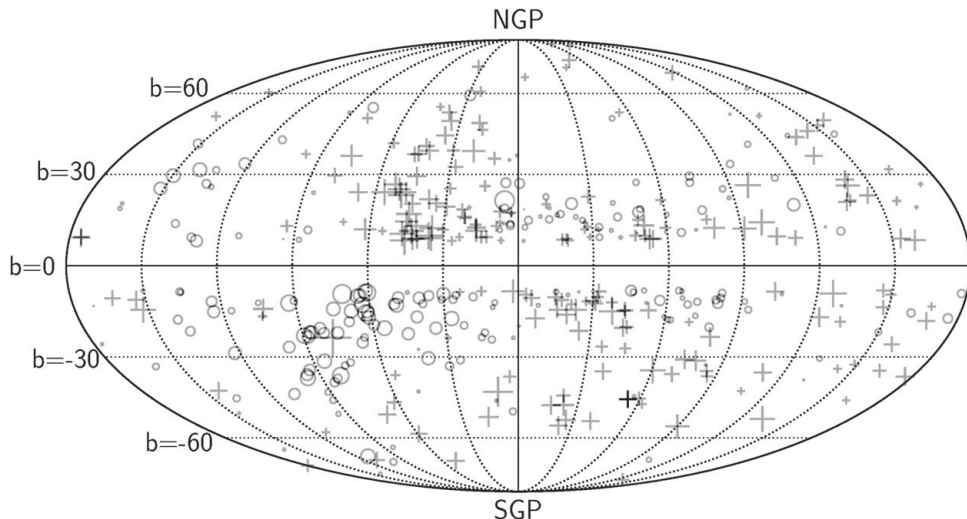


Figure 20.3 The distribution of B-field values for pulsars with Galactic latitude $|b| > 8$ deg. Positive values are shown as pluses and their sizes are proportional to the field strength (Data provided by C. Sobey).

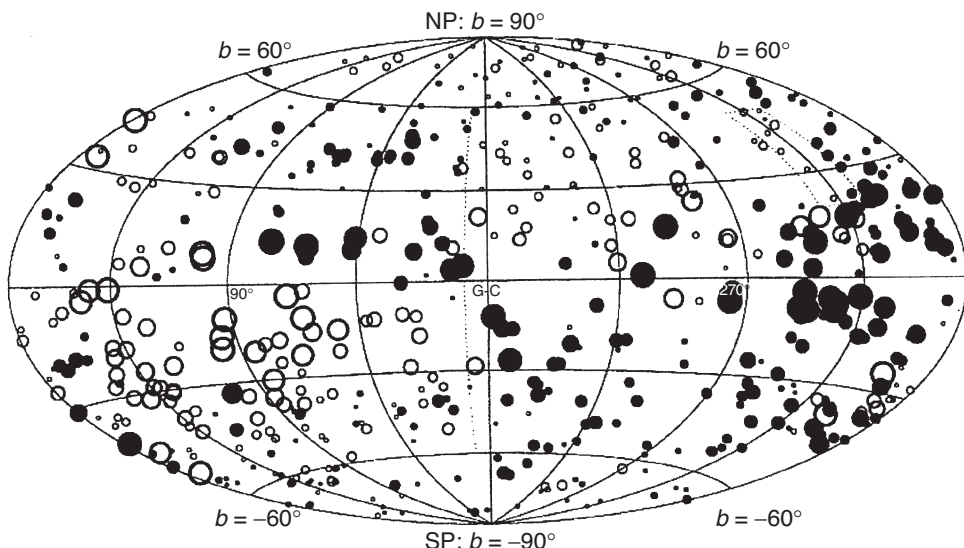


Figure 20.4 The distribution of rotation measures R for extragalactic radio sources (Han *et al.* 1999).

show that the contributions to magnetic energy density of ordered and random fields are approximately equal on the Galactic plane.

The overall effect of the spiral arm magnetic fields, in terms of a dipole field for the whole Galaxy, may be small, since the field within the arms is cancelled by the reverse field in the interarm spaces. Outside the plane there appears to be very

little organised field. As there are few pulsars there, most information comes from extragalactic sources (Figure 20.4). Mao *et al.* (2010) assembled RM values for 1000 sources for $|b| \geq 77$ deg and found no consistent pattern of rotation measures that embrace both Galactic poles; there was, however, a significant field in the south Galactic pole.

20.4 The Effect of H II Regions and Other Structure

The random component of the field, as seen in the distribution of rotation measures, might be expected from observations of the polarisation of background radio emission; Wilkinson and Smith (1974), Spoelstra (1984) and Beuermann, Kanbach and Berkhuijsen (1985) showed that irregularities in the magnetic field exist on a scale of some tens of parsecs and with a strength comparable with the mean field. There is probably also an extensive irregularity associated with the north Galactic spur, which is believed to be the remnant of a supernova shell (Rand & Kulkarni 1989). An investigation of rotation measures in an area of sky containing the local (Perseus) spiral arm by Mitra *et al.* (2003) demonstrates large effects due to ionised hydrogen regions (H II regions), which account for the large deviations from simple patterns in the distribution of rotation measures. As expected, a pulsar located behind an H II region will have a large value of R ; this can be seen by relating R values to thermal radio emission from individual H II regions.

There are, however, cases of reversals of the sign of R between pulsars that are close together on the sky and at similar distances. This indicates that there are distortions of field direction in addition to the increases in electron density. Such distortions are presumably due to differential movement of ionised clouds containing frozen-in magnetic fields. By detailed study of the selected area of sky containing the spiral arm, Mitra *et al.* (2003) were able to evaluate both the mean field and the magnitude of the irregularities in the local arm. They concluded that the mean field strength is $1.7 \pm 1.0 \mu\text{G}$, with local random components up to $5.7 \mu\text{G}$. These very large irregularities emphasise the importance of detailed study of foreground objects in delineating the overall field pattern in the Galaxy.

Further discussion on the magnetic fields in spiral galaxies may be found in Beck (2015). Han, Manchester, van Straten and Demorest (2018) combined the rotation measures of 477 pulsars with those of extragalactic sources to describe the magnetic field of the Milky Way, including details of local irregularities superposed on large-scale structure.

20.5 The Intergalactic Magnetic Field

In a comprehensive review of galactic and intergalactic magnetic fields, Han (2017) discusses the possibilities of measuring intergalactic magnetic fields. Within the

local group of galaxies, there may eventually be sufficient pulsars discovered to allow an exploration of the magnetic field between galaxies, although it will be difficult to distinguish the intergalactic field from fields within the galaxies. Pulsar observations at present extend only to the Magellanic Clouds. On a larger scale, the “cosmic web” of magnetic fields may become accessible through rotation measures of fast radio bursts.

21

Prospects

At the time of writing (2021), it is nearly 90 years since the discovery of the neutron, 87 years since the proposal by Baade and Zwicky that neutron stars might be the result of supernova explosions and just over 54 years since the discovery of the first neutron star. In the intervening decades, we have discovered more than 3000 pulsars and hundreds of other manifestations of neutron stars. If you have read your way through the book to this stage, then you will have already established that there is a wide range of science that can be undertaken by studying or using pulsars. If you have skipped to the end to read this section, then the sheer size of this book will already have given you the same impression.

In this final chapter, we take a look forward into the near future to give the reader some idea of what we might expect to learn about, and from, pulsars. This cannot be a comprehensive consideration of all possible science, because, for example, the pulsar science case for the SKA (Square Kilometre Array) alone is a couple of hundred pages. We will therefore just give a flavour, and we will not be able to touch on all planned or proposed future missions.

We are entering a rich era of new radio telescopes. The completion of the FAST (Five-hundred-meter Aperture Spherical Telescope) and MeerKAT (more Karoo Array Telescope) telescopes has added excellent sensitivity in the Northern and Southern Hemisphere, respectively, significantly boosting the capabilities for all radio studies of pulsars, from emission physics to precision timing and discovering new sources, while LOFAR (LOw Frequency ARray) has allowed us to push this sensitivity boost to the lowest radio frequencies. ASKAP (Australian SKA Pathfinder) and MWA (Murchison Wide-field Array) are revealing new sources that look like they may be either different manifestations of radio-emitting neutron stars or extreme versions of the ones we already know. These are all precursors for the SKA, which will have the MID (in South Africa) and LOW (in Australia) telescopes due to come on line before the end of this decade. The SKA will be an exceptionally sensitive telescope which, combined with its wide range of

frequencies and flexibility, will revolutionise our understanding of neutron stars and their use as probes of gravity and super-nuclear-density matter and for detecting gravitational waves.

Initially with FAST and MeerKAT and ultimately with the SKA, we can expect a significant increase in the number of radio pulsars known in the Galaxy. There are at least 30,000 pulsars predicted to be detectable from Earth. This increase in the population of radio-emitting pulsars will impact many areas of astrophysics. For example, we can expect to constrain the maximum and minimum spin-period of radio-emitting neutron stars, which will impact on our understanding of the physics of accretion, of the neutron star equation of state and of the emission mechanism. At the time of going to press, we are already aware of two record breaking pulsars/magnetars with spin periods of 76 seconds and 18 minutes respectively. Improved implementations of search methods like the fast-folding algorithm, and the increased sensitivity to single pulses (the method by which both these new sources were found) will add to the filling out of the $P - \dot{P}$ diagram and reveal evolutionary trends – and no doubt throw up new mysteries.

As mentioned above, it is 54 years since the discovery of the first pulsar, and some of the longest continuous data sets for pulsar timing are approaching 50 years! This provides the opportunity to start to look at longer-term timing effects, such as prospects for measuring braking indices and further understanding the relationship between spin-noise and magnetospheric effects. Two new large glitch catalogues are about to be published, and these exceptional samples will provide vital new input into our understanding of the glitch mechanism but will also be used to probe the physics of the neutron star interiors. This will be extremely interesting in the era where neutron star mergers are seen by gravitational wave observatories, which will also probe the equation of state.

The ever-improved sensitivity of existing and new telescopes will also reveal new and weaker manifestations of all of these effects, revealing more about the associated physical mechanisms. However, the competition for observing time with all of the new sources that are being discovered is a real issue that will need to be addressed as the pressure to do instant science rather than long-term studies rises, as will the pressure on the older facilities that provide vital supporting roles to the new shiny facilities.

It is not only at radio wavelengths where we can expect to see significant steps forward in capabilities in the near term. We are already seeing how the sensitivity and high time resolution of NICER (Neutron star Interior Composition ExploreR) are revolutionising our understanding of x-ray emission from neutron stars, from pulsars to magnetars, but also in measuring their sizes. At the time of writing,

e-ROSITA (extended ROentgen Survey with an Imaging Telescope Array) has produced stunning all-sky images of the x-ray sky, which will be an excellent resource for x-ray studies of neutron stars and their interactions with the ISM and supernova remnants. In 2022, XRISM (X-Ray Imaging and Spectroscopy Mission) will be launched: this is an imaging and spectroscopy mission with significantly improved spectral resolution over Chandra and XMM-Newton. eXTP (enhanced X-ray Timing and Polarimetry) is expected to be launched towards the end of the 2020s and has neutron stars at the core of its science mission. It will use spectroscopy and timing measurements to measure the equation of state of neutron star interiors and use polarisation observations to understand their x-ray emission properties. Early in the next decade, ATHENA (Advanced Telescope for High ENergy Astrophysics) will be launched. This is expected to be up to two orders of magnitude more sensitive than present x-ray instruments and, amongst other things, will provide more neutron star mass and radius measurements.

The Fermi-LAT (Fermi Large Area Telescope) gamma-ray telescope has revolutionised our understanding of pulsar emission, directed us to the locations of previously undiscovered radio pulsars and unveiled a population of sources emitting only gamma rays. Fermi-LAT will continue to bring important information on timing and properties of pulsars, which is especially important as no new pulsar-optimised gamma-ray satellite is on the horizon. There will, however, be a big step up in studying the TeV emission from pulsars with the completion of the CTA (Cerenkov Telescope Array) in the 2020s. Telescopes like HESS (High Energy Stereoscopic System), MAGIC (Major Atmospheric Gamma Imaging Cherenkov) and VERITAS (Very Energetic Radiation Imaging Telescope Array System) have revealed important attributes of the high-energy emission of pulsars and their interactions with their environments. The CTA will have the sensitivity and resolution to improve our understanding of pulsar emission physics, the interstellar medium and the wind properties of the companion stars, and possibly to detect magnetars beyond our Galaxy.

The rich data set provided by the Fermi-LAT and the revelation of the relationship between pulsar spin and emission properties has revitalised the study of the pulsar emission theory. When combined with improved computing and enhanced models and modelling, we are getting ever closer to a detailed understanding of the way that pulsars shine. It is very likely that this will continue to advance as the next generation of computing becomes available and comparisons can be made with the ever-richer multi-wavelength data sets.

The LIGO (Laser Interferometer Gravitational-Wave Observatory) and Virgo gravitational wave detectors have made amazing strides in the last decade, and

the direct detection of gravitational waves from neutron star–neutron star mergers provides an exciting new tool for understanding gravity but also the interiors of neutron stars. The continued improvement of LIGO and Virgo, and the addition of KAGRA (Kamioka Gravitational Wave Detector) and LIGO-India, will enable the detection of dozens of such mergers per year, and the improved localisation will enable the slew of follow-up instruments to catch any resultant electro-magnetic signatures. This sample will revolutionise our understanding of neutron star binaries and properties and may ultimately also reveal elusive neutron star–black hole systems. On the further horizon (2034) is the space-based gravitational wave interferometer LISA (Laser Interferometer Space Antenna), which will have the sensitivity to watch neutron star binaries across the orbital period range, provide unique tests of gravity and measure the neutron star equation of state.

Recent work has shown that the detection of the stochastic gravitational wave signal from a population of merging supermassive black holes in the early Universe is tantalisingly close. The last decade has already seen a dramatic increase in the population of MSPs, and, when combined with the improvements in pulsar timing precision with MeerKAT and FAST, there is a strong prospect that a first detection will happen this decade. In the era of the SKA, we can then expect to measure the gravitational wave spectrum to better determine the origin and physics of the source population. This will allow us to constrain and study Galaxy evolution and the physics of black hole in-spiral. It will also be possible to undertake tests of gravity through studying the polarisation modes and measure, or strongly constrain, the mass of the graviton.

We will continue to see increased and new constraints on theories of gravity from high precision timing of pulsars in binary systems. With the SKA we can expect to detect Lense–Thirring effects in the Double Pulsar system and eventually constrain the moment of inertia.

Another by-product of the large increase in the known pulsar population is the expectation that at least one neutron star–black hole binary should be discovered, and other exotic systems such as a binary with two MSPs, or even a triple MSP system might be found. A pulsar–black hole binary would provide us with an excellent tool for studying theories of gravity and the properties of the black hole. An MSP in orbit around the black hole at the centre of the Galaxy would allow us to measure a black hole mass and spin with a precision of 1% or better. It would therefore allow one to test the cosmic censorship conjecture and to test the no-hair theorem of black holes.

We have touched briefly in this book on the possibility that at least some FRBs are associated with neutron stars. In the coming decade, we will discover many thousands of new FRBs, and many hundreds will likely be localised to their host galaxies. Thus we will be able to ascertain whether they are associated with (young)

Magnetars, super giant pulses, lensed radio emission from binary MSPs, merging neutron stars or other manifestations involving neutron stars. Or they may indeed come from all of these proposed origins. It is clear that the next generation of this book will have a significantly larger section on FRBs!

We make these predictions with confidence, but we also can expect the new generation of telescopes to bring us many further and unexpected discoveries. We look forward to the next decade of research in pulsar astronomy.

References

- Abbott, B. P., Abbott, R., Abbott, T. D., and 1153 others. 2017. GW170817: Observation of gravitational waves from a binary neutron star inspiral. *Phys. Rev. Lett.*, **119**(16), 1101.
- Abbott, B. P., Abbott, R., Abbott, T. D., and 1149 others. 2018. GW170817: Measurements of neutron star radii and equation of state. *Phys. Rev. Lett.*, **121**(16), 1101.
- Abdo, A. A., Allen, B., Berley, D., and 31 others. 2007. TeV gamma-ray sources from a survey of the Galactic plane with Milagro. *ApJ*, **664**(Aug.), L91–L94.
- Abdo, A. A., Ackermann, M., Ajello, M., and 177 others. 2009a. Detection of 16 gamma-ray pulsars through blind frequency searches using the Fermi LAT. *Science*, **325**(Aug.), 840–844.
- Abdo, A. A., Ackermann, M., Ajello, M., and 199 others. 2009b. A population of gamma-ray millisecond pulsars seen with the Fermi Large Area Telescope. *Science*, **325**, 848.
- Abdo, A. A., Ackermann, M., Ajello, M., and 232 others. 2010a. Fermi Large Area Telescope first source catalog. *ApJS*, **188**, 405–436.
- Abdo, A. A., Ackermann, M., Ajello, M., and 189 others. 2010b. Fermi Large Area Telescope observations of the Crab Pulsar and Nebula. *ApJ*, **708**, 1254–1267.
- Abdo, A. A., Ackermann, M., Ajello, M., and 214 others. 2010c. The first Fermi Large Area Telescope catalog of gamma-ray pulsars. *ApJS*, **187**, 460–494.
- Abdo, A. A., Ajello, M., Allafort, A., and 208 others. 2013. The Second Fermi Large Area Telescope catalog of gamma-ray pulsars. *ApJS*, **208**(2), 17.
- Acciari, V. A., Aliu, E., Arlen, T., and 79 others. 2010. Discovery of very high energy γ -ray emission from the SNR G54.1+0.3. *ApJ*, **719**(1), L69–L73.
- Ackermann, M., Ajello, M., Allafort, A., and 166 others. 2013. Detection of the characteristic pion-decay signature in supernova remnants. *Science*, **339**(6121), 807–811.
- Aharonian, F., Akhperjanian, A. G., Aye, K.-M., and 96 others. 2005. Discovery of extended VHE gamma-ray emission from the asymmetric pulsar wind nebula in MSH 15–52 with HESS. *A&A*, **435**, L17–L20.
- Aharonian, F., Akhperjanian, A. G., Bazer-Bachi, A. R., and 103 others. 2006. First detection of a VHE gamma-ray spectral maximum from a cosmic source: HESS discovery of the Vela X nebula. *A&A*, **448**, L43.
- Aharonian, F., Akhperjanian, A. G., Bazer-Bachi, A. R., and 125 others. 2007. Discovery of two candidate pulsar wind nebulae in very-high-energy gamma rays. *A&A*, **472**(2), 489–495.
- Akgün, T., Link, B., and Wasserman, I. 2006. Precession of the isolated neutron star PSR B1828-11. *MNRAS*, **365**, 653–672.

- Alam, Md F., Arzoumanian, Z., Baker, P. T., and 67 others. 2020. The NANOGrav 12.5-year data set: Wideband timing of 47 millisecond pulsars. *arXiv e-prints*, May, arXiv:2005.06495.
- Allen, B., Knispel, B., Cordes, J. M., and 43 others. 2013. The Einstein@Home search for radio pulsars and PSR J2007+2722 discovery. *ApJ*, **773**(Aug.), 91.
- Alpar, M. A., Anderson, P. W., Pines, D., and Shaham, J. 1981. Giant glitches and the pinned vorticity in the Vela and other pulsars. *ApJ*, **249**, L29–L33.
- Alpar, M. A., Cheng, A. F., Ruderman, M. A., and Shaham, J. 1982. A new class of radio pulsars. *Nature*, **300**, 728–730.
- Alpar, M. A., Cheng, K. S., and Pines, D. 1989. Vortex creep and the internal temperature of neutron stars: Linear and nonlinear response to a glitch. *ApJ*, **346**, 823–832.
- Alpar, M. A., Chau, H. F., Cheng, K. S., and Pines, D. 1996. Postglitch relaxation of the Crab Pulsar after its first four glitches. *ApJ*, **459**, 706–716.
- Andersen, B. C., and Ransom, S. M. 2018. A Fourier domain “Jerk” search for binary pulsars. *ApJ*, **863**(1), L13–L18.
- Andersen, B. C., Bandura, K. M., Bhardwaj, M., and 68 others. 2020. A bright millisecond-duration radio burst from a Galactic magnetar. *Nature*, **587**(7832), 54–58.
- Anderson, P. W., and Itoh, N. 1975. Pulsar glitches and restlessness as a hard superfluidity phenomenon. *Nature*, **256**, 25–27.
- Anderson, S. B. 1993 (Jan.). *A Study of Recycled Pulsars in Globular Clusters*. Ph.D. thesis, California Institute of Technology, Pasadena.
- Antoniadis, J., Freire, P. C. C., Wex, N., and 19 others. 2013. A massive pulsar in a compact relativistic binary. *Science*, **340**(6131), 448.
- Antonopoulou, D., Espinoza, C. M., Kuiper, L., and Andersson, N. 2018. Pulsar spin-down: The glitch-dominated rotation of PSR J0537-6910. *MNRAS*, **473**(2), 1644–1655.
- Archibald, A. M., Stairs, I. H., Ransom, S. M., and 15 others. 2009. A radio pulsar/X-ray binary link. *Science*, **324**(5933), 1411.
- Archibald, R. F., Kaspi, V. M., Tendulkar, S. P., and Scholz, P. 2016. A magnetar-like outburst from a high-B radio pulsar. *ApJ*, **829**(1), L21.
- Arendt, P. N., and Eilek, J. A. 2002. Pair creation in the pulsar magnetosphere. *ApJ*, **581**, 451–469.
- Armstrong, J. W., Rickett, B. J., and Spangler, S. R. 1995. Electron density power spectrum in the local interstellar medium. *ApJ*, **443**, 209–221.
- Arons, J., and Barnard, J. J. 1986. Wave propagation in pulsar magnetospheres: Dispersion relations and normal modes of plasmas in superstrong magnetic fields. *ApJ*, **302**, 120.
- Arzoumanian, Z., Nice, D. J., Taylor, J. H., and Thorsett, S. E. 1994. Timing behavior of 96 radio pulsars. *ApJ*, **422**, 671–680.
- Arzoumanian, Z., Joshi, K., Rasio, F. A., and Thorsett, S. E. 1996. Orbital parameters of the PSR B1620-26 triple system. *PASP Conf. Ser.*, **105**, 525–530.
- Ash, M. E., Shapiro, I. I., and Smith, W. B. 1967. Astronomical constants and planetary ephemerides deduced from radar and optical observations. *AJ*, **72**, 338–350.
- Ashton, G., Lasky, P. D., Gruber, V., and Palfreyman, J. 2019. Rotational evolution of the Vela pulsar during the 2016 glitch. *Nature Astronomy*, **3**, 1143–1148.
- Ashworth, M. 1982. *The Emission Mechanism of Radio Pulsars*. Ph.D. thesis, The University of Manchester.
- Asseo, E., Pellat, R., and Sol, H. 1983. Radiative or two-stream instability as a source for pulsar radio emission. *ApJ*, **266**, 201–214.
- Atwood, W. B., Ziegler, M., Johnson, R. P., and Baughman, B. M. 2006. A time-differencing technique for detecting radio-quiet gamma-ray pulsars. *ApJ*, **652**(1), L49–L52.

- Atwood, W. B., Abdo, A. A., Ackermann, and 237 others. 2009. The Large Area Telescope on the Fermi Gamma-Ray Space Telescope mission. *ApJ*, **697**(2), 1071–1102.
- Baade, W. 1942. The Crab Nebula. *ApJ*, **96**, 188–198.
- Baade, W., and Zwicky, F. 1934. On super-novae. *Proc. Nat. Acad. Sci.*, **20**, 254–259.
- Bachetti, M., Harrison, F. A., Walton, D. J., and 21 others. 2014. An ultraluminous X-ray source powered by an accreting neutron star. *Nature*, **514**(7521), 202–204.
- Backer, D. C. 1970. Pulsar nulling phenomena. *Nature*, **228**, 42–43.
- Backer, D. C. 1976. Pulsar average wave forms and hollow-cone beam models. *ApJ*, **209**, 895–907.
- Backer, D. C., and Hellings, R. W. 1986. Pulsar timing and general relativity. *Ann. Rev. Astr. Ap.*, **24**, 537–575.
- Backer, D. C., Rankin, J. M., and Campbell, D. B. 1976. Orthogonal mode emission in geometric models of pulsar polarisation. *Nature*, **263**, 202–207.
- Backer, D. C., Kulkarni, S. R., Heiles, C., Davis, M. M., and Goss, W. M. 1982. A millisecond pulsar. *Nature*, **300**, 615–618.
- Bailes, M., Manchester, R. N., Kesteven, M. J., Norris, R. P., and Reynolds, J. E. 1990. The proper motion of six southern radio pulsars. *MNRAS*, **247**, 322–326.
- Baldo, M., and Burgio, G. F. 2012. Properties of the nuclear medium. *Reports on Progress in Physics*, **75**(2), 026301.
- Bamba, A., Mori, K., and Shibata, S. 2010. Chandra view of pulsar wind nebula tori. *ApJ*, **709**, 507–511.
- Barat, C., Chambon, G., Hurley, K., Niel, M., Vedrenne, G., Estulin, I. V., Kurt, V. G., and Zenchenko, V. M. 1979. Evidence for periodicity in a gamma ray burst. *A&A*, **79**, L24–L25.
- Barnard, J. J. 1986. Probing the magnetic field of radio pulsars: A reexamination of polarization position angle swings. *ApJ*, **303**, 280–291.
- Barr, E. D., Champion, D. J., Kramer, M., and 13 others. 2013. The Northern High Time Resolution Universe pulsar survey – I. Setup and initial discoveries. *MNRAS*, **435**(3), 2234–2245.
- Bartel, N., Sieber, W., and Wolszczan, A. 1980. Pulse to pulse intensity modulation from radio pulsars with particular reference to frequency dependence. *A&A*, **90**, 58–60.
- Bartel, N., Morris, D., Sieber, W., and Hankins, T. H. 1982. The mode-switching phenomenon in pulsars. *ApJ*, **258**, 776–789.
- Bartel, N., Chandler, J. F., Ratner, M. I., Shapiro, I. I., Pan, R., and Capallo, R. J. 1996. Towards a frame-tie via millisecond pulsar VLBI. *AJ*, **112**, 1690–1696.
- Bassa, C. G., Pleunis, Z., Hessels, J. W. T., Ferrara, E. C., Kondratiev, V. I., Sanidas, S., Lyne, A. G., Stappers, B. W., Ransom, S. M., and Fermi Pulsar Search Consortium. 2018 (Aug.). Targeted millisecond pulsar surveys of Fermi γ -ray sources with LOFAR. Pages 33–36 of: Weltevrede, P., Perera, B. B. P., Preston, L. L., and Sanidas, S. (eds), *Pulsar Astrophysics the Next Fifty Years*, vol. 337.
- Bastian, T. S. 1994. Angular scattering of solar radio emission by coronal turbulence. *ApJ*, **426**(May), 774.
- Basu, R., and Mitra, D. 2019. Radio emission features in different modes of PSR J0826+2637 (B0823+26). *MNRAS*, **487**(4), 4536–4549.
- Basu, R., Mitra, D., Melikidze, G. I., Maciesiak, K., Skrzypczak, A., and Szary, A. 2016. Meterwavelength Single-pulse Polarimetric Emission Survey. II. The phenomenon of drifting subpulses. *ApJ*, **833**(1), 29.
- Baym, G., Pethick, C. J., and Sutherland, P. 1971. The ground state of matter at high densities: Equation of state and stellar models. *ApJ*, **170**, 299–317.

- Baym, G., Hatsuda, T., Kojo, T., Powell, P. D., Song, Y., and Takatsuka, T. 2018. From hadrons to quarks in neutron stars: A review. *Reports on Progress in Physics*, **81**(5), 056902.
- Baym, G., Furusawa, S., Hatsuda, T., Kojo, T., and Togashi, H. 2019. New neutron star equation of state with quark-hadron crossover. *ApJ*, **885**(1), 42.
- Beck, R. 2009 (Apr.). Measuring interstellar magnetic fields by radio synchrotron emission. Pages 3–14 of: Strassmeier, K. G., Kosovichev, A. G., and Beckman, J. E. (eds), *Cosmic Magnetic Fields: From Planets, to Stars and Galaxies*. IAU Symposium, vol. 259.
- Beck, R. 2015. Magnetic fields in spiral galaxies. *Astron. Astrophys. Rev.*, **24**(Dec.), 4.
- Becker, W., and Trümper, J. 1997. The X-ray luminosity of rotation-powered neutron stars. *A&A*, **326**, 682–691.
- Belian, R. D., Conner, J. P., and Evans, W. D. 1976. The discovery of X-ray bursts from a region in the constellation Norma. *ApJ*, **206**, L135–L138.
- Bell, J. F. 1998. Radio pulsar timing. *Adv. Space Res.*, **21**, 137–147.
- Bell, J. F., and Bailes, M. 1996. A new method for obtaining binary pulsar distances and its implications for tests of general relativity. *ApJ*, **456**, L33–L36.
- Bell, J. F., Bailes, M., Manchester, R. N., Weisberg, J. M., and Lyne, A. G. 1995. The proper motion and wind nebula of the nearby millisecond pulsar J0437–4715. *ApJ*, **440**, L81–L83.
- Bergeron, P., Dufour, P., Fontaine, G., Couture, S., Blouin, S., Genest-Beaulieu, C., Bédard, A., and Rolland, B. 2019. On the measurement of fundamental parameters of white dwarfs in the Gaia era. *ApJ*, **876**(1), 67.
- Bertotti, B., Carr, B. J., and Rees, M. J. 1983. Limits from the timing of pulsars on the cosmic gravitational wave background. *MNRAS*, **203**, 945–954.
- Bertotti, B., Iess, L., and Tortora, P. 2003. A test of general relativity using radio links with the Cassini spacecraft. *Nature*, **425**, 374–376.
- Beskin, V. S. 1999. Radio pulsars. *Physics Uspekhi*, **42**, 1071.
- Beskin, V. S., Gurevich, A. V., and Istomin, Ya. N. 1993. *Physics of the Pulsar Magnetosphere*. Cambridge University Press.
- Beuermann, K., Kanbach, G., and Berkhuijsen, E. M. 1985. Radio structure of the Galaxy – Thick disk and thin disk at 408 MHz. *A&A*, **153**, 17–34.
- Bhandari, S., Sadler, E. M., Prochaska, J. X., and 16 others. 2020. The host galaxies and progenitors of fast radio bursts localized with the Australian Square Kilometre Array Pathfinder. *ApJ*, **895**(2), L37.
- Bhat, N. D. R., Cordes, J. M., Camilo, F., Nice, D. J., and Lorimer, D. R. 2004. Multifrequency observations of radio pulse broadening and constraints on interstellar electron density microstructure. *ApJ*, **605**(2), 759–783.
- Bhat, N. D. R., Gupta, Y., Kramer, M., Karastergiou, A., Lyne, A. G., and Johnston, S. 2007. Simultaneous single-pulse observations of radio pulsars. V. On the broadband nature of the pulse nulling phenomenon in PSR B1133+16. *A&A*, **462**(1), 257–268.
- Bhattacharya, D., Wijers, R. A. M. J., Hartman, J. W., and Verbunt, F. 1992. On the decay of magnetic fields of single radio pulsars. *A&A*, **254**, 198–212.
- Bhattacharya, D., Gupta, Y., and Gil, J. 2009 (Sept.). Wide profile drifting pulsars: An elegant way to probe pulsar magnetospheres. Page 313 of: Saikia, D. J., Green, D. A., Gupta, Y., and Venturi, T. (eds), *The Low-Frequency Radio Universe*. Astronomical Society of the Pacific Conference Series, vol. 407.
- Bietenholz, M. F., Kassim, N., and Weiler, K. 2002. The radio spectral index of 3C58. *Proc. IAU Symp.* **199**, 303.
- Biggs, J. D. 1990. Meridional compression of radio pulsar beams. *MNRAS*, **245**, 514–521.

- Biggs, J. D., Hamilton, P. A., McCulloch, P. M., and Manchester, R. N. 1985a. The drifting subpulses of PSR 0148–06. *MNRAS*, **214**, 47P–52P.
- Biggs, J. D., McCulloch, P. M., Hamilton, P. A., Manchester, R. N., and Lyne, A. G. 1985b. A study of PSR 0826–34 – A remarkable pulsar. *MNRAS*, **215**, 281–294.
- Bignall, H. E., Jauncey, D. L., Lovell, J., Macquart, J.-P., Kedziora-Chudczer, L., and Tzioumis, A. K. 2003 (Jan.). The rapidly scintillating quasar, PKS 1257-326. Page E12 of: *IAU Joint Discussion*. IAU Joint Discussion.
- Bignami, G. F., Caraveo, P. A., De Luca, A., and Mereghetti, S. 2003. Discovery of X-ray cyclotron absorption lines measures the magnetic field of an isolated neutron star. *Nature*, **423**, 725–727.
- Bilous, A. V., Pennucci, T. T., Demorest, P., and Ransom, S. M. 2015. A broadband radio study of the average profile and giant pulses from PSR B1821-24A. *ApJ*, **803**(2), 83.
- Bilous, A. V., Watts, A. L., Harding, A. K., Riley, T. E., Arzoumanian, Z., Bogdanov, S., Gendreau, K. C., Ray, P. S., Guillot, S., Ho, W. C. G., and Chakrabarty, D. 2019. A NICER view of PSR J0030+0451: Evidence for a global-scale multipolar magnetic field. *ApJ*, **887**(1), L23.
- Björnsson, C.-I. 1998. A direct method to determine the geometry of the hollow cones in pulsars. *A&A*, **338**, 971–976.
- Blaauw, A. 1985. The progenitors of the local pulsar population. Pages 211–224 of: Boland, W., and van Woerden, H. (eds), *Birth and Evolution of Massive Stars and Stellar Groups*. Dordrecht: Reidel.
- Blandford, R., and Teukolsky, S. A. 1976. Arrival-time analysis for a pulsar in a binary system. *ApJ*, **205**, 580–591.
- Blaskiewicz, M., Cordes, J. M., and Wasserman, I. 1991. A relativistic model of pulsar polarization. *ApJ*, **370**, 643–669.
- Bochenek, C. D., Ravi, V., Belov, K. V., Hallinan, G., Kocz, J., Kulkarni, S. R., and McKenna, D. L. 2020. A fast radio burst associated with a galactic magnetar. *Nature*, **587**(7832), 59–62.
- Bogdanov, S., Rybicki, G. B., and Grindlay, J. E. 2007. Constraints on neutron star properties from X-ray observations of millisecond pulsars. *ApJ*, **670**(1), 668–676.
- Boldt, E. A., Desai, U. D., Holt, S. S., Serlemitsos, P. J., and Silverberg, R. F. 1969. Pulsed X-ray emission of NP 0532 in March 1968. *Nature*, **223**, 280–281.
- Bolton, J. G., Stanley, G. J., and Slee, O. B. 1949. Positions of three discrete sources of galactic radio-frequency radiation. *Nature*, **164**, 101–102.
- Boriakoff, V., Ferguson, D. C., and Slater, G. 1981. Pulsar microstructure quasi-periodicity. Pages 199–204 of: Sieber, W., and Wielebinski, R. (eds), *Pulsars, IAU Symposium 95*. Dordrecht: Reidel.
- Boriakoff, V., Buccieri, R., and Fauci, F. 1983. Discovery of a 6.1-ms binary pulsar, PSR 1953+29. *Nature*, **304**, 417–419.
- Bradt, H., Rappaport, S., Mayer, W., Nather, R. E., Warner, B., Macfarlane, M., and Kristian, J. 1969. X-ray and optical observations of the pulsar NP 0532 in the Crab Nebula. *Nature*, **222**, 728–730.
- Bradt, H. V. D., and McClintock, J. E. 1983. The optical counterparts of compact galactic X-ray sources. *Ann. Rev. Astr. Ap.*, **21**, 13–66.
- Brambilla, G., Kalapotharakos, C., Timokhin A., Harding, A., and Kazanas, D. 2018. Electron-positron pair flow and current composition in the pulsar magnetosphere. *ApJ*, **858**(2), 81.
- Breton, R. P., Kaspi, V. M., Kramer, M., McLaughlin, M. A., Lyutikov, M., Ransom, S. M., Stairs, I. H., Ferdman, R. D., Camilo, F., and Possenti, A. 2008. Relativistic spin precession in the Double Pulsar. *Science*, **321**, 104.

- Brisken, W. F., Benson, J. M., Goss, W. M., and Thorsett, S. E. 2002. Very Long Baseline Array measurement of nine pulsar parallaxes. *ApJ*, **571**, 906–917.
- Brisken, W. F., Macquart, J.-P., Gao, J. J., Rickett, B. J., Coles, W. A., Deller, A. T., Tingay, S. J., and West, C. J. 2010. 100 as resolution VLBI imaging of anisotropic interstellar scattering toward pulsar B0834+06. *ApJ*, **708**, 232–243.
- Bühler, R., and Blandford, R. 2014. The surprising Crab pulsar and its nebula: A review. *Rep. Prog. Phys.*, **77**(6), 066901.
- Burgay, M., D'Amico, N., Possenti, A., and 10 others. 2003. An increased estimate of the merger rate of double neutron stars from observations of a highly relativistic system. *Nature*, **426**, 531–533.
- Burgay, M., Joshi, B. C., D'Amico, N., Possenti, A., Lyne, A. G., Manchester, R. N., McLaughlin, M. A., Kramer, M., Camilo, F., and Freire, P. C. C. 2006. The Parkes High-Latitude pulsar survey. *MNRAS*, **368**(May), 283–292.
- Burgay, M., Keith, M. J., Lorimer, D. R., and 11 others. 2013. The Perseus Arm pulsar survey. *MNRAS*, **429**(1), 579–588.
- Burgay, M., Stappers, B., Bailes, M., and 21 others. 2019. The High Time Resolution Universe pulsar survey – XV. Completion of the intermediate-latitude survey with the discovery and timing of 25 further pulsars. *MNRAS*, **484**(4), 5791–5801.
- Cadelano, M., Ransom, S. M., Freire, P. C. C., Ferraro, F. R., Hessels, J. W. T., Lanzoni, B., Pallanca, C., and Stairs, I. H. 2018. Discovery of three new millisecond pulsars in Terzan 5. *ApJ*, **855**(2), 125.
- Cairns, I. H., Johnston, S., and Das, P. 2004. Intrinsic variability and field statistics for pulsars B1641-45 and B0950+08. *MNRAS*, **353**(1), 270–286.
- Cameron, A. D., Champion, D. J., Kramer, M., and 27 others. 2018. The High Time Resolution Universe pulsar survey – XIII. PSR J1757-1854, the most accelerated binary pulsar. *MNRAS*, **475**(1), L57–L61.
- Camilo, F., Thorsett, S. E., and Kulkarni, S. R. 1994. The magnetic fields, ages and original spin periods of millisecond pulsars. *ApJ*, **421**, L15–L18.
- Camilo, F., Nice, D. J., and Taylor, J. H. 1996a. A search for millisecond pulsars at galactic latitudes $-50^\circ < b < -20^\circ$. *ApJ*, **461**, 812–819.
- Camilo, F., Nice, D. J., Shrauner, J. A., and Taylor, J. H. 1996b. Princeton-Arecibo all-sky survey for millisecond pulsars. I. *ApJ*, **469**, 819–827.
- Camilo, F., Lorimer, D. R., Freire, P., Lyne, A. G., and Manchester, R. N. 2000. Observations of 20 millisecond pulsars in 47 Tucanae at 20 cm. *ApJ*, **535**, 975–990.
- Camilo, F., Lorimer, D. R., Bhat, N. D. R., Gotthelf, E. V., Halpern, J. P., Wang, Q. D., Lu, F. J., and Mirabal, N. 2002a. Discovery of a 136 millisecond radio and X-ray pulsar in supernova remnant G54.1+0.3. *ApJ*, **574**, L71–L74.
- Camilo, F., Manchester, R. N., Gaensler, B. M., Lorimer, D. L., and Sarkissian, J. 2002b. PSR J1124-5916: A young and energetic pulsar in supernova remnant G292.0+1.8. *ApJ*, **567**, L71–L75.
- Camilo, F., Stairs, I. H., Lorimer, D. R., Backer, D. C., Ransom, S. M., Klein, B., Wielebinski, R., Kramer, M., McLaughlin, M. A., Arzoumanian, Z., and Müller, P. 2002c. Discovery of radio pulsations from the X-ray pulsar J0205+6449 in supernova remnant 3C 58 with the Green Bank Telescope. *ApJ*, **571**, L41–L44.
- Camilo, F., Ransom, S. M., Gaensler, B. M., Slane, P. O., Lorimer, D. R., Reynolds, J., Manchester, R. N., and Murray, S. S. 2006a. PSR J1833-1034: Discovery of the central young pulsar in the supernova remnant G21.5-0.9. *ApJ*, **637**, 456–465.
- Camilo, F., Ransom, S. M., Halpern, J. P., Reynolds, J., Helfand, D. J., Zimmerman, N., and Sarkissian, J. 2006b. Transient pulsed radio emission from a magnetar. *Nature*, **442**, 892–895.

- Camilo, F., Reynolds, J., Johnston, S., Halpern, J. P., and Ransom, S. M. 2008. The magnetar 1E 1547.0-5408: Radio spectrum, polarimetry, and timing. *ApJ*, **679**(May), 681–686.
- Camilo, F., Ransom, S. M., Gaensler, B. M., and Lorimer, D. R. 2009a. Discovery of the energetic pulsar J1747-2809 in the supernova remnant G0.9+0.1. *ApJ*, **700**, L34–L38.
- Camilo, F., Ray, P. S., Ransom, S. M., and 24 others. 2009b. Radio detection of LAT PSRs J1741-2054 and J2032+4127: No longer just gamma-ray pulsars. *ApJ*, **705**(Nov.), 1–13.
- Camilo, F., Ransom, S. M., Chatterjee, S., Johnston, S., and Demorest, P. 2012. PSR J1841-0500: A radio pulsar that mostly is not there. *ApJ*, **746**(Feb.), 63.
- Campana, R., Massaro, E., Mineo, T., and Cusumano, G. 2009. The multi-component model of the Crab Pulsar at energies above 25 GeV. *A&A*, **499**, 847–850.
- Caswell, J. L., Murray, J. D., Roger, R. S., Cole, D. J., and Cooke, D. J. 1975. Neutral hydrogen absorption measurements yielding kinematic distances for 42 continuum sources in the Galactic plane. *A&A*, **45**, 239–258.
- Cerutti, B., and Beloborodov, A. M. 2017. Electrodynamics of pulsar magnetospheres. *Space Sci. Rev.*, **207**(1-4), 111–136.
- Chakrabarty, D., and Morgan E. H. 1998. The two-hour orbit of a binary millisecond X-ray pulsar. *Nature*, **394**, 346–348.
- Chakrabarty, D., Morgan, E. H., Munro, M. P., Galloway, D. K., Wijnands, R., van der Klis, M., and Markwardt, C. B. 2003. Nuclear-powered millisecond pulsars and the maximum spin frequency of neutron stars. *Nature*, **424**, 42–44.
- Chakraborty, A., and Bagchi, M. 2020. Understanding the Galactic population of normal pulsars: A leap forward. *arXiv e-prints*, Dec., arXiv:2012.13243.
- Champion, D. J., Lorimer, D. R., McLaughlin, M. A., Cordes, J. M., Arzoumanian, Z., Weisberg, J. M., and Taylor, J. H. 2004. PSR J1829+2456: A relativistic binary pulsar. *MNRAS*, **350**, L61–L65.
- Chandrasekhar, S. 1931. The maximum mass of ideal white dwarfs. *ApJ*, **74**, 81–82.
- Chatterjee, S., and Cordes, J. M. 2002. Bow shocks from neutron stars: Scaling laws and HST observations of the Guitar Nebula. *ApJ*, **575**, 407–418.
- Chatterjee, S., Brisken, W. F., Vlemmings, W. H. T., Goss, W. M., Lazio, T. J. W., Cordes, J. M., Thorsett, S. E., Fomalont, E. B., Lyne, A. G., and Kramer, M. 2009. Precision astrometry with the Very Long Baseline Array: Parallaxes and proper motions for 14 pulsars. *ApJ*, **698**, 250–265.
- Chau, H. F., Cheng, K. S., and Ding, K. Y. 1992. Implications of 3P2 superfluidity in the interior of neutron stars. *ApJ*, **399**, 213.
- Chen, J. L., and Wang, H. G. 2014. Frequency dependence of pulse width for 150 radio normal pulsars. *ApJS*, **215**(1), 11.
- Cheng, A. F., and Ruderman, M. 1979. A theory of subpulse polarization patterns from radio pulsars. *ApJ*, **229**, 348–360.
- Chevalier, R. A. 1977. Was SN 1054 a type II supernova? Pages 53–61 of: Schramm, D. N. (ed), *Supernovae*. Dordrecht: Reidel.
- Chevalier, R. A. 1992. Early expansion and luminosity evolution of supernovae. *ApJ*, **394**, 599–602.
- Chiang, J., and Romani, R. W. 1994. An outer gap model of high-energy emission from rotation-powered pulsars. *ApJ*, **436**, 754–761.
- Chiu, H. Y., and Salpeter, E. E. 1964. Surface X-ray emission from neutron stars. *Phys. Rev. Lett.*, **12**, 413.
- Chung, C. T. Y., and Melatos, A. 2011. Stokes tomography of radio pulsar magnetospheres – I. Linear polarization. *MNRAS*, **411**, 2471–2529.

- Cieślar, M., Bulik, T., and Osłowski, S. 2018. Markov chain Monte Carlo population synthesis of single radio pulsars in the Galaxy. *arXiv e-prints*, Mar., arXiv:1803.02397.
- Clark, C. J., Wu, J., Pletsch, H. J., and Guillemot, L. 2018. The Einstein@Home Survey for Gamma-ray Pulsars. Pages 21–24 of: Weltevrede, P., Perera, B. B. P., Preston, L. L., and Sanidas, S. (eds), *Pulsar Astrophysics the Next Fifty Years*, vol. 337.
- Clark, D. H., and Caswell, J. L. 1976. A study of Galactic supernova remnants, based on Molonglo–Parkes observational data. *MNRAS*, **174**, 267–305.
- Clark, D. H., and Stephenson, F. R. 1977. Do all Galactic supernovae produce long-lived remnants? *MNRAS*, **179**, 87P–92P.
- Clemence, G. M., and Szebehely, V. 1967. Annual variation of an atomic clock. *AJ*, **72**, 1324–1326.
- Clifton, T. R., and Lyne, A. G. 1986. High-radio-frequency survey for young and millisecond pulsars. *Nature*, **320**, 43–45.
- Clifton, T. R., Lyne, A. G., Jones, A. W., McKenna, J., and Ashworth, M. 1992. A high frequency survey of the Galactic plane for young and distant pulsars. *MNRAS*, **254**, 177–184.
- Cocke, W. J., Disney, M. J., and Taylor, D. J. 1969. Discovery of optical signals from pulsar NP 0532. *Nature*, **221**, 525–527.
- Cognard, I., Bourgois, G., Lestrade, J.-F., Biraud, F., Aubry, D., Darchy, B., and Drouhin, J.-P. 1996. High-precision timing observations of the millisecond pulsar PSR 1821–24 at Nancay. *A&A*, **311**, 179–188.
- Cognard, I., Freire, P. C. C., Guillemot, L., and 10 others. 2017. A massive-born neutron star with a massive white dwarf companion. *ApJ*, **844**(2), 128.
- Cohen, M. H., Gunderman, E. J., Handebeck, H. E., and Sharp, L. E. 1967. Interplanetary scintillations. II. Observations. *ApJ*, **147**, 449–466.
- Cole, T. W. 1970. Pulsar subpulses and the emission process. *Nature*, **227**, 788–791.
- Coles, W. A., Rickett, B. J., Gao, J. J., Hobbs, G., and Verbiest, J. P. W. 2010. Scattering of pulsar radio emission by the interstellar plasma. *ApJ*, **717**, 1206–1221.
- Comella, J. M., Craft, H. D., Lovelace, R. V. E., Sutton, J. M., and Tyler, G. L. 1969. Crab Nebula pulsar NP 0532. *Nature*, **221**, 453–454.
- Cordes, J. M. 1986. Space velocities of radio pulsars from interstellar scintillations. *ApJ*, **311**, 183–196.
- Cordes, J. M. 2002. *Pulsar Observations I. – Propagation Effects, Searching Distance Estimates, Scintillations and VLBI*. Astronomical Society of the Pacific Conference Series, vol. 278. Pages 227–250.
- Cordes, J. M., and Chatterjee, S. 2019. Fast radio bursts: An extragalactic enigma. *Ann. Rev. Astr. Ap.*, **57**(Aug.), 417–465.
- Cordes, J. M., and Chernoff, D. F. 1997. Neutron star population dynamics. I. Millisecond pulsars. *ApJ*, **482**, 971–992.
- Cordes, J. M., and Lazio, T. J. W. 2002. NE2001. I. A new model for the Galactic distribution of free electrons and its fluctuations. preprint (arXiv:astro-ph/0207156).
- Cordes, J. M. 2004. NE2001: A new model for the Galactic electron density and its fluctuations. *ASP Conf. Ser.*, **317**, 211.
- Cordes, J. M., and Lazio, T. J. W. 2003. NE2001. II. Using radio propagation data to construct a model for the Galactic distribution of free electrons. preprint (arXiv:astro-ph/0301598).
- Cordes, J. M., and McLaughlin, M. A. 2003. Searches for fast radio transients. *ApJ*, **596**, 1142–1154.
- Cordes, J. M., Romani, R. W., and Lundgren, S. C. 1993. The Guitar Nebula: A bow-shock from a slow-spin, high-velocity neutron star. *Nature*, **362**, 133–135.

- Cordes, J. M., Freire, P. C. C., Lorimer, D. R., and 21 others. 2006a. Arecibo pulsar survey using ALFA. I. Survey strategy and first discoveries. *ApJ*, **637**, 446–455.
- Cordes, J. M., Rickett, B. J., Stinebring, D. R., and Coles, W. A. 2006b. Theory of parabolic arcs in interstellar scintillation spectra. *ApJ*, **637**, 346–365.
- Cordes, J. M., Shannon, R. M., and Stinebring, D. R. 2016. Frequency-dependent dispersion measures and implications for pulsar timing. *ApJ*, **817**(1), 16.
- Crossley, J. H., Eilek, J. A., Hankins, T. H., and Kern, J. S. 2010. Short-lived radio bursts from the Crab Pulsar. *ApJ*, **722**, 1908–1920.
- Crusius-Waetzl, A. R., and Lesch, H. 2002 (Jan.). Emission mechanisms in high energy pulsars: From gamma rays to infrared. Page 162 of: Becker, W., Lesch, H., and Trümper, J. (eds), *Neutron Stars, Pulsars, and Supernova Remnants*.
- Dai, S., Hobbs, G., Manchester, R. N., and 23 others. 2015. A study of multifrequency polarization pulse profiles of millisecond pulsars. *MNRAS*, **449**(3), 3223–3262.
- Damashek, M., Taylor, J. H., and Hulse, R. A. 1978. Parameters of 17 newly discovered pulsars in the northern sky. *ApJ*, **225**, L31.
- Damashek, M., Backus, P. R., Taylor, J. H., and Burkhardt, R. K. 1982. Northern hemisphere pulsar survey: A third radio pulsar in a binary system. *ApJ*, **253**, L57–L60.
- D’Amico, N., Lyne, A. G., Manchester, R. N., Possenti, A., and Camilo, F. 2001. Discovery of short-period binary millisecond pulsars in four globular clusters. *ApJ*, **548**, L171–L174.
- Damour, T., and Esposito-Farèse, G. 1998. Gravitational-wave versus binary-pulsar tests of strong-field gravity. *Phys. Rev. D*, **58**, 1–12.
- Damour, T., and Esposito-Farèse, G. 1992. Testing local Lorentz invariance of gravity with binary pulsar data. *Phys. Rev. D*, **46**, 4128–4132.
- Damour, T., and Taylor, J. H. 1991. On the orbital period change of the binary pulsar PSR 1913+16. *ApJ*, **366**, 501–511.
- Damour, T., and Taylor, J. H. 1992. Strong-field tests of relativistic gravity and binary pulsars. *Phys. Rev. D*, **45**, 1840–1868.
- Davies, J. G., Horton, P. W., Lyne, A. G., Rickett, B. J., and Smith, F. G. 1968. Pulsating radio source at $\alpha = 19^{\text{h}}19^{\text{m}}$, $\delta = +22^{\circ}$. *Nature*, **217**, 910–913.
- Davies, J. G., Lyne, A. G., and Seiradakis, J. H. 1973. Thirteen new pulsars. *Nature Phys. Sci.*, **244**, 84–85.
- De, K., Gupta, Y., and Sharma, P. 2016. Detection of polarized quasi-periodic microstructure emission in millisecond pulsars. *ApJ*, **833**(1), L10.
- de Jager, G., Lyne, A. G., Pointon, L., and Ponsonby, J. E. B. 1968. Measurement of the distance of pulsar CP 0328. *Nature*, **220**, 128–129.
- de Plaa, J., Kuiper, L., and Hermsen, W. 2003. Hard X-ray timing and spectral properties of PSR B0540-69. *A&A*, **400**(Mar.), 1013–1019.
- de Vaucouleurs, G., and Corwin, H. G. 1985. S. Andromedae 1885: A centennial review. *ApJ*, **295**, 287–304.
- Degenaar, N., and Suleimanov, V. F. 2018 (Jan.). Testing the equation of state with electromagnetic observations. Page 185 of: Rezzolla, L., Pizzochero, P., Jones, D. I., Rea, N., and Vidaña, I. (eds), *Astrophysics and Space Science Library*. Astrophysics and Space Science Library, vol. 457.
- Deller, A. T., Tingay, S. J., Bailes, M., and Reynolds, J. E. 2009. Precision southern hemisphere VLBI pulsar astrometry. II. Measurement of seven parallaxes. *ApJ*, **701**, 1243–1257.
- Deller, A. T., Weisberg, J. M., Nice, D. J., and Chatterjee, S. 2018. A VLBI distance and transverse velocity for PSR B1913+16. *ApJ*, **862**(2), 139.

- Deller, A. T., Goss, W. M., Brisken, W. F., and 8 others. 2019. Microarcsecond VLBI pulsar astrometry with PSR π II. Parallax distances for 57 pulsars. *ApJ*, **875**(2), 100.
- Demorest, P. B., Pennucci, T., Ransom, S. M., Roberts, M. S. E., and Hessels, J. W. T. 2010. A two-solar-mass neutron star measured using Shapiro delay. *Nature*, **467**(7319), 1081–1083.
- Deneva, J. S., Cordes, J. M., and Lazio, T. J. W. 2009. Discovery of three pulsars from a Galactic Center pulsar population. *ApJ*, **702**, L177–L181.
- Deneva, J. S., Stovall, K., McLaughlin, M. A., Bates, S. D., Freire, P. C. C., Martinez, J. G., Jenet, F., and Bagchi, M. 2013. Goals, strategies and first discoveries of AO327, the Arecibo all-sky 327 MHz drift pulsar survey. *ApJ*, **775**(1), 51.
- Deshpande, A. A., and Rankin, J. M. 1999. Pulsar magnetospheric emission mapping: Images and implications of polar CAP weather. *ApJ*, **524**, 1008–1013.
- Desvignes, G., Kramer, M., Lee, K., van Leeuwen, J., Stairs, I., Jessner, A., Cognard, I., Kasian, L., Lyne, A., and Stappers, B. W. 2019. Radio emission from a pulsar's magnetic pole revealed by general relativity. *Science*, **365**(6457), 1013–1017.
- Detweiler, S. 1979. Pulsar timing measurements and the search for gravitational waves. *ApJ*, **234**, 1100.
- Dewey, R. J., Taylor, J. H., Weisberg, J. M., and Stokes, G. H. 1985. A search for low-luminosity pulsars. *ApJ*, **294**, L25–L29.
- Dib, R., Kaspi, V. M., and Gavriil, F. P. 2009. Rossi X-ray timing explorer monitoring of the anomalous X-ray pulsar 1E 1048.1 – 5937: Long-term variability and the 2007 march event. *ApJ*, **702**(1), 614–630.
- Diehl, R., Halloin, H., Kretschmer, K., and 12 others. 2006. 26Al in the inner Galaxy. Large-scale spectral characteristics derived with SPI/INTEGRAL. *A&A*, **449**, 1025–1031.
- Dodson, R. G., McCulloch, P. M., and Lewis, D. R. 2002. High time resolution observations of the January 2000 glitch in the Vela Pulsar. *ApJ*, **564**, L85–L88.
- Dombrovsky, V. A. 1954. On the nature of the radiation from the Crab Nebula. *Dokl. Akad. Nauk. USSR*, **94**, 1021.
- Driessen, L. N., Janssen, G. H., Bassa, C. G., Stappers, B. W., and Stinebring, D. R. 2019. Scattering features and variability of the Crab Pulsar. *MNRAS*, **483**(1), 1224–1232.
- Dubner, G., and Giacani, E. 2015. Radio emission from supernova remnants. *Astron. Astrophys. Rev.*, **23**(Sept.), 3.
- Duffet-Smith, P. J., and Readhead, A. C. S. 1976. The angular broadening of radio sources by scattering in the interstellar medium. *MNRAS*, **174**, 7–17.
- Duncan, J. C. 1939. Second report on the expansion of the Crab Nebula. *ApJ*, **89**, 482.
- Duncan, R. C., and Thompson, C. 1992. Formation of very strongly magnetized neutron stars: Implications for gamma-ray bursts. *ApJ*, **392**, L9–L13.
- Durdin, J. M., Large, M. I., Little, A. G., Manchester, R. N., Lyne, A. G., and Taylor, J. H. 1979. An unusual pulsar – PSR 0826–34. *MNRAS*, **186**, 39P–41P.
- Duyvendak, J. J. L. 1942. Further data bearing on the identification of the Crab Nebula with the supernova of A.D. 1054, Part I: The ancient Oriental chronicles. *PASP*, **54**, 91–94.
- Dyks, J., and Harding, A. K. 2004. Rotational sweepback of magnetic field lines in geometric models of pulsar radio emission. *ApJ*, **614**(Oct.), 869–880.
- Dyks, J., and Rudak, B. 2003. Two-pole caustic model for high-energy light curves of pulsars. *ApJ*, **598**, 1201–1206.
- Dyks, J., Rudak, B., and Harding, A. K. 2004. On the methods of determining the radio emission geometry in pulsar magnetospheres. *ApJ*, **607**, 939–948.
- Eatough, R. P., Keane, E. F., and Lyne, A. G. 2009. An interference removal technique for radio pulsar searches. *MNRAS*, **395**(1), 410–415.

- Eatough, R. P., Falcke, H., Karuppusamy, R., and 20 others. 2013. A strong magnetic field around the supermassive black hole at the centre of the Galaxy. *Nature*, **501**(7467), 391–394.
- Edwards, R. T., and Stappers, B. W. 2002. Drifting sub-pulse analysis using the two-dimensional Fourier transform. *A&A*, **393**(Oct.), 733–748.
- Edwards, R. T., Bailes, M., van Straten, W., and Britton, M. C. 2001. The Swinburne intermediate-latitude pulsar survey. *MNRAS*, **326**(Sept.), 358–374.
- Edwards, R. T., Hobbs, G. B., and Manchester, R. N. 2006. TEMPO2, a new pulsar timing package – II. The timing model and precision estimates. *MNRAS*, **372**, 1549–1574.
- Eilek, J. A., Arendt, P. N., Jr., Hankins, T. H., and Weatherall, J. C. 2002. The radio-loud plasma in pulsars. *Proceedings of the 270 WE-Heraeus seminar on neutron stars, pulsars, and supernova remnants*, MPE Report 278, 249.
- Esamdin, A., Lyne, A. G., Kramer, M., Graham-Smith, F., and Manchester, R. N. 2004 (Jan.). Thirteen drift bands in PSR B0826-34. Page 341 of: Camilo, F., and Gaensler, B. M. (eds), *Young Neutron Stars and Their Environments*. IAU Symposium, vol. 218.
- Espinoza, C. M., Lyne, A. G., Kramer, M., Manchester, R. N., and Kaspi, V. M. 2011. The braking index of PSR J1734–333 and the magnetar population. *ApJ*, **741**, 13.
- Espinoza, C. M., Lyne, A. G., and Stappers, B. W. 2017. New long-term braking index measurements for glitching pulsars using a glitch-template method. *MNRAS*, **466**(1), 147–162.
- Esposito-Farèse, G. 1999. Binary-pulsar tests of strong-field gravity. *Pulsar Timing, General Relativity and the Internal Structure of Neutron Stars*, 13.
- Evans, W. D., Klebesadel, R. W., Laros, J. G., and 11 others. 1980. Location of the gamma-ray transient event of 1979 March 5. *ApJ*, **237**, L7–L9.
- Faber, J. A., and Rasio, F. A. 2002. Post-Newtonian SPH calculations of binary neutron star coalescence. III. Irrotational systems and gravitational wave spectra. *Phys. Rev. D*, **65**(8), 084042.
- Fahlman, G. G., and Gregory, P. C. 1981. An X-ray pulsar in SNR G109.1–1.0. *Nature*, **293**, 202–204.
- Fantin, N. J., Côté, P., Hanes, D. A., Gwyn, S. D. J., Bianchi, L., Ferrarese, L., Cuillandre, J.-C., McConnachie, A., and Starkenburg, E. 2017. The next generation Virgo Cluster survey. XXVIII. Characterization of the Galactic white dwarf population. *ApJ*, **843**(1), 53.
- Faucher-Giguère, C.-A., and Kaspi, V. M. 2006. Birth and evolution of isolated radio pulsars. *ApJ*, **643**, 332–355.
- Faulkner, A. J., Kramer, M., Lyne, A. G., Manchester, R. N., McLaughlin, M. A., Stairs, I. H., Hobbs, G., Possenti, A., Lorimer, D. R., D’Amico, N., Camilo, F., and Burgay, M. 2005. PSR J1756–2251: A new relativistic double neutron star system. *ApJ*, **618**, L119–L122.
- Ferdman, R. D., Stairs, I. H., Kramer, M., and 14 others. 2010. A precise mass measurement of the intermediate-mass binary pulsar PSR J1802 – 2124. *ApJ*, **711**(2), 764–771.
- Ferdman, R. D., Archibald, R. F., Gourgouliatos, K. N., and Kaspi, V. M. 2018. The glitches and rotational history of the highly energetic young pulsar PSR J0537-6910. *ApJ*, **852**(2), 123.
- Fichtel, C. E., Hartman, R. C., Kniffen, D. A., Thompson, D. J., Bignami, G. F., Ögelman, H., Özel, M. E., and Tümer, T. 1975. High-energy gamma-ray results from the Second Small Astronomy Satellite. *ApJ*, **198**, 163–182.
- Filippenko, A. V. 1997. Optical spectra of supernovae. *Ann. Rev. Astr. Ap.*, **35**, 309–355.
- Filippenko, A. V., and Radhakrishnan, V. 1982. Pulsar nulling and drifting subpulse phase memory. *ApJ*, **263**, 828–834.

- Finger, M. H., Koh, D. T., Nelson, R. W., Prince, T. A., Vaughan, B. A., and Wilson, R. B. 1996. Discovery of hard X-ray pulsations from the transient source GRO J1744-28. *Nature*, **381**, 291–293.
- Fishman, G. J., Harnden, F. R., and Haymes, R. C. 1969. Observation of pulsed hard X-radiation from NP 0532 from 1967 data. *ApJ*, **156**, L107–L110.
- Flanagan, C. S. 1990. Rapid recovery of the Vela Pulsar from a giant glitch. *Nature*, **345**, 416–417.
- Fomalont, E. B., Goss, W. M., Lyne, A. G., and Manchester, R. N. 1984. Astrometry of 59 pulsars: A comparison of interferometric and timing positions. *MNRAS*, **210**, 113–130.
- Fomalont, E. B., Goss, W. M., Lyne, A. G., Manchester, R. N., and Justtanont, K. 1992. Positions and proper motions of pulsars. *MNRAS*, **258**, 497–510.
- Fonseca, E., Stairs, I. H., and Thorsett, S. E. 2014. A comprehensive study of relativistic gravity using PSR B1534+12. *ApJ*, **787**(1), 82.
- Fontaine, G., Brassard, P., and Bergeron, P. 2001. The potential of white dwarf cosmochronology. *PASP*, **113**(782), 409–435.
- Foster, R. S., and Backer, D. C. 1990. Constructing a pulsar timing array. *ApJ*, **361**, 300.
- Foster, R. S., Cadwell, B. J., Wolszczan, A., and Anderson, S. B. 1995. A high Galactic latitude pulsar survey of the Arecibo sky. *ApJ*, **454**, 826–830.
- Frail, D. A., and Kulkarni, S. R. 1991. Unusual interaction of the high-velocity pulsar PSR 1757–24 with the supernova remnant G5.4–1.2. *Nature*, **352**, 785–787.
- Frail, D. A., and Weisberg, J. M. 1990. A critical evaluation of pulsar distance measurements. *AJ*, **100**, 743–757.
- Frail, D. A., Goss, W. M., and Whiteoak, J. B. Z. 1994. The radio lifetime of supernova remnants and the distribution of pulsar velocities at birth. *ApJ*, **437**, 781–793.
- Freire, P., Ransom, S., Begin, S., and Stairs, I. 2008. Eight new millisecond pulsars in NGC 6440 and NGC 6441. *ApJ*, **675**, 670–682.
- Freire, P. C., Kramer, M., Lyne, A. G., Camilo, F., Manchester, R. N., and D’Amico, N. 2001a. Detection of ionized gas in the globular cluster 47 Tucanae. *ApJ*, **557**, L105–L108.
- Freire, P. C., Kramer, M., and Lyne, A. G. 2001b. Determination of the orbital parameters of binary pulsars. *MNRAS*, **322**, 885–890.
- Freire, P. C., Camilo, F., Lorimer, D. R., Lyne, A. G., Manchester, R. N., and D’Amico, N. 2001c. Timing the millisecond pulsars in 47 Tucanae. *MNRAS*, **326**(Sept.), 901–915.
- Freire, P. C., Camilo, F., Kramer, M., Lorimer, D. R., Lyne, A. G., Manchester, R. N., and D’Amico, N. 2003. Further results from the timing of the millisecond pulsars in 47 Tucanae. *MNRAS*, **340**, 1359–1374.
- Freire, P. C. C., and Wex, N. 2010. The orthometric parametrization of the Shapiro delay and an improved test of general relativity with binary pulsars. *MNRAS*, **409**, 199–212.
- Fritz, G., Henry, R. C., Meekins, J. F., Chubb, T. A., and Friedmann, H. 1969. X-ray pulsar in the Crab Nebula. *Science*, **164**, 709–712.
- Fruchter, A. S., Stinebring, D. R., and Taylor, J. H. 1988a. A millisecond pulsar in an eclipsing binary. *Nature*, **333**, 237–239.
- Fruchter, A. S., Gunn, J. E., Lauer, T. R., and Dressler, A. 1988b. Optical detection and characterization of the eclipsing pulsar’s companion. *Nature*, **334**, 686–689.
- Fuentes, J. R., Espinoza, C. M., Reisenegger, A., Shaw, B., Stappers, B. W., and Lyne, A. G. 2017. The glitch activity of neutron stars. *A&A*, **608**, A131.
- Gaensler, B. M., and Slane, P. O. 2006. The evolution and structure of pulsar wind nebulae. *Ann. Rev. Astr. Ap.*, **44**(1), 17–47.

- Gaensler, B. M., and Wallace, B. J. 2003. A multi-frequency radio study of supernova remnant G292.0+1.8 and its pulsar wind nebula. *ApJ*, **594**, 326–339.
- Gaensler, B. M., Slane, P. O., Gotthelf, E. V., and Vasisht, G. 2001. Anomalous X-Ray pulsars and soft gamma-ray repeaters in supernova remnants. *ApJ*, **559**, 963–972.
- Gaensler, B. M., Arons, J., Kaspi, V. M., Pivovaroff, M. J., Kawai, N., and Tamura, K. 2002a. High-resolution X-ray imaging of pulsar B1509–58 and its environment. *ApJ*, **569**, 878–893.
- Gaensler, B. M., Jones, D. H., and Stappers, B. W. 2002b. An optical bow shock around the nearby millisecond pulsar J2124–3358. *ApJ*, **580**, L137–L141.
- Gaensler, B. M., Madsen, G. J., Chatterjee, S., and Mao, S. A. 2008. The vertical structure of warm ionised gas in the Milky Way. *PASA*, **25**, 184–200.
- Galloway, D. K., and Keek, L. 2017. Thermonuclear X-ray bursts. *arXiv e-prints*, Dec., arXiv:1712.06227.
- Galt, J. A., and Lyne, A. G. 1972. The interstellar scintillation pattern of PSR 0329+54. *MNRAS*, **158**, 281–290.
- Gandolfi, S., Lippuner, J., Steiner, A. W., Tews, I., Du, X., and Al-Mamun, M. 2019. From the microscopic to the macroscopic world: From nucleons to neutron stars. *J. Phys. G Nucl. Phys.*, **46**(10), 103001.
- Gardner, F. F., Morris, D., and Whiteoak, J. B. 1969. The linear polarization of radio sources between 11 and 20 cm wavelength. II Influence of the Galaxy on source depolarization and Faraday rotation. *Aust. J. Phys.*, **22**, 813–819.
- Gavril, F. P., Kaspi, V. M., and Woods, P. M. 2002. Magnetar-like X-ray bursts from an anomalous X-ray pulsar. *Nature*, **419**, 142–144.
- Gavril, F. P., Gonzalez, M. E., Gotthelf, E. V., Kaspi, V. M., Livingstone, M. A., and Woods, P. M. 2008. Magnetar-like emission from the young pulsar in Kes 75. *Science*, **319**, 1802–1805.
- Gedalin, M., Gruman, E., and Melrose, D. B. 2002. New mechanism of pulsar radio emission. *Phys. Rev. Lett.*, **88**, 121101.
- Gehrels, N., and Chen, W. 1993. The Geminga supernova as a possible cause of the local interstellar bubble. *Nature*, **361**, 706–707.
- Gelfand, J. D., Gaensler, B. M., Slane, P. O., Patnaude, D. J., Hughes, J. P., and Camilo, F. 2007. The radio emission, X-ray emission, and hydrodynamics of G328.4+0.2: A comprehensive analysis of a luminous pulsar wind nebula, its neutron star, and the progenitor supernova explosion. *ApJ*, **663**, 468–486.
- Geppert, U., Page, D., and Zannias, T. 1999. Submergence and re-diffusion of the neutron star magnetic field after the supernova. *A&A*, **345**, 847–854.
- Geyer, M., Karastergiou, A., Kondratiev, V. I., and 8 others. 2017. Scattering analysis of LOFAR pulsar observations. *MNRAS*, **470**(3), 2659–2679.
- Giacconi, R. 1974. Page 27 of: *Proc. 16th Int. Conf. on Physics*. Editions de l’Université de Bruxelles.
- Giacconi, R., Gursky, H., Paolini, F. R., and Rossi, B. 1962. Evidence for X-rays from sources outside the solar system. *Phys. Rev. Lett.*, **9**, 439–443.
- Gil, J. A., and Han, J. L. 1996. Geometry of pulsar emission and pulse width distribution. *ApJ*, **458**, 265.
- Gil, J. A., and Kijak, K. 1993. Period dependence of radio emission altitudes in the pulsar magnetosphere. *A&A*, **273**, 563–569.
- Gil, J. A., Kijak, J., and Seiradakis, J. H. 1993. On the Two-dimensional structure of pulsar beams. *A&A*, **272**, 268.
- Glendenning, N. K. 2000. *Compact Stars: Nuclear Physics, Particle Physics, and General Relativity*. New York: Springer.

- Gold, T. 1968. Rotating neutron stars as the origin of the pulsating radio sources. *Nature*, **218**, 731–732.
- Gold, T. 1969. Rotating neutron stars and the nature of pulsars. *Nature*, **221**, 25–27.
- Goldreich, P., and Julian, W. H. 1969. Pulsar electrodynamics. *ApJ*, **157**, 869–880.
- Golenetskii, S. V., Ilyinskii, V. N., and Mazets, E. P. 1984. Recurrent bursts in GBS 0526–66, the source of the 5 March 1979 gamma-ray burst. *Nature*, **307**, 41–43.
- Gómez, G. C., Benjamin, R. A., and Cox, D. P. 2001. A reexamination of the distribution of Galactic free electrons. *AJ*, **122**, 908–920.
- Gonthier, P. L., Ouellette, M. S., Berrier, J., O'Brien, S., and Harding, A. K. 2002. Galactic populations of radio and gamma-ray pulsars in the polar cap model. *ApJ*, **565**, 482–499.
- Gotthelf, E. V., Vasisht, G., Boylan-Kolchin, M., and Torii, K. 2000. A 700 year-old pulsar in the supernova remnant Kesteven 75. *ApJ*, **542**(Oct.), L37–L40.
- Gould, D. M., and Lyne, A. G. 1998. Multifrequency polarimetry of 300 radio pulsars. *MNRAS*, **301**, 235–260.
- Graham, D. A., Mebold, U., Hesse, K. H., Hills, D. L., and Wielebinski, R. 1974. HI absorbtion of nine pulsars. *A&A*, **37**, 405–410.
- Graham-Smith, F., Dolan, J. F., Boyd, P. T., Biggs, J. D., Lyne, A. G., and Percival, J. 1996. The ultraviolet polarization of the Crab Pulsar. *MNRAS*, **282**, 1354–1358.
- Grenier, I. A., and Harding, A. K. 2015. Gamma-ray pulsars: A gold mine. *Comptes Rendus Physique*, **16**(6–7), 641–660.
- Grewing, M., and Warmsley, M. 1971. On the interpretation of the pulsar dispersion measure. *A&A*, **11**, 65–69.
- Grindlay, J., Gursky, H., Schnopper, H., Parsignault, D. R., Heise, J., Brinkman, A. C., and Shriner, J. 1976. Discovery of intense X-ray bursts from the globular cluster NGC 6624. *ApJ*, **205**, L127–L130.
- Gunn, J. E., and Ostriker, J. P. 1970. On the nature of pulsars. III. Analysis of observations. *ApJ*, **160**, 979–1002.
- Gupta, Y., and Gangadhara, R. T. 2003. Understanding the radio emission geometry of multiple-component radio pulsars from retardation and aberration effects. *ApJ*, **584**, 418–426.
- Gupta, Y., Rickett, B. J., and Lyne, A. G. 1994. Refractive interstellar scintillation in pulsar dynamic spectra. *MNRAS*, **269**, 1035–1068.
- Haberl, F. 2007. The magnificent seven: Magnetic fields and surface temperature distributions. *ApJS*, **73**.
- Haensel, P., Salgado, M., and Bonazzola, S. 1995. Equation of state of dense matter and maximum rotation frequency of neutron stars. *A&A*, **296**, 745.
- Hall, J. S., and Mikesell, A. H. 1950. Polarization of light in the Galaxy as determined from observations of 557 early-type stars. *Pub. of US Naval Obs Second Ser.*, **17**, 1–62.
- Hamilton, T. T., Helfand, D. J., and Becker, R. H. 1985. A search for millisecond pulsars in globular clusters. *AJ*, **90**, 606–608.
- Han, J. L. 2017. Observing interstellar and intergalactic magnetic fields. *Ann. Rev. Astr. Ap.*, **55**(1), 111–157.
- Han, J. L., and Manchester, R. N. 2001. The shape of pulsar radio beams. *MNRAS*, **320**, L35–L39.
- Han, J. L., Manchester, R. N., and Qiao, G. J. 1999. Pulsar rotation measures and the magnetic structure of our Galaxy. *MNRAS*, **306**, 371–380.
- Han, J. L., Demorest, P. B., van Straten, W., and Lyne, A. G. 2009. Polarization observations of 100 pulsars at 774 MHz by the Green Bank Telescope. *ApJS*, **181**, 557–571.

- Han, J. L., Manchester, R. N., van Straten, W., and Demorest, P. 2018. Pulsar rotation measures and large-scale magnetic field reversals in the galactic disk. *ApJS*, **234**(1), 11.
- Hankins, T. H. 1971. Microsecond intensity variation in the radio emission from CP 0950. *ApJ*, **169**, 487–494.
- Hankins, T. H., and Cordes, J. M. 1981. Interpulse emission from pulsar 0950+08: How many poles? *ApJ*, **249**, 241–253.
- Hankins, T. H., and Eilek, J. A. 2007. Radio emission signatures in the Crab Pulsar. *ApJ*, **670**(1), 693–701.
- Hankins, T. H., and Rickett, B. J. 1975. Pulsar signal processing. Pages 55–129 of: *Methods in Computational Physics Volume 14 – Radio Astronomy*. New York: Academic Press.
- Hankins, T. H., Eilek, J. A., and Jones, G. 2016. The Crab Pulsar at centimeter wavelengths. II. Single pulses. *ApJ*, **833**(1), 47.
- Harding, A. K., Contopoulos, I., and Kazanas, D. 1999. Magnetar spin-down. *ApJ*, **525**, L125–L128.
- Harding, A. K., Stern, J. V., Dyks, J., and Frackowiak, M. 2008. High-altitude emission from pulsar slot gaps: The Crab Pulsar. *ApJ*, **680**, 1378–1393.
- Harding, A. K., Kalapotharakos, C., Barnard, M., and Venter, C. 2018. Multi-TeV emission from the Vela Pulsar. *ApJ*, **869**(1), L18.
- Harrison, E. R., and Tademaru, E. 1975. Acceleration of pulsars by asymmetric radiation. *ApJ*, **201**, 447–461.
- Harrison, P. A., and Lyne, A. G. 1993. Pulsar velocities and the scale height of scattering in the Galaxy. *MNRAS*, **265**, 778–780.
- Harrison, P. A., Lyne, A. G., and Anderson, B. 1993. New determinations of the proper motions of 44 pulsars. *MNRAS*, **261**, 113–124.
- Hartman, J. W., Bhattacharya, D., Wijers, R., and Verbunt, F. 1997. A study of the evolution of radio pulsars through improved population synthesis. *A&A*, **322**, 477–488.
- Hartnett, J. G., and Luiten, A. 2010. Comparison of astrophysical and terrestrial frequency standards. *arXiv:1004.0115*.
- Hartnett, J. G., and Luiten, A. N. 2011. Colloquium: Comparison of astrophysical and terrestrial frequency standards. *Rev. Mod. Phys.*, **83**(1), 1–9.
- Haskell, B., and Melatos, A. 2015. Models of pulsar glitches. *Int. J Modern Phys. D*, **24**(3), 1530008.
- Hayakawa, S., and Matsouka, M. 1964. Origin of Cosmic X-rays. *Prog. Theor. Phys. Suppl.*, **30**, 204.
- Heinke, C. O., and Ho, W. C. G. 2010. Direct observation of the cooling of the Cassiopeia A neutron star. *ApJ*, **719**, L167–L171.
- Helfand, D. J., Fowler, L. A., and Kuhlman, J. V. 1977a. Pulsar flux observations: Long-term intensity and spectral variations. *AJ*, **82**, 701–705.
- Helfand, D. J., Taylor, J. H., and Manchester, R. N. 1977b. Pulsar proper motions. *ApJ*, **213**, L1–L4.
- Helfand, D. J., Gotthelf, E. V., and Halpern, J. P. 2001. The Vela Pulsar and its synchrotron nebula: Aftermath of a glitch. *ApJ*, **556**(July), 380–391.
- Hellings, R. W. 1986. Relativistic effects in astronomical timing measurements. *AJ*, **91**, 650.
- Hellings, R. W., and Downs, G. S. 1983. Upper limits on the isotropic gravitational radiation background from pulsar timing analysis. *ApJ*, **265**, L39.
- Hessels, J. W. T., Ransom, S. M., Stairs, I. H., Freire, P. C. C., Kaspi, V. M., and Camilo, F. 2006. A radio pulsar spinning at 716 Hz. *Science*, **311**(Mar.), 1901–1904.
- Hessels, J. W. T., Ransom, S. M., Stairs, I. H., Kaspi, V. M., and Freire, P. C. C. 2007. A 1.4-GHz Arecibo survey for pulsars in globular clusters. *ApJ*, **670**, 363–378.

- Hessels, J. W. T., Nice, D. J., Gaensler, B. M., and 21 others. 2008a. PSR J1856+0245: Arecibo discovery of a young, energetic pulsar coincident with the TeV gamma-ray source HESS J1857+026. *ApJ*, **682**, L41–L44.
- Hessels, J. W. T., Ransom, S. M., Kaspi, V. M., Roberts, M. S. E., Champion, D. J., and Stappers, B. W. 2008b (Feb.). The GBT350 survey of the northern Galactic plane for radio pulsars and transients. Pages 613–615 of: Bassa, C., Wang, Z., Cumming, A., and Kaspi, V. M. (eds), *40 Years of Pulsars: Millisecond Pulsars, Magnetars and More*. American Institute of Physics Conference Series, vol. 983.
- Hessels, J. W. T., Spitler, L. G., Seymour, A. D., and 23 others. 2019. FRB 121102 bursts show complex time-frequency structure. *ApJ*, **876**(2), L23.
- Hewish, A. 1980. Frequency–time structure of pulsar scintillation. *MNRAS*, **192**, 799–804.
- Hewish, A., Bell, S. J., Pilkington, J. D. H., Scott, P. F., and Collins, R. A. 1968. Observation of a rapidly pulsating radio source. *Nature*, **217**, 709–713.
- Hibscher, J. A., and Arons, J. 2001. Polarization sweeps in rotation-powered pulsars. *ApJ*, **546**, 382–393.
- Hill, A. S., Stinebring, D. R., Barnor, H. A., Berwick, D. E., and Webber, A. B. 2003. Pulsar scintillation arcs. I. Frequency dependence. *ApJ*, **599**, 457–464.
- Hillebrandt, W., and Niemeyer, J. C. 2000. Type IA supernova explosion models. *Ann. Rev. Astr. Ap.*, **38**, 191–230.
- Hiltner, W. A. 1949. Polarization of stellar radiation III. The polarisation of 841 stars. *ApJ*, **114**, 241–271.
- Ho, P.-Y. 1962. Ancient and mediaeval observations of comets and novae in Chinese sources. *Vistas Astron.*, **5**, 127–225.
- Ho, W. C. G., Ng, C. Y., Lyne, A. G., Stappers, B. W., Coe, M. J., Halpern, J. P., Johnson, T. J., and Steele, I. A. 2017. Multiwavelength monitoring and X-ray brightening of Be X-ray binary PSR J2032+4127/MT91 213 on its approach to periastron. *MNRAS*, **464**(1), 1211–1219.
- Hobbs, G., Lyne, A. G., and Kramer, M. 2003. Jodrell Bank timing astrometry. Pages 215–218 of: Bailes, M., Nice, D. J., and Thorsett, S. E. (eds), *Radio Pulsars*. San Francisco: Astronomical Society of the Pacific.
- Hobbs, G., Lyne, A. G., Kramer, M., Martin, C. E., and Jordan, C. 2004. Long-term timing observations of 374 pulsars. *MNRAS*, **353**, 1311–1344.
- Hobbs, G., Lorimer, D. R., Lyne, A. G., and Kramer, M. 2005. A statistical study of 233 pulsar proper motions. *MNRAS*, **360**, 974–992.
- Hobbs, G., Lyne, A. G., and Kramer, M. 2010. An analysis of the timing irregularities for 366 pulsars. *MNRAS*, **402**, 1027–1048.
- Hobbs, G., Archibald, A., Arzoumanian, Z., and 55 others. 2010. The International Pulsar Timing Array project: Using pulsars as a gravitational wave detector. *Classical and Quantum Gravity*, **27**, 084013.
- Hobbs, G., Guo, L., Caballero, R. N., and 57 others. 2020. A pulsar-based time-scale from the International Pulsar Timing Array. *MNRAS*, **491**(4), 5951–5965.
- Hoyle, F., Narlikar, J., and Wheeler, J. A. 1964. Electromagnetic waves from very dense stars. *Nature*, **203**, 914–916.
- Hui, C. Y., and Becker, W. 2008. Resolving the bow-shock nebula around the old pulsar PSR B1929+10 with multi-epoch Chandra observations. *A&A*, **486**, 485–491.
- Hulse, R. A., and Taylor, J. H. 1974. A high sensitivity pulsar survey. *ApJ*, **191**, L59–L61.
- Hurley, K. 2000. The 4.5 +/- 0.5 soft gamma repeaters in review. Page 515 of: McConnell, M. L., and Ryan, J. M. (eds), *The Fifth Compton Symposium; AIP Conference Proceedings No. 510*. New York: AIP Press.

- Hurley, K., Cline, T., Mazets, E., and 11 others. 1999. A giant periodic flare from the soft gamma-ray repeater SGR1900+14. *Nature*, **397**, 41–43.
- Hurley-Walker, N., Gaensler, B. M., Leahy, D. A., and 18 others. 2019a. Candidate radio supernova remnants observed by the GLEAM survey. *PASA*, **36**(Nov.), e048.
- Hurley-Walker, N., Filipović, M. D., Gaensler, B. M., and 18 others. 2019b. New candidate radio supernova remnants detected in the GLEAM survey. *PASA*, **36**(Jan.), e045.
- Ibrahim, A. I., Safi-Harb, S., Swank, J. H., Parke, W., Zane, S., and Turolla, R. 2002. Discovery of cyclotron resonance features in the soft gamma repeater SGR 1806-20. *ApJ*, **574**, L51–L55.
- Ibrahim, A. I., Swank, J. H., and Parke, W. 2003. New evidence of proton-cyclotron resonance in a magnetar strength field from SGR 1806-20. *ApJ*, **584**, L17–L21.
- Ibrahim, A. I., Markwardt, C. B., Swank, J. H., and 10 others. 2004. Discovery of a transient magnetar: XTE J1810-197. *ApJ*, **609**, L21–L24.
- Ilie, C. D., Weltevrede, P., Johnston, S., and Chen, T. 2020. The drifting sub-pulses of PSR B0031-07 and its synchronously modulated radio polarization. *MNRAS*, **491**(3), 3385–3394.
- Ilovaisky, S. A., and Lequeux, J. 1972. A study of galactic supernova remnants I. Distances, radio luminosity function and galactic distribution. *A&A*, **18**, 169–185.
- Israel, G., Covino, S., Mignani, R., and 9 others. 2005. Discovery and monitoring of the likely IR counterpart of SGR 1806-20 during the 2004 gamma-ray burst-active state. *A&A*, **438**, L1–L4.
- Jackson, M. S., Halpern, J. P., Gotthelf, E. V., and Mattox, J. R. 2002. A high-energy study of the Geminga Pulsar. *ApJ*, **578**(2), 935–942.
- Jacoby, B. A., Bailes, M., van Kerkwijk, M. H., Ord, S., Hotan, A., Kulkarni, S. R., and Anderson, S. B. 2003. PSR J1909-3744: A binary millisecond pulsar with a very small duty cycle. *ApJ*, **599**(2), L99–L102.
- Jacoby, B. A., Cameron, P. B., Jenet, F. A., Anderson, S. B., Murty, R. N., and Kulkarni, S. R. 2006. Measurement of orbital decay in the double neutron star binary PSR B2127+11C. *ApJ*, **644**, L113–L116.
- Jacoby, B. A., Bailes, M., Ord, S. M., Edwards, R. T., and Kulkarni, S. R. 2009. A large-area survey for radio pulsars at high Galactic latitudes. *ApJ*, **699**(2), 2009–2016.
- Jaffe, T. R., Leahy, J. P., Banday, A. J., Leach, S. M., Lowe, S. R., and Wilkinson, A. 2010. Modelling the Galactic magnetic field on the plane in two dimensions. *MNRAS*, **401**, 1013–1028.
- Jahan-Miri, M. 2010. Rotational coupling of the pinned core superfluid. *ApJ*, **725**, 29–35.
- Janka, Hans-Thomas. 2012. Explosion mechanisms of core-collapse supernovae. *Annual Review of Nuclear and Particle Science*, **62**(1), 407–451.
- Janssen, G. H., and van Leeuwen, J. 2004. Intermittent nulls in PSR B0818–13, and the subpulse-drift alias mode. *A&A*, **425**(Oct.), 255–261.
- Janssen, G. H., Stappers, B. W., Kramer, M., Purver, M., Jessner, A., and Cognard, I. 2008a. European Pulsar Timing Array. *40 Years of Pulsars: Millisecond Pulsars, Magnetars and More. AIP Conference Proceedings, Volume 983*, 633–635.
- Janssen, G. H., Stappers, B. W., Kramer, M., Nice, D. J., Jessner, A., Cognard, I., and Purver, M. B. 2008b. Multi-telescope timing of PSR J1518+4904. *A&A*, **490**, 753–761.
- Jansson, R., and Farrar, G. R. 2012. The Galactic magnetic field. *ApJ*, **761**(1), L11.
- Jauncey, D., Bignall, H., Kedziora-Chudczer, L., Koay, J., Lovell, J., Macquart, J.-P., Ojha, R., Pursimo, T., Reynolds, C., and Rickett, B. 2016. Interstellar scintillation and scattering of micro-arc-second AGN. *Galaxies*, **4**(4), 62.
- Jensen, H. J. 1998. *Self-organised Critical Systems*. Cambridge University Press.

- Jennings, R. J., Kaplan, D. L., Chatterjee, S., Cordes, J. M., and Deller, A. T. 2018. Binary pulsar distances and velocities from Gaia Data Release 2. *ApJ*, **864**(1), 26–34.
- Jha, S. W., Maguire, K., and Sullivan, M. 2019. Observational properties of thermonuclear supernovae. *Nat. Astron.*, **3**(Aug.), 706–716.
- Johnston, H. M., and Kulkarni, S. R. 1991. On the detectability of pulsars in close binary systems. *ApJ*, **368**, 504–514.
- Johnston, S., and Karastergiou, A. 2019. The period-width relationship for radio pulsars revisited. *MNRAS*, **485**(1), 640–647.
- Johnston, S., Lyne, A. G., Manchester, R. N., Kniffen, D. A., D’Amico, N., Lim, J., and Ashworth, M. 1992. A high frequency survey of the southern Galactic plane for pulsars. *MNRAS*, **255**, 401–411.
- Johnston, S., Koribalski, B. S., Weisberg, J., and Wilson, W. 1996. HI line measurements of pulsars towards the Gum Nebula and Carina Arm. *MNRAS*, **279**, 661–668.
- Johnston, S., Koribalski, B., Weisberg, J. M., and Wilson, W. 2001. HI line measurements of pulsars towards the Galactic Center and the electron density in the inner Galaxy. *MNRAS*, **322**, 715–722.
- Johnston, S., Kramer, M., Lorimer, D. R., Lyne, A. G., McLaughlin, M., Klein, B., and Manchester, R. N. 2006. Discovery of two pulsars towards the Galactic centre. *MNRAS*, Oct., L96+.
- Johnston, S., Smith, D. A., Karastergiou, A., and Kramer, M. 2020. The Galactic population and properties of young, highly energetic pulsars. *MNRAS*, **497**(2), 1957–1965.
- Jones, D. I., and Anderson, N. 2001. Freely precessing neutron stars: Model and observations. *MNRAS*, **324**, 811–824.
- Jones, P. B. 2002. Post-glitch relaxation in pulsars. *MNRAS*, **335**, 733–740.
- Joss, P. C., and Rappaport, S. A. 1984. Neutron stars in interacting binary systems. *Ann. Rev. Astr. Ap.*, **22**, 537–592.
- Kalapotharakos, C., Brambilla, G., Timokhin, A., Harding, A., and Kazanas, D. 2018. Three-dimensional kinetic pulsar magnetosphere models: Connecting to gamma-ray observations. *ApJ*, **857**(1), 44.
- Kaplan, D. L., Escoffier, R. P., Lacasse, R. J., O’Neil, K., Ford, J. M., Ransom, S. M., Anderson, S. B., Cordes, J. M., Lazio, T. J. W., and Kulkarni, S. R. 2005. The Green Bank Telescope pulsar spigot. *PASP*, **117**(June), 643–653.
- Kaplan, G. H. 2005. The IAU resolutions on astronomical reference systems, time scales, and earth rotation models: Explanation and implementation. *U.S. Naval Observatory Circular*, **179**.
- Karuppusamy, R., Stappers, B. W., and van Straten, W. 2010. Giant pulses from the Crab Pulsar. A wide-band study. *A&A*, **515**(June), A36.
- Kaspi, V. M. 1995. Millisecond pulsar timing: Recent advances. Pages 345–356 of: Fruchter, A. S., Tavani, M., and Backer, D. C. (eds), *Millisecond Pulsars – A Decade of Surprise*, vol. 72. Astronomical Society of the Pacific.
- Kaspi, V. M., and Beloborodov, A. M. 2017. Magnetars. *Ann. Rev. Astr. Ap.*, **55**(1), 261–301.
- Kaspi, V. M., and Helfand, D. J. 2002. Constraining the birth events of neutron stars. *ASP Conf. Ser.*, **271**, 3.
- Kaspi, V. M., Lackey, J. R., Mattox, J., Manchester, R. N., Bailes, M., and Pace, R. 2000. High-energy gamma-ray observations of two young, energetic radio pulsars. *ApJ*, **528**, 445–453.

- Katgert, P., and Oort, J. H. 1967. On the frequency of supernova outbursts in galaxies. *Bull. Astr. Inst. Netherlands*, **19**, 239–245.
- Keane, E. F., and Kramer, M. 2008. On the birthrates of Galactic neutron stars. *MNRAS*, **391**, 2009–2016.
- Keane, E. F., Ludovici, D. A., Eatough, R. P., Kramer, M., Lyne, A. G., McLaughlin, M. A., and Stappers, B. W. 2010. Further searches for rotating radio transients in the Parkes Multi-beam pulsar survey. *MNRAS*, **401**, 1057–1068.
- Keith, M. J., Kramer, M., Lyne, A. G., Eatough, R. P., Stairs, I. H., Possenti, A., Camilo, F., and Manchester, R. N. 2009. PSR J1753-2240: A mildly recycled pulsar in an eccentric binary system. *MNRAS*, **393**(2), 623–627.
- Keith, M. J., Jameson, A., van Straten, W., and 14 others. 2010. The High Time Resolution Universe pulsar survey – I. System configuration and initial discoveries. *MNRAS*, **409**, 619–627.
- Keith, M. J., Coles, W., Shannon, R. M., and 16 others. 2013. Measurement and correction of variations in interstellar dispersion in high-precision pulsar timing. *MNRAS*, **429**(3), 2161–2174.
- Kemp, J. C. 1970. Circular polarization of thermal radiation in a magnetic field. *ApJ*, **162**(Oct.), 169.
- Kerr, F. J. 1969. The large scale distribution of hydrogen in the Galaxy. *Ann. Rev. Astr. Ap.*, **7**, 39–66.
- Kerr, M., Hobbs, G., Johnston, S., and Shannon, R. M. 2016. Periodic modulation in pulse arrival times from young pulsars: a renewed case for neutron star precession. *MNRAS*, **455**(2), 1845–1854.
- Kiel, P. D., and Hurley, J. R. 2009. Populating the Galaxy with pulsars – II. Galactic dynamics. *MNRAS*, **395**, 2326–2346.
- Kijak, J., and Gil, J. 1997. Radio emission altitudes in pulsar magnetospheres. *MNRAS*, **288**, 631–637.
- Klose, S., Henden, A. A., Geppert, U., Greiner, J., Guetter, H. H., Hartmann, D. H., Kouveliotou, C., Luginbuhl, C. B., Stecklum, B., and Vrba, F. J. 2004. A near-infrared survey of the N49 region around the soft gamma repeater SGR 0526-66. *ApJ*, **609**, L13–L16.
- Koester, D. 2002. White dwarfs: Recent developments. *Astron. Astrophys. Rev.*, **11**(1), 33–66.
- Kolonko, M., Gil, J., and Maciesiak, K. 2004. On the pulse-width statistics in radio pulsars. *A&A*, **428**(Dec.), 943–951.
- Komesaroff, M. M. 1970. Possible mechanism for the pulsar radio emission. *Nature*, **225**, 612–614.
- Komesaroff, M. M., Morris, D., and Cooke, D. J. 1970. Linear polarization and pulse shape measurements of nine pulsars. *Astrophys. Lett.*, **5**, 37–41.
- Komissarov, S., and Lyubarsky, Y. 2004. MHD simulations of Crab's jet and torus. *Ap&SS*, **293**, 107–113.
- Konacki, M., and Wolszczan, A. 2003. Masses and orbital inclinations of planets in the PSR B1257+12 system. *ApJ*, **591**, L147–L150.
- Kondratiev, V. I., Verbiest, J. P. W., Hessels, J. W. T., and 29 others. 2016. A LOFAR census of millisecond pulsars. *A&A*, **585**(Jan.), A128.
- Kopeikin, S. M. 1995. On possible implications of orbital parallaxes of wide orbit binary pulsars and their measurability. *ApJ*, **439**, L5–L8.
- Koribalski, B. S., Johnston, S., Weisberg, J., and Wilson, W. 1995. HI line measurements of eight southern pulsars. *ApJ*, **441**, 756.

- Kostyuk, S. V., Kondratiev, V. I., Kuzmin, A. D., Popov, M. V., and Soglasnov, V. A. 2003. Peculiarities of giant pulses from the Crab Pulsar at frequencies of 594 and 2228 MHz. *Astronomy Letters*, **29**(June), 387–393.
- Kosugi, G., Ogasawara, R., and Terada, H. 2005. A variable infrared counterpart to the soft gamma-ray repeater SGR 1806–20. *ApJ*, **623**, L125–L128.
- Kouveliotou, C., Dieters, S., Strohmayer, T., van Paradijs, J., Fishman, G. J., Meegan, C. A., Hurley, K., Kommers, J., Smith, I., Frail, D., and Murakami, T. 1998. An X-ray pulsar with a superstrong magnetic field in the soft γ -ray repeater SGR 1806–20. *Nature*, **393**, 235–237.
- Kouveliotou, C., Strohmayer, T., Hurley, K., Van Paradijs, J., Finger, M. H., Dieters, S., Woods, P., Thompson, C., and Duncan, R. C. 1999. Discovery of a magnetar associated with the soft gamma repeater SGR 1900+14. *ApJ*, **510**, L115–L118.
- Kramer, M. 1998. Determination of the geometry of the PSR B1913+16 system by geodetic precession. *ApJ*, **509**, 856–860.
- Kramer, M., and Stairs, I. H. 2008. The double pulsar. *Ann. Rev. Astr. Ap.*, **46**, 541–572.
- Kramer, M., Lange, C., Lorimer, D. R., Backer, D. C., Xilouris, K. M., Jessner, A., and Wielebinski, R. 1999. The characteristics of millisecond pulsar emission: III. From low to high frequencies. *ApJ*, **526**, 957–975.
- Kramer, M., Johnston, S., and van Straten, W. 2002. High-resolution single-pulse studies of the Vela Pulsar. *MNRAS*, **334**, 523–532.
- Kramer, M., Lyne, A. G., O'Brien, J. T., Jordan, C. A., and Lorimer, D. R. 2006a. A periodically active pulsar giving insight into magnetospheric physics. *Science*, **312**, 549–551.
- Kramer, M., Stairs, I. H., Manchester, R. N., and 12 others. 2006b. Tests of general relativity from timing the Double Pulsar. *Science*, **314**, 97–102.
- Krishnakumar, M. A., Maan, Yogesh, Joshi, B. C., and Manoharan, P. K. 2019. Multi-frequency scatter-broadening evolution of pulsars. II. Scatter-broadening of nearby pulsars. *ApJ*, **878**(2), 130.
- Krishnamohan, S., and Downs, G. S. 1983. Intensity dependence of the pulse profile and polarization of the Vela pulsar. *ApJ*, **265**, 372.
- Kronberg, P. P., and Newton-McGee, K. J. 2009. Remarkable symmetries in the Milky Way disk's magnetic field. *arXiv:0909.4753*.
- Kuiper, L., and Hermsen, W. 2009. High-energy characteristics of the schizophrenic pulsar PSR J1846-0258 in Kes 75. Multi-year RXTE and INTEGRAL observations crossing the magnetar-like outburst. *A&A*, **501**(3), 1031–1046.
- Kulkarni, S. R. 1986. Optical identification of binary pulsars: Implications for magnetic field decay in neutron stars. *ApJ*, **306**, L85–L89.
- Kumar, H. S., and Safi-Harb, S. 2008. Variability of the high magnetic field X-ray pulsar PSR J1846-0258 associated with the supernova remnant Kes 75 as revealed by the Chandra X-ray observatory. *ApJ*, **678**, L43–L46.
- Kuzmin, A. 2001. Scattering of the low frequency pulsar radiation. *Astrophys. Space Sci.*, **278**, 53–56.
- Kuzmin, A. D., Hamilton, P. A., Shitov, Y. P., McCulloch, P. M., McConnell, D., and Pugatchev, V. D. 2003. High temporal resolution observations of the pulsar microstructure at 102 MHz. *MNRAS*, **344**, 1187–1192.
- Lai, D. 2001. Matter in strong magnetic fields. *Rev. Modern Phys.*, **73**(July), 629.
- Lam, M. T., Cordes, J. M., Chatterjee, S., and 22 others. 2017. The NANOGrav nine-year data set: Excess noise in millisecond pulsar arrival times. *ApJ*, **834**(1), 35.
- Lampland, C. O. 1921. Observed changes in the structure of the Crab Nebula (NGC 1952). *PASP*, **33**, 79–84.
- Lang, K. R. 1971. Interstellar scintillation of pulsar radiation. *ApJ*, **164**, 249–264.

- Lange, C., Camilo, F., Wex, N., Kramer, M., Backer, D. C., Lyne, A. G., and Doroshenko, O. 2001. Precision timing measurements of PSR J1012+5307. *MNRAS*, **326**, 274–282.
- Large, M. I., and Vaughan, A. E. 1971. A search of the Galactic plane for high dispersion pulsars. *MNRAS*, **151**, 277–287.
- Large, M. I., Vaughan, A. E., and Wielebinski, R. 1968a. Pulsar searches at the Molonglo radio observatory. *Nature*, **220**, 753–756.
- Large, M. I., Vaughan, A. E., and Mills, B. Y. 1968b. A pulsar supernova association. *Nature*, **220**, 340–341.
- Laros, J. G., Fenimore, E. E., Klebesadel, R. W., and 14 others. 1987. A new type of repetitive behavior in a high-energy transient. *ApJ*, **320**, L111–L115.
- Lattimer, J. M., and Prakash, M. 2001. Neutron star structure and the equation of state. *ApJ*, **550**, 426–442.
- Lattimer, J. M. 2012. The nuclear equation of state and neutron star masses. *ARNPS*, **62**(1), 485–515.
- Lazaridis, K., Wex, N., Jessner, A., and 10 others. 2009. Generic tests of the existence of the gravitational dipole radiation and the variation of the gravitational constant. *MNRAS*, **400**, 805–814.
- Lazio, T. J. W., and Cordes, J. M. 1998. Hyperstrong radio-wave scattering in the Galactic center. II. A likelihood analysis of free electrons in the Galactic Center. *ApJ*, **505**, 715–731.
- Lazio, T. J. W., Bhaskaran, S., Cutler, C., Folkner, W. M., Park, R. S., Ellis, J. A., Ely, T., Taylor, S. R., and Vallisneri, M. 2018 (Aug.). Solar system ephemerides, pulsar timing, gravitational waves, & navigation. Pages 150–153 of: Weltevrede, P., Perera, B. B. P., Preston, L. L., and Sanidas, S. (eds), *Pulsar Astrophysics the Next Fifty Years*, vol. 337.
- Lee, L. C. 1976. Strong scintillations in astrophysics. *ApJ*, **206**, 744–752.
- Lee, L. C., and Jokipii, J. R. 1976. The irregularity spectrum in interstellar space. *ApJ*, **206**, 735–743.
- Lentati, L., Shannon, R. M., Coles, W. A., and 80 others. 2016. From spin noise to systematics: Stochastic processes in the first International Pulsar Timing Array data release. *MNRAS*, **458**(2), 2161–2187.
- Lesch, H., Jessner, A., Kramer, M., and Kunzl, T. 1998. On the possibility of curvature radiation from radio pulsars. *A&A*, **332**, L21–L24.
- Levin, L., Bailes, M., Bates, S., and 12 others. 2010. A radio-loud magnetar in X-ray quiescence. *ApJ*, **721**, L33–L37.
- Lewandowski, W., Rożko, K., Kijak, J., Bhattacharyya, B., and Roy, J. 2015. The study of multi-frequency scattering of 10 radio pulsars. *MNRAS*, **454**(3), 2517–2528.
- Lewin, W. H. G., and Joss, P. C. 1981. X-ray bursters and the X-ray sources of the galactic bulge. *Space Sci. Rev.*, **28**, 3–87.
- Lewin, W. H. G., and van Paradijs, J. 1986. Quasi-periodic oscillations, the ‘latest’ in X-ray astronomy. *Comm. Astrophys.*, **11**, 127–134.
- Lewin, W. H. G., Doty, J., Clark, G. W., and 11 others. 1976. The discovery of a rapidly repetitive X-ray burst from a new source in Scorpius. *ApJ*, **207**, L95–L99.
- Li, J., Torres, D. F., Lin, T. T., Grondin, M.-H., Kerr, M., Lemoine-Goumard, M., and de Oña Wilhelmi, E. 2018. Observing and modeling the gamma-ray emission from pulsar/pulsar wind nebula complex PSR J0205+6449/3C 58. *ApJ*, **858**(2), 84.
- Li, X. H., and Han, J. L. 2003. The effect of scattering on pulsar polarization angle. *A&A*, **410**, 253–256.
- Linares, M.. 2019. Super-massive neutron stars and compact binary millisecond pulsars. *arXiv e-prints*, Oct., arXiv:1910.09572.

- Link, B. 2006. Incompatibility of long-period neutron star precession with creeping neutron vortices. *A&A*, **458**, 881–884.
- Link, B., and Epstein, R. I. 2001. Precession interpretation of the isolated pulsar PSR 1828–11. *ApJ*, **556**, 392–398.
- Link, B., Epstein, R. I., and Baym, G. 1992. Postglitch behaviour of the Crab Pulsar: Evidence for external torque variations. *ApJ*, **390**, L21–L22.
- Liu, K., Young, A., Wharton, R., and 20 others. 2019. Detection of pulses from the Vela pulsar at millimeter wavelengths with Phased ALMA. *ApJ*, **885**(1), L10.
- Liu, Q. Z., van Paradijs, J., and van den Heuvel, E. P. J. 2005. High-mass X-ray binaries in the Magellanic Clouds. *A&A*, **442**, 1135–1138.
- Liu, Q. Z., van Paradijs, J., and van den Heuvel, E. P. J. 2006. Catalogue of high-mass X-ray binaries in the Galaxy (4th edition). *A&A*, **455**, 1165–1168.
- Liu, Q. Z., van Paradijs, J., and van den Heuvel, E. P. J. 2007. A catalogue of low-mass X-ray binaries in the Galaxy, LMC, and SMC (Fourth edition). *A&A*, **469**, 807–810.
- Livingstone, M. A., Kaspi, V. M., Gavriil, F. P., Manchester, R. N., Gotthelf, E. V. G., and Kuiper, L. 2007. New phase-coherent measurements of pulsar braking indices. *Astrophys. Space Sci.*, **308**(Apr.), 317–323.
- Livingstone, M. A., Kaspi, V. M., and Gavriil, F. P. 2010. Timing behavior of the magnetically active rotation-powered pulsar in the supernova remnant Kesteven 75. *ApJ*, **710**(2), 1710–1717.
- Lockhart, W., Gralla, S. E., Özel, F., and Psaltis, D. 2019. X-ray light curves from realistic polar cap models: Inclined pulsar magnetospheres and multipole fields. *MNRAS*, **490**(2), 1774–1783.
- Löhmer, O., Kramer, M., Driebe, T., Jessner, A., Mitra, D., and Lyne, A. G. 2004a. The parallax, mass and age of the PSR J2145–0750 binary system. *A&A*, **426**, 631–640.
- Löhmer, O., Mitra, D., Gupta, Y., Kramer, M., and Ahuja, A. 2004b. The frequency evolution of interstellar pulse broadening from radio pulsars. *A&A*, **425**, 569–575.
- Löhmer, O., Jessner, A., Kramer, M., Wielebinski, R., and Maron, O. 2008. Observations of pulsars at 9 millimetres. *A&A*, **480**, 623–628.
- Lorimer, D. R. 2008. Binary and millisecond pulsars. *Living Rev. Rel.*, **11**.
- Lorimer, D. R. 2010. The Galactic pulsar population. *Highlights of Astronomy*, **15**(Nov.), 807–807.
- Lorimer, D. R. 2013. The galactic millisecond pulsar population. Pages 237–242 of: van Leeuwen, Joeri (ed), *Neutron Stars and Pulsars: Challenges and Opportunities after 80 Years*, vol. 291.
- Lorimer, D. R., Bailes, M., Dewey, R. J., and Harrison, P. A. 1993. Pulsar statistics: The birthrate and initial spin periods of radio pulsars. *MNRAS*, **263**, 403–415.
- Lorimer, D. R., Festin, L., Lyne, A. G., and Nicastro, L. 1995. Birth rate of millisecond pulsars. *Nature*, **376**, 393.
- Lorimer, D. R., Bailes, M., and Harrison, P. A. 1997. Pulsar statistics IV: Pulsar velocities. *MNRAS*, **289**, 592–604.
- Lorimer, D. R., Lyne, A. G., and Camilo, F. 1998. A search for pulsars in supernova remnants. *A&A*, **331**, 1002–1010.
- Lorimer, D. R., McLaughlin, M. A., Arzoumanian, Z., Xilouris, K. M., Cordes, J. M., Lommen, A. N., Fruchter, A. S., Chandler, A. M., and Backer, D. C. 2004. PSR J0609+2130: A disrupted binary pulsar? *MNRAS*, **347**, L21–L25.
- Lorimer, D. R., Stairs, I. H., Freire, P. C., and 33 others. 2006a. Arecibo pulsar survey using ALFA. II. The young, highly relativistic binary pulsar J1906+0746. *ApJ*, **640**, 428–434.

- Lorimer, D. R., Faulkner, A. J., Lyne, A. G., and 11 others. 2006b. The Parkes Multibeam pulsar survey – VI. Discovery and timing of 142 pulsars and a Galactic population analysis. *MNRAS*, **372**, 777–800.
- Lorimer, D. R., Bailes, M., McLaughlin, M. A., Narkevic, D. J., and Crawford, F. 2007. A bright millisecond radio burst of extragalactic origin. *Science*, **318**, 777.
- Lu, F. J., Wang, Q. D., Aschenbach, B., Durouchoux, P., and Song, L. M. 2002. Chandra observation of supernova remnant G54.1+0.3: A close cousin of the Crab Nebula. *ApJ*, **568**, L49–L52.
- Luken, K. J., Filipović, M. D., and 18 others. 2020. Radio observations of supernova remnant G1.9+0.3. *MNRAS*, **492**(2), 2606–2621.
- Lundgren, S. C., Cordes, J. M., Ulmer, M., Matz, S. M., Lomatch, S., Foster, R. S., and Hankins, T. 1995. Giant pulses from the Crab Pulsar: A joint radio and gamma-ray study. *ApJ*, **453**(Nov.), 433.
- Lundmark, K. 1921. Suspected new stars recorded in old chronicles and among recent meridian observations. *PASP*, **33**, 225–238.
- Lynch, R. S. 2018 (Aug.). The Green Bank North Celestial Cap pulsar survey: Status and future. Pages 13–16 of: Weltevrede, P., Perera, B. B. P., Preston, L. L., and Sanidas, S. (eds), *Pulsar Astrophysics the Next Fifty Years*, vol. 337.
- Lynch, R. S., Ransom, S. M., Freire, P. C. C., and Stairs, I. H. 2011. Six new recycled globular cluster pulsars discovered with the Green Bank Telescope. *arXiv:1101.1467*.
- Lynch, R. S., Swiggum, J. K., Kondratiev, V. I., and 37 others. 2018. The Green Bank North Celestial Cap pulsar survey. III. 45 new pulsar timing solutions. *ApJ*, **859**(2), 93.
- Lynden-Bell, D. 1969. Galactic nuclei as collapsed old quasars. *Nature*, **223**(5207), 690–694.
- Lyne, A. G. 1971. The comparative properties of the pulsars. Pages 182–194 of: Davies, R. D., and Smith, F. G. (eds), *IAU Symp. 46*. Reidel.
- Lyne, A. G. 1984. Orbital inclination and mass of the binary pulsar PSR 0655+64. *Nature*, **310**, 300–302.
- Lyne, A. G. 1987. A massive glitch in an old pulsar. *Nature*, **326**, 569–571.
- Lyne, A. G., and Ashworth, M. 1983. The effect of nulls upon subpulse drift in PSRs 0809+74 and 0818–13. *MNRAS*, **204**, 519–536.
- Lyne, A. G., and Lorimer, D. R. 1994. High birth velocities of radio pulsars. *Nature*, **369**, 127–129.
- Lyne, A. G., and Manchester, R. N. 1988. The shape of pulsar radio beams. *MNRAS*, **234**, 477–508.
- Lyne, A. G., and Rickett, B. J. 1968. Measurements of the pulse shape and spectra of the pulsating radio sources. *Nature*, **218**, 326–330.
- Lyne, A. G., and Smith, F. G. 1968. Linear polarization in pulsating radio sources. *Nature*, **218**, 124–126.
- Lyne, A. G., and Smith, F. G. 1982. Interstellar scintillation and pulsar velocities. *Nature*, **298**, 825–827.
- Lyne, A. G., and Thorne, D. J. 1975. Anomalous scattering in the Crab Nebula. *MNRAS*, **172**, 97–108.
- Lyne, A. G., Smith, F. G., and Graham, D. A. 1971. Characteristics of the radio pulses from the pulsars. *MNRAS*, **153**, 337–382.
- Lyne, A. G., Anderson, B., and Salter, M. J. 1982. The proper motions of 26 pulsars. *MNRAS*, **201**, 503–520.
- Lyne, A. G., Manchester, R. N., and Taylor, J. H. 1985. The Galactic population of pulsars. *MNRAS*, **213**, 613–639.

- Lyne, A. G., Brinklow, A., Middleditch, J., Kulkarni, S. R., Backer, D. C., and Clifton, T. R. 1987. The discovery of a millisecond pulsar in the globular cluster M28. *Nature*, **328**, 399–401.
- Lyne, A. G., Pritchard, R. S., and Smith, F. G. 1988a. Crab Pulsar timing 1982–1987. *MNRAS*, **233**, 667–676.
- Lyne, A. G., Biggs, J. D., Brinklow, A., Ashworth, M., and McKenna, J. 1988b. Discovery of a binary millisecond pulsar in the globular cluster M4. *Nature*, **332**, 45–47.
- Lyne, A. G., Manchester, R. N., D’Amico, N., Staveley-Smith, L., Johnston, S., Lim, J., Fruchter, A. S., Goss, W. M., and Frail, D. 1990. An eclipsing millisecond pulsar in the globular cluster Terzan 5. *Nature*, **347**, 650–652.
- Lyne, A. G., Pritchard, R. S., and Smith, F. G. 1993. 23 years of Crab Pulsar rotational history. *MNRAS*, **265**, 1003–1012.
- Lyne, A. G., Pritchard, R. S., Graham-Smith, F., and Camilo, F. 1996. Very low braking index for the Vela Pulsar. *Nature*, **381**, 497–498.
- Lyne, A. G., Manchester, R. N., Lorimer, D. R., Bailes, M., D’Amico, N., Tauris, T. M., Johnston, S., Bell, J. F., and Nicastro, L. 1998. The Parkes Southern pulsar survey – II. Final results and population analysis. *MNRAS*, **295**, 743–755.
- Lyne, A. G., Camilo, F., Manchester, R. N., and 8 others. 2000. The Parkes Multibeam pulsar survey: PSR J1811–1736 – A pulsar in a highly eccentric binary system. *MNRAS*, **312**, 698–702.
- Lyne, A. G., Pritchard, R. S., and Graham-Smith, F. 2001. Pulsar reflections in the Crab Nebula. *MNRAS*, **321**, 67–70.
- Lyne, A. G., Burgay, M., Kramer, M., and 9 others. 2004. A double-pulsar system: A rare laboratory for relativistic gravity and plasma physics. *Science*, **303**, 1153–1157.
- Lyne, A. G., Hobbs, G., Kramer, M., Stairs, I., and Stappers, B. 2010. Switched magnetospheric regulation of pulsar spin-down. *Science*, **329**, 408.
- Lyne, A. G., Jordan, C. A., Graham-Smith, F., Espinoza, C. M., Stappers, B. W., and Weltevrede, P. 2015. 45 years of rotation of the Crab Pulsar. *MNRAS*, **446**(Jan.), 857–864.
- Lyne, A. G., Stappers, B. W., Freire, P. C. C., and 31 others. 2017. Two long-term intermittent pulsars discovered in the PALFA survey. *ApJ*, **834**(1), 72.
- Lyne, A., Levin, L., Stappers, B., Mickaliger, M., Desvignes, G., and Kramer, M. 2018. Intense radio flare from the magnetar XTE J1810-197. *The Astronomer’s Telegram*, **12284**(Dec.), 1.
- Ma, C., Arias, E. F., Bianco, G., and 30 others. 2009. The second realization of the international celestial reference frame by very long baseline interferometry. *IERS Technical Note*, **35**(Jan.), 1.
- Maciesiak, K., Gil, J., and Ribeiro, V. A. R. M. 2011. On the pulse-width statistics in radio pulsars – I. Importance of the interpulse emission. *MNRAS*, **414**(2), 1314–1328.
- Macquart, J. P., Prochaska, J. X., McQuinn, M., and 13 others. 2020. A census of baryons in the Universe from localized fast radio bursts. *Nature*, **581**(7809), 391–395.
- Malov, I. F., and Timirkeeva, M. A. 2019. On X-ray emission of radio pulsars. *MNRAS*, **485**(4), 5319–5328.
- Manchester, R. N., and Lyne, A. G. 1977. Pulsar interpulses – Two poles or one? *MNRAS*, **181**, 761–767.
- Manchester, R. N., and Peterson, B. A. 1996. A search for optical pulsations in SN 1987A. *ApJ*, **456**, L107–L109.
- Manchester, R. N., and Taylor, J. H. 1981. Observed and derived parameters for 330 pulsars. *AJ*, **86**, 1953–1973.

- Manchester, R. N., Taylor, J. H., and Van, Y.-Y. 1974. Detection of pulsar proper motion. *ApJ*, **189**, L119–L122.
- Manchester, R. N., Taylor, J. H., and Huguenin, G. R. 1975. Observations of pulsar radio emission II. Polarisation of individual radio pulses. *ApJ*, **196**, 83–102.
- Manchester, R. N., Lyne, A. G., Taylor, J. H., Durdin, J. M., Large, M. I., and Little, A. G. 1978. The second Molonglo pulsar survey – Discovery of 155 pulsars. *MNRAS*, **185**, 409–421.
- Manchester, R. N., Lyne, A. G., Robinson, C., D’Amico, N., Bailes, M., and Lim, J. 1991. Discovery of ten millisecond pulsars in the globular cluster 47 Tucanae. *Nature*, **352**, 219–221.
- Manchester, R. N., Lyne, A. G., D’Amico, N., Bailes, M., Johnston, S., Lorimer, D. R., Harrison, P. A., Nicastro, L., and Bell, J. F. 1996. The Parkes southern pulsar survey I. Observing and data analysis systems and initial results. *MNRAS*, **279**, 1235–1250.
- Manchester, R. N., Lyne, A. G., Camilo, F., and 9 others. 2001. The Parkes multi-beam pulsar survey – I. Observing and data analysis systems, discovery and timing of 100 pulsars. *MNRAS*, **328**, 17–35.
- Manchester, R. N., Bell, J. F., Camilo, F., and 9 others. 2002. Young pulsars from the Parkes multibeam pulsar survey and their associations. *ASP Conf. Ser.*, **271**, 31.
- Manchester, R. N., Fan, G., Lyne, A. G., Kaspi, V. M., and Crawford, F. 2006. Discovery of 14 radio pulsars in a survey of the Magellanic Clouds. *ApJ*, **649**, 235–242.
- Mao, S. A., Gaensler, B. M., Havercorn, M., Zweibel, E. G., Madsen, G. J., McClure-Griffiths, N. M., Shukurov, A., and Kronberg, P. P. 2010. A survey of extragalactic Faraday rotation at high Galactic latitude: The vertical magnetic field of the Milky Way toward the Galactic poles. *ApJ*, **714**, 1170–1186.
- Maoz, D., Mannucci, F., Li, W., Filippenko, A. V., Della Valle, M., and Panagia, N. 2011. Nearby supernova rates from the Lick observatory supernova search – IV. A recovery method for the delay-time distribution. *MNRAS*, **412**(3), 1508–1521.
- Markwardt, C. B., Swank, J. H., Strohmayer, T. E., Zand, J. J., and Marshall, F. E. 2002. Discovery of a second millisecond accreting pulsar: XTE J1751-305. *ApJ*, **575**, L21–L24.
- Marsh, T. R., Gänsicke, B. T., Hümmerich, S., and 23 others. 2016. A radio-pulsing white dwarf binary star. *Nature*, **537**(7620), 374–377.
- Martinez, J. G., Stovall, K., Freire, P. C. C., Deneva, J. S., Jenet, F. A., McLaughlin, M. A., Bagchi, M., Bates, S. D., and Ridolfi, A. 2015. Pulsar J0453+1559: A double neutron star system with a large mass asymmetry. *ApJ*, **812**(2), 143.
- Martinez, J. G., Gentile, P., Freire, P. C. C., Stovall, K., Deneva, J. S., Desvignes, G., Jenet, F. A., McLaughlin, M. A., Bagchi, M., and Devine, T. 2019. The discovery of six recycled pulsars from the Arecibo 327 MHz drift-scan pulsar survey. *ApJ*, **881**(2), 166.
- Matheson, H., and Safi-Harb, S. 2010. The Plerionic supernova remnant G21.5-0.9 powered by PSR J1833-1034: New spectroscopic and imaging results revealed with the Chandra X-ray observatory. *ApJ*, **724**, 572–587.
- Matsakis, D. N., Taylor, J. H., Eubanks, T. M., and Marshall, T. 1997. A statistic for describing pulsar and clock stabilities. *A&A*, **326**, 924–928.
- Mayer-Hasselwander, H. A., Bennett, K., Bignami, G. F., and 13 others. 1982. Large-scale distribution of galactic gamma radiation observed by COS-B. *A&A*, **105**(1), 164–175.
- Maza, J., and van den Berg, S. 1976. Statistics of extragalactic supernovae. *ApJ*, **204**, 519–529.
- Mazets, E. P., Golenetskii, S. V., and Gur’yan, Yu. A. 1979. Soft gamma-ray bursts from the source B1900+14. *Sov. Astron. Lett.*, **5**, 343–344.

- Mazets, E. P., Golenskii, S. V., Aptekar, R. L., Guryan, Y. A., and Ilyinskii, V. N. 1981. Cyclotron and annihilation lines in gamma-ray bursts. *Nature*, **290**, 378–382.
- McCarthy, D. D., and Petit, G. (eds). 2004. *IERS Conventions 2003, IERS Technical Note 32*. Frankfurt am Main: Verlag des Bundesamts für Kartographie und Geodäsie.
- McConnell, D., McCulloch, P. M., Hamilton, P. A., Ables, J. G., Hall, P. J., Jacka, C. E., and Hunt, A. J. 1991. Radio pulsars in the Magellanic Clouds. *MNRAS*, **249**, 654–657.
- McCulloch, P. M., Hamilton, P. A., Royle, G. W. R., and Manchester, R. N. 1983. Daily observations of a large period jump of the Vela Pulsar. *Nature*, **302**, 319–321.
- McKee, J. W., Janssen, G. H., Stappers, B. W., and 17 others. 2016. A glitch in the millisecond pulsar J0613-0200. *MNRAS*, **461**(3), 2809–2817.
- McKee, J. W., Lyne, A. G., Stappers, B. W., Bassa, C. G., and Jordan, C. A. 2018. Temporal variations in scattering and dispersion measure in the Crab Pulsar and their effect on timing precision. *MNRAS*, **479**(3), 4216–4224.
- McKee, J. W., Stappers, B. W., Bassa, C. G., and 13 others. 2019. A detailed study of giant pulses from PSR B1937+21 using the Large European Array for pulsars. *MNRAS*, **483**(4), 4784–4802.
- McKinnon, M. M. 1997. Birefringence as a mechanism for the broadening and depolarization of pulse average profiles. *ApJ*, **475**, 763–769.
- McKinnon, M. M., and Stinebring, D. R. 2000. The mode-separated pulse profiles of pulsar radio emission. *ApJ*, **529**, 435–446.
- McLaughlin, M. A., Lyne, A. G., Lorimer, D. R., and 11 others. 2006. Transient radio bursts from rotating neutron stars. *Nature*, **439**, 817–820.
- Medin, Z., and Lai, D. 2007. Condensed surfaces of magnetic neutron stars, thermal surface emission, and particle acceleration above pulsar polar caps. *MNRAS*, **382**(4), 1833–1852.
- Melatos, A., and Drummond, L. V. 2019. Pulsar glitch activity as a state-dependent poisson process: Parameter estimation and epoch prediction. *ApJ*, **885**(1), 37–52.
- Melatos, A., and Warszawski, L. 2009. Superfluid vortex unpinning as a coherent noise process, and the scale invariance of pulsar glitches. *ApJ*, **700**, 1524–1540.
- Melrose, D. B. 1979. Propagation effects on the polarization of pulsar radio emission. *Aust. J. Phys.*, **32**, 61–70.
- Melrose, D. B., and Gedalin, M. E. 1999. Relativistic plasma emission and pulsar radio emission: A critique. *ApJ*, **521**, 351–361.
- Melrose, D. B., and Stoneham, R. J. 1977. The natural wave modes in a pulsar magnetosphere. *PASA*, **3**, 120.
- Melzer, D. W., and Thorne, K. S. 1966. Normal modes of radial pulsation of stars at the end-point of thermo nuclear evolution. *ApJ*, **145**, 514–543.
- Mestel, L. 2003. *Stellar Magnetism*. Oxford University Press.
- Michilli, D., Hessels, J. W. T., Donner, J. Y., and 17 others. 2018. Low-frequency pulse profile variation in PSR B2217+47: Evidence for echoes from the interstellar medium. *MNRAS*, **476**(2), 2704–2716.
- Mickaliger, M. B., McLaughlin, M. A., Lorimer, D. R., Langston, G. I., Bilous, A. V., Kondratiev, V. I., Lyutikov, M., Ransom, S. M., and Palliyaguru, N. 2012. A giant sample of giant pulses from the Crab Pulsar. *ApJ*, **760**(1), 64.
- Middleditch, J., and Pennypacker, C. 1985. Optical pulsation in the Large Magellanic Cloud remnant 0540–69.3. *Nature*, **313**, 659–661.
- Middleditch, J., Marshall, F. E., Wang, Q. D., Gotthelf, E. V., and Zhang, W. 2006. Predicting the starquakes in PSR J0537–6910. *ApJ*, **652**(Dec.), 1531–1546.
- Mignani, R. P., Paladino, R., Rudak, B., and 8 others. 2017. The first detection of a pulsar with ALMA. *ApJ*, **851**(1), L10.

- Mignani, R. P., Shearer, A., de Luca, A., and 9 others. 2019. The first ultraviolet detection of the Large Magellanic Cloud pulsar PSR B0540-69 and its multi-wavelength properties. *ApJ*, **871**(2), 246.
- Miller, M. C., and Lamb, F. K. 1998. Bounds on the compactness of neutron stars from brightness oscillations during X-ray bursts. *ApJ*, **499**(1), L37–L40.
- Miller, M. C., and Lamb, F. K. 2016. Observational constraints on neutron star masses and radii. *Eur. Phys. J. A*, **52**, 63.
- Minkowski, R. 1964. Supernovae and supernova remnants. *Ann. Rev. Astr. Ap.*, **2**, 247–266.
- Mirabel, I. F., and Rodrigues, I. 2003. The origin of Scorpius X-1. *A&A*, **398**, L25–L28.
- Mitra, D., Wielebinski, R., Kramer, M., and Jessner, A. 2003. The effect of HII regions on rotation measure of pulsars. *A&A*, **398**, 993–1005.
- Mitra, D., Arjunwadkar, M., and Rankin, J. M. 2015. Polarized quasiperiodic structures in pulsar radio emission reflect temporal modulations of non-stationary plasma flow. *ApJ*, **806**(2), 236.
- Moehler, S., and Bono, G. 2008. White dwarfs in globular clusters. *arXiv:0806.4456*.
- Morii, M., Sato, R., Kataoka, J., and Kawai, N. 2003. Chandra observation of the anomalous X-Ray pulsar 1E 1841–045. *PASJ*, **55**, L45–L48.
- Morsink, S. M., Stergioulas, N., and Blattnig, S. R. 1999. Quasi-normal modes of rotating relativistic stars: Neutral modes for realistic equations of state. *ApJ*, **510**, 854–861.
- Mukherjee, S., and Kembhavi, A. 1997. Magnetic field decay in single radio pulsars: A statistical study. *ApJ*, **489**, 928.
- Murakami, T., Fujii, M., Hayashida, K., and 10 others. 1988. Evidence for a cyclotron absorption from spectral features in gamma-ray bursts seen with Ginga. *Nature*, **335**, 234–235.
- Murray, S. S., Slane, P. O., Seward, F. D., Ransom, S. M., and Gaensler, B. M. 2002. Discovery of X-ray pulsations from the compact central source in the supernova remnant 3C 58. *ApJ*, **568**, 226–231.
- Muslimov, A., and Page, D. 1996. Magnetic and spin history of very young pulsars. *ApJ*, **458**, 347–354.
- Mutel, R. L., Broderick, J. J., Carr, T. D., Lynch, M., Desch, M., Warnock, W. W., and Klemperer, W. K. 1974. VLB observations of the Crab Nebula and the wavelength dependence of interstellar scattering. *ApJ*, **193**, 279–282.
- Narayan, R. 1987. The birthrate and initial spin period of single radio pulsars. *ApJ*, **319**, 162–179.
- Narayan, R., and Vivekanand, M. 1983. Evidence for evolving elongated pulsar beams. *A&A*, **122**, 45–53.
- Navasardyan, H., Petrosian, A. R., Turatto, M., Cappellaro, E., and Boulesteix, J. 2001. Supernovae in isolated galaxies, in pairs and in groups of galaxies. *MNRAS*, **328**, 1181–1192.
- Nice, D. J., Fruchter, A. S., and Taylor, J. H. 1995. A search for fast pulsars along the Galactic plane. *ApJ*, **449**, 156–163.
- Nice, D. J., Sayer, R. W., and Taylor, J. H. 1996. PSR J1518+4904: A mildly relativistic binary pulsar system. *ApJ*, **466**, L87–L90.
- Noutsos, A., Sobey, C., Kondratiev, V. I., and 52 others. 2015. Pulsar polarisation below 200 MHz: Average profiles and propagation effects. *A&A*, **576**(Apr.), A62.
- Olausen, S. A., and Kaspi, V. M. 2014. The McGill magnetar catalog. *ApJS*, **212**(1), 6.
- Olausen, S. A., Kaspi, V. M., Lyne, A. G., and Kramer, M. 2010. XMM-Newton X-ray observation of the high-magnetic-field radio pulsar PSR J1734-3333. *ApJ*, **725**, 985–989.

- Oort, J., and Walraven, Th. 1956. Polarization and composition of the Crab Nebula. *Bull. Astr. Inst. Netherlands*, **12**, 285–308.
- Oppenheimer, J. R., and Volkoff, G. 1939. On massive neutron cores. *Phys. Rev.*, **55**, 374–381.
- Ord, S. M., van Straten, W., Hotan, A. W., and Bailes, M. 2004. Polarimetric profiles of 27 millisecond pulsars. *MNRAS*, **352**, 804–814.
- Ostriker, J. P. 1968. Possible model for a rapidly pulsating radio source. *Nature*, **217**, 1227–1228.
- Oswald, L., Karastergiou, A., and Johnston, S. 2020. Pulsar polarimetry with the Parkes ultra-wideband receiver. *MNRAS*, **496**(2), 1418–1429.
- Oswald, L. S., Karastergiou, A., Posselt, B., and 13 others. 2021. The Thousand-Pulsar-Array programme on MeerKAT – V. Scattering analysis of single-component pulsars. *arXiv e-prints*, Apr., arXiv:2104.01081.
- Özel, F., and Freire, P. 2016. Masses, radii, and the equation of state of neutron stars. *Ann. Rev. Astr. Ap.*, **54**(Sept.), 401–440.
- Pacini, F. 1967. Energy emission from a neutron star. *Nature*, **216**, 567–568.
- Pacini, F. 1968. Rotating neutron stars, pulsars, and supernova remnants. *Nature*, **219**, 145–146.
- Pacini, F., and Salpeter, E. E. 1968. Some models for pulsed radio sources. *Nature*, **218**, 733–734.
- Papitto, A., Hessels, J. W. T., Burgay, M., Ransom, S., Rea, N., Possenti, A., Stairs, I., Ferrigno, C., and Bozz, E. 2013. The transient low-mass X-ray binary IGR J18245-2452 is again active as a radio pulsar. *The Astronomer's Telegram*, **5069**(May), 1.
- Parent, E., Kaspi, V. M., Ransom, S. M., and 18 others. 2019. Eight millisecond pulsars discovered in the Arecibo PALFA survey. *ApJ*, **886**(2), 148.
- Paschalidis, V., and Stergioulas, N. 2017. Rotating stars in relativity. *Living Rev. Rel.*, **20**(1), 7.
- Pechenick, K. R., Ftaclas, C., and Cohen, J. M. 1983. Hot spots on neutron stars – The near-field gravitational lens. *ApJ*, **274**(Nov.), 846–857.
- Pen, Ue-Li, and Levin, Yuri. 2014. Pulsar scintillations from corrugated reconnection sheets in the interstellar medium. *MNRAS*, **442**(4), 3338–3346.
- Perera, B. B. P., McLaughlin, M. A., Kramer, M., and 9 others. 2010. The evolution of PSR J0737-3039B and a model for relativistic spin precession. *ApJ*, **721**, 1193–1205.
- Perera, B. B. P., Stappers, B. W., Lyne, A. G., Bassa, C. G., Cognard, I., Guillemot, L., Kramer, M., Theureau, G., and Desvignes, G. 2017. Evidence for an intermediate-mass black hole in the globular cluster NGC 6624. *MNRAS*, **468**(2), 2114–2127.
- Perera, B. B. P., Barr, E. D., Mickaliger, M. B., and 11 others. 2019a. The dynamics of Galactic centre pulsars: Constraining pulsar distances and intrinsic spin-down. *MNRAS*, **487**(1), 1025–1039.
- Perera, B. B. P., DeCesar, M. E., Demorest, P. B., and 72 others. 2019b. The International Pulsar Timing Array: Second data release. *MNRAS*, **490**(4), 4666–4687.
- Peters, P. C. 1964. Gravitational radiation and the motion of two point masses. *Phys. Rev.*, **136**, 1224–1232.
- Pethick, C. J., and Ravenhall, D. G. 1991. An introduction to matter at subnuclear densities. Pages 3–20 of: Ventura, J., and Pines, D. (eds), *Neutron Stars: Theory and Observation*. Dordrecht: Kluwer.
- Pethick, C. J., and Ravenhall, D. G. 1995. The physics of neutron star crusts. Pages 59–70 of: Alpar, A., Kizilöglü, Ü, and van Paradis, J. (eds), *The Lives of the Neutron Stars (NATO ASI Series)*. Dordrecht: Kluwer.

- Petroff, E., Hessels, J. W. T., and Lorimer, D. R. 2019. Fast radio bursts. *Astron. Astrophys. Rev.*, **27**(1), 4.
- Philippov, A., Timokhin, A., and Spitkovsky, A. 2020. Origin of pulsar radio emission. *Phys. Rev. Lett.*, **124**(24), 245101.
- Phillips, J. A. 1992. Radio emission altitudes in the pulsar magnetosphere. *ApJ*, **385**, 282.
- Phinney, E. S. 1992. Pulsars as probes of newtonian dynamical systems. *Philos. Trans. Roy. Soc. London A*, **341**, 39–75.
- Phinney, E. S., and Blandford, R. D. 1981. Analysis of the pulsar $P - \dot{P}$ distribution. *MNRAS*, **194**, 137–148.
- Pilia, M., Hessels, J. W. T., Stappers, B. W., and 84 others. 2016. Wide-band, low-frequency pulse profiles of 100 radio pulsars with LOFAR. *A&A*, **586**(Feb.), A92.
- Pilkington, J. D. H., Hewish, A., Bell, S. J., and Cole, T. W. 1968. Observations of some further pulsed radio sources. *Nature*, **218**, 126–129.
- Pitkin, M., Reid, S., Rowan, S., and Hough, J. 2011. Gravitational wave detection by interferometry (ground and space). *arXiv:1102.3355*.
- Pivovaroff, M. J., Kaspi, V. M., Camilo, F., Gaensler, B. M., and Crawford, F. 2001. X-ray observations of the new pulsar-supernova remnant system PSR J1119-6127 and SNR G292.2-0.5. *ApJ*, **554**, 161–172.
- Platts, E., Weltman, A., Walters, A., Tendulkar, S. P., Gordin, J. E. B., and Kandhai, S. 2019. A living theory catalogue for fast radio bursts. *Phys. Rep.*, **821**(Aug.), 1–27.
- Pletsch, H. J., Guillemot, L., Fehrmann, H., and 150 others. 2012. Binary millisecond pulsar discovery via gamma-ray pulsations. *Science*, **338**(6112), 1314.
- Podsiadlowski, P., Langer, N., Poelarends, A. J. T., Rappaport, S., Heger, A., and Pfahl, E. 2004. The effects of binary evolution on the dynamics of core collapse and neutron star kicks. *ApJ*, **612**, 1044–1051.
- Polzin, E. J., Breton, R. P., Clarke, A. O., and 10 others. 2018. The low-frequency radio eclipses of the black widow pulsar J1810+1744. *MNRAS*, **476**(2), 1968–1981.
- Pons, J. A., Walter, F. M., Lattimer, J. M., Prakash, M., Neuhauser, R., and An, P. 2002. Towards a mass and radius determination of the nearby isolated neutron star RX J185635–3754. *ApJ*, **564**, 981–1006.
- Popov, M. V., Bartel, N., Gwinn, C. R., and 13 others. 2017. PSR B0329+54: Substructure in the scatter-broadened image discovered with RadioAstron on baselines up to 330 000 km. *MNRAS*, **465**(1), 978–985.
- Popov, M. V., Andrianov, A. S., Burgin, M. S., Zuga, V. A., Rudnitskii, A. G., Smirnova, T. V., Soglasnov, V. A., and Fadeev, E. N. 2019. Anisotropic scattering of the radio emission of the pulsar B0833-45 in the Vela supernova remnant. *Astron. Rep.*, **63**(5), 391–403.
- Popov, S. B., Pons, J. A., Miralles, J. A., Boldin, P. A., and Posselt, B. 2010. Population synthesis studies of isolated neutron stars with magnetic field decay. *MNRAS*, **401**(4), 2675–2686.
- Possenti, A., Cerutti, R., Colpi, M., and Mereghetti, S. 2002. Re-examining the X-ray versus spin-down luminosity correlation of rotation powered pulsars. *A&A*, **387**, 993–1002.
- Prager, B. J., Ransom, S. M., Freire, P. C. C., Hessels, J. W. T., Stairs, I. H., Arras, P., and Cadelano, M. 2017. Using long-term millisecond pulsar timing to obtain physical characteristics of the bulge globular cluster Terzan 5. *ApJ*, **845**(2), 148.
- Prentice, A. J. R., and ter Haar, D. 1969. On H II regions and pulsar distances. *MNRAS*, **146**, 423–444.
- Prince, T. A., Anderson, S. B., Kulkarni, S. R., and Wolszczan, A. 1991. Timing observations of the 8 hour binary pulsar 2127 + 11C in the globular cluster M15. *ApJ*, **374**, L41–L44.

- Psaltis, D., Özel, F., and Chakrabarty, D. 2014. Prospects for measuring neutron-star masses and radii with X-ray pulse profile modeling. *ApJ*, **787**(2), 136.
- Putney, A. 1999. Magnetic white dwarf stars - A review. Page 195 of: Solheim, S. E., and Meistas, E. G. (eds), 11th European Workshop on White Dwarfs. Astronomical Society of the Pacific Conference Series, vol. 169.
- Radhakrishnan, V., and Cooke, D. J. 1969. Magnetic poles and the polarization structure of pulsar radiation. *Astrophys. Lett.*, **3**, 225–229.
- Radhakrishnan, V., and Manchester, R. N. 1969. Detection of a change of state in the pulsar PSR 0833–45. *Nature*, **222**, 228–229.
- Rajwade, K. M., Lorimer, D. R., and Anderson, L. D. 2017. Detecting pulsars in the Galactic Centre. *MNRAS*, **471**(1), 730–739.
- Rajwade, K., Chennamangalam, J., Lorimer, D., and Karastergiou, A. 2018. The Galactic halo pulsar population. *MNRAS*, **479**(3), 3094–3100.
- Ramachandran, R., Mitra, D., Deshpande, A. A., McConnell, D. M., and Ables, J. G. 1997. Measurement of scatter broadening for 27 pulsars at 327 MHz. *MNRAS*, **290**, 260–264.
- Rand, R. J., and Kulkarni, S. R. 1989. The local Galactic magnetic field. *ApJ*, **343**, 760–772.
- Rankin, J. M. 1990. Toward an empirical theory of pulsar emission. IV. Geometry of the core emission region. *ApJ*, **352**, 247–257.
- Rankin, J. M. 1993. Toward an empirical theory of pulsar emission. VI. The geometry of the conal emission region. *ApJ*, **405**, 285–297.
- Ransom, S. M. 2007. Parsec-scale constraints on the ionized interstellar medium with the Terzan 5 pulsars. Page 265 of: Havercorn, M., and Goss, W. M. (eds), *SINS – Small Ionized and Neutral Structures in the Diffuse Interstellar Medium*. Astronomical Society of the Pacific Conference Series, vol. 365.
- Ransom, S. M., Eikenberry, S. S., and Middleditch, J. 2002. Fourier techniques for very long astrophysical time-series analysis. *AJ*, **124**, 1788–1809.
- Ransom, S. M., Hessels, J. W. T., Stairs, I. H., Freire, P. C. C., Camilo, F., Kaspi, V. M., and Kaplan, D. L. 2005. Twenty-one millisecond pulsars in Terzan 5 using the Green Bank Telescope. *Science*, **307**(Feb.), 892–896.
- Ravi, V., Manchester, R. N., and Hobbs, G. 2010. Wide radio beams from gamma-ray pulsars. *ApJ*, **716**, L85–L89.
- Ray, P. S., Thorsett, S. E., Jenet, F. A., van Kerkwijk, M. H., Kulkarni, S. R., Prince, T. A., Sandhu, J. S., and Nice, D. J. 1996. A survey for millisecond pulsars. *ApJ*, **470**, 1103–1110.
- Ray, P. S., Abdo, A. A., Parent, D., and 29 others. 2012. Radio searches of Fermi LAT sources and blind search pulsars: The Fermi Pulsar Search Consortium. *arXiv e-prints*, May, arXiv:1205.3089.
- Raymond, J. C. 1984. Observations of supernova remnants. *Ann. Rev. Astr. Ap.*, **22**, 75–95.
- Rea, N., and Esposito, P. 2011. Magnetar outbursts: An observational review. *Astrophys. Space Sci. Proc.*, **21**(Jan.), 247.
- Readhead, A. C. S., and Duffett-Smith, P. J. 1975. The scale-height of interstellar ionised hydrogen. *A&A*, **42**, 151–153.
- Reardon, D. J., Hobbs, G., Coles, W., and 18 others. 2016. Timing analysis for 20 millisecond pulsars in the Parkes Pulsar Timing Array. *MNRAS*, **455**(2), 1751–1769.
- Reardon, D. J., Coles, W. A., Hobbs, G., Ord, S., Kerr, M., Bailes, M., Bhat, N. D. R., and Venkatraman Krishnan, V. 2019. Modelling annual and orbital variations in the scintillation of the relativistic binary PSR J1141-6545. *MNRAS*, **485**(3), 4389–4403.

- Reardon, D. J., Coles, W. A., Bailes, M., and 17 others. 2020. Precision orbital dynamics from interstellar scintillation arcs for PSR J0437-4715. *arXiv e-prints*, Sept., arXiv:2009.12757.
- Redman, S. L., Wright, G. A. E., and Rankin, J. M. 2005. Pulsar PSR B2303+30: A single system of drifting subpulses, moding and nulling. *MNRAS*, **357**(3), 859–872.
- Reichley, P. E., and Downs, G. S. 1969. Observed decrease in the periods of pulsar PSR 0833–45. *Nature*, **222**, 229–230.
- Renaud, M., Marandon, V., Gotthelf, E. V., Rodriguez, J., Terrier, R., Mattana, F., Lebrun, F., Tomsick, J. A., and Manchester, R. N. 2010. Discovery of a highly energetic pulsar associated with IGR J14003-6326 in the young uncataloged Galactic supernova remnant G310.6-1.6. *ApJ*, **716**, 663–670.
- Reynolds, S. P., Borkowski, K. J., Green, D. A., Hwang, U., Harrus, I., and Petre, R. 2008. The youngest Galactic supernova remnant: G1.9+0.3. *ApJ*, **680**, L41–L44.
- Richards, D. W., and Comella, J. M. 1969. The period of pulsar NP 0532. *Nature*, **222**, 551–552.
- Rickett, B. J. 1969. Frequency structure of pulsar intensity fluctuations. *Nature*, **221**, 158–159.
- Rickett, B. J. 1990. Radio propagation through the turbulent interstellar plasma. *Ann. Rev. Astr. Ap.*, **28**, 561–605.
- Rickett, B. J. 2007 (July). What do scintillations tell us about the ionized ISM? Page 207 of: Havercorn, M., and Goss, W. M. (eds), *SINS – Small Ionized and Neutral Structures in the Diffuse Interstellar Medium*. Astronomical Society of the Pacific Conference Series, vol. 365.
- Rickett, B. J., Hankins, T. H., and Cordes, J. M. 1975. The radio spectrum of micropulses from pulsar PSR 0950+08. *ApJ*, **201**, 425–430.
- Rickett, B. J., Coles, W. A., and Bourgois, G. 1984. Slow scintillation in the interstellar medium. *A&A*, **134**, 390–395.
- Rickett, B. J., Lyne, A. G., and Gupta, Y. 1997. Interstellar fringes from PSR B0834+06. *MNRAS*, **287**, 739–752.
- Ridley, J. P., Crawford, F., Lorimer, D. R., Bailey, S. R., Madden, J. H., Anella, R., and Chennamangalam, J. 2013. Eight new radio pulsars in the Large Magellanic Cloud. *MNRAS*, **433**(1), 138–146.
- Rigoselli, M., Mereghetti, S., Suleimanov, V., Potekhin, A. Y., Turolla, R., Taverna, R., and Pintore, F. 2019. XMM-Newton observations of PSR J0726-2612, a radio-loud XDINS. *A&A*, **627**(July), A69.
- Roberts, J. A., and Ables, J. G. 1982. Dynamic spectra of pulsar scintillations at frequencies near 0.34, 0.41, 0.63, 1.4, 1.7, 3.2 and 5.0 GHz. *MNRAS*, **201**, 1119–1138.
- Roberts, M. S. E. 2011. New black widows and redbacks in the galactic field. Pages 127–130 of: Burgay, M., D'Amico, N., Esposito, P., Pellizzoni, A., and Possenti, A. (eds), *Radio Pulsars: An Astrophysical Key to Unlock the Secrets of the Universe*. American Institute of Physics Conference Series, vol. 1357.
- Romani, R. W. 1996. Gamma-ray pulsars: Radiation processes in the outer magnetosphere. *ApJ*, **470**, 469–478.
- Romani, R. W., and Yadigaroglu, I.-A. 1995. Gamma-ray pulsars: Emission zones and viewing geometries. *ApJ*, **438**, 314–321.
- Rookyard, S. C., Weltevrede, P., and Johnston, S. 2015. Constraints on viewing geometries from radio observations of γ -ray-loud pulsars using a novel method. *MNRAS*, **446**(4), 3367–3388.
- Ruderman, M. 1974. Matter in superstrong magnetic fields. Pages 117–131 of: Hansen, C. J. (ed), *IAU Symposium 53*. Reidel.

- Ruderman, M. 1991. Neutron star crustal plate tectonics. I. Magnetic Dipole evolution in millisecond pulsars and low-mass X-Ray binaries. *ApJ*, **366**, 261–269.
- Ruderman, M., Zhu, T., and Chen, K. 1998. Neutron star magnetic field evolution, crust movement, and glitches. *ApJ*, **492**, 267–280.
- Ruderman, M. A., and Sutherland, P. G. 1975. Theory of pulsars: Polar gaps, sparks, and coherent microwave radiation. *ApJ*, **196**, 51–72.
- Ryba, M. F., and Taylor, J. H. 1991. High-precision timing of millisecond pulsars. II – Astrometry, orbital evolution, and eclipses of PSR 1957+20. *ApJ*, **380**, 557–563.
- Safi-Harb, S., Harrus, I. M., Petre, R., Pavlov, G. G., Koptsevich, A. B., and Sanwal, D. 2001. X-ray observations of the supernova remnant G21.5–0.9. *ApJ*, **561**, 308–320.
- Sanchez, N., and Romani, R. W. 2017. B-ducted heating of black widow companions. *ApJ*, **845**(1), 42.
- Sanidas, S., Cooper, S., Bassa, C. G., and 20 others. 2019. The LOFAR Tied-Array All-Sky Survey (LOTAAS): Survey overview and initial pulsar discoveries. *A&A*, **626**(June), A104.
- Saz Parkinson, P. M., Dormody, M., Ziegler, M., and 34 others. 2010. Eight γ -ray pulsars discovered in blind frequency searches of Fermi LAT data. *ApJ*, **725**(1), 571–584.
- Scargle, J., and Harlan, E. 1970. Activity in the Crab Nebula following the pulsar spin-up of 1969 September. *ApJ*, **159**, L143–L146.
- Scheuer, P. A. G. 1968. Amplitude variations of pulsed radio sources. *Nature*, **218**, 920–922.
- Schönhardt, R. E., and Sieber, W. 1973. Pulsars: Properties of PSR 0301+19 and PSR 2020+28. *Astrophys. Lett.*, **14**, 61–64.
- Segelstein, D. J., Rawley, L. A., Stinebring, D. R., Fruchter, A. S., and Taylor, J. H. 1986. New millisecond pulsar in a binary system. *Nature*, **322**, 714–717.
- Seidelmann, P. K., and Fukushima, T. 1992. Why new time scales? *A&A*, **265**, 833–838.
- Seward, F. D., and Charles, P. A. 1995. *Exploring the X-Ray Universe*.
- Seward, F. D., and Harnden Jr., F. R. 1982. A new, fast X-ray pulsar in the supernova remnant MSH 15–52. *ApJ*, **256**, L45–L47.
- Shannon, R. M., and Cordes, J. M. 2010. Assessing the role of spin noise in the precision timing of millisecond pulsars. *ApJ*, **725**(2), 1607–1619.
- Shapiro, I. I. 1964. Fourth test of general relativity. *Phys. Rev. Lett.*, **13**, 789.
- Shapiro, S. L., and Teukolsky, S. A. 1983. *Black Holes, White Dwarfs and Neutron Stars. The Physics of Compact Objects*. New York: Wiley–Interscience.
- Shearer, A., Redfern, R. M., Gorman, G., and 8 others. 1997. Pulsed optical emission from PSR 0656+14. *ApJ*, **487**, L181–L185.
- Shearer, A., Golden, A., Harfst, S., and 9 others. 1998. Possible pulsed optical emission from Geminga. *A&A*, **335**(July), L21–L24.
- Shearer, A., Stappers, B., O'Connor, P., Golden, A., Strom, R., Redfern, M., and Ryan, O. 2003. Enhanced optical emission during Crab giant radio pulses. *Science*, **301**, 493–495.
- Shemar, S. L., and Lyne, A. G. 1996. Observations of pulsar glitches. *MNRAS*, **282**, 677–690.
- Shishov, V. I., Smirnova, T. V., Gwinn, C. R., Andrianov, A. S., Popov, M. V., Rudnitskiy, A. G., and Soglasnov, V. A. 2017. Interstellar scintillations of PSR B1919+21: Space-ground interferometry. *MNRAS*, **468**(3), 3709–3717.
- Shitov, Yu. P. 1983. Period dependence of the spectrum and the phenomenon of twisting of the magnetic fields of pulsars. *Sov. Astron.*, **27**, 314–321.
- Shklovsky, I. S. 1970. Possible causes of the secular increase in pulsar periods. *Sov. Astron.*, **13**, 562–565.

- Shklovsky, I. S. 1953. On the nature of the radiation from the Crab Nebula. *Dokl. Akad. Nauk. USSR*, **90**, 983.
- Shklovsky, I. S. 1967. On the nature of the source of X-ray emission of SCO XR-1. *ApJ*, **148**, L1.
- Sieber, W. 1973. Pulsar spectra – A summary. *A&A*, **28**, 237–252.
- Sieber, W. 1982. Causal relationship between pulsar long-term intensity variations and the interstellar medium. *A&A*, **113**, 311–313.
- Sieber, W., and Oster, L. 1975. Drifting subpulse behavior of PSRs 0943+10 and 2303+30. *A&A*, **38**, 325–327.
- Siemens, X., Ellis, J., Jenet, F., and Romano, J. D. 2013. The stochastic background: Scaling laws and time to detection for pulsar timing arrays. *Classical and Quantum Gravity*, **30**(22), 224015.
- Sigurdsson, S., and Thorsett, S. E. 2005. Update on pulsar B1620-26 in M4: Observations, models, and implications. *ASP Conf. Ser.*, **328**, 213.
- Simard, D., Pen, U. L., Marthi, V. R., and Brisken, W. 2019. Disentangling interstellar plasma screens with pulsar VLBI: Combining auto- and cross-correlations. *MNRAS*, **488**(4), 4963–4971.
- Slee, O. B., Dulk, G. A., and Otrupcek, R. E. 1980. Culgoora radio heliograph measurements of interstellar scattering of pulsar signals. *PASA*, **4**, 100–106.
- Slowikowska, A., Kanbach, G., Kramer, M., and Stefanescu, A. 2009. Optical polarization of the Crab Pulsar: Precision measurements and comparison to the radio emission. *MNRAS*, **397**, 103–123.
- Smart, W. M. 1977. *Textbook on Spherical Astronomy*. Cambridge University Press.
- Smith, D. A., Guillemot, L., Kerr, M., Ng, C., and Barr, E. 2017. Gamma-ray pulsars with Fermi. *arXiv e-prints*, June, arXiv:1706.03592.
- Smith, F. G. 1968. Measurement of the interstellar magnetic field. *Nature*, **218**, 325–326.
- Smith, F. G. 1973. The pulse energy distribution in pulsars. *MNRAS*, **161**, 9P.
- Smith, F. G., and Wright, N. C. 1985. Frequency drift in pulsar scintillation. *MNRAS*, **214**, 97–107.
- Sobey, C., Bilous, A. V., Grießmeier, J. M., and 22 others. 2019. Low-frequency Faraday rotation measures towards pulsars using LOFAR: Probing the 3D Galactic halo magnetic field. *MNRAS*, **484**(3), 3646–3664.
- Spitkovsky, A. 2006. Time-dependent force-free pulsar magnetospheres: Axisymmetric and oblique rotators. *ApJ*, **648**, L51–L54.
- Spitler, L. G., Cordes, J. M., Hessels, J. W. T., and 29 others. 2014. Fast radio burst discovered in the Arecibo pulsar ALFA survey. *ApJ*, **790**(Aug.), 101.
- Splaver, E. M., Nice, D. J., Stairs, I. H., Lommen, A. N., and Backer, D. C. 2005. Masses, parallax, and relativistic timing of the PSR J1713+0747 binary system. *ApJ*, **620**, 405–415.
- Spoelstra, T. A. T. 1984. Linear polarization of the galactic radio emission at frequencies between 408 and 1411 MHz. II – Discussion. *A&A*, **135**, 238–248.
- Spolon, A., Zampieri, L., Burtovoi, A., Naletto, G., Barbieri, C., Barbieri, M., Patruno, A., and Verroi, E. 2019. Timing analysis and pulse profile of the Vela Pulsar in the optical band from Iqueye observations. *MNRAS*, **482**(1), 175–183.
- Staelin, D. H. 1969. Fast folding algorithm for detection of periodic pulse trains. *Proc. I. E. E.*, **57**, 724–725.
- Staelin, D. H., and Reifenstein, III, E. C. 1968. Pulsating radio sources near the Crab Nebula. *Science*, **162**, 1481–1483.
- Stairs, I. H. 2002. Pulsar observations II. Coherent dedispersion polarimetry, and timing. *ASP Conf. Proc.*, **278**, 251–269.

- Stairs, I. H., Splaver, E. M., Thorsett, S. E., Nice, D. J., and Taylor, J. H. 2000a. A baseband recorder for radio pulsar observations. *MNRAS*, **314**, 459–467. (astro-ph/9912272).
- Stairs, I. H., Lyne, A. G., and Shemar, S. 2000b. Evidence for free precession in a pulsar. *Nature*, **406**, 484–486.
- Stairs, I. H., Thorsett, S. E., Taylor, J. H., and Wolszczan, A. 2002. Studies of the relativistic binary pulsar PSR B1534+12: I. Timing analysis. *ApJ*, **581**, 501–508.
- Stairs, I. H., Thorsett, S. E., and Arzoumanian, Z. 2004. Measurement of gravitational spin-orbit coupling in a binary-pulsar system. *Phys. Rev. Lett.*, **93**, 141101.
- Standish, E. M. 1982. Orientation of the JPL ephemerides, DE200/LE200, to the dynamical equinox of J 2000. *A&A*, **114**, 297–302.
- Standish, E. M. 2004. An approximation to the errors in the planetary ephemerides of the Astronomical Almanac. *A&A*, **417**, 1165–1171.
- Stappers, B. W., Bessell, M. S., and Bailes, M. 1996. Detection of an irradiated pulsar companion. *ApJ*, **473**, L119–L121.
- Stappers, B. W., Jones, D. H., and Gaensler, B. M. 2002. The H-alpha bow-shock nebula around PSR B0740-28. *ASP Conf. Ser.*, **271**, 141.
- Stappers, B. W., Archibald, A., Bassa, C., Hessels, J., Janssen, G., Kaspi, V., Lyne, A., Patruno, A., and Hill, A. B. 2013. State-change in the “transition” binary millisecond pulsar J1023+0038. *The Astronomer’s Telegram*, **5513**(Oct.), 1.
- Steiner, A. W., Gandolfi, S., Fattoyev, F. J., and Newton, W. G. 2015. Using neutron star observations to determine crust thicknesses, moments of inertia, and tidal deformabilities. *Phys. Rev. C*, **91**(1), 015804.
- Stinebring, D. 2007 (July). Pulsar scintillation arcs and the ionized ISM. Page 254 of: Havercorn, M., and Goss, W. M. (eds), *SINS – Small Ionized and Neutral Structures in the Diffuse Interstellar Medium*. Astronomical Society of the Pacific Conference Series, vol. 365.
- Stinebring, D. R., Cordes, J. M., Rankin, J. M., Weisberg, J. M., and Boriakoff, V. 1984. Pulsar polarization fluctuations. I. 1408 MHz statistical summaries. *ApJS*, **55**, 247–277.
- Stinebring, D. R., McLaughlin, M. A., Cordes, J. M., Becker, K. M., Goodman, J. E. E., Kramer, M. A., Sheckard, J. L., and Smith, C. T. 2001. Faint scattering around pulsars: Probing the interstellar medium on Solar System size scales. *ApJ*, **549**, L97–L100.
- Stokes, G. H., Taylor, J. H., Weisberg, J. M., and Dewey, R. J. 1985. A survey for short period pulsars. *Nature*, **317**, 787–788.
- Stollman, G. M. 1986. A possible discrimination between two luminosity laws for radio pulsars. *A&A*, **170**, 48–54.
- Story, S. A., Gonther, P. L., and Harding, A. K. 2007. Population synthesis of radio and γ -ray millisecond pulsars from the Galactic disk. *ApJ*, **671**(1), 713–726.
- Stovall, K., Lynch, R. S., Ransom, S. M., and 29 others. 2014. The Green Bank Northern Celestial Cap pulsar survey. I. Survey description, data analysis, and initial results. *ApJ*, **791**(1), 67.
- Strader, J., Swihart, S., Chomiuk, L., and and 12 others. 2019. Optical spectroscopy and demographics of redback millisecond pulsar binaries. *ApJ*, **872**(1), 42–58.
- Strömgren, B. 1939. The physical state of interstellar hydrogen. *ApJ*, **89**, 526–547.
- Sutton, J. M., Staelin, D. H., and Price, R. M. 1971. Individual radio pulses from NP 0531. Pages 97–102 of: Davies, R. D., and Smith, F. G. (eds), *IAU Symp. No. 46*. Reidel.
- Swartz, D. A., Ghosh, K. K., McCollough, M. L., Pannuti, T. G., Tennant, A. F., and Wu, K. 2003. Chandra X-ray observations of the spiral galaxy M81. *ApJS*, **144**, 213–242.
- Szary, A., van Leeuwen, J., Weltevrede, P., and Maan, Y. 2020. Single-pulse modeling and the bi-drifting subpulses of radio pulsar B1839-04. *ApJ*, **896**(2), 168.

- Tammann, G. A., Löffler, W., and Schröder, A. 1994. The galactic supernova rate. *ApJS*, **92**, 487–493.
- Tan, C. M., and LOTAAS Group. 2018 (Aug.). The LOFAR Tied-Array All-Sky Survey for pulsars and fast transients. Pages 9–12 of: Weltevrede, P., Perera, B. B. P., Preston, L. L., and Sanidas, S. (eds), *Pulsar Astrophysics the Next Fifty Years*, vol. 337.
- Tan, C. M., Bassa, C. G., Cooper, S., and 16 others. 2018. LOFAR discovery of a 23.5 s radio pulsar. *ApJ*, **866**(1), 54.
- Tauris, T. M., and Konar, S. 2001. Torque decay in the pulsar ($P - \dot{P}$) diagram. *A&A*, **376**, 543–552.
- Tauris, T. M., and Manchester, R. N. 1998. On the evolution of pulsar beams. *MNRAS*, **298**, 625–636.
- Tavani, M., Barbiellini, G., Argan, A., and 49 others. 2008. The AGILE space mission. *Nuclear Instruments and Methods in Physics Research A*, **588**(1-2), 52–62.
- Taylor, J. H. 1974. A sensitive method for detecting dispersed radio emission. *A&AS*, **15**, 367–369.
- Taylor, J. H. 1992. Pulsar timing and relativistic gravity. *Philos. Trans. Roy. Soc. London A*, **341**, 117–134.
- Taylor, J. H., and Cordes, J. M. 1993. Pulsar distances and the Galactic distribution of free electrons. *ApJ*, **411**, 674–684.
- Taylor, J. H., and Huguenin, G. R. 1971. Observations of rapid fluctuations of intensity and phase in pulsar emissions. *ApJ*, **167**, 273–291.
- Taylor, J. H., and Weisberg, J. M. 1982. A new test of general relativity – Gravitational radiation and the binary pulsar PSR 1913+16. *ApJ*, **253**, 908–920.
- Taylor, J. H., Huguenin, G. R., Hirsch, R. M., and Manchester, R. N. 1971. Polarisation of the drifting subpulses of pulsar 0809+74. *Astrophys. Lett.*, **9**, 205–208.
- Tendulkar, S. P., Cameron, P. B., and Kulkarni, S. R. 2012. Proper motions and origins of SGR 1806-20 and SGR 1900+14. *ApJ*, **761**(1), 76.
- Tendulkar, S. P., Bassa, C. G., Cordes, J. M., and 24 others. 2017. The host galaxy and redshift of the repeating fast radio burst FRB 121102. *ApJ*, **834**(2), L7.
- Thompson, C., and Duncan, R. C. 1995. The soft gamma repeaters as very strongly magnetized neutron stars – I. Radiative mechanism for outbursts. *MNRAS*, **275**, 255–300.
- Thompson, C., and Duncan, R. C. 1996. The soft gamma repeaters as very strongly magnetized neutron stars. II. Quiescent neutrino, X-ray, and Alfvén wave emission. *ApJ*, **473**, 322–342.
- Thompson, C., Blandford, R. D., Evans, C. R., and Phinney, E. S. 1994. Physical processes in eclipsing pulsars: Eclipse mechanisms and diagnostics. *ApJ*, **422**, 304–335.
- Thorne, K. S., and Zytkow, A. N. 1977. Stars with degenerate neutron cores. I. Structure of equilibrium models. *ApJ*, **212**(Mar.), 832–858.
- Thornton, D., Stappers, B., Bailes, M., and 17 others. 2013. A population of fast radio bursts at cosmological distances. *Science*, **341**(6141), 53–56.
- Thorsett, S. E. 1991. Frequency dependence of pulsar integrated profile. *ApJ*, **377**, 263–267.
- Thorsett, S. E., and Dewey, R. J. 1996. Pulsar timing limits on very low frequency stochastic gravitational radiation. *Phys. Rev. D*, **53**, 3468.
- Tiburzi, C., and Verbiest, J. P. W. 2018 (Aug.). The effect of the solar wind on low-frequency observations of pulsars. Pages 279–282 of: Weltevrede, P., Perera, B. B. P., Preston, L. L., and Sanidas, S. (eds), *Pulsar Astrophysics the Next Fifty Years*, vol. 337.
- Timokhin, A. N. 2010. A model for nulling and mode changing in pulsars. *MNRAS*, **408**, L41–L45.

- Tong, H., and Kou, F. F. 2017. Possible evolution of the pulsar braking index from larger than three to about one. *ApJ*, **837**(2), 117.
- Toscano, M., Britton, M. C., Manchester, R. N., Bailes, M., Sandhu, J. S., Kulkarni, S. R., and Anderson, S. B. 1999. Parallax of PSR J1744–1134 and the local interstellar medium. *ApJ*, **523**, L171–L175.
- Trang, F. S., and Rickett, B. J. 2007. Modeling of interstellar scintillation arcs from pulsar B1133+16. *ApJ*, **661**(2), 1064–1072.
- Trümper, J., Pietsch, W., Reppin, C., Voges, W., Staubert, R., and Kendziorra, E. 1978. Evidence for strong cyclotron line emission in the hard X-ray spectrum of Hercules X-1. *ApJ*, **219**, L105–L110.
- Unwin, S. C., Readhead, A. C. S., Wilkinson, P. N., and Ewing, M. S. 1978. Phase stability in the drifting subpulse pattern of PSR 0809+74. *MNRAS*, **182**, 711–721.
- Uscinski, B. J. 1968. The multiple scattering of waves in irregular media. *Philos. Trans. Roy. Soc. London A*, **262**, 609–640.
- Uscinski, B. J. 1974. The propagation and broadening of pulses in weakly irregular media. *Philos. Trans. Roy. Soc. London A*, **336**, 379–392.
- Usov, V. V. 1987. On two-stream instability in pulsar magnetospheres. *ApJ*, **320**, 333–335.
- Uyaniker, B., Reich, W., Yar, A., and Fürst, E. 2004. Radio emission from the Cygnus Loop and its spectral characteristics. *A&A*, **426**(Nov.), 909–924.
- van den Bergh, S. 1988. Classification of supernovae and their remnants. *ApJ*, **327**, 156–163.
- van den Bergh, S., and McClure, R. D. 1994. Rediscussion of extragalactic supernova rates derived from Evans's 1980–1988 observations. *ApJ*, **425**, 205–209.
- van den Heuvel, E. P. J. 1992. Formation and evolution of neutron star binaries. Pages 233–256 of: van den Heuvel, E. P. J., and Rappaport, S. A. (eds), *X-ray Binaries and Recycled Pulsars*. Dordrecht: Kluwer.
- van der Hulst, H. C. 1967. Observing the Galactic magnetic field. *Ann. Rev. Astr. Ap.*, **5**, 167–182.
- van der Klis, M. 2000. Millisecond oscillations in X-ray binaries. *Ann. Rev. Astr. Ap.*, **38**, 717–760.
- van Kerkwijk, M. H., and Kaplan, D. L. 2007. Isolated neutron stars: Magnetic fields, distances, and spectra. *Astrophys. Space Sci.*, **308**, 191–201.
- van Kerkwijk, M. H., Breton, R. P., and Kulkarni, S. R. 2011. Evidence for a massive neutron star from a radial-velocity study of the companion to the black-widow pulsar PSR B1957+20. *ApJ*, **728**, 95–102.
- van Leeuwen, A. G. J., Stappers, B. W., Ramachandran, R., and Rankin, J. M. 2003. Probing drifting and nulling mechanisms through their interaction in PSR B0809+74. *A&A*, **399**, 223–229.
- van Straten, W., Bailes, M., Britton, M., Kulkarni, S. R., Anderson, S. B., Manchester, R. N., and Sarkissian, J. 2001. A test of general relativity from the three-dimensional orbital geometry of a binary pulsar. *Nature*, **412**, 158–160.
- Vandenberg, N. R., Clark, T. A., Erickson, W. C., Resch, G. M., Broderick, J. J., Payne, R. R., Knowles, S. H., and Youmans, A. B. 1973. VLBI observations of the Crab Nebula pulsar. *ApJ*, **180**, L27–L29.
- Vashakidze, M. A. 1954. Polarization observations of nearby extragalactic nebulae and the Crab Nebula. *Astr. Circ.*, **147**, 11–13.
- Vaughan, A. E., and Large, M. I. 1969. Pulsar observations at Molonglo. *PASA*, **1**, 220–223.
- Verbist, J. P. W., Bailes, M., van Straten, W., Hobbs, G. B., Edwards, R. T., Manchester, R. N., Bhat, N. D. R., Sarkissian, J. M., Jacoby, B. A., and Kulkarni, S. R. 2008. Precision timing of PSR J0437–4715: An accurate pulsar distance, a high pulsar mass, and a limit on the variation of Newton's gravitational constant. *ApJ*, **679**, 675–680.

- Verbiest, J. P. W., Bailes, M., Coles, W. A., and 11 others. 2009. Timing stability of millisecond pulsars and prospects for gravitational-wave detection. *MNRAS*, **400**, 951–968.
- Verbiest, J. P. W., Weisberg, J. M., Chael, A. A., Lee, K. J., and Lorimer, D. R. 2012. On pulsar distance measurements and their uncertainties. *ApJ*, **755**(1), 39.
- Verbunt, F., Igoshev, A., and Cator, E. 2017. The observed velocity distribution of young pulsars. *A&A*, **608**(Dec.), A57.
- Voges, W., Aschenbach, B., Boller, T., and 17 others. 1999. The ROSAT all-sky survey bright source catalogue. *A&A*, **349**, 389–405.
- von Hoensbroech, A., and Xilouris, K. M. 1997. Effelsberg multifrequency pulsar polarimetry. *A&AS*, **126**, 121–149.
- von Hoensbroech, A., Kijak, J., and Krawczyk, A. 1998. On the high frequency polarization of pulsar radio emission. *A&A*, **334**, 571–584.
- Vranešević, N., and Melrose, D. B. 2011. Pulsar current revisited. *MNRAS*, **410**, 2363–2369.
- Wakatsuki, S., Hikita, A., Sato, N., and Itoh, N. 1992. The nonexponential evolution of pulsar magnetic fields. *ApJ*, **392**, 628–636.
- Walker, M. A., Koopmans, L. V. E., Stinebring, D. R., and van Straten, W. 2008. Interstellar holography. *MNRAS*, **388**, 1214–1222.
- Wallace, P. T., Peterson, B. A., Murdin, P. G., and 9 others. 1977. Detection of optical pulses from the Vela Pulsar. *Nature*, **266**, 692–694.
- Wang, J. B., Coles, W. A., Hobbs, G., and 23 others. 2017. Comparison of pulsar positions from timing and very long baseline astrometry. *MNRAS*, **469**(1), 425–434.
- Wang, N., Manchester, R. N., and Johnston, S. 2007. Pulsar nulling and mode changing. *MNRAS*, **377**(3), 1383–1392.
- Warszawski, L., and Melatos, A. 2008. A cellular automaton model of pulsar glitches. *MNRAS*, **390**, 175–191.
- Watts, A. L. 2012. Thermonuclear burst oscillations. *Ann. Rev. Astr. Ap.*, **50**(Sept.), 609–640.
- Weatherall, J. C. 1998. Pulsar radio emission by conversion of plasma wave turbulence: Nanosecond time structure. *ApJ*, **506**, 341–346.
- Weekes, T. C., Cawley, M. F., Fegan, D. J., and 9 others. 1989. Observation of TeV gamma rays from the Crab Nebula using the atmospheric Cerenkov imaging technique. *ApJ*, **342**, 379–395.
- Weiler, K. W., and Sramek, R. A. 1988. Supernovae and Supernova Remnants. *Ann. Rev. Astr. Ap.*, **26**, 295–341.
- Weiler, K. W., Van Dyk, S. D., Sramek, R. A., and Panagia, N. 1996. Radio supernovae. Pages 283–297 of: McCray, R., and Wang, Z. (eds), *IAU Colloquium 145: Supernovae and Supernova Remnants*. Cambridge University Press.
- Weisberg, J. M., and Huang, Y. 2016. Relativistic measurements from timing the binary pulsar PSR B1913+16. *ApJ*, **829**(1), 55.
- Weisberg, J. M., and Taylor, J. H. 1984. Observations of post-Newtonian timing effects in the binary pulsar PSR 1913+16. *Phys. Rev. Lett.*, **52**, 1348–1350.
- Weisberg, J. M., and Taylor, J. H. 2002. General relativistic geodetic spin precession in binary pulsar B1913+16: Mapping the emission beam in two dimensions. *ApJ*, **576**, 942–949.
- Weisberg, J. M., and Taylor, J. H. 2005. The relativistic binary pulsar B1913+16: Thirty years of observations and analysis. *ASP Conf. Ser.*, **328**, 25.
- Weisberg, J. M., Romani, R. W., and Taylor, J. H. 1989. Evidence for geodetic spin precession in the binary pulsar 1913+16. *ApJ*, **347**, 1030–1033.

- Weisberg, J. M., Cordes, J. M., Lundgren, S. C., Dawson, B. R., Despotes, J. T., Morgan, J. J., Weitz, K. A., Zink, E. C., and Backer, D. C. 1999. Arecibo 1418 MHz polarimetry of 98 pulsars: Full Stokes profiles and morphological classifications. *ApJS*, **121**, 171–217.
- Weisberg, J. M., Nice, D. J., and Taylor, J. H. 2010. Timing measurements of the relativistic binary pulsar PSR B1913+16. *ApJ*, **722**, 1030–1034.
- Weisskopf, M. C., Hester, J. J., Tenant, A. F., and 8 others. 2000. Discovery of spatial and spectral structure in the X-ray emission from the Crab Nebula. *ApJ*, **536**, L81–L84.
- Weltevrede, P., and Johnston, S. 2008. The population of pulsars with interpulses and the implications for beam evolution. *MNRAS*, **387**, 1755–1760.
- Weltevrede, P., Edwards, R. T., and Stappers, B. W. 2006. The subpulse modulation properties of pulsars at 21 cm. *A&A*, **445**(Jan.), 243–272.
- Weltevrede, P., Stappers, B. W., and Edwards, R. T. 2007. The subpulse modulation properties of pulsars at 92 cm and the frequency dependence of subpulse modulation. *A&A*, **469**(2), 607–631.
- Weltevrede, P., Johnston, S., and Espinoza, C. M. 2011. The glitch-induced identity changes of PSR J1119-6127. *MNRAS*, **411**(Mar.), 1917–1934.
- Wheeler, J. A. 1966. Superdense stars. *Ann. Rev. Astr. Ap.*, **4**, 393–432.
- Whelan, J., and Iben, I. 1973. Binaries and supernovae of Type I. *ApJ*, **186**, 1007–1014.
- White, N. E., Swank, J. H., and Holt, S. S. 1983. Accretion-powered X-ray pulsars. *ApJ*, **270**, 711–734.
- White, N. E., Nagase, F., and Parmar, A. N. 1995. The properties of X-ray Binaries. Pages 1–57 of: Lewin, W. H. G., van Paradijs, J., and van den Heuvel, E. P. J. (eds), *X-ray Binaries*. Cambridge University Press.
- Wijnands, R., and van der Klis, M. 1998. A millisecond pulsar in an X-ray binary system. *Nature*, **394**, 344–346.
- Wilkinson, A., and Smith, F. G. 1974. Characteristics of the local Galactic magnetic field determined from background polarization surveys. *MNRAS*, **167**, 593–611.
- Will, C. M. 1993. *Theory and Experiment in Gravitational Physics*. Cambridge University Press.
- Williamson, I. P. 1973. Pulse broadening due to multiple scattering in the interstellar medium. *MNRAS*, **163**, 345–356.
- Williamson, I. P. 1974. Pulse broadening due to irregular scattering in the interstellar medium – III. *MNRAS*, **166**, 499–512.
- Willstrop, R. V. 1969. Optical flashes from the Crab Nebula M1. *Nature*, **221**, 1023–1025.
- Wolszczan, A. 1982. A frequency correlation analysis of pulsar scintillation Spectra. *MNRAS*, **204**, 591–602.
- Wolszczan, A. 1991. A nearby 37.9 ms radio pulsar in a relativistic binary system. *Nature*, **350**, 688–690.
- Wolszczan, A., and Frail, D. A. 1992. A planetary system around the millisecond pulsar PSR 1257+12. *Nature*, **355**, 145–147.
- Woltjer, L. 1972. Supernova remnants. *Ann. Rev. Astr. Ap.*, **10**, 129–158.
- Woods, P. M., and Thompson, C. 2006. Soft gamma repeaters and anomalous X-ray pulsars: Magnetar candidates. *Compact Stellar X-Ray Sources*. Vol. 39. Cambridge University Press. Pages 547–586.
- Woosley, S. E., and Weaver, T. A. 1986. The physics of supernova explosions. *Ann. Rev. Astr. Ap.*, **24**, 205–253.
- Wright, G. A., and Fowler, L. A. 1981. Mode-changing and quantized subpulse drift-rates in pulsar PSR 2319+60. *A&A*, **101**, 356–361.

- Wright, G., and Weltevrede, P. 2017. Pulsar bi-drifting: Implications for polar cap geometry. *MNRAS*, **464**(3), 2597–2608.
- Xilouris, K. M., Kramer, M., Jessner, A., Wielebinski, R., and Timofeev, M. 1996. Emission properties of pulsars at mm-wavelengths. *A&A*, **309**, 481.
- Xilouris, K. M., Kramer, M., Jessner, A., von Hoensbroech, A., Lorimer, D., Wielebinski, R., Wolszczan, A., and Camilo, F. 1998. The characteristics of millisecond pulsar emission: II. Polarimetry. *ApJ*, **501**, 286–306.
- Yan, W. M., Manchester, R. N., van Straten, W., and 14 others. 2011. Polarization observations of 20 millisecond pulsars. *arXiv 1102.2274*.
- Yao, J. M., Manchester, R. N., and Wang, N. 2017. A new electron-density model for estimation of pulsar and FRB distances. *ApJ*, **835**(1), 29.
- Young, M. D., Manchester, R. N., and Johnston, S. 2000. A radio pulsar with an 8.5-s period challenges emission models. *ASP Conf. Ser.*, **202**, 185.
- Yuen, R., and Melrose, D. B. 2014. Visibility of pulsar emission: Motion of the visible point. *PASA*, **31**(Oct.), e039.
- Zdunik, J. L., Fortin, M., and Haensel, P. 2017. Neutron star properties and the equation of state for the core. *A&A*, **599**(Mar.), A119.
- Zel'dovich, Ya. B., and Guseynov, O. K. 1964. Collapsed stars in binaries. *ApJ*, **144**, 840–841.
- Zhu, W. W., Freire, P. C. C., Knispel, B., and 15 others. Mass Measurements for Two Binary Pulsars Discovered in the PALFA Survey. *ApJ*, **881**(2), 165–174.
- Zoccali, M., Renzini, A., Ortolani, S., and 9 others. 2001. The white dwarf distance to the globular cluster 47 Tucanae and its age. *ApJ*, **553**, 733–743.
- Zou, W. Z., Hobbs, G., Wang, N., Manchester, R. N., Wu, X. J., and Wang, H. X. 2005. Timing measurements and proper motions of 74 pulsars using the Nanshan radio telescope. *MNRAS*, **362**, 1189–1198.

Index

- aberration, 283, 287
accretion, 201, 202
accretion induced collapse, 303
accretion powered pulsar, 193
ages of pulsars, 64, 84, 85
Alfvén surface, 202
Alfvén waves, 292, 295
Allan Variance, 88
angular diameter, 114
anomalous x-ray pulsars (AXPs), 184
astrometric reference frames, 80
- Baade's star, 3, 310, 313, 315
Baade,W., 3, 299, 309
barycentre, 75, 91
barycentric arrival times, 76
barycentric correction, 77
beam geometry, 135, 263
beaming factor, 135
beamshape, 135
beamwidth, 137, 265
 frequency dependence, 131
Bell, Jocelyn, 5
binary orbit, 9, 90, 196
 Keplerian parameters, 93
 parameters, 91
 post-newtonian, 94
 precession, 96
 relativistic effects, 94
binary pulsars
 double neutron star, 230
 black widow, 171, 233
 double neutron (DNS), 166
 dynamics, 229
 eclipsing, 170
 evolution, 95, 164, 167
 redback, 168, 233
 searches, 43
 white dwarf, 113, 167, 232
binary stars, 214
- black hole, 201, 213, 302
black widow binaries, 168
bow shock, 317
braking index, 84, 85, 186, 189, 190, 240
brightness temperature, 290
- cascade process, 281
Cassiopeia A, 305, 307, 314
Cerenkov airshower telescopes, 32
 CTA, 33
 HESS, 32
Chandra x-ray telescope, 28
Chandrasekhar limit, 214, 303
characteristic age, 85
circular polarisation, 272, 274, 294
coherent radiation, 290
core and cone components, 133, 142
Crab Nebula, 3, 11, 12, 15, 299, 308, 310, 316
 distance, 310
 scattering, 343
Crab Pulsar, 105
 discovery, 14
 giant pulses, 160
 glitches, 237, 242, 243
 nanoshots, 160
 optical pulses, 14
 scattering, 342
 scintillation, 346
 spectrum, 286
 x-ray pulses, 14
crust quakes, 246, 250
crust, of neutron star, 216
curvature radiation, 285
cyclotron absorption lines, 221
cyclotron resonance, 185, 203
 absorption, 203
- de-dispersion, 36, 37
 coherent, 37
- death line, 70, 145

- degeneracy, 215
- dispersion, 34
- dispersion constant (D), 35
- dispersion measure (DM), 352
 - changes, 347
- dispersion measure(DM), 35
- double neutron star binaries, 99, 166
- Double Pulsar PSR J0737–3039A/B, 102, 166
- dynamical distances, 106
- Earth's orbit, 74, 79
- eccentric anomaly, 93
- eccentricity, 90, 166
- Eddington limit, 202
- Einstein@Home, 42
- electron distribution, Galactic, 114, 115
- electron lifetime, 312
- elliptical beam, 135
- emission height, 277
- emission mechanism
 - millisecond pulsars, 287
 - radio, 294
- energy density, 290
- energy outflow, 225
- ephemeris, 78
- equation of state, 216
- equatorial current sheet, 280
- Faraday rotation, 21, 349, 350, 352
- fast Fourier transform FFT, 38
- fast radio bursts (FRBs), 22, 155, 187, 291
- Fermi Observatory, 17
- frequency dispersion, 34
- Fresnel distance, 327
- GAIA astrometric satellite, 114
- Galactic centre, 67, 68
- Galactic electron distribution, 115
- Galactic population, 55, 63
- gamma-ray bursts (GRBs), 181
- gamma-ray pulsars, 71
- gamma-ray repeaters (SGRs), 181
- gamma-ray spectrum, 287
- gamma-ray telescopes, 29
 - AGILE, 30
 - CGRO, 29, 30
 - Fermi LAT, 30
 - INTEGRAL, 30, 195
- Geminga Pulsar, 16
- general relativity (GR), 78
 - tests, 100
- giant pulses, 143, 160, 296
 - location, 296
- gigahertz break, 288
- glitch, 219, 220, 235
 - Crab Pulsar, 237, 242, 243
 - PSR B1758–23, 251
 - recovery, 240, 243, 248
- theories, 245
 - Vela Pulsar, 240, 243, 246
- globular cluster, 22, 47, 113, 215
 - 47 Tuc, 22, 46, 84, 174
 - Terzan 5, 175
- globular cluster pulsars, 173
- Gold,T., 10
- Goldreich–Julian magnetosphere, 222, 280
- gravitational acceleration, 83
- gravitational radiation, 9, 20, 98, 167
- gravitational redshift, 79
- gravitational waves, 102, 256
- group velocity, 35
- Guitar Nebula, 317
- H II regions, 115, 357
- H-I line absorption, 110
- height of emission, 284, 294
- Her X-1, 196
- Hewish, A., 5
- HMXBs, 193, 197
- Hulse–Taylor binary, 90, 164, 172
- HZ Her, 201
- integrated pulse profiles
 - high energy, 258
 - radio, 128
- interpulse, 128
- interstellar magnetic field, 349
 - random component, 356, 357
- interstellar scattering, 39, 114
- inverse Compton effect, 185, 282
- ionised hydrogen H II, 115
- isolated x-ray neutron stars (XDINSs), 187
- Keplerian parameters, 93
- kinematic distances, 106, 109
- kinetic ages, 65
- Kolmogorov turbulence, 328
- Langmuir waves, 295
- LAT, 17
- LMXBs, 197
- luminosity
 - decay, 70
 - distribution, 60
 - spin-down, 287
- Magellanic Clouds, 22
- magnetars, 181
 - origin, 188
 - radio emission, 185
- magnetic field
 - alignment, 131
 - decay, 66
 - evolution, 189
 - intergalactic, 357
 - interstellar, 349, 353

- magnetic field (Cont.)
 magnetars, 203
 millisecond pulsars, 176
 multipole, 267
 quantum limit, 203
 strength, 85, 203
 sweep-back, 284
magnetic field strength, 84
magnetobremssstrahlung, 311
magnetosphere, 13, 221, 222
 equatorial current sheet, 225, 260, 281
 null charge surface, 222
 outer slot gap, 258, 281, 285
 polar cap, 261, 281, 290
 structure, 295
 vacuum gaps, 224
Magnus force, 248
mass function, 92
micropulses, 157
microstructure, 142, 157
millisecond pulsars, 22, 162
 magnetic fields, 176
 ages, 67
 discovery, 16, 162, 164
 emission location, 277
 glitches, 237
 polarisation, 277
 population, 66
 searches, 46
 solitary, 173
 surveys, 46
mode changing, 145, 274
 polarisation, 274
mode switching, 294
multipath propagation, 114
- NANOGrav, 254
nanoshots, 160
neutral hydrogen absorption, 110
neutron star, 3, 7, 12, 213
 crust, 217, 246
 crust cracking, 245, 250
 crust quakes, 246
 density, 216, 217
 equation of state, 215, 216
 magnetic field, 13, 220
 magnetic flux tubes, 221, 251
 masses, 13, 92
 moment of inertia, 219
 quark core, 217
 redshift at surface, 227
 rotation rate, 219
 superfluid interior, 218, 246
neutron superfluid, 246
North Galactic Spur, 357
nudot switching, 254
nulling, 143
- optical identifications, 113
orbital inclination, 196
oscillation, of stars, 8
outer gap, 280
- Pacini, F., 3, 11, 12
pair creation, 281, 285
parallax, 105, 107
 timing, 108
VLBI, 106
Parkes multi-beam survey, 51, 68
periastron advance, 96
period
 $P - \dot{P}$ diagram, 60, 162
 changes, 80
 lower limit, 10
periodogram analysis, 40
 harmonic addition, 40
pinned vortices, 247
planetary orbits, 9
planetary pulsar systems, 103
plasma frequency, 34, 291, 294
plasma instability, 295
plasma waves, 291
plerion, 307
polar cap, 280
polarisation, 135
 angle swing, 157, 263, 269, 270, 276
 geometry, 268
 limiting radius, 294
 millisecond pulsars, 137
 orthogonal modes, 274, 293
population
 Galactic, 21, 55, 67
 scale height, 63
precession, 96, 98, 135, 256
propagation
 magnetospheric, 292
proper motion, 64, 82, 177
Prospects, 359
PSR B0525+21, 269
PSR B0655+64, 166
PSR B0818–13, 144
PSR B0826–34, 144, 146, 153
PSR B0833–45, 289
PSR B0943+10, 153
PSR B0950+08, 139, 157
PSR B1133+16, 82
PSR B1237+25, 149, 152
PSR B1257+12, 103
PSR B1757–24, 317
PSR B1913+16, 20, 90, 98, 164
PSR B1919+21, 7
PSR B1929+10, 157
PSR B1931+24, 254
PSR B1937+21, 46
PSR B1957+20, 169
PSR B2224+65, 317

- PSR B2319–07, 151
 PSR J0205+6449, 85
 PSR J0437–4715, 317
 PSR J0537–6910, 237, 249
 PSR J0737–3039A/B, 99, 102
 PSR J1124–5916, 316
 PSR J1734–3333, 189
 pulsar
 birthrate, 68
 current, 70
 distances, 55, 57
 pulsar timing array, 102
 pulsar wind nebula (PWN), 225, 314, 315
 pulsars as clocks, 256
 pulse
 drift rates, 151
 mode changing, 254
 nulling, 142, 254
 width, 128, 263
 pulse lengthening, 337, 338, 342
 pulse power distribution, 142
 pulse profiles
 components, 128, 131
 frequency dependence, 266
 high energy, 121, 258
 integrated, 121
 MSPs, 178
 optical, 125
 polarisation, 272
 radio, 128
 width, 265
 x-ray, 123
 quasi-periodic oscillations (QPOs), 206, 228
 Römer delay, 74, 77
 radiated power, 290
 radiation beam geometry, 263
 radio interference (RFI), 52
 radio spectra, 289
 spectral index, 289
 radio telescopes, 25
 ALMA, 25
 Arecibo, 25
 Effelsberg, 25
 FAST, 25
 GMRT, 25
 Green Bank, 25
 LOFAR, 25, 26
 Lovell, 25
 MeerKAT, 26
 MWA, 25, 26
 Parkes, 26
 phased array, 26
 SKA, 26
 radius to frequency mapping (RFM), 266
 redback, 168
 reference frames, 80
 refractive index, 292, 323
 interstellar, 34
 refractive scintillation, 347
 relativistic binary pulsar, 90
 relativity effects
 diameters, 228
 luminosity, 227
 retardation, 283, 287
 Roche lobe, 197
 rotating radio transients (RRATs), 155, 187, 188
 rotating vector model (RVM), 269
 rotation measure (RM), 351
 rotation slowdown, 10, 12, 84, 85
 scale height, in Galaxy, 63, 64, 67, 117
 scattering
 angular diameter, 345
 multiple, 341
 pulse length, 337
 scattering coefficient, 326
 scintillation, 5, 114, 322
 angular spectrum, 327
 apparent source diameter, 345
 arcs, 333
 bandwidth, 330
 coherence scale, 328
 diffraction theory, 325
 dynamic spectrum, 329, 333
 frequency drifting, 331
 Fresnel distance, 327
 interplanetary, 5
 pattern, 325
 pattern velocity, 335
 refractive, 347
 slow, 346
 spectrum, 329
 strong and weak, 327
 thick screen, 326
 thin-screen, 323
 time-scale, 330
 search techniques
 periodic pulses, 40
 single pulses, 39
 self-lensing, 208, 227, 228
 self-organised criticality, 248
 Shapiro delay, 76, 78, 79, 94
 Shklovsky effect, 83, 94, 98, 108
 Shklovsky, I., 311
 signal averaging, 48
 slow scintillation, 346
 slowdown
 rate switching, 254
 SNR 3C 58, 85
 soft gamma-ray repeaters (SGRs), 181
 spatial distribution, 60
 specific luminosity, 55
 spectral index, 287

- spectrum
 gamma-ray, 179
spin-orbit coupling, 100, 135
spin-down luminosity, 258, 287, 290
Square Kilometre Array (SKA), 26, 52
standard clocks, 87
stellar evolution, 301
stellar oscillations, 8
Strömgren sphere, 115
strong equivalence principle (SEP), 101
sub-pulses, 139
 drifting, 147, 267
 polarisation, 142, 157
 width, 141
superfluid
 rotation, 247
 vortices, 218
 vorticity, 246
supernova, 299
 in binary, 302
 light curve, 300, 303, 304
 precursors, 301
 progenitors, 213, 302
 rate, 71, 304, 306
 remnants, 306
 types, 300
supernova remnants (SNR), 47,
 113, 305
 3C58, 314
 composite, 314
 Crab, 308
 Cygnus Loop, 307
 IC443, 307
 Kepler, 307
 Tycho, 307
supernovae
 types, 300
surveys, 42, 54, 67
 sensitivity limits, 48, 59
synchrotron radiation, 311, 349
 polarisation, 311
- TEMPO analysis system, 74
thermal x-ray sources, 314
thermal x-rays
 isolated neutron stars, 207
timing noise, 81, 251, 254
 activity parameter, 253
timing residuals, 81
transient x-ray sources, 201
transitional millisecond pulsars, 169
transverse Doppler effect, 94
transverse velocity, 83, 108, 336
- true anomaly, 93
two pole caustic model, 287
- Universal Time (UTC), 87
- Vela Nebula, 317
Vela Pulsar, 10
 glitches, 235, 237, 244, 249
 polarisation, 267
velocities of pulsars, 64, 67, 177, 317
 MSPs, 67
velocity of light cylinder, 222
vortex pinning, 248
- white dwarf, 7, 167, 175, 213, 214
 AR Sco, 13
 mass, 213
 pulsar, 215
wind nebulae, 121
Wolter x-ray telescope, 28
- x-ray binaries, 4, 22, 221, 233
 masses, 230
x-ray flares, 228
- x-ray sources
- binary, 195
 - bursters, 204, 206
 - companion masses, 196
 - extragalactic, 198
 - HMXBs, 198
 - LMXBs, 192, 199
 - rotation powered, 193
 - Sco X-1, 192
 - thermal, 192, 226, 227
 - transients, 201
- x-ray telescopes, 27, 194
- Astrosat, 195
 - ATHENA, 29
 - Chandra, 28
 - eRosita, 195
 - HEAO-2, 28
 - INTEGRAL, 30
 - Nustar, 29
 - ROSAT, 28, 194
 - RXTE, 29
 - UHURU, 192
 - XMM-Newton, 28
- x-rays
- thermal, 192
- XDINS, 188
- Zeeman effect, 350
Zwicky, F., 3, 299

